8-3-2015

Scattering and Sympathetic Cooling within an Ion-Neutral Hybrid Trap

Douglas S. Goodman
University of Connecticut - Storrs, douglas.goodman2@gmail.com

Scattering and Sympathetic Cooling within an Ion-Neutral Hybrid Trap

Douglas S. Goodman, Ph.D.

University of Connecticut, 2015

Abstract

Dilute ion-neutral gas mixtures are an interesting system to study due to the rich variety and enormous strength of their scattering interactions, especially in the cold and ultracold regimes. Ion-neutral collisions are dominated by long-range polarization potentials that lead to cross sections several orders of magnitude larger than typical neutral-neutral van der Waals interactions. These large ion-neutral interactions can play an important role in atomic and molecular optical physics, astrophysics, and quantum chemistry. Thanks to advances in theoretical modeling of ion-neutral scattering and the development of new ion-neutral hybrid trapping and cooling technology, interest in this previously unexplored area of cold atomic and molecular physics has surged over the past decade.

The ion-neutral hybrid trap, composed of a magneto-optical trap concentric within a linear Paul trap, offers the ideal playground for studying and manipulating ion-neutral interactions over a wide energy range ($\sim$ 1 μK - 10^4 K). This dissertation discusses the development of UConn's hybrid trap, compares experimental measurements of the Na^+- Na system and Ca^+- Na system's low-energy collision rates with previously reported theory, and reports on experimental and simulation results of the sympathetic cooling of Na^+ ions by laser cooled Na atoms.

Scattering and Sympathetic Cooling within an Ion-Neutral Hybrid Trap

B.S., Trinity College, 2006

M.S., University of Connecticut, 2010

A Dissertation

Submitted in Partial Fullfillment of the

Requirement for the Degree of

Doctor of Philosophy

at the

University of Connecticut

2015

APPROVAL PAGE

Doctor of Philosophy Dissertation

Scattering and Sympathetic Cooling within an Ion-Neutral Hybrid Trap

Presented by

Douglas S. Goodman, B.S., M.S.

1. Major Advisor _____

Winthrop W. Smith

2. Associate Advisor _____

Susanne F. Yelin

3. Associate Advisor _____

George N. Gibson

University of Connecticut

2015

Acknowledgment

Financial support for this research was provided in part by the University of Connecticut Foundation and the National Science Foundation under NSF Grant No. 0855570 and 1307874.

The path from matriculation to dissertation has been long, circuitous, sometimes painful, exciting, frightening, and very rewarding. I most certainly could not have navigated this journey alone and I would like to thank all the wonderful people who have helped me reach the end.

To begin with, I would like to thank all the amazing staff in the UConn Physics Department. The front office staff have helped me overcome many of the logistical nightmares that come with being a student and an employee of UConn. I would especially like to thank Kim Giard for all her assistance with the space committee, her record keeping and student wrangling came in very handy. Another space committee member, Dr. Dave Perry, has been a wonderful resource to both me and all the graduate students. Whether he is teaching, helping take data, or moving equipment, he is always single handedly keeps this department moving in a forward direction. I would also like to thank Heather Osborne, the Manager of Laboratory Services, for all that she has taught me about physics education research. She is a great resource for the graduate students and an excellent supervisor.

Our group is grateful to Alan Chasse, the department's machinist. Having a great machine shop is an invaluable resource to an experimentalist. I cannot thank him enough for the beautiful and complicated parts he has made for our group over the years. I also thank him for training me to use many of the machines within the shop. I also enjoyed our time together on the shop committee.

I would like to thank all my teachers, both undergraduate and graduate, who have taught

me a great deal of physics and a great deal about teaching physics. I can definitely say that my class experiences are my most cherished memories of the Trinity and UConn physics programs. From Trinity College, I would especially like to thank Dr. Dave Branning for all of his career guidance and continued assistance well after my Trinity conferral. From UConn, I would especially like to thank Dr. Robin Côté for teaching my atomic and molecular physics courses, having thoughtful discussions and collaborations with our research group, and for taking the time to meet with me to flesh out the semiclassical scattering theory treatment discussed in this dissertation. I would also like to thank Dr. William Stwalley for a wonderful special topics course on ultracold physics, as well as nominating me for the Frisius Memorial Fund Fellowship.

My co-advisors, Dr. George Gibson and Dr. Susanne Yelin have been critical resources for me throughout this process. I really enjoyed initially working in Dr. Gibson's research group my first summer here and I thank Dr. Yelin's for her assistance with the written and oral qualifying examination preparation. I also thank both of them for their comments, edits, and discussions regarding my plan of study, dissertation proposal, and this dissertation.

However, the most important and influential faculty member during my time at UConn has been my advisor Dr. Winthrop Smith. I am not only a better physicist for having known him, but also better person. I cannot thank him enough for his encouraging, supportive, approachable, and thoughtful advising style. My feelings of admiration for Dr. Smith are not unique, as he is definitely a faculty and student favorite within the department due to his friendly attitude and steadfast advocacy for faculty and student success.

In working for Dr. Smith I have also had the pleasure of collaborating with Navy scientist Dr. Francesco Narducci and Wesleyan Physics Department Chair Dr. Reinhold Blümel. Dr. Narducci has been a critical collaborator since the beginning of the project.

He has loaned us equipment, but more importantly loaned us his time and expertise in the field of neutral atom trapping. I am always amazed by his willingness to always drop what he is doing at a moment's notice and have lengthy discussions answering my questions regarding our experiment. Dr. Blümel has become a recent and welcomed addition to our team. Fortunately, he is also always available for thoughtful discussions about our ion trap, for which I thank him. We began our collaboration during the Na^+- Na rate coefficient measurement. During that collaboration we uncovered some very interesting and unexpected follow-up theory and experimentation that has proved successful and we hope to publish those results shortly.

The support of family and friends have made the often frustrating graduate school experience much more pleasant, fun, and memorable. It is not only cathartic to discuss problems from the research or classroom with your peers, but it is a great way to debug and problem solve. For example, our group has been saved by Marco Ascolli's dye laser skills many many times. We have also received assistance regarding research problems from Kishan Yerubandi, Charles Talbot, Ryan Carollo, Jen Carini, Chad Rogers, Leland Aldridge, Vincent Tagliamonti, Nick Lewkow, and Michael Bellos. From my classroom days, I would also like to acknowledge my studying buddies Kristen Basiaga, Thomas O'Connell, Michael Ambroselli, and Lahiru Narangammana.

For their blood, sweat, and tears, I thank Ilamaran Sivarajah, James Wells, and Jon Kwolek, all of whom worked on the hybrid trap project with me. Collaborating with all of them has been a pleasure and I have tried to credit their enormous contributions throughout this dissertation. A special thanks to James who has been on this journey with me since the beginning. Sometimes I like to think he and I should earn a second degree in counseling, as we have managed to keep each others spirits high in the face of utter laboratory despair.

My family, W. Michael Goodman, Cary Goodman, and Paul Goodman have been very

supportive of all my endeavors in life, and graduate school was no exception. I am so lucky to have parents and a brother who care so much about my success and well being. All three of you are in everything I do and I love you all. Additionally, I thank my great-uncle Morris Goodman for his generous financial assistance with both my undergraduate and graduate education.

Last, and certainly not least, I must thank my wife Katherine Goodman, to whom I dedicate this dissertation. Your love and support knows no limits and trust me, graduate school has tested that statement. Having *actually* earned a degree in counseling your skills have been greatly appreciated on the bad days when something breaks or does not turn out as expected in the laboratory. I can always turn to you to make me feel better and more confident that, just like the last time and the time before that, this problem will be solved too. On the good days, there is no one better with which to celebrate than your best friend and soul mate. Katie is an excellent writer and an even better editor, so I thank her for reading and editing everything I have written in graduate school. I know that whatever the next adventure may be, we will come out stronger and more committed, because as a team we can do anything. I love you with all my heart and cannot wait to meet our baby girl.

This dissertation is dedicated to my wife Katherine B. Goodman.

Contents

Chapter 1

Introduction

1.1 Cold atomic, molecular, and optical physics

Imagine a container of hot or room temperature gas ($\sim$ 100 K) with Avogadro's number of atoms and molecules incoherently moving at high speeds ($\sim$ 100 m/s). Typically, the atoms in this gas are well approximated as ideal non-interacting hard spheres, like billiard balls, undergoing elastic collisions with the container's walls and each other. Due to their high-speed incoherent motion it is difficult to control, manipulate, study, or take advantage of the quantum nature of the atoms and molecules within the gas, which reside in an incoherent mixed quantum state. Traditional chemistry controls the warm gases' chemical properties or reactions by changing state variables like pressure and volume. However, atomic physics seeks to achieve much greater control to access each atom or molecule's quantum mechanical degrees-of-freedom.

Alternatively, we could imagine trapping a small number of atoms or molecules ($\sim 1-10^7$ atoms) and cooling the gas down to near absolute zero temperatures in the cold ($\lesssim 1$ mK) or ultracold ($\lesssim 1\mu$K) regime. In doing so, we can freeze out all the unwanted

degrees-of-freedom in the gas, thus removing nearly all translational incoherent motion and internal molecular motion. This trapped, suspended, and cold gas of a small number of particles represents a well controlled environment containing atoms in pure quantum states, which can much more easily be manipulated or studied in a laboratory setting. This experimentally achievable pure quantum system becomes nearly identical to the idealized systems assumed in many textbooks or theoretical calculations.

Thanks to the invention of laser cooling and trapping [1], physicists have reached temperatures near absolute zero [2, 3], thus controlling the velocity and spatial distribution of a dilute gas with surgical precision. Steven Chu, Claude Cohen-Tannoudji, and William D. Phillips were awarded the 1997 Nobel prize in Physics for their pioneering work in the field of laser cooling and trapping. Once the dilute gas is ultracold, additional lasers can be used to manipulate the internal quantum state of cold trapped atoms to do useful things like tune the strength of their interatomic interaction [4, 5], store information in their quantum degrees-of-freedom [6], simulate many-body quantum systems [7], or use their quantum states as the frequency standard for clocks [8] that are so precise that it would take more than twice the current age of the universe for them to be off by one second. By lowering the temperature of a system of particles to near absolute zero, scientists have brought the microscopic quantum nature of matter into the macroscopic every-day world in which we live.

One dramatic example of ultracold macroscopic quantum phenomena is the Bose-Einstein condensate (BEC) [9]. When a cooled and trapped dilute gas of, e.g., rubidium (Rb) or sodium (Na) atoms are cooled below a critical temperature ($\sim 1\mu$K), the de Broglie matter wavelength

$$\lambda_{\mathrm{dB}} = \frac{h}{p} = \frac{h}{\sqrt{3mk_BT}} \tag{1.1}$$

becomes comparable in size to the interatomic spacing, and all the indistinguishable atoms in the gas condense to the trap's lowest energy state (where p is an atom's momentum, m the mass of the atom, k_B is Boltzmann's constant, T is the gas's temperature, and h is Planck's constant). At this point the atoms act like a single macroscopic quantum particle and exhibit quantum behavior on a macroscopic scale. The realization of Rb and Na BECs earned Wolfgang Ketterle, Carl Wiemen, and Eric Cornell the 2001 Nobel prize in Physics.

To experimentally achieve such cold temperatures almost every cold atomic, molecular and optical (AMO) physics laboratory in the world employs one of two trapping/cooling apparatuses: magneto-optical traps (MOT) or ion traps. The MOT is used to trap and cool neutral atoms (although neutral molecular MOTs have also recently been successfully developed [10]) and the ion trap is used to trap atomic or molecular ions. These apparatuses are used individually in many applications, such as quantum information processing [11–16], atomic clocks [8, 17–19], inertial sensors [20], magnetometers [21], precision spectroscopy [22–25], quantum simulators [7], and tests of fundamental constants [26–30].

The MOT was first developed in a collaboration led by David Pritchard (MIT) and 1997 Nobel laureate and President Obama's former Secretary of Energy Steven Chu [31] at Bell laboratories in the mid-1980s. The MOT, as seen in Fig. 1.1 (a), operates on the principle of velocity and spatially dependent light-pressure forces exerted on a low-density gas held within an ultra-high vacuum (UHV) chamber. The light-pressure force, known as "Doppler-cooling," comes from six intersecting laser beams within a magnetic field gradient, which causes the atoms in the low-density gas to undergo damped harmonic oscillation about the trap's center.

Ion traps primarily come in two flavors – Penning traps [32], which utilize static electric fields and static magnetic fields to trap ions, and Paul traps [33], which utilize radio frequency (rf) electrodynamic fields to trap ions. The Penning trap is named after Frans

Michel Penning by its inventor, 1989 Nobel laureate Hans Georg Dehmelt. The Paul trap is directly named after its inventor, 1989 Nobel laureate Wolfgang Paul.[1] One particularly useful aspect of the ion trap is that it can achieve very deep trap depths (~ 1 eV) that allow for very long trapping times, in some cases indefinitely [34].

If the trapped ions have an optically accessible transition, then the translational motion can be damped by velocity dependent light-pressure forces, while the spatial confinement is provided by electrodynamic (Paul) or magnetostatic (Penning) forces. Unlike the MOT, the spatial confinement is not approximately spring-like and the ions undergo a more complicated motion than simple harmonic oscillations. The particular kind of ion trap employed by our group at the University of Connecticut (UConn) is called a quadrupole linear Paul trap (LPT) due to its characteristic four parallel rod electrode design, as seen in Fig. 1.1 (b).

1.2 The ion-neutral hybrid trap

The apparatus What is unique about our group's apparatus is that it is a combination of these two normally separate technologies, making it capable of simultaneously trapping and cooling neutral atoms and atomic (or molecular) ions. Therefore, we call the apparatus an ion-neutral hybrid trap, shown in Fig. 1.1 (c). This apparatus is ideal for studying the interaction between ions and neutrals over a very wide temperature range ($\sim 1\ \mu$K - 10^4 K). Thus the hybrid trap allows experimentalists to study and manipulate cold ($\lesssim 1$ mK) ion-neutral interactions, which had remained a relatively unexplored regime before the early 2000s. It is this new found access to low temperature ion-neutral reactions that motivated the UConn group's pioneering work in developing the ion-neutral hybrid trap [35–40].

The hybrid trap was originally proposed in 2001 at the conference for Coherence

[1] Wolfgang Paul was also humorously referred to as Wolfgang Pauli's imaginary counterpart

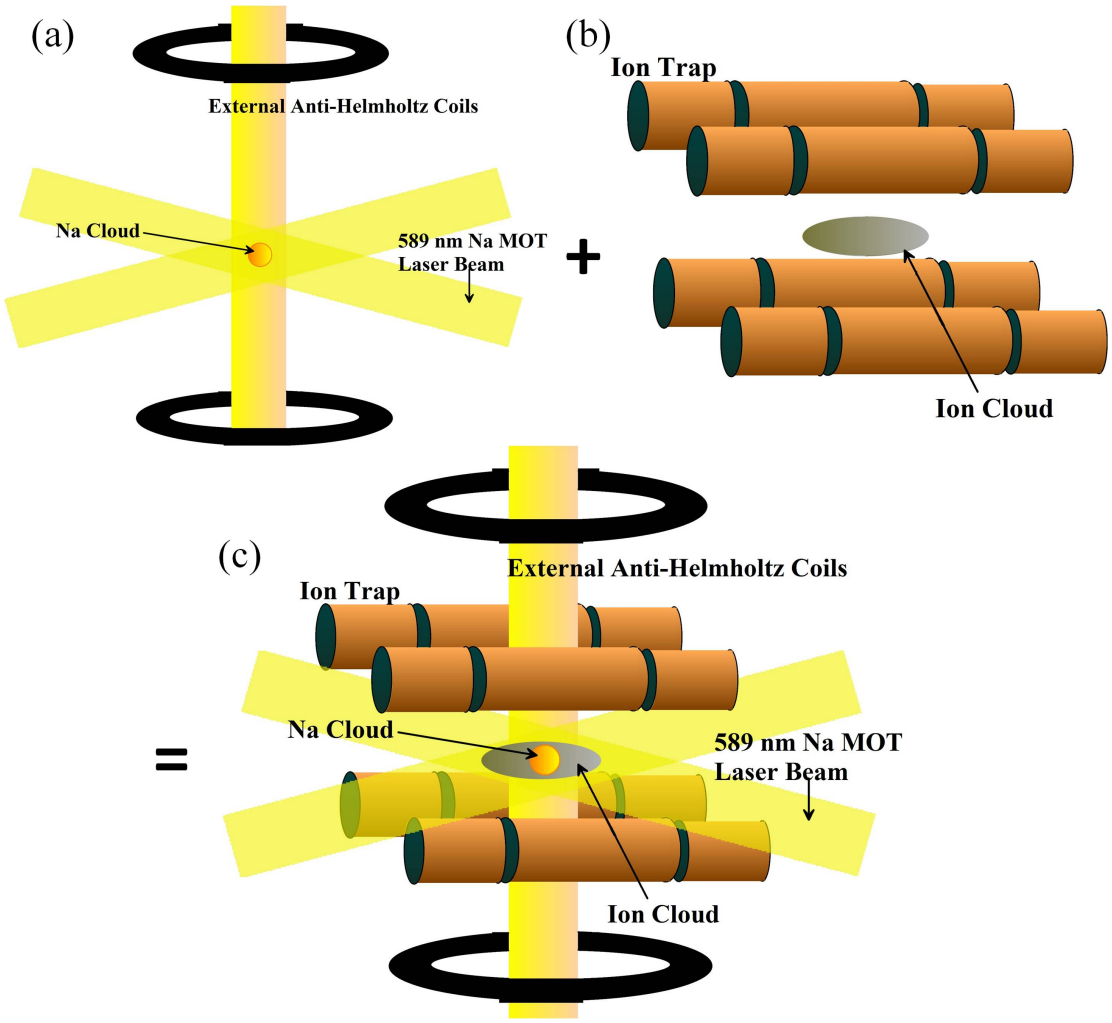

Figure 1.1: Schematic of UConn's hybrid trap apparatus. (a) The cold sodium (Na) cloud held within the MOT consisting of six 589 nm laser beams intersecting at the minimum of a magnetic field gradient produced by the anti-Helmholtz electromagnets. (b) The segmented LPT rf and dc electrodes confining a Na^+ ion cloud. (c) The composite Na^+-Na clouds within the ion-neutral hybrid apparatus, which is a combination of the neutral MOT and ion LPT.

and Quantum Optics VIII [35] and since its inception, several experimental groups have developed various kinds of hybrid traps throughout the world. Most notably Vuletić's group at MIT [41–43], Hudson's group at UCLA [44–49], Köhl's group at Cambridge (which use a BEC-LPT hybrid trap) [5, 50–52], Willitsch's group at the University of

Basel [53–55], Denschlag's group at IQST [56, 57], Mukaiyama's group at University of Electro-Communications [58], Weidemüller's group at University of Innsbruck (which uses a MOT-octupole-rf hybrid trap) [59], and Rangwala's group at the Raman Research Institute (which use a MOT-optical-cavity-LPT hybrid trap) [60–63]. Needless to say, both theoretical [64–72] and experimental interest in cold ion-neutral interactions have surged over the past decade.

The ion-neutral interaction One of the most important and interesting aspects of ion-neutral interactions are the long-range interaction potentials, which play an important role in understanding the properties of quantum gases. The size of these interactions are quantified by an interaction cross section. The cross section does not refer to the physical size of the collision partners, but rather their effective size, were they to collide like hard spheres or billiard balls. For example, the neutral Na on Na system's scattering cross section at ultracold temperatures has a radius or effective size of about 3 nm, which is about an order of magnitude greater than the size of the physical electronic cloud of Na [73].

Typical neutral-neutral van der Waals interactions have cross sections of a few atomic units (a.u.) or 1 square Bohr ($a_0^2 \sim 1\ \mathring{A}^2$), whose interaction potential energy falls off like R^{-6}, where R is the internuclear distance in the binary neutral atom system. Ion-ion interactions are effectively infinite, due to the $1/R$ Coulomb interaction potential. Cold ion-neutral reactions are of intermediate range between ion-ion and neutral-neutral collisions, and can have cross sections of $\sim 10^6$ a.u. [36, 68, 71]. Ion-neutral interactions are dominated by universal long-range polarization potentials [74], with the principal long range term

$$V = -\frac{C_4}{2R^4}, \tag{1.2}$$

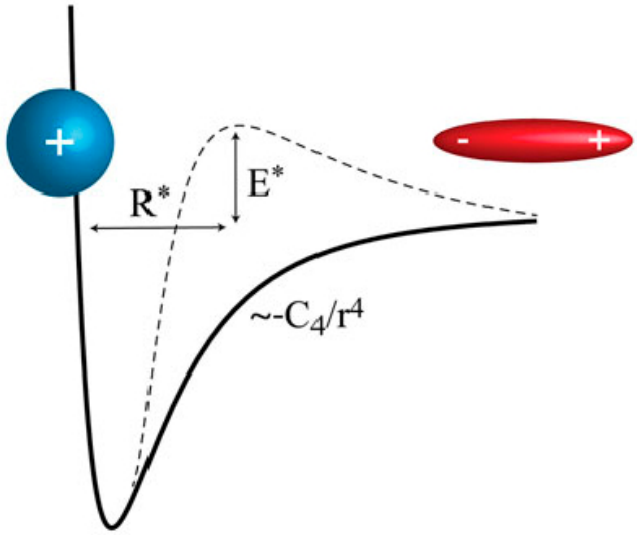

Figure 1.2: Originally from Ref. [57]. As illustrated, the ion-neutral interaction polarizes the neutral atom. Solid line shows the potential energy of the s-wave $(l = 0)$ interaction and dashed line includes the p-wave $(l = 1)$ centrifugal potential energy barrier.

here C_4 is proportional to the dipole polarizability of the neutral collision partner. The R^{-4} dependence results from the fact that the ion's electric field polarizes the neutral collision partner distorting the atom's electron cloud, which creates an induced dipole moment in the neutral atom, as illustrated in Fig. 1.2. It is the stronger ion + induced dipole interaction that leads to such a large cross section. If we include the centrifugal potential (which is energy associated with the two-body ion-neutral orbital angular momentum l) we see that there is a centrifugal barrier for p-wave scattering $(l = 1)$, as seen in Fig. 1.2. The barrier's peak defines the characteristic size of the interaction R^* and an energy scale E^*, which marks the onset of the s-wave $(l = 0)$ scattering regime.[2]

There are a rich variety of interactions to study and manipulate in cold ion-neutral hybrid traps, which can result in several reaction pathways: elastic collisions, which

[2]The terms "s" and "p" are abbreviations given to spectral lines of alkali atoms associated with different angular momentum states of the atom's valance electrons. The lowest energy line was called "sharp" and the next highest was called "principal."

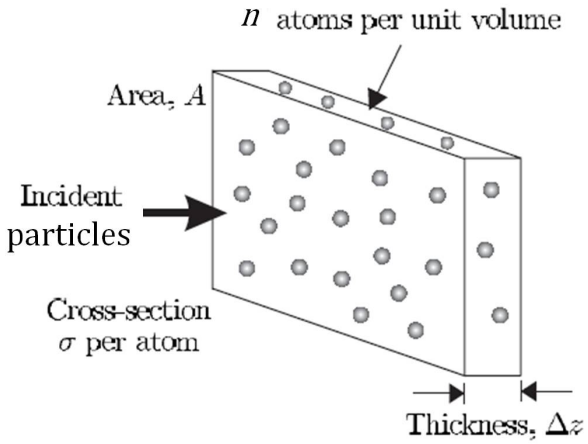

Figure 1.3: Modified figure originally from Ref. [73]. Ions incident on a hypothetical slab of target atomic collision partners.

conserve the kinetic energy of the colliding partners (A and B^+) or inelastic collisions, which do not conserve kinetic energy. An inelastic collision might release energy (exothermic) from some internal degree-of-freedom during the collision, e.g., quenching collisions, $A^* + B^+ \rightarrow A + B^+ + h\nu$, that relax the internal electronic state of the atom or ion releasing a photon. Another possible outcome of an exothermic inelastic collision might be the formation of a molecular ion, $A + B^+ \rightarrow (AB)^+ + h\nu$. Charge-exchange collisions, a subset of ion-neutral collisions, have been extensively studied in hybrid traps [39, 40, 42, 45, 46, 53, 54, 58]). These types of collisions result in the the elastic or inelastic exchange of an electron, $A + B^+ \rightarrow A^+ + B$, where *A* and *B* can be in ground or excited $(^*)$ state.

As illustrated in the Fig. 1.3, the probability $\mathscr{P}_x$ of any of these ion-neutral reactions per incident collision partner depends on the collisional cross section σ_x associated with that particular reaction pathway *x* and the number of target collision partners per unit area $n\Delta z$. It can be described as

$$\mathscr{P}_x = \sigma_x n \Delta z. \tag{1.3}$$

Therefore, adjusting the cross section of each reaction pathway σ_x, by tuning the temperature or internal quantum states of the ion-neutral pair, controls (or tests predictions of) the relative likelihood or branching ratio of a particular ion-neutral interaction.

Furthermore, in the semi-classical regime ($\sim$ 10 μK - 10^4 K), the cross sections for several kinds of reactions increases with decreasing collision energy or gas temperature. When many partial waves contribute to the scattering cross section (which can still occur with cold collisions) the cross sections can be well approximated by power laws that exhibit the inverse proportionality to the collisions energy E, such as $\sigma \propto E^{-1/3}$ or classical Langevin [75] cross section $\sigma \propto E^{-1/2}$. Here,

$$E = (1/2)\mu v^2, \tag{1.4}$$

where μ is the reduced mass of the collision partners and v is their relative velocity. However, the reaction rate $k = \langle \sigma v \rangle$ (averaged over the thermal ensemble) is fairly temperature insensitive (or completely temperature insensitive for the Langevin case).

1.3 Motivation for cold ion-neutral studies

Four interesting characteristics about the study of ion-neutral interactions have been discussed thus far, (i) in the past these interactions had been essentially unexplored in the cold-ultracold regime (ii) the size of these ion-neutral interactions are much larger than neutral-neutral interactions (iii) there is a rich variety of interactions to study (iv) that collision cross sections increases with reduced temperatures. It is these factors that motivate our studies and consequently explains why cold ion-neutral collisions play a significant

role in quantum chemistry, astrophysics, and sympathetic cooling applications. However, recent efforts show that ion-neutral hybrid systems may become important to quantum information processing [52] and quantum simulation of many-body systems [76] as well.

Quantum chemistry Typically, classical chemistry uses bulk state variables like pressure and volume to control chemical reactions. Quantum chemistry seeks to theoretically calculate and experimentally control chemical reactions on the quantum level, e.g., using lasers to control the reactant's internal quantum states, which in turn controls branching ratios of reaction pathways [5]. Consequently, there is great theoretical interest in understanding the myriad of reaction pathways associated with different ion-neutral systems that can be manipulated via lasers within a hybrid trap. Additionally, quantum chemistry theory has predicted new quantum gas effects that can be studied with a hybrid trap as the temperature is reduced to the ulracold regime, e.g., mesoscopic molecues [70] and unique charge transport properties [69]

It is important that ion-neutral hybrid experiments continually verify the accuracy of these quantum chemistry theoretical calculations and predictions, since theory uses many different models and procedures to produce molecular potential curves like the ones in Fig. 1.4, which are subsequently used to calculate interaction cross sections [54]. For example, the Côté theory group at UConn has produced new theoretical curves for the Ca^+-Na system that differ significantly from the McLaughlin group's theoretical predictions on the same system. Hopefully, our future (improved) experiments on this system will have the necessary accuracy to settle any theoretical debate. Furthermore, we hope to demonstrate the ability to turn on and off reaction pathways by controlling the hyperfine level populations of the colliding reactants.

In another example, Tacconi *et al*. [67] have calculated the total cold charge exchange

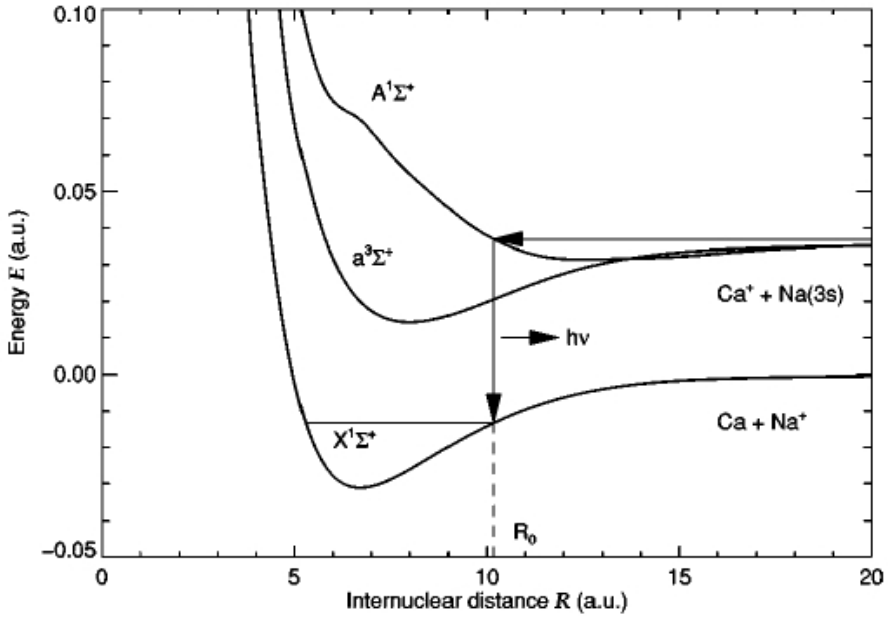

Figure 1.4: Originally from Ref. [71], showing the three lowest potential energy curves for $NaCa^+$, i.e., the potential energy of the interaction during an Ca^+- Na collision. This plot serves as an example of theoretically generated potential curves used to calculate collision cross sections.

cross section in the $(CaRb)^+$ system for various final channels, starting with the entrance channel $Ca^+(4S)$ + Rb (ground state). At 1 mK, charge exchange to the Ca(4P) + Rb^+ has a calculated cross section $\sim 4 \times 10^3$ a.u., fairly large, but show good agreement with experiment [53]. Near-resonant charge-exchange between different isotopes at 1 mK can be even larger (e.g., Be^+ on Be [77]). Thus far, excellent agreement between theory and experiment has been found by other hybrid trap groups [42, 45, 46, 53, 54, 58], which have studied interactions (primarily charge exchange) with species such as Rb^+- Rb, Yb^+- Rb, Ba^+- Rb, Yb^+ -Yb, Yb^+- Ca, Ba^+- Ca, and Ca^+- Li; and by our own group for the Ca^+- Na system [39] and the Na^+- Na system [40]. The measurements of the last two collision rates will constitute some of the major results discussed in this dissertation.

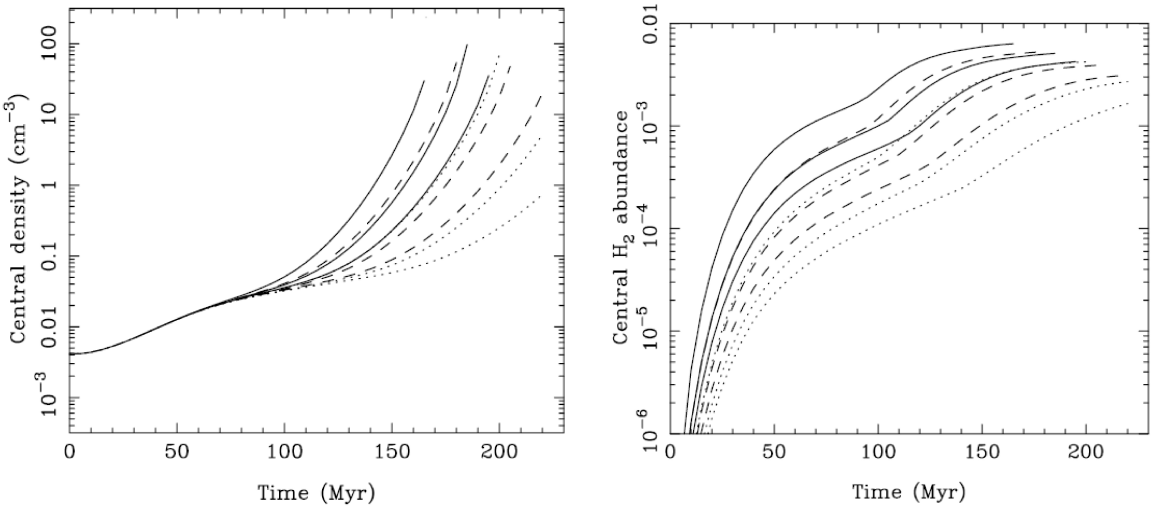

Figure 1.5: Originally from Ref. [82]. The left plot shows a simulated result of the time dependence of the central density of a protogalaxy undergoing collapse and the right plot shows the simulated central H_2 abundance of the same protogalaxy. Each line corresponds to a different theoretically predicted ion-neutral reaction rate, which results in orders of magnitude discrepancies in the theoretical model's predicted central density or central H_2 abundance.

Astrophysics Accurate measurements of ion-neutral collision rates are also of great interest to the astrophysical community. It is not surprising that in the low density environment of outer space ion-neutral collisions play a significant role, due to the large interaction cross sections associated with ion-neutral collisions. Although, the temperature of space is a relatively warm ~ 3 K, there are still cold ion-neutral exothermic processes in the interstellar medium [78, 79]. Low-energy ion-neutral charge-exchange is of interest for studies of chemical reactions relevant to the early universe [80] and important to studies of the upper atmosphere, e.g., secondary ions from solar-wind collisions can undergo further ion-molecule reactions [81].

Additionally, accurate modeling of cooling primordial gas or newly forming protogalaxies in formerly ionized regions requires accurate experimental measurements of ion-neutral reaction rates. In a paper by Glover *et al.* [82], the cosmological implications

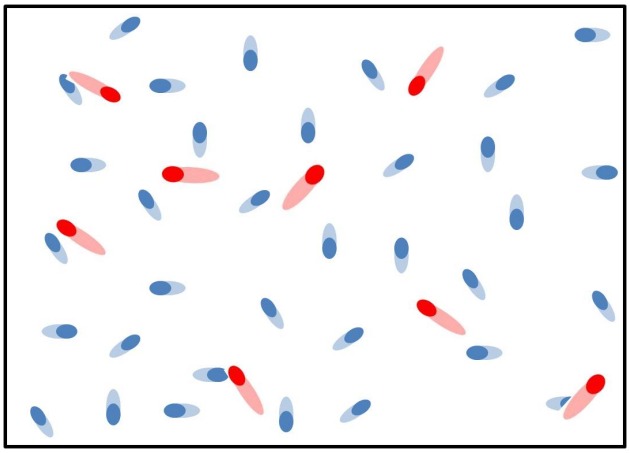

Figure 1.6: The hotter red gas is translationally cooled via elastic collisions with the colder blue gas and internally cooled via inelastic collisions with the colder blue gas. However, because the blue gas is directly laser cooled the blue and red gas mixture equilibrates at the blue gas' initial temperature, rather than some intermediate temperature.

of the uncertainty in ion-neutral reaction rates, like the associative detachment reaction $H^- + H \rightarrow H_2 + e^-$, are explored. They find that the $(< 50\%)$ variation in the theoretically predicted reactions rates leads to orders of magnitude discrepancies in protogalactic collapse models, as seen in Fig. 1.5.

Sympathetic cooling In addition to its contributions to the fields of quantum chemistry and astrophysics, one of the most promising applications of the hybrid trap is to use the the large intermediate range ion-neutral scattering cross sections to sympathetically cool internal and translational degrees-of-freedom of atomic or molecular ions.[3] As illustrated in Fig. 1.6, sympathetic cooling is the process of cooling an atomic or molecular species (hot red gas) by elastic and inelastic interaction with a second directly-cooled species (cold blue gas), thus equilibrating at the temperature of the directly cooled species and not some intermediate temperature.

[3]The strong ion-neutral elastic interaction makes translational cooling efficient. The possibility of short-range inelastic collisions also make internal cooling possible.

One of the first examples of ion-ion sympathetic cooling was $^{198}Hg^+$ ions sympathetically cooled for an optical frequency standard by 2012 Nobel laureate David Wineland's group at NIST, using laser cooled $^9Be^+$ in the same ion trap [83]. Interest in ion-ion sympathetic cooling continues today [84], e.g., in quantum information schemes [85], atomic clocks [86], and spectroscopy [87].

In earlier experiments by others, the neutral species used in ion-neutral collisional cooling was usually a cold noble buffer gas [88, 89]. Since the interaction depends on the electric polarizability of the neutral noble gas, the neutral species in buffer-gas cooling typically has a smaller cross section than in the case of the alkali neutral atom interactions in a hybrid trap. Therefore, hybrid trap sympathetic cooling offers the possibility of improved cooling, down to lower temperatures than buffer gas cooling.

Translational sympathetic cooling has been successfully demonstrated experimentally within hybrid traps by us and by others [38, 50, 60, 63]. However, it is not likely that translationally cold or ultracold temperatures can be reached via hybrid trap sympathetic cooling for multiple trapped ions [37, 43, 49, 59], as will be discussed in this dissertation.

Our group's future interests are primarily in demonstrating sympathetic cooling of the internal vibrational state of homonuclear Na_2^+. In contrast to ion-ion cooling, the shorter range non-Coulombic ion-neutral interactions allow for the sympathetic cooling of internal degrees-of-freedom. Molecular internal-state sympathetic cooling [44, 59] has recently been demonstrated experimentally for a heteronuclear molecule, $BaCl^+$, in a hybrid trap and may prove to be a very general cooling technique [47].

1.4 Dissertation outline

The dissertation is organized as follows: Chs. 2 and 3 give a brief overview of underlying classical and quantum physics involved with ion-neutral scattering and atomic interaction

with electromagnetic radiation. Ch. 4 discusses the construction and operation of the hybrid trap apparatus's two components, the MOT and the LPT. Next, results from sympathetic cooling investigations are discussed in Ch. 5 and results from ion-neutral reaction rate measurements are discussed in Ch. 6. Last, Ch. 7 covers possible future hybrid trap experiments.

Chapter 2

Scattering

The goal of our experimental efforts is to study and manipulate ion-neutral scattering reactions in the cold regime, and when possible, compare with theoretical reaction rate models. This chapter will outline much of the underlying physics associated with classical and quantum mechanical ion-neutral scattering models. For example, in the simplest "hard-sphere" classical model two particles move toward one another and have no long-range interaction. Upon contact, they elastically bounce off one another like billiard balls, as shown in Fig. 2.1 (a). Alternatively, if we consider the wave-like nature of the colliding particles, we can describe the collision system in terms of quantum mechanical matter-wave interference, as depicted in Fig. 2.1 (b).

2.1 Classical scattering

The dynamics of the classical hard-sphere model will be the subject of Sec. 2.1.1. The Langevin model, a more advanced, but still classical, model that includes the long-range forces between the collision partners, will be discussed in Sec. 2.1.2

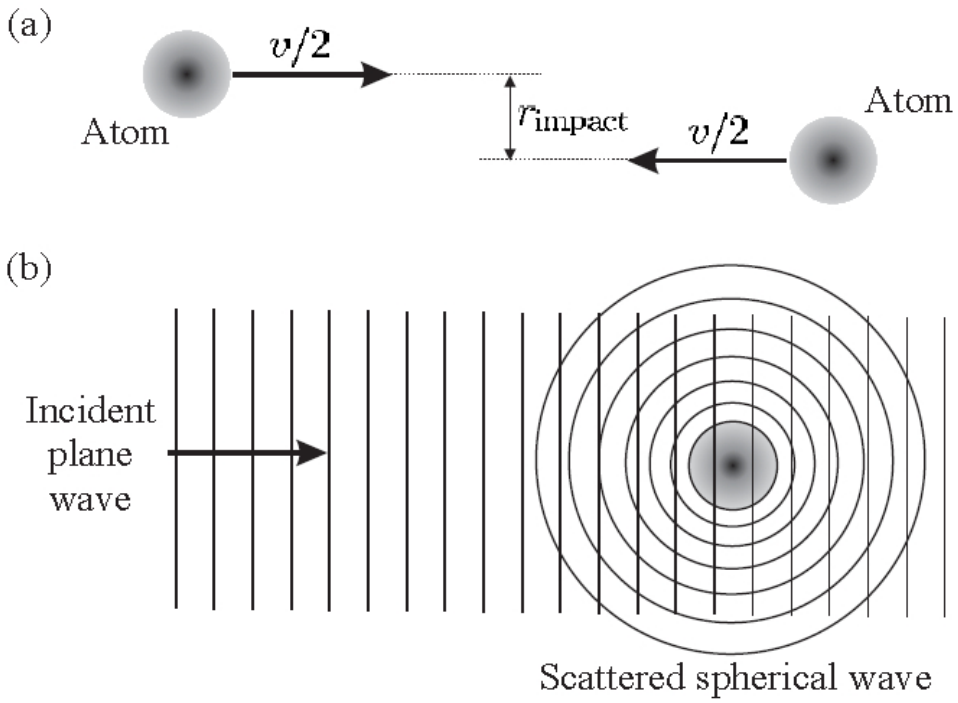

Figure 2.1: Originally from Ref. [73], (a) the classical scattering of two particles with relative velocity v as seen in the center-of-mass frame with an impact parameter $r_{\text{impact}} \equiv b$ and (b) the quantum mechanical matter-wave description of the scattering of two particles with an incident plane wave and outgoing superposition of a plane wave and a spherical wave.

2.1.1 Hard sphere model

Final speed and scattering angle A hard sphere is an idealized body that has no long-range interactions (only contact forces) and that undergoes perfectly elastic collisions, meaning that the total kinetic energy of the hard spheres is conserved. Billiard ball collisions are a good analogy for these hard-sphere collisions, because they do not experience long-range interactions and nearly all the kinetic energy from the cue ball is transfered to the colliding object ball in a head-on collision.

Let us begin by considering the initial and final velocity vectors of a two-body hard-sphere collision. Consider two hard spheres: I with radius r_I and N with radius r_N, where

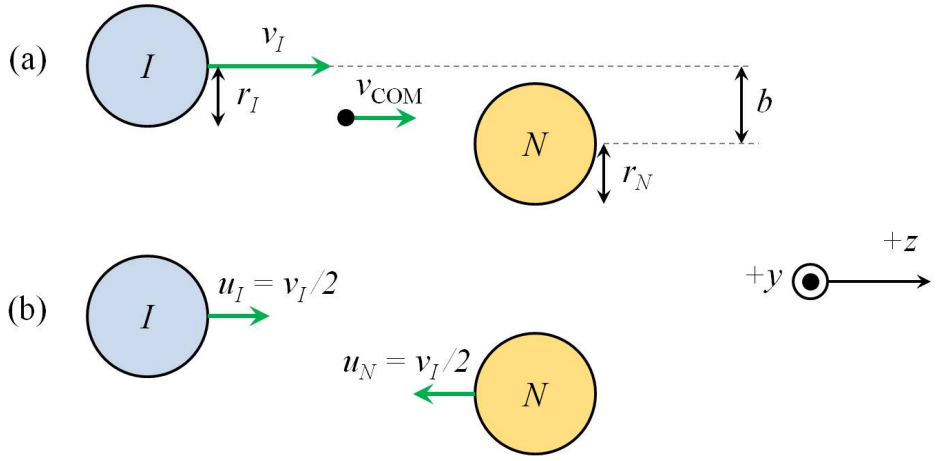

Figure 2.2: Illustration of hard sphere's I and N before the collision in the laboratory rest frame (a) and center-of-mass rest frame (b) for the special case of equally massive hard spheres $m_I = m_N$. The $+\hat{z}$ orientation is the same in both frames and is parallel to the pre-collision velocity of hard sphere I.

I is moving with relative velocity $\vec{v}_I = v\hat{z}$ and N is initially at rest $\vec{v}_N = 0$ in the laboratory reference frame, as seen in Fig. 2.2 (a). The z dimension is chosen to be aligned with I's initial velocity and y dimension is out of the page. The collision is not head-on, rather there is some perpendicular x displacement between the spheres' centers (as defined in Fig. 2.2) commonly called the impact parameter b, where $b = 0$ would correspond to a head-on collision. We also assume collisions are azimuthally symmetric, in which case we can restrict our discussion to the 2D plane defined by the azimuthal angle $\phi = 0$. The impact parameter b, the $+z$-axis orientation, and the assumption of azimuthal symmetry do not change when transforming between the COM and laboratory reference frames, as seen in Fig. 2.2.

The velocity of the system's center-of-mass can be written in general as

$$\vec{v}_{\mathrm{COM}} = \frac{m_I\vec{v}_I + m_N\vec{v}_N}{m_I + m_N} \rightarrow \frac{m_I\vec{v}_I}{m_I + m_N} \quad \text{for} \quad v_N = 0, \tag{2.1}$$

where m_I and m_N are the masses of the I and N hard spheres, respectively. For the special case where $m_I = m_N$, each hard sphere carries half the initial kinetic energy and $v_{\text{COM}} = v_I/2$ in the center-of-mass (COM) reference frame, as seen in Fig. 2.2 (b). In general, the pre-collision velocity vectors in the COM frame can be written as

$$\vec{u}_I = \vec{v}_I - \vec{v}_{\text{COM}} \text{ and } \vec{u}_N = \vec{v}_N - \vec{v}_{\text{COM}}, \tag{2.2}$$

for I and N, respectively.

In the absence of external forces, the hard sphere collision is isolated and the system should conserve the total kinetic energy and total momentum in laboratory reference frame

$$\begin{aligned} \frac{1}{2}m_I v_I^2 &= \frac{1}{2}m_I (v_I')^2 + \frac{1}{2}m_N (v_N')^2 \\ m_I \vec{v}_I &= m_I \vec{v}_I{}' + m_N \vec{v}_N{}' \\ \vec{v}_{\text{COM}} &= \vec{v}_{\text{COM}}' \end{aligned} \tag{2.3}$$

and in the COM reference frame

$$\begin{aligned} \frac{1}{2}m_I u_I^2 + \frac{1}{2}m_N u_N^2 &= \frac{1}{2}m_I (u_I')^2 + \frac{1}{2}m_N (u_N')^2 \\ m_I \vec{u}_I + m_N \vec{u}_N &= m\vec{u}_I{}' + m\vec{u}_N{}' = 0 \\ \vec{v}_{\text{COM}} &= 0 \end{aligned} \tag{2.4}$$

where primed quantities are post-collision [90]. Using Eq. (2.3), we can determine the post-collision velocities

$$\begin{aligned} v_I' &= \frac{v_I m_I}{m_I + m_N}\left(\cos(\chi) + \sqrt{\frac{m_N^2}{m_I^2} - \sin^2(\chi)}\right) \text{ and} \\ v_N' &= \frac{v_I m_I}{m_I + m_N}\sqrt{2\left[m_I + m_N - \left(\cos(\chi) + \sqrt{\frac{m_N^2}{m_I^2} - \sin^2(\chi)}\right)\cos(\chi)\right]} \end{aligned} \tag{2.5}$$

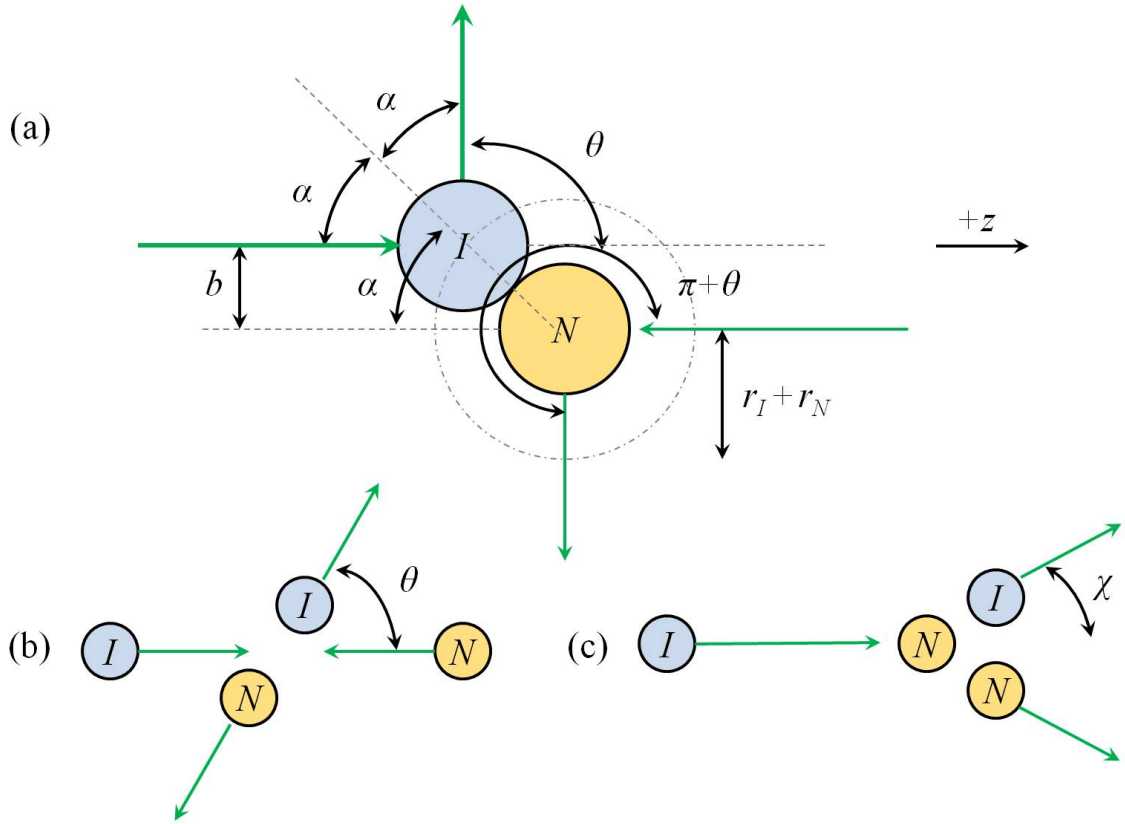

Figure 2.3: Panel (a) shows a detailed view of the trajectories (green arrows) and geometry of the hard sphere collision in the COM reference frame with impact parameter b. The polar scattering angle is defined as the angle between the $+z$ axis and hard sphere I's final trajectory. It is convenient to think of hard sphere I as a point-like object colliding with another hard sphere whose radius is $r_I + r_N$ (dot-dashed sphere). Due to the conservation of energy and momentum, the angle of incidence α is equivalent to the deflection or reflection angle α, which results in a scattering angle $\theta = \pi - 2\alpha$. Hard sphere N scatters at an angle of $\pi + \theta$. Panels (b) and (c) show the same hard sphere collision [with a different impact parameter from that shown in panel (a)] as seen from the COM reference frame characterized by scattering angle θ and the laboratory reference frame characterized by the scattering angle χ, respectively.

in terms of the initial conditions and collision partner I's laboratory scattering angle χ, as defined in Fig. 2.3 (c).

Consequently, in the COM reference frame, where $\vec{p}_I = -\vec{p}_N$, the magnitude of the pre- and post-collision velocities remain the same $u_I = u_I'$ and $u_N = u_N'$. We can write the final

velocity vectors in the laboratory reference frame as

$$\vec{v}_I\,' = u_I\,[\sin(\theta)\hat{x} + \cos(\theta)\hat{z}] + v_{\rm COM}\hat{z} \;\text{ and }\; \vec{v}_N\,' = u_N\,[-\sin(\theta)\hat{x} - \cos(\theta)\hat{z}] + v_{\rm COM}\hat{z} \quad (2.6)$$

for I and N (respectively), which are expressed in terms of speeds u and scattering angle θ associated with the COM reference frame, as defined in Fig. 2.3 (a). The magnitude of the velocities in the laboratory reference frame can also be written as a function of the COM coordinates as,

$$(v_I')^2 = u_I^2 + v_{\rm COM}^2 + 2v_{\rm COM}u_I\cos(\theta) \;\text{ and }\; (v_N')^2 = u_N^2 + v_{\rm COM}^2 - 2v_{\rm COM}u_N\cos(\theta), \quad (2.7)$$

where we used the fact that the angle between $\vec{u}_I\,'$ and $v_{\rm COM}$ is equivalent to θ and the angle between $\vec{u}_N\,'$ and $v_{\rm COM}$ is equivalent to $\pi + \theta$.

To relate the scattering angle in the COM frame θ to that of the scattering angle in the laboratory frame χ, we need only consider the dot product of the initial and final velocity vectors $\vec{v}_I$ and $\vec{v}_I\,'$

$$\vec{v}_I \cdot \vec{v}_I\,' = v_I v_I' \cos(\chi) = v_I(u_I\cos(\theta) + v_{\rm com}), \quad (2.8)$$

which are already expressed in terms of the COM scattering angle θ according to Eq. (2.7). By substituting Eqs. (2.7) [or (2.5)] for v_I', Eq. (2.2) for u_I, and Eq. (2.1) for $v_{\rm COM}$ into Eq. (2.8), manipulation yields

$$\tan(\chi) = \frac{\sin(\theta)}{\frac{m_I}{m_N} + \cos(\theta)}, \quad (2.9)$$

which simplifies to $2\chi = \theta$ for the $m_I = m_N$ case. Alternatively we could have arrived at the same result by equating Eqs. (2.7) and the square of (2.5). Furthermore, using the

geometry of Fig. 2.3, we can see the impact parameter is related to the scattering angle by

$$b = (r_I + r_N)\cos(\theta/2). \tag{2.10}$$

From Eq. (2.10), for $b \geq r_I + r_N$ there is no deflection, the scattering angle $\theta = 0^\circ$ (forward scattering), and v_I' is at a maximum [according to Eq. (2.7)]. Alternatively, for $b = 0$ the scattering angle $\theta = 180^\circ$ (back scattering) and v_N' is at a maximum. For the special case of $b = 0$ equal-mass collisions all the kinetic energy is transfered from I into hard sphere N, as seen in the laboratory reference frame [90].

Differential and total scattering cross section If we imagine a beam of hard spheres with beam intensity I_0 (number of spheres per unit area per unit time) approaching the target hard sphere, we might ask the question what fraction of the incident hard spheres are deflected or scattered into the solid angle $d\Omega$? From the illustration in Fig. 2.4 and

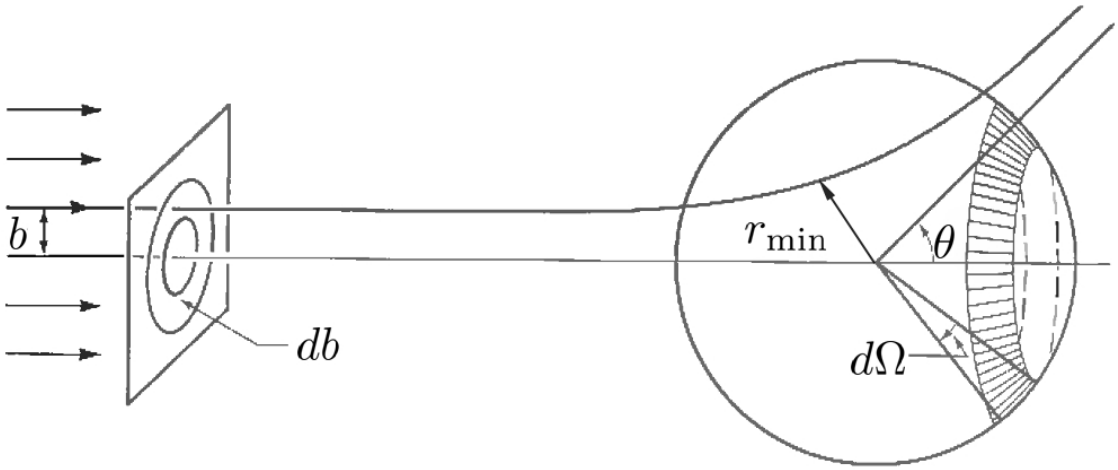

Figure 2.4: A modified version of a figure from Ref. [91]. Many hard spheres are incident on a scattering target. Assuming azimuthal symmetry, we see that a fraction of the incident beam within an infinitesimal width db at impact parameter b scatter at an angle θ into an infinitesimal solid angle $d\Omega$. For hard sphere scattering, the closest hard sphere center-to-center distance is $r_{\min} = r_I + r_N$.

following the treatment of two-body scattering from Refs. [91–93], we see that an infinitesimal strip of area $d\sigma = bd\phi db$ has an infinitesimal number of particles $dN_{\rm sc} = I_0 d\sigma$ scatter through the infinitesimal solid angle $d\Omega$ per unit time, where $d\sigma = D(\theta)d\Omega$. Here, $D(\theta)$ is the proportionality constant known as the differential scattering cross section [92]

$$D(\theta) \equiv \frac{d\sigma}{d\Omega} = \frac{b}{\sin(\theta)}\left|\frac{db}{d\theta}\right| = \frac{1}{I_0}\frac{dN_{\rm sc}}{d\Omega}. \tag{2.11}$$

If we integrate $D(\theta)$ over all solid angles we can arrive at the total collisional cross section

$$\sigma \equiv \int D(\theta)d\Omega. \tag{2.12}$$

The probability distribution function (PDF) for scattering is isotropic in solid angle. Therefore, we can write the azimuthal distribution function as being equally probable for each angle ϕ and the normalized polar angle PDF must have the form

$$\rho(E,\theta) = \frac{2\pi\sin(\theta)D(\theta,E)}{\sigma(E)}, \tag{2.13}$$

where we have allowed for the possibility that the cross section and differential cross section depend on the relative collision energy E defined in Eq. (1.4).

Using Eq. (2.11) and Eq. (2.10), we find that for the specific case of hard sphere scattering $D(\theta) = (r_I + r_N)/4$ and is both isotropic and energy independent. The total cross section is $\pi(r_I + r_N)^2$, which is equivalent to thinking of the incident beam as being comprised of point like particles I on spherical target's N with effective radius $r_I + r_N$. Therefore, the distance of closest approach must be always be $r_{\rm min} = r_I + r_N$ for $b \leq r_I + r_N$. Also, we find that $\rho = \sin(\theta)/2$, which is plotted along side the azimuthal hard sphere scattering angles' distribution function in Fig. 2.5.

As we saw earlier with Fig. 1.3 and Eq. (1.3), we can also express the total number of scattered hard spheres $N_{\rm sc}$ from an incident beam with N_0 total hard spheres on a group of

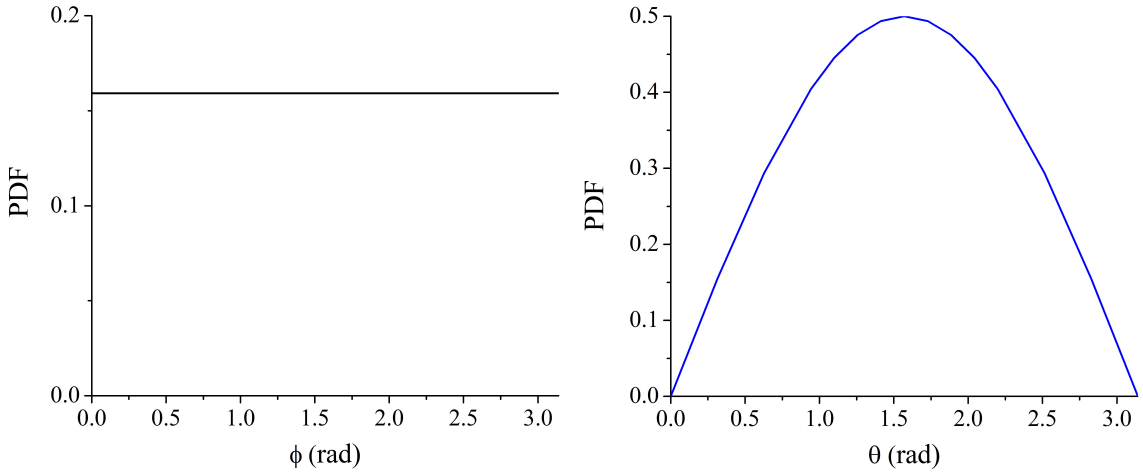

Figure 2.5: Isotropic solid angle normalized hard sphere scattering distributions. On the left is the constant PDF for azimuthal angle ϕ and on the right is the PDF for θ, which is $\rho = \sin(\theta)/2$. Together, they form an isotropic distribution for the solid angle.

scattering targets with number density n_{tar} as

$$N_{sc}^{\text{COM}} = N_0^{\text{COM}} \sigma^{\text{COM}} n_{\text{tar}}^{\text{COM}} \quad \text{and} \quad N_{sc}^{L} = N_0^{L} \sigma^{L} n_{\text{tar}}^{L}, \tag{2.14}$$

in both the COM and laboratory reference frame, respectively [93]. We have assumed that densities are low enough that only two-body collisions are occurring between the incident and scattering target hard spheres. In both reference frames the total incident number of hard spheres $N_0^{\text{COM}} = N_0^L$, the scattering target density $n_{\text{tar}}^{\text{COM}} = n_{\text{tar}}^L$, and the total number of scatter hard spheres $N_{sc}^{\text{COM}} = N_{sc}^L$ must be equivalent, thus the total cross section must be the same in both reference frames $\sigma^{\text{COM}} = \sigma^L = \sigma$. In a similar vein, using Eq. (2.11) we can express the number of particles scattered into some solid angle $d\Omega$ as

$$dN_{\text{sc}} \text{ (into } d\Omega) = N_0 n_{\text{tar}} D(x) d\Omega, \tag{2.15}$$

where x could refer to θ or χ depending on your reference frame. Again by equating N_{sc} (into $d\Omega$), N_0, and n_{tar} in both the COM and laboratory reference frames, we find that

$$D(\theta)d\Omega^{\mathrm{COM}} = D(\chi)d\Omega^{L} \implies D(\chi) = D(\theta)\frac{\left[1+2\frac{m_I}{m_N}\cos(\theta)+\left(\frac{m_I}{m_N}\right)^2\right]^{3/2}}{\left|1+\frac{m_I}{m_N}\cos(\theta)\right|}, \quad (2.16)$$

where the relationship between θ and χ found in Eq. (2.9) was substituted into each respective solid angle $\left(\text{e.g., } d\Omega^{L} = d[\cos(\chi)]\right)$ in the last step [93].

In short, we have considered the case of non-interacting hard sphere elastic collisions. In doing so, we have determined the pre- and post- collision velocity vectors of two-body hard sphere collision, the corresponding scattering angles in both the laboratory and COM reference frames, and related the incident impact parameter b to the final scattering angle θ in the COM reference frame. We have also considered the case of multiple two-body collisions between a group of incident and target collision partners. In the process, we have defined parameters that characterize the scattering outcomes of such collisions, such as the impact parameter b, the scattering cross section $\sigma(E)$, and the differential scattering cross section $D(\theta,E)$, for both the laboratory and COM reference frames. These three parameters will continue to be used and characterized in each progressively more advanced scattering model presented throughout this chapter.

2.1.2 Langevin model

The effective potential Although instructive, the hard sphere model is a poor description for low-energy or cold ($\sim$ 100 K - 100 μK) atomic collisions. This is because atomic two-body collisions are dominated by long-range electrical forces and do not simply interact by contact forces alone, as was assumed in Sec. 2.1.1. Ironically, it turns out that the overall effect of quantum scattering models at ultracold temperatures ($\sim$ 100 nK) are

essentially hard-sphere like [73, 92], as will be discussed in Sec. 2.2.1. However, since we are interested in low-energy or cold collisions, we need to develop a scattering model that incorporates the long-range interaction potential $V(R)$, which only depends on the interatom spacing R between collision partners I and N.

The total energy of the collision system in the laboratory reference frame is

$$E = \frac{m_I + m_N}{2} v_{\mathrm{COM}}^2 + \frac{1}{2}\frac{m_I m_N}{m_I + m_N} v^2 + V(R), \tag{2.17}$$

which is the sum of the COM kinetic, the relative kinetic energy, and the long-range potential $V(R)$.

By switching to the COM reference frame and making the substitution for the reduced mass $\mu = m_I m_N/(m_I + m_N)$, we can simplify the problem to the equivalent one-body problem in the presence of a conservative fixed central field with potential $V(R)$, which is centered at the origin of the coordinate system [91]. Furthermore, because the potential is spherically symmetric, the angular motion must be cyclic and thus angular momentum $l = mr^2\dot{\Theta}$ is conserved. Here, $v^2 = \dot{R}^2 + R^2\dot{\Theta}$, where Θ is the cyclic polar angle in the new COM coordinate system. In short, we have reduced the two-body problem to a one-body problem in two dimensions (2D), and the total energy is

$$E = \frac{1}{2}\mu\dot{R}^2 + \frac{l^2}{2mR^2} + V(R), \tag{2.18}$$

where the second term is referred to as the centrifugal term.

However, it would be more convenient to express our result in terms of the following independent parameters: the conserved total relative collision energy E (where $E = \frac{1}{2}\mu v_0^2$ at large R) and the impact parameter b, which together determine l. This re-expression is accomplished by substituting $l = b\mu v_0 = b\sqrt{2mE}$ giving

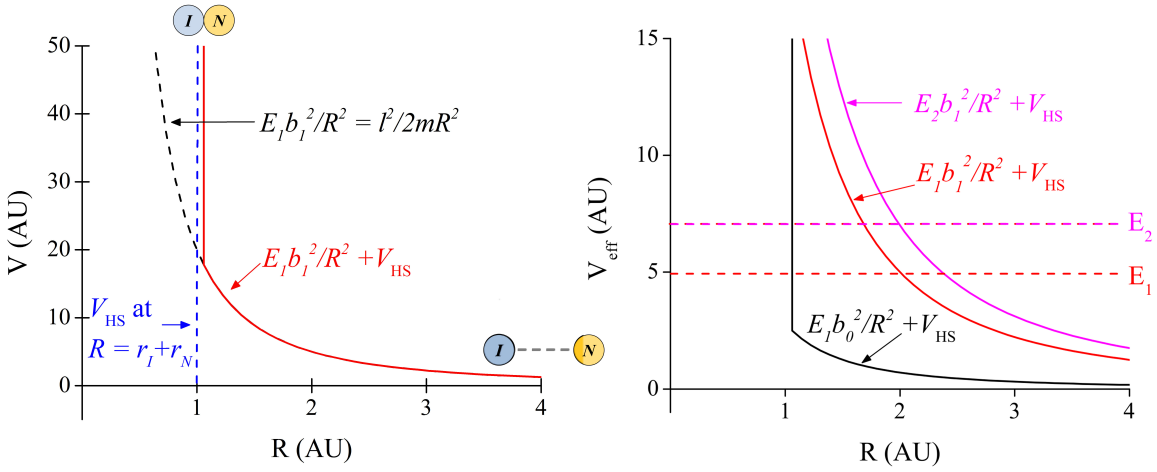

Figure 2.6: The left plot shows the effective potential for hard sphere scattering (red solid curve) as a function of the interatomic distance R in arbitrary units (AU). The effective potential is the sum of the centrifugal term (black dashed curve) and the hard sphere potential barrier at the hard sphere radius $R = r_I + r_N = 1$ AU. The right plot shows three different effective potentials. Two of the curves (black and red) have the same collision energy E_1, one of which has an impact parameter $b_0 < r_I + r_N$ (black curve) resulting in a collision, while the other has a larger impact parameter $b_1 > r_I + r_N$ (red curve) and shows no collision. The magenta curve has the same impact parameter as the orange curve b_1 but a larger collision energy E_2, which results in the same distance of closest approach $r_{\min} = 2$ AU and no deflection. For hard sphere scattering, the impact parameter alone determines the distance of closest approach.

$$E = \frac{1}{2}\mu\dot{R}^2 + \frac{b^2 E}{R^2} + V(R) = \frac{1}{2}\mu\dot{R}^2 + V_{\text{eff}}(E, b, R). \tag{2.19}$$

In the last step the centrifugal term and the long-range potential are combined in a single term called the effective potential V_{eff}.

If we temporarily return to to the hard sphere approximation, then we would describe the hard sphere potential as

$$V_{\text{HS}}(R) = \begin{cases} \infty, & \text{if } R \leq r_I + r_N \\ 0, & \text{if } R > r_I + r_N \end{cases}. \tag{2.20}$$

Both the hard sphere potential, a centrifugal contribution, and effective potential for a hard

sphere collision are plotted as a function of interatomic separation in Fig. 2.6. These plots are called interatomic potential curves and the hard sphere model represents the simplest possible non-trivial potential.

Due to the lack of long-range interaction, the distance of closest approach $r_{\min}$ [as shown in Fig. 2.4 and defined by the interatomic distance at which $V_{\text{eff}} = E$] is only affected by the size of the impact parameter. If the impact parameter is larger than $r_I + r_N$, then $r_{\min} = b$ regardless of the collision energy, as is the case for the magenta and orange curves on the right plot of Fig. 2.6. If the impact parameter is smaller than $r_I + r_N$, then the interatomic distance reaches the closets possible distance $r_I + r_N$, regardless of the collision energy, as is the case for the black curve on the right plot of Fig. 2.6.

Long-range polarization potential Now let us consider the actual long-range electrical potential between the two collision partners, an atomic ion I and the neutral atom N. As compared to neutral-neutral interactions, which involve two induced dipoles, the case of ion-neutral interactions result in a much stronger attractive potential from the monopole-induced-dipole potential, as depicted in Fig. 2.7.

Following the standard electrostatic treatment [94], each charge in an atom q experiences a force $\vec{F} = q\vec{\mathscr{E}}$, in the presence of an external electric field $\vec{\mathscr{E}}$. If we think of the atom's electron cloud as a point charge $-q$ and the nucleus as a point charge $+q$, an electric dipole $\vec{d} = q\vec{r}$ is formed (where q and d are defined in Fig. 2.7). The dipole experiences a torque $\vec{d} \times \vec{\mathscr{E}}$ in the presence of a uniform electric field. However, in the presence of a spatially non-uniform field, which is the case for the field produced by a monopole, there is a net force $\vec{F} = (\vec{d} \cdot \vec{\nabla})\vec{\mathscr{E}}$, due to the inhomogeneity of the field over the dipole length r.

We can express the induced dipole moment of an atom in terms of its linear atomic

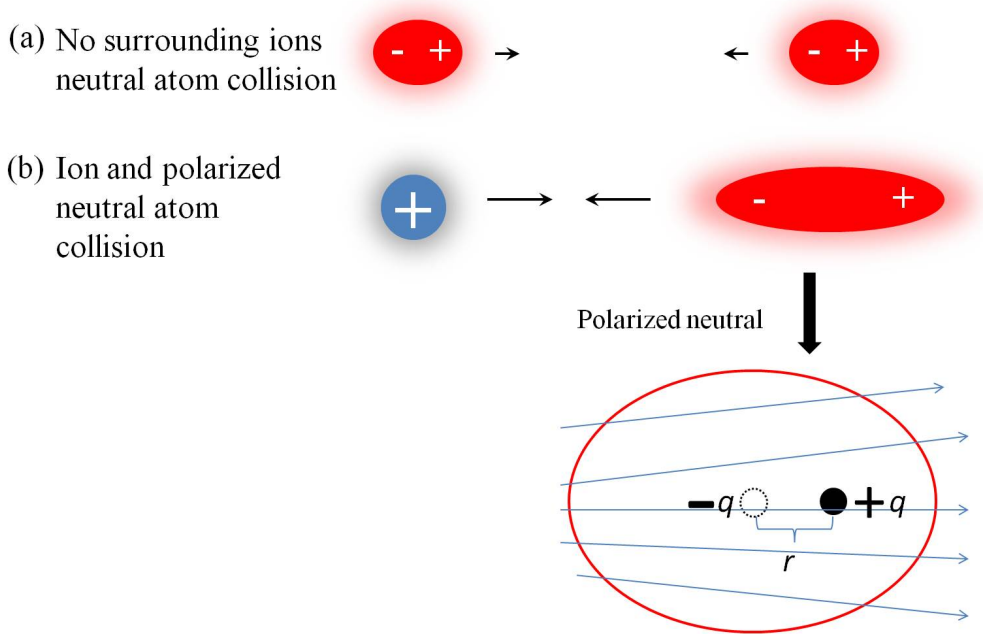

Figure 2.7: Panel (a) shows a neutral-neutral interaction or an induced-dipole-induced-dipole interaction. Panel (b) shows an ion-neutral interaction or a monopole-induced-dipole interaction. The ion-neutral interaction polarizes or distorts the neutral atom's charge distribution more dramatically than in the neutral-neutral case, which leads to a stronger attractive force between the collision partners. The positive nucleus and negative electron cloud form a dipole $\vec{d}$.

polarizability α as $\vec{d} = \alpha\vec{\mathscr{E}}$. For example, a typical value for an easily polarized alkali Na is $\alpha = 24.1 \times 10^{-30}$ m^3, while a less easily polarized noble gas like He is two orders of magnitude smaller [94].

To determine the potential energy we can used the vector identity

$$\begin{aligned}\vec{\nabla}(\vec{d}\cdot\vec{\mathscr{E}}) &= \vec{d}\times(\vec{\nabla}\times\vec{\mathscr{E}}) + \vec{\mathscr{E}}\times(\vec{\nabla}\times\vec{d}) + (\vec{d}\cdot\vec{\nabla})\vec{\mathscr{E}} + (\vec{\mathscr{E}}\cdot\vec{\nabla})\vec{d} \\ &= 2(\vec{d}\cdot\vec{\nabla})\vec{\mathscr{E}} = 2\vec{F},\end{aligned} \tag{2.21}$$

where we have simplified the expression using the fact that $\vec{\nabla}\times\vec{\mathscr{E}} = 0$ for the electrostatic case and that $(\vec{\mathscr{E}}\cdot\vec{\nabla})\vec{d} = 2\alpha(\vec{\mathscr{E}}\cdot\vec{\nabla})\vec{\mathscr{E}} = (\vec{d}\cdot\vec{\nabla})\vec{\mathscr{E}}$. Therefore, we can express the potential energy as

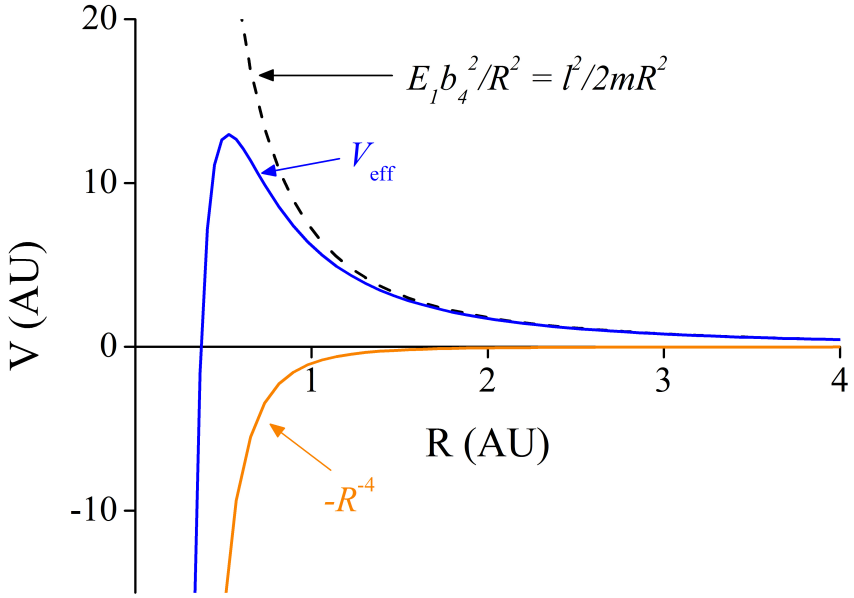

Figure 2.8: The Langevin model's effective potential V_{eff} (solid blue curve) as a function of interatomic distance (in arbitrary units) for an ion-neutral collision is the sum of the centrifugal term (dashed black curve) and the long-range polarization potential (solid orange curve). The centrifugal term causes a hump in V_{eff} called the centrifugal barrier.

$$V_{\text{in}}(R) = -\int \vec{F}\cdot d\vec{R} = -\int \frac{1}{2}\vec{\nabla}(\vec{d}\cdot\vec{\mathscr{E}})\cdot d\vec{R} = -\frac{1}{2}\vec{d}\cdot\vec{\mathscr{E}} = -\frac{\alpha}{2}\vec{\mathscr{E}}\cdot\vec{\mathscr{E}} = -\frac{C_4}{2R^4}, \qquad (2.22)$$

where $\vec{\mathscr{E}}$ is now specifically the electric field from the monopole ion with net charge Q and $C_4 = \alpha(Q/4\pi\varepsilon_0)^2$. This is the same result reported earlier in Eq. (1.2).

Incorporating the formula for V_{in} into Eq. (2.19) gives the Langevin model's effective potential energy as a function of the interatomic spacing, as seen in Fig. 2.8. The collision partners cannot get indefinitely close to one another. Once close enough, the electron clouds will exhibit a repulsive electrical forces and Pauli repulsion. Typically, an *ad hoc* hard-sphere like repulsive term for the short-range interactions is added to V_{eff} (not shown in Fig. 2.8). For example, the Lennard-Jones potential uses a repulsive $1/R^{12}$ term at short-

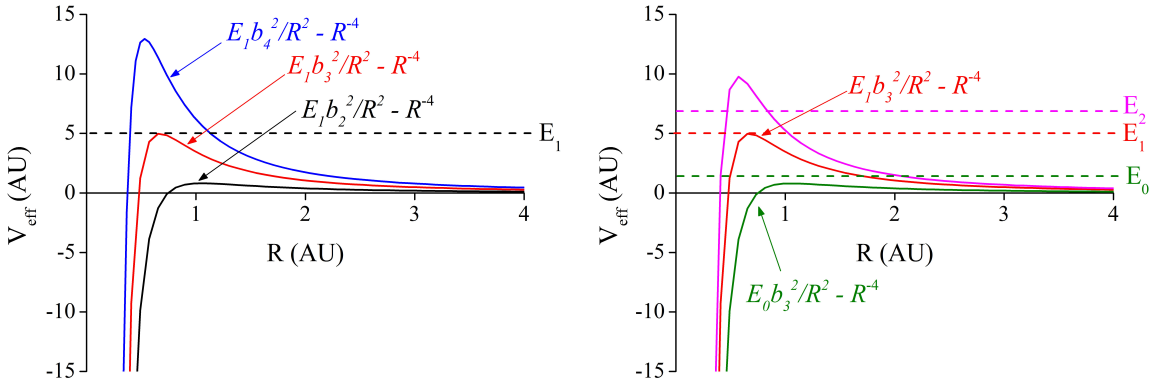

Figure 2.9: The left plot shows three different ion-neutral effective potentials all with the same energy E_1, but with different impact parameters $b_2 < b_3 < b_4$ and thus three different angular momenta. The distance of closest approach and the trajectory of the collision partners are affected by the impact parameter. For example, the red curve will result in an unstable circular orbit, thus $b_3 = b_0$ for $E = E_1$, as shown by the dashed trajectory in Fig. 2.10. The right plot shows three ion-neutral effective potentials for the same impact parameter, but three different energies $E_0 < E_1 < E_2$. Unlike the hard sphere model, the collision energy also affects the distance of closest approach.

range [95], while the Buckingham potential uses a decaying exponential [96]. However, because of the centrifugal barrier, the details of the potential at short-range do not significantly impact the low-energy ion-neutral collision cross section with $b > 0$, so they are not of major concern for this chapter or this dissertation as a whole and will not be discussed further.

The attractive electrical potential and repulsive centrifugal term result in the centrifugal barrier, characterized by the V_{eff}'s hump seen in Fig. 2.8. The location and height of the hump indicate the previously mentioned characteristic radius R^* and E^* from chapter 1. By differentiating the effective potential, we find that the hump's maximum is at a radius

$$R^* = \frac{1}{b}\left(\frac{C_4}{E}\right)^{1/2}, \tag{2.23}$$

and substituting that result back into V_{eff} gives the maximum effective potential energy

$$E^* = \frac{E^2 b^4}{2C_4}. \tag{2.24}$$

If the collision energy $E = E^*$, then a critical impact parameter is reached

$$b_0 = \left(\frac{2C_4}{E}\right)^{1/4}, \tag{2.25}$$

resulting in an unstable circular orbit with radius $R^* = b_0/\sqrt{2}$ between the ion and neutral. This is the case for the red curve with energy E_1 and impact parameter $b_3 = b_0$ in the left and right plots of Fig. 2.9 and corresponds to the dashed trajectory depicted in the trajectory diagram, Fig. 2.10.

For a fixed energy collision energy E_1 there are three possible cases to consider. First, if the impact parameter is small compared to b_0, then the distance of closest approach can be very small, because the energy of the particle is above the centrifugal barrier, as seen in the left plot's black curve of Fig. 2.9 or for the trajectories whose impact parameter $b < b_0$ in Fig. 2.10. These small impact parameter collisions result in spiral trajectories and a larger R^*. Second, if $b = b_0$, then the ion and neutral will undergo a unstable circular orbit, as discussed before. Third, if the impact parameter is large compared to b_0, the collision partners are slightly deflected from the barrier and the distance of closest approach is $r_{\min} \approx b$, as seen in the left plot's blue curve of Fig. 2.9 (where $b_4 = 1.2$ AU) and for trajectories whose $b > b_0$ in Fig. 2.10. These large impact parameter collisions result in a smaller R^*. Both the first and third case show a similar behavior to the hard-sphere results associated with the black and orange curves in the right plot of Fig. 2.6.

However, unlike the hard sphere case, the collision energy can also affect the distance of closest approach. As shown in the right plot of Fig. 2.9 and as seen in Eq. (2.23), both

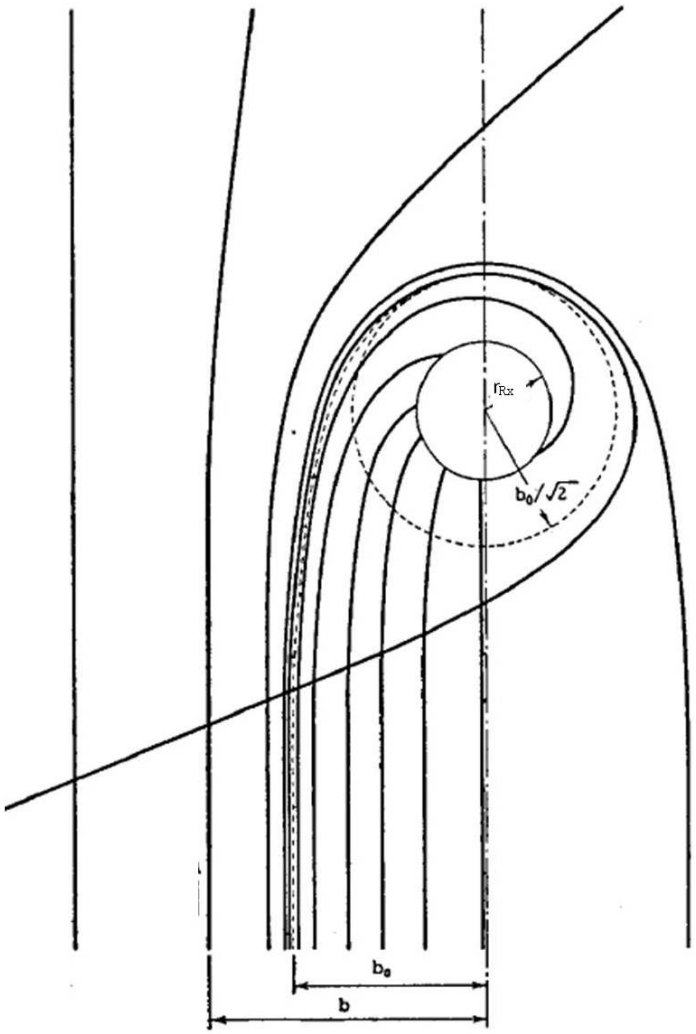

Figure 2.10: Modified version of a figure originally from Ref. [75] showing various scattering trajectories of equivalent initial energy, but different impact parameters for an ion-neutral collision following the Langevin model. If the impact parameter is below a critical impact parameter b_0 shown by the dashed (unstable) circular orbit, then the partners will undergo a spiraling short-range collision. The collision pair reaches the desired reaction radius r_{Rx} with 100% efficiency, such that $r_{\mathrm{Rx}} < b_0/\sqrt{2}$.

the total collision energy and the impact parameter can affect R^*. Now, for a fixed impact parameter, a smaller collision energy gives a larger R^* and smaller r_{min} [as seen in the green curve of Fig. 2.9] and a larger collision energy gives a smaller R^* and larger r_{min} [as seen in the magenta curve of Fig. 2.9].

The cross section and rate coefficient If there exists a critical or minimum distance of closest approch for a particular kind of ion-neutral reaction to occur (e.g, charge-exchange reaction), then the Lagnevin model predicts that as long as the critical reaction radius r_{Rx} is smaller than the unstable circular orbit radius $b_0/\sqrt{2}$, the reaction will proceed with 100% efficiency for all $b < b_0$, as shown in Fig. 2.10. Using the critical impact mobel, Langevin's power-law energy dependent collisional cross section is

$$\sigma_L(E) = \pi b_0^2 = \pi \left[R^*(b_0)\right]^2 = \pi\sqrt{2C_4}E^{-1/2} \equiv C_{\mathrm{ce}}E^{-1/2}. \tag{2.26}$$

It turns out that the Langevin model works well for predicting ion-neutral charge-exchange reactions (up to a factor of 4 or 2), so in the last part of Eq. (2.26) we have defined the classical charge-exchange power-law coefficient $C_{\mathrm{ce}} = \pi\sqrt{2C_4}$.

In the laboratory, one typically measures the reaction rate coefficient k_x, where the subscript x refers to either the reactants or the model associated with the reaction. The Langevin reaction rate k_L is defined as

$$k_L = \langle \sigma_L v \rangle = \int_0^\infty \sigma_L(E) f_{\mathrm{MB}}(E)\, dE = 2\pi\sqrt{\frac{C_4}{\mu}}, \tag{2.27}$$

where we have averaged over the relative, presumably Maxwell-Boltzmann (MB) energy distribution $f_{\mathrm{MB}}(E)$. Typically, because the neutral atoms are so cold ($\lesssim 1mK$), their COM reference frame distribution can be approximated as delta-function like. Therefore, it is sufficiently accurate to average over the ion energy COM reference frame distribution at temperature T_I, rather than the actual relative energy distribution. This approximation will be assumed throughout the dissertation. Thus, unless otherwise specified, the relative energy distribution and the ion energy distribution refer to essentially the same thing and will be used interchangeably. Furthermore, Eq. (2.27) shows that the Langevin reaction rate is energy independent, which is a consequence of the electrical potential's R^{-4} behavior.

The reaction rate coefficient determines the total number of collisions that will happen per second in an ion-neutral gas mixture with approximately uniform density within the overlap volume V by,

$$R_{\text{coll}} = k_L \frac{N_I N_a}{V}, \tag{2.28}$$

where N_I is the total number of ions and N_a is the total number of atoms within the volume of overlap.

In summary, the Langevin model incorporates an effective potential that is a sum of the centrifugal term and the electrical interaction potential. The long-range electrical potential is that of a monopole-induced-dipole interaction for ion-neutral collisions, leading to the characteristic R^{-4} behavior. For values of E and b that lead to spiral trajectories, short-range collisions are possible. These short range collisions (possibly resulting in charge-exchange reactions) are characterized by the classical power-law Langevin cross section $\sigma_L(E)$ at characteristic radius R^* and reaction rate k_L, which is collision-energy independent.

2.2 Quantum scattering

So far our scattering discussion has been entirely classical. Now we will consider the fact that the ion-neutral collision partners have de Broglie matter wavelengths λ_{dB} [defined in Eq. (1.1)] and scatter or interfere much like water waves bouncing off a rock.

2.2.1 Quantum and semiclassical model

The partial wave amplitude We will again assume the equivalent one-body problem with total collision energy E in the presence of a spherically symmetric potential V. We can write the three-dimensional (3D) time independent Schröedinger equation (TISE)

$$-\frac{\hbar^2}{2m}\nabla^2\psi + V(R)\psi = E\psi. \tag{2.29}$$

Using the separable solution $\psi = U(R)Y_l^{m_l}(\theta,\phi)$, where $Y_l^{m_l}(\theta,\phi)$ are the spherical harmonics, the radial equation for $\Phi(R) = RU(R)$ reduces to

$$-\frac{\hbar^2}{2\mu}\frac{d^2\Phi(R)}{dR^2} + \left[\frac{\hbar^2}{2\mu}\frac{l(l+1)}{r^2} + V(R)\right]\Phi(R) = E\,\Phi(R). \tag{2.30}$$

Again, the second term (in square brackets) is the effective potential, which combines the potential $V(R)$ and the quantum mechanical centrifugal eigenvalue associated with the solution to the angular part of ∇^2 operator. As was the case for the Langevin and hard-sphere model, at large interatomic distances known as the "radiation zone," the effective potential vanishes ($V_{\text{eff}} \approx 0$) and radial equation reduces to

$$-\frac{\hbar^2}{2\mu}\frac{d^2\Phi(R)}{dR^2} = E\,\Phi(R) \;\text{ or }\; \frac{d^2\Phi(R)}{dR^2} = -k^2\Phi(R), \tag{2.31}$$

which has spherical wave solutions with wave number

$$k \equiv \frac{\sqrt{2\mu E}}{\hbar} = \frac{2\pi}{\lambda_{\text{dB}}}. \tag{2.32}$$

The general solution to $\Phi(R)$ in the radiation zone is just that of a plane wave,

$$\Phi(R) = Ae^{ikR} + Be^{-ikR}. \tag{2.33}$$

The "intermediate" region is between the "scattering region," where $V(R)$ dominates and the radiation zone where $V_{\text{eff}} \approx 0$, as seen in Fig. 2.11. In the intermediate region V can be ignored, but the centrifugal term in Eq. (2.30) cannot. The exact solution to the TISE (up to a normalization constant A) outside the scattering region expressed completely in polar coordinates can be written as

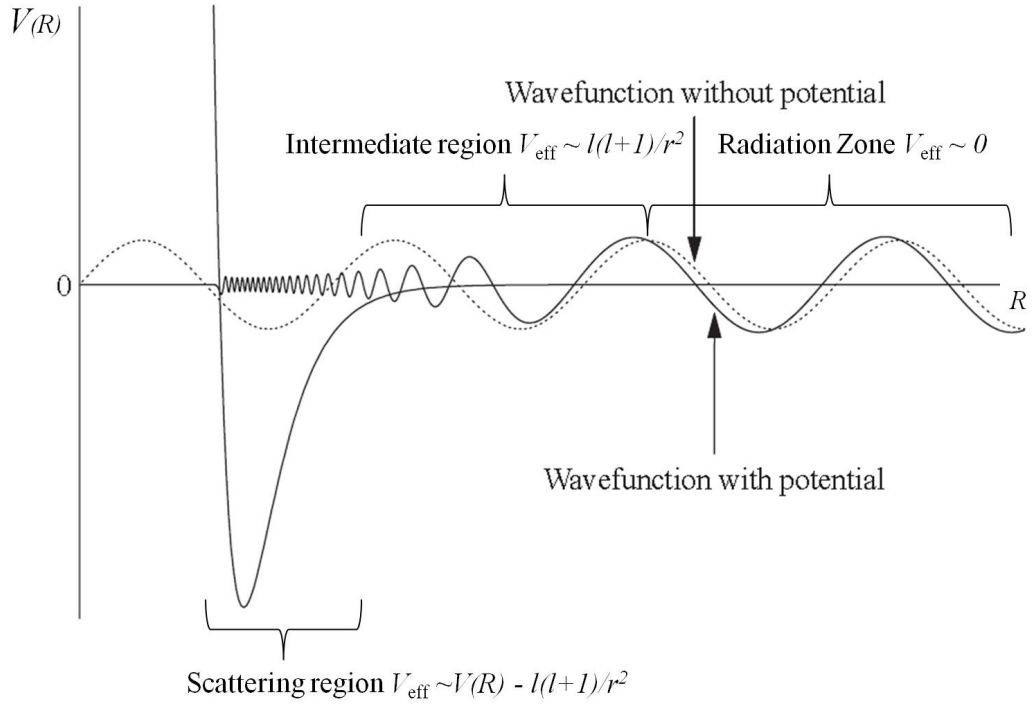

Figure 2.11: Modified figure originally from Ref. [73] shows plot of interatomic potential, wavefunction $\Phi(R)$ (solid sinusoidal curve) and approximate low-energy hard sphere wavefunction (dashed sinusoidal curve). The scattering from the actual potential at ultracold temperatures is indistinguishable from that of a hard sphere potential with radius (scattering length) a that gives the same asymptotic phase shift.

$$\psi(R,\theta) = A\sum_{l=0}^{\infty}\frac{\Phi(R)}{R}Y_l^0(\theta) = A\sum_{l=0}^{\infty} i^l(2l+1)\left(j_l(kR)+ika_l h_l^{(1)}(kR)\right)P_l[\cos(\theta)], \tag{2.34}$$
$$\text{where}\quad \Phi_l(R) = A\sqrt{4\pi(2l+1)}i^l R\left(j_l(kR)+ika_l h_l^{(1)}(kR)\right).$$

We have again taken advantage of the azimuthal symmetry and dropped the ϕ dependence by setting $m = 0$. The solution to the TISE is an expansion of the spherical Bessel functions $j_l(x)$, the spherical Hankel function of the first kind $h_l^{(1)} = j_l(x) + in_l(x)$ (where n_l is the Neumann spherical Bessel function), the expansion coefficient a_l, and the Legendre polynomials P_l.

We approach the asymptotic limit for R in the radiation zone, and we can use the asymptotic forms of the Bessel and Hankel functions [97] to rewrite the exact solution in the asymptotic limit as

$$\psi(R,\theta) \overset{R\to\infty}{\approx} A\sum_{l=0}^{\infty}\frac{(2l+1)P_l[\cos(\theta)]}{R}\left[\frac{1}{2ik}\left(e^{ikR}-(-1)^l e^{-ikR}\right)+a_l e^{i(kR-\frac{l\pi}{2})}\right], \quad (2.35)$$

$$\overset{R\to\infty}{\approx} A\sum_{l=0}^{\infty}\frac{(2l+1)P_l[\cos(\theta)]}{R}\left[\frac{1}{k}\sin(kr-\frac{l\pi}{2})+a_l e^{i(kR-\frac{l\pi}{2})}\right], \quad (2.36)$$

$$\overset{R\to\infty}{\approx} A\left(e^{ikz}+f(\theta)\frac{e^{ikR}}{R}\right), \quad (2.37)$$

where we have used Rayleigh's formula

$$e^{ikz}=\sum_{l=0}^{\infty} i^l(2l+1)j_l(kR)P_l[\cos(\theta)] \overset{R\to\infty}{\approx} \sum_{l=0}^{\infty} i^l(2l+1)\frac{\sin(kR-\frac{l\pi}{2})}{kR}P_l[\cos(\theta)]. \quad (2.38)$$

Equation (2.37) gives the expected form for the wavefunction in the radiation zone [92], which is a combination of traveling wave with wave number k in the +z direction and a spherical wave with forward scattering amplitude $f(\theta)$, as seen in Fig. 2.1 (b). The solution is very similar to the classical scattering of water waves or sound waves off a spherical obstacle. The scattering amplitude only depends on θ due to the symmetry of the potential. The scattering amplitude squared is proportional to the probability $|\psi|^2$ that a particle scatters at an angle θ and thereby determines the differential scattering cross section

$$D(\theta)=|f(\theta)|^2 \quad (2.39)$$

and comparison between Eqs. (2.37) and (2.35) gives

$$f(\theta)=\sum_{l=0}^{\infty}(2l+1)a_l P_l[\cos(\theta)], \quad (2.40)$$

where the a_l has absorbed the phase factor of $e^{il\pi/2}$. Therefore, the forward scattering amplitude is directly related to a_l. The differential cross section can be determined using Eq. (2.39) and integrating that result [as described by Eq. (2.12)] yields the total cross section

$$\sigma = 4\pi \sum_{l=0}^{\infty} (2l+1)|a_l|^2. \tag{2.41}$$

The forward scattering amplitude depends on the details of the potential via a_l, which is known as the partial wave amplitude. By solving the TISE in the scattering region with the specific $V(R)$ and then matching solutions to Eq (2.34), a_l can be determined and the cross section realized using Eq. (2.41).

As an example, if we return to the hard sphere potential Eq (2.20) and define $r_I + r_N = a$, then the solution in the scattering zone is zero. Meanwhile, at the boundary $\psi(a,\theta) = 0$ and by plugging in $R = a$ into Eq. (2.34) and setting it equal to zero, the partial wave amplitude becomes

$$a_l = i\frac{j_l(ka)}{kh_l^{(1)}(ka)}, \tag{2.42}$$

which can be substituted in Eq. (2.41) to get the exact total cross section

$$\sigma = \frac{4\pi}{k^2} \sum_{l=0}^{\infty} (2l+1) \left| \frac{j_l(ka)}{kh_l^{(1)}(ka)} \right|^2 \tag{2.43}$$

In the ultracold regime $ka \ll 1$ or $a \ll \lambda_{\mathrm{dB}}$, as can be seen by the fact that λ_{dB} grows with decreasing temperature according to Eq. (1.1). In this regime, Eq. (2.43) reduces to a series that is proportional to $(ka)^{4l+2}$ [92], thus only the first term $l = 0$ (or the "s-wave") partial wave significantly contributes to the sum. Therefore, Eq. (2.43) can be reduced to the first term,

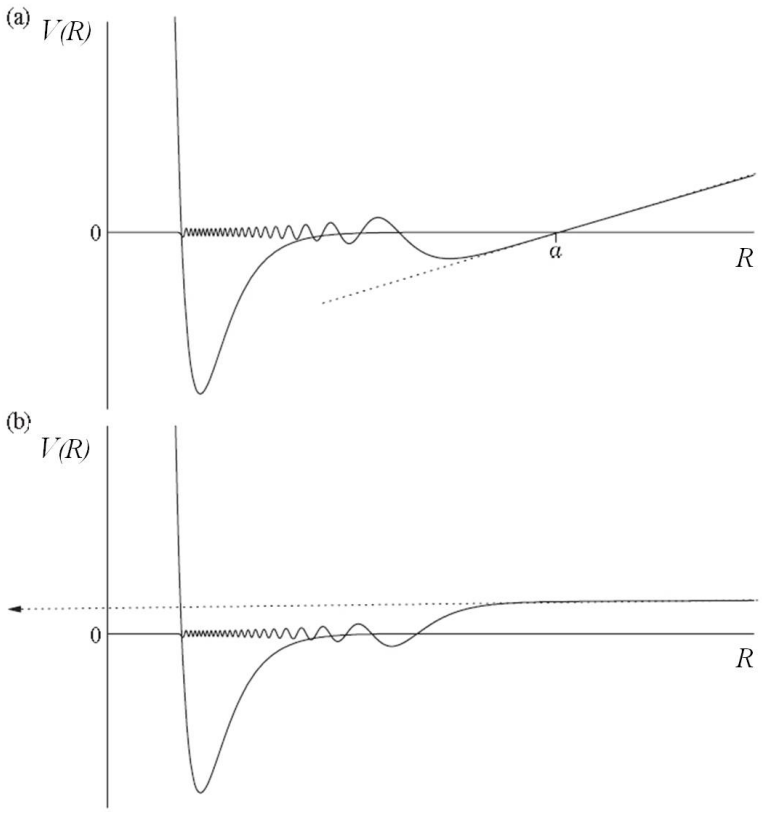

Figure 2.12: Modified figure originally from Ref. [73], wavefunctions $\Phi(R)$ (solid sinusoidal curves) for low energy scattering with positive scattering lengths (a) and negative scattering length (b). The dashed line shows the fit of $\Phi(R) = R\psi(R)$ to the large R or radiation zone part of the wavefunction, where $\psi(R)$ comes from Eq. (2.46). The scattering length is proportional to the dashed line's Y-intercept.

$$\sigma \approx 4\pi a^2. \tag{2.44}$$

The total ultracold cross section is equivalent to the surface area of the hard sphere with radius a. The quantum mechanical factor of four enhancement comes from the fact that matter waves can bend and "feel" the entire sphere's surface area, unlike classical hard spheres that only see the head on cross section [92]. Furthermore, this ultracold result applies to real potentials as well. As seen in the radiation zone of Fig. 2.11, the actual

wavefunction only differs from the equivalent hard-sphere wavefunction by a phase shift, meaning that the details of the potential well are insignificant in the ultracold regime.

Alternatively, if we started the ultracold quantum hard-sphere exercise knowing that only the s-wave ($l = 0$) partial wave contributes to the wavefunction, then using Eqs. (2.34) and (2.42) we could have initially reduced the TISE solution to

$$\psi(R)_{l=0} = A\left(j_0(kR) - \frac{j_0(ka)}{h_0^{(1)}(ka)} h_0^{(1)}(kR)\right) P_0[\cos(\theta)]. \tag{2.45}$$

Using the fact that kR is small over the range of interaction $0 < R < a$ then $j_0(kR) \approx 1$ and $h_0^{(1)}(kR) \approx 1/kR$, Eq. (2.45) can be further simplified to

$$\psi(R)_{l=0} \propto 1 - \frac{a}{R}, \tag{2.46}$$

which still meets the boundary condition $\psi(a,\theta) = 0$. The size of the effective hard sphere a associated with ultracold scattering is often called the "scattering length" and can be negative or positive, as seen in Fig. 2.12.

The partial wave phase shift When solving the TISE in the scattering region, it is useful to recast Eq. (2.34) in terms of the physically meaningful partial wave shift parameter δ_l. When the incident wave bounces off the repulsive hard-sphere like wall or centrifugal barrier, the probability must be conserved, thus the outgoing wave amplitude B and the incoming wave amplitude A obey $B = -A$. If we assume the effective potential is approximately zero for all points beyond the barrier then the waves are in phase with a node at the potential barrier. In 1D the wavefunction would have the form

$$\psi(x) = A\left(e^{ikx} - e^{ikx}\right) \quad \text{for } V = 0. \tag{2.47}$$

However, if there is a potential $V \neq 0$ within the scattering region, then the reflected wavefunction undergoes a relative phase shift 2δ, i.e., $B = Ae^{i2\delta}$, $\tan(2\delta) = B/A$ and $|B| = |A|$ still holds. With the potential localized over some finite scattering region, the 1D wavefunction becomes

$$\psi(x) = A\left(e^{ikx} - e^{i(2\delta - kx)}\right) \text{ for } V \neq 0, \tag{2.48}$$

where the factor of two is just conventional.

We can re-express the 3D TISE solution using the partial wave phase shift formalism by first noting that each partial wave l that is part of the incident plane wave e^{ikz} scatters independently with no change in amplitude. In the radiation zone the effective potential is zero (just a plane wave solution and $a_l = 0$). As we saw with Eq. (2.35) the wavefunction of the plane wave can be approximated as

$$\psi_l \overset{R\to\infty}{\approx} A\frac{(2l+1)}{2ikR}\left(e^{ikR} - (-1)^l e^{-ikR}\right) P_l[\cos(\theta)] \text{ for } V = 0 \text{ and } R \gg 1. \tag{2.49}$$

Just like in the 1D case, the outgoing (spherical) wave e^{ikr} acquires a phase shift from the scattering region. Thus ψ_l becomes

$$\psi_l \overset{R\to\infty}{\approx} A\frac{(2l+1)}{2ikR}\left(e^{i(kR+2\delta_l)} - (-1)^l e^{-ikR}\right) P_l[\cos(\theta)] \text{ for } V \neq 0. \tag{2.50}$$

By comparing the asymptotic form of the wavefunction from Eq. (2.35) with Eq. (2.50), we find that the partial wave amplitude a_l and the partial wave phase shift δ_l are related by

$$a_l = \frac{e^{i\delta_l}}{k}\sin(\delta_l) \text{ and } f(\theta) = \frac{1}{k}\sum_{l=0}^{\infty}(2l+1)e^{i\delta_l}\sin(\delta_l)P_l[\cos(\theta)]. \tag{2.51}$$

Substituting Eq. (2.51) into Eq. (2.34) gives the exact solution outside the scattering

zone as

$$\begin{aligned}\psi(R,\theta) &= A\sum_{l=0}^{\infty} i^l(2l+1)\left(j_l(kR)+ie^{i\delta_l}\sin(\delta_l)h_l^{(1)}(kR)\right)P_l[\cos(\theta)],\\ \text{where}\ \ \Phi_l(R) &= A\sqrt{4\pi(2l+1)}i^lR\left(j_l(kR)+ie^{i\delta_l}\sin(\delta_l)h_l^{(1)}(kR)\right).\end{aligned} \tag{2.52}$$

To cast the wavefunction in Eq. (2.50) in the asymptotic form that is typically used [68], we substitute Eq. (2.51) into Eq. (2.36), which simplifies to

$$\psi(R,\theta) \overset{R\to\infty}{\approx} A\sum_{l=0}^{\infty}\frac{i^l(2l+1)P_l[\cos(\theta)]}{kR}\sin(kr-\frac{l\pi}{2}-\delta_l). \tag{2.53}$$

Furthermore, by substituting Eq. (2.51) into Eq. (2.41) the cross section can be expressed in terms of the phase shift,

$$\sigma = \frac{4\pi}{k^2}\sum_{l=0}^{\infty}(2l+1)\sin^2(\delta_l). \tag{2.54}$$

Again, the procedure is to first solve the TISE for the specific potential $V(R)$ in the scattering region. Then by matching the wavefunctions at the boundaries between regions, the partial wave phase shifts can be determined and subsequently the scattering cross section.

For example, if we return to the quantum hard sphere case, we find that comparison of Eqs. (2.51) and (2.42) for a_l imply that the partial wave phase shift is $\delta_l = \tan^{-1}[j_l(ka)/n_l(ka)]$. In the ultracold limit ($ka \ll 1$ and for $l=0$) we have $\tan(\delta_0) = -ka \approx \pm\sin(\delta_0) \approx \delta_0$. As expected, substituting this result into Eq. (2.54) gives back our earlier result for the ultracold cross section, Eq. (2.44). Furthermore, by substituting $\delta_0 = ka$ into Eq. (2.54) and again assuming $k(r-a) \ll 1$, we find that the asymptotic wavefunction reduces to the previous result, Eq. (2.46).

Another instructive example is the scattering states $E > 0$ of the attractive finite well potential

$$V_{\mathrm{w}}(R) = \begin{cases} \infty, & \text{if } R = 0 \\ -V_0, & \text{if } r_0 \geq R > 0 \\ 0, & \text{if } R > r_0 \end{cases}, \tag{2.55}$$

which looks like a crude interatomic potential. This potential is plotted as the the black curve in Fig. 2.13. Using Eq. (2.52), we can write the lth radial solution as

$$\Phi_l(R) = \sqrt{4\pi(2l+1)}i^l R \begin{cases} A_l j_l(\kappa R), & \text{if } r_0 \geq R \geq 0 \\ B_l j_l(kR) + ie^{i\delta_l}\sin(\delta_l)h_l^{(1)}(kR), & \text{if } R > r_0 \end{cases} \tag{2.56}$$

inside the scattering region and outside the scattering region, respectively. We have dropped the spherical Hankel function because it is poorly behaved at the origin where the boundary conditions require a node. Also, in the scattering region $R < r_0$ we use the wavenumber $\kappa = \sqrt{2m(E+V_0)/\hbar^2}$.

We can determine the phase shift by matching the wavefunction ϕ_l and its first derivative ϕ_l' with respect to R evaluated at $R = r_0$. It is convenient to take the ratio of these conditions

$$\begin{aligned} \frac{\Phi_{l,\, r\leq r_0}(R=r_0)}{\Phi'_{l,\, r\leq r_0}(R=r_0)} &= \frac{\Phi_{l,\, r>r_0}(R=r_0)}{\Phi'_{l,\, r>r_0}(R=r_0)} \implies \\ \frac{r_0 j_l(\kappa r_0)}{[Rj_l(kR)]'\Big|_{R_0}} &= \frac{r_0 j_l(\kappa r_0) + r_0 ie^{i\delta_l}\sin(\delta_l)h_l^{(1)}(kr_0)}{[Rj_l(kR)]'\Big|_{R_0} + ie^{i\delta_l}\sin(\delta_l)\left[Rh_l^{(1)}(kR)\right]'\Big|_{R_0}}. \end{aligned} \tag{2.57}$$

In principle we can solve for any partial wave phase shift using Eq (2.57), for simplicity let's consider the s-wave scattering ($l = 0$), which by multiplying both the numerator and

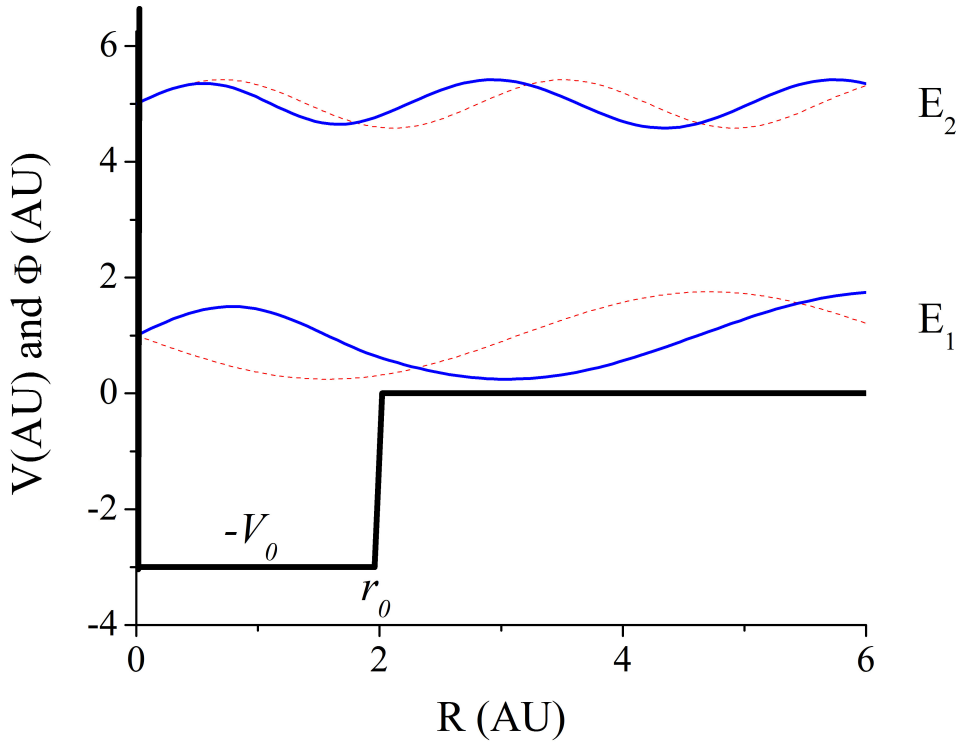

Figure 2.13: Black line shows finite attractive square well potential described by Eq. (2.55). Each dashed red line shows the free radial s-wave solution $\sim \sin(kR)$ at two different energies $E_2 = 5E_1$. The solid blue lines shows the exact radial s-wave solution described by Eq. (2.59), at the corresponding energies.

denominator of the right-hand-side of Eq. (2.57) by its denominator's complex conjugate simplifies to

$$\frac{\tan(\kappa_0)}{\kappa} = \frac{\tan(kr_0+\delta_0)}{k} \implies \delta_0 = -kr_0 + \tan^{-1}\left[\frac{k}{\kappa}\tan(\kappa r_0)\right], \tag{2.58}$$

thus allowing us to solve for the phase shift and the s-wave partial scattering cross section using Eq. (2.54). We also note that in the deep well or ultracold limit $E \ll V_0 \implies k \ll \kappa$ the phase shift can be approximated as $-kr_0$. Armed with the phase shift and using the continuity of the wavefunction at r_0, we can solve for B_0 in terms of the remaining nor-

malization constant A_0. The exact s-wave radial solution simplifies to

$$\Phi_0(R) = \begin{cases} A_0 \frac{\sin(\kappa R)}{\kappa}, & \text{if } r_0 \geq R \geq 0 \\ A_0 \sin(kr_0 + \delta_0) \frac{\sin(\kappa r_0)}{\kappa \sin(kr_0 + \delta_0)}, & \text{if } R > r_0 \end{cases}. \tag{2.59}$$

Figure 2.13 shows some plots of the unnormalized radial free wave solution (dashed red lines) for s-wave scattering at two energies and the corresponding exact solution at the same two energies (solid blue lines).

Scattering of identical particles Thus far we have considered the scattering of two non-identical species, like the scattering of an ion and a neutral atom. However, in this section we will briefly mention the consequences of scattering reactions between identical particles each with total half integer spin (e.g., ^{40}K -^{40}K) called fermions or total integer spin called bosons (e.g., Na - Na).

When describing the total wavefunction of identical particles, the wavefunction cannot be a simple outer product state, but rather a linear combination of product states. This is because we cannot tell which (identical) particle is in ψ_1 or ψ_2, so the wavefunction must be such that each particle has an equal probability of being in each state, namely that

$$\psi(R_I, R_N) = \begin{cases} \psi_1(R_I)\psi_2(R_N) & \text{not identical} \\ \frac{1}{\sqrt{2}}\left[\psi_1(R_I)\psi_2(R_N) + \psi_2(R_I)\psi_1(R_N)\right], & \text{identical bosons} \\ \frac{1}{\sqrt{2}}\left[\psi_1(R_I)\psi_2(R_N) - \psi_2(R_I)\psi_1(R_N)\right], & \text{identical fermions,} \end{cases} \tag{2.60}$$

where $R = |R_I - R_N|$. The parity or exchange operator O (which commutes with the TISE, allowing for simultaneous diagonalization), results in no change on the bosonic wavefunction and these wavefunctions are called symmetric. The linear combination

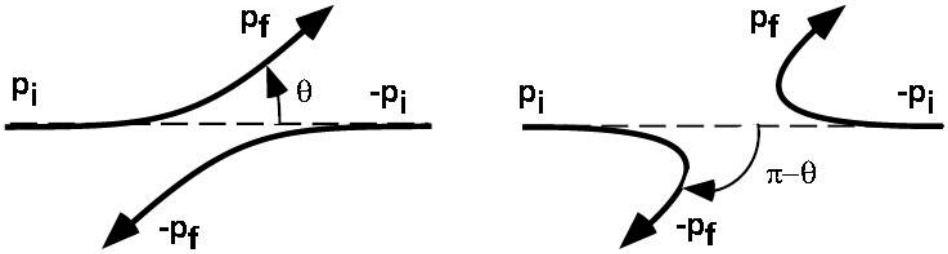

Figure 2.14: Originally from Ref. [98], showing the indistinguishable final scattering outcome for two identical particles scattering in the COM reference frame with initial momentum P_i and final momentum P_f.

describing fermionic wavefunctions are called antisymmetric, since they pick up an overall factor of -1 under interchange in Eq. (2.62).

Equivalently for scattering problems, we cannot tell which particle has scattered by an angle θ vs. scattering $\pi-\theta$ (as seen in Fig. 2.14) and the symmetry requires that each outcome be equally probable, namely that $\psi_l(R) = \pm\psi_l(-R)$. The asymptotic form of the symmetric/antisymmetirc wavefunction [98] can be written as

$$\psi(R) \sim \frac{1}{\sqrt{2}}\left\{e^{ikz} \pm e^{-ikz} + [f(\theta) \pm f(\pi-\theta)]\frac{e^{ikR}}{R}\right\}. \tag{2.61}$$

Integrating $D(\theta) = |f(\theta) \pm f(\pi-\theta)|^2$ gives the cross sections

$$\begin{aligned} \sigma_B &= \frac{8\pi}{k^2}\sum_{l\ \text{even}}^{\infty}(2l+1)\sin^2(\delta_l), \ \text{ for identical bosons} \\ \sigma_F &= \frac{8\pi}{k^2}\sum_{l\ \text{odd}}^{\infty}(2l+1)\sin^2(\delta_l), \ \text{ for identical fermions.} \end{aligned} \tag{2.62}$$

Upon integrating $D(\theta)$, we find that only the even partial waves survive and contribute to the scattering of identical bosons and only the odd partial waves contribute to the scattering of identical fermions. This is a consequence of the parity of the Legendre polynomials $P_l(-x) = (-1)^l P_l(x)$, the orthogonality of the Legendre polynomials, and the fact that

$-\cos(\theta) = \cos(\pi - \theta)$. In the end, Eq. (2.62) has a factor of 2 enhancement in the size of the cross sections, as compared to Eq. (2.54) for the non-identical particle cross section. Physically, this enhancement is due to constructive partial wave interference. Also, s-wave scattering does not exist for identical fermion collisions.

Semiclassical approximation For large values of l (e.g., for $l > 50$ for the Na^+- Na system [68]) the centrifugal barrier prevents the scattering region from affecting the phase shifts and the long-range ion-neutral potential determines the phase shifts. Within this so-called semiclassical regime for $l \gg 1$ it is appropriate to use the WKB approximation [92, 99], where we make the ansatz that the scattering wavefunction outside the scattering region has the form

$$\psi_{\mathrm{WKB}}(R) = A(R)e^{\pm i\phi(R)}, \tag{2.63}$$

where A is the amplitude and ϕ is a phase. Both the amplitude and phase may depend on R and the general solution is a linear combination of the right moving $+$ and left moving $-$ wavefunctions. We can also assume that the effective potential varies slowly compared to the equivalent one body de Broglie wavelength, thus $d^2A/dR^2 \approx 0$.

We can rewrite the radial TISE Eq. (2.30) in terms of the classical momentum

$$p = \sqrt{k^2 - \frac{2\mu V(R)}{\hbar^2} - \frac{l(l+1)}{R^2}} \tag{2.64}$$

as

$$\frac{d^2\psi_{\mathrm{WKB}}(R)}{dR^2} + \frac{p^2}{\hbar^2}\psi_{\mathrm{WKB}}(R) = 0 \tag{2.65}$$

Substituting our ansatz Eq. (2.63) into the TISE, with the $+i\phi$ phase, we get

$$\frac{d^2A}{dR^2} - A\left(\frac{d\phi}{dR}\right)^2 + i\left[2\frac{dA}{dR}\frac{d\phi}{dR} + A\frac{d^2\phi}{dR^2}\right] = -\frac{p^2}{\hbar^2}A. \tag{2.66}$$

This can be divided into two equations, one for the real part and one for the imaginary part. The slowly varying amplitude approximation allows us to drop the A'' term and the two first order differential equations lead to the results

$$A = \frac{C}{\sqrt{\frac{d\phi}{dR}}}, \quad \frac{d\phi}{dR} = \pm\frac{p}{\hbar}, \quad \text{and} \quad \phi = \frac{1}{\hbar}\int p(R)\,dR, \tag{2.67}$$

where C is a real constant. Therefore, the general solution becomes

$$\psi_{\mathrm{WKB}}(R) = \frac{C}{\sqrt{p(R)}}\mathrm{Exp}\left[\frac{1}{\hbar}\int p(R)\,dR\right] + \frac{D}{\sqrt{p(R)}}\mathrm{Exp}\left[\frac{-1}{\hbar}\int p(R)\,dR\right]. \tag{2.68}$$

Following the treatment of Ref. [99], we need to match the wavefunction on the left and right side of the classical turning point R_0, where $p \to 0$ at $V_{\mathrm{eff}}(R_0) = E$. We make the approximation that at R_0 the potential is approximately linear $V \approx \alpha(R - R_0)$, which leads to the matching condition $A = -iD\exp(i\phi/4)$ and $B = iD\exp(-i\phi/4)$, where D is a normalization constant. Now, the WKB wavefunction goes like

$$\begin{aligned}\psi_{\mathrm{WKB}}(R) &\sim \sin\left(\frac{\pi}{4} + \int_{R_0}^{R}[p(R) - k + k]\,dR\right) \\ &\sim \sin\left(\frac{\pi}{4} + \int_{R_0}^{R}[p(R) - k]\,dR + k[R - R_0]\right).\end{aligned} \tag{2.69}$$

To create a factor of kR in the argument of the sine function, we have added a factor of $0 = k - k$. We are interested in the asymptotic form of Eq. (2.69), so we let the upper bound $R \to \infty$. By comparing the argument of the sine functions between the asymptotic form of the WKB wavefunction in Eq. (2.69) with the asymptotic form of the previously derived scattering wavefunction of Eq. (2.53), the phase shift must be

$$\delta_l^V = -kR_0 + \frac{\pi}{4} - \frac{l\pi}{2} + \int_{R_0}^{\infty}\sqrt{k^2 - \frac{2\mu V(R)}{\hbar^2} - \frac{l(l+1)}{R^2}} - k\,dR \tag{2.70}$$

We are interested in the relative phase shift between the plane wave solution $V = 0$ and that of the solution with the potential $V \neq 0$, namely $\delta_l = \delta_l^V - \delta_l^{V=0}$. Therefore, using Eq. (2.70) as the definition of each absolute phase shift, we find that the relative phase shift becomes

$$\delta_l = \int_{R_0}^{\infty} \sqrt{k^2 - \frac{2\mu V(R)}{\hbar^2} - \frac{l(l+1)}{R^2}} - \sqrt{k^2 - \frac{l(l+1)}{R^2}}\, dR, \tag{2.71}$$

as stated in Ref. [100].

In the limit of large l, we can use the approximation that $l(l+1) \approx (l+1/2)^2$ and by expanding [101] about $2\mu V(R)/\{\hbar^2[k^2 - (l+1/2)^2]\}$, the the phase shift can be approximated as

$$\delta_l \overset{l\to\infty}{\approx} -\frac{\mu}{\hbar^2} \int_{R_0}^{\infty} \frac{V(R)}{\sqrt{k^2 - (l+\frac{1}{2})^2/R^2}}\, dR, \tag{2.72}$$

where $V(R)$ is defined by Eq. (2.22) for an ion-neutral collision [100]. Integration yields

$$\delta_l \overset{l\to\infty}{\approx} \frac{\pi\mu^2 C_4 E}{4\hbar^2 l^3} \tag{2.73}$$

for the phase shift [68]. In the last step we used the fact that for large l the classical turning point is approximately in the intermediate region, meaning that we can make the substitution $R_0 \approx \sqrt{(l+1/2)^2/E}$.

To approximate the cross section, we break up the discrete sum in Eq. (2.54) into two integrals, one from zero to L and the other from L to infinity. The partial wave L must be a number large enough so that Eq. (2.73) is valid. The resulting total cross section is

$$\begin{aligned} \sigma &\overset{l\to\infty}{\approx} \frac{4\pi}{k^2}\left(\int_0^L l\, dl + \int_L^{\infty} 2l\delta(l)^2\, dl\right) \\ &\overset{l\to\infty}{\approx} \frac{2\pi}{k^2}L^2 + \frac{4\pi}{k^2}\int_L^{\infty} 2l\left(\frac{\pi\mu^2 C_4 E}{4\hbar^2 l^3}\right)^2 dl \\ &\overset{l\to\infty}{\approx} \frac{2\pi}{k^2}L^2(1+\delta_L^2), \end{aligned} \tag{2.74}$$

where we have approximated that for $l < L$ the $\sin^2(\delta_l)$ averages out to $1/2$, so $(2l+1)\sin^2(\delta_l) \approx l$. We have also assumed that for $l > L$ the phase shifts are small and $(2l+1)\sin^2(\delta_l) \approx 2l\delta_l^2$. A reasonable choice for L is $\delta_L = \pi/4$ or $\sin^2(\delta_l) = 1/2$ as described in Ref. [68]. Using Eqs. (2.73) and (2.74) and choosing $\delta_L = \pi/4$, the total ion-neutral semiclassical cross section can be written as

$$\sigma_{\text{tot}} \overset{l\to\infty}{\approx} \pi \left(\frac{\mu C_4^2}{\hbar^2}\right)^{1/3} \left(1 + \left[\frac{\pi}{4}\right]^2\right) E^{1/3} \equiv C_{\text{tot}} E^{1/3}, \tag{2.75}$$

The total cross section formula has a $E^{1/3}$ power-law collision energy dependence that is due to the R^{-4} long range potential. The total scattering constant C_{tot} scales like $(\mu {C_4}^2)^{1/3}$. The expression in Eq. (2.75) is incorrectly identified as the semiclassical elastic scattering cross section σ_{el} in Refs. [68, 71], but is correctly identified as the total (elastic + charge exchange) cross section in Ref. [72], where $\sigma_{\text{tot}} = \sigma_{el} + \sigma_{\text{ce}}$. The distinction will be discussed further in Sec. 2.2.3.

As we did with Eq. (2.27) for the Langevin cross section, we write the rate coefficient for the total semiclassical ion-neutral (ion-atom) cross section [71] in atomic units as

$$k_{\text{ia}} = \langle \sigma_{\text{tot}} v \rangle = \int_0^\infty \sigma_{\text{tot}}(E) f_{\text{MB}}(E)\, dE = C_{\text{tot}} \frac{8}{\pi\mu} \Gamma\left(\frac{5}{3}\right) (k_B T_I)^{1/6}, \tag{2.76}$$

where Γ is the gamma function, k_B is the Boltzmann constant, and T_I is the temperature of the ion cloud.

In this section we have solved the TISE and determined the partial wave scattering wavefunction, which is characterized by a partial wave phase shift associated with the scattered wave's forward scattering amplitude. The phase shift determines the differential and total scattering cross section. As illustrative examples for finding the phase shift, we have considered ultracold s-wave scattering for a hard sphere and finite square well potential. We have also considered the consequences of identical particle scattering. Last,

we determined the phase shifts, the cross section as a function of collision energy E, and the rate coefficient for the semiclassical ion-neutral collisions.

2.2.2 Molecular potential for H_2^+

Variational method for finding H_2^+ potential Accurate knowledge of the interatomic or molecular potential within which ions and neutral atoms scatter is necessary for solving the TISE in the scattering region. Knowing these potentials allows theorists to determine the partial phase shifts δ_l and scattering cross sections σ using the formalism developed in the previous section. To illustrate how these molecular potentials are calculated, we will consider the simplest possible case as an illustrative example – the molecular electronic Hamiltonian for the H_2^+. Although the H_2^+ system can be solved exactly in elliptical coordinates, using the variational approximation to solve this system is more illustrative, since this method can be applied to more complicated systems.

Our goal is to determine the potential energy $U_e(R)$ seen by the nuclei of the colliding H^+- H system, which is the eigenvalue of the diatomic molecular electronic Hamiltonian $\hat{H}_e$ for the H_2^+ molecule. The coordinates that describe the diatomic molecule are defined in Fig. 2.15. A diatomic molecule in the COM reference frame with N_e electrons having mass m_e, charge q, and two nuclei with charge q and mass m_I and m_N, respectively, has the Hamiltonian operator

$$\hat{H} = -\underbrace{\frac{\hbar}{2m_e}\sum_i^{N_e}\nabla_{r_i}^2}_{\hat{T}_e} + V(r,R) - \underbrace{\frac{\hbar}{2\mu}\nabla_R^2}_{\hat{T}_{\text{nuc}}} \tag{2.77}$$

In writing $\hat{H}$ we have assumed the Born-Oppenheimer (BO) approximation to be valid. In doing so, we approximate that the fast electronic motion is instantaneous relative the slower nuclear motion. Therefore, the approximately frozen internuclear separation R is treated more like a parameter than a variable. As a consequence of the BO approximation,

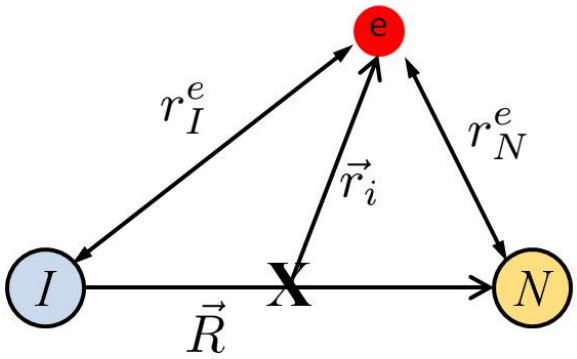

Figure 2.15: Illustration of the diatomic ion-neutral molecule with atomic core nuclei I and N and a single electron, just like the H_2^+ system. The COM is marked with an X. The vector between the COM and the ith electron is $\vec{r}_i$ and the relative vector between the nuclei is $\vec{R}$. The distance between the electron and each atomic nuclei are also shown.

we have already dropped cross terms that go like $\nabla_{r_i}\nabla_{r_j}$ or $\nabla_R\nabla_{r_i}$ in Eq. (2.77). Also, we can treat the nuclear motion $\hat{T}_{\text{nuc}}$ as a perturbation, making the unperturbed Hamiltonian

$$\hat{H}_0 = \hat{H}_e = -\frac{\hbar}{2m_e}\nabla_{r_i}^2 + \frac{q^2}{4\pi\varepsilon_0 r_I^e} + \frac{q^2}{4\pi\varepsilon_0 r_N^e} - \frac{q^2}{4\pi\varepsilon_0 R} \tag{2.78}$$

for the H_2^+ system. Thanks to the BO approximation we can construct a separable solution $\Psi = \chi_{\text{nuc}}\phi_e$ to Eq. (2.77), specifically

$$\hat{H}\Psi = (\hat{H}_e + \hat{T}_{\text{nuc}})\chi_{\text{nuc}}\phi_e = \underbrace{(U_e(R) + \hat{T}_{\text{nuc}})}_{\hat{H}_{\text{nuc}}}\chi_{\text{nuc}}\phi_e = (U_e(R) + E)\chi_{\text{nuc}}\phi_e. \tag{2.79}$$

Let us focus our attention on $\hat{H}_e\phi_e = U_e(R)\phi_e$, since we are interested in determining $U_e(R)$. We will make the ansatz that $\phi_e = C_I\psi_I + C_N\psi_N$, a linear combination of atomic orbitals (LCAO). Using the variational method [92], we can write the energy as

$$U_e(R) = \frac{\langle\phi_e|\hat{H}_e|\phi_e\rangle}{\langle\phi_e|\phi_e\rangle} = \frac{C_I^2 E_{\text{II}} + C_N^2 E_{\text{NN}} + 2C_I C_N E_{\text{IN}}}{C_I^2 E_{\text{II}} + C_N^2 E_{\text{NN}} + 2C_I C_N \mathscr{S}}, \tag{2.80}$$

where

$$\begin{aligned} E_{\rm II} = E_{\rm NN} &\equiv \langle \psi_I | \hat{H}_e | \psi_I \rangle \\ E_{\rm IN} = E_{\rm NI} &\equiv \langle \psi_I | \hat{H}_e | \psi_N \rangle \cdot \\ \mathscr{S} &\equiv \langle \psi_I | \psi_N \rangle \end{aligned} \tag{2.81}$$

If we minimize the energy $U_e(R)$ with respect to both C_I and C_N, we get the secular equation

$$\begin{vmatrix} E_{\rm II} - U_e & E_{\rm IN} - U_e \mathscr{S} \\ E_{\rm IN} - U_e \mathscr{S} & E_{\rm II} - U_e \end{vmatrix} = 0, \tag{2.82}$$

whose eigenvalues are

$$U_e^g = \frac{E_{\rm IN} - E_{\rm II}}{\mathscr{S} - 1} \text{ and } U_e^u = \frac{E_{\rm IN} + E_{\rm II}}{\mathscr{S} + 1} \tag{2.83}$$

with corresponding wavefunctions

$$\phi_e^g = \frac{\psi_I + \psi_N}{\sqrt{2(1+\mathscr{S})}} \text{ and } \phi_e^u = \frac{\psi_N - \psi_I}{\sqrt{2(1-\mathscr{S})}}, \tag{2.84}$$

respectively. In general the electron is in a superposition of these two states. The terms g and u refer to the German words "gerade" and "ungerade", which connote "even" (symmetric) and "odd" (antisymmetric) wavefunctions with respect to interchanging nucleus I and N, respectively.

In the separated atom limit $R \to \infty$ these eigenvalues are degenerate, since the ion and atom are not identical and the electron is clearly part of neutral atom N. However, when the atom and ion approach each other the single electron is in a superposition of orbits about both nuclear cores. This leads to the degeneracy being broken as R decreases. The lower gerade or bonding energy state is associated with constructive in-phase interference of the LCAO. The higher ungerade or antibonding energy state is associated with the destructive

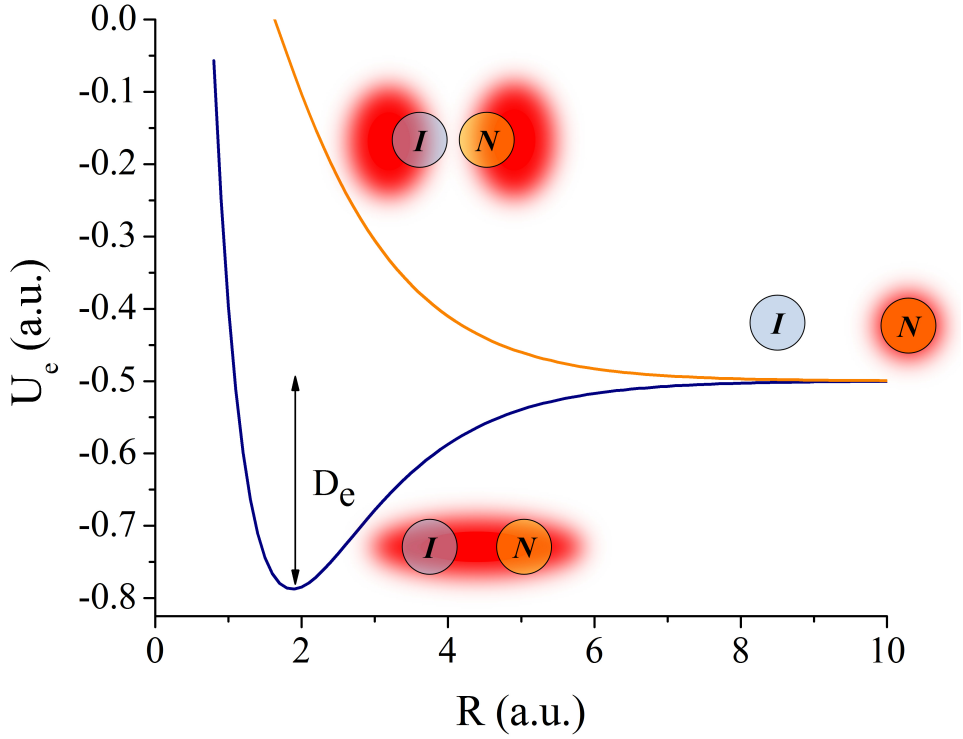

Figure 2.16: Plot of interatomic BO molecular potentials $U_e^g(R)$ (navy) and $U_e^u(R)$ (orange) for the H_2^+ system in atomic units with illustrations of the electron cloud wavefunction (red) for the separated atom and ion, antibonding, and bonding wavefunctions.

out-of-phase interference of the LCAO. The energy difference between the bonding and antibonding states is called the exchange energy.

As mentioned earlier, by converting the operators in our Hamiltonian to elliptical coordinates [102] the integrals in Eq. (2.81) can be evaluated using (1s) atomic hydrogen wavefunction for ψ_I and ψ_N, which determines the solutions to the two lowest energy electronic states in Eq. (2.84) as a function of interatomic distance R for the H_2^+ system. Figure 2.16 shows that solution for U_e^g and U_e^u for the H_2^+ system. The result in Fig. 2.16 has a dissociation energy D_e that is off from the exact value by about 50%. To improve on the accuracy of our variational calculation one must include higher atomic orbitals in the

LCAO leading to more accurate ground state energies and fairly inaccurate excited state energies.

2.2.3 Charge-exchange vs. elastic cross sections

Using the BO approximation, we determined that the molecular wavefunction could be written as a separable solution Ψ involving the product state of a nuclear wavefunction χ_{nuc} and electronic wavefunction ϕ_e. If we use the radiation zone asymptotic scattering wavefunction of Eq. (2.37) as χ_{nuc}, we can define the g or u total wavefunction as

$$\Psi_{\text{sc}}^{g/u} \sim \left(\chi_{\text{in}} + \chi_{\text{out}}^{g/u}\right) \phi_e^{g/u} = e^{ikz}\phi_e^{g/u} + \frac{e^{ikR}}{R} f^{g/u}\phi_e^{g/u}, \tag{2.85}$$

where "in" and "out" refer to the incoming plane wave and the outgoing spherical waves. The forward scattering amplitude f^g or f^u each have their own associated phase shift δ_l^g and δ_l^u (respectively), which can be calculated with knowledge of their respective potentials $U_e^{g/u}$ using the methods discussed in Sec. 2.2.1.

If we prepare the system with the electron on the neutral atom N (in the separated atom limit), then the incoming total wavefunction would go like $\sim \chi_{\text{in}}\left(\phi_e^g + \phi_e^u\right) = e^{ikz}\psi_N$ according to Eqs (2.84) and (2.86). The outgoing wave would also be a linear combination of the g and u product nuclear-electronic states. Putting that all together we get

$$\begin{aligned} \Psi_{\text{sc}} &\sim e^{ikz}\psi_N + \frac{e^{ikR}}{R}\left[f^g\phi_e^g + f^u\phi_e^u\right] \\ &\sim e^{ikz}\psi_N + \frac{e^{ikR}}{R}\left[\left(f^g + f^u\right)\psi_N + \left(f^g - f^u\right)\psi_I\right]. \end{aligned} \tag{2.86}$$

If the outgoing wave goes into the state ψ_N, this is considered elastic scattering reaction, because nothing was changed and kinetic energy was conserved. Therefore, the elastic differential cross sections $D_{\text{el}}(\theta) = |f^g + f^u|^2$. If the outgoing scattering channel is ψ_I, then the electron was transfered to the ion, which constitutes a charge-exchange event. The

charge-exchange process is considered resonant if the internal states are exchanged without changing the total internal energy [40].

According to Eq. (2.86) the differential cross section for charge exchange is $D_{\rm ce}(\theta) = |f^g - f^u|^2$ and integrating $D_{\rm ce}(\theta)$ over the solid angle yields the charge-exchange total cross section

$$\sigma_{\rm ce} = \frac{\pi}{k^2} \sum_{l=0}^{\infty} (2l+1) \sin^2(\delta_l^g - \delta_l^u). \tag{2.87}$$

2.2.4 Molecular potentials and cross sections for Na_2^+ and $NaCa^+$

Na_2^+ potential curves and cross sections R. Côté and A. Dalgarno have performed a fully quantal calculation of the scattering cross sections on the Na^+- Na (ground state) system using *ab initio* [103] data from 5.0 to 20.0 Bohr in the two lowest energy potential curves [68] shown in Fig. 2.17. The short range potential is an exponential wall and the long-range potential matches Eq. (2.22) with the addition of the exchange energy splitting the g and u states.

The fully quantal calculations use the asymptotic form of the radial part of the scattering wavefunction Eq. (2.53) to determine the phase shifts and subsequently the total and charge exchange quantal cross section using Eq. (2.54) and Eq. (2.87), respectively. These data are compared to the semiclassical power-law cross section model for large numbers of partial waves using Eq. (2.54) and the classical Langevin charge-exchange power-law cross section model using Eq. (2.26). By fitting the power-law model to the quantal data [as seen in Figs. 2.18 and 2.19], the values $C_{\rm tot} = 4174$ a.u. and $C_{\rm ce} \approx \pi\sqrt{2C_4}/4 \approx 14.4$ a.u. were determined [68]. The fitted value for $C_{\rm tot}$ is very close to the value calculated using the anaylitical model described by Eq. (2.75), which predicts $C_{\rm tot} = 4183$ a.u.

Comparison between the fully quantal and semiclassical data show excellent agreement

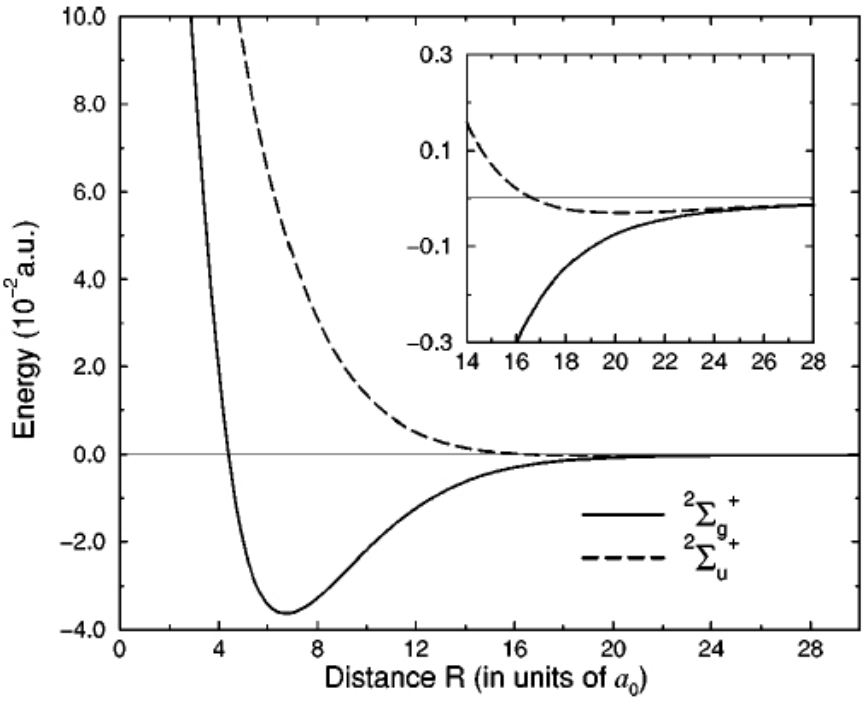

Figure 2.17: Originally from Ref. [68], shows lowest two molecular potential curves for the Na_2^+ system.

in the cold and low-energy regime, as seen in Fig. 2.18. Not surprisingly, the semiclassical approximation in Fig. 2.18 fails at ultracold energies $E < 10^{-12}$ a.u., where only a few partial waves contribute to the total cross section. Due to the stronger ion-neutral long range interaction, the Na^+- Na cross sections are orders of magnitude larger than the Na - Na cross sections, also shown in Fig. 2.18. In Sec. 6.2, we report on measurements of the total Na^+- Na cross section [40] that show good agreement with the semiclassical and fully quantal treatment discussed here [68].

The resonant charge-exchange cross section shows good agreement with the classical Langevin model up to a factor of four. It is not surprising that the Langevin cross section overestimates the charge-exchange, since it assumes 100% efficiency when the ion-neutral pair have an impact parameter less than the critical value b_0. Furthermore, the factor of

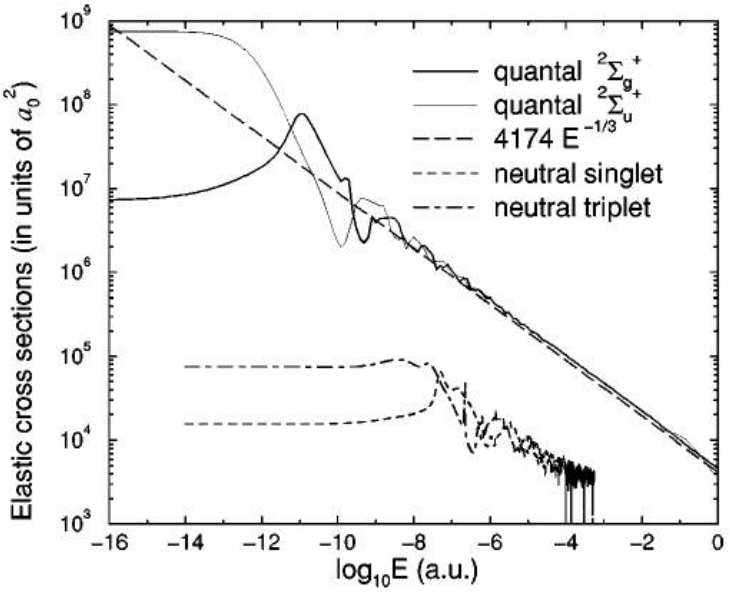

Figure 2.18: Originally from Ref. [68], shows the (incorrectly labeled) total (elastic + charge-exchange) cross section as a function of the log of the collision energy for the Na_2^+ system. The semiclassical result from Eq. (2.75) fits the quantal calculations well over a wide energy range.

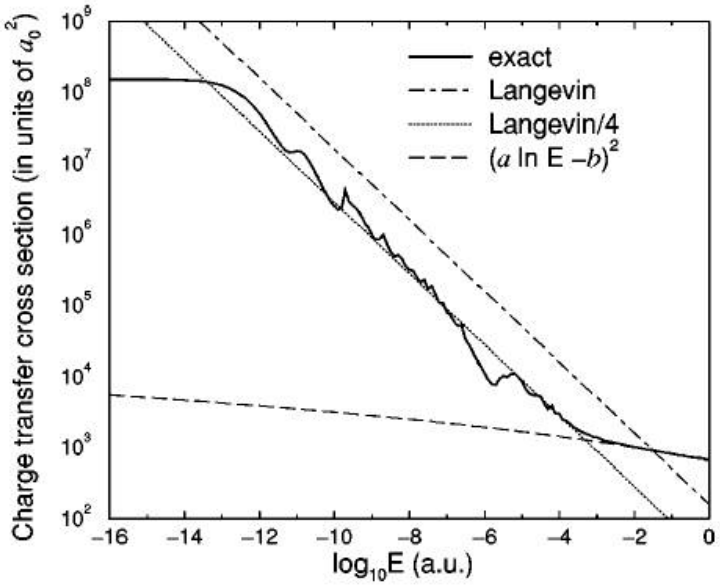

Figure 2.19: Originally from Ref. [68], shows the charge-exchange cross section as a function of the log of the collision energy for the Na_2^+ system. The classical Langevin model Eq. (2.26) fits the quantal calculations well, up to a factor of four.

four may be due to the ratio between a classical hard sphere cross section Eq. (2.26) and the quantum (surface area) hard sphere cross section Eq. (2.44), which includes interference effects. Also, Côté and Dalgarno found that the charge-exchange cross section is orders of magnitude smaller than the total cross section, so the distinction between elastic and total cross section is negligible over the energy ranges considered in Ref. [68].

$NaCa^+$ potential curves In Ref. [39] we presented some preliminary theoretical BO molecular potential curves that were calculated by H. Michels and S. Banerjee shown here in Fig. 2.20. Paraphrasing Ref. [39], the ground and low lying excited states in $(NaCa)^+$ were calculated using the equation of motion coupled cluster (EOM-CCSD) method. In the case of $(NaCa)^+$, the valence space consists of two electrons, and CCSD theory is equivalent to full configuration interaction (FCI). The core electrons have been efficiently described by an effective-core potential (ECP) along with a core polarization potential (CPP), as discussed in [104, 105]. Basis sets corresponding to the ECP for Na were obtained from [106], while those for Ca were taken from [107].

In the experiments reported in Ref. [39] and Sec. 6.1 of this dissertation, we were surprised to find a significant Ca^+- Na charge-exchange pathway given our earlier theoretical predictions [71] of a weak radiative charge-exchange rate (only one exchange event every couple of hours at 1 mK with MOT densities $\sim 10^{10}$ cm^{-3}) between the $A\,^1\Sigma^+$ state and the $X\,^1\Sigma^+$ state shown in Fig. 1.4. The earlier theoretical work also predicted total cross sections $C_{\rm tot} = 5310$ a.u. for the $A\,^1\Sigma^+$ state and $C_{\rm tot} = 5070$ a.u. for the $a\,^3\Sigma^+$ state [71], by again fitting fully quantal scattering data to the power-law formula in Eq. (2.75).

It appears that the process we observed in Ref. [39] most likely uses the entrance channel $Ca^+(4s) + Na^*(3p)$, which has a collision barrier (~ 0.17 eV) at large internuclear distance $R \sim 11$ Bohr. The neighboring state D with the asymptote $Na^+ + Ca(4\,^1P)$ can be

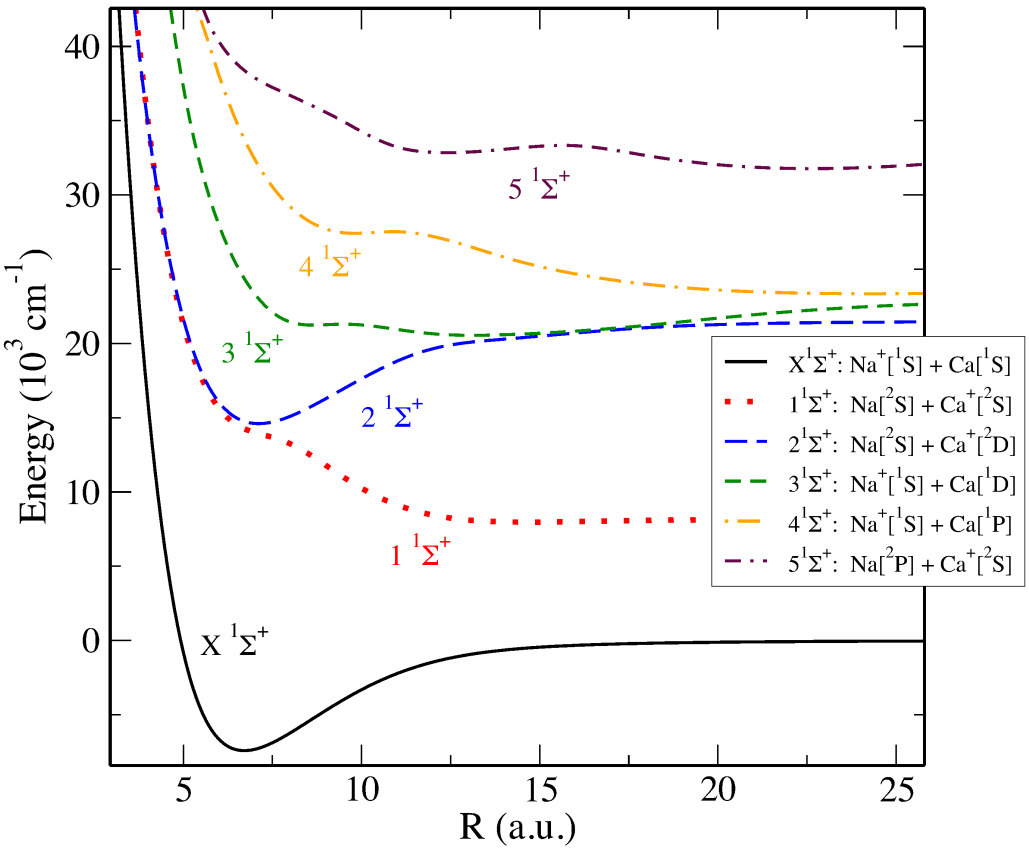

Figure 2.20: Originals from Ref. [39], interatomic molecular potential curves for the $NaCa^+$ system.

populated via an avoided crossing (near 10 Bohr) from the entrance quasimolecular state of $Ca^+ + Na(3p)$, as seen in Fig. 2.20.

In conclusion, we have developed the underlying theory for scattering reactions in both the classical and quantum regimes, allowing us to compare theoretically predicted rates with experiments involving cold ion-neutral collisions within the hybrid trap apparatus. Specifically, we will discuss the preliminary Ca^+- Na charge-exchange rate measurements [39] in Ch. 6 and some of the future measurements on this system in Ch. 7. In Ch. 5 we will utilize the theoretically predicted cross sections to perform simulations of

sympathetic cooling for both the Ca^+- Na and Na^+- Na system [37] and compare with sympathetic cooling experiments [38]. Furthermore, in Ch. 6 we will compare quantitative measurements of low-energy Na^+- Na total collision rates [40] with the semiclassically predicted rates presented earlier in this section [68].

Chapter 3

Interactions of atoms with light

In Ch. 1, we discussed our novel hybrid ion-neutral trap apparatus used to experimentally study the cold ion-neutral scattering interaction, whose theoretical treatment was the subject of Ch. 2. However, the cooling and trapping of these ions and atoms within the hybrid apparatus is primarily based upon their interaction with electromagnetic radiation, specifically laser light. Furthermore, the scattering reactions themselves can be manipulated by preparing atoms or ions in specific electronic states via absorption or emission of laser light. Clearly, understanding the matter-light interaction is crucial to the discussion of the experiments in Chs. 4 – 7. In this chapter we will outline the fundamental classical and quantum physics associated with atomic matter-light interaction.

3.1 The atom

3.1.1 Hydrogenic atom

Non-relativistic hydrogenic atom We would like to characterize a hydrogen-like valence electron's energy eigenvalues and wavefunctions. We begin with the non-

relativistic Hamiltonian of the hydrogenic (single-electron atom) in the COM reference frame

$$H_{\text{tot}} = \frac{\hat{p}^2}{2\mu} + V(r) = -\frac{\hbar^2}{2\mu}\nabla^2_{r,\theta,\phi} + \frac{Ze^2}{r}. \tag{3.1}$$

As we saw in Ch. 2, working in the COM frame reduces the two-body (electron-proton) problem to the equivalent one-body problem within a central field. Here, $e^2 = q^2/(4\pi\varepsilon_0)$, q is the elemental charge, ε_0 is the vacuum permittivity, $\hat{p}$ is the momentum operator, and r is the position of the electron with mass m_e relative to the COM. The COM is essentially located at the massive nucleus with Z protons each having mass m_p. If the total mass of the nucleus is m_n the reduced mass is

$$\mu = \frac{m_e m_n}{m_n + m_e} \approx m_e. \tag{3.2}$$

The total electron wavefunction $|\Psi\rangle$ must fulfill the time dependent Schröedinger equation

$$i\hbar\frac{\partial}{\partial t}|\Psi\rangle = \hat{H}_{\text{tot}}|\Psi\rangle = E_\alpha|\Psi_n\rangle. \tag{3.3}$$

The total wavefunction is separable in space and time and the series solution is

$$\langle\vec{x},t|\Psi\rangle = \Psi(\vec{r},t) = \sum_x^\infty e^{-iE_x(t-t_0)/\hbar}|\psi_x(t_0)\rangle, \tag{3.4}$$

where $|\psi_x\rangle$ are the solution to the TISE at the initial time t_0. Each TISE solution has an energy eigenvalues E_x where x denotes the good quantum number(s). For example, x might refer to the principal energy level n or some angular momentum quantum numbers like l, whatever diagonalizes the Hamiltonian. The solution to the TISE can also be separated into a radial and angular solution [92] (associated with the angular momentum operator $\hat{L}$)

$$\begin{aligned} \left|\psi_{n,l,m_l}\right\rangle &= \left|n,l,m_l\right\rangle, \text{ and} \\ \left\langle\vec{x}\middle|\psi_{n,l,m_l}\right\rangle &= R_{n,l}(r)Y_l^{m_l}(\theta,\phi) = \frac{1}{n}\sqrt{\frac{(n-l-1)!}{(n+l)!}}\frac{\rho_n^{l+1}}{\sqrt{a}}e^{\frac{-ln}{2}}\mathscr{L}_{n-l-1}^{2l+1}(\rho_n), \end{aligned} \tag{3.5}$$

where $\mathscr{L}$ is the Laguerre polynomial, m_l is the angular momentum projection qunatum number,

$$\begin{aligned} \hat{L}^2\left|l,m_l\right\rangle = \hbar^2 l(l+1)\left|l,m_l\right\rangle, \;\; \hat{L}_z\left|l,m_l\right\rangle = \hbar m_l\left|l,m_l\right\rangle, \\ \rho_n \equiv \frac{2r}{na}, \;\; a \equiv \frac{\hbar^2}{Z\mu e^2}, \;\; R_\infty \overset{\mu\to m_e}{\equiv} \frac{m_e e^4}{2\hbar^2 hc}, \end{aligned} \tag{3.6}$$

and c is the speed of light in vacuum. We can see that the atomic unit for length, one Bohr, is $a_0 = a(Z=1,\mu\approx m_e)$. Upon integrating the expectation value, we find that the energy of a single electron atom with atomic number Z and $\mu \approx m_e$ reduces to

$$\left\langle\hat{H}_{\text{tot}}\right\rangle = \int \psi^*_{nlm_l}(r,\theta,\phi)\hat{H}_{\text{tot}}\psi_{nlm_l}(r,\theta,\phi)\,d^3\vec{r} = E_n = -Z^2hc\frac{R_\infty}{n^2} = -Z^2\frac{13.6\text{ eV}}{n^2}, \tag{3.7}$$

which is degenerate with respect to the angular momentum and projection quantum numbers.

Relativistic and hyperfine corrections We must consider the relativistic Hamiltonian to obtain a more accurate result for the energy eigenvalues that will break the degeneracy of $\hat{H}_{\text{tot}}$. We can accomplish this without the need for the full quantum electrodynamics (QED) treatment by instead using the relativistic Dirac equation

$$i\hbar\frac{\partial}{\partial t}\left|\Psi\right\rangle = \hat{H}_{\text{tot}}\left|\Psi\right\rangle \;\text{ and }\; \hat{H}_{\text{tot}}\left|\psi\right\rangle = \left[c\hat{\alpha}\cdot\hat{p} + \hat{\beta}m_e c^2 + V(r)\right]\left|\psi\right\rangle. \tag{3.8}$$

Dirac reformulated the Hamiltonian into a first order differential equation (making the time dependent Schröedinger equation covariant) [108], so that when $V=0$, the square of the

energy reproduces Einstein's total kinetic energy $\hat{H}^2 = E^2 = \hat{p}^2c^2 + m_e^2c^4$. However, this only works if $\hat{\alpha}$ and $\hat{\beta}$ are chosen to be represented by the 4 x 4 matrices

$$\hat{\alpha}_i = \begin{pmatrix} 0 & \hat{\sigma}_i \\ \hat{\sigma}_i & 0 \end{pmatrix} \text{ and } \hat{\beta} = \begin{pmatrix} \mathbb{1} & 0 \\ 0 & -\mathbb{1} \end{pmatrix}, \tag{3.9}$$

where the $\hat{\sigma}_i$s are the 2 x 2 Pauli spin matrices and $\mathbb{1}$ is the 2 x 2 identity matrix. Using $|\psi\rangle = \binom{\psi_a}{\psi_b}$, where ψ_a and ψ_b are two-component spinors, leads to the coupled equations

$$\hat{\sigma}\cdot\hat{p}\psi_b = \frac{E - V - m_ec^2}{c}\psi_a \tag{3.10}$$

$$\text{and } \hat{\sigma}\cdot\hat{p}\psi_a = \frac{E - V - m_ec^2}{c}\psi_b. \tag{3.11}$$

Using the coupled equations to eliminate ψ_b and approximating that $E \ll m_ec^2$ gives

$$\hat{\sigma}\cdot\hat{p}\left[1 - \frac{E - m_ec^2 - V}{2m_ec^2}\right]\hat{\sigma}\cdot\hat{p}\frac{\psi_a}{2m_ec^2} \approx (E - m_ec^2 - V)\psi_a. \tag{3.12}$$

Further manipulation [108] and the substitutions $\hat{L} = \hat{r}\times\hat{p}$ and $\hbar\hat{\sigma} = 2\hat{S}$ reduces Eq. (3.12) to

$$\hat{H}_{\text{tot}} \approx \underbrace{\frac{\hat{p}^2}{2m_e} + V(r)}_{\hat{H}_0} - \underbrace{\frac{\hat{p}^4}{8m_e^3c^2}}_{\hat{H}_T} + \underbrace{\frac{Ze^2}{2m_e^2c^2r^3}\hat{L}\cdot\hat{S}}_{\hat{H}_{\text{so}}} + \underbrace{\frac{Ze^2\pi\hbar^2}{8m_e^2c^2}\delta(\vec{r})}_{\hat{H}_D}, \tag{3.13}$$

where $\hat{S}$ is the electron's intrinsic spin operator (whose eigenvectors only exist in Hilbert space) and $\delta(\vec{r})$ is a 3D Dirac delta function. We have also dropped the constant rest energy offset m_ec^2.

We have already solved for the eigenvalues and eigenvectors of the unperturbed Hamiltonian $\hat{H}_0$ in Eqs. (3.7) and (3.5), respectively. Next, we will identify the physical significance and evaluate the expectation value of each relativistic correction term $\hat{H}_D$, $\hat{H}_T$, and $\hat{H}_{\text{so}}$.

The Darwin perturbation $\hat{H}_D$ is a consequence of the Coulomb potential and does not have a classical physical interpretation. The expectation value of the perturbation gives the Darwin energy shift

$$\langle ln|\hat{H}_D|nl\rangle = \frac{Z^4\alpha^4 m_e c^2}{2n^3}\delta_{l0}, \tag{3.14}$$

where $\alpha = e^2/(\hbar c)$ is the fine structure constant and δ_{ij} is a Kronecker delta. The δ_{l0} comes form the fact that the hyrdogenic wavefunction vanishes at the origin except for $l = 0$. Therefore, the Darwin perturbation only shifts the s orbital, as seen in Fig. 3.1.

The relativistic kinetic energy pertubation $\hat{H}_T$ can be independently derived by expanding the Einstein's relativistic kinetic energy about $p^2/(m_e^2c^2) \ll 1$, which gives

$$E = \sqrt{p^2c^2 - m_e^2c^4} \approx m_e c^2 + \frac{\hat{p}^2}{2m_e} + \frac{\hat{p}^4}{8m_e^3c^2}. \tag{3.15}$$

The energy shift from this perturbation is

$$\langle ln|\hat{H}_T|nl\rangle = -\frac{\left\langle \left(\hat{H}_0 - V\right)^2 \right\rangle}{2m_e c^2} = -\frac{Z^4\alpha^4 m_e c^2}{2n^3}\left[\frac{1}{l+1/2} - \frac{3}{4n}\right]. \tag{3.16}$$

Unlike the Darwin term, the $\hat{H}_T$ perturbation contributes to all orbital angular momentum states l, as seen in Fig. 3.1.

The last relativistic perturbation $\hat{H}_{\rm so}$ is the spin-orbit coupling, refered to as the "fine structure" or "fine splitting." This correction can be independently derived by considering the work $\hat{H} = \hat{\mu}\cdot\vec{\mathscr{B}}$ associated with the torque on the electron's magnetic dipole moment $\hat{\mu}_e = (-|q|/m_e)\hat{S}$. The magnetic field is created by the moving proton (with relative velocity v) in the electron's rest frame $\vec{\mathscr{B}} = -\frac{v}{c^2}\times\vec{E}$ (see Ref. [109]).

The quantum numbers l and s are no longer good because of the mixing of $\hat{L}$ and $\hat{S}$, where $[\hat{H}_{\rm so}, \hat{L}_z] \neq 0$ and $[\hat{H}_{\rm so}, \hat{S}_z] \neq 0$. However, the magnitude squared of the total angular momentum operator $\hat{J}^2 = (\hat{L}+\hat{S})^2$ and its z projection operator $\hat{J}_z$ commute with the $\hat{H}_{\rm so}$,

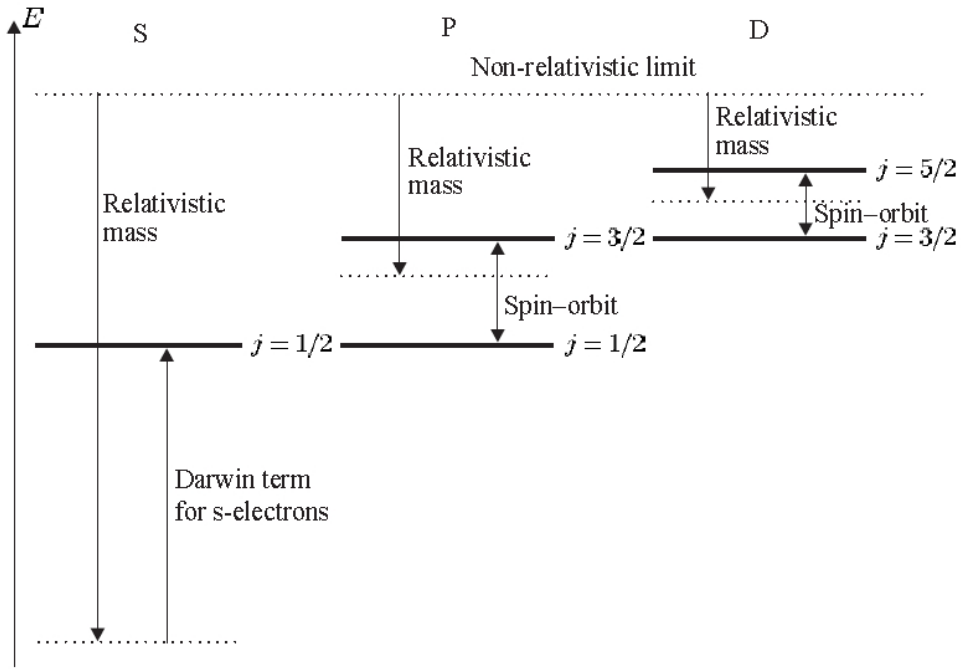

Figure 3.1: Originally from Ref. [73], showing relativistic energy corrections to the non-relativistic S, P, and D energy levels for hydrogen. The term "Relativistic mass" in Ref. [73] is equivalent to our $\hat{H}_T$ correction here.

making j and projection m_j the good quantum numbers for $2\langle \hat{L}\cdot\hat{S}\rangle = \langle J^2 - L^2 - S^2\rangle$. The expectation value of the spin-orbit perturbation gives an energy shift of

$$\begin{aligned}\left\langle m_j jsln\right| \hat{H}_{\rm so} \left|nlsjm_j\right\rangle &\propto \frac{\hbar^2}{2}\left[j(j+1)-l(l+1)-s(s+1)\right]\left\langle nl\right|\frac{1}{r^3}\left|nl\right\rangle \\ &= -\frac{Z^4\alpha^4 m_e c^2}{2n^3}\frac{j(j+1)-l(l+1)-3/4}{l(l+1/2)(l+1)}.\end{aligned} \tag{3.17}$$

In Eq. (3.17) we have used the fact that for the hyrdrogenic wavefunction $s = 1/2$, which means that for each $l > 0$ there are two total angular momentum quantum numbers $j = l + 1/2$ and $j = l - 1/2$, as seen in Fig. 3.1. We can write the energy splitting as

$$\Delta E_{\rm so} = E_{j=l+1/2} - E_{j=l-1/2} = -\frac{Z^4\alpha^4 m_e c^2}{2n^3 l(l+1)}. \tag{3.18}$$

Putting it all together gives the total energy of the hydrogenic electron is approximately

$$\left\langle m_j jsln\right| \hat{H}_{\text{tot}} \left|nlsjm_j\right\rangle = E_{n,l,s,j} \approx -\frac{Z^2 hcR_\infty}{n^2}\left[1+\frac{Z^2\alpha^2}{n^2}\left(\frac{n}{j+1/2}-\frac{3}{4}\right)\right]. \tag{3.19}$$

All of the relativistic corrections are of order $\sim \alpha^4 m_e c^2$. However, corrections that are about 2000 times smaller $\sim \alpha\hbar^3/(m_e m_p c)$ are also important to our discussion of the energy shifts. In fact, these "hyperfine" energy levels are the ones that we use for optical transitions.

These hyperfine perturbations $\hat{H}_{\text{hf}}$ are due to the work associated with the torque on the magnetic dipole moment of the nucleus $\hat{\mu}_I = g_I \mu_n \hat{I}/\hbar$ from the magnetic field produced by the dipole associated with the electron's intrinsic spin μ_e and its orbital angular momentum. The total nuclear spin operator is $\hat{I}$, the nuclear Bohr magneton is $\mu_n = \hbar|q|/(2m_p)$, the nuclear g-factor is g_I, and the product of the electron Bohr magneton and its g-factor is $g_s\mu_B \approx \hbar|q|/m_e$. Following the treatment of Ref. [73], when an atom has a nuclear spin $I > 0$, the total energy due to the dipole contribution can be written as

$$\hat{H}_{\text{hf}} = -\hat{\mu}_I \cdot B_e = -\hat{\mu}_I \cdot \left[\frac{\mu_0}{4\pi}\frac{-e\vec{v}\times -\vec{r}}{r^3} - \frac{\mu_e - 3\hat{r}(\hat{r}\cdot\mu_e)}{r^3} + \frac{8\pi}{3}\mu_e \delta(\vec{r})\right], \tag{3.20}$$

where μ_0 is the vacuum permeability. The first term comes from the Biot-Savart law [109] and $-r$ refers to the position of the nucleus relative to the electron. The second and third terms are associated with the magnetic field of a dipole at distance r from the origin in the direction of unit vector $\hat{r}$, which includes the Fermi-contact (third) term with the Dirac

delta function [109]. Substituting for μ_I, μ_e and $\hat{L}$ into Eq. (3.20) gives

$$\begin{aligned}\hat{H}_{\rm hf} &= -\frac{\mu_0}{4\pi}\frac{2\mu_B\mu_n g_I}{\hbar^2}\hat{I}\cdot\left[\frac{\hat{L}}{r^3}-\frac{\hat{S}-3\hat{r}(\hat{r}\cdot\hat{S})}{r^3}+\frac{8\pi}{3}\hat{S}\delta(\vec{r})\right] \\ &= -\frac{\mu_0}{4\pi}\frac{2\mu_B\mu_n g_I}{\hbar^2}\hat{I}\cdot\left[\hat{X}+\frac{8\pi}{3}\hat{S}\delta(\vec{r})\right].\end{aligned} \tag{3.21}$$

When evaluating the expectation value of Eq. (3.21) for the $l=0$ case, only the Fermi-contact term remains, due to the integral over the Dirac delta function $\propto \left|\psi_{n,0,0}(0)\right|^2$, just like in the Darwin relativistic correction. For $l=0$ hydrogenic atoms $\hat{S}=\hat{J}$ (where $s=1/2$), thus $\hat{H}_{\rm hf}\propto\hat{I}\cdot\hat{J}$. This mixing has the same form as the fine structure perturbation, but with $\hat{I}$ instead of $\hat{S}$. Therefore, the good quantum numbers for the hyperfine structure are $F=J+I$.

When evaluating the expectation value of of Eq. (3.21) $l>0$, only the $\hat{X}$ term remains. We can make a hand waving argument about the components of the angular momenta vectors perpendicular to $\hat{J}$ averaging out to zero and not contribute to the expectation value [73]. Therefore, we can continue to use the quantum numbers f and projection m_f by projecting $\hat{X}$ onto $\hat{J}$

$$\langle\hat{X}\cdot\hat{I}\rangle=\frac{\langle\hat{X}\cdot\hat{J}\rangle}{\langle\hat{J}^2\rangle}\langle\hat{J}\cdot\hat{I}\rangle=\frac{\langle\hat{X}\cdot\hat{J}\rangle}{j(j+1)}\langle\hat{J}\cdot\hat{I}\rangle \tag{3.22}$$

which again gives $\hat{H}_{\rm hf}\propto\hat{I}\cdot\hat{J}$. Therefore, using the form of the solution to the mixed angular momentum expectation value [as seen in Eq. (3.17)] we find that the hyperfine energy shift can be given by

$$\left\langle m_f fijsln\right|\hat{H}_{\rm hf}\left|nlsjifm_f\right\rangle=\frac{A^{(2)}_{n,l,s,j}}{2}\left[f(f+1)-l(l+1)-I(I+1)\right] \tag{3.23}$$

for all l with proportionality constant $A^{(2)}$. The energy spacing between consecutive hyperfine levels for a fixed j is

$$\Delta E_{\rm hf} = E_f - E_{f-1} = A^{(2)} f. \tag{3.24}$$

For the details of determining $A^{(2)}$ using the Wigner Eckart theorem and spherical tensors see [110], the final result is

$$A^{(2)}_{n,l,s=1/2,j} = \frac{2\mu_0\mu_n\mu_B g_I}{4\pi h}\left[\frac{l(l+1)}{j(j+1)}\left\langle r^{-3}\right\rangle + \frac{4Z^3}{3a_0^3 n^3}\delta_{l0}\right]. \tag{3.25}$$

When the total nuclear spin $I > 1/2$ there can be higher order electric quadrupole $B^{(4)}$ and magnetic octupole contributions. The hyperfine energy shift including higher order contributions give

$$\begin{gathered}\frac{A^{(2)}}{2}k + B^{(4)}\frac{\frac{3}{2}k(k+1) - 2I(I+1)j(j+1)}{2I(2I-1)2j(2j-1)} + ..., \\ \text{where } \; k = f(f+1) - j(j+1) - I(I+1)\end{gathered} \tag{3.26}$$

as described in Ref. [111].

3.1.2 Alkali atoms

We can tweak our results for the single electron hydrogenic atom to develop a model that describes the multi-electron alkali atoms or alkali earth ions that have a single valance electron using the effective principal quantum number $n^* = n - \eta_l$ and the effective atomic number $Z_{\rm eff}(r)$, as discussed in Ref. [73]. We model the alkali-like atom in the central-field approximation, where the atom is considered hydrogenic with an effective nuclear core that consists of the actual nucleus and the inner electrons. The term η_l is called the quantum defect and can be determined if the specific functional form of $Z_{\rm eff}(r)$ is known. For example, the non-relativistic energy uses $Z_{\rm eff} = 1$, because the non-valance inner electrons screen the nucleus's positive core. The quantum defect values for Na are $\eta_0 = 1.35$, $\eta_1 = 0.86$, and $\eta_{l\geq 2} \approx 0$. The defect gets smaller for higher-l orbitals because

the screening effect is more pronounced.

According to Eq. (3.19), the relativistic perturbations go like $\sim Z^4/n^3$. It is again customary to replace the quantum number n by n^*. The atomic number Z^4 is replaced by $Z^4 \to (Z_{\max})^2(Z_{\min})^2$. For Na, the largest effective $Z_{\text{eff}}(r \to 0) = Z_{\max} = Z = 11$, while the smallest $Z_{\text{eff}}(r \to \infty) = Z_{\min} = 1$, which is associated with the greatest screening effect. Using a similar logic for the hyperfine perturbations that go like $\sim Z^3/n^3$ [according to Eq. (3.25)], becomes $Z_{\max}(Z_{\min})^2/(n^*)^3$. Putting it all together gives

$$\begin{aligned} E \approx & -\frac{hcR_\infty}{(n-\eta_L)^2}\left[1+\frac{(Z_{\max})^2(Z_{\min})^2\alpha^2}{(n-\eta_L)^2}\left(\frac{(n-\eta_L)}{J+1/2}-\frac{3}{4}\right)\right] \\ & +\frac{A_{n^*,L,S,J}}{2}\left[F(F+1)-J(J+1)-I(I+1)\right]. \end{aligned} \tag{3.27}$$

In the hydrogenic atom, which only has a single electron, the distinction between total angular momentum and individual angular momentum is irrelevant. For example, total angular momentum quantum number $\vec{L} = \sum_i \vec{l}$ is denoted by a capital letter and the ith electron's quantum individual number l is denoted by a lowercase letter. With our alkali-like atom model, the lack of distinction is essentially still true, since we are treating the valance electron as a single electron within an effective central-field. However, in keeping with the convention of capital letters denoting total angular momentum in muli-electron atoms, we have switch to capital letters in Eq. (3.27).

For a multi-electron system we can use the shell model to describe the electron configuration of the atoms, as seen in Fig. 3.2 for Na, Na^+, Ca, and Ca^+. Electrons are fermions and must obey the Pauli principle discussed in Ch. 2. As a consequence of the Pauli principle, each shell associated with principal quantum number n has $l = n-1$ possible angular momenta and 2(2l+1) available states within a specific nl sub shell, as depicted in Fig. 3.2. There are various possible vector sums of the different total angular momentum

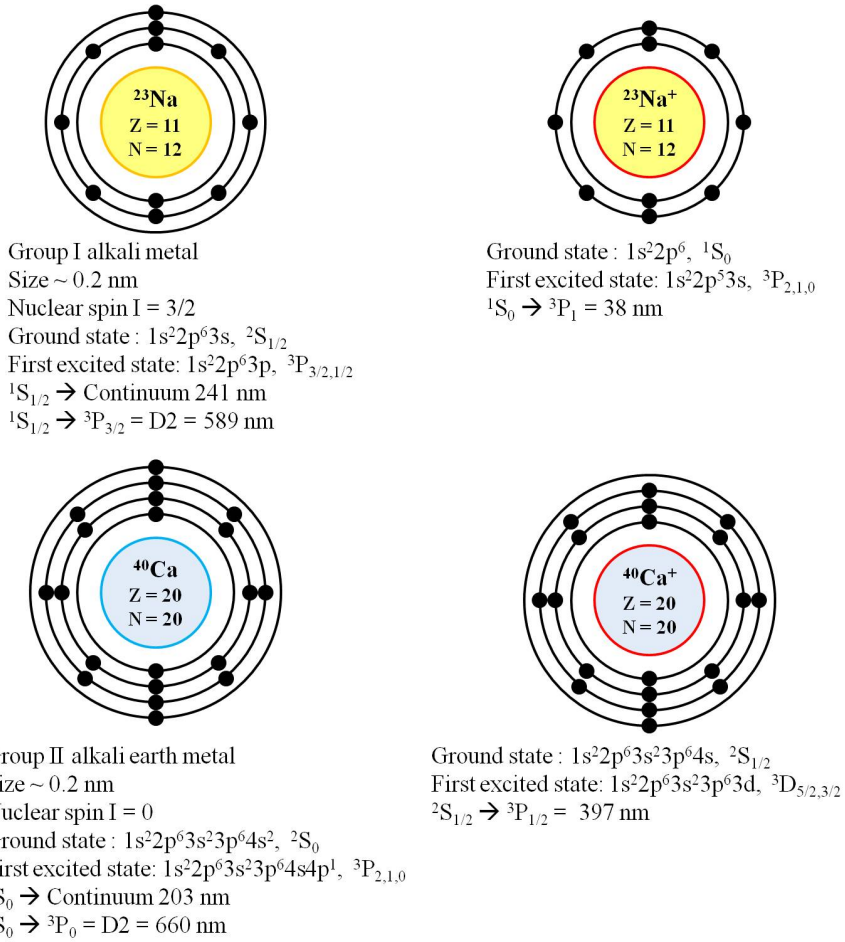

Figure 3.2: Electron configurations for Na, the singly ionized closed shell Na^+ (yellow), Ca, and Ca^+ (blue).

operators S, L, and J associated with a principal quantum number n. We can distinguish a particular vector sum of angular momenta using the spectroscopic notation

$$n^{2S+1}L_J, \tag{3.28}$$

which is used in Figs. 3.2 and 3.3, as well as throughout this dissertation.

Some of the important chemical properties and characteristics of the atoms and ions studied in this dissertation[1] are given in Fig. 3.2. We also show the energy level spacing

[1]It is worth noting that there are resonant laser excitable optical transitions for Na and Ca^+, but not for Na^+, which has a closed shell structure. Furthermore, both excited Na^* and Ca^* can be optically ionized.

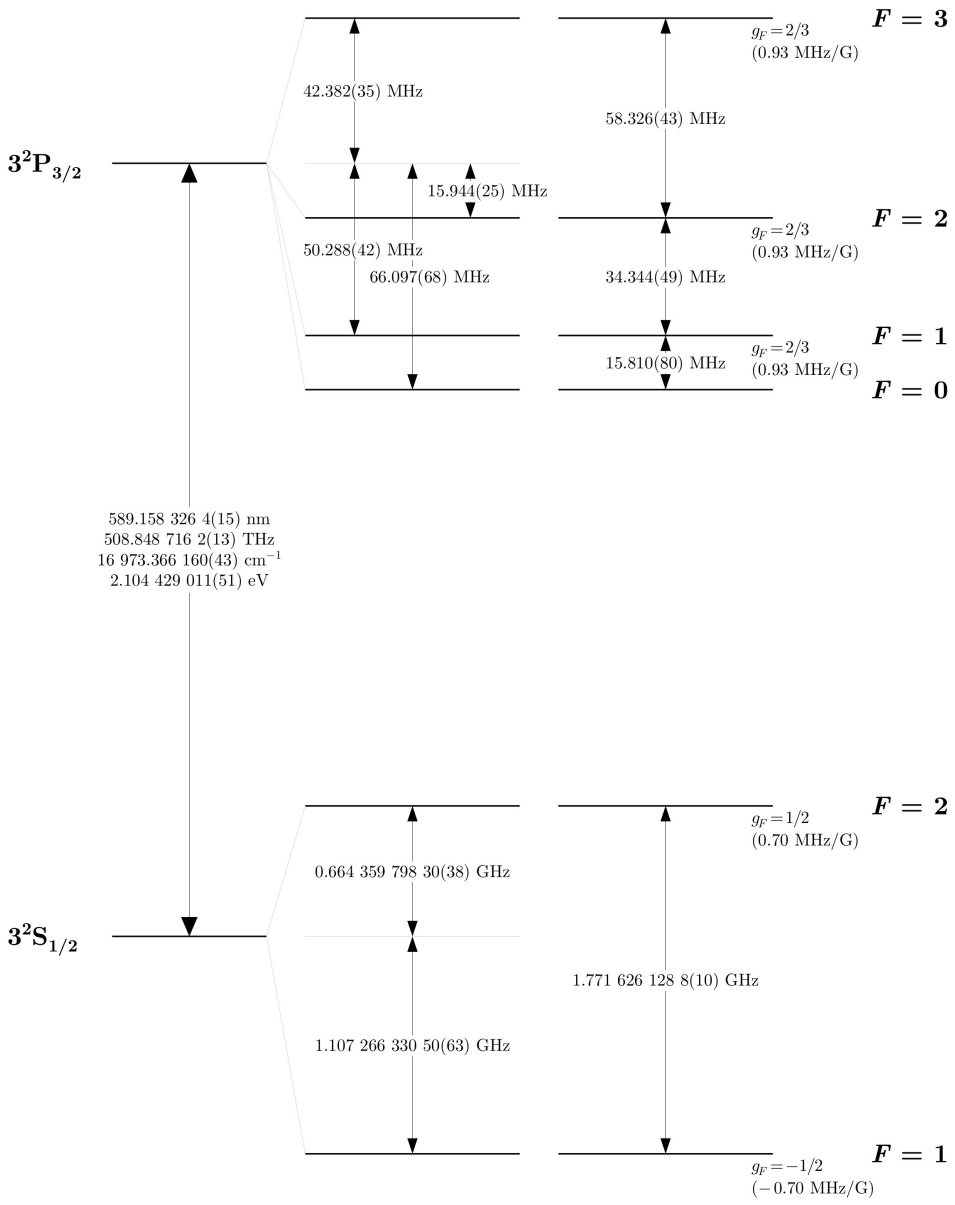

Figure 3.3: Energy level diagram that is originally from Ref. [111], showing the neutral ^{2}3 Na atom's D2 line (the lowest energy ground state and $^2P_{3/2}$ excited state) with relativistic (fine structure) and hyperfine structure corrections. The D1 line (590 nm) is associated with the $^2P_{1/2}$ excited state. The single ionization threshold is 41449.481 cm^{-1} or $\approx$ 5.14 eV above the ground state. Neither the D1 line nor the ionization threshold are shown in this figure.

including the relativistic corrections and hyperfine levels for the Na D2 line[2] associated with the $^2P_{3/2}$ excited state in Fig. 3.3.

3.2 Classical atom-light model

3.2.1 Electromagnetic waves

To describe atomic interaction with light we must first characterize the electromagnetic radiation seen by the atom. We will assume that the atom is far from the radiation source and we will choose to work in the Coulomb gage $\vec{\nabla}\cdot\vec{A}=0$ and $\mathscr{V}=0$. Here $\vec{A}$ is the vector potential, $\vec{\mathscr{B}}=\vec{\nabla}\times\vec{A}$ is the magnetic field, $\vec{\mathscr{E}}$ is the electric field, and $\mathscr{V}$ is the electrical potential. We will assume that the light is composed of transverse plane waves [109], which satisfy Maxwell's wave equations

$$\vec{\mathscr{E}}=-\frac{\partial\vec{A}}{\partial t}, \tag{3.29}$$

$$\text{and } \nabla^2\vec{A}=\frac{1}{c}\frac{\partial^2\vec{A}}{\partial t^2}. \tag{3.30}$$

The plane wave solution to Eq. (3.29) and Eq. (3.30) for monochromatic light with wavelength λ, wavenumber $k=2\pi/\lambda$, propagation direction $\hat{k}$, perpendicular polarization direction $\hat{\varepsilon}$, and angular frequency ω as a function of space and time t is

$$\begin{aligned}\vec{\mathscr{E}}(x,t)=E_0\hat{e}_0\cos\left(\vec{k}\cdot\vec{r}-\omega t\right)&=\frac{\hat{\varepsilon}}{2}\left[E_0e^{i\left(\vec{k}\cdot\vec{r}-\omega t\right)}+\text{c.c}\right],\\ \text{and } \vec{A}(x,t)&=\frac{\hat{\varepsilon}}{2i\omega}\left[E_0e^{i\left(\vec{k}\cdot\vec{r}-\omega t\right)}+\text{c.c.}\right],\end{aligned} \tag{3.31}$$

respectively. To ensure that the fields are real we add the complex conjugate (c.c.). However, to reduce notational clutter we will not continue to explicitly write the c.c., yet

[2] We will be using the Na D2 line to make our MOT, as discussed in Ch. 4.

know that it is there.

Customarily one makes the dipole approximation, which assumes that the size of the interaction is equivalent to the size of the atom and that the atom's size is much smaller than the optical wavelength. For example, the size of a Na atom is ~ 0.2 nm and the D2 line optical transition is at $\lambda_{D2} = 589$ nm, so the approximation is valid. The dipole approximation implies that if we expand $\vec{\mathscr{E}}$ and $\vec{A}$ about kr, we can drop all terms to first order in $kr \ll 1$ and higher, thus the fields in Eq. (3.31) become spatially independent

$$\begin{aligned} \vec{\mathscr{E}}(t) &= \frac{1}{2}\hat{\varepsilon}E_0 e^{-i\omega t} + \text{c.c.}, \\ \text{and } \vec{A}(t) &= \frac{1}{2i\omega}E_0\hat{\varepsilon}e^{-i\omega t} + \text{c.c.} \end{aligned} \tag{3.32}$$

The intensity of the wave is given by the time averaged Poynting vector

$$I = |\langle \vec{S} \rangle| = \frac{|\langle \vec{\mathscr{E}} \times \vec{\mathscr{B}} \rangle|}{\mu_0} = \frac{E_0^2 \varepsilon_0 c}{2}, \tag{3.33}$$

and the classical time averaged momentum density is given by

$$\vec{p}_d = \frac{\langle \vec{S} \rangle}{c^2} = \frac{E_0^2 \varepsilon_0}{2c} = \frac{I}{c^2}\hat{k}, \tag{3.34}$$

as explained in Ref. [94].

3.2.2 Lorentz model

In the Lorentz model of the atom the single valance electron is at position r relative to the COM. We assume the electron is within a harmonic potential $V = 1/2 m\omega_0^2 r^2$ and experiences a driving force from the electric field $\vec{F}(t) = q\vec{\mathscr{E}}(t)$. The oscillating charge is accelerating and is emitting radiation itself, causing it to lose energy at a rate γ. The loss of energy can be thought of as a damping force. The differential equation that describes the electron's motion in this model [94, 112] is that of a damped driven harmonic oscillator

$$m\ddot{\vec{r}} - m\gamma\dot{\vec{r}} + m\omega_0^2\vec{r} = \vec{F}(t) = -qE_0\hat{\varepsilon}e^{-i\omega t}. \tag{3.35}$$

Using the ansatz that the solution has the same time dependence as the driving force and plugging that into Eq. (3.35) yields the solution

$$\vec{r}(t) = \frac{qE_0\hat{\varepsilon}}{m\left(\omega^2 - \omega_0^2 + i\gamma\omega\right)}e^{-i\omega t} \equiv r_0E_0\hat{\varepsilon}e^{-i\omega t}. \tag{3.36}$$

The solution to the equation of motion suggests that the electron acts like an oscillating dipole with dipole moment $\vec{d}(t) = q\vec{r}(t)$ and polarizability

$$\begin{aligned}\vec{d} = \alpha\vec{\mathscr{E}}(t) \implies \alpha &= \frac{q^2}{m\left(\omega^2 - \omega_0^2 + i\gamma\omega\right)} \\ &= \frac{q^2}{m}\left[\frac{\omega^2 - \omega_0^2}{(\omega^2 - \omega_0^2)^2 + \gamma^2\omega^2} - \frac{i\gamma\omega}{(\omega^2 - \omega_0^2)^2 + \gamma^2\omega^2}\right].\end{aligned} \tag{3.37}$$

We can relate the dipole moment to the bulk polarization density of a dilute gas with number density N via the susceptibility [94, 112] as $\chi = N\alpha/\varepsilon_0$. Using Eq. (3.37) we find that the complex index of refraction [112] for small χ is

$$n \approx 1 + \frac{\chi}{2} = 1 + \frac{Nq^2}{2m\varepsilon_0}\left[\frac{\omega^2 - \omega_0^2}{(\omega^2 - \omega_0^2)^2 + \gamma^2\omega^2} - \frac{i\gamma\omega}{(\omega^2 - \omega_0^2)^2 + \gamma^2\omega^2}\right]. \tag{3.38}$$

From the spatial dependence of Eq. (3.31), assuming $\hat{k} = \hat{r}$ we know that

$$\vec{\mathscr{E}}(r) = \hat{\varepsilon}E_0e^{ikr} = \hat{\varepsilon}E_0e^{ink_0r} = \left(\hat{\varepsilon}E_0e^{-\mathrm{Im}[n]kr}\right)e^{i\mathrm{Re}[n]k_0r}, \tag{3.39}$$

where $k_0 = \omega/c$ is the wavenumber in vacuum and Im[] and Re[] denote imaginary and real parts, respectively. The intensity of the wave, according to Eq. (3.33), becomes

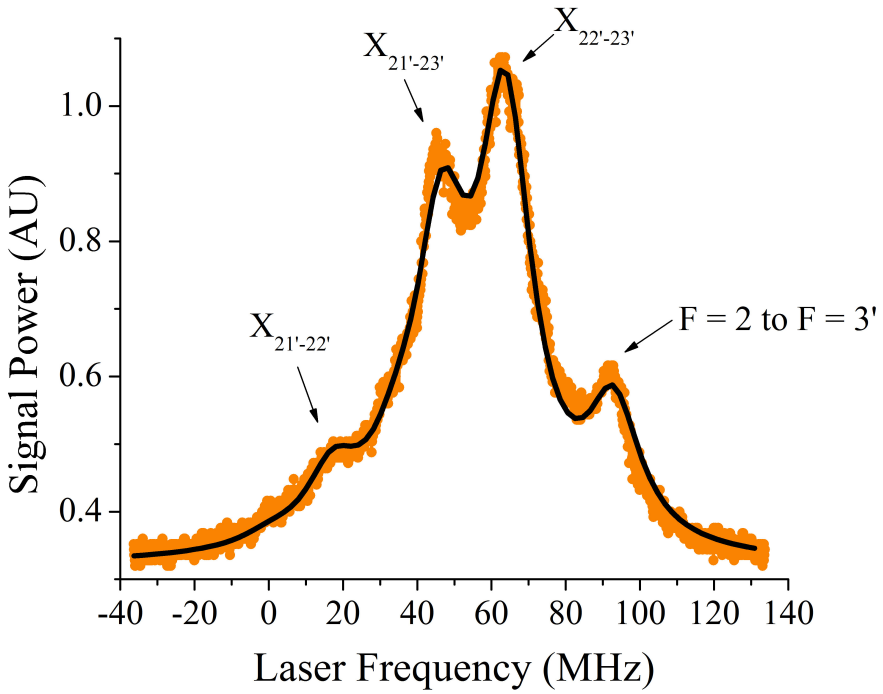

Figure 3.4: Experimental Na Doppler-free saturation absorption spectrum of the $F = 2 \rightarrow F' = 1, 2, 3$ hyperfine manifold of the D2 line (orange) with corresponding fit to a sum of Lorentzian functions[3](black). The most resolvable peaks are labeled. The peaks marked with an X are called crossover peaks, which will be discussed in Sec. 4.2.3.

$$I = \frac{E_0^2 \varepsilon_0 c}{2} e^{-2\mathrm{Im}[n]kr} = I_0 e^{-\kappa r}, \tag{3.40}$$

where κ is the absorption coefficient and it has the expected Lorentzian behavior

$$\frac{Nq^2}{2m\varepsilon_0 \gamma c}\left[\frac{(\gamma/2)^2}{(\omega-\omega_0)^2+(\gamma/2)^2}\right]. \tag{3.41}$$

In Eq. (3.41), we have assumed that we are near resonance $|\omega - \omega_0| \ll \omega_0$, thus

$$\omega_0^2 - \omega^2 \approx 2\omega(\omega_0 - \omega). \tag{3.42}$$

[3]The Lorentzian lineshape is predicted classically by Eq. (3.43) and quantum mechanically by Eq. (3.87)

For multiple allowed transitions to states $x = 1,2,3,...$ we would turn Eq. (3.41) into a sum over each possible resonant transition with frequency ω_{0x} weighted by the transition strength f_x giving an absorption spectrum

$$\kappa = \sum_x \frac{Nq^2 f_x}{2m\varepsilon_0 \gamma c} \left[\frac{(\gamma/2)^2}{(\omega - \omega_{0x})^2 + (\gamma/2)^2} \right]. \tag{3.43}$$

We can also assign an absorption cross section by equating $dI/dz = -\kappa I = N\sigma_a I$. Thus σ_a is equivalent to Eq. (3.43) without the factor of N [73]. The classical absorption cross section works well for low intensity absorption, wherein stimulated emission (discussed in the next section) does not play a significant role.

As an example, Fig. 3.4 shows the Na D2 line hyperfine Doppler-free absorption spectrum taken by our group, which is fit to a series of Lorentzian line shapes. This spectrum is used to frequency stabilize our lasers. A more detailed discussion of the spectroscopy of Na and laser stabilization can be found in Sec. 4.2.3.

Electric dipole radiation decay As mentioned earlier, we can think of the electron as an oscillating dipole source that emits radiation. If we are far from the induced electron's oscillating induced dipole moment $d/q \ll r$ in the radiation zone $r \gg c/\omega$, then the driven oscillating dipole produces fields that approximate as

$$\vec{\mathscr{E}}(r,t) \approx -\frac{\mu_o \omega^2 (q r_0)}{4\pi} \left(\frac{\sin(\theta)}{r} \right) \cos(\omega t - kr)\hat{\theta}, \text{ and } \vec{\mathscr{B}}(r,t) = \frac{\vec{\mathscr{E}}(r,t)}{c}\hat{\phi}, \tag{3.44}$$

where for convenience we have now defined the dipole to be oscillating in the polarization direction $\hat{\varepsilon} = \hat{z}$, as described in Ref. [94]. Also, we are using the dipole amplitude from Eq. (3.36). The time-averaged power of the oscillating dipole radiation in the radiation zone is determined by the Poynting vector, namely

$$P = \int \langle \vec{S} \rangle \cdot d\vec{a} = \int \langle \vec{S} \rangle \cdot \hat{r} r^2 d\Omega = \frac{\mu_0 (q r_0)^2 \omega^4}{12\pi c}, \tag{3.45}$$

which has the characteristic ω^4 dependence.[4]

We can use the result in Eq. (3.45) to establish the value of the decay or damping rate γ [73]. The total energy of the electron in the Lorentz model can be expressed in terms of its maximum displacement as $E = (1/2) m_e \omega^2 r_0$ and when substituted into Eq. (3.45) gives

$$P = \frac{dE}{dt} = -\frac{q^2 \omega^2}{6\pi \varepsilon_0 c^3} E = -\gamma E \implies \tau = \frac{6\pi \varepsilon_0 c^3}{q^2 \omega^2}, \tag{3.46}$$

where the transition lifetime $\tau = 1/\gamma$. The classical decay rate and corresponding lifetime gives the shortest possible lifetime. Quantum mechanical effects can only lengthen the lifetime, sometimes indefinitely for cases involving forbidden transitions [73]. However, for strong transitions like the D2 line in Na, Eq. (3.45) gives a value of 16 ns, which is very close to the experimental value. Allowed optical transitions for alkali-like atoms and ions are typically have lifetimes $\sim$ 10 - 100 ns.

3.3 Quantum two-level atom

3.3.1 Emission and absorption

In Sec. 3.2 we used the Lorentz model to describe an atom in a harmonic well that was driven by an oscillating electromagnetic wave. This was a completely classical model, since the energy of the electron and the radiation fields were not quantized. In this section we will assume that the atom's valance electron can only have discrete quantized energies

[4] The strong ω^4 dependence in Eq. (3.45) is why the sky is blue. Sunlight is white, meaning it is composed of all the visible wavelengths. The blue light (higher frequency) within white sunlight is more strongly scattered (reradiated) by particles in the atmosphere than the red light (lower frequency), thus making the sky overhead appear blue. Similarly, during a sunset the sky is dark overhead and red in the horizon, because most of the blue light has been scattered away by the atmosphere leaving only red light [92, 109].

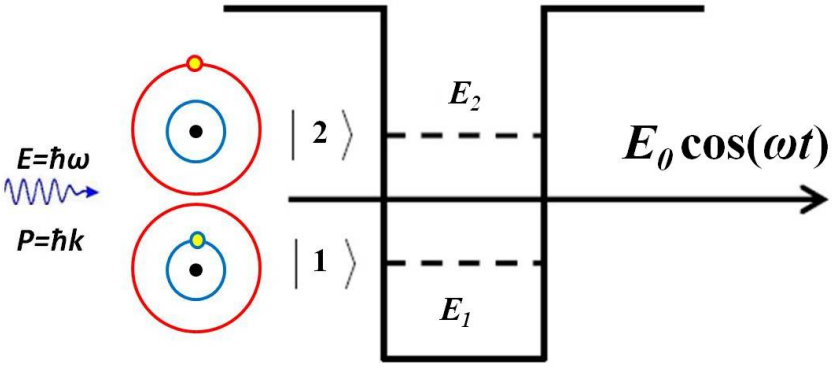

Figure 3.5: Illustration of two level atom absorbing a photon and the valance electron transitions between a lower atomic bound state to an upper state.

associated with good quantum numbers like n, L, ,J, S, and F, as discussed in Sec. 3.1.

For simplicity, we will consider that the atom is restricted to making transitions between just two atomic bound states after absorbing energy from the light field, as illustrated in Fig. 3.5. For example, the ground (lower) atomic states could be that of sodium's hyperfine state $3^2S_{1/2}F = 2$, which we will refer to as state 1, ψ_1, or $|1\rangle$, having energy E_1 transitioning to its excited state $3^2P_{3/2}F' = 3$, which we will refer to as state 2, ψ_2, or $|2\rangle$, having energy E_2. This is the D2 line optical transition associated with the laser cooling of one of our Na MOTs. We will also assume the electromagnetic radiation with angular frequency ω is quantized in discrete energy packets called photons. Each photon has energy $\hbar\omega$ and integer spin that is associated with its polarization. If the radiation is restricted to modes of an optical cavity (quantized volume) [112] then the total light energy is

$$E = (n+1/2)\hbar\omega, \tag{3.47}$$

where n is the number of photons with frequency ω. The energy difference between the two atomic energy levels can be written as

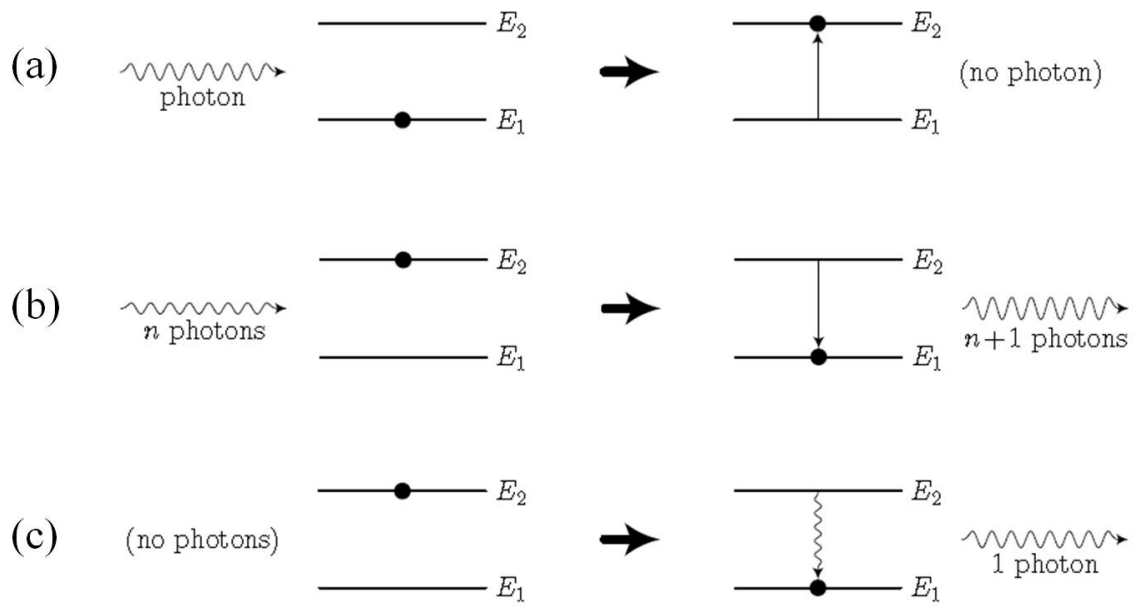

Figure 3.6: Three panels showing absorption of a photon (a), stimulated emission of a photon (b), and spontaneous emission of a photon (c). Each panel's illustration is originally from Ref. [112].

$$\begin{aligned}\Delta E_{\rm hf} = E_2 - E_1 &= -\frac{hcR_\infty}{(3-\eta_1)^2}\left[1+\frac{(11)^2\alpha^2}{(3-\eta_1)^2}\left(\frac{(3-\eta_1)}{1}-\frac{3}{4}\right)\right]+\frac{A_{3^*,1,1/2,1/2}}{2}[6-(3/4)] \\ &+\frac{hcR_\infty}{(3-\eta_0)^2}\left[1+\frac{(11)^2\alpha^2}{(3-\eta_0)^2}\left(\frac{(3-\eta_0)}{2}-\frac{3}{4}\right)\right]-\frac{A_{3^*,0,1/2,3/2}}{2}[12-(15/4)] \\ &= \hbar\omega_0 \\ &\approx \hbar c\frac{2\pi}{589\text{ nm}},\end{aligned} \tag{3.48}$$

where we have used Eqs (3.27) to evaluate the energy difference (excluding the small quadrupole contribution to the excited state). Following our Lorentz model in Sec. 3.2, we know that when $\omega \approx \omega_0$ the electron resonantly absorbs the photon's quantized energy, leading to a transition.

There are three kinds of photon-atom interactions depicted in Fig. 3.6. An atom can absorb a photon, which is likely to occur if the photon energy is resonant with the two-level energy difference and the polarization of the photon allows for angular momentum to conserved during the transition. An excited atom can be stimulated to emit a photon by interacting with an incident resonant photon, a process known as stimulated emission. The probability of stimulated emission is equal to that of absorption. Alternatively, the atom may randomly or spontaneously emit a photon, known as spontaneous emission. The truth is that spontaneous emission is actually the same as stimulated emission, except it is stimulated by vacuum field fluctuations [92]. However, we are not going to quantize the electromagnetic fields here, so we will continue to use the spontaneous emission model.

3.3.2 Quantum model

The atom-light Hamiltonian We will now include the energy associated with the radiation in our time dependent Hamiltonian for the atom-light interaction. The canonical momentum operator $\hat{p} \rightarrow \hat{p} - q\vec{A}$ incorporated into our Hamiltonian gives

$$i\hbar\frac{\partial\Psi}{\partial t} \approx \left[\underbrace{\hat{p}^2 + V}_{\hat{H}_0} - \underbrace{\frac{q}{m_e}\vec{A}\cdot\hat{p}}_{\hat{H}_{\mathrm{E1}}+\hat{H}_{\mathrm{M1}}+\ldots}\right]\Psi, \tag{3.49}$$

where we have dropped the small $\vec{A}^2$ terms. Again we are using the dipole approximation where the vector potential is defined by Eq. (3.32). The first part to the TISE is the unperturbed Hamiltonian $\hat{H}_0$ or atomic Hamiltonian, whose energies and wavefunctions were the subject of Sec. 3.1. Although not explicitly shown in Eq. (3.49), we can assume that $\hat{H}_0$ includes all the relativistic and hyperfine corrections, too.

The second term can be written as a series expansion of the vector potential where E1

refers to the strongest term, the electric dipole term,[5] $(q/m_e)\vec{A}\cdot\hat{p} \approx q\vec{\mathscr{E}}\cdot\vec{r} = \vec{d}\cdot\vec{\mathscr{E}}$. Here, we will only consider transitions that couple to the atom's electric dipole, aptly called "electric dipole" or "E1" transitions.

Now we have

$$i\hbar\frac{\partial}{\partial t}|\Psi\rangle = \hat{H}_{\text{tot}}|\Psi\rangle \approx \left[\hat{H}_0 + \hat{H}_{\text{E1}}\right]|\Psi\rangle, \tag{3.50}$$

$$\text{where } \hat{H}_0|1\rangle = E_1|1\rangle = \hbar\omega_1|1\rangle,\ \hat{H}_0|2\rangle = E_2|1\rangle = \hbar\omega_2|2\rangle,\ \langle 1|2\rangle = 0, \tag{3.51}$$

$$\text{and } |\Psi\rangle = c_1(t)e^{-i\omega_1 t}|1\rangle + c_2(t)e^{-i\omega_2 t}|2\rangle. \tag{3.52}$$

We have expressed Eq. (3.52) in the interaction picture, thus $|1\rangle$ and $|2\rangle$ are time independent. It is convenient to write the time-dependent Hamiltonian as

$$\hat{H}_{\text{tot}} = \hbar\omega_1|1\rangle\langle 1| + \hbar\omega_2|2\rangle\langle 2| + \left(\langle 1|q\vec{r}\vec{\mathscr{E}}(t)|2\rangle\right)|1\rangle\langle 2| + \left(\langle 2|q\vec{r}\vec{\mathscr{E}}(t)|1\rangle\right)|2\rangle\langle 1|, \tag{3.53}$$

where we have assumed that the major diagonal elements of H_{E1} must be zero. This is due to the fact that the parity operator $\hat{\Pi}$ transforms the diagonal elements $\hat{\Pi}\langle\vec{r}\cdot\hat{\varepsilon}\rangle = -\langle\vec{r}\cdot\hat{\varepsilon}\rangle$, because if the bra and ket states have the same parity, the integral's overall party is solely determined by r making it antisymmetric. However, the overall parity for the perturbation must be symmetric due to the symmetry of the atom's Coulomb potential, thus the major diagonal terms must be zero to avoid the contradiction [73]. We will show this again later when we discuss selection rules.

Looking ahead, substituting $\vec{\mathscr{E}}(t)$ from Eq. (3.32) into $\hat{H}_{\text{tot}}$ yields off diagonal terms that oscillate like $e^{i(\omega_0+\omega)t}$ and $e^{i(\omega_0-\omega)t}$. We can assume that close to resonance $\omega_0 + \omega \gg$

[5] Alternatively, from the dipole approximation we know that the work done on a the electron $W = -\int q\vec{\mathscr{E}}(t)\,d\vec{r} = -q\vec{r}\cdot\vec{\mathscr{E}}(t)$, which gives the same result. This argument uses an electrostatic formula, which implicitly assumes that the field's oscillation period is long compared to the electron's orbital period [92].

$|\omega_0 - \omega|$ and we can drop the $e^{i(\omega_0+\omega)t}$, which oscillates quickly and averages to zero. This is called the rotating wave approximation. In anticipation of this approximation it is acceptable to drop the necessary terms at this stage [92] and write the $\vec{\mathscr{E}}(t)$ in Eq. (3.53) as

$$\hat{H}_{\text{tot}} = \hbar\omega_1 |1\rangle\langle 1| + \hbar\omega_1 |2\rangle\langle 2| + \frac{\hbar\Omega_R}{2}\left(e^{i\omega t}|1\rangle\langle 2| + e^{-i\omega t}|2\rangle\langle 1|\right), \tag{3.54}$$

where we have grouped the angular and spatial integral into the so-called "Rabi frequency"

$$\Omega_R \equiv \frac{qE_0}{\hbar}\langle 2|\vec{r}\cdot\hat{\varepsilon}|1\rangle = \frac{qE_0}{\hbar}\langle 1|\vec{r}\cdot\hat{\varepsilon}|2\rangle = \frac{E_0}{\hbar}\langle 1|\vec{d}\cdot\hat{\varepsilon}|2\rangle, \tag{3.55}$$

where $\vec{d}$ is the atomic dipole moment.

Selection rules Evaluating the Rabi frequency determines the strength of the transition [112] as well as whether or not the dipole transition is allowed. This leads to a set of "selection rules" for allowed transitions [73]. Evaluating the angular integrals is easiest if we rewrite the dipole operator in spherical tensors and use the Wigner Eckart theorem. The dot product in the Rabi frequency becomes $r(\hat{C}_1^{(1)}\varepsilon_1 + \hat{C}_0^{(1)}\varepsilon_0 + \hat{C}_{-1}^{(1)}\varepsilon_{-1})$, where $q = 1, 0, -1$ means circular right σ^+, linear, and circular left σ^-, respectively. If we assume that the polarization has just one q then the angular integral in the Rabi frequency becomes $\langle 1|r\hat{C}_q^{(1)}|2\rangle$, where $\hat{C}_q^{(1)}$ is the angular part of the position vector written as a rank 1 spherical tensor (equivalent to a spherical harmonic) [113]. For our example of the hyperfine D2 transition in Na, Ref. [111] gives

$$\langle xm_F F|r\hat{C}_q^{(1)}|x'F'm_{F'}\rangle = \langle xF\|\vec{r}\|x'F'\rangle(-1)^{F'-1+m_F}\sqrt{2F+1}\begin{pmatrix} F' & 1 & F \\ m_{F'} & q & -m_F \end{pmatrix}, \tag{3.56}$$

where x and x' are all the other quantum numbers within $|1\rangle$ and $|2\rangle$. The double bar term is the reduced matrix element and the matrix is the Wigner (3-j) symbol, which is equivalent to Clebsch-Gordan coefficients [113] . The top row of the 3j requires that $\Delta F = 0, \pm 1$

(triangle rule) and that $m_F = m_{F'} + q$ (this is equivalent to conserving angular momentum), else the 3j's value is zero. Hence the 3j determines the angular momentum selection rules. We see that a $F = 2$ to $F' = 3$ transition is an allowed E1 transition.

We can further reduce the reduced matrix element using the $\{6-j\}$ symbol and show that $\langle xIJF\|\vec{r}\|F'J'I'x'\rangle$ is equivalent to

$$\langle xJ\|\vec{r}\|x'J'\rangle(-1)^{F'+J+1+I}\sqrt{(2F'+1)(2J+1)}\begin{Bmatrix} J' & J & 1 \\ F' & F & -I \end{Bmatrix}, \tag{3.57}$$

as discussed in Ref. [111]. Naturally, more and more reduction can be done. Eventually, one reduces down to the orbital angular momentum basis and we can use the known result for the spherical harmonics

$$\langle l\|\vec{r}\|l'\rangle = \langle l\|\hat{C}^{(1)}\|l'\rangle = (-1)^l\sqrt{(2l'+1),(2l+1)}\begin{pmatrix} l & 1 & l' \\ 0 & 0 & 0 \end{pmatrix}. \tag{3.58}$$

In Eq. (3.58), the 3-j symbol requires that $\Delta l = \pm 1, \neq 0$ to be non vanishing. Therefore, E1 transitions between states with the same l are forbidden. This is also what we concluded earlier on the basis of parity transformations, namely that $\langle 1|\hat{H}_{\mathrm{E1}}|1\rangle = \langle 2|\hat{H}_{\mathrm{E1}}|2\rangle = 0$.

3.3.3 Population transfer

Probability of coherent population transfer Assuming that we can solve the integral in the Rabi frequency, we would like to determine the probability of a transition as a function of time. To do this we need to use the time-dependent Schröedinger equation Eq. (3.53) with our Hamiltonian from Eq. (3.54) and our time-dependent wavefunction from Eq. (3.52), which leads to the coupled first-order differential equations

$$\begin{aligned} \dot{c}_1 &= \frac{i\Omega_R}{2} c_2 e^{-i\delta t} \\ \text{and } \dot{c}_2 &= \frac{i\Omega_R}{2} c_1 e^{i\delta t}, \end{aligned} \tag{3.59}$$

where $\delta = \omega_0 - \omega$ is the the detuning from resonance. If we assume the atom is initially in the ground state $|\Psi(t=0)\rangle = |1\rangle$ the solution to Eq. (3.59) is

$$\begin{aligned} c_1(t) &= \left[\cos\left(\frac{\Omega t}{2}\right) + \frac{i\delta}{\Omega}\sin\left(\frac{\Omega t}{2}\right)\right] e^{-i\delta t/2} \\ \text{and } c_2(t) &= \frac{i\Omega_R}{\Omega}\sin\left(\frac{\Omega t}{2}\right) e^{i\delta t/2}, \end{aligned} \tag{3.60}$$

as discussed in Refs. [73, 92, 112]. In Eq. (3.60) we have also introduced the frequency $\Omega = \sqrt{\Omega_R^2 + \delta^2}$. From Eq. (3.60) we see that the population of each state, which is equivalent to the probability of being in a particular state (e.g., $\langle 1| e^{i\hbar\omega_1} |\Psi\rangle = |c_1(t)|^2$), oscillates due to absorption and stimulated emission. Figure 3.7 shows the excited state population's on-resonance temporal dependence ($|c_2(t)|^2$ for $\delta = 0$) and the population's dependence on detuning at $|c_2(t = \pi/\Omega_R)|^2$.

Spontaneous lifetime In the limit of low intensity where the population mostly stays in the ground state $\Omega_R \ll \delta$ or $\Omega \approx \delta$, the probability of being in the excited state can be approximated by

$$|c_2(t)|^2 = \frac{\Omega_R^2}{\delta^2}\sin^2\left(\frac{\delta t}{2}\right) = \frac{2u|\langle 1|\vec{d}\cdot\hat{\varepsilon}|2\rangle|^2}{\varepsilon_0\hbar^2\delta^2}\sin^2\left(\frac{\delta t}{2}\right), \tag{3.61}$$

as discussed in Refs. [73, 92]. In the last part of Eq. (3.60), we have used Eq. (3.33) to make a substitution for the $|E_0|^2$ in the Rabi frequency in terms of the energy density u.

We can use Eq. (3.61) to derive an expression for calculating the spontaneous emission

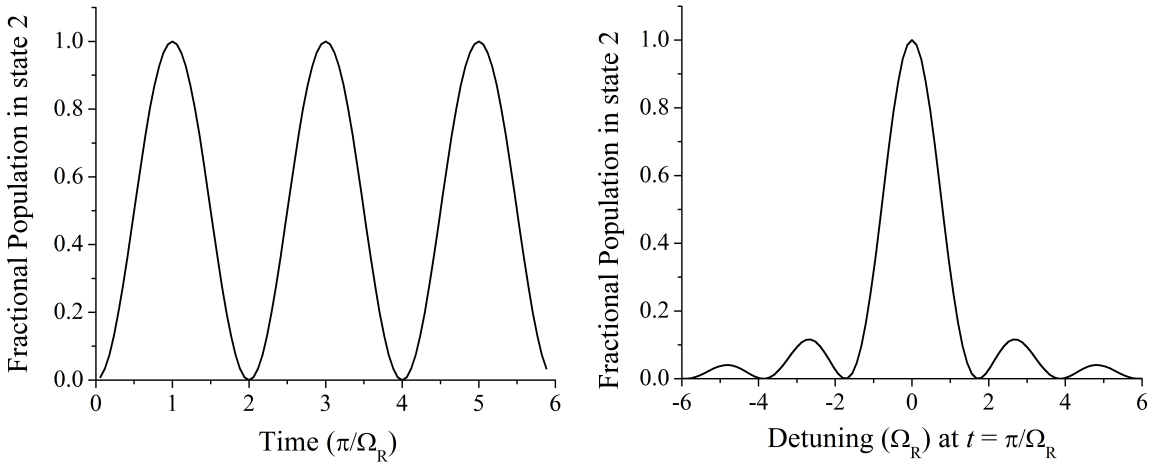

Figure 3.7: Left plot shows time dependence of coherent population transfer of the excited state $|2\rangle$ (with $\delta = 0$) only due to absorption and stimulated emission [according to modulus squared of Eq. (3.60]. When incoherent spontaneous emission can be ignored and the atom is exposed to radiation for a time π/Ω_R, making the argument of the Sine $\pi/2$, the initial population is completely transfered to the excited state. That process is called a $\pi/2$ pulse. The right plot shows how the population in $|2\rangle$ depends on the detuning at time $t = \pi/\Omega_R$. The maximum population transfer occurs when the light is on resonance $\delta = 0$.

rate in the presence of broadband radiation. When the atom experiences broadband radiation, most of the population remains in the ground state, thus validating our earlier assumption and the energy density can be written as $u \to \rho(\omega)d\omega$. Here, we have modeled the broadband radiation as having an energy density distribution with energy density $\rho(\omega)d\omega$ in the range $d\omega$, which must be integrated over all frequencies. Typically $\rho(\omega)$ is broad and slowly varying while the $\sin(\delta t/2)/\delta$ is sharply peaked around ω_0 (as seen in Fig. 3.7). Therefore, when the integrand is non-zero the energy density is fairly constant and can come out of the integral [92]. The approximate result is

$$|c_2(t)|^2 = \frac{2|\langle 1|\vec{d}\cdot\hat{\varepsilon}|2\rangle|^2}{\varepsilon_0\hbar^2\delta^2}\rho(\omega_0)\int_0^\infty \frac{\sin^2(\delta(\omega)t/2)}{\delta(\omega)^2}\,d\omega \approx \frac{\pi|\langle 1|\vec{d}\cdot\hat{\varepsilon}|2\rangle|^2}{\varepsilon_0\hbar^2}\rho(\omega_0)t \quad (3.62)$$

and the rate (first time derivative) becomes constant

$$R_2 \approx \frac{\pi |\langle 1|\vec{d}\cdot\hat{\varepsilon}|2\rangle|^2}{\varepsilon_0\hbar^2}\rho(\omega_0). \tag{3.63}$$

Let us assume that the light does not have a single polarization and propagation direction, but is instead isotropic in $\hat{k}$ and $\hat{\varepsilon}$. When the light is isotropic we need to replace $|\langle 1|\vec{d}\cdot\hat{\varepsilon}|2\rangle|^2$ with its average value [92]. Using $\vec{d} = d\sin(\theta)\hat{y} + d\cos(\theta)\hat{z}$ in the yz-plane, $\hat{\varepsilon} = \cos(\phi)\hat{x} + \sin(\phi)\hat{y}$ in the xy-plane, and integrated over all possible orientations gives the average value of

$$|\langle 1|\vec{d}\cdot\hat{\varepsilon}|2\rangle|^2_{\text{av}} = \frac{|\langle 1|\vec{d}|2\rangle|^2}{4\pi}\int \sin^2(\theta)\sin^2(\phi)d\Omega = \frac{q^2|\langle 1|\vec{r}|2\rangle|^2}{3}, \tag{3.64}$$

The isotropic rate is therefore

$$R_2^{\text{av}} \approx \frac{\pi q^2|\langle 1|\vec{r}|2\rangle|^2}{3\varepsilon_0\hbar^2}\rho(\omega_0) = B_{12}\rho(\omega_0), \tag{3.65}$$

where B_{12} is the Einstein B coefficient [73].

The Einstein coefficients come from Einstein's rate equation developed before quantum mechanics was actually formalized [114]. The rate equation is

$$\frac{dN_2}{dt} = \underbrace{-A_{21}N_2}_{\text{spont.}} - \underbrace{B_{21}N_2\rho(\omega_0)}_{\text{stim.}} - \underbrace{B_{12}N_1\rho(\omega_0)}_{\text{absorp.}} \tag{3.66}$$

as discussed in Refs. [73, 92]. Amazingly, the steady-state solution along with Plank's blackbody formula for the energy density distribution allowed Einstein to correctly predict that the stimulated emission rate should equal the absorption rate, $B_{21} = B_{12}$. Additionally, he predicted that the net spontaneous emission rate is related to the stimulated emission rate by

$$A_{21} = \frac{\hbar\omega_0^3}{\pi^2c^3}B_{21}. \tag{3.67}$$

Thus using Eq. (3.65) we can express the spontaneous emission rate as

$$A_{21} = \frac{4\alpha |\langle 1|\vec{r}|2\rangle|^2 \omega_0^3}{3c^2} = \Gamma. \tag{3.68}$$

For a two-level atom we can equate the spontaneous emission rate with Γ, whose maximum value is the classical dipole radiation decay rate γ from Sec. 3.2. However, in a multilevel atom that has several possible lower states, we would need to sum over all possible rates to get the net rate $\Gamma = A_{21} + A_{20} + ...$

Decoherence from spontaneous emission Thus far we have only solved for the probability of coherent emission and absorption of radiation, whose results apply for transitions with a very small Γ. However, we would like to include the incoherent spontaneous decay in our model, too. This is most easily accomplished by switching to the density matrix formalism, which describes both pure and mixed quantum states [73, 108]. The density matrix operator is defined as a sum of pure states, weighted by their probability $\tilde{p}$ or $\hat{\rho} = \sum_x \tilde{p}_x |x\rangle \langle x|$. For a single pure state there is just one term in the sum $|\Psi\rangle \langle \Psi|$, so for our two-level atom pure state defined in Eq. (3.52)

$$\begin{aligned} \hat{\rho} = |\Psi\rangle \langle \Psi| &= |c_1|^2 |1\rangle \langle 1| + |c_2|^2 |2\rangle \langle 2| + c_1 c_2^* e^{-i\omega_0 t} |1\rangle \langle 2| + c_2 c_1^* e^{i\omega_0 t} |2\rangle \langle 1| \\ &= \begin{pmatrix} |c_1|^2 & c_1 c_2^* e^{-i\omega_0 t} \\ c_2 c_1^* e^{i\omega_0 t} & |c_2|^2 \end{pmatrix}, \end{aligned} \tag{3.69}$$

where the trace $\mathrm{Tr}(\hat{\rho}) = 1$, so that the total probability of finding the state in $|1\rangle$ or $|2\rangle$ is unity. Additionally, the expectation value of an operator $\hat{A}$ is now given by $\langle \hat{A} \rangle = \mathrm{Tr}(\hat{\rho}\hat{A})$. The diagonal terms of the density matrix represent the fractional population and the off-diagonal terms are called coherences. The time dependence of the density matrix is

determined by the Liouville-von Neumann equation

$$-i\hbar\frac{\partial\hat{\rho}}{\partial t}=\left[\hat{H}_{\text{tot}},\hat{\rho}\right],\ \text{ so }\ -i\hbar\frac{\partial\hat{\rho_{nm}}}{\partial t}=\langle n|\left[\hat{H}_{\text{tot}},\hat{\rho}\right]|m\rangle, \tag{3.70}$$

where [...] denotes commutators [112].

Substituting our expressions for $\hat{H}_{\text{tot}}$ and $\hat{\rho}$ into Eq. (3.70) yields four coupled first-order differential equations known as the optical Bloch equations

$$\begin{aligned}
\frac{d\hat{\rho}_{11}}{dt}&=\frac{i\Omega_R}{2}\left[\hat{\rho}_{21}e^{i\omega t}-\hat{\rho}_{12}e^{-i\omega t}\right],\\
\frac{d\hat{\rho}_{22}}{dt}&=-\frac{i\Omega_R}{2}\left[\hat{\rho}_{21}e^{i\omega t}-\hat{\rho}_{12}e^{-i\omega t}\right],\\
\frac{d\hat{\rho}_{12}}{dt}&=i\omega\hat{\rho}_{12}+\frac{i\Omega_R}{2}e^{i\omega t}\left[\hat{\rho}_{22}-\hat{\rho}_{21}\right],\\
\frac{d\hat{\rho}_{21}}{dt}&=i\omega\hat{\rho}_{21}+\frac{i\Omega_R}{2}e^{-i\omega t}\left[\hat{\rho}_{22}-\hat{\rho}_{21}\right].
\end{aligned} \tag{3.71}$$

At this stage we could solve the coupled equations for $\hat{\rho}_{22}$ and we would arrive at the modulus squared of our earlier result Eq. (3.60). Instead we will now add the decoherence of the spontaneous emission, which decays at a rate Γ. In adding the decay term, we would like the population to exponentially decay from $|2\rangle$ down to $|1\rangle$ as it did in the classical model Eq. (3.46), namely when $\Omega_R=0$, $\hat{\rho}_{22}=\hat{\rho}_{22}(0)e^{-\Gamma_{22}t}$ or $d\hat{\rho}_{22}/dt=-\Gamma_{22}\hat{\rho}_{22}$. Adding these decay terms to Eq. (3.71) gives new coupled equations[6]

$$\begin{aligned}
\frac{d\hat{\rho}_{11}}{dt}&=\Gamma\hat{\rho}_{22}+\frac{i\Omega_R}{2}\left[\hat{\rho}_{21}e^{i\omega t}-\hat{\rho}_{12}e^{-i\omega t}\right],\\
\frac{d\hat{\rho}_{22}}{dt}&=-\Gamma\hat{\rho}_{22}-\frac{i\Omega_R}{2}\left[\hat{\rho}_{21}e^{i\omega t}-\hat{\rho}_{12}e^{-i\omega t}\right],\\
\frac{d\hat{\rho}_{12}}{dt}&=-\frac{\Gamma\hat{\rho}_{12}}{2}+i\omega\hat{\rho}_{12}+\frac{i\Omega_R}{2}e^{i\omega t}\left[\hat{\rho}_{22}-\hat{\rho}_{21}\right],\\
\text{and }\ \frac{d\hat{\rho}_{21}}{dt}&=-\frac{\Gamma\hat{\rho}_{21}}{2}+i\omega\hat{\rho}_{21}+\frac{i\Omega_R}{2}e^{-i\omega t}\left[\hat{\rho}_{22}-\hat{\rho}_{21}\right].
\end{aligned} \tag{3.72}$$

[6]We have used the fact that the spontaneous decay rate $\Gamma=\Gamma_2=(\Gamma_2+\Gamma_2)/2$ and that $\Gamma_{12}=\Gamma_{21}=(\Gamma_2+0)/2=\Gamma/2$, since there is no decay Γ_1 from the ground state in a two-level atom.

To solve these equations it is customary to define three new coupled equations $V_x(t)$, $V_y(t)$, and $V_z(t)$, which can be thought of as components of a vector $\vec{V}$. The first two components have to do with the coherences and the third has to do with the populations,

$$\begin{aligned} V_x(t) &= \left[\hat{\rho}_{21}e^{i\omega t} + \hat{\rho}_{12}e^{-i\omega t}\right], \\ V_y(t) &= i\left[\hat{\rho}_{21}e^{i\omega t} - \hat{\rho}_{12}e^{-i\omega t}\right], \\ \text{and } V_z(t) &= [\hat{\rho}_{22} - \hat{\rho}_{11}] = 2\hat{\rho}_{22} - 1, \end{aligned} \tag{3.73}$$

where we used the fact that the trace of the density matrix is unity in the last step. The differential equations from Eq. (3.72) can now be rewritten with three equations

$$\begin{aligned} \frac{dV_x(t)}{dt} &= -\frac{\Gamma}{2}V_x - \delta V_y, \\ \frac{V_y(t)}{dt} &= -\frac{\Gamma}{2}V_y + \delta V_x + \Omega_R V_z, \\ \text{and } \frac{V_z(t)}{dt} &= -\Gamma(V_z + 1) - \Omega_R V_y, \end{aligned} \tag{3.74}$$

which have well known steady-state solutions [73]. Using the steady-state solutions for the components of $\vec{V}$ and Eq. (3.74) to relate those solutions to the population density matrix elements gives

$$\begin{aligned} V_z(t \to \infty) &= \frac{\delta^2 + \Gamma^2/4}{\delta^2 + \Omega_R^2/2 + \Gamma^2/4}, \\ \text{and } \hat{\rho}_{22}(t \to \infty) &= \frac{\Omega_R^2/4}{\delta^2 + \Omega_R^2/2 + \Gamma^2/4}, \end{aligned} \tag{3.75}$$

which saturates rather than oscillates. In the limit of large intensity, where $\Omega_R^2 \propto |E_0|^2 \to \infty$, we find that $\hat{\rho}_{22} = 1/2$.

We can also express the excited state fraction $\hat{\rho}_{22}$ in terms of the saturation intensity I_s

as

$$\hat{\rho}_{22}(t \to \infty) = \frac{1}{2}\frac{I/I_s}{1+4(\delta/\Gamma)^2+I/I_s}, \tag{3.76}$$

$$\text{and} \quad \frac{I}{I_s} = \frac{2\Omega_R^2}{\Gamma^2}. \tag{3.77}$$

When $I = I_s$ the spontaneous emission angular frequency is on the same order of magnitude as the stimulated emission angular frequency. Sometimes the saturation intensity in Eq. (3.77) is defined with the factor of two [73, 111] and sometimes without [115], in the latter case the spontaneous and stimulated frequencies are exactly equivalent at saturation. Using the definition for intensity in Eq. (3.33) and the definition of the Rabi frequency in Eq. (3.55) gives the saturation intensity formula

$$I_s = \frac{c\varepsilon_0\Gamma^2\hbar^2}{4|\langle 1|\vec{d}\cdot\hat{\varepsilon}|2\rangle|^2}. \tag{3.78}$$

The saturation intensity can then be empirically determined [115–117] or calculated [111] for a specific transition with a known light polarization with Eq. (3.78).

From Eq. (3.76), the total photon scattering rate per atom in steady state becomes

$$\Gamma\hat{\rho}_{22} = \frac{\Gamma}{2}\frac{I/I_s}{1+4(\delta/\Gamma)^2+I/I_s}. \tag{3.79}$$

3.3.4 Optical cross section

In the same spirit as the ion-neutral scattering cross section in Ch. 2, we can also assign a cross section for the atom-light interaction. We would interpret the cross section size as being proportional to the likelihood of an atom absorbing a photon and reradiating it, similar to how the ion-neutral scattering cross section was related to the likelihood of a collision.

We already saw with our classical model in Sec. 3.2 that the absorption cross section was proportional to the absorption coefficient. However, to account for the stimulated emission offset we want the rate of absorbed energy $N_1\sigma(\omega)I$ that exceeds the stimulated rate $N_2\sigma(\omega)I$, so

$$-\kappa I = -(N_1 - N_2)\sigma I = -N_2\Gamma\hbar\omega_0, \tag{3.80}$$

where again $N = N_1 + N_2$ refers to the total atom number density [73]. In the last part of Eq. (3.80), we have equated the net rate of energy absorbed to the rate at which energy is scattered spontaneously out of the N_2 excited atoms per unit volume. Using our steady-state solution for $V_z = (N_2 - N_1)/N$ and $\hat{\rho}_{22} = N_2/N$ in Eq. (3.80) gives the cross section as

$$\sigma(\omega) = \frac{N_2}{N_1 - N_2}\frac{\Gamma\hbar\omega_0}{I} = \frac{(\Omega_R^2)\Gamma\hbar\omega_0}{4I(\delta^2 + \Gamma^2/4)}. \tag{3.81}$$

When the laser is on resonance $\delta = 0$ we see that $\sigma(\omega_0) = \sigma_0$ is at a maximum and using Eq. (3.77) we can express the saturation intensity as

$$I_s = \frac{\hbar\omega_0\Gamma}{2\sigma_0}. \tag{3.82}$$

Explicitly including the intensity dependence of Rabi frequency using Eq. (3.33)

$$\Omega_R^2 = \frac{e^2|\langle 1|\vec{r}\cdot\hat{\varepsilon}|2\rangle|^2 E_0^2}{\hbar^2} = \frac{2Ie^2|\langle 1|\vec{r}\cdot\hat{\varepsilon}|2\rangle|^2}{\hbar^2\varepsilon_0 c} = \frac{2Ie^2}{\hbar^2\varepsilon_0 cQ}\frac{A_{21}3c^2}{4\alpha\omega_0^3} = \frac{2I\pi\Gamma 3c^2}{Q\hbar\omega_0^3} \tag{3.83}$$

shows that Eq. (3.81) is actually intensity independent and the cross section can be expressed as a Lorentzian

$$\sigma(\omega) = \frac{3\pi^2 c^2\Gamma}{Q\omega_0^2}\left(\frac{1}{2\pi}\frac{\Gamma}{\delta^2 + \Gamma^2/4}\right) \tag{3.84}$$

as was found to be the case classically in Sec. 3.2. In going from the third term to the fourth

in Eq. (3.83) we let $|\langle 1|\vec{r}\cdot\hat{\varepsilon}|2\rangle|^2 \rightarrow |\langle 1|\vec{r}\cdot\hat{\varepsilon}|2\rangle|^2_{\text{av}}$, as was done in Eq. (3.64), and then made a substitution for $|\langle 1|\vec{r}|2\rangle|^2$ using the A_{21} expression in Eq. (3.68). However, the result of the averaging amounts to a prefactor Q that can take on a value between 1 and 3 depending on the polarization of the light field and atomic alignment. If there is an isotropic light field then Q = 3 [as we saw in Eq. (3.64)] when averaged over all orientations. If the light field is polarized for a single optimum orientation then Q = 1.

Using Eq. (3.84), the maximum cross section for the two level atom with zero detuning can be written as $\sigma_0 = 6\pi c^2/(Q\omega_0^2)$, making the I_s from Eq. (3.86) equal to

$$I_s = \frac{Q\hbar\omega_0^3\Gamma}{12\pi c^2}. \tag{3.85}$$

This expression for I_s is actually equivalent to our earlier result in Eq. (3.78), if we average the dipole term in the denominator over multiple orientations and make the substitution for $|\langle 1|\vec{r}|2\rangle|^2$ using Eq. (3.68).

We end by returning to the absorption coefficient κ, which according to Eq. (3.80) can be written as $\kappa = (N_1 - N_2)\sigma(\omega)$, and following Ref. [73]'s manipulation equals

$$\kappa = \frac{N\sigma(\omega)}{1+2N_2/(N_1-N_2)} = \frac{N\sigma(\omega)}{1+2I\sigma(\omega)/[\hbar\omega_0\Gamma]}, \tag{3.86}$$

using $N = N_1 + N_2$ and Eq. (3.80). Using our expression for σ_0 and substituting our earlier expression for the cross section Eq. (3.84) gives the quantal absorption coefficient

$$\kappa = N\sigma_0\frac{\Gamma^2/4}{\delta^2+\Gamma^2/4(1+I/I_s)}, \tag{3.87}$$

which includes the homogeneous power broadening term [73] giving an effective linewidth $\Gamma\sqrt{1+I/I_s}$. In the spectra shown in Fig. 3.4, the fitting parameter for the measured effective linewidth is slightly larger than the known value of the atomic linewidth $\Gamma \approx (2\pi)10$ MHz. The difference is due to the power broadening. Although the broadening is

undesirable, it is necessary to achieve a strong enough signal to noise ratio.

In conclusion, we have discussed the energy levels and wavefunctions of a hyrdrogenic atom, including relativistic corrections and hyperfine splitting. We also discussed extending the hydrogenic model to alkali-like atoms and ions using the central-field model. Last, we discussed classical and quantum models of the matter-light interaction in a two-level atom, yielding expressions for the coherent population transfer probability, spontaneous emission rate, steady-state photon scattering rate, and optical absorption cross section. In the following chapters we will utilize the underlying background explored here to better explain the workings of the hybrid apparatus and our experimental results.

Chapter 4

Hybrid trap apparatus

In this chapter we will fully describe the underlying physics and technical details behind the operation and design of our group's hybrid trap apparatus. This chapter is divided into three sections: the optical table layout, the neutral atom trap, and the ion trap. In each section we will discuss the design and engineering of our group's traps, how the traps are characterized, how the traps are loaded, and how neutral atom and/or ion measurements are performed.

4.1 Optical table layout

The experimental apparatus sits on a standard breadboard optical table. Due to a lack of environmental controls in the laboratory we had to correct for significant dust accumulation on the optical table. To prevent dust buildup we shrouded the optical table with freezer-door type plastic flaps from Singer Safety Co. Above the table hangs a single piece of polyurethane-coated plywood with steel beam reinforcement. The plywood rack holds an industrial laminar airflow fan with a HEPA filter from CleanAir Solutions Inc. that causes a positive overpressure inside the shroud, further preventing dust from getting into the

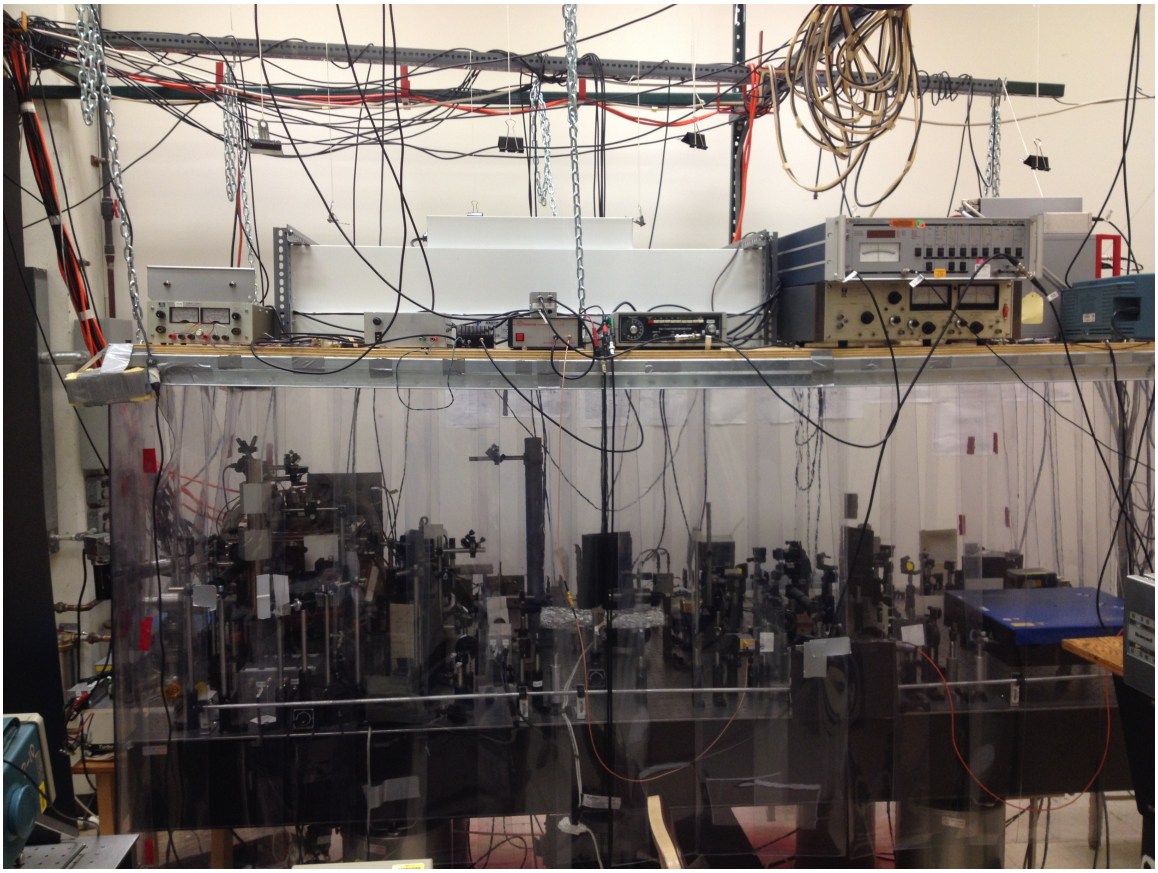

Figure 4.1: Optical table in plastic flaps shroud. The plywood rack holds a HEPA filter air filtration system and various electronics.

shrouded table. The plywood rack also holds much of the electronic controls. The complete system can be seen in the photograph in Fig. 4.1. Once the shroud was implemented the necessity to clean optics dropped from being a daily concern to a tri-annual one.

An illustration of the optical table layout is shown in Fig. 4.2. The optical layout shows the following lasers: the Toptica TA-SHG Pro 589 nm laser used for laser cooling on the Na D2 line, the RGBLase 405 nm diode laser used for photoionizing (PI) the excited Na^* to create Na^+, the Toptica DL100 379 nm diode laser used for laser cooling Ca^+, and the 866 nm laser used as a repumper for the Ca^+ cooling. All laser radiation leads to the vacuum chamber where the hybrid trap is formed.

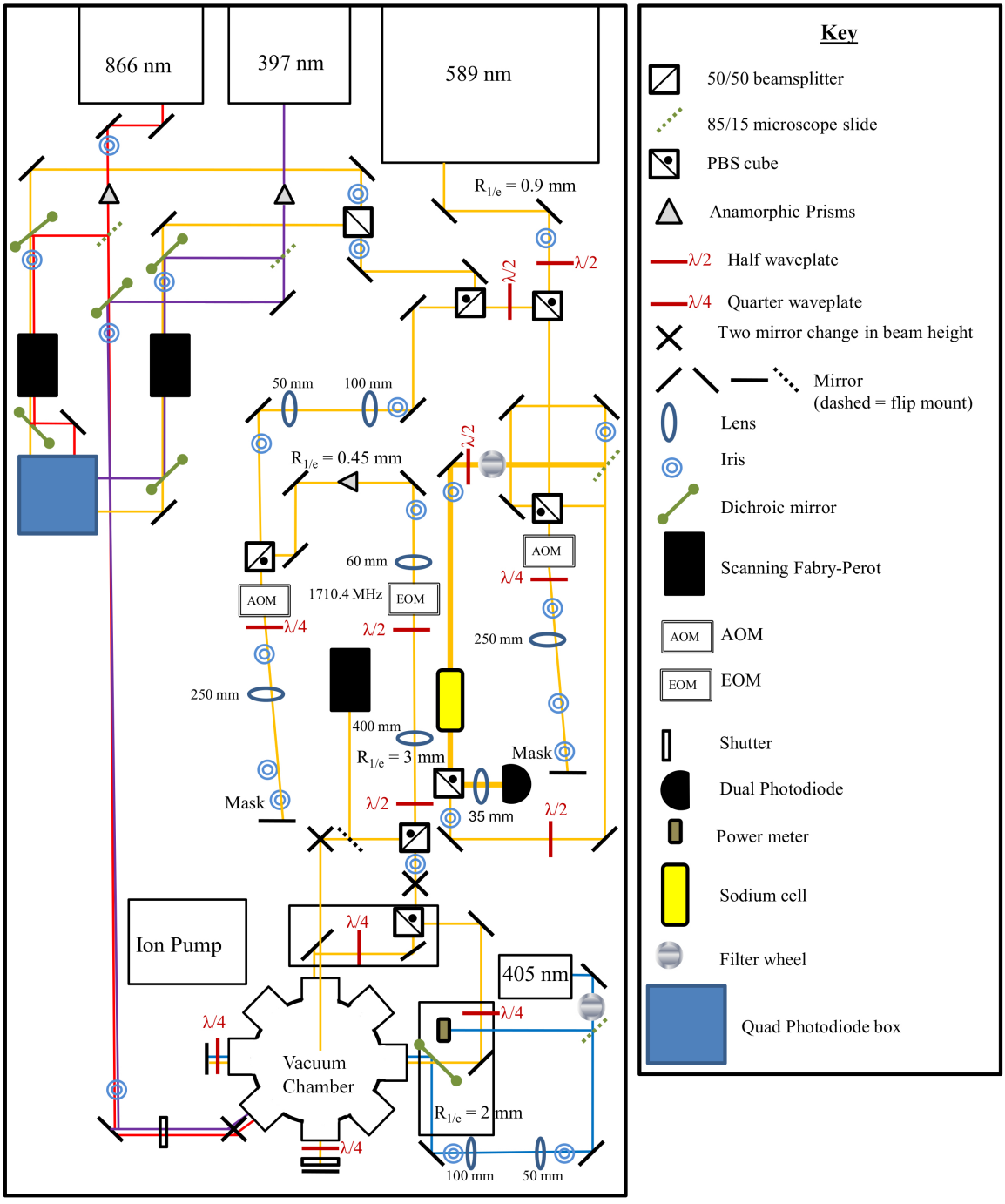

Figure 4.2: Detailed schematic (not to scale) of optical table layout. The CMOS camera, PMT, and several electromagnets all near or on the vacuum chamber are not shown in this figure [instead, see Figs 4.33 and 4.60 for location of those components]. For most of the experiments presented here the 397 nm laser and 866 nm laser are not used and the CMOS camera was located at the lower left diagonal viewport.

The optics in between the laser source and the chamber are primarily used for laser frequency stabilization (locking) and beam shaping, so that the beams are the necessary size, polarization, and wavelength for cooling, trapping, or ionizing purposes. A major part of our discussion in the remaining sections will be devoted to the use of these lasers and how they are frequency-stabilized.

4.2 Magneto-optical trap

4.2.1 Doppler cooling and trapping in a MOT

The neutral atom trap in our hybrid apparatus is a MOT [31]. The MOT cools and traps a dilute cloud of Na atoms in the center of our vacuum chamber, concentric within the LPT. The cooling and trapping is accomplished by carefully choreographed radiation pressure forces acting on a warm background Na vapor. In this section we begin by discussing the radiation pressure force's damping or velocity dependence and how this results in cooling. Next we will discuss the spatial spring force dependence of the radiation force.

Classical radiation pressure It has been known that light carries a momentum since Maxwell, before the formulation of quantum mechanics. The classical momentum $\vec{p}_d$ per unit volume V carried by light is described in Eq. (3.34). When light with intensity I is absorbed by an object there is an impulse at the scattering rate R_{scatt} and a pressure

$$P = \frac{F_{\text{rad}\perp}}{A} = \frac{\Delta\vec{p}_{d\perp} V R_{\text{scatt}}}{A} = \frac{I}{c^2}(Ac)\frac{1}{A} = \frac{I}{c}, \tag{4.1}$$

where there is an extra factor of two if the light is reflected, because Δp is doubled. This radiation pressure is what gives a solar sail its thrust, as illustrated in Fig. 4.3. In fact, on a sunny day at the beach incident sunlight with $I = 1.4\ \text{kWm}^{-2}$ provides a very weak pressure 5 μNm^{-2}. This radiation pressure is so small compared to atmospheric pressure

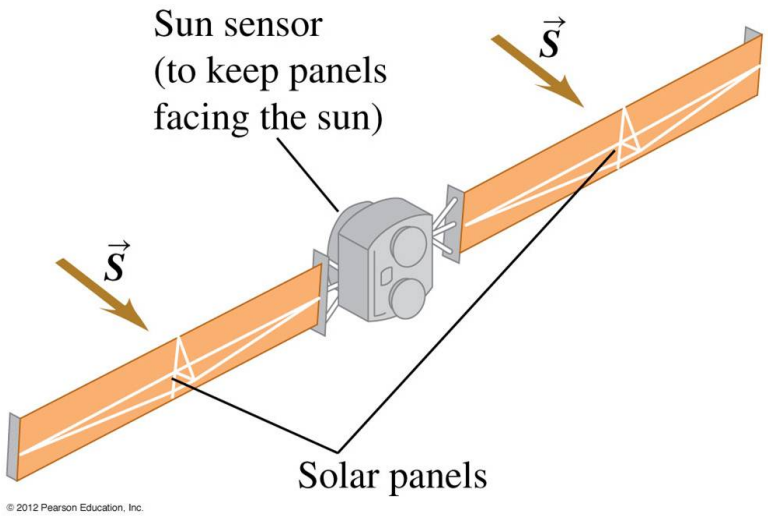

Figure 4.3: Originally from Ref. [118] showing solar panels experiencing a radiation pressure from sunlight.

(about 10^{-10} times weaker) that we do not notice a pressure difference between day and night [73, 118].

Quantum radiation force Instead of describing the atomic radiation pressure semi-classically in terms of the absorption cross section $F_{\text{rad}} = \sigma I/c$, it is convenient to use the quantum mechanical atom-photon interaction. As discussed in Ch. 3, there are three kinds of interactions: absorption, spontaneous emission, and stimulated emission. The absorption of a counter-propagating photon is a 1D inelastic collision. The total momentum and energy conservation associated with the absorption of a photon leads to the relations

$$\begin{aligned} -\hbar\frac{\omega}{c} &= -m_N u_a', \\ \text{and } \hbar\omega &= \frac{1}{2}m(u_a')^2 + \hbar\omega_0, \end{aligned} \tag{4.2}$$

in the atom's rest frame, respectively. In Eq. (4.2) m_N is the mass of the atom, $p_{\text{photon}} = \hbar k = \hbar\omega/c$ is the photon momentum, and u_a' is the post collision atom velocity.

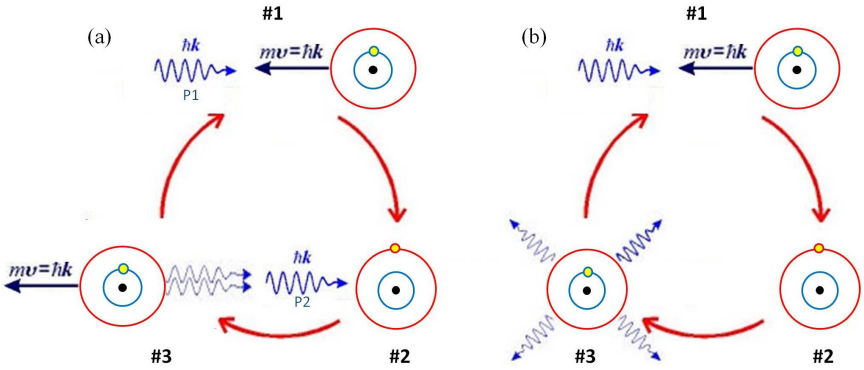

Figure 4.4: Panel (a) shows the process of absorption followed by stimulated emission in the laboratory reference frame resulting in no-net momentum or energy change for the atom. Panel (b) shows the process of absorption followed by spontaneous emission, which emits photons isotropically, resulting in an average momentum decrease.

Thus the photon must have slightly more energy than the transition energy $\hbar\omega_0$, since some of its energy goes into the atom's final kinetic energy. However the difference is small and $\omega \approx \omega_0$.

In the laboratory frame we similarly have

$$\begin{aligned} m_N v_a - \hbar\frac{\omega_L}{c} &= m_N v_a', \\ \text{and } \frac{1}{2}mv_a^2 + \hbar\omega_L &= \frac{1}{2}m(v_a')^2 + \hbar\omega_0, \\ \text{where } \omega_L &\approx \omega - k_L v. \end{aligned} \tag{4.3}$$

In the last line of Eq. (4.3) we used the first order Doppler shift of the counter-propagating light frequency, which tells us that the frequency in the lab frame must be less than the atomic transition frequency. In general, $\omega \approx \omega_0 \approx \omega_L - \vec{k}_L \cdot \vec{v}$. From Eq. (4.3) we find that $v_a' < v_a$, when absorbing a counter-propagating photon decreasing momentum and kinetic energy, if the atom initially has momentum $p_a > p_{\text{photon}}$.

The emission of radiation leads to similar expressions to that of Eqs. (4.2) and (4.3) due to the conservation of momentum and energy. If the atom is only absorbing counter-

propagating photons (for reasons explained later), then the stimulated emission will always result in a recoil momentum equal and opposite to the absorption momentum, giving no net momentum change, as seen in Fig. 4.4 (a). However, the spontaneous emission process is isotropic, so the emission has an average zero momentum change. Therefore, each absorption followed by spontaneous emission cycle at worst will have no net momentum change and at best decrease the momentum by $2\hbar k_L$, as seen in Fig. 4.4 (b). The net effect is an average $\hbar k_L$ momentum decrease per counter-propagating photon absorbed and then spontaneously emitted.[1]

Knowing the mean impulse per scattering event allows us to calculate the radiation force on an atom using the steady-state scattering rate Eq. (3.79) from the optical Bloch equations and the photon impulse $\hbar\vec{k}_L$, which gives

$$\vec{F}_{\text{rad}} = \Delta\vec{p}R_{\text{scatt}} = \hbar\vec{k}_L\Gamma\hat{\rho}_{22} = \hbar\vec{k}_L\frac{\Gamma}{2}\frac{I/I_s}{1+4(\delta/\Gamma)^2+I/I_s}. \tag{4.4}$$

Although each absorption event has a relatively small impulse, on resonance the rate of events goes like Γ, which is large. In fact, according to Eq. (4.4) at $I \gg I_s$ and $\delta = 0$ the maximum radiation force on a Na atom is $\sim 10^5$ times stronger than the force due to gravity.

The temperature T of the background Na gas depends on the statistical distribution of speeds that we will assume follow a MB distribution. Therefore, in 1D, the velocity v distribution must be Gaussian

$$f(v)_{\text{1DMB}} \propto e^{-m_N v^2/2k_B T}, \tag{4.5}$$

[1]The energy of the spontaneously emitted photon that is part of an absorption/emission cycle that results in a net decrease in momentum must have a higher emission frequency than the initial absorption frequency for energy to be conserved. Another way to think of it is that the absorbed photon is less than the atomic transition frequency (in the laboratory frame) and the emitted photon is co-propagating with the atom and will be Doppler shifted above the atomic transition (in the laboratory frame), thus the atom's loss in kinetic energy goes into the re-radiated photon's energy.

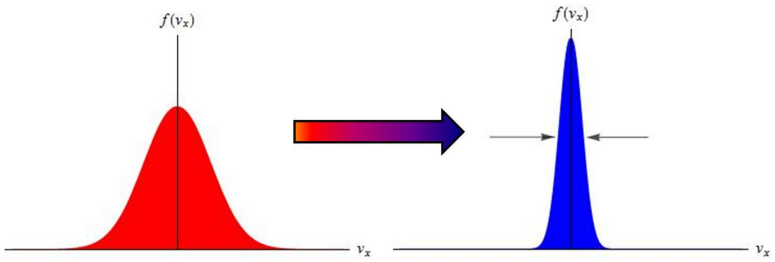

Figure 4.5: A gas that obeys MB statistic has a Gaussian 1D velocity distribution. When a gas is cooled the distribution becomes more narrowly peaked about its center, zero velocity. To change the gas's distribution we need a velocity dependent force.

where m_N is the mass of the Na atom. Cooling a gas is equivalent to narrowing the 1D velocity distribution for each dimension, as illustrated in Fig. 4.5. To change the distribution one needs a net damping force that opposes the atom's motion and is proportional to the atom's speed, thus squeezing the distribution. Therefore, we want the net radiation force to have a damping dependence $F = -\alpha v$, vanishing at $v = 0$.

Damping radiation force We are able to control the velocity dependence and directionality of the force by red-detuning the laser radiation below the atomic resonance, as seen in the laboratory (or laser source's) rest frame. As illustrated in Fig. 4.6, let us imagine an atom restricted to move in 1D in the presence of highly monochromatic laser radiation incident from the right and the left. If the laser light is detuned below the atomic resonance in the laboratory reference frame, then atoms that are at rest in the laboratory rest frame weakly interact with the radiation, because the probability of absorption is small according to Eq. (3.60) and Fig. 3.7, making the force on low velocity atoms zero. However, atoms that are counter-propagating the laser radiation in the laboratory frame will see the radiation Doppler shifted up in the atom's own reference frame, making absorption likely. The co-propagating beam is Doppler shifted even further out of resonance, which gives the directionality or overall minus sign in our resulting radiation force.

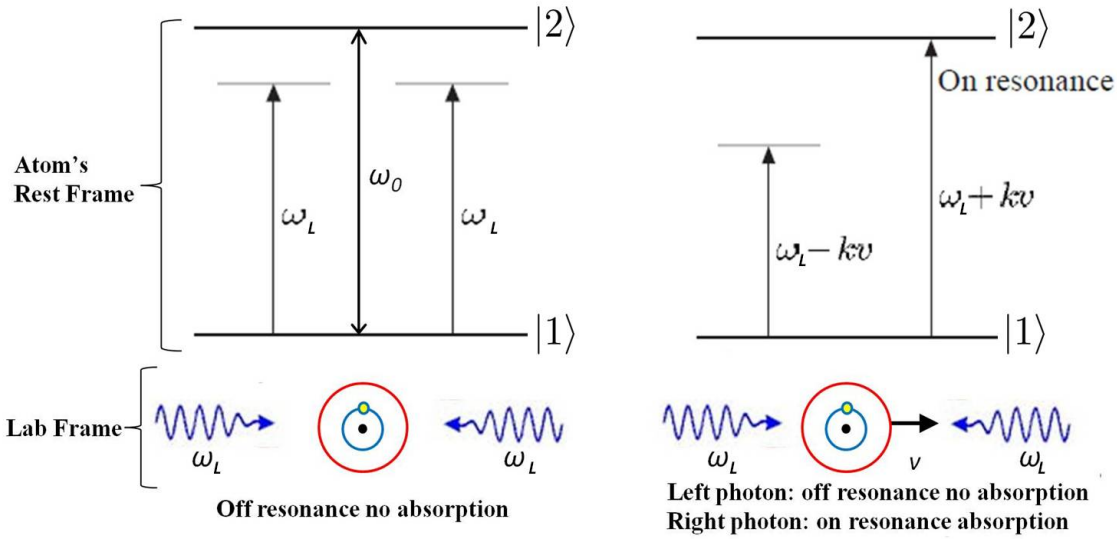

Figure 4.6: Modified version of a figure from Ref. [73]. The top two pictures show the energy level diagram for a two-level transition in the atom's rest frame. The bottom two illustrations correspond to the same situations, but in the laboratory reference frame where the laser source is at rest. On the left, the atom is stationary relative to the laser sources in the laboratory and the atom sees all the incident light as off resonant. On the right, the atom is moving relative to the laboratory frame and sees the opposing laser beam as Doppler shifted toward resonance within its own rest frame.

The detuning in Eq. (4.4) can be written as $\delta = \omega - \omega_0 \approx (\omega_L + k_L v) - \omega_0$ for the negative (leftward) propagating beam and as $\delta \approx (\omega_L - k_L v) - \omega_0$ for the positive (rightward) propagating. Substituting the detuning into Eq. (4.4) gives 1D net force

$$\begin{aligned} F_{\text{net}} &= \hbar \frac{\omega_L}{c} \frac{\Gamma}{2} \left\{ \frac{-I/I_s}{1+4\left[(\omega_L-\omega_0+k_L v)/\Gamma\right]^2 + I/I_s} + \frac{I/I_s}{1+4\left[(\omega_L-\omega_0-k_L v)/\Gamma\right]^2 + I/I_s} \right\} \\ &\approx -2\frac{\partial F}{\partial \omega_L} k_L v. \end{aligned} \tag{4.6}$$

In the last line of Eq. (4.6) we have restricted ourselves to the case of small velocities $k_L v \ll \Gamma$, as discussed in Ref. [73]. The approximate result is a damping force with

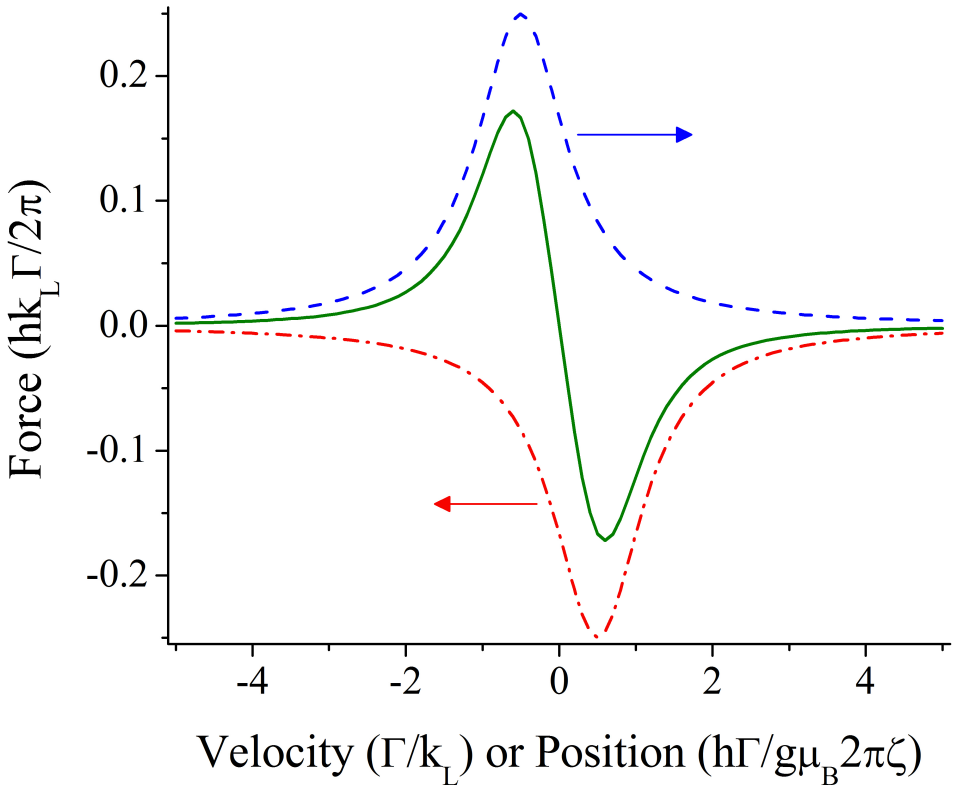

Figure 4.7: 1D radiation force due to velocity dependence or spatial dependence with detuning $\omega_L - \omega_0 = -\Gamma/2$. The dashed blue line shows the force from the rightward propagating laser beam and the dashed red line shows the force from the leftward propagating laser beam. The net force is the green solid line. Between $\pm 1\ \Gamma/k_L$ [or $\hbar\Gamma/(g\mu_B\zeta)$] the net force has an approximately constant negative slope and $F = 0$ y-intercept, making the velocity dependence that of a damping force and the spatial dependence that of a spring force near the origin.

$$\alpha = 2\frac{\partial F}{\partial \omega_L}k_L \approx 2k_L(\hbar k_L)\frac{\partial R_{\text{scatt}}}{\partial \omega_L} = 2\hbar k^2 \frac{4(I/I_s)(-\delta)/\Gamma}{1+4(\delta/\Gamma)^2+I/I_s}. \tag{4.7}$$

In Eq. (4.7), we dropped the term $(\hbar/c)R_{\text{scatt}} \ll \hbar k \partial R_{\text{scatt}}/\partial \omega_L$, as discussed in Ref. [73]. Additionally, the detuning $\delta = \omega_L - \omega_0 < 0$ when the MOT beams are red-detuned, making $\alpha > 0$, which is required for damping. Figure 4.7 shows a plot of each laser beam's force (with $\omega_L - \omega_0 = \Gamma/2$) as a function of laboratory frame velocity and the resulting net force

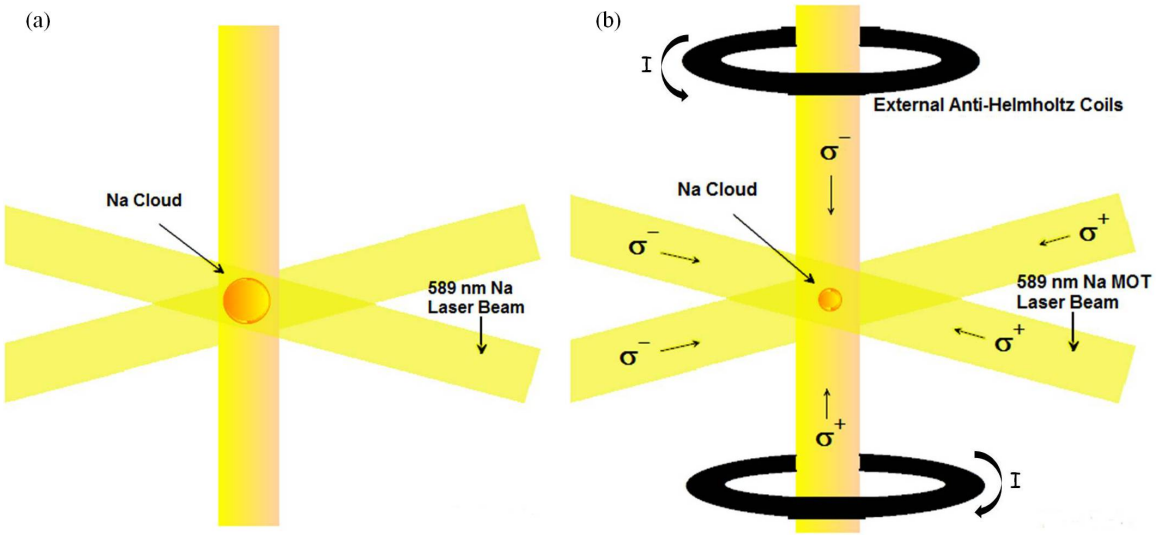

Figure 4.8: Panel (a) shows a 3D optical molasses, six intersection laser beams red detuned yielding a damping force. Panel (b) shows a MOT, which is optical molasses inside a magnetic field gradient. The magnetic field gradient and the polarization of the light beams create an additional spatial dependence to the radiation force.

Eq. (4.6), which has a negative nearly linear slope for small velocities less than Γ/k_L.

Detuning the laser below resonance is critical to the Doppler cooling technique. In order to have a precise detuning one needs a laser with a narrow linewidth. Typically, experimentalists want laser linewidths of $\Delta\omega_L \ll \Gamma$, e.g., $(2\pi) \times 1$ MHz or better for Na.

Thus far we have restricted ourselves to 1D. However, by using three pairs of counter-propagating laser beams (one for each spatial dimension) the damping force in Eq. (4.6) applies to all three dimensions creating what Steven Chu called "optical molasses," as seen in Fig. 4.8 (a). Because the total intensity is from all six beams $I \to I_{\rm tot}$ in Eq. (4.4), where $I_{\rm tot}$ is the total intensity from all six beams at the location of the molasses.

Limiting temperatures Following the treatment of Ref. [119], there are three temperature limits associated with this technique that we will discuss here. The first is the recoil temperature limit T_r. We could imagine starting with a $T = 0$ gas that experiences

one cycle of absorption and emission (recoil) having mean impulse $\Delta p = \hbar\vec{k}_L$. The average energy would be

$$\sim k_B T \sim \frac{\langle \Delta p^2 \rangle}{2m_N} \sim \frac{\hbar^2\omega^2}{m_N c^2} \implies T_r \sim \frac{\hbar^2\omega^2}{2k_B m_N c^2}. \tag{4.8}$$

For Na atoms the recoil temperature is an ultracold $T_r \sim 1\mu$K.

If initially hot atoms are cooled such that their Doppler linewidth $\Gamma_D \sim (\omega_0/c)\sqrt{2k_BT/m_N}$ (to be derived in Sec. 4.2.3) is comparable to the natural linewidth $\Gamma \approx \Gamma_D$, then the cloud is at the natural linewidth temperature limit

$$T^* \sim \frac{\Gamma^2 m_N c^2}{2k_B\omega_0^2}. \tag{4.9}$$

For Na the natural linewidth temperature is a balmy $T^* \sim 40$ mk.

The third temperature limit is the Doppler limit, associated with the optical molasses technique we just derived. We can easily generalize our results to 3D, so for convenience let us take the 1D case. The characteristic velocity of the atoms is

$$\bar{v} = \frac{\sqrt{\langle p^2 \rangle}}{m_N}, \tag{4.10}$$

and the thermal energy is

$$E = \frac{k_B T}{2} = \frac{\langle p^2 \rangle}{2m_N}, \tag{4.11}$$

where $\langle p \rangle = 0$. The cooling power $P_{\text{cool}} = F_{net}\bar{v}$, which using Eq. (4.6) in the limit of $I \ll I_s$ reduces to

$$P_{\text{cool}} \approx -\alpha\bar{v}^2 \approx -8\hbar k_L^2 \frac{I}{I_s} \frac{\bar{v}^2\delta}{\Gamma\left[1+4\delta^2/\Gamma^2\right]^2}. \tag{4.12}$$

The heating power is associated with two random momentum kicks each absorption/emission cycle, so the rate of change of momentum for two beams is ap-

proximately twice the scattering rate at twice the recoil energy. Therefore, the heating power can be expressed as

$$P_{\text{heat}} = 2\Gamma\hat{\rho}_{22}\frac{\hbar^2 k_L^2}{m_N} \overset{I\ll I_s}{\approx} \left(\frac{I}{I_s}\right)\frac{\Gamma}{1+4\delta^2/\Gamma^2}\frac{\hbar^2 k_L^2}{m_N}. \tag{4.13}$$

At equilibrium the two rates are equal and manipulation [73] yields

$$P_{\text{cool}} = P_{\text{heat}} \implies \frac{1}{2}m_N\bar{v}^2 = \left(\frac{\hbar\Gamma}{16}\right)\frac{1+4\delta^2/\Gamma^2}{-2\delta} = \frac{k_B T}{2}, \tag{4.14}$$

which is at a minimum for $\delta = -\Gamma/2$, giving the minimum temperature of

$$T_D = \frac{\hbar\Gamma}{2k_B}. \tag{4.15}$$

For Na this gives a cold value of $\sim 240\ \mu$k, which is comparable to the temperatures we can achieve experimentally,[2] as discussed in Sec. 4.2.6.

Evidently the three temperature limits are related by $T_D^2 = T^* T_r$, as shown in Ref. [119].

Trapping radiation force The optical molasses force provides cooling, but does not provide trapping. A background gas atom that crosses the laser beams will be slowed, but can leave the area of intersection because there is no restoring or spring-like force $F = -\kappa x$, with spring constant κ. By adding a magnetic field gradient and circularly polarizing the molasses beams, we can add a spatial component to the radiation pressure,[3] as seen in Fig. 4.8 (b).

To understand this spring force we must first discuss the Zeeman effect. In Ch. 3 we saw that the electron acquired a hyperfine energy shift due to its magnetic dipole moment in

[2]Interestingly, the original optical molasses experiments measured temperatures $T \ll T_D$, see Ref. [3]. In reality, the atoms are not simple two-level systems and this complication is what leads to sub-Doppler cooling mechanisms [3, 73]. It is fortuitous that the more realistic model should lower the temperature's lower bound rather than raise it!

[3]It is the radiation force that provides the trapping, not the magnetostatic field itself. Magnetostatic traps require much larger magnetic field gradients than MOTs

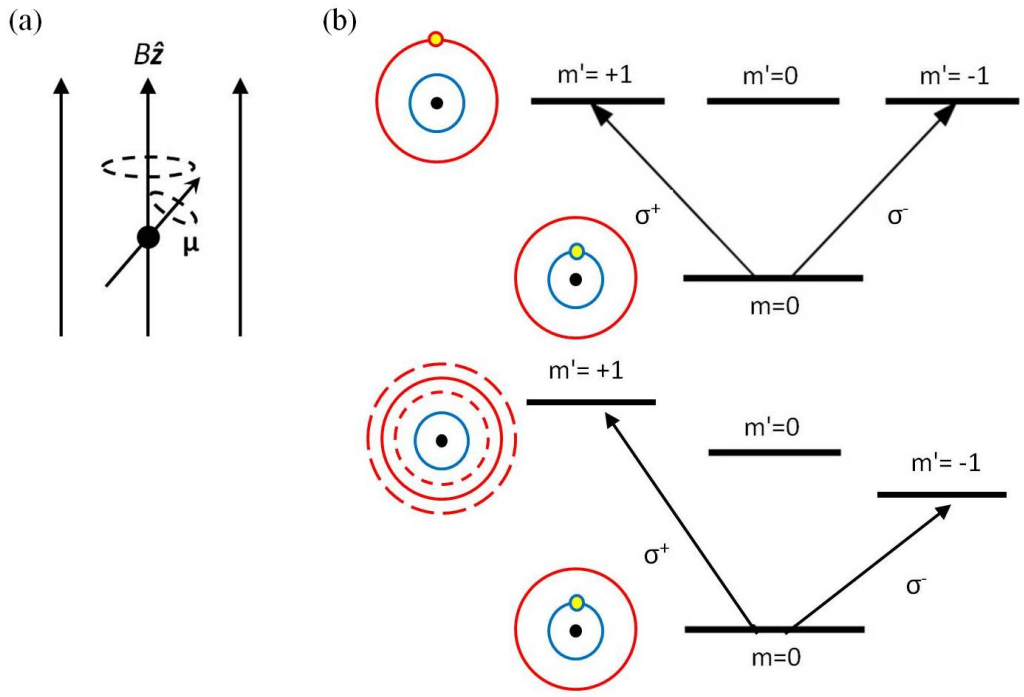

Figure 4.9: Panel (a) shows an electron with a magnetic dipole moment experiencing a torque in the presence of an external magnetic field. Panel (b) shows that the Zeeman effect breaks the degeneracy of the hyperfine sub-levels m_F.

the presence of the magnetic field produced by the atom's nuclear spin and orbital angular momentum. If an external magnetic field is also applied causing yet another torque on the the valance electron's magnetic dipole, there is another energy shift

$$\hat{H}_Z = \hat{\mu} \cdot \vec{\mathscr{B}}_{\text{ext}} = -g_J \mu_B \hat{J} + g_I \mu_n \hat{I} \cdot \vec{\mathscr{B}}_{\text{ext}} \overset{\mu_B \gg \mu_n}{\approx} -g_J \mu_B \hat{J} \cdot \vec{\mathscr{B}}_{\text{ext}}, \tag{4.16}$$

as stated in Ref. [73].

When the external field is weak, $\hat{\mu}$ slowly rotates about the magnetic local field lines, as seen in Fig. 4.9 (a), and F and m_F are still the good quantum numbers. The Zeeman Hamiltonian is treated as a perturbation and we must project $\hat{J}$ on to $\hat{F}$, giving the

expectation value with the hyperfine quantum numbers as

$$\begin{aligned} E_z &= g_J \mu_B \frac{\langle \hat{J}\cdot\hat{F}\rangle}{F(F+1)} \langle \mathscr{B}_{\text{ext}}\hat{z}\cdot\hat{F}\rangle \\ &= \frac{F(F+1)-J(J+1)-I(I+1)}{2F(F+1)}\left(\frac{3}{2}+\frac{S(S+1)-L(L+1)}{2J(J+1)}\right)\mu_B\langle \mathscr{B}_{\text{ext}}F_z\rangle \\ &= g_F \mu_B \mathscr{B} m_F, \end{aligned} \tag{4.17}$$

where the z-axis is defined by the magnetic field direction. In the absence of a field the hyperfine splitting is m_F degenerate, but with the field the degeneracy is lifted. The polarization of the light must be circular to couple to one of the $m_F \neq 0$ states, so as to conserve angular momentum, as seen in Fig. 4.9. Mathematically this is a consequence of the E1 selection rule's 3j-symbol in Eq. (3.56).

The MOT uses a quadrupole magnetic field produced by external electromagnets that sit on the top and bottom of the chamber in an anti-Helmholtz configuration. A detailed discussion of the electromagnet configuration, construction, and water cooling can be found in Appendix B. The end result is a fairly linear magnetic field gradient of ≈ 45 Gauss/cm along the z-direction [as defined in Fig. 4.10 (a) and (b)] and half the negated z gradient along the x- and y-directions, since $\vec{\nabla}\cdot\vec{\mathscr{B}} = 0$.

Let us again return to the 1D case with the net magnetic field $\vec{\mathscr{B}}_{\text{ext}} \approx \zeta z\hat{z}$ near the center of the trap. Here, $z = 0$ corresponds to the center of the trap and ζ is the nearly constant magnetic field gradient, as seen Fig. 4.10 (a) and (b). Using Eq. (4.17) we can write the atomic energy level as

$$\begin{aligned} E = \hbar\omega_0 + g'_F\mu_B\zeta z m'_F - g_F\mu_B\zeta z m_F &\approx \hbar\omega_0 + g\mu_B\zeta z q \\ &\equiv \hbar\omega_0 + \hbar\beta z, \end{aligned} \tag{4.18}$$

where we have assumed that $g_F \approx g'_F = g \sim 1$, as is often the case Ref. [73]. To conserve

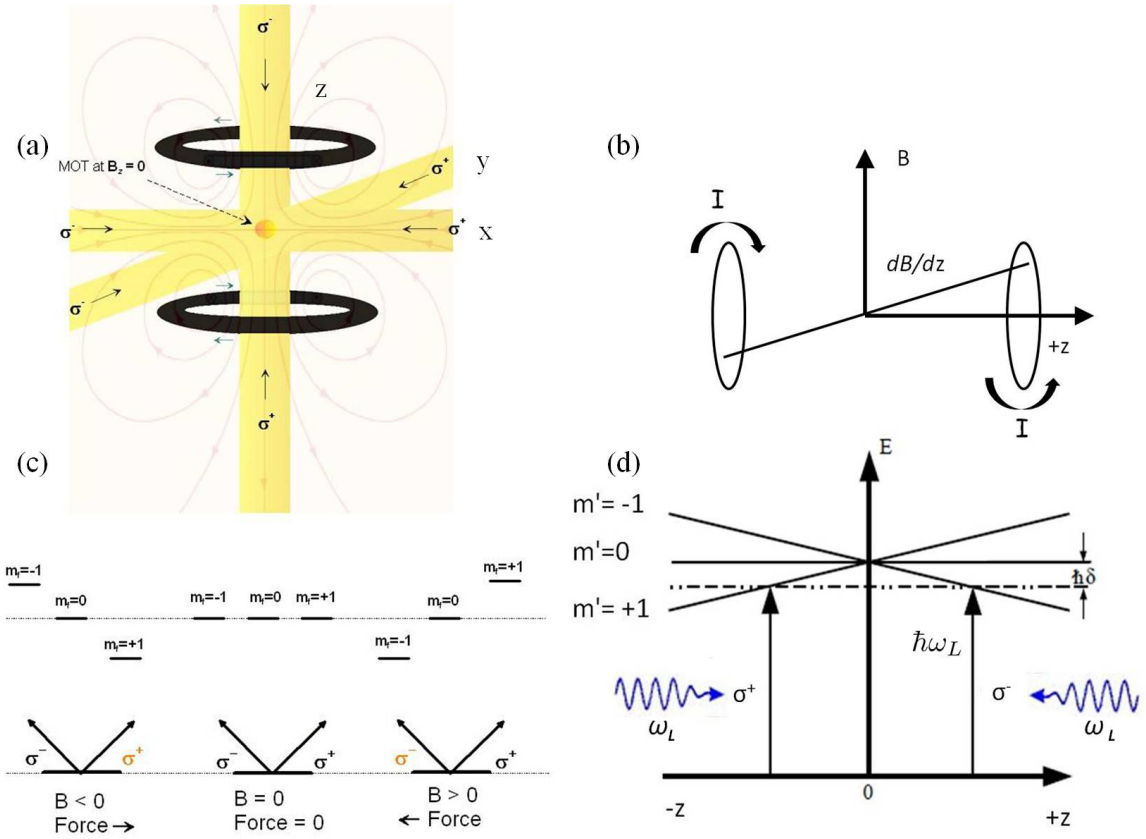

Figure 4.10: Panel (a) shows the magnetic field lines in the zx-plane for the anti-Helmholtz magnetic field configuration and the six circularly polarized beams. Panel (b) shows that the net magnetic field gradient along any beam direction is approximately linear. Panel (c) shows the resulting spatial force due to the Zeeman effect. Panel (d) shows the atomic energy level splitting due to the Zeeman effect as a function of the position in the trap.

angular momentum (see Sec. 3.3.2) the polarization q must equal Δm_F, where polarization $q = 1$ for right circular σ^+ and $q = -1$ for left circular σ^-.

As seen in Fig. 4.10 (d), if we make our negative (leftward) propagating beam σ^- then the atomic transition frequency shift is $\omega_0 - \beta z$. Similarly, the counter-propagating beam has polarization σ^+ and atomic transition frequency shift is $\omega_0 + \beta z$.

Substituting this into the expression for the detuning $\delta_\pm = \omega_L - (\omega_0 \pm \beta z) \mp k_L v$ gives the detuning a spatial dependence, which gives the force a spatial dependence. If we just

consider the spatial force, when the atom is in the center there is no net force because $z = 0$ and each laser applies the same force. Meanwhile if the atom is displaced from center the most probable transition will come from the laser that would apply a restoring force back to center, as seen in Fig. 4.10 (d).

Inserting the spatial component into the detuning gives the new net force

$$\begin{aligned} F_{\text{net}} &= \hbar \frac{\omega_L}{c} \frac{\Gamma}{2} \left\{ \frac{-I/I_s}{1+4\left[\delta_-/\Gamma\right]^2 + I/I_s} + \frac{I/I_s}{1+4\left[\delta_+/\Gamma\right]^2 + I/I_s} \right\} \\ &\approx -2\frac{\partial F}{\partial \omega_L} k_L v + 2\frac{\partial}{\partial \omega_0} \beta z = -\alpha v - \underbrace{\alpha \beta k_L}_{\kappa} z, \end{aligned} \tag{4.19}$$

thus the trapped atoms undergo damped harmonic oscillations about the $\vec{\mathscr{B}}_{\text{ext}} = 0$ location [73]. From Eq. (4.19), the equation of motion becomes

$$\ddot{x} - \frac{\alpha}{m_N}\dot{x} + \frac{\kappa}{m_N} x = 0. \tag{4.20}$$

Under typical trapping conditions $\alpha > 2\sqrt{\kappa m_N} \implies$ overdamping with time constants ~ 1 ms [31].

By circularly polarizing the beams in the manner indicated in Fig. 4.10 (a), the spatial trapping is extended to all three dimensions. Also, by adding additional uniform magnetic fields with shim coils, the magnetic field minimum can be translated spatially, which changes the location of the MOT within the UHV chamber.

The spatial force is a consequence of the detuning, which depends linearly on z, just like the Doppler detuning depended linearly on v. Therefore, for a fixed velocity the 1D force plot from the left and right beams will look just like the Doppler force, except position is now the independent variable, as seen in Fig. 4.7.

From Fig. 4.7, we see that the capture speed for the optical molasses is about $v_c \sim \Gamma/k_L$, which for Na is around 6 m/s. However, in the MOT, the magnetic field gradient increases

the capture velocity. As an atom is slowed its speed becomes off resonant with the laser, but the magnetic field gradient essentially adjusts the transition energy to compensate, giving a nearly constant deceleration. Typical MOT beams have a $r \sim 5$ mm radius, so the largest initial velocity that is constantly decelerated to zero velocity over the distance r using the maximum radiation force is

$$v_c^2 \sim 2\frac{F_{\text{net}}(I \gg I_s)}{m_N} r, \tag{4.21}$$

which equals ≈ 80 m/s for Na, at most. Consequently, MOT densities are typically much larger than optical molasses densities. Furthermore, we can assign a trap depth associated with the size of the MOT beams

$$D_{\text{MOT}} = \frac{1}{2}\kappa r^2. \tag{4.22}$$

For typical settings this gives depths $D_{\text{MOT}}/k_B \sim 1$ K, which is about an order of magnitude deeper than typical optical molasses depths [31, 73].

4.2.2 UConn's Na MOT

Although we have occasionally made reference to our group's Na MOT [36, 38–40], we have been primarily discussing MOTs as a general concept. Here and in the next few sections, we will discuss some of the technical details specifically associated with our group's Na MOT.

Type I and II MOTs There are two Na MOTs that can be formed using the D2 Na line. A camera image of each of our Na MOTs can be seen in Fig. 4.11 and the relevant optical transition are shown in Fig. 4.12.

The type I MOT [31, 120, 121] uses a stronger hyperfine cooling transition 3S $F = 2 \rightarrow$ 3P $F' = 3$, giving it a larger α and thus more damping, a greater spring

constant, and an overall denser colder MOT, as compared to the type II [visualized in Fig. 4.11]. The type II MOT [122] uses a weaker cooling transition from the lower ground state 3S $F = 1 \rightarrow$ 3P $F' = 0, 1$.

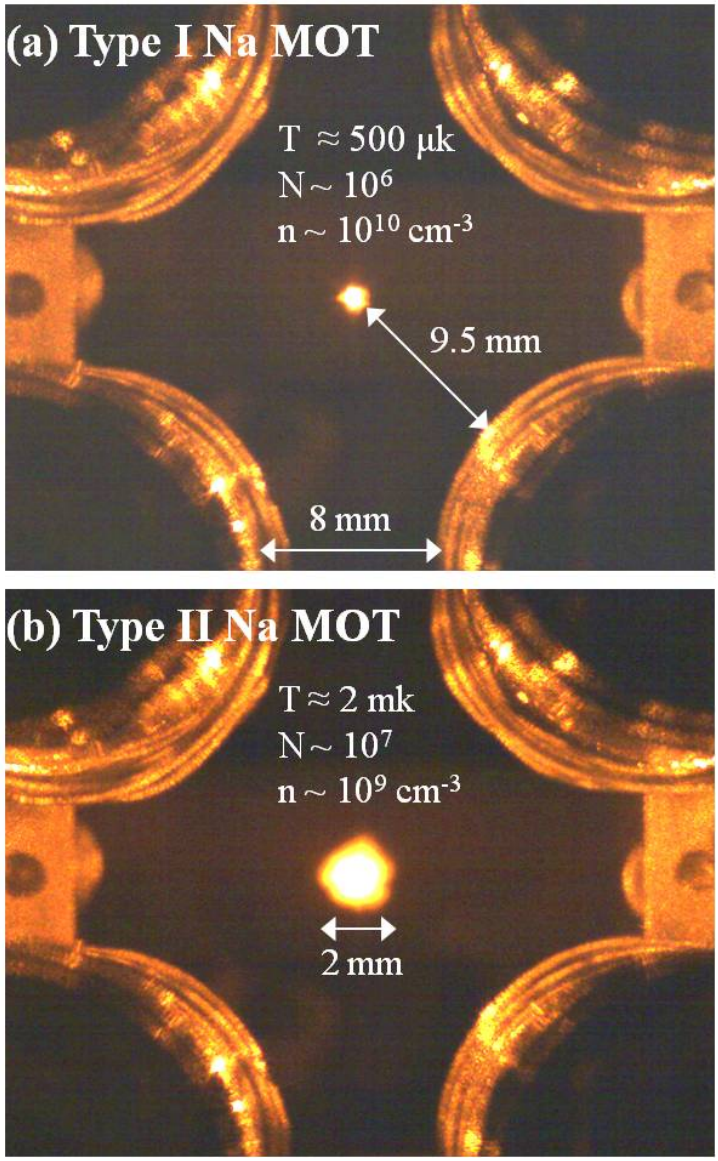

Figure 4.11: Modified figure from [40] showing the type I Na MOT (a) and the type II Na MOT (b). The images were taken with our CMOS camera looking through a vacuum chamber viewport along the long axis of the LPT. The type I MOT is colder, smaller, and denser than the type II, but has fewer atoms.

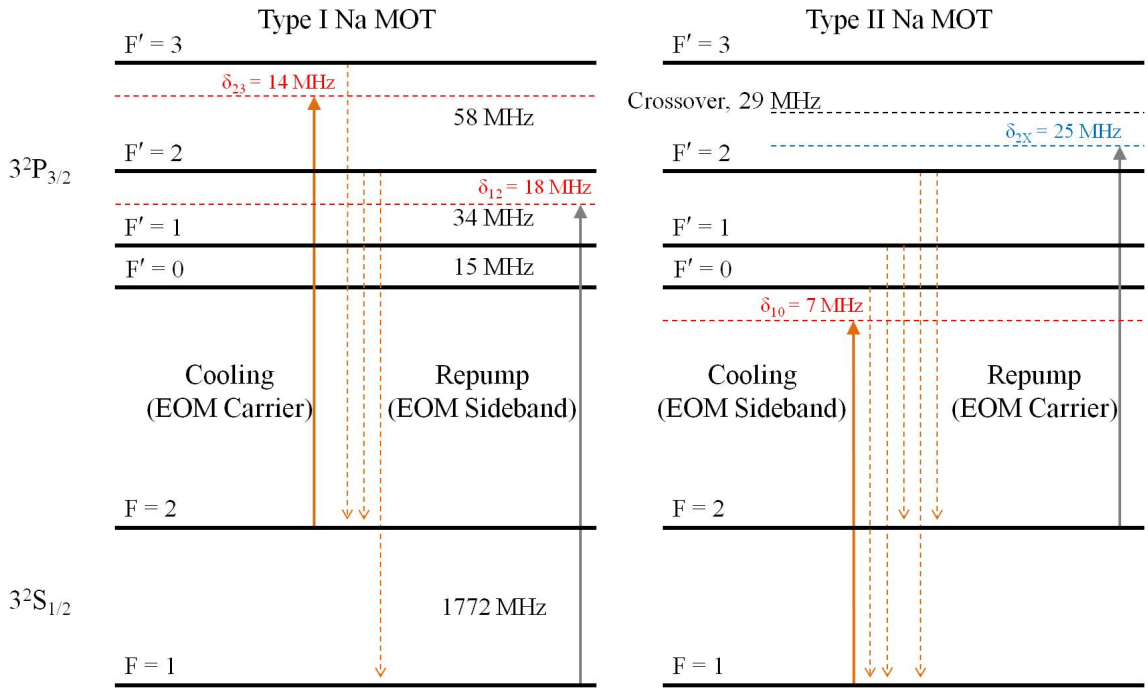

Figure 4.12: Energy level diagram showing optical E1 excitation (solid), decay (dashed) pathways. The cooling transitions are orange and repumping transitions are gray for the type I (left) and type II (right) MOTs.

Both MOT cooling transitions are not simple two-level systems. For example, in the type I MOT, the $F' = 2$ state rather than the desired $F' = 3$ state will occasionally become excited. Unfortunately, $F' = 2$ state can sometimes decay to the $F = 1$ ground state and that atom is then stuck in the wrong ground state. The atom will be in a state that is ≈ 1772 MHz detuned away from ω_L and will no longer be cooled. The solution is to use additional laser light, called the "repumper," to pump these atoms out of the dark state back up to the $F' = 2$ excited state so that they have a chance to get back into the cooling cycle. All the E1 optical transitions and laser detunings used in our experiments are shown in Fig. 4.12 for both MOTs.

If we assume that the transition strengths are comparable and that $I \ll I_s$, the scattering

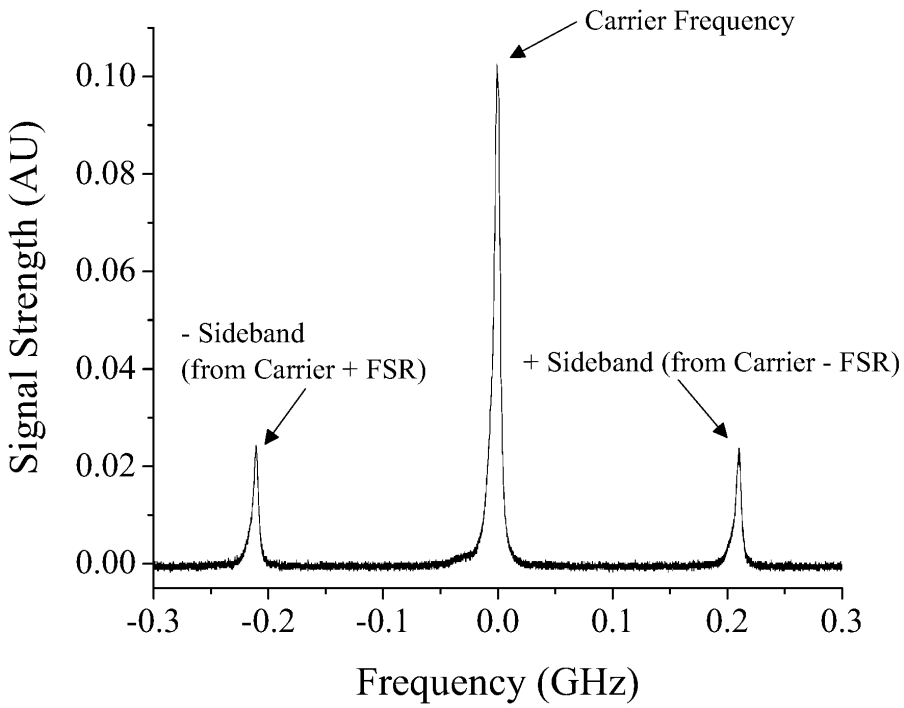

Figure 4.13: Scanning Fabry-Perot interferometer (FPI) signal of EOM output showing the carrier signal and sideband laser frequencies from carrier signals ± one free spectral range (FSR) = 1.5 GHz (not seen in plot). This is unfortunately nearly coincident with the 1.7 GHz sideband.

rates[4] for the type I cooling transition and the wrong $F' = 2$ transition are

$$\begin{aligned} R_{23} &= \frac{I}{I_s}\frac{\Gamma/2}{1+(-2\delta_{23}/\Gamma)^2} \\ \text{and } R_{22} &= \frac{I}{I_s}\frac{\Gamma/2}{1+\{2[2\pi(58\text{ MHz})-\delta_{23}]/\Gamma\}^2}, \end{aligned} \tag{4.23}$$

respectively. By taking the ratio of these two rates we get a back-of-the-envelope estimate that on average the wrong excited state is populated once every ~ 10 cooling cycles.

The additional repumper laser frequency for the type I MOT is provided by passing the 589 nm cooling laser through a New Focus 4421 electro-optical modulator (EOM)

[4]The assumption that $I \ll I_s$ is actually not valid for normal MOT operation. However, since we are only performing a back-of-the-envelope estimate we do not care.

before reaching the vacuum chamber, as seen in Fig. 4.2. The EOM modulates the phase of the laser radiation via the electro-optic effect, which results in a carrier signal at the input frequency and two collinear sideband laser beams at the modulation frequency $\delta_{\pm\mathrm{sb}} = \pm 1710.7$ MHz. The particular modulation frequency was chosen so that both the type I and II yielded the optimal (i.e., brightest) possible MOT. We found that both MOTs yielded their maximum populations in the range of 1708 - 1712 MHz.

Figure 4.13 shows a trace from a scanning Fabry-Perot interferometer of the laser output from the EOM, which shows that the optical power in the sidebands is approximately 25% of the power at the carrier frequency. A detailed explanation of the EOM's operation can be found in Appendix E.

The output of the EOM plays different roles in each MOT, as seen in Fig. 4.12. For the type I MOT, the carrier frequency output is used for the cooling cycle and the sideband is used for the repumper transition. The carrier frequency is laser locked to transitions from the $F = 2$ Na D2 line ground state, so the carrier detuning δ_c from atomic resonance is known and the tunable first order EOM sideband shift $\delta_{+\mathrm{sb}}$ is also known. For the type I MOT the relevant experimental detunings of the carrier and the repumper light to their respective transitions are determined using the hyperfine energy level spacing ΔF, δ_c, and $\delta_{+\mathrm{sb}}$, which gives

$$\begin{aligned} \delta_{23} &= \delta_c = -(2\pi)(14 \pm 1)\ \mathrm{MHz} \\ \text{and}\ \ \delta_{22} &= -\Delta F_{12} + \delta_{+\mathrm{sb}} + (\Delta F_{2'3'} + \delta_{23}) \\ &\approx (2\pi)\,(-177.626 + 1710.7 + 58.326 - 14)\ \mathrm{MHz} \\ &\approx -(2\pi)18\ \mathrm{MHz}, \end{aligned} \tag{4.24}$$

respectively, as seen in Fig. 4.12. The experimentally chosen value of δ_c corresponds to the

optimal MOT and is discussed in Sec. 4.2.3. We also note that the power of the radiation for the cooling transition P_c and the repumper transition P_r can be determined using the carrier-sideband power ratio $R_{\rm cs} = P_r/P_c = 0.25$ and the measured total power $P_{\rm tot}$ as

$$\begin{aligned} P_c + 2P_r = P_{\rm tot} \implies P_c &= \frac{P_{\rm tot}}{1+2R_{\rm cs}} \approx \frac{2}{3}P_{\rm tot} \\ \text{and } P_r &= \frac{P_{\rm tot}}{2+1/R_{\rm cs}} \approx \frac{1}{6}P_{\rm tot}. \end{aligned} \tag{4.25}$$

The total beam power $(0.5nW < P_{\rm tot} < 0.5$ W$)$ is measured using the Thorlabs S130C photodiode power meter sensor. For powers greater than 0.5 W a thermal meter is used.

We lock the type II MOT using the carrier frequency as the repumper and use the first order EOM sideband shift $\delta_{+\rm sb}$ as the cooling transition.[5] Thus, the analog to Eq. 4.24 for the type II MOT is

$$\begin{aligned} \delta_{10} &= -\Delta F_{12} + \delta_{+\rm sb} + \left(\frac{\Delta F_{2'3'}}{2} + \Delta F_{0'2'} + \delta_{2X}\right) \\ &\approx (2\pi)\left[-1771.626 + 1710.7 + 29.163 + 50.154 - (25 \pm 1)\right] \text{ MHz} \\ &\approx (2\pi)7 \text{ MHz} \\ \text{and } \delta_{22} &= \frac{\Delta F_{2'3'}}{2} + \delta_{2X} \\ &\approx (2\pi)\left(29.163 - 25\right) \text{ MHz} \approx (2\pi)4 \text{ MHz}, \end{aligned} \tag{4.26}$$

where $\Delta F_{23}/2$ is the location of the saturation absorption spectroscopy crossover peak (as discussed in Sec. 4.2.3) relative to $F' = 2$ level. The detuning $\delta_{2X} = \delta_c$ is directly measured relative to the crossover peak.

[5] Alternatively, the type II MOT could be locked to the spectrum of the lower ground state $F = 1$, making the carrier frequency address the cooling transition, as was the case for the type I MOT. However, when locked to the lower ground state we found that the MOT's density did not increase, but its size increased by about 25%. Because our experiments benefit from a smaller type II MOT, we did not choose to lock to the lower ground state.

We can also write the analog of Eq. 4.25 for the power of the type II MOT's cooling and repumper radiation as

$$P_c \approx \frac{1}{6}P_{\text{tot}} \quad \text{and} \quad P_r \approx \frac{2}{3}P_{\text{tot}}, \tag{4.27}$$

respectively.

MOT laser beam polarization The six trapping beams must have the correct circular polarizations, as shown in Fig. 4.10 (a) and Fig. 4.8 (b), to create the radiation force's spatial dependence. The laser light after the EOM is linearly polarized and is subsequently split into an x, y, and z input MOT beams with polarization beamsplitting cubes and half waveplates $\lambda/2$, as seen in Fig. 4.2. The $\lambda/2$ waveplates, xy-z, and x-y, polarization beamsplitting cubes are used to control the relative intensities of the MOT beams. The principles of waveplate operation are discussed in detail in Appendix G.

The linearly polarized x, y, and z beams go through a quarter waveplate $\lambda/4$ before entering the vacuum chamber. It is convenient to think of the waveplate as a transformation operator and the polarization as a column vector, known as a Jones vector [123, 124]. For example, horizontal polarized light $|H\rangle = \begin{pmatrix} 1 \\ 0 \end{pmatrix}$ incident on a $\lambda/4$ waveplate with its fast axis at $+45^\circ$ clockwise (CW) yields[6]

$$\frac{1}{\sqrt{2}}\begin{pmatrix} 1 & -i \\ -i & 1 \end{pmatrix}\begin{pmatrix} 1 \\ 0 \end{pmatrix} = \frac{1}{\sqrt{2}}\begin{pmatrix} 1 \\ -i \end{pmatrix} = |L\rangle\,, \tag{4.28}$$

where $|L\rangle$ is left hand circular σ^- polarization. This process is shown at the beginning of the rightward propagating beam in Fig. 4.14. The Jones vector formalism is discussed in Appendix G.

[6]Rotating CW relative to the +x horizontal as viewed along the light's propagation direction.

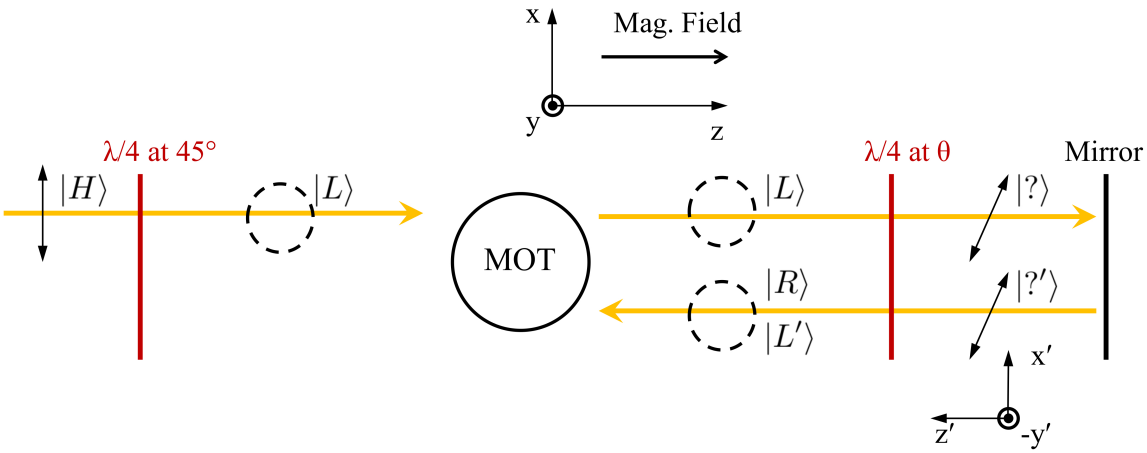

Figure 4.14: Illustration of one MOT beam incident from the left initially propagating positively (as defined by the magnetic field) with linear horizontal polarization. The linear polarization passes through a $\lambda/4$ waveplate resulting in a left circular polarization. The light passes through another$\lambda/4$ waveplate at an arbitrary angle resulting in linear polarization. The light is then retro-reflected and it passes through the $\lambda/4$ waveplate again with positive propagation in the primed coordinate system (which amounts to inverting the vertical component to the polarization vector). As viewed in the atom's unprimed frame, the light incident from the left has the opposite handedness as the light incident from the right.

Upon exiting the vacuum chamber viewport, the circularly polarized light passes through a second $\lambda/4$ waveplate, is retro-reflected, and then passes through the waveplate again, before taking a second pass through the vacuum chamber. Thus, the initial three input beams are all retro-reflected, effectively acting like six MOT beams. The orientation of the second waveplate's fast axis is arbitrary since the effective $\lambda/2$ retarding done by the two passes through the $\lambda/4$ waveplate always reverses the light's handedness, as seen by the atom. For example, the Jones matrix transformation for left circular input $|L\rangle$ on the first pass through the second $\lambda/4$ waveplate with the fast axis at $+\theta$ CW orientation, followed by a reflection (inverts y-axis, so $-\hat{k}$ becomes $\hat{k}'$), and ends with the second pass

with the fast access at $-\theta$ counterclockwise (CCW) yields[7]

$$\begin{aligned}
&\begin{pmatrix} \cos^2(\theta)+i\sin^2(\theta) & -(1-i)\sin(\theta)\cos(\theta) \\ -(1-i)\sin(\theta)\cos(\theta) & i\cos^2(\theta)+\sin^2(\theta) \end{pmatrix} \begin{pmatrix} 1 & 0 \\ 0 & -1 \end{pmatrix} \\
&\times \begin{pmatrix} \cos^2(\theta)+i\sin^2(\theta) & (1-i)\sin(\theta)\cos(\theta) \\ (1-i)\sin(\theta)\cos(\theta) & i\cos^2(\theta)+\sin^2(\theta) \end{pmatrix} \frac{1}{\sqrt{2}} \begin{pmatrix} 1 \\ -i \end{pmatrix} \qquad (4.29) \\
&= \frac{1}{2\sqrt{2}} \begin{pmatrix} \cos(2\theta) & \sin(2\theta) \\ -\sin(2\theta) & \cos(2\theta) \end{pmatrix} \begin{pmatrix} 1 \\ -i \end{pmatrix} = \frac{e^{-i2\theta}}{\sqrt{2}} \begin{pmatrix} 1 \\ -i \end{pmatrix} \propto \left|L'\right\rangle .
\end{aligned}$$

However, we want to know what the atom sees in the z-direction as defined by the magnetic field (unprimed coordinate system), so we need to take our result and invert the y-axis again, which gives

$$\begin{pmatrix} 1 & 0 \\ 0 & -1 \end{pmatrix} \frac{e^{-i2\theta}}{\sqrt{2}} \begin{pmatrix} 1 \\ -i \end{pmatrix} \propto |R\rangle , \qquad (4.30)$$

as seen by the atom. Here, $|R\rangle$ is right hand circular σ^+ polarization. This process is also illustrated in Fig. 4.14.

The $\lambda/4$ waveplates are initially set using a procedure described in Appendix G, such that the relative handedness of the polarization follows Fig. 4.10 (a) and Fig. 4.8 (b). When setting the input $\lambda/4$ waveplate orientations, all that matters is the relative circular handedness between the three input beams. For example, if the wrong absolute handedness is chosen, but the relative handedness is correct, the MOT will work once the electromagnet anti-Helmholtz coils' gradient is reversed. In other words, reversing ζ is the same as reversing $\sigma^{\pm}$. Experimentally, it is easy to reverse the anti-Helmholtz coils' power supply

[7]Rotating CCW relative to the +x′ horizontal as viewed along the now retro-reflected light propagation direction.

lead connection, which reverses the coils' current directions, negating the direction of the gradient ζ.

The majority of the $\lambda/2$ and the initial MOT beam $\lambda/4$ waveplates are Thorlabs 633 zero order waveplates. We found that the Thorlabs 633 nm waveplates outperformed custom 589 nm waveplates from CVI. The Thorlabs waveplates rotated linearly polarized light passing a maximum of 87% of the incident power as compared to CVI's maximum 78% through the same polarizing beamsplitting cube. The retro-reflecting $\lambda/4$ waveplates are multi-order, since they are not as critical as the initial $\lambda/4$ waveplates. In fact, the MOT will sometimes still work (poorly) with the second $\lambda/4$ waveplate removed.

MOT laser beam size As we saw in Sec. 4.2.1 and we will see again in Secs. 4.2.3 and 4.2.5, it is important to experimentally determine the ratio I_{tot}/I_s, which requires knowledge of the physical MOT beam inteisites I_{tot}. To experimentally find the intensity of our laser beams, we measure the beam's total power P_{tot} and determine the size of the beam. Assuming our laser beams are well approximated by a Gaussian TEM_{00} mode, the peak intensity is defined as

$$I_0 = \frac{P_{\text{tot}}}{\pi(r_{x,1/e})(r_{y,1/e})}, \tag{4.31}$$

where $r_{x,y,1/e}$ is the (horizontal and vertical, respectively) distance associated with a $1/e$ intensity drop from the center of the laser beam. For a round beam $r_{x,1/e} = r_{y,1/e}$. The collimated $r_{1/\text{e}}$ beam sizes for all the laser beams throughout the table are labeled in Fig. 4.2, as lenses are used to magnify, shrink, and re-collimate the laser beams.

The size and mode of the laser beams are experimentally characterized by performing a "razor-blade test." This is performed by measuring the beam power incident on a power meter while a razor blade is translated horizontally or vertically across the transverse plane of the laser beam across the front of the power meter's sensor. For a Gaussian TEM_{00}

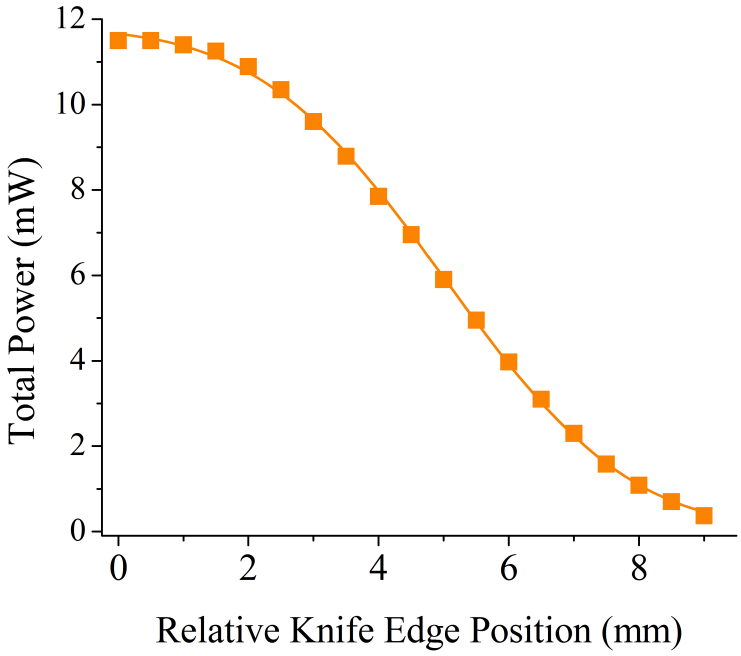

Figure 4.15: The plot shows the measurement results of a vertical razor-blade test on the 589 nm laser beam at the location of the MOT after the last collimating lens. The uncertainty in the plot's data is smaller than the plot markers. From the fit (solid line) to Eq. (4.32) we find that the 589 nm beam has a vertical radius $r_{y,1/e} = 3.18 \pm 0.04$ mm.

mode, the power measured as a function of the horizontal knife translation distance X is

$$P(X) = \frac{P_{\text{tot}}}{2}\left[1 - \text{erf}\left(\frac{X - x_0}{r_{x,1/e}}\right)\right], \tag{4.32}$$

where erf is the error function and x_0 is the center of the laser beam relative to the arbitrarily chosen origin, $X = 0$. The details of the razor-blade test including a derivation of Eq. (4.32) can be found in Appendix F. The results of typical beam tests are shown in Fig. 4.15 with corresponding fit to Eq. (4.32) for a MOT beam.

Although our lasers have internal beam shaping that produce TEM_{00} round Gaussian laser modes, the light that reaches the vacuum chamber does not. This is due to the laser propagation through all the optics on the table, which can in some cases dramatically

change the size and mode of the beam in undesirable ways.

For example, we found that the Isomet acousto-optical modulator (AOM) located in the center of the table in Fig. 4.2 creates an astigmatism. To maximize diffraction efficiency and throughput at the AOM's entrance and exit apertures, the beam is reduced in size and collimated with a biconvex lens pair. After the beam makes a double pass through the AOM we found that the mode becomes elliptical due to the astigmatism developed from each pass through the AOM.

When turning off the AOM's rf driver, we found that the astigmatism went away and the beam shape returned to the initial round beam shape over a slow ~ 5 second transformation period. Due to the slow relaxation time we concluded that this was a thermal effect. Unfortunately, attempts to cool the AOM proved futile. We theorized that the astigmatism was likely a temperature gradient effect in the crystal that causes the the horizontal beam waist location to shift relative to the vertical beam waist location.

The best way to correct for the astigmatism is to use a pair of cylindrical lenses, where each one separately collimates the horizontal and vertical beam divergences. However, in an attempt to make due with the optics currently available to us, we used an anamorphic prism pair to create a circular beam. This does not correct for the mismatched divergence and only creates a circular beam at a single distance relative to the prism pair, which we will call z_c.

At this point in the beam path the beam needs to be magnified and collimated using a two biconvex lens pair telescope with the beam waist located within the EOM (so as to fit the beams within the EOM's 2 mm entrance and exit apertures). Magnification is desired so that the beams are as large as possible, giving the MOT the largest possible capture velocity (as discussed in Sec. 4.2.1). By magnifying and collimating the beam with the first collimation lens placed at z_c, the relative divergences will not change, but both the

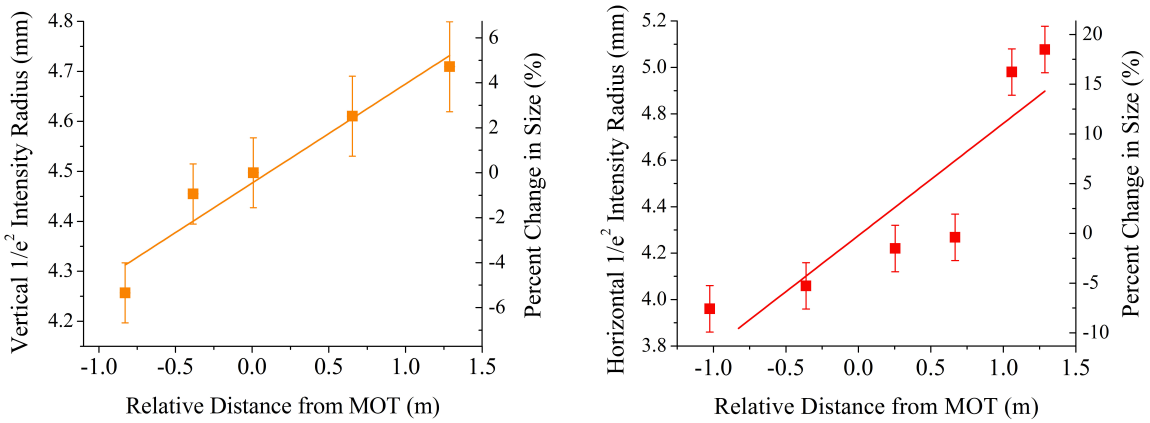

Figure 4.16: Plot of $1/e^2$ intensity radius w of MOT beams as a function of distance from the MOT. Left plot (orange) shows the horizontal divergence and the right (red) shows the vertical divergence, which is different due to the astigmatism. The beam is fairly round near the MOT and fairly well collimated near the MOT.

horizontal and vertical absolute divergence will be greatly reduced. For Gaussian beams with minimum $1/e^2$ intensity waist w_0, the far-field half angle of divergence [125] is

$$\theta_{\mathrm{FF}} = \frac{w_{\mathrm{FF}}}{z} = \frac{\lambda}{\pi w_0}, \tag{4.33}$$

where z is the far-field distance from w_0 along the beam and w_{FF} is the waist at z. Because magnification increases w_0, the absolute divergence decreases according to Eq. (4.33).

Figure 4.16 shows the horizontal and vertical beam size as a function of position relative to the MOT's location. These plots are produced by repeating razor-blade tests at several locations beyond the last collimation lens just after the EOM. The data are fit to the expected $1/e^2$ intensity beam size dependence on z for Gaussian beams, namely

$$w(z) = w_0\sqrt{1+\left(\frac{z}{z_R}\right)^2}, \tag{4.34}$$

z_R is the Rayleigh range, as discussed in Appendix F.

Table 4.1 gives the estimated values of the $1/e$ intensity radius of all six MOT beams at the location of the MOT based on the fitting results from Fig. 4.16. The plots and table show that despite not actually correcting the astigmatism, the MOT beams are still fairly round and collimated at the location of the MOT.

Table 4.1: Table of $1/e$ intensity radius for all six MOT beams at the location of the MOT

Beam	Horizontal $\pm$ 0.1 (mm)	Vertical $\pm$ 0.1 (mm)
r_x	3.0	3.2
r_x (retro)	3.2	3.2
r_y	2.9	3.1
r_y (retro)	3.1	3.2
r_z	3.0	3.2
r_z (retro)	3.2	3.2

4.2.3 Na lasers and laser stabilization

In this section we will discuss the lasers used for cooling and trapping Na in our MOT and how these lasers are frequency stabilized.

589 nm dye laser and Toptica laser The MOT 589 nm laser radiation was initially provided by a Coherent continuous wave (cw) 699-21 ring dye laser on loan from our collaborator Francesco A. Narducci. This kind of laser was independently developed by P. P. Sorokin and F. P. Schäfer [128, 129]. A schematic of the dye laser is shown in Fig. 4.17 (a). Our dye laser is pumped by a Coherent cw Ar^+ gas laser with a net output of approximately 10 W at several different wavelengths. The pump laser is used to achieve the population inversion in the gain medium necessary for lasing. The gain medium is a flowing dye jet comprised of Rhodamine 590 Chloride (R6G) within an ethylene glycol solution. The dye laser primarily absorbs the 502 nm, 514, and 529 nm Ar^+ pump radiation

and fluoresces broadband from 550 nm - 625 nm, according to Fig. 4.17 (b).

The dye laser cavity has light traveling in both directions forming a kind of ring of light, with laser emission through the partially reflective output coupler mirror. Some of the output radiation is picked off and fed to a temperature stabilized reference cavity used for active feedback frequency stabilization. The feedback to the optical cavity is controlled by changing the effective cavity length by rotating the Brewster plate (woofer) for low frequency corrections and translating the M1 mirror (tweeter) for high frequency

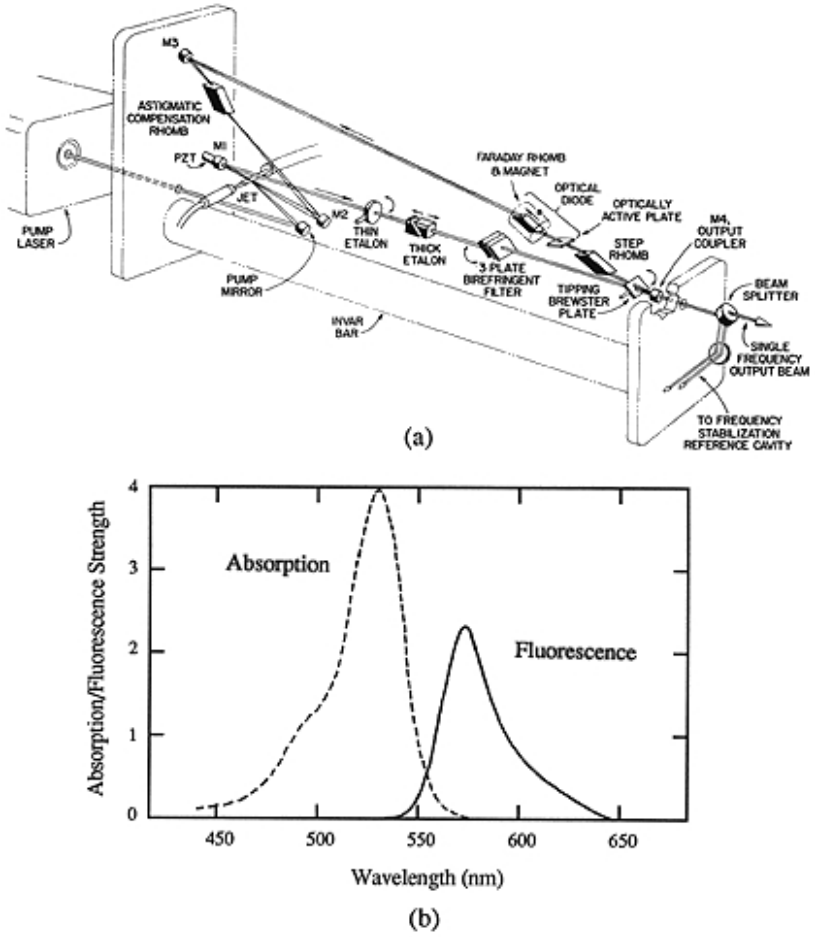

Figure 4.17: Originally from Ref. [126], panel (a) shows the coherent cw 699-21 dye laser schematic. Originally from Ref. [127], panel (b) shows the R6G dye pump beam absorption and output lasing fluorescence strength as a function of wavelength.

corrections. At best, we achieved long term frequency stability of about 1 MHz drift per minute, locked only to the reference cavity.

To keep the light traveling in only one direction, an optical diode or Faraday isolator is formed with a Faraday rotating magnet and a waveplate inside the cavity. The Faraday rotator causes a polarization rotation on the light traveling in one of the two directions (and not the other), creating a polarization dependence to the propagation direction. When the light hits the Brewster plate oriented at Brewster's angle, 4% of the s-type polarized light (propagating in the wrong direction) is deflected per pass, keeping the radiation propagating in the wrong direction below the lasing threshold.

To achieve narrowband radiation a birefringent filter and etalons are added to the cavity. The maximum narrowband power achieved was approximately 750 mW at 588.996 nm.

Although our earlier experiments presented in Sec. 5.3.4 and 6.1 used the dye laser, we recently abandoned this laser's usage for MOT cooling. The dye laser is unreliable and difficult to use. Achieving adequate power output and consistent frequency stability proved a daily battle.[8]

The dye laser was replaced by a diode seeded tapered-amplified second-harmonic-generation (TA-SHG) DL Pro 589 nm laser head made by Toptica. The schematic of the TA-SHG Pro 589 nm laser is shown in Fig. 4.18. The new Toptica laser is very reliable and can consistently achieve sub MHz long term stability with active feedback.

The TA-SHG Pro 589 nm uses a seed 1178 nm cw diode laser that is amplified via a tapered amplifier and is then frequency doubled by passing the beam through an independently locked SHG cavity.[9] The output radiation is at the second harmonic of the seed laser yielding 589 nm radiation. The maximum output power is 1.14 W at 589 nm

[8]No tears were shed when this laser was retired... tears of joy, maybe.

[9]The specific non-linear optic within the SHG cavity is not known to us, as it is proprietary.

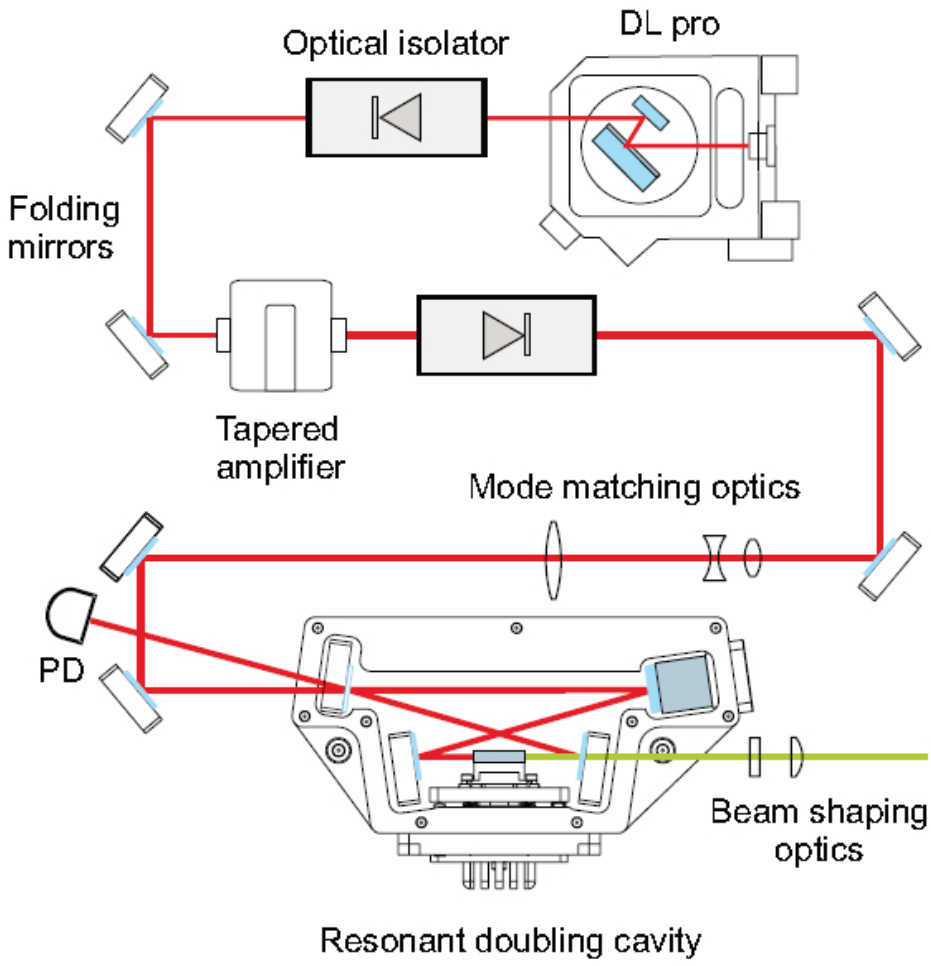

Figure 4.18: Toptica TA-SHG Pro 589 nm laser schematic. See text for detials

with the TA current at 6.4 A. However, we typically run the TA at 5.75 A with an output power of 960 mW.

The SHG is locked using a Pound-Drever-Hall lock [130], monitoring the feedback via the photodiode (PD in Fig. 4.18) signal from the partial reflection off the entrance of the SHG cavity. The TA-SHG Pro laser is long-term frequency stabilized by a top of fringe lock to the Doppler-free saturation absorption spectroscopy of atomic Na vapor cell. The feedback loop schematic is depicted in Fig. 4.19. The loop sequence is as follows:

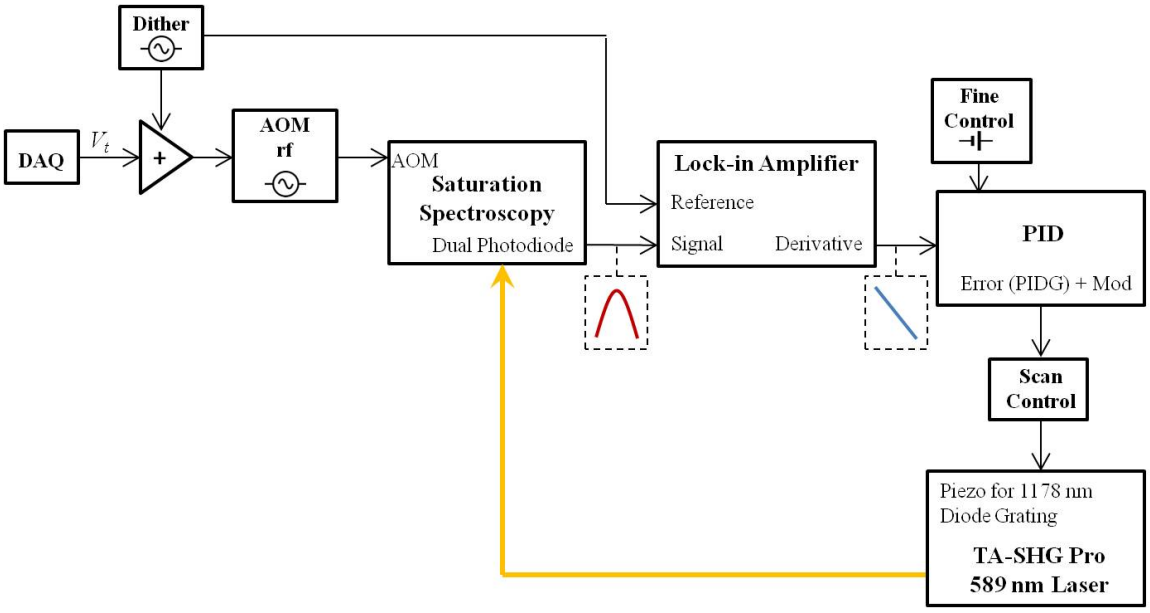

Figure 4.19: Top of fringe laser locking feedback loop schematic. The details of the schematic's sequence is outlined in the text. For details on the optical setup see Fig. 4.21. For details on the fine-tune control circuit see Fig. 4.20. For details on the dual photodiode circuit see Fig. 4.22. Typical saturation spectrum signal (red) and derivative lock-in signal (blue) are shown in Figs. 4.24. The lock-in amplifier is also discussed in Appendix D.

1. The AOM gets an rf input from a dc tuning voltage V_t input. This tuning voltage comes from the National Instruments' (NI) data acquisition hardware (DAQ) analog output.

2. The tuning voltage is quickly modulated with the addition of a sinusoidal signal $V_{\text{dither}} \sin(\Omega t)$. The dither amplitude is typically $V_{\text{dither}} \approx 225$ mV with frequency $\Omega \approx (2\pi)11.0$ kHz.[10] The two signals are added using an operational amplifier (op-amp) adding circuit.

3. The saturation spectroscopy (detailed in Fig. 4.21) receives optical input from the laser head and electrical input to control the AOM.

[10]Higher frequencies are desirable since this frequency places an upper bound on the feedback speed. However, we wanted to stay within the Brimrose AOM specifications.

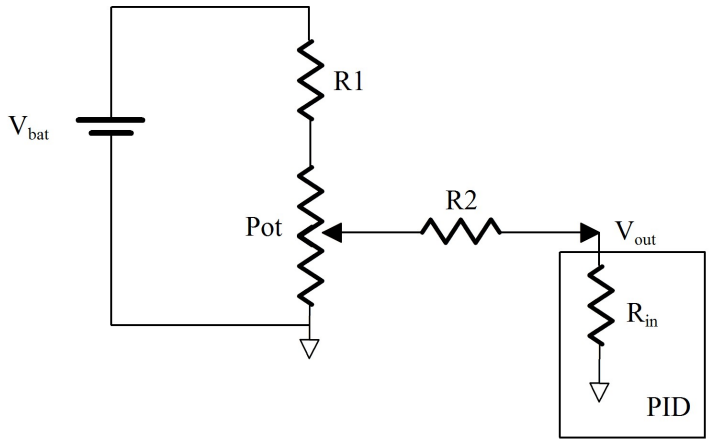

Figure 4.20: Circuit diagram for fine-tune control of Piezo-controlled 1178 nm diode laser grating voltage. The fine tune control voltage V_{out} goes to the modulation input on the Toptica PID control box, which is added to the Scan control voltage. The circuit uses the variable resistance of a potentiometer to adjust the effective voltage drop across the PID's internal resistance R_{in} at the modulation input. We get ≈ 120 GHz of total range with Pot $= 10$ kΩ, $R_1 = 2$ kΩ, $R_2 = 560$ kΩ, and a quiet V_{bat} = 9V battery source.

4. The saturation absorption spectroscopy signal is input into the lock-in amplifier along with the dither modulation signal. The lock-in amplifier outputs the derivative of the spectrum. A detailed discussion of the lock-in amplifier can be found in Appendix D.

5. The derivative is sent to the proportional-integral-derivative control (PID) module.

   - An error signal Err comprised of the derivative of the spectrum signal minus the lock point voltage $Err = S - L$. Because we lock to the top of the spectrum feature (which has a null derivative) the lock voltage is chosen to be ground.
   - The error signal is multiplied by the gain G and then sent into the PID controller, giving $Err' = (S-L)G$.
   - The PID controller adjusts the error signal to create clean, stable, and correctly proportioned feedback $Err'' = P(Err') + I\int Err'(t)\,dt + D(dErr'/dt)$, where

P, I, and D, give the relative strength of each control.[11]

- A dc offset is also added to shift the entire spectrum by small amounts (fine tune control) using the simple homebuilt dc circuit shown in Fig. 4.20.

6. The net error signal from the PID controller is added to the output of the Toptica scan control module,[12] which feeds to the piezo-controlled grating within the DL Pro 1178 nm diode seed laser. The seed laser grating changes the TA-SHG Pro laser radiation output that is fed back to the saturation absorption spectroscopy, thus completing the loop.

Optical setup for spectroscopy We employ a Doppler-free saturation absorption spectroscopy scheme, as shown in Fig. 4.21. We use a Na vapor cell held at 125° C to achieve the necessary Na vapor density for the spectroscopy. To cross the so-called "pump" and "probe" beams [73], we split the beams and then rotate the pump beams polarization by 90° allowing the probe beam to pass through the Na cell and be deflected by a polarization beamsplitter into a dual-photodiode detector. The pump beam passes through the same beamsplitter, resulting in near perfect co-axial counter-propagating overlap with the probe beam.

We also use a slightly weaker beam parallel to and horizontally displaced from the probe beam that we call the "reference beam." This beam comes from the partial reflection off the back of the rectangular glass beam splitter that also separates the pump and probe beams. Therefore, the probe and reference horizontal displacement is a function of the thickness and parallelism of the front and back surfaces of the glass beamsplitter. The dual

[11] When the Toptica scan control modual is in HV mode, the PID dip switches should be set to the lowest possible settings $I/100$, $P/100$ and $D/3$.

[12] When locking the dye laser the error signal went to the so-called "magic spot," which added the reference cavity error signal voltage to the PID error signal voltage.

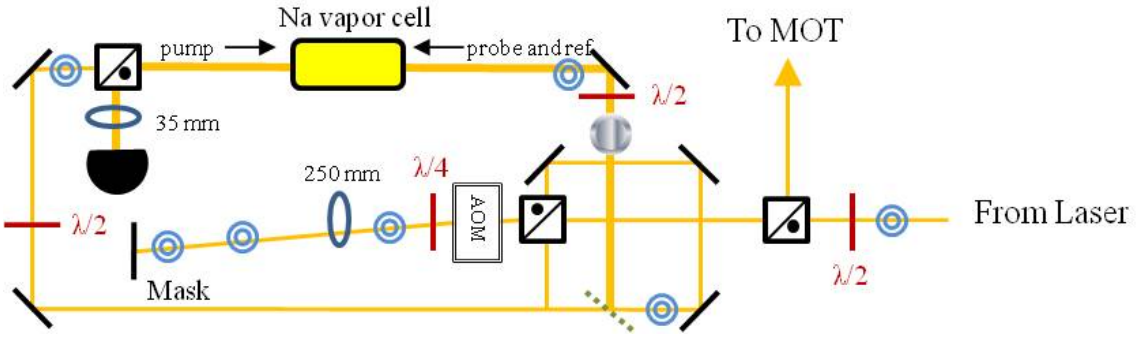

Figure 4.21: Optical setup for Doppler free saturation absorption spectroscopy of Na. The thicker orange line represents the two physically displaced and parallel beams, the probe beam and reference beam, which pass through the Na cell going right to left. Overlapping the probe beam in the cell is the counter-propagating pump beam. There is a double pass on the Brimrose AOM, which shifts the pump, probe, and reference beam frequencies by $2f_a$. The double-pass retro-mirror and AOM are exactly one focal length distance away from the $f = 250$ mm lens. Using a slow lens in the double-pass makes blocking or masking the unwanted diffraction orders with an iris easy. Each optical element's symbolic representation adheres to the same key used in Fig. 4.2.

photodiode receives both the reference signal and probe signal, as schematically shown later in Fig. 4.23. By subtracting these two signals from each other, the Doppler profile can be removed from the saturation spectrum. The dual-photodiode circuit is shown in Fig. 4.22.

To achieve the correct proportionality between the reference and probe beams, the dual photodiode is placed on a translating mount that translates perpendicular to the incident beams. The translation takes advantage of the spatially dependent sensitivity of each photodiode cell, which decreases as one moves away from the juncture between the two cells (anode lead) toward the edge of either cell.

The spot size of the probe and reference beams can be adjusted by translating the 35 mm lens away from or towards the front of the detector. A larger spot size $\varnothing \sim 2$ mm is desirable, so as to not saturate the photodiodes and to reduce any noise produced by fluctuations in the beam propagation direction. However, if the spot is too large then the

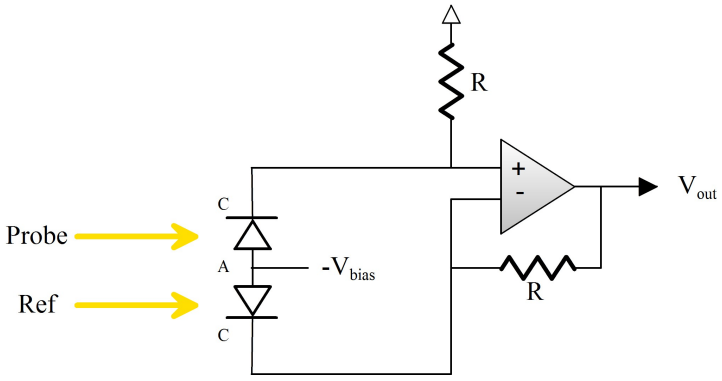

Figure 4.22: Circuit diagram for the dual photodiode. The op-amp circuit [131] changes the photocurrent into a voltage measurement and then subtracts the reference signal from the probe signal.

signal strength drops and the reference and pump beam spots start to overlap.

As discussed in Sec. 4.2.1, the MOT beams must be red-detuned from the atomic resonance. In order to lock to the top of a spectrum feature we need to shift the spectrum relative to the MOT laser beams by the detuning associated with optimal MOT operation. This is accomplished using AOMs, which diffract light with a traveling sound wave in a crystal known as the acousto-optical effect. Each diffracted order maximum is Doppler shifted by the sound wave frequency times the order number. The principles of AOM operation are discussed in detail in Appendix E.

The desired detuning is around $\Gamma \sim (2\pi)10$ MHz, however AOMs are not typically capable of operating at such small frequency shifts. Therefore, we use two AOMs whose relative shift equals the desired detuning. The MOT beams' AOM is made by Isomet and typically operates at a double-pass (first-order and first-order) diffraction efficiency of 75%. The saturation spectrum Brimrose AOM operates at a double-pass (first-order and first-order) diffraction efficiency of 51%. Typical values of the two AOM settings are listed in Table 4.2. The settings are chosen for optimal MOT operation, which corresponds to the brightest possible MOT.

We note that since both the Isomet and Brimrose AOM's are double positive first order passed, each AOM's output is $2f_a$, where f_a is the acoustic wave frequency. Therefore, the relative shift f_r between the two AOM's is

$$f_r = 2\left(f_a^{\mathrm{MOT}} - f_a^{\mathrm{SS}}\right), \tag{4.35}$$

where the superscripts refer to the MOT AOM and saturation spectrum AOM, respectively. The relative detuning becomes the cooling cycle detuning for the type I MOT and the repumper detuning for the type II MOT, as discussed in Sec. 4.2.2.

Table 4.2: Table of experimental AOM settings. The driving frequency or first order frequency shift is f_a and the relative frequency shift is f_r, as defined in Eq. (4.35). Neither frequency is an angular frequency.

MOT Type	V_t^{MOT}(V)	f_a^{MOT}(MHz)	V_t^{SS}(V)	f_a^{SS}(MHz)	f_r (MHz)
I	4.500 ± 0.005	74.6 ± 0.5	7.360 ± 0.005	67.4 ± 0.5	14.4 ± 0.7
II	4.500 ± 0.005	74.6 ± 0.5	6.500 ± 0.005	62.2 ± 0.5	24.8 ± 0.7

Saturation-absorption spectroscopy Here, we will discuss the principles behind the Doppler-full and Doppler-free saturated absorption spectroscopy, following the treatment of Ref. [73]. We also discuss the resulting spectrum, detuning optimization, and laser lock.

Let us begin with a single monochromatic reference beam passing through the Na vapor cell having intensity $I_{\mathrm{ref}} \ll I_s$. As we defined in Sec. 4.2.1, the laser frequency in the laboratory frame and the atom's frame is related by the Doppler shift, $\omega = \omega_L - k_L v$, so the absorption cross section from Eq. (3.84) becomes $\sigma(\omega - k_L v)$. We will also assume that the total number density in Eq. (3.87) can be written as $N(v) = N f_{\mathrm{MB}}(v)$, where $f_{\mathrm{MB}}(v)$ is the MB speed distribution [73]. Integrating over the distributions yields the net absorption coefficient

$$\kappa = \int \kappa(v)\, dv \propto \int f_{\mathrm{MB}}(v) \frac{\Gamma}{(\omega_L - \omega_0 - k_L v)^2 + (\Gamma/2)^2 (1 + I/I_s)}. \tag{4.36}$$

When $T \gg T^*$ [defined in Eq (4.9)], the power-broadened Lorentzian lineshape acts like a delta function compared to the wide MB distribution with $(\omega_L - \omega_0)/k = v$ and the integral in Eq. (4.36) can be evaluated to be

$$\kappa \propto e^{-\left(c\frac{\omega_L - \omega_0}{\omega_0}\right)^2 \frac{m_N}{2k_B T}}, \tag{4.37}$$

where m_N is the mass of the Na atom and k_B is the Boltzmann constant. The MB distribution causes inhomogeneous broadening and the Gaussian linewidth is related to the temperature by

$$\Gamma_D^2 = \frac{\omega_0^2}{c^2} \frac{2k_B T}{m_N}, \tag{4.38}$$

according to Eq. (4.37). An example of the Doppler full spectrum for Na can be found in Fig. 4.42, taken on the background Na vapor in the UHV chamber.[13]

As mentioned earlier, a single beam is split into three beams by a glass rectangular beam spliter. The partial reflections off the piece of glass becomes the weak $(I_{\mathrm{probe}} \approx I_{\mathrm{ref}} \lesssim I_s)$ probe and reference beams and the transmitted light is the strong $(I_{\mathrm{pump}} \gg I_s)$ pump beam. The strong counter-propagating pump beam addresses the same speed class as the probe/reference beams, but addresses the opposite (negative) velocity class. Each beam selectively addresses or "burns a hole" in the fractional population of the gas in the ground state having velocity $v = (\omega_L - \omega_0)/(\pm k_L)$. Without an overlapping beam the pump or probe beam alone would be attenuated in the same manner as the reference beam shown in Fig. 4.23 (a). However, when the pump and probe beam are overlapped and $\omega_L \approx \omega_0$, i.e.,

[13] To avoid confusion about the sign of the signal in Fig. 4.42, we note that in this section (Sec. 4.2.3) we are interested in measuring beam attenuation. However, in Fig. 4.42 atomic fluorescence is measured, where maximum fluorescence is analogous to maximum attenuation.

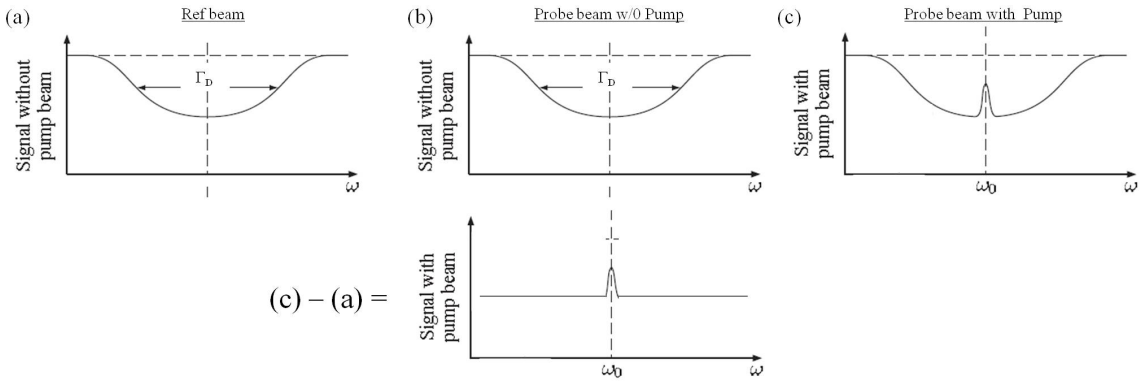

Figure 4.23: Modified version of a figure originally from Ref. [73]. Panel (a) shows beam attenuation due to inhomogeneous Doppler-full broadening associated with the reference beam. Panel (b) shows the same signal associated with the probe beam when there is not an overlapping counter-propagating pump beam. Panel (c) shows the probe beam attenuation is reduced for the Doppler-free velocity class when the saturated hole burned from the overlapping pump beam addresses the same zero velocity class. The dual photodiode subtracts the Doppler-full profile from the spectrum leaving only the Doppler-free peak.

$v \approx 0$, then the two beams address the same zero velocity (Doppler-free) atoms at rest in the laboratory frame. When this happens the weaker probe beam is less attenuated, since the pump beam has already saturated the transition by burning a large hole in the zero velocity class, as seen in Fig. 4.23 (c).

The Doppler-free spectra absorption coefficient is associated with $f_{\mathrm{MB}}(v = 0)$ in Eq. (4.36). Therefore, there is no integral to evaluate in Eq. (4.36) and κ reverts back to Eq. (3.87) derived in Sec. 3.3.4. The linewidth of the Doppler free peak remains limited by the power broadening, as was discussed in Sec. 3.3.4.

The actual Doppler-free saturated-absorption spectrum used to lock our TA-SHG Pro laser is shown in Fig. 4.24. We have fit the resulting spectra to a sum of Lorentzian line functions weighted by the relative transition strengths [111]. By dithering the AOM frequency, we can sample the local derivative of each point along the spectrum and use a

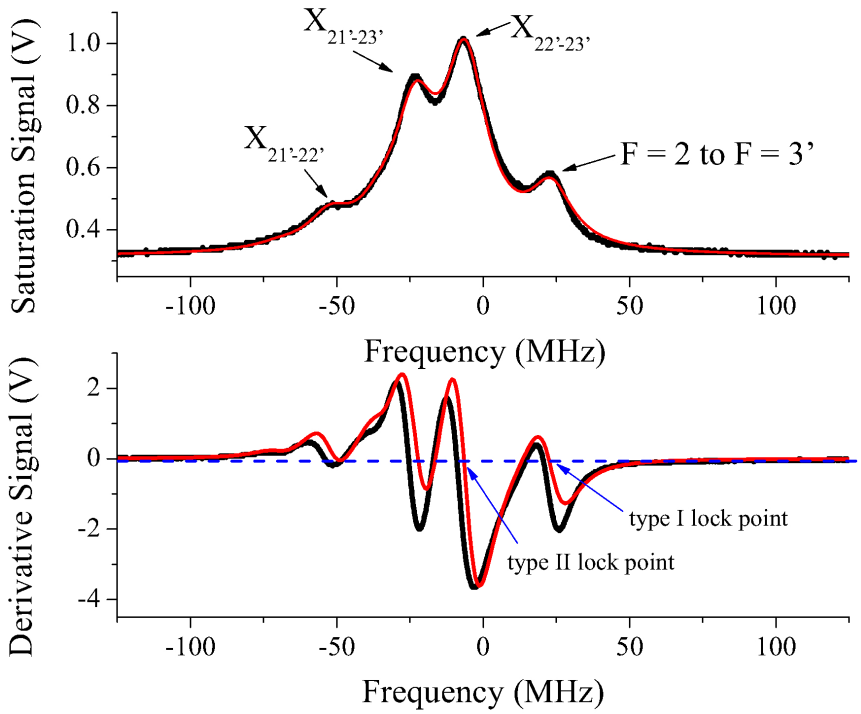

Figure 4.24: The top plot shows the Doppler-free saturation absorption spectrum of the $F = 2$ ground state manifold of the Na D2 line. The signal is in black and the fit to a sum of Lorentzian lineshape functions is in red. The bottom plot shows the actual derivative signal from the lock-in amplifier in black and the derivative of the spectrum's fit from the top plot in red. The red curve in the bottom plot is not a direct fit to the derivative signal.

lock-in amplifier to obtain the real time derivative of the spectrum, also shown in Fig. 4.24. Using the derivative signal and setting the lock point to ground allows us to lock to the top of a feature. The principles of the lock-in amplifier's operation is the subject of Appendix D.

By locking to the side (linearly sloped part) of the derivative signal at ground voltage, we are effectively locking to the top of the saturation spectrum peak, which is called a "top of fringe" lock. The advantage to locking to the top of fringe rather than to the side of the original spectrum is that the derivative signal has a greater signal-to-noise ratio and the top of fringe is less sensitive to laser power fluctuations than the side of fringe.

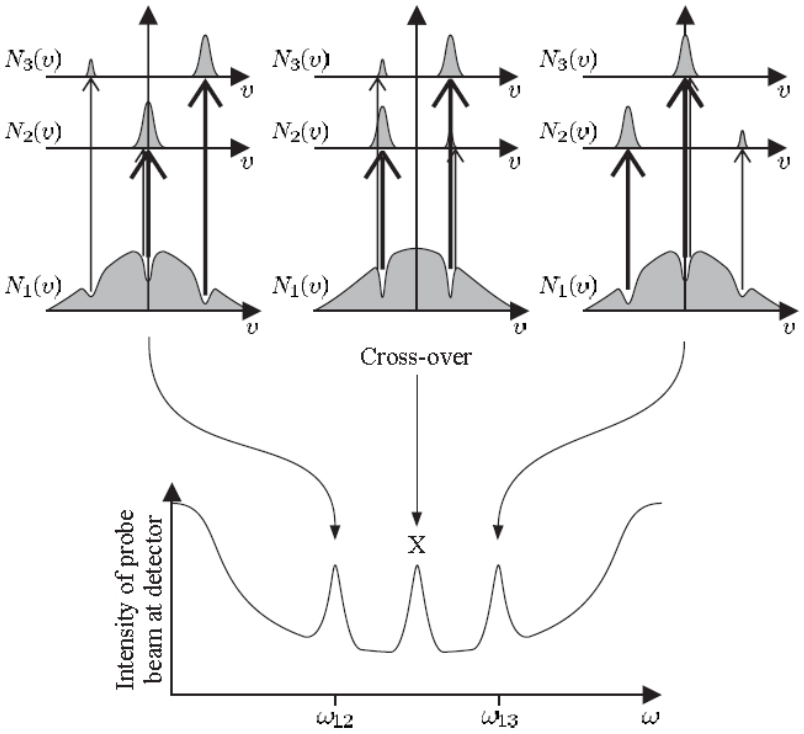

Figure 4.25: Modified schematic of crossover peak originally from [73]. Each laser burns two holes in the atomic population associated with transitions from state 1 to 2 or state 1 to 3. The pump beam transitions are represented by the thick arrow and the probe beam transitions are represented by the thin arrow. The probe beam's attenuation is reduced when the pump and probe address the zero velocity class at each transition and when the laser detuning is halfway between the two transition frequencies, which creates the crossover peak.

The type I MOT carrier signal is locked to the shifted (detuned by f_r) top of the $2 \rightarrow 3'$ transition, but the type II MOT's carrier signal is locked to the shifted "crossover" peak denoted by $X_{22'-23'}$ in Fig. 4.24. When there are multiple excited states associated with the same ground state both the pump and probe beams address two velocity classes, making a total of four simultaneous holes burned, as schematically depicted in Fig. 4.25 . A single beam burns a hole for the velocity class that is resonant with the $1 \rightarrow 2$ transition and another velocity class resonant with the $1 \rightarrow 3$ transition in Fig. 4.25. When ω_L is tuned halfway between these two excited states the pump beam's $1 \rightarrow 2$ burned hole reduces

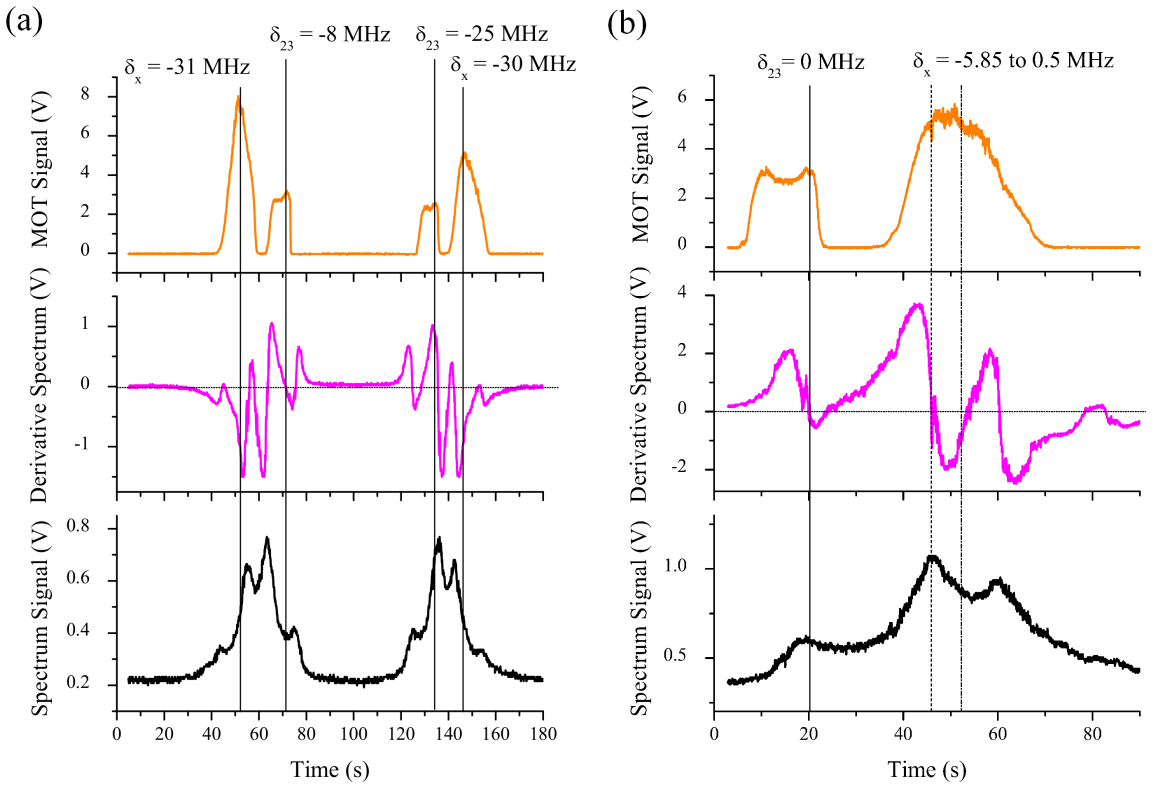

Figure 4.26: The MOT fluorescence signal [discussed in Sec. 4.2.5], the saturation spectrum, and its derivative are shown in the left and right stacked plots. The left stacked plots have no relative AOM shift $f_r = 0$ and $f_a = 70.4 \pm 0.5$ MHz for both AOMs. The scan control ramp is symmetrically scanned, initially increasing laser frequency then decreasing laser frequency. The frequency detuning between the MOT signal's peak fluorescence and the spectrum's $2 \rightarrow 3'$ peak or the $X_{22'-23'}$ crossover peak are indicated in both plots. The right stacked plot just shows the decreasing frequency scan when the AOMs have a relative shift of $f_r = 24.8 \pm 0.5$ MHz. Both plots time to frequency domain conversion is calibrated by the known frequency separation between the $2 \rightarrow 3'$ peak and $X_{22'-23'}$ peak.

the attenuation of the probe beam's simultaneous $1 \rightarrow 3$ hole. Simultaneously, the pump's $1 \rightarrow 3$ hole reduces the attenuation of the probe beam's $1 \rightarrow 2$ hole. This results in a strong peak at the frequency $\omega_L = \omega_{12} + 2\pi\Delta f_{13-12}/2$, called the crossover peak [73].

On the left side of Fig. 4.26 we show the spectrum, its derivative, and the resulting MOT fluorescence measured with out photomultiplier tube (PMT). The Toptica scan

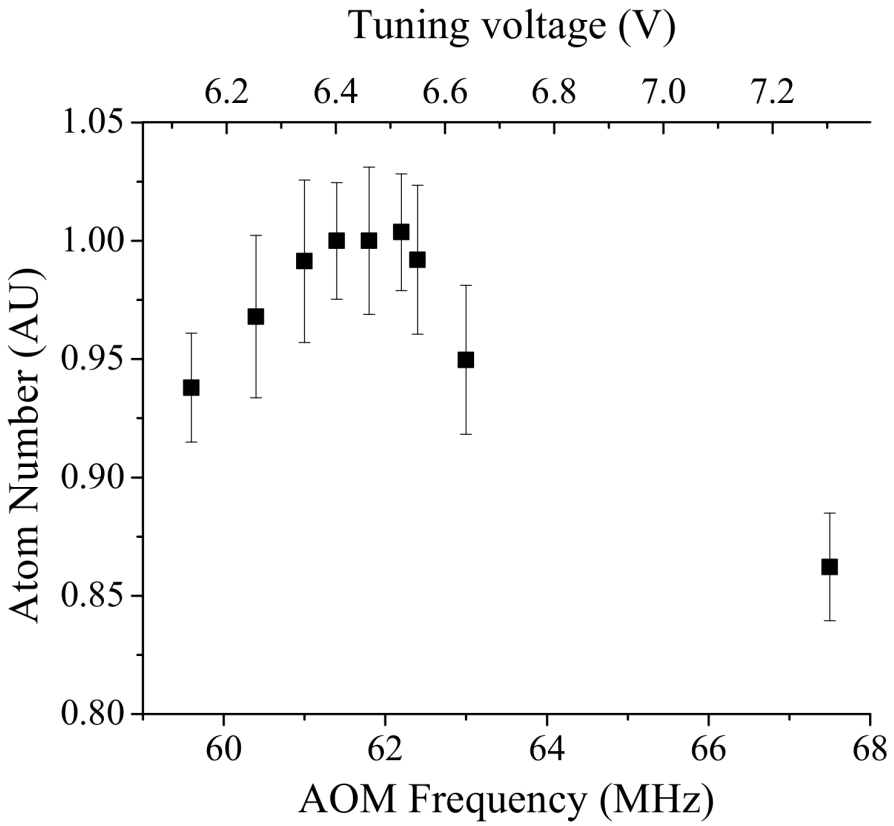

Figure 4.27: Plot of atom fluorescence in arbitrary units (1 AU $\approx 10^7$ atoms) as a function of saturation spectrum AOM detuning. The MOT beam AOM is fixed at 74.6 ± 0.5 MHz. These results correspond to a manual scan not a scan control saw tooth ramp.

control outputs a sawtooth voltage ramp on the seed diode laser's piezo-controlled grating, resulting in a scan in laser frequency. The left side of Fig. 4.26 shows the forward and backward frequency ramp. Even at the slowest obtainable ramp speeds the MOT loads so slowly (over 3 - 5 seconds) that the ramp precedes the MOT steady-state formation, giving poor accuracy as to the optimal or brightest MOT detuning relative to the lock point peaks. This is evident by the disagreement of the observed detuning between the forward going and backward going scans. In the infinitely slow scan speed limit the forward and backward scans should yield the same detunings and the same MOT fluorescence peak signals for each MOT, respectively.

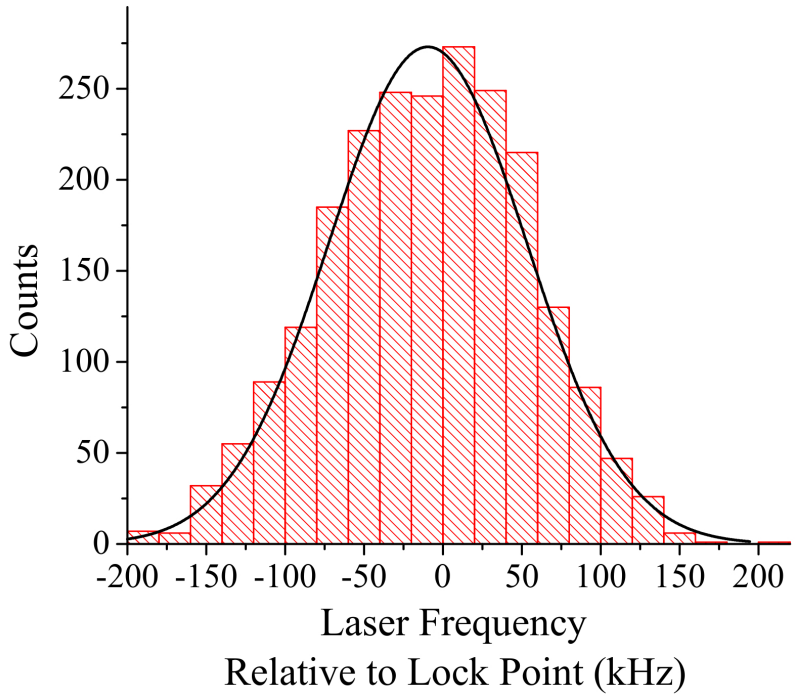

Figure 4.28: Histogram and corresponding Gaussian fit of frequency jitter of the Toptica TA-SHG Pro 589 nm laser for approximately one minute of lock time. Gaussian fit gives a standard deviation of approximately 63 kHz, so the locked long-term laser linewidth is about 126 kHz.

A better way to determine the detuning is to manually scan the MOT fluorescence as a function of f_r. The manual scan could be thought of as an infinitely slow scan speed. For example, the manual scan is shown in Fig. 4.27 for the type II MOT. The optimal detuning is in the $f_r/2 = 12.2$ to 13.6 MHz range. The right plot in Fig. 4.26 shows the backward going ramped MOT signal and spectrum signals when the AOMs have a relative shift $f_r = 24.8$ MHz, which still has the systematic detuning error of about 3 MHz due to the slow MOT loading time.

Using the saturation spectrum derivative signal near the $X_{22'-23'}$ and the $2 \rightarrow 3'$ peak (separated by ≈ 29 MHz) we calibrated the change in the derivative signal's voltage to

change in laser frequency. Next, the locked derivative signal was monitored for a little over one minute and a histogram of the change in voltage relative to the lock point (converted to the frequency domain) was recorded and fit to a Gaussian lineshape, as seen in Fig. 4.28. We found that the resulting long-term laser linewidth is about 126 kHz.

4.2.4 Vacuum chamber and getters

In this section we will discuss experimental details pertaining to the vacuum system and the getters used to load the background Ca and Na vapor. The vacuum chamber, seen in

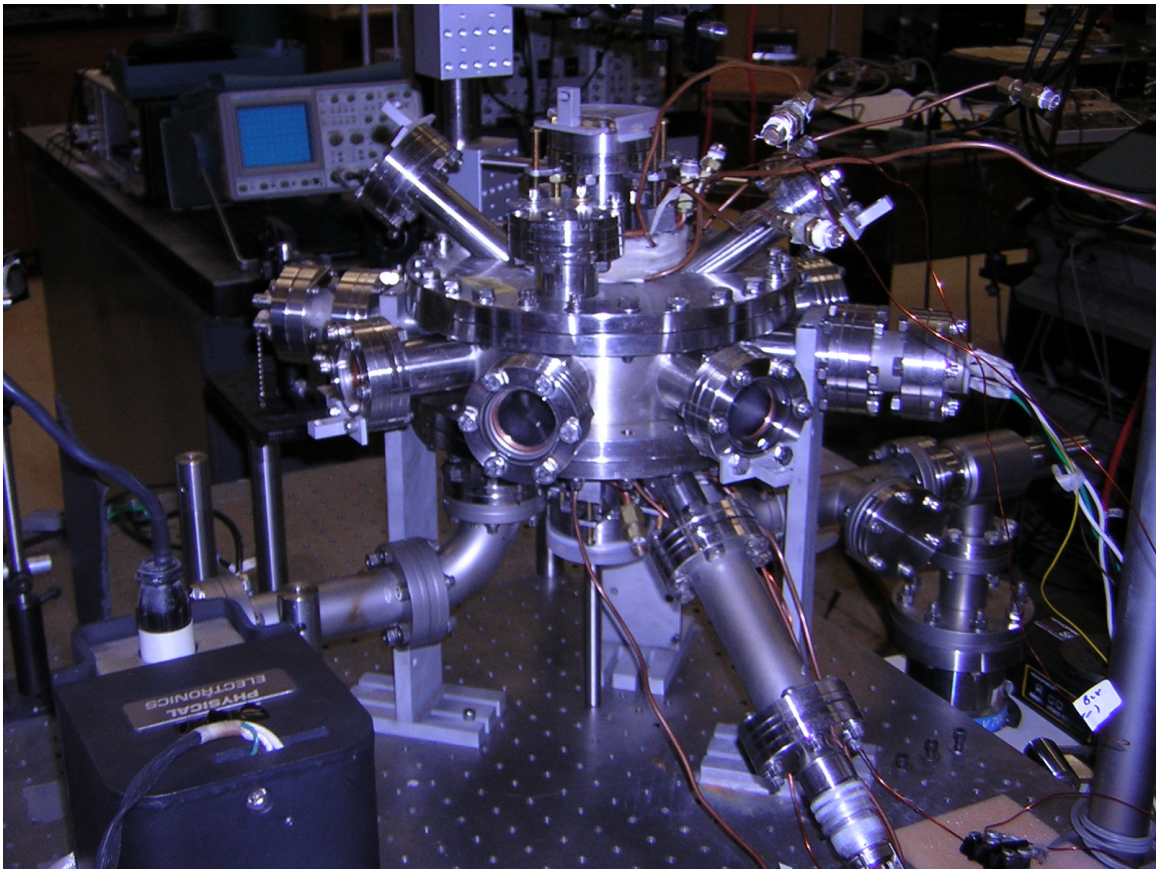

Figure 4.29: Image of the outside of the vacuum chamber with the optics stripped away. The anti-Helmhotlz magnets are attached and some of the electrical feedthroughs are in place. The ion pump can be seen in the lower left corner.

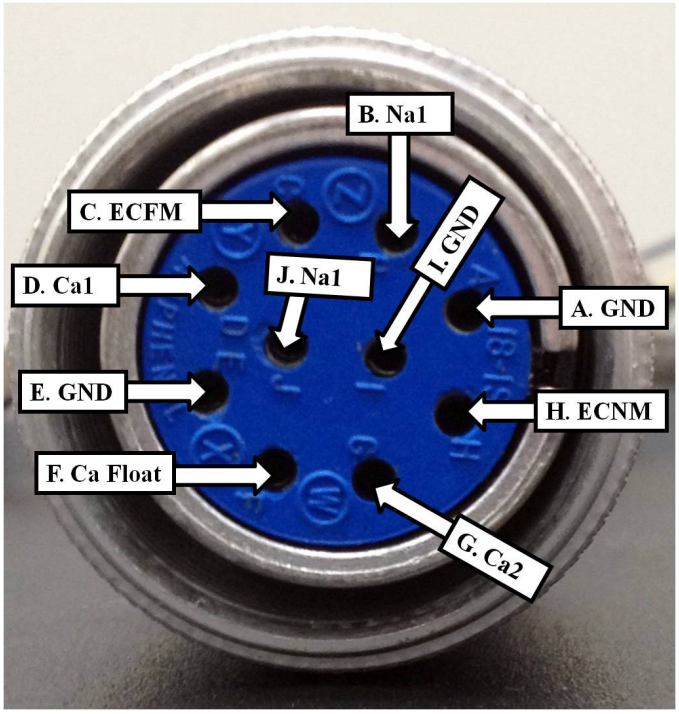

Figure 4.30: Image of vacuum chamber plug with several electrical feedthroughs for the Alvatec Na getters, Alvatec Ca getters, and the LPT end cap voltages.

Fig. 4.29, is made of stainless steel walls that are 5.08 mm thick. There are three quartz window viewports on the top of the chamber and seven viewports on the perimeter of the chamber's center section. The viewports have diameter $\varnothing = 35$ mm. The retro-reflection (second) viewports associated with the MOT beams are anti-reflection (AR) coated for visible wavelengths. When testing the viewports for optical transmission we found approximately 92 - 98% transmission at all wavelengths.

The vacuum chamber also has several electrical feedthroughs and an electron gun in one of the center section arms. Two of the electrical feedthrough plugs are shown in Figs. 4.30 and 4.31.

Whenever possible we try to not use aluminum metal or nylon as an electric insulator due to their high vapor pressure. However, using these materials in the chamber was

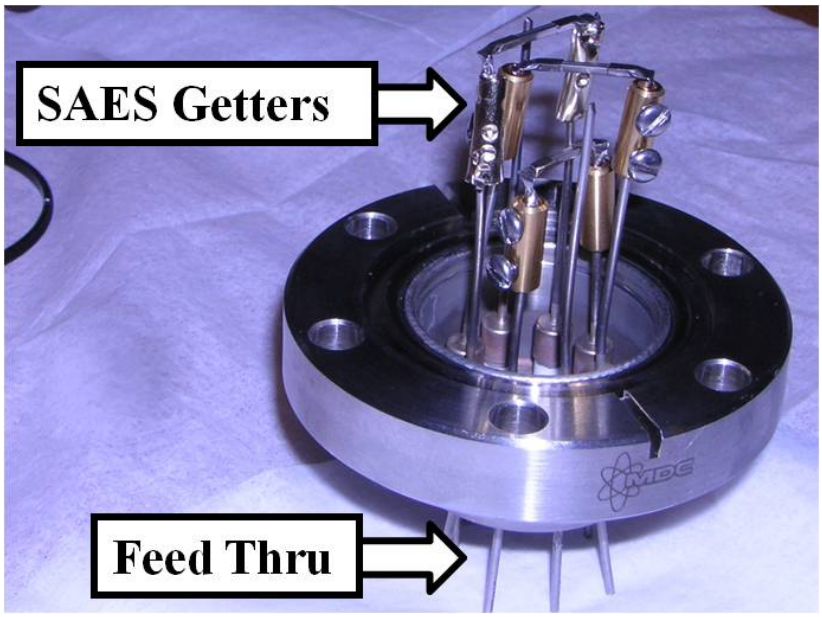

Figure 4.31: Image of electrical feedthrough at the top of the chamber for the SAES Na getters.

unavoidable, luckily is appeared not to prevent us from reaching UHV. To avoid the high vapor pressure, we mostly use materials made of stainless steel, OFHC copper, or Macor (as an insulator).

The chamber feedthroughs and viewports are sealed using stainless steel screws, nuts, and copper gaskets. After sealing the chamber it was baked at temperatures around $150°C$ for approximately one week, allowing the chamber to outgas. When the chamber is baking, we use a Varian turbo-pump, which lowers the chamber pressure down to $\sim 10^{-8}$ Torr. The turbo-pump can be closed off from the chamber and a Dunaway ion pump is used to bring the pressure down even further to $\lesssim 10^{-10}$ Torr, which is the lowest possible reading on our ion pump's gauge.

The neutral Ca and Na gas is produced within the chamber using Alvatec Ca and Alvatec Na ovens, as well as SAES Na getters. Some of the getters are within the main body of the chamber (Fig. 4.32) and some are within one of the top chamber arms (Fig. 4.31).

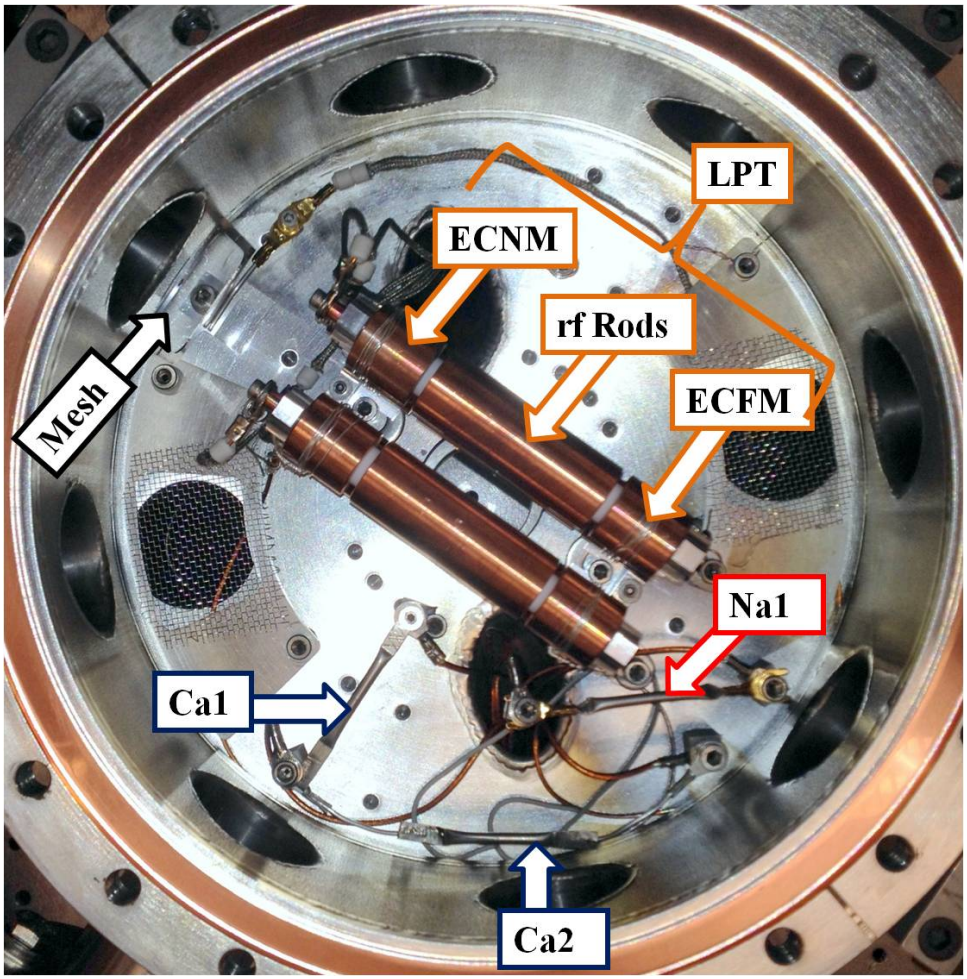

Figure 4.32: Image of inside of UHV chamber viewed from above the chamber. See text for details.

The getters' openings are aimed away from the center of the trap, to avoid a locally high background pressure at the location of the hybrid trap.

Passing an electrical current through the sources resistively heats them, boiling the Ca or Na inside releasing the gas into the chamber. The SAES getters operate at a 6.5 A current and the Na Alvatec oven at 5.5 A. The Ca ovens run at a larger 8 A current setting. At these current settings the sources do not increase the UHV chamber's pressure in any measurable way.

Thermionic emission occurs when the thermal energy of a getter is larger than the work function of the getter's metal case [132]. As a result, the metal becomes ionized causing the release of electrons that in turn ionize the boiled Ca or Na gas like an electron gun. To hinder the release of background ions produced via thermionic emission, the getters are negatively biased by a few volts.

4.2.5 MOT population and size

In this section we discuss measurements of the MOT's atomic steady-state population $\tilde{N}_a$ and its volume.

To measure the atom population we can use our photomultiplier tube (PMT) or our Thorlabs CMOS camera, whose placements are shown in Fig. 4.33. The lens in front of the PMT is used to image the MOT onto a mask at the front end on the PMT mount. We used one of two masks labeled in Fig. 4.34. The PMT mount creates another image from the real image at the location of the mask (passing through a neutral density ND filter and bandpass filter) onto a rectangular active target area within the PMT's vacuum tube. The target area has dimensions 27 mm x 10 mm.

When exposed to radiation the PMT outputs a photo-current proportional to the input radiation power. The proportionality constant is called the gain. To calibrate the relationship between input radiation power and output voltage we send in low power collimated 589 nm laser light and measure the corresponding linear voltage response, as seen in Fig 4.35. We will define the ratio between power and voltage as κ_{PMT}. The high voltage (HV) setting on the PMT determines the gain, which is expected to have an exponential dependence. By fitting the individual calibration results for several different HV settings to an exponential (with a non-zero offset), we can approximate a continuous calibration as a function of HV setting, as seen in Fig 4.35.

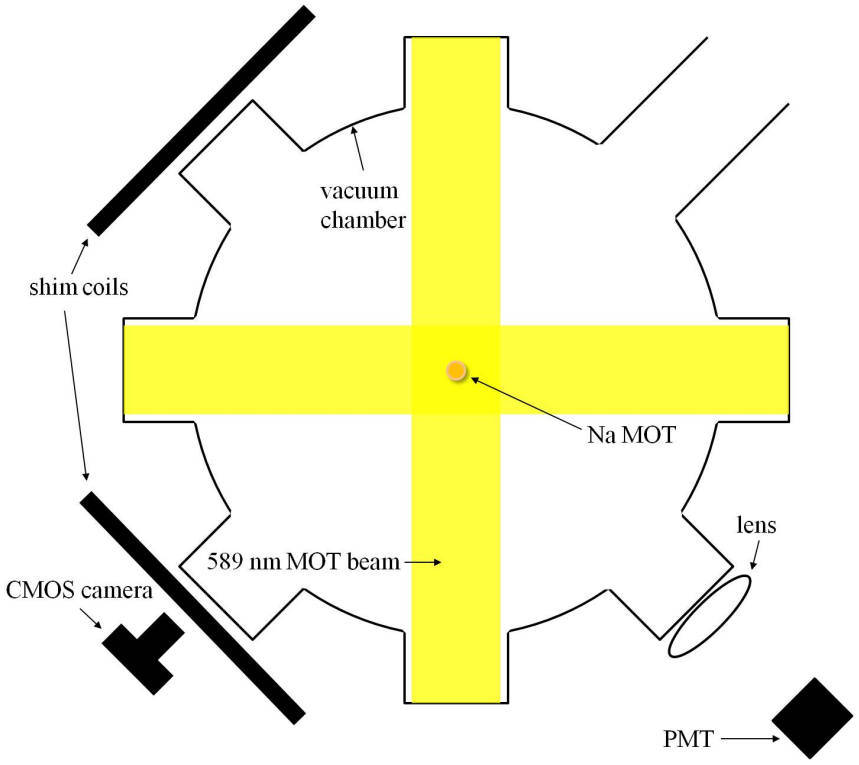

Figure 4.33: Top view of vacuum chamber (not to scale) with the orientation matching that of Fig. 4.2. The MOT beams intersect in the center of the chamber where the magnetic field gradient (from the external anti-Helmholtz coils that are not shown) is zero. To adjust the location of the magnetic field minimum electromagnet shim coils are used, which are designed with a large enough radius so as to produce a fairly uniform magnetic field normal to their coil plane. The x and y coils are shown here, but the z coil is not. The CMOS camera and the PMT fluorescence imaging system is also shown in front of the two lower diagonal viewports, unlike what is depicted in Fig. 4.2.

The output of the PMT is a current measurement. However, we would like to read a more robust voltage measurement that is not sensitive to the capacitance of our BNC cables and can be measured using our NI DAQ hardware. To convert the current measurement to a voltage measurement we use an op-amp current-to-voltage circuit with an active low-pass Sallen-Key filter [131], as illustrated in Fig. 4.36. For slow measurements a resistor is chosen so that the time constant is ≈ 0.3 ms, and for fast measurements a smaller resistance is chosen to give a time constant of $\approx 9\ \mu$s.

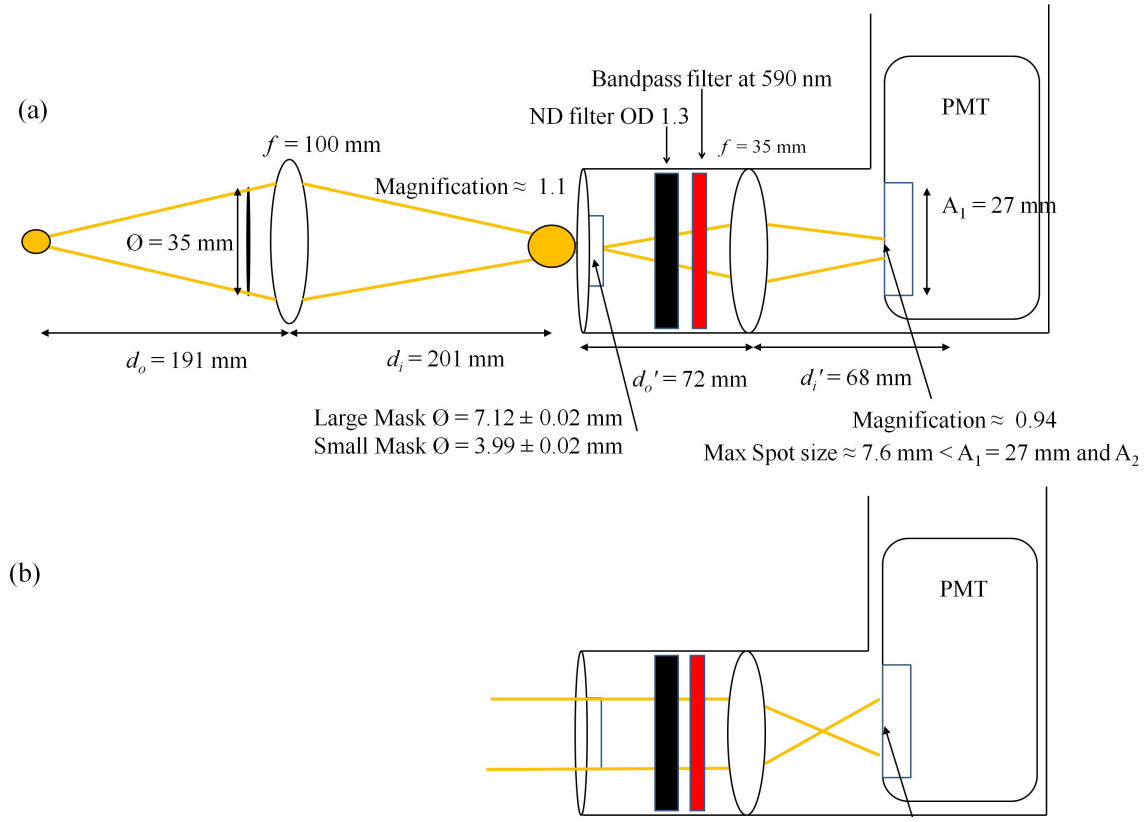

Figure 4.34: Panel (a) shows the schematic (not to scale) of the imaging system for the PMT used to determine the MOT's atomic population. Panel (b) shows that even collimated light will be incident within the PMT's active area. Collimated light is used for the calibration procedure. See text for details.

With the PMT calibrated we can relate the PMT's output voltage to the emitted optical fluorescence power from the MOT atoms. Now we need to relate the optical fluorescence power to the number of atoms held within the MOT at any time N_a. To do this we note that the fraction of excited atoms $\hat{\rho}_{22}$ release photons in steady-state at a rate Γ with each photon having energy $\hbar\omega_L$. Therefore, the total output power P_{MOT} can be written as

$$P_{\text{MOT}} = N_a \hat{\rho}_{22} \Gamma \hbar \omega_L. \tag{4.39}$$

However, the PMT or CMOS camera only measure a fraction of the power subtended

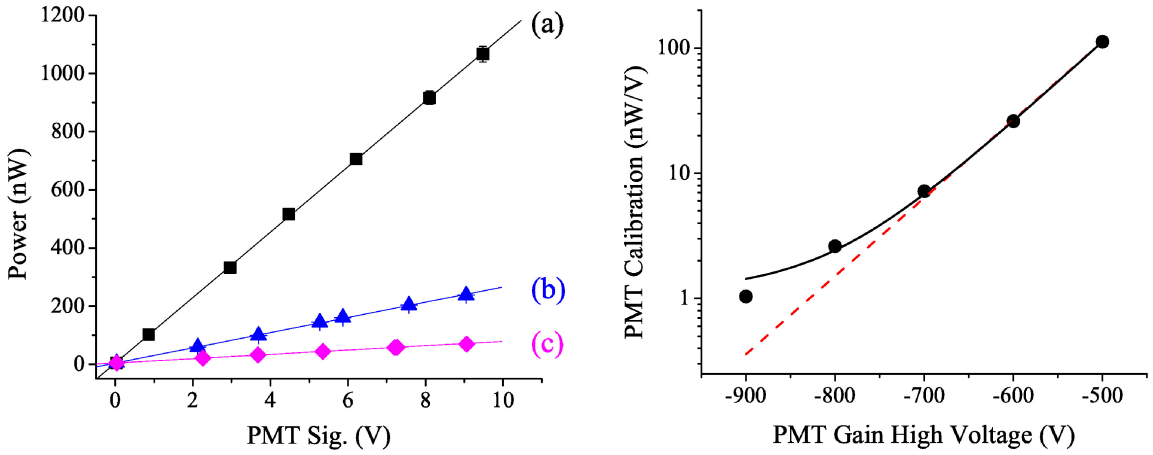

Figure 4.35: Left plot shows PMT calibration data for three different PMT-HV gain settings (a) -700 V , (b) -600 V, (c) -500 V. The calibration shows a linear relationship between incident 589 nm laser power and resulting PMT signal. Right plot shows the calibration value as a function of PMT-HV setting on a log-linear plot. The dashed red line shows exponential gain with zero offset. We use the exponential fit (solid black line) to predict the calibration as a continuous function of HV gain setting. The uncertainty in the data points is smaller than the size of the plot markers in both plots.

by the observable solid angle $\pi R_v^2/(4\pi d_o^2)$ and the fraction of light f_T transmitted though the UHV viewports and various external optics. Here, R_v is the radius of the UHV viewport (or CMOS camera lens) and d_o is the radial distance from the MOT to the imaging object. We have made the approximation that $d_o \gg R_v$. Correcting for the fractional transmission and the observable solid angle allows us to express the atom number as a function of the measured PMT signal voltage $\mathscr{V}_{\rm PMT}$ according to

$$N_a = \frac{(\mathscr{V}_{\rm PMT} - \mathscr{V}_{\rm back})\kappa_{\rm PMT} 4\pi d_o^2}{\pi R_v^2 f_T \hbar\omega_L}\left(\frac{1+4(\delta/\Gamma)^2 + I_{\rm tot}/I_s}{I_{\rm tot}/I_s}\right). \tag{4.40}$$

In Eq. (4.40) we subtract out any background light signal $\mathscr{V}_{\rm back}$, separately measured when the magnets are turned off, thus destroying the MOT. From Eq. (4.40) we see that the total intensity, saturation intensity, and detuning need to be precisely known to establish an accurate atom population measurement. The determination of the detuning is discussed in

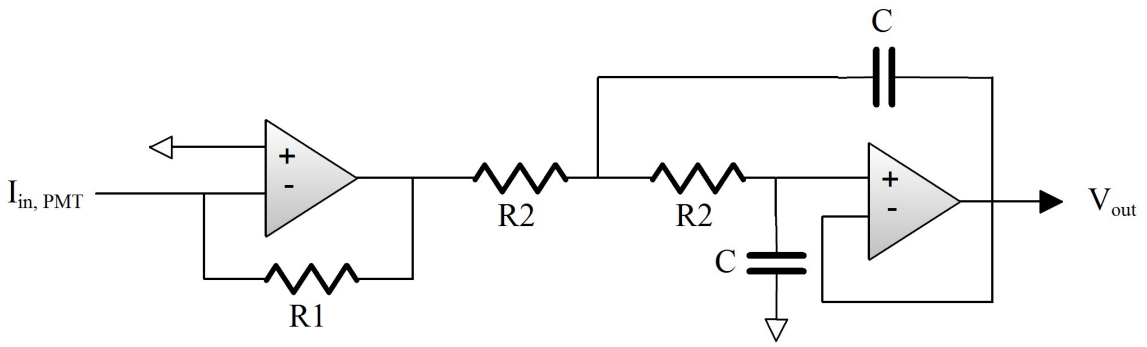

Figure 4.36: Circuit diagram of PMT current to voltage converter $R_1 = 1$ MΩ and an active Sallen-Key low-pass filter. The capacitor used in the filter has capacitance $C = 100$ pF, and the resistor R_2 is variable.

Secs. 4.2.2 and 4.2.3. The peak intensity is found using Eq. (4.31), where the measured size of the beams are listed in Table 4.1. The beam's effective power is only the fraction of the total power actually at the cooling transition frequency, which is the EOM carrier power for the type I MOT and the EOM sideband power for the type II MOT described by Eqs. (4.25) and (4.27), respectively.

As we will discuss further in Sec. 6.2, we have performed measurements [116] to determine the effective saturation intensities for the two MOTs and found that $I_s = 17 \pm 2$ mW/cm^2 for the type I MOT and $I_s = 38 \pm 4$ mW/cm^2 for the type II MOT. The theoretical value for isotropic polarization at the cooling transitions is $I_s \approx 13.4$ mW/cm^2, according to Ref. [111]. The discrepancy is because the theoretical value assumes an ideal two-level system, which is not the case in practice.[14] In fact, it is even less so for the type II MOT, which has greater leakage into states other than the cooling cycle, thus requiring greater intensity to saturate the transition.

We use our LabVIEW data acquisition program to automate the PMT data collection, which outputs the atom number and can record atom number measurements to file. For a

[14] "There are no two-level atoms and sodium is not one of them" – Bill Phillips

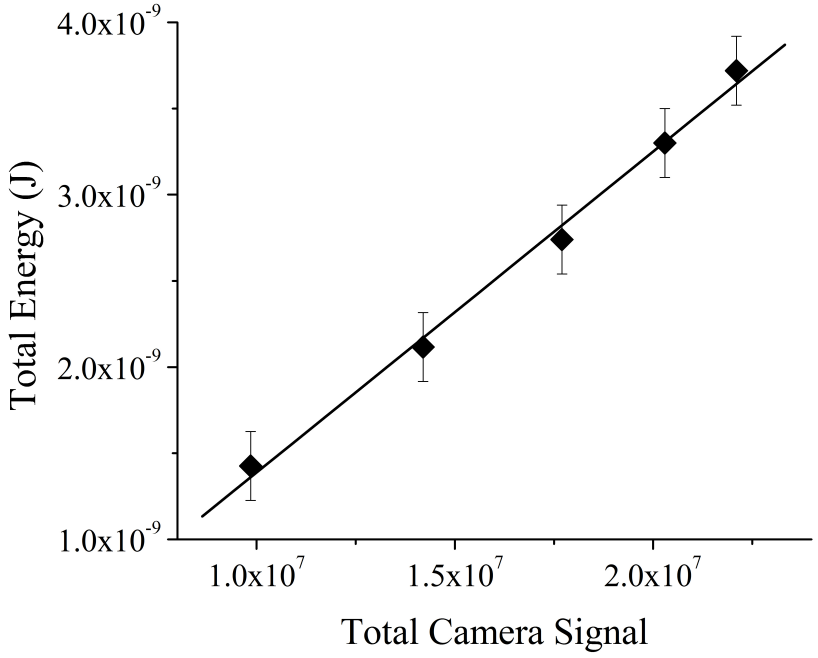

Figure 4.37: Camera signal calibration relating the total energy incident on the camera's active area (no lens) during a fixed exposure time.

detailed discussion of the LabVIEW data acquisition program see Appendix C.

Alternatively, we can use our CMOS camera to calculate the atom number and determine the MOT's spatial distribution, which allows us to determine the MOT's peak volume and density. Using an identical procedure to that used for the PMT, we can independently calibrate the CMOS camera's signal as a function of optical power input. When light is incident on the camera our software can read a 8 bit value (between 0 and 256) that we will call "csig," which is proportional to the amount of energy incident on that pixel during a finite exposure time. The ratio of input energy to output signal gives the camera calibration $\kappa_{\text{cam}} = 1.86 \pm 0.08 \times 10^{-16}$ J/csig, as seen in Fig. 4.37.

The camera also needs to be spatially calibrated to determine the ratio between the object (MOT) size and the image number of pixels α_{cam}. To establish this spatial calibration we first image the MOT and lock the camera lens position so that the MOT is in focus. Next,

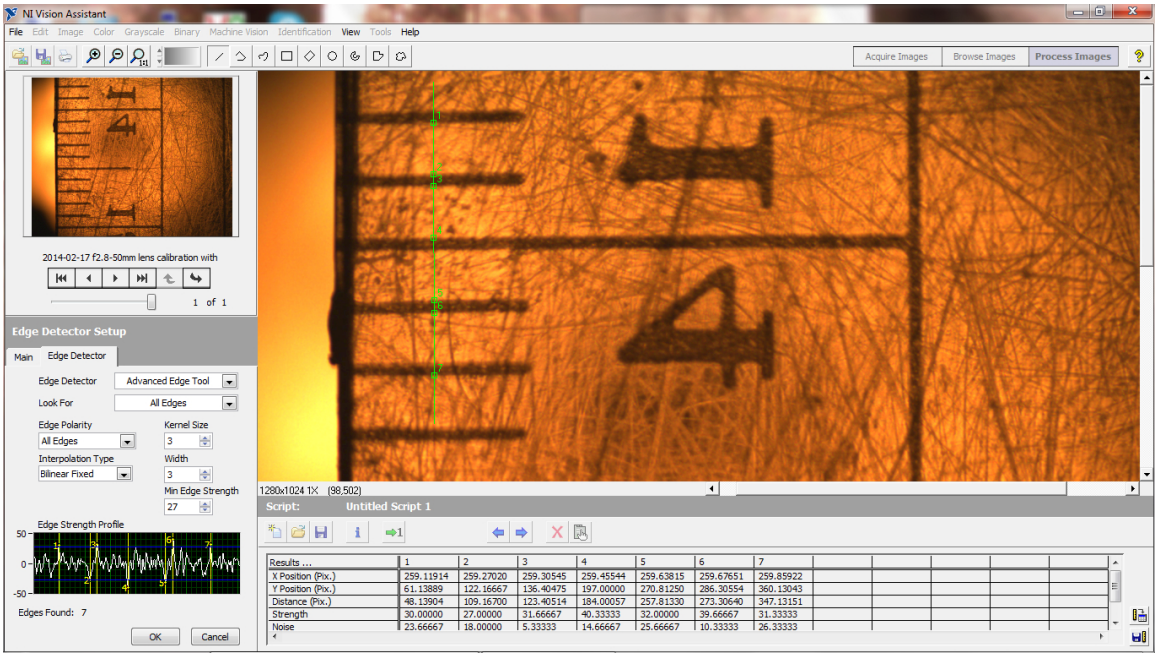

Figure 4.38: Screen shot showing the NI Vision software analysis of the calibration image of a ruler taken with our CMOS camera.

we aim the camera at a ruler and position the ruler so that it comes into focus, putting it at the same distance as the MOT, relative to the camera lens. Last, we use NI Vision software to measure the number of pixels associated with a 1 mm distance on the ruler, as seen in Fig. 4.38. Our calibration yields a value of $\alpha_{\text{cam}} = 75.11$ pixels/mm, which is in good agreement with an independent back-of-the-envelop estimate using geometric optics and the relevant camera dimensions given the camera's specification.

With the calibrated camera we can now use another LabVIEW program to capture and analyze the MOT image. A screen shot of the LabVIEW MOT image program's front panel is shown in Fig. 4.39. To obtain an accurate atom number we first subtract an image of the background fluorescence with the MOT turned off from the image of the MOT turned on. Analysis is then performed on the subtracted image.

The total signal integrated across the entire resulting image is used along with κ_{cam}

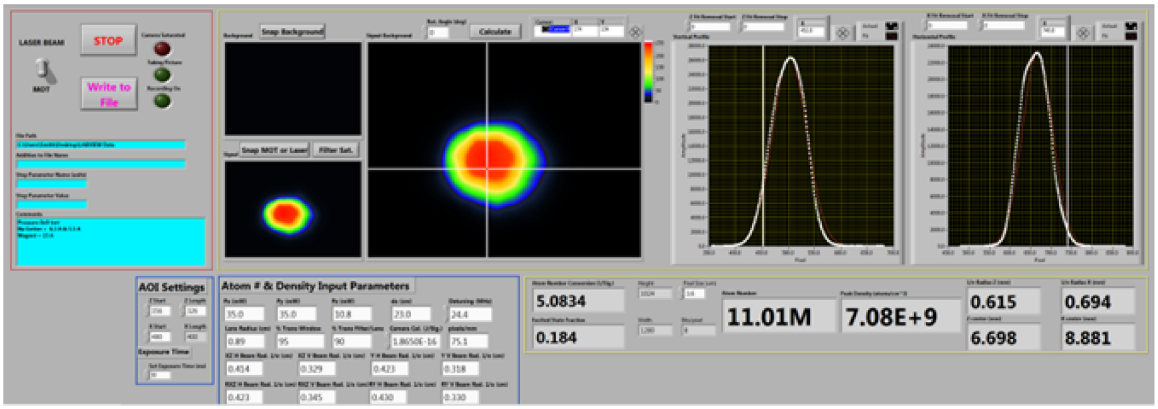

Figure 4.39: Screen shot of MOT image program's front panel. See text for details

and Eq. (4.40) to determine the total atom number. By separately integrating the pixel values vertically and horizontally we obtain projections of the horizontal and vertical spatial distribution, which is approximately Gaussian due to the harmonic trap potential. The pixel numbers can be converted into distances using α_{cam}.

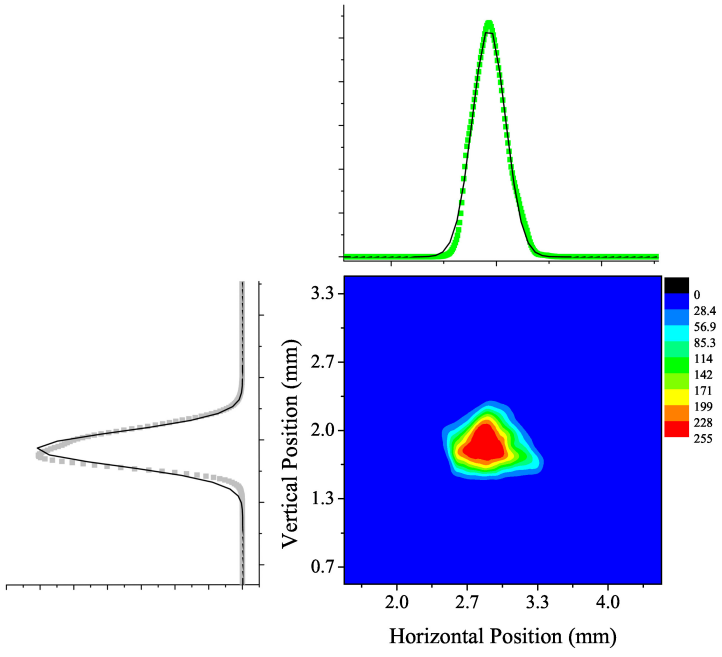

Figure 4.40: Type I MOT image data represented in a contour plot and corresponding vertical and horizontal spatial profile.

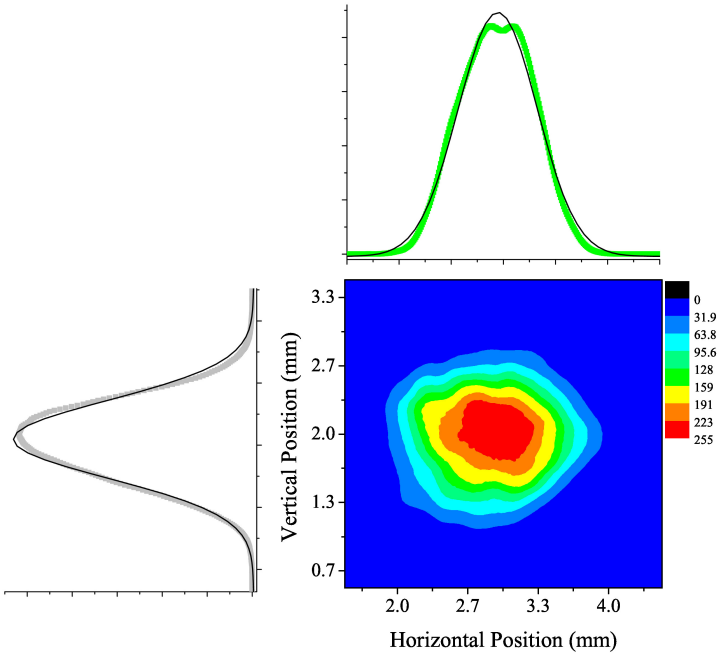

Figure 4.41: Type II MOT image data represented in a contour plot and corresponding vertical and horizontal spatial profile.

By adjusting the relative MOT cooling beam intensities, both MOTs can be formed with approximately spherical Gaussian spatial distributions, as seen in Figs. 4.40 and 4.41. As mentioned earlier, we can measure the total number of atoms using the MOT fluorescence with our camera or PMT; both measurements typically agree within 5% of one another despite using different collection optics, different viewpoints, and having been independently calibrated.

Because the type I MOT has a stronger cycling transition strength, it forms a denser and colder MOT, with typical measured densities $n_{\mathrm{MOT}} \sim 10^{10}$ cm^{-3}, $N_a \sim 10^6$, and $1/e$ density radius $r_a \approx 0.025$ cm. The type II MOT is larger and warmer, typically having measured $n_{\mathrm{MOT}} \sim 10^9$ cm^{-3}, $N_a \sim 10^7$, and $r_a \approx 0.075$ cm.

4.2.6 MOT temperature

In this section we will discuss the determination of the background Na gas temperature and the type I and II MOT temperatures.

Background gas temperature The background gas is illuminated by the six MOT beams, but the anti-Helmholtz coils are turned off so the MOT cannot be formed. We scan the 589 nm radiation over both hyperfine ground state transitions, about 2 GHz. The corresponding Doppler free saturation absorption spectrum signal within our Na cell during the MOT beam scan is shown in the blue curve of Fig. 4.42. The PMT signal from the background gas fluorescence in the UHV chamber is shown in the orange curve of Fig. 4.42, which corresponds to a Doppler broadened spectrum, described by Eq. (4.37).

Fitting the two Doppler broadened ground states to a least square fit of the sum of two Gaussian functions yields the temperature of the background gas $T = 346 \pm 3$ K. Here, the Doppler-full spectrum follows a Gaussian function, whose width is related to the temperature according to Eq. (4.38). The two dips in the spectrum result from the fact that both the forward going and retro-reflected beams address the same speed class, but address negated velocity classes. Therefore, half of the atoms fluorescing are associated with all the forward beams and the other half are associated with all the retro-reflected beams. However, when the laser beams are tuned to the middle of the transition, both the forward and retro-reflected beams address the same speed and velocity class, $v = 0$. If the transition is saturated then half as many atoms will be fluorescing near resonance as compared to non-zero velocity classes, giving a dip in the signal called the Lamb dip.[15] The dip is removed when all the retro-reflected beams are blocked.

[15]The Lamb dip in the observed background gas fluorescence occurs for the same reason that the saturation absorption pump beam reduces the probe beam's attenuation.

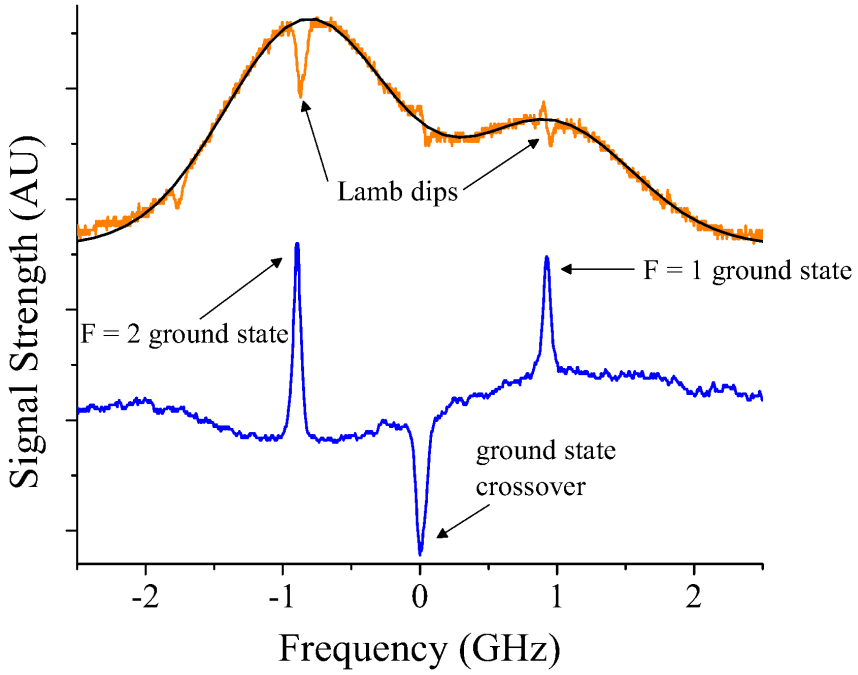

Figure 4.42: The plot shows the saturation absorption spectroscopy of both hyperfine ground states on the D2 line (blue) and the background gas fluorescence with the MOT turned off (orange). The x-axis is calibrated such that the F = 1 and F = 2 features are 1772 MHz apart (as seen in Fig. 3.3). The fitting parameters to Eq. (4.37) in black determines the temperature. See text for details.

MOT temperature We use the release and recapture method to measure the MOT's temperature [1]. The method involves three steps: (i) fully loading the MOT into steady-state, (ii) suddenly turning off all six trapping laser beams for a time t_{off}, and (iii) suddenly turning the laser beams back on, thus illuminating the remaining atoms and recapturing the MOT to saturation. The process can be repeated for several values of t_{off}. When the MOT beams are off, the atom cloud is no longer trapped and expands ballistically and isotropically. The fraction of atoms recaptured after t_{off} can be related to the MOT temperature using the following argument.

The PMT images a finite volume within the vacuum chamber, specifically $R_d = R_m/M$. Here, R_m is the physical radius of the PMT mask, M is the magnification of the fluorescence

image [as discussed in Sec. 4.2.5] and R_d is the effective radius of PMT detection inside the UHV chamber. Any atom moving with speed $v_0 = R_d/t_{\text{off}}$ (assuming it starts at the center of the detection radius) will escape the detection radius and not be detected when the MOT beams are switched back on. Thus, the number of detectable atoms remaining N_d is proportional to the number of atoms with speeds less than v_0. Assuming that the MOT atoms adhere to a MB speed distribution f_{MB} we find that

$$\begin{aligned} N_d &= \tilde{N}_a \int_0^{v_0} f_{\text{MB}}(v)\, dv = \tilde{N}_a \int_0^{\frac{R_d}{t_{\text{off}}}} f_{\text{MB}}(v)\, dv \implies \\ \frac{N_d}{\tilde{N}_a} &= \text{erf}\left(\frac{R_d}{t_{\text{off}}}\sqrt{\frac{m_N}{2k_BT}}\right) - \frac{R_d}{t_{\text{off}}}\sqrt{\frac{2m_N}{\pi k_BT}}e^{-m_N R_d^2/(2k_BTt_{\text{off}}^2)}, \end{aligned} \tag{4.41}$$

where m_N is the mass of the atom, T is the temperature of the MOT, and k_B is the Boltzmann constant.

We use our LabVIEW data acquisition program to automate the data collection. The power supply for the MOT beam Isomet AOM can be triggered on and off with a TTL pulse generated via our NI DAQ board. The AOM shut-on/off time is $\lesssim 10\ \mu$s and can be approximated as sudden. The PMT analog input is triggered when the light is shut off, with a short pre-trigger data collection to establish the initial steady-state population. The mean PMT signal during the pre-trigger window is proportional to $\tilde{N}_a$ according to Eq. (4.40). When the MOT beams are turned back on after t_{off} the recapture PMT signal is determined, which is proportional to N_d. The value of the recapture signal is determined by having the LabVIEW data acquisition program average the PMT waveform right after the lasers are turned back on over a time window of ≈ 0.2 ms. The ratio of these two PMT signals gives the fraction of atoms recaptured when the laser light is turned back on.

Because of the necessary temporal resolution, the PMT current to voltage circuit in Fig. 4.36 uses a short time constant of $\approx 9\ \mu$s. The data are recorded to file and the

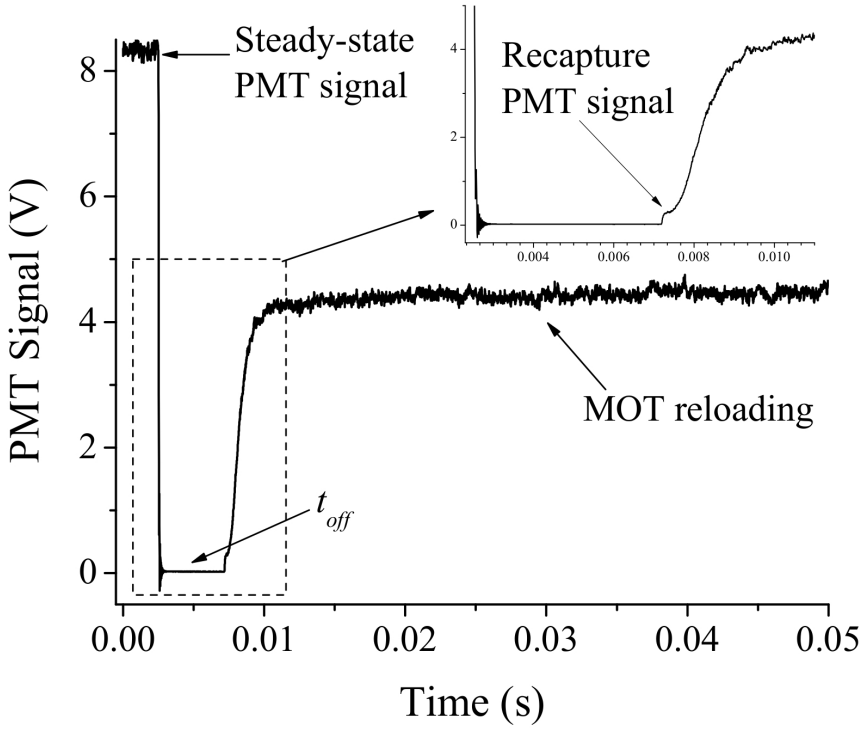

Figure 4.43: PMT signal for a single release and recapture measurement sequence. The insert shows a magnified view of the recapture voltage.

LabVIEW data acquisition program also performs a least-squares fit using Eq. (4.41), with the MOT temperature T as the fitting parameter.

The resulting PMT signal for a single release and recapture sequence is shown in Fig. 4.43, where the magnified inset shows that the recapture signal is actually at a slightly earlier time than can easily be seen when viewing the unmagnified PMT signal. The net results from measurements on the type I and II MOTs are shown in Fig. 4.44, which yield $T_{\mathrm{MOT}} = 0.38 \pm 0.18$ mK for the type I MOT and $T_{\mathrm{MOT}} = 2.3 \pm 1.0$ mk for the type II MOT.

The procedure contains two systematic errors worth discussing. First, the anti-Helmholtz coils' field can couple to the atom's quadrupole moment. This coupling causes a force that tends to prevent ballistic expansion and recaptures more atoms than would have otherwise been captured had the magnets also been turned off during t_{off}. Another error is

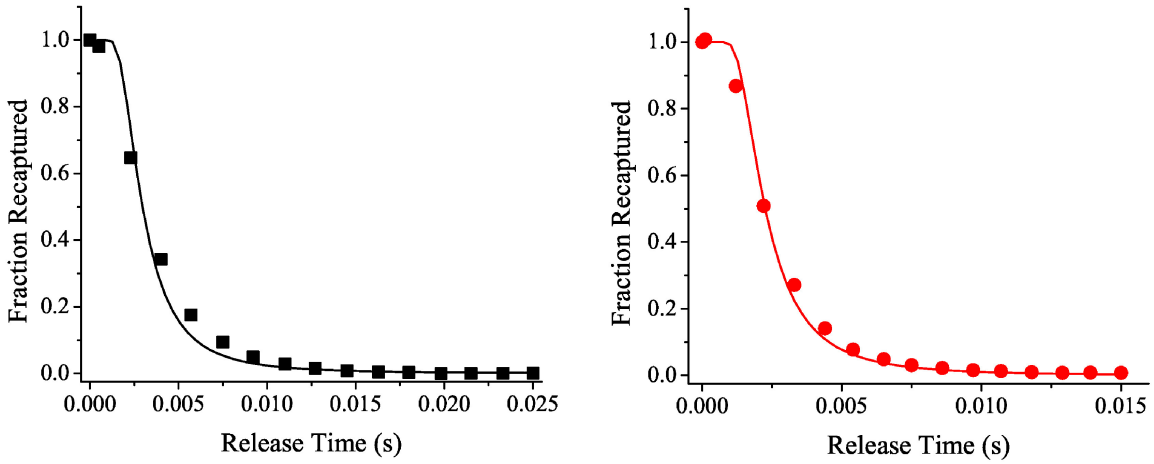

Figure 4.44: The left plot (black) shows the release and recapture data for the type I MOT using the small PMT mask with $R_d \approx 1.68$ mm. The right plot (red) shows the release and recapture data for the type II MOT using the large PMT mask with $R_d \approx 3.15$ mm. The corresponding fits to Eq. (4.41) are shown as solid lines and give a temperature of $T_{\mathrm{MOT}} = 0.38 \pm 0.18$ mK for the type I MOT and $T = 2.3 \pm 1.0$ mk for the type II MOT. The statistical uncertainty in the data is smaller than the plot markers.

the fact that the COM of the MOT falls under the influence of gravity, making R_d's center location time dependent. This has the opposite systematic effect from the magnetic field, since it tends to reduce the number of atoms recaptured.[16] We do not do anything to correct for these systematic errors either experimentally or post-analysis, but merely mention them here for thoroughness

4.2.7 MOT loading model

In this section we will consider the loading dynamics of the MOT and the resulting rate equation that leads to the the MOT's steady-state population $\tilde{N}_a$.

In the temperature-limited regime [121, 133], the volume of the MOT V_{MOT} remains constant while the MOT density n_{MOT} increases linearly with atom increasing population

[16] The systematic error due to the cloud falling under the influence of gravity may be problematic for our system, since an atom with zero initial velocity falls approximately 1 mm in 0.015 s near the surface of the earth. This is not an insignificant distance compared to R_d. Choosing a larger R_d might be advantageous.

$\tilde{N}_a$. Collisions between two MOT atoms lead to a non-exponential two-body loss rate βn_{MOT} [134], while collisions with constant density background Na atoms result in a linear loss rate γ_b. Because we operate in the temperature-limited regime, we model the MOT loading behavior with a non-linear rate equation

$$\frac{dN_a}{dt} = L_{\mathrm{MOT}} - \gamma_t N_a - \frac{\beta}{V_{\mathrm{MOT}}} N_a^2, \tag{4.42}$$

where L_{MOT} is the constant rate at which atoms are loaded into the MOT and γ_t is the total single-body linear loss rate [121]. The total single body loss rate is a sum of all the single body loss rates, e.g., $\gamma_t = \gamma_b + \gamma_{\mathrm{pi}}$ when there are losses due to photoionization (PI) radiation at rate γ_{pi} per atom in addition to background collisional losses. The solution to Eq. (4.42) is

$$N_a(t) = \frac{2L_{\mathrm{MOT}}\left(1 - e^{-\gamma_e t}\right)}{\gamma_e + \gamma_t + (\gamma_e - \gamma_t)\, e^{-\gamma_e t}}, \tag{4.43}$$

where

$$\gamma_e = \sqrt{\gamma_t^2 + \frac{4\beta L_{\mathrm{MOT}}}{V_{\mathrm{MOT}}}}. \tag{4.44}$$

The steady-state solution can be found by taking $t \to \infty$ in Eq. (4.43) giving

$$\tilde{N}_a = \frac{2L_{\mathrm{MOT}}}{\gamma_b + \zeta I_{\mathrm{pi}} + \sqrt{\left(\gamma_b + \zeta I_{\mathrm{pi}}\right)^2 + \frac{4\beta L_{\mathrm{MOT}}}{V_{\mathrm{MOT}}}}}. \tag{4.45}$$

We found that using Eq. (4.43) significantly improved our fits to the MOT fluorescence loading data, as seen by comparing Figs. 4.45 and 4.46. This model is different from the the more commonly used density limited (constant density) linear rate equation

$$\frac{dN_a}{dt} = L_{\mathrm{MOT}} - \gamma_t N_a, \tag{4.46}$$

whose solution is

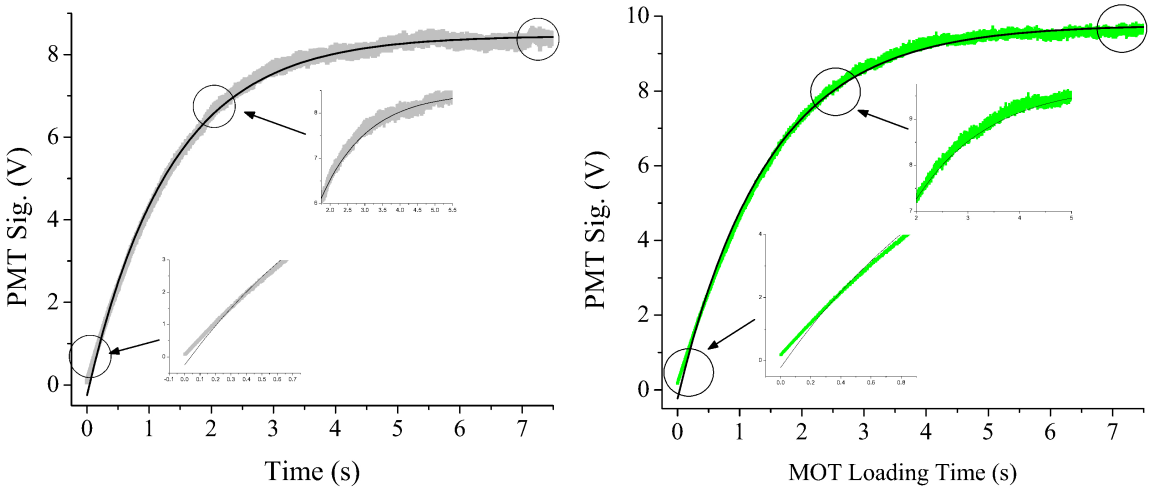

Figure 4.45: Left and right plot show the MOT fluorescence loading data for the type I (gray) and II (green) MOTs, respectively. Both plots show the fit to the density limited model Eq. (4.47). The insets magnify the areas of the fit with the worst discrepancy.

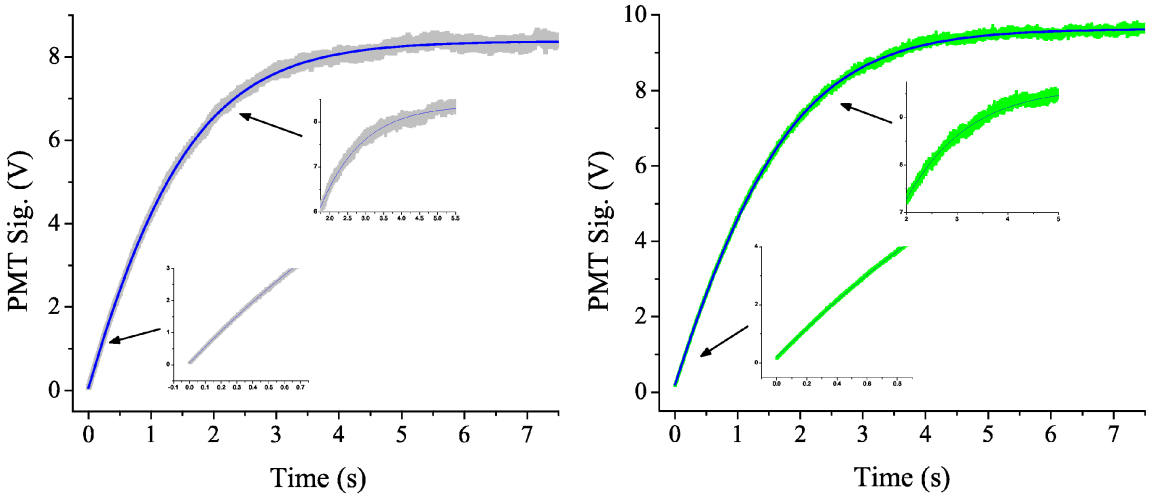

Figure 4.46: Left and right plot show the MOT fluorescence loading data for the type I (gray) and II (green) MOTs, respectively. Both plots shows the fit to the temperature limited model Eq. (4.43). The insets show the improvement over Fig. 4.45.

$$N_a(t) = \frac{L_{\mathrm{MOT}}}{\gamma_t}\left(1 - e^{-\gamma_t t}\right), \tag{4.47}$$

which assumes constant density, so γ_b absorbs the now constant $\beta N_a / V_{\mathrm{MOT}}$ term, as

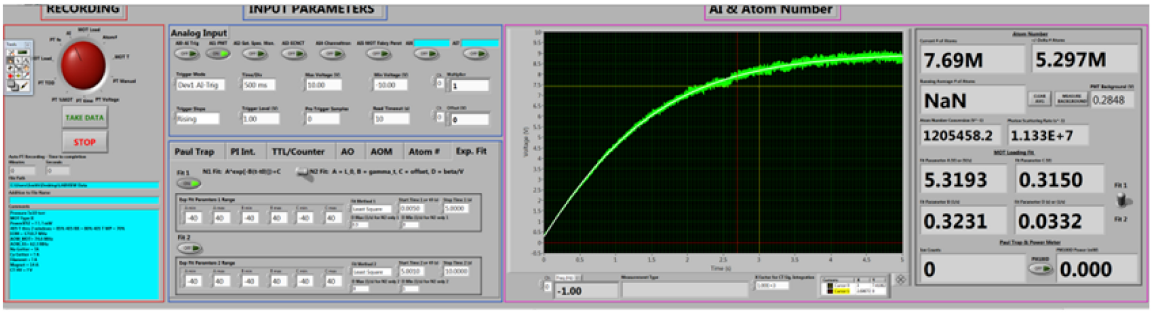

Figure 4.47: Screen shot of the LabVIEW data acquisition program's front panel showing a MOT loading measurement and corresponding fit. See text for details.

discussed in Refs. [62, 121, 135]. However, to reduce the number of free parameters using the temperature limited model, we found that constraining β to a value of $\approx 1.0 \times 10^{-11}$ cm^3/s for the type I MOT and a value of $\approx 1.0 \times 10^{-10}$ cm^3/s for the type II MOT gave the most consistent fits. These values are fairly close to the previously reported value of β for a Na MOT of 4×10^{-11} cm^3/s, which has a factor of five uncertainty [134].

We find that the MOT loading rate L_{MOT} is larger for the type II MOT then the type I by a factor of ≈ 2.3. We also found that each individual MOT's loading rate is insensitive to the presence of additional loss mechanisms, e.g., PI radiation or ion-atom collisions within the hybrid trap. Similar insensitivity has been observed elsewhere [62, 135]. For example, an experiment that modeled changes to L_{MOT} in a Na MOT due to PI found that the modification was small [121], therefore we neglect it in the experiments presented here in the interest of simplicity.

We use our LabVIEW data acquisition program to automate the data collection. The front panel for a MOT loading measurement is shown in Fig. 4.47. The MOT is initially unloaded by closing the electronic shutter that blocks the MOT retro-reflection y beam, as seen in Fig. 4.2. The shutter is controlled via a TTL pulse from the NI DAQ board and has a closed default state. When the shutter is opened the analog input is triggered to start

reading the PMT fluorescence data and a least squares fit to Eq. (4.43) or Eq. (4.47) is performed. The raw data and fit results are recorded to file.

This concludes our discussion of the neutral atom component to the hybrid apparatus. We have discussed the physical principles associated with Doppler laser cooling and trapping, as well as many of the technical details associated with our group's Na MOT. We will now move onto the LPT ion-trapping component to the hybrid apparatus.

4.3 Linear Paul trap

In the previous section we have extensively discussed neutral atom cooling and trapping by radiation pressure forces within a MOT. In this section we will extend our discussion of trapping and cooling to ionic atoms or molecules, which are trapped in an ion trap called a linear Paul trap (LPT). We will also discuss the combination of the MOT and LPT into the hybrid trap system.

4.3.1 Earnshaw's theorem

All traps must provide a restoring force, like a spring force $\vec{F} = (-kx)\hat{x}$ in each dimension. In 3D all the force lines would point back to the center of the trap, thus always restoring a displaced particle back to the trap's center. When all the force lines point to the center of the trap, the divergence of the force must be negative, satisfying the inequality

$$\vec{\nabla} \cdot \vec{F} = \vec{\nabla} \cdot (-\vec{\nabla} V) = -\nabla^2 V < 0. \tag{4.48}$$

For a 1D spring Eq. (4.48) gives

$$\vec{\nabla} \cdot (-kx)\hat{x} = -\nabla^2 \left(\frac{kx^2}{2} \right) = -k < 0, \tag{4.49}$$

as advertised.

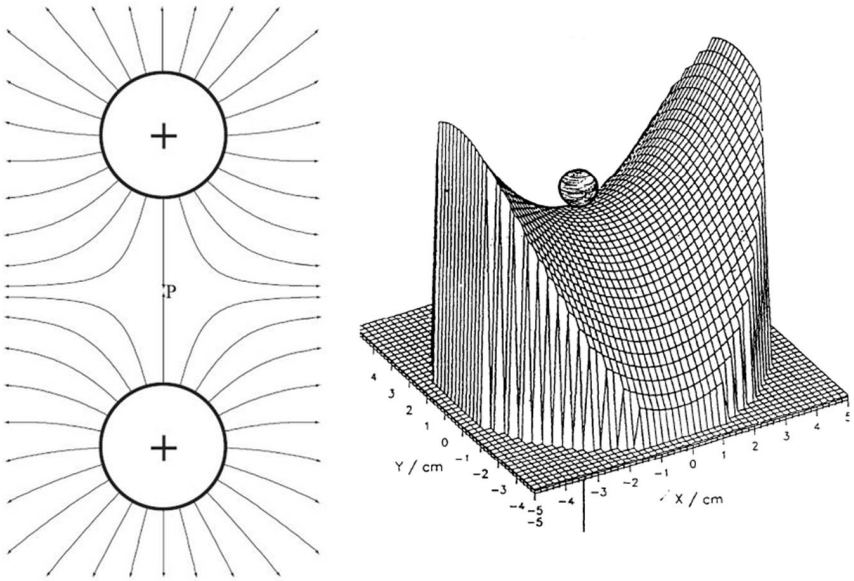

Figure 4.48: Originally from Ref. [73], left panel shows an electrostatic trap with electric field lines. A positively charged point particle is stably trapped in the vertical direction, but can escape (unstable) if perturbed horizontally. The right panel, originally from Ref [33], shows the spatial dependence of the saddle potential.

However, all electrostatic configurations have electrical potentials that obey Laplace's equation

$$\nabla^2 \mathscr{V} = 0 \implies -\nabla^2 V = 0 \tag{4.50}$$

within the source free region, where one might try to create an electrostatic trap. According to Eqs. (4.48) and (4.50), it is impossible to create an electrostatic trap in three dimensions, a result known as Earnshaw's theorem. When the potential satisfies Laplace's equation it has a saddle dependence that provides stable trapping in one dimension and unstable trapping in the perpendicular dimension, as seen in Fig. 4.48.

There are some electrostatic or magnetostatic trap loopholes associated with traps that couple to dipole moments of particles. For example, we know from our earlier discussion that the energy on a magnetic dipole in a magnetostatic field is $V = -\vec{\mu} \cdot \vec{\mathscr{B}}$. Permanent

dipoles (ferromagnets) satisfy Eq. (4.50) and are subject to Earnshaw's theorem. However, if the dipole moment is proportional to the local magnetic field lines, as is the case for paramagnets, then $V \propto |B|^2$ and $\nabla^2 V \geq 0$ when the proportionality constant is positive. Therefore, when the potential is proportional to the square of the field's magnitude, the potential satisfies the inequality in Eq. (4.48) and the particle is restored to points of low field magnitude, this behavior is called low-field seeking.[17]

4.3.2 Harmonic pseudopotential

To get around Earnshaw's theorem for ionic monopoles, Wolfgang Paul developed a dynamic electromagnetic field to create his ion trap [136]. By using an electrodynamic field, the saddle potential oscillates, where the stable axis continuously rotates its orientation by 90° at the electrodynamic rf angular driving field frequency Ω_{rf}. The net result is an effective harmonic pseudopotential, as illustrated in Fig. 4.49.

We would like to describe the motion of the trapped ion within the pseudopotential approximation, as illustrated by the black line in Fig. 4.49 (B). We begin by describing the force on the particle in one dimension due to static dc electric fields and ac dynamic electric fields as

$$\begin{aligned} F_{\text{dc}} &= qE_{\text{dc}}(x) = -q\frac{d\mathscr{V}_{\text{dc}}}{dx} \\ \text{and } F_{\text{ac}} &= qE_{\text{ac}}(x,t) = qE_0(x)\cos(\Omega_{\text{rf}}t) = -q\frac{d\mathscr{V}_{\text{ac}}(x,t)}{dx}, \end{aligned} \tag{4.51}$$

respectively.

Following the treatment of Refs. [84, 137], we can separate the ion's motion into a slow secular motion $X_s(t)$ and fast smaller oscillation about the secular trajectory $X_m(t)$ called the micromotion. The net displacement of an ion with mass m_I becomes

[17] This magnetostatic loophole is what makes magnetically trapped BECs possible [73].

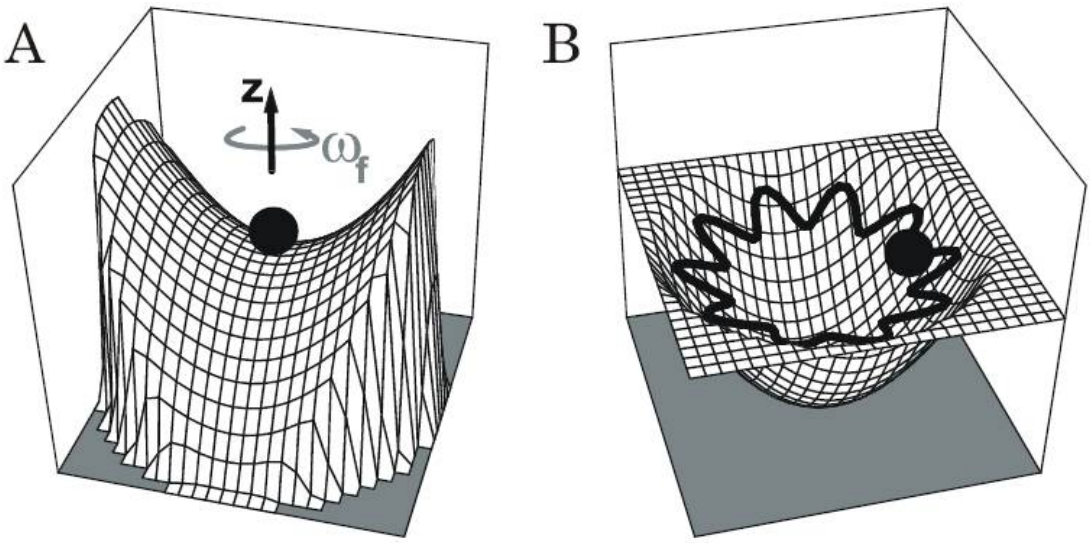

Figure 4.49: Originally from Ref. [84], left panel shows an electrostatic saddle potential and right panel shows the effective pseudopotential. The ion takes a trajectory that is a superposition of secular motion around the pseudopotential with small oscillations called micromotion about the secular trajectory at the driving frequency.

$$x(t) = X_s(t) + X_m(t), \quad \text{where} \quad m_I \ddot{x} = F_{\text{dc}}(x) + F_{\text{ac}}(x,t) \tag{4.52}$$

by Newton's second law. Because $X_s \gg X_m = x - X_s$ we can Taylor expand Eq. (4.52) in $X_m = x - X_s$ about X_s giving

$$\begin{aligned} m_I \left(\ddot{X}_s + \ddot{X}_m\right) \approx & F_{\text{dc}}(X_s) + qE_0(X_s)\cos(\Omega_{\text{rf}} t) \\ & + X_m \left(\left.\frac{\partial F_{\text{dc}}(x)}{\partial x}\right|_{x=X_s} + q\cos(\Omega_{\text{rf}} t) \left.\frac{\partial E_0(x)}{\partial x}\right|_{x=X_s} \right) \end{aligned} \tag{4.53}$$

to first order in $X_m = x - X_s$.

Equating the fast oscillating parts [84] in Eq. (4.55) allows us to solve for the micromotion dynamics via integration

$$m_I \ddot{X}_m \approx qE_0(X_s)\cos(\Omega_{\text{rf}} t) \implies X_m(t) = \frac{-qE_0}{m_I \Omega_{\text{rf}}^2}\cos(\Omega_{\text{rf}} t), \tag{4.54}$$

where we have assumed that $E_0(X_s)$ is approximately static over the period of the micromotion oscillation and comes out of the integral.

Using the micromotion solution from Eq. (4.57) in Eq. (4.55) and time averaging over the driving field's period τ_{rf} gives the equation of motion for the secular motion

$$\begin{aligned}
\left\langle m_I\left(\ddot{X}_s+\ddot{X}_m\right)\right\rangle_t \approx& \left\langle F_{\text{dc}}(X_s)+E_0(X_s)\cos(\Omega_{\text{rf}}t)\right\rangle_t \\
&+\left\langle \frac{-E_0}{m_I\Omega_{\text{rf}}^2}\cos(\Omega_{\text{rf}}t)\left(\left.\frac{\partial F_{\text{dc}}(x)}{\partial x}\right|_{x=X_s}+\cos(\Omega_{\text{rf}}t)\left.\frac{\partial E_0(x)}{\partial x}\right|_{x=X_s}\right)\right\rangle_t \\
\implies m_I\ddot{X}_s \approx& F_{\text{dc}}(X_s)+\frac{-E_0}{m_I\Omega_{\text{rf}}^2\tau_{\text{rf}}}\left(\left.\frac{\partial E_0(x)}{\partial x}\right|_{x=X_s}\right)\int_0^{\tau_{\text{rf}}}\cos^2(\Omega_{\text{rf}}t)\,dt \\
\approx& F_{\text{dc}}(X_s)+\frac{-E_0}{2m_I\Omega_{\text{rf}}^2}\left(\left.\frac{\partial E_0(x)}{\partial x}\right|_{x=X_s}\right).
\end{aligned} \tag{4.55}$$

The secular equation of motion can be expressed in terms of a secular potential energy V_{sec} function

$$\begin{aligned}
m_I\ddot{X}_s &\approx -q\left.\frac{\partial \mathscr{V}_{\text{dc}}(x)}{\partial x}\right|_{x=X_s}+\left.\frac{-q^2}{4m_I\Omega_{\text{rf}}^2}\frac{\partial}{\partial x}\left(\frac{\partial \mathscr{V}_{\text{ac}}(x)}{\partial x}\right)^2\right|_{x=X_s} \\
&\equiv -\frac{\partial V_{\text{sec}}}{\partial x}=-\frac{\partial}{\partial x}(V_{\text{dc}}+V_{\text{sp}}),
\end{aligned} \tag{4.56}$$

where V_{ds} is the potential energy due to the static field and V_{sp} is the potential energy due to the pseudopotential. The pseudopotential energy V_{sp} is proportional to the square of the field amplitude, making it a low-field seeking potential and satisfies the inequality of Eq. (4.48) necessary for trapping.

From Eq. (4.57) and Eq. (4.56) we find that the time average micromotion kinetic energy K_m is equal to the pseudopotential's potential energy

$$\langle K_m\rangle_t = V_{\text{sp}}=\frac{E_0^2(X_s)}{4m_I\Omega_{\text{rf}}^2}. \tag{4.57}$$

4.3.3 UConn's LPT and hybrid trap design

LPT electrical potentials For an ion trap in the linear quadrupole configuration, as seen in Fig. 4.50, the electrical potential near the center of the trap $r = \sqrt{x_1^2 + x_2^2} \ll r_0$ (where $x_i \in \{x, y, z\}$) can be approximated as

$$\begin{aligned}\mathscr{V}(x_i,t) \approx [V_{\rm rf}\cos(\Omega_{\rm rf}t) + V_{\rm rad}\cos(\omega_{\rm rad}t)]\frac{x_1^2 - x_2^2}{r_0^2} + V_{\rm dc}(x_i) \\ + \frac{\eta V_{\rm end}}{z_0^2}\left(x_3^2 - \frac{x_1^2 + x_2^2}{2}\right) + V_{\rm ax}(x_i)\cos(\omega_{\rm ax}t).\end{aligned} \tag{4.58}$$

As shown in Fig. 4.51, the rf/radial (rad) voltages are applied to the four middle segmented electrodes and the end/axial (ax) voltages are applied to the end segmented electrodes. If we ignore the additional perturbing dc ($V_{\rm dc}$) and ac potentials ($V_{\rm rad}$ and $V_{\rm ax}$) discussed and defined in Sec. 4.3.7, we can simplify Eq. (4.58) to[18]

$$\mathscr{V}(x_i,t) \approx \underbrace{V_{\rm rf}\cos(\Omega_{\rm rf}t)\frac{x_1^2 - x_2^2}{r_0^2}}_{\mathscr{V}_{\rm ac}} + \underbrace{\frac{\eta V_{\rm end}}{z_0^2}\left(x_3^2 - \frac{x_1^2 + x_2^2}{2}\right)}_{\mathscr{V}_{\rm dc}}, \tag{4.59}$$

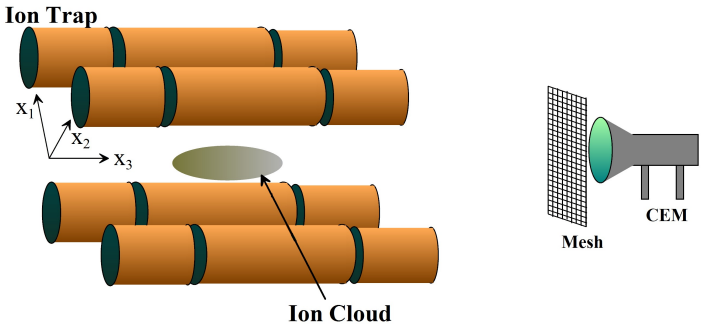

Figure 4.50: Diagram of cloud of trapped ions within the segmented LPT copper electrodes, detection ion optics (electrified mesh), and CEM. The ion optics and CEM are discussed in Sec. 4.3.6. Although the coordinate system is drawn at the end of the trap, the trap's center $x_i = 0$ is in the middle of the ion cloud.

[18] Equation (4.59) is exactly correct for hyperbolic electrodes, but is approximately correct for more easily constructed cylindrical electrodes. In either case the boundary conditions are satisfied.

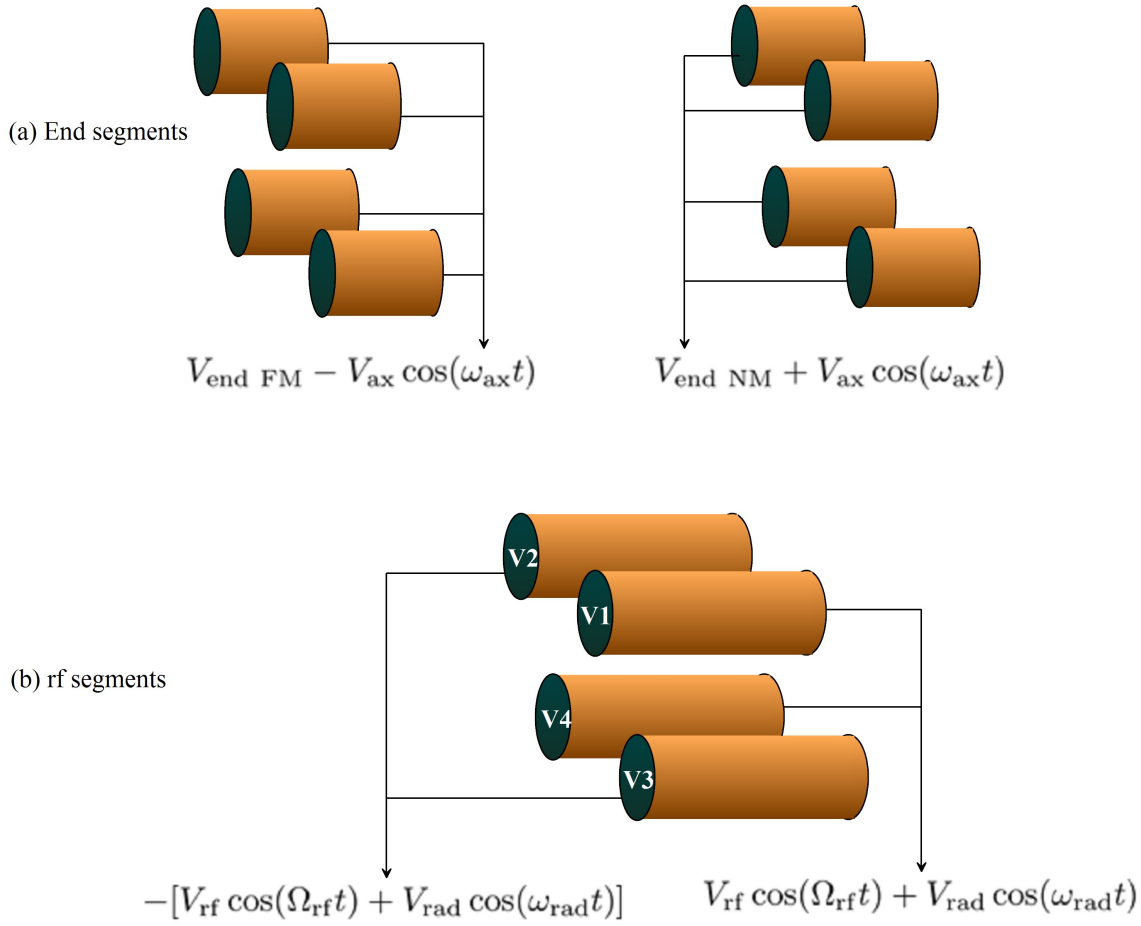

Figure 4.51: Diagram of electrical potentials applied to the LPT segmented electrodes [138]. A detailed discussion of the voltage sources can be seen in Figs. 4.56 and 4.59. The perturbing fields V_{ax} and V_{rad} are discussed in Sec. 4.3.7.

where V_{rf} is the driving field's voltage amplitude relative to ground on each rod and V_{end} is the dc voltage applied to the end segments, sometimes called end caps. The rf voltage provides radial confinement (pseudopotential) and the end voltages provide axial confinement.[19] When trapping, the end segment voltages on both sides of the trap are held at the same electrical potential $V_{\text{end FM}} = V_{\text{end NM}} = V_{\text{end}}$. The subscripts FM and NM refer to far from mesh and near mesh, respectively.

[19]Because the two confinement gradients are typically not equivalent, ion clouds typically form ellipsoidal spatial distributions, as illustrated in Fig. 4.50.

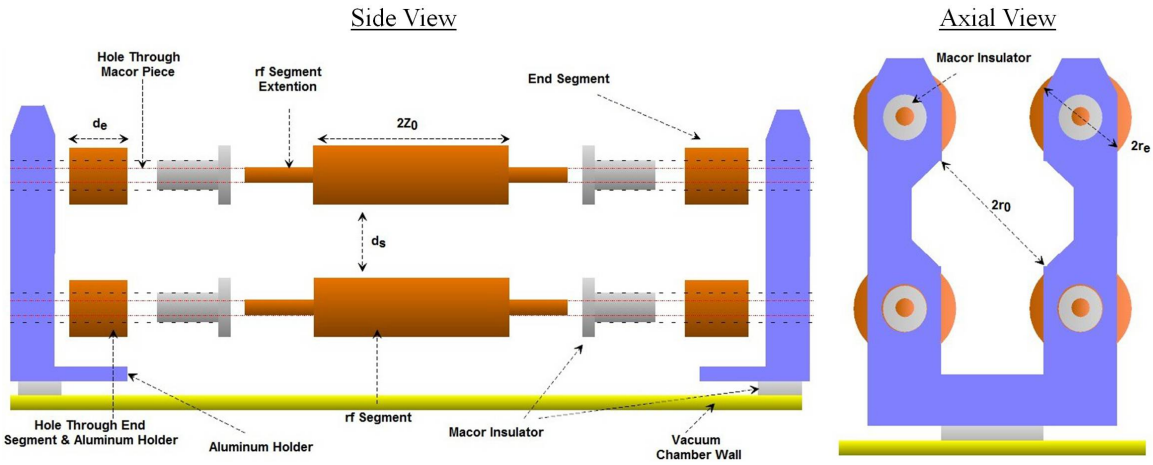

Figure 4.52: Mechanical schematic of disassembled UConn LPT [138]. The blue fixtures at the end are made of aluminum, the white insulating material is macor, and the orange electrodes are OFHC copper. The trap dimension are listed in Table 4.3, and prints for the trap components can be found in Appendix A. An image of the actual LPT is shown in 4.53.

A schematic of the actual segmented ion trap's construction is shown in Fig. 4.52, where the geometric parameters r_0 and z_0 from Eqs. (4.58) and (4.59) are defined. The values of all the relevant geometric parameters are listed in Table 4.3.

When designing the LPT we needed to be mindful of the hybrid nature of the trap, so that the LPT dimensions did not impede the formation of the MOT. Unfortunately, the two traps have competing interests for optimization and can pose constraints on each other's design. First, electrical ground is approximated as being infinitely far away from the LPT

Table 4.3: Table of mechanical dimensions of the LPT.

Dimension	Value (mm)
r_0	9.5
r_e	8.8
d_s	8.5
z_0	24.2
d_e	17.0

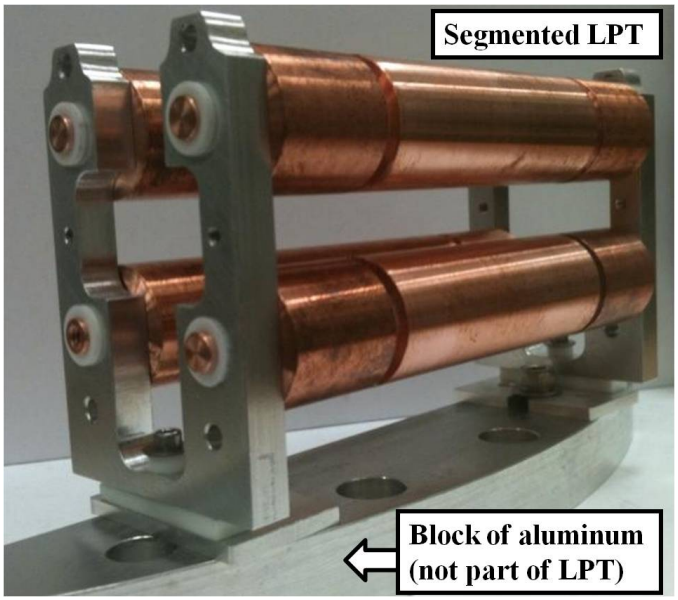

Figure 4.53: Image of the actual fully assembled LPT.

electrodes outside of the trapping region. If ground is too close, image charges can form on grounded surfaces creating contributions from undesirable higher-order multipoles within the trapping region. The UHV chamber is at ground, so the LPT electrodes should not be placed close to the chamber walls. Our current (generation II) trap has a clearance of ≈ 16 mm or about $2r_e$ between the OFHC electrodes and the nearest UHV chamber wall.[20]

Second, for optimal suppression of higher-order multipoles within the trapping region one wants an LPT with an electrode size to spacing ratio of $r_e/r_0 \approx 1.147$, as discussed in Ref. [139]. However, as r_e is increased the optical MOT beam clearance d_s is reduced. Unlike ion trap laser cooling beams, MOT beams are typically much larger $\varnothing \sim 10$ mm, since the capture velocity is proportional to the size of the beam, as seen in Eq. (4.21). We found a happy medium using the dimensions listed in Table 4.3, with a MOT beam clearance of ≈ 8.5 mm and an electrode size to spacing ratio of ≈ 0.93.

[20] A taller chamber would allow for the construction of a larger LPT, which is a possible design improvement.

Our hybrid trap design is similar to E. Hudson's [46] or S. Willitsch's [140] in that the LPT has a large r_0 compared to most conventional LPTs, to allow MOT beam optical axis. The hybrid (magnetically or optical-dipole trapped) ion-BEC traps can use much smaller LPTs since they form their BEC outside of the trap and then transport the condensate into the center of the trap by slowly translating the location of the magnetic or optical-dipole trap minimum [50, 56]. Because our MOT is formed within the trap we do not require transport mechanisms. However, we still have MOT position maneuverability from the electromagnet shim coils. Alternatively, Rangwala's hybrid trap group [61] translates their MOT's position by translating the entire anti-Helmholtz electromagnet coil fixture.

The third design consideration is the ion optics associated with the extraction and detection of ions, which motivated our choice to use a segmented electrode design [141]. We will be discuss this design choice in more detail in Sec. 4.3.6.

The inter-electrode separation $2r_0$ can be approximated as the physical electrode separation of the rf segments, but it is more accurate to determine its value by fitting the trap geometry's simulated electrical potential to Eq. (4.59) at $x_3 = 0$, as was done in Ref. [61]. The simulated potential (left) and the numerically generated fitting results (right) have good agreement and are shown in Fig. 4.54. Evidently, the effective $r_0 \approx 9.6$ mm, which is quite close to the physical dimension listed in Table 4.3.

We were able to numerically model the potential created from our actual electrode geometry using software called SIMION [142].[21] To create the potentials we first input the trap and UHV chamber dimensions into what SIMION calls a geometry file. The software then numerically simulates the trajectories of charged particles within the static and time-varying electric field's produced by the custom electrode geometry. As the charged particles move through the simulation, characteristics such as the particle's trajectory and local

[21] Our SIMION simulations are discussed in greater detail in Sec. 5.2

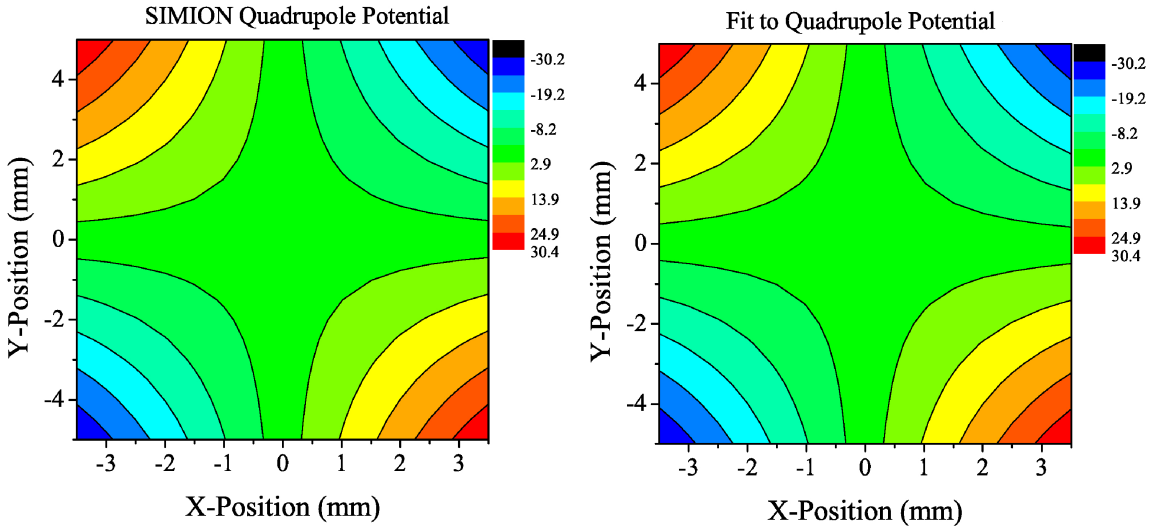

Figure 4.54: The spatial dependence of the radial voltage (V) as modeled using SIMION with our actual electrode geometry (left) and the equivalent potential from Eq. (4.59) with $r_0 \approx 9.6$ mm and $\eta = 0.3$ (right).

electrical potential can be output to file. By simulating multiple particles regularly spaced across the x_1 - x_2 plane at $x_3 = 0$, we outputted the 2D electrical quadrupole potential's spatial dependence, as seen in the left plot of Fig. 4.54.

The geometric factor η can also be determined by fitting the SIMION generated potential along the x_3 axis at $r = 0$. Using the fit to the potential we found $\eta \approx 0.3$, slightly larger than the value 0.1 reported in earlier Refs. [37, 38, 143] by our group. The value of 0.1 had been determined by numerically simulating the axial secular period, which should be insensitive to the ion's kinetic energy (as discussed in Sec. 4.3.4). However, we find that the η parameter changes with ion energy, thus making the earlier method of determination suspect. As can be seen in Fig. 4.55, the axial potential was designed with the end segments too far apart, which leads to a quartic (non-harmonic) spatial dependence on the axial potential.[22] The quartic spatial dependence may explain η's apparent energy

[22]This axial design flaw will be corrected should a generation III trap be constructed. The reasoning behind the end segment spacing was to keep $z_0 \gg r_0$, which is another constraint for LPT design.

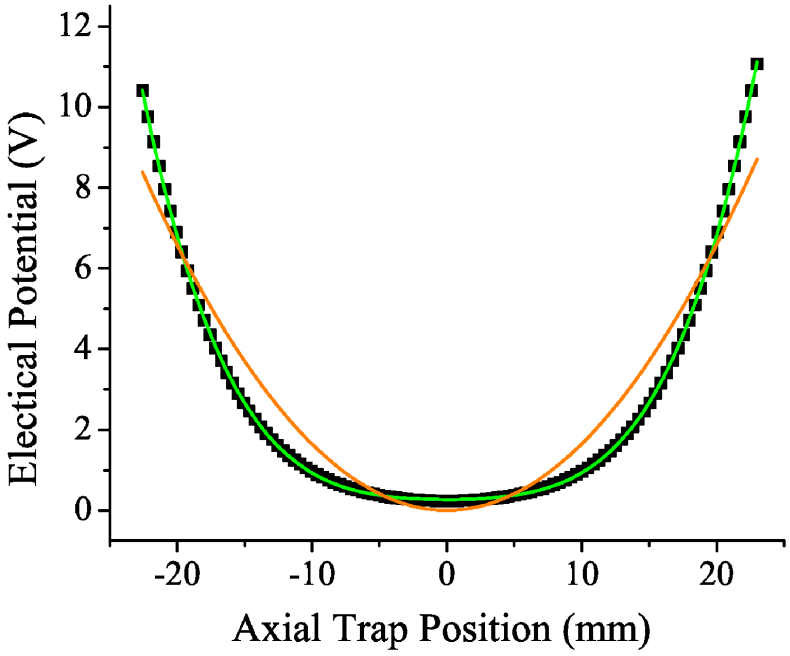

Figure 4.55: The resulting axial voltage as modeled using SIMION with our actual electrode geometry (black squares) and a fit to a Eq. (4.59) with $r = 0$ (orange curve), as well as a fit to a quartic potential (green curve).

dependence. If the ion's energy is low, the ion only experiences the lower flatter part of the axial potential, as opposed to higher energy particles that experience the walls of the quartic potential. Therefore, the effective quadratic potential for low energy ions is wide with a small η and higher energy ions have a narrower effective quadratic potential with a larger effective η.

LPT voltage sources and circuits Here we will briefly discuss the generation of the trapping voltages on the LPT's middle segments used for radial confinement and the generation of voltages on the LPT's end segments used for the axial confinement and ion extraction.

A circuit diagram of the voltage source for the middle segments' electrical potentials is shown in Fig. 4.56 with the values of the electrical components listed in Table 4.4.

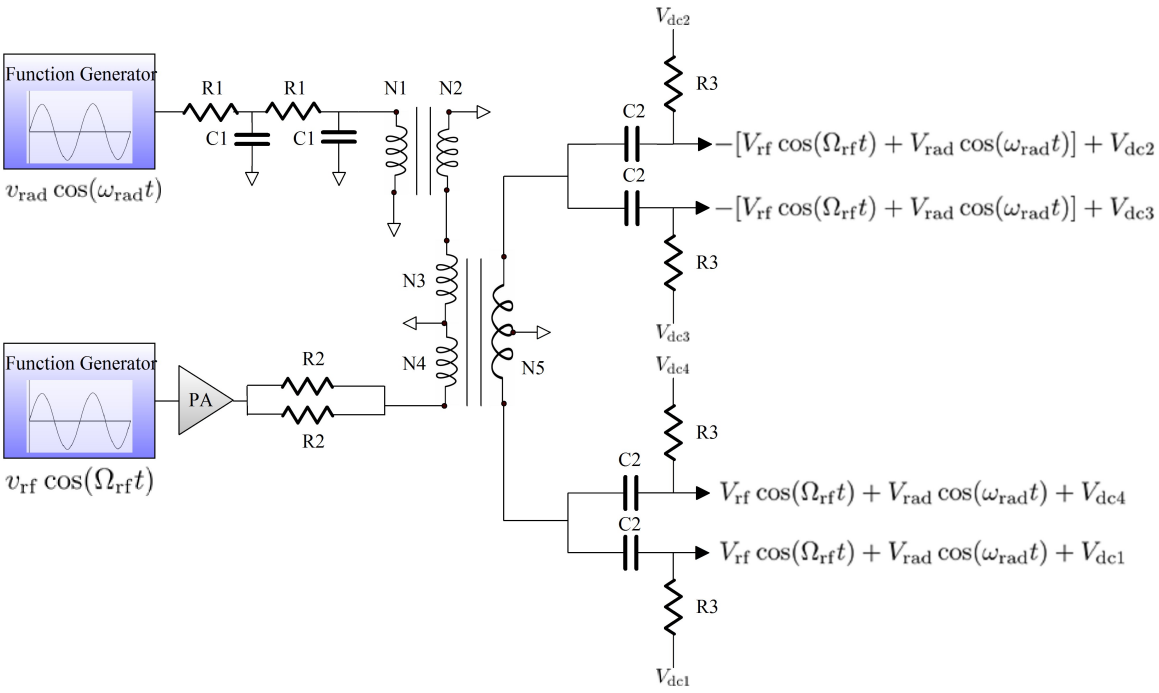

Figure 4.56: Circuit diagrams for the radial potential, the values of the circuit elements are listed in Table 4.4. See text for details.

The output consists of three components: an rf voltage $V_{\mathrm{rf}}\cos(\Omega_{\mathrm{rf}}t)$ used for the electrodynamic quadrupole radial confinement, a small ac perturbation $V_{\mathrm{rad}}\cos(\Omega_{\mathrm{rad}}t)$ used for mass selective resonance quenching (MSRQ) [24, 143–145] discussed in Sec. 4.3.7, and a dc component V_{dc} used to shift the location of the ion cloud, control excess micromotion heating (see Sec. 4.3.8), or shift the ion's secular frequency (see Sec. 4.3.7).

Table 4.4: Table of values for electrical elements in Fig. 4.56.

Resistors		Capacitors		Transformers	
Resistor	Value	Capacitor	Value	Loop	Value
R1	24 Ω	C1	12 nF	N1	37
R2	100 Ω	C2	70 nF	N2	2
R3	2.25 MΩ			N3	1
				N4	2
				N5	25

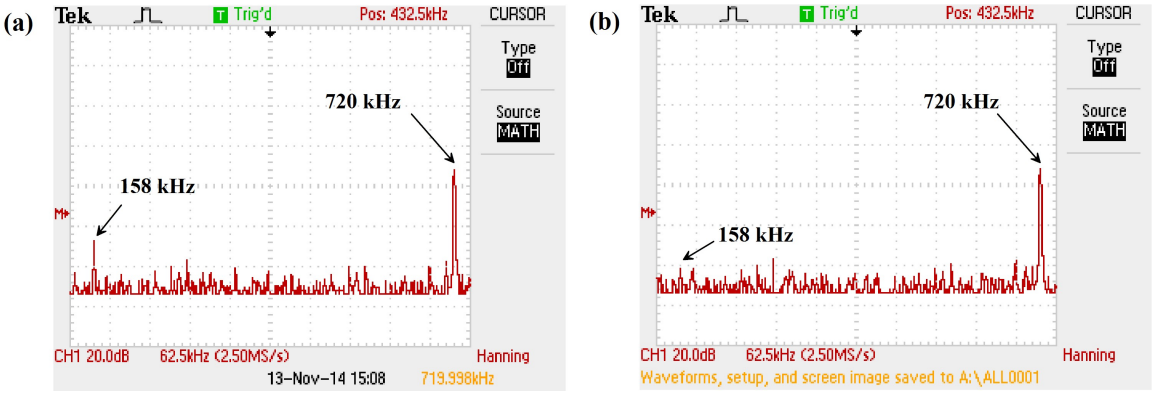

Figure 4.57: Digital oscilloscopes fast-Fourier-transform of one middle electrode segment's electrical potential. The rf driving frequency $\Omega_{\rm rf} = 720$ kHz with $V_{\rm rf} = 160$ V peak-to-peak and the (weak) radial 158 kHz MSRQ signal $V_{\rm rad} = 3$ V peak-to-peak in (a) and $V_{\rm rad} = 1.5$ V peak-to-peak in (b) are seen in the frequency spectrum. MSRQ will be discussed in Sec. 4.3.7.

The rf voltage is created with a function generator that can be modulated on and off. The rf goes through a power amplifier and then through a homebuilt voltage step-up transformer with a high-frequency ferrite toroidal core before reaching the rods. The secondary loop $N5$

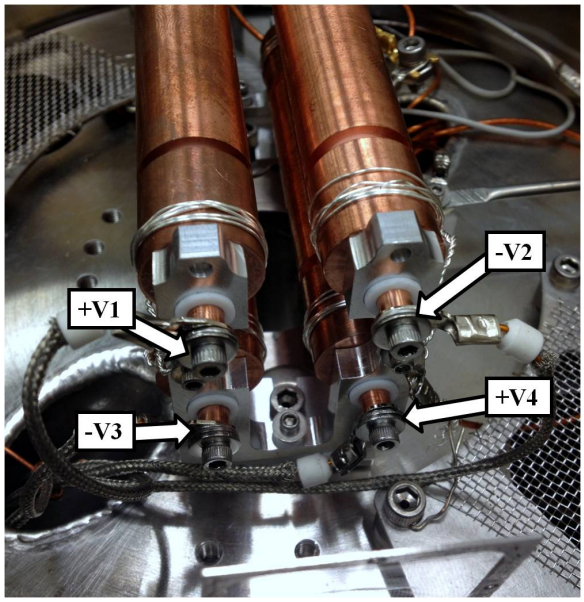

Figure 4.58: Electrical wiring of the four middle LPT electrodes within the UHV chamber.

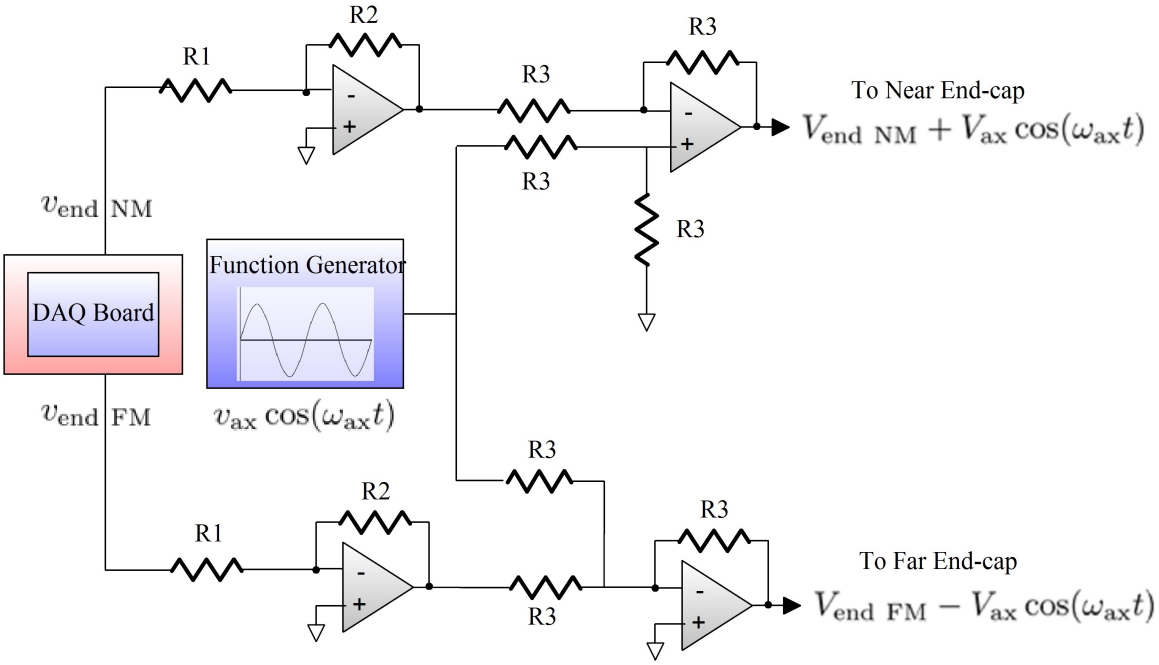

Figure 4.59: Circuit diagrams for the axial potential, the values of the circuit elements are listed in Table 4.5. See text for details.

is center-tapped to ground to ensure a 180° phase difference on the rf waveform between diagonal rod pairs $V1$ - $V4$ and $V2$ - $V3$.

An additional low power radial sinusoidal waveform v_{rad} is generated with another function generator. This signal is fed through a passive low-pass filter[23], goes through a voltage step-down transformer (N1 - N2), and is added to the rf voltage waveform by

Table 4.5: Table of resistances in Fig. 4.59.

Resistance	Value (kΩ)
R1	8.2
R2	39
R3	18

[23]The passive low-pass filter is used to block pickup from the rf voltage back onto the v_{rad} function generator, so as to prevent damage to the function generator.

connecting the secondary coil for the step-down transformer to the primary of the final step-up transformer.[24] By stepping down in voltage we are stepping up in current I_{rad}, which gives a larger final (stepped up) voltage amplitude V_{rad} on the rods. The Fourier transform of one middle segment's resulting waveform is shown in Fig. 4.57.

The four LPT middle segment signals are sent through a BNC feedthrough and pass though coaxial shielded wires within the vacuum chamber. The connection within the vacuum chamber is shown in Fig. 4.58.

The end segment's voltage source circuit diagram is shown in Fig. 4.56 with the values of the electrical components listed in Table 4.5. The NI DAQ board, controlled by the LabVIEW data acquisition program, outputs a separate analog signal for each set of four end segments, near and far from the mesh. Each signal is amplified by a gain factor of ≈ 4.75 with high voltage op-amps OPA445 that have a maximum symmetric voltage range of ± 45. The amplified signal is then summed with an additional low power axial sinusoidal signal[25] with the OPA445 op-amps, such that each set of end segments are 180° out of phase.

Hybrid trap The ion trap is placed in the vacuum chamber as illustrated in Fig. 4.60 and digitally imaged in Fig. 4.32. The MOT is formed concentrically within the center of the LPT and the location of the MOT can be adjusted relative to the center of the LPT with the electromagnet shim coils. We found no measurable evidence that one trap disrupts the operation of the other and both traps can be run simultaneously [38].

[24] The secondary of the step-up transformer $N5$ will pick up the sum of the two primary coils $N3$ and $N4$.
[25] The amplified DAQ signal becomes an offset to the sinusoidal waveform.

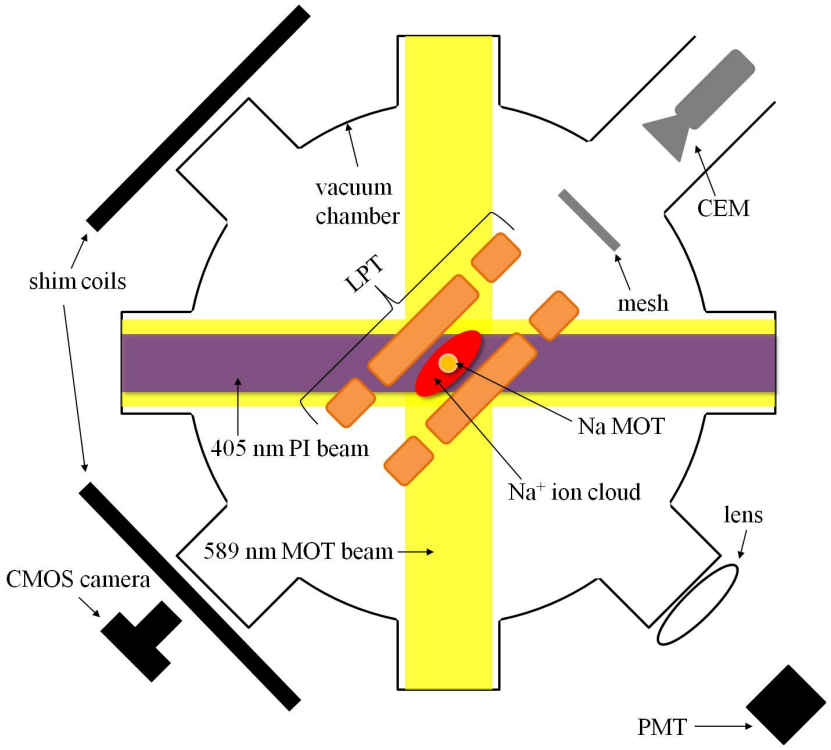

Figure 4.60: The complete hybrid system (not to scale), originally from Ref. [40]. This figure is identical to Fig. 4.33, but with the LPT, PI laser, mesh electrode, and CEM added within the vacuum chamber.

4.3.4 Dynamics of a single trapped ion in an LPT

Having fully explained the LPT design and applied electrode voltages, we will now solve the equation of motion for a single ion held within the LPT's effective secular potential and the physical (ideal quadrupole) LPT electrodynamic potential. In doing so, we will formulate the constraints on the electrical potentials introduced in Sec. 4.3.3 that are required for stable trapping.

LPT secular potential Using Eqs (4.59) and (4.56) within the pseudopotential approximation, we can express the LPT's secular potential energy[26] as

[26]The "center" of the trap is located at the secular potential energy minimum $x_i = 0$, which corresponds to the geometric center of the LPT's electrode configuration.

$$V_{\text{sec}} = \left[\frac{q^2}{m_I \Omega_{\text{rf}}^2}\left(\frac{V_{\text{rf}}^2}{r_0^2}\right) - \frac{\eta q V_{\text{end}}}{2z_0^2}\right] r^2 + \frac{\eta q V_{\text{end}}}{z_0^2} x_3^2. \tag{4.60}$$

We identify the potential energy at the electrode boundaries

$$D_r = \left[\frac{q^2}{m_I \Omega_{\text{rf}}^2}\left(\frac{V_{\text{rf}}^2}{r_0^2}\right) - \frac{\eta q V_{\text{end}}}{2z_0^2}\right] r_0^2 \text{ and } \eta q V_{\text{end}}, \tag{4.61}$$

as the largest possible radial and axial trap depths, respectively [22, 84].

For typical trap settings the trap depths predicted by Eq. (4.61) are very deep ~ 1 eV (or $\sim 10^4$ K), as compared to MOTs, which have depths closer to $\sim 10^{-4}$ ev (or ~ 1 K) [31]. The deep trapping leads to long trapped ion lifetimes [34], making the LPT an ideal apparatus for studying reactions with low reaction rates.

Equation (4.61) applies for a single trapped ion in an ideal trap with no higher-order multipoles. In practice the depth is actually much smaller, so we will think of Eq. (4.61) as an upper bound on the trap depth associated with an upper bound on the ellipsoidal cloud size r_0 and z_0.

We can re-express the pseudopotential energy in Eq. (4.60) in terms of the ion's secular motional frequencies [84, 137, 146] by

$$V_{\text{sec}} = \frac{m_I}{2}\omega_{\text{sp}}^2 r^2 + \frac{m_I}{2}\omega_3^2 x_3^2, \tag{4.62}$$

where the pseudopotential, axial, and radial secular angular frequencies are defined as

$$\begin{aligned} \omega_{\text{sp}} &\equiv \sqrt{2}\frac{qV_{\text{rf}}}{m_I \Omega_{\text{rf}} r_0}, \\ \omega_3 &\equiv \frac{2\eta q V_{\text{end}}}{m_I z_0^2}, \\ \text{and } \omega_1^2 = \omega_2^2 = \omega_r &\equiv \omega_{\text{sp}}^2 - \frac{\omega_3^2}{2}, \end{aligned} \tag{4.63}$$

respectively.

Electrodynamic potential Using Eq. (4.59) we can express the electric field within the idealized trap as

$$\vec{\mathscr{E}} = -\vec{\nabla}\mathscr{V} = \left[\frac{-2V_{\text{rf}}\cos(\Omega_{\text{rf}}t)}{r_0^2} + \frac{\eta V_{\text{end}}}{z_0^2}\right]\{x_1\hat{x}_1 - x_2\hat{x}_2\} - \frac{2\eta V_{\text{end}}}{z_0^2}x_3\hat{x}_3, \tag{4.64}$$

making the force on a single ion

$$\vec{F} = q\vec{\mathscr{E}} - q\left[\frac{-2V_{\text{rf}}\cos(\Omega_{\text{rf}}t)}{r_0^2} + \frac{\eta V_{\text{end}}}{z_0^2}\right]\{x_1\hat{x}_1 - x_2\hat{x}_2\} - \frac{2\eta V_{\text{end}}}{z_0^2}x_3\hat{x}_3. \tag{4.65}$$

Making a change of variable

$$\begin{aligned} \tau &= \frac{\Omega_{\text{rf}}t}{2}, \\ a_1 = a_2 = -\frac{a_3}{2} &= \frac{-4q\eta V_{\text{end}}}{m_I z_0^2 \Omega_{\text{rf}}^2}, \\ \text{and } q_3 = 0,\ \ q_1 = -q_2 = q_r = &= \frac{4qV_{\text{rf}}}{m_I r_0^2 \Omega_{\text{rf}}^2}, \end{aligned} \tag{4.66}$$

where a_i and q_i are known as the "stability parameters," we can re-write Eq. (4.65) in the form of the well known Mathieu equation[27] [102, 148]

$$\frac{d^2x_i}{d\tau^2} + [a_i - 2q_i\cos(2\tau)]x_i = 0. \tag{4.67}$$

The general (series) solution to the Mathieu equation [137] has the form

$$x_i(\tau) = Ae^{i\beta_i\tau}\sum_n C_{2n}e^{i2n\tau} + Be^{-i\beta_i\tau}\sum_n C_{2n}e^{-i2n\tau}, \tag{4.68}$$

where $\beta_i(a_i, q_i)$ is a function of the stability parameters, C_{2n} is the continued fraction [84, 148], and the initial conditions determine A and B.

Stable solutions exist when $0 \leq \beta_i \leq 1$, shown in Fig. 4.61 within the $a_i - q_i$ plane. The

[27] The Mathieu equations comes up in other areas of physics, such as the inverted pendulum problem [147].

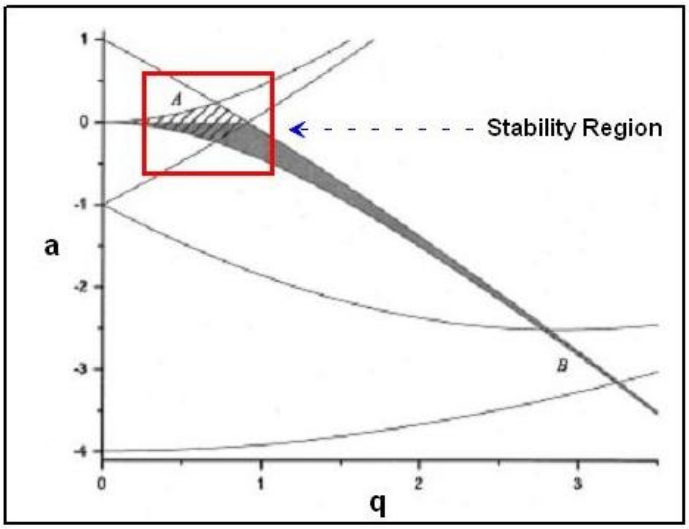

Figure 4.61: Diagram of region of stable solutions from Ref. [141], modified in Ref. [138]. See text for details

stability region constrains the range of allowable values for a_i and q_i, which constrains the possible trap settings, $V_{\rm rf}$, $V_{\rm end}$, $\Omega_{\rm rf}$, for a given trap geometry, according to Eq. (4.66).

Typically, we use trap settings such that $|a_i| \ll 1$ and $q_i^2 \ll 1$,[28] which implies that $\beta \ll 1$. In this limit $\beta_i \approx \sqrt{a_i + q_i^2/2}$. Furthermore, expanding Eq. (4.68) to first order in n [137, 146] and changing back to time t gives

$$x_i(t) \approx X_{0i}\cos(\omega_i t + \phi_{0i})\left[1 + \frac{q_i}{2}\cos(\Omega_{\rm rf} t)\right], \tag{4.69}$$

where the secular amplitude X_{0i} and phase ϕ_{0i} are determined by the ion's initial conditions.

As expected, Eq. (4.69) has a micromotion component oscillating at $\Omega_{\rm rf}$ about the secular amplitude and a slow secular motion oscillating at frequency

$$\omega_i \equiv \frac{\beta_i \Omega_{\rm rf}}{2} \approx \frac{\Omega_{\rm rf}}{2}\sqrt{a_i + \frac{q_i^2}{2}}, \tag{4.70}$$

[28] Our actual trap settings are typically at $a_1 \sim 0.01$ and $q_1^2 \sim 0.1$, so this is a good approximation.

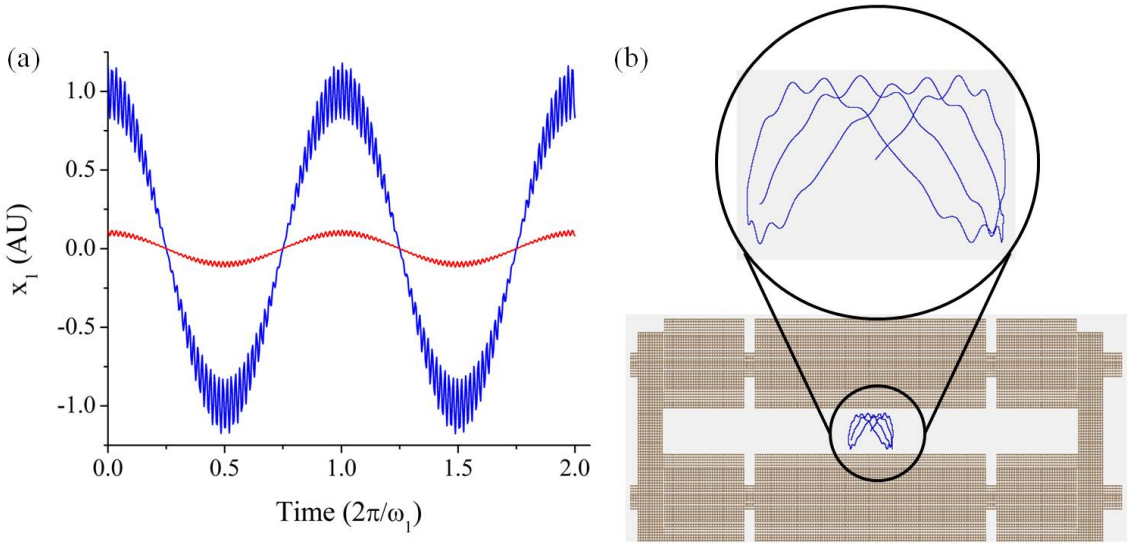

Figure 4.62: Panel (a) shows plot of the x_1 component from Eq. (4.69) with a large secular amplitude (blue) and a small secular amplitude (red). Panel (b) shows SIMION simulated trajectory (blue tracks) of ion motion within our LPT. The plot in (a) and the magnified view of the ion tracks in (b) clearly show the superposition of large secular oscillations and smaller micromotion oscillations

as seen in Fig. 4.62 for the x_1 component [panel (a)] or the SIMION generated trajectory viewed from the side of the trap [panel (b)]. Equation 4.70 is consistent with Eq. (4.63) using the definition of stability parameters from Eq. (4.66).

The ion's kinetic energy averaged over the secular period $2\pi/\omega_r$ in each dimension is

$$\langle E_i \rangle = \frac{1}{2} m_I \langle \dot{x}_i^2 \rangle \approx \frac{m_I X_{0i}^2}{4} \left(\omega_i^2 + \frac{q_i^2 \Omega_{\mathrm{rf}}^2}{8} \right), \tag{4.71}$$

where the first term is associated with the secular motion (thermal) and the second term is associated with the micromotion [146]. Following the treatment of Ref. [146], a dimensional temperature T_i can be assigned to the axial secular, radial secular, and micromotion T_{mi} degrees-of-freedom

$$\begin{aligned} \langle E_3 \rangle &= \frac{k_B T_3}{2} = \frac{k_B T_I}{2} \approx \frac{m X_{03}^2 \omega_3^2}{4}, \\ \text{and } \langle E_1 \rangle = \langle E_2 \rangle &= \frac{k_B T_1}{2} + \frac{k_B T_{m1}}{2} \approx k_B T_I = \frac{m X_{01}^2 \omega_1^2}{2}, \end{aligned} \tag{4.72}$$

respectively. The temperatures are equivalent for each degree-of-freedom $T_i = T_{mi} = T_I$, and the mean energy $\langle E \rangle = \frac{5}{2} k_B T_I$ [149, 150]. In Eq. (4.72), we have used the fact that $q_3 = 0$ and $|a_{i=1,2}| \ll q_{i=1,2}^2$, which implies that the mean micromotion and secular motion kinetic energies are approximately equivalient [146].

Although our analysis was for a single trapped ion, the formula and qualitative conclusions found here can be applied to an ion cloud within the so-called Mathieu regime. In this regime the cloud is typically hot and/or low enough density, such that the coupling parameter

$$\Gamma_c = \frac{q^2}{4\pi\varepsilon_0 a k_B T} \tag{4.73}$$

is much less than unity [137]. Equation (4.73) is a ratio of the nearest-neighbor Coulomb repulsion energy and the thermal energy, where a is the Wigner-Seitz radius related to the mean ion density by $\langle n_I \rangle = (4/3)\pi a^3$.

4.3.5 Loading the LPT

In this section we will describe how the ion trap is loaded and initialized either by photoionization (PI) [151] or electron impact ionization (EI) [152].

Photoionization We create Na^+ ions with a two-step process using a resonant 589 nm photon and a 405 nm photon, $Na + h\nu_{589} + h\nu_{405} \rightarrow Na^+$, as shown in Fig. 4.63. The 589 nm radiation is the same light used in our MOT beams that excites the D2 line transitions for the type I or II MOTs. The 405 nm radiation is superimposed coaxially to one of the MOT beams with a dichroic mirror, as seen in Fig. 4.2.

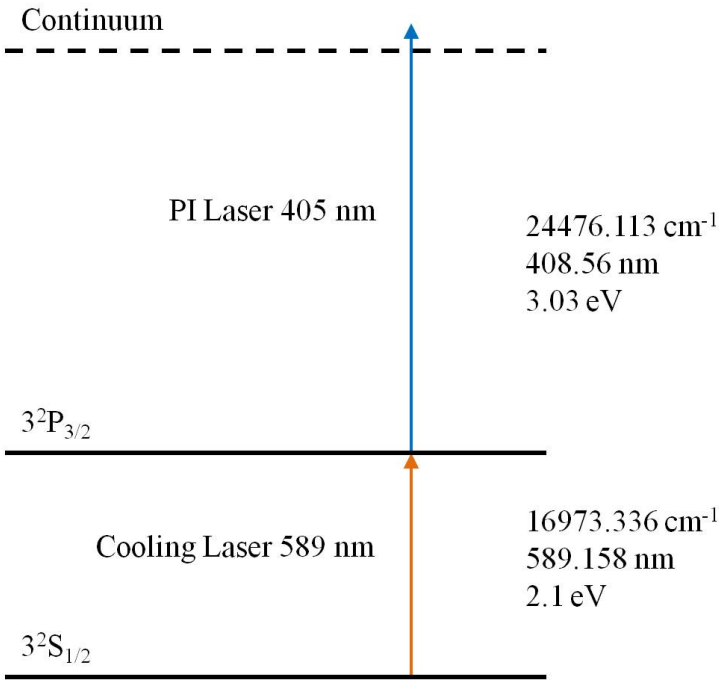

Figure 4.63: Energy level diagram for two-step resonant PI of excited Na^* by a 405 nm photon. Having the laser close to the continuum threshold maximizes the PI cross section [121, 153]

The PI radiation is provided by a diode laser manufactured by RGBLase.[29] The laser can be shuttered on and off with a TTL signal and its output power can be controlled with an analog tuning voltage in the range of $0-5$ V corresponding to $90-0$ mW. The TTL shutter and analog power control allows our LabVIEW data acquisition program to control the PI power and timing during data collection via the NI DAQ hardware. We measure a 2% output power fluctuation and the center wavelength is ≈ 404.45 nm, according to the manufacturer. We do not need to frequency or temperature stabilize the laser, since it is not used for any resonant atomic transitions.

To ensure that the PI beam is larger than the MOT we expand and then re-collimate the beam with a lens pair, as depicted in Fig. 4.2. Like the MOT beams, the intensity of

[29] Thanks to their use in Blu-Ray players, 405 nm diode lasers have become readily available and cheap.

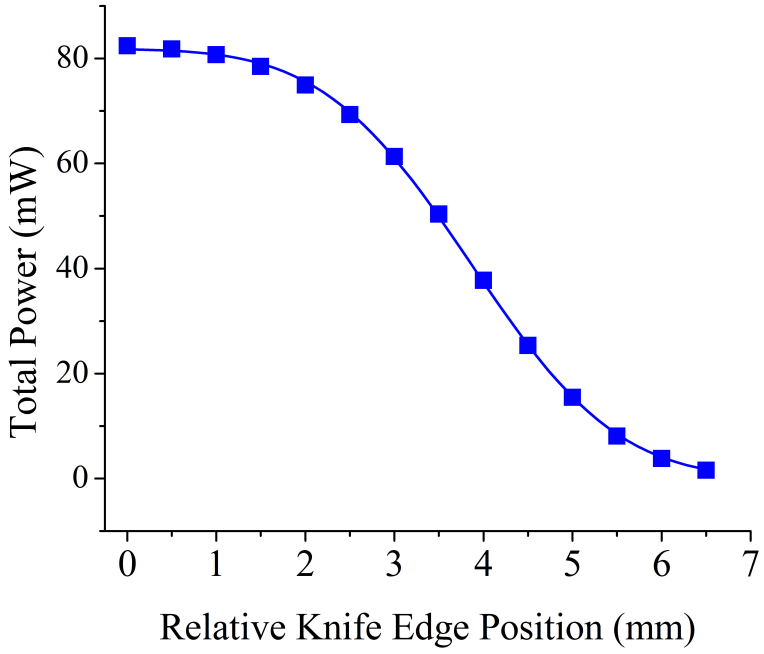

Figure 4.64: The results for a razor-blade test on the 405 nm PI laser after the magnifying telescoping lens pair. The fit to Eq. (4.32) (solid line) predicts a beam size of $r_{x,1/e} \approx r_{y,1/e} = 1.84 \pm 0.02$ mm. The uncertainty in the plot's data is smaller than the plot markers.

the PI beam is measured using power measurements of the PI radiation and razor-blade measurements to establish the beam's $1/e$ intensity radius $r_{1/e}$. Figure 4.64 shows the results of a razor-blade test on the PI laser beam.

We found that the PI beam was circular and has an approximate beam size within the LPT trapping region of $r_{1/e} = 1.9 \pm 0.1$ mm on its first pass and $r'_{1/e} = 2.1 \pm 0.1$ mm on its second (retro-reflected) pass. The total peak PI intensity within the trapping region becomes

$$I_{\text{pi}} = \frac{P_{\text{in}} f_T}{\pi r_{1/e}^2} + \frac{P_{\text{in}} f_T^3 (f'_T)^2 f_R}{\pi (r'_{1/e})^2}, \tag{4.74}$$

where P_{in} is the PI power incident on the first UHV chamber window, $f_T \approx 92\%$ is the fractional transmission of 405 nm radiation, $f'_T \approx 70\%$ is the fractional transmission

through the MOT beam retro-reflection $\lambda/4$ waveplate, and $f_R \approx 80\%$ is the fractional reflectivity of the 405 nm radiation off the MOT beam retro-reflection mirror.

The total rate of PI Na^+ production is

$$R_{\rm pi} = \gamma_{\rm pi} N_a = \gamma_{\rm pi} n_a \pi \langle r_{1/e} \rangle^2 L \tag{4.75}$$

where n_a is the atomic number density, N_a is total number of atoms within the average volume of the PI beam (within the trapping region having length L), and $\gamma_{\rm pi}$ is the PI rate per atom.

When ionizing the excited background gas we can determine the atomic density using the ideal gas law [118]

$$P = n_a k_B T, \tag{4.76}$$

where P is absolute gas pressure. At the previously mentioned background pressure 1×10^{-10} Torr and temperature 346 K, the background gas number density is $\approx 2.7 \times 10^6$ cm^{-3}, according to Eq. (4.76). The ionized background gas density is several orders of magnitude smaller than the MOT densities $\sim 10^{10}$ cm^{-3} and the MOT is always smaller than and completely overlapped by the PI beam. Thus, when photoionizing the MOT we can always approximate N_a as being the total number of MOT atoms.

At low enough PI intensity $I_{\rm pi}$, the PI loss rate $\gamma_{\rm pi}$ is linearly proportional to $I_{\rm pi}$ and can be expressed as

$$\gamma_{\rm pi} = \frac{\sigma_{\rm pi} \hat{\rho}_{22} I_{\rm pi}}{h \nu_{\rm pi}} \equiv \xi I_{\rm pi}, \tag{4.77}$$

where $\sigma_{\rm pi}$ is the PI cross section, h is Plank's constant, and $\nu_{\rm pi}$ is the frequency of the PI radiation, and again $\hat{\rho}_{22}$ is the fraction of MOT atoms in the excited state [40, 62, 121, 135].

Figure 4.65 shows the Na type I MOT fluorescence fit to Eq. (4.43) for two different loss rates γ_t. The total loss rate depends upon the loss mechanisms that are present at the

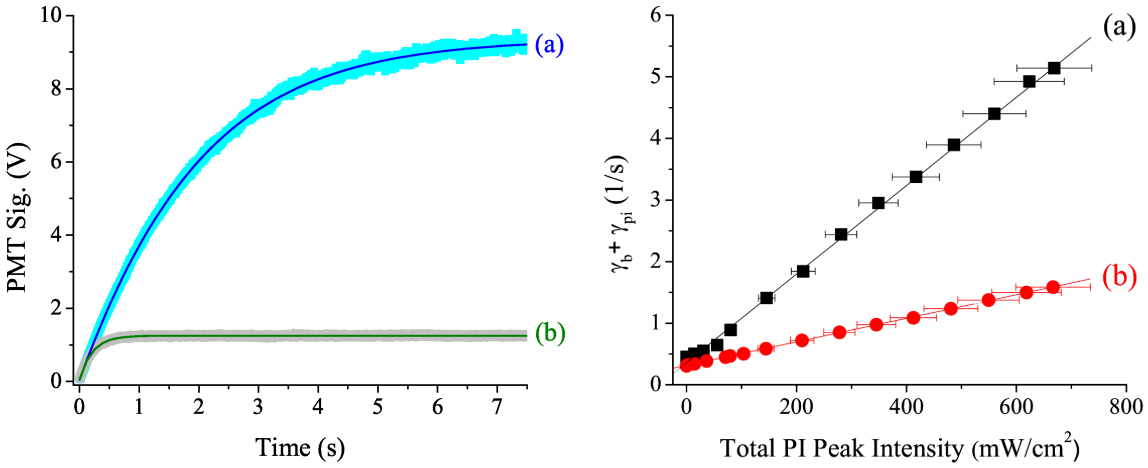

Figure 4.65: Left panel shows the PMT fluorescence signal of type I MOT loading (a) without PI and (b) with PI $I_{pi} \approx 560$ mW/cm^2 and corresponding fits to Eq. (4.43). Right panel, originally from Ref. [40], shows a plot of the total MOT loss rate in the presence of PI ($\gamma_t = \gamma_b + \gamma_{pi}$) as a function of the total peak PI intensity and corresponding linear fits. Curve (a) shows type I MOT data and curve (b) shows type II MOT data. The statistical uncertainty in the rates are smaller than the plot markers. The uncertainty in the intensity is primarily due to the propagated error [154] from the power fluctuations and the precision of the beam waist measurement.

time the MOT is loaded, as discussed in Sec. 4.2.5. The left panel in Fig. 4.65 curve (a) is for an isolated MOT loaded from background Na vapor, where $\gamma_t = \gamma_b$. When the MOT is exposed to the PI radiation, there is an additional atom loss rate γ_{pi}, which increases the total atomic loss rate to $\gamma_t = \gamma_b + \gamma_{pi}$. As predicted by Eqs. (4.43) and (4.45), the PI loaded MOT has a faster time constant and lower steady-state population, as seen by comparing the left panel curves (a) and (b) in Fig. 4.65.

By taking several measurements at different PI laser powers, we found that the directly measured γ_t is linearly proportional with I_{pi} for both MOTs over the full PI intensity range achieved with our setup, as shown in the right panel of Fig. 4.65 from Ref [40]. The y-intercept (at $I_{pi} = 0$) of Fig. 4.65 is equal to γ_b, while the slope can be used to determine $\xi \propto \sigma_{pi}$. The slope of curve (a) for the type I MOT gives $\sigma_{pi} = 1.1 \pm 0.2 \times 10^{-17}$ cm^2 and the

slope of curve (b) for the type II MOT gives $\sigma_{\text{pi}} = 4.1 \pm 0.9 \times 10^{-18}$ cm^2. Both results are fairly close to the previously reported experimental value of $\sigma_{\text{pi}} = 9.1 \pm 1.4 \times 10^{-18}$ cm^2 for 404 nm PI radiation from Ref. [121], which also had very good agreement with theory [153].

Electron impact ionization For the experiment discussed in Sec. 6.1, we load Ca^+ ions via EI rather than PI. An electron beam is generated by applying a current through a tungsten filament. The current in the filament causes resistive heating which results in thermionic emission of electrons. The emitted electrons pass through the gun's ion optics (einzel lens and deflector plates) that collimate and steer the electron beam [155], as seen in Fig. 4.66. The electrons then pass through an opening in the trap electrodes and scatter off the background Ca gas ionizing it. The electron gun electrical feedthourgh is illustrated in Fig. 4.67, and typical voltage settings are listed in Table 4.6.

The electron energy within the beam (in eV units) is equivalent to the center potential on the tungsten filament V_{fil} relative to ground. The filament current power supply is bridged

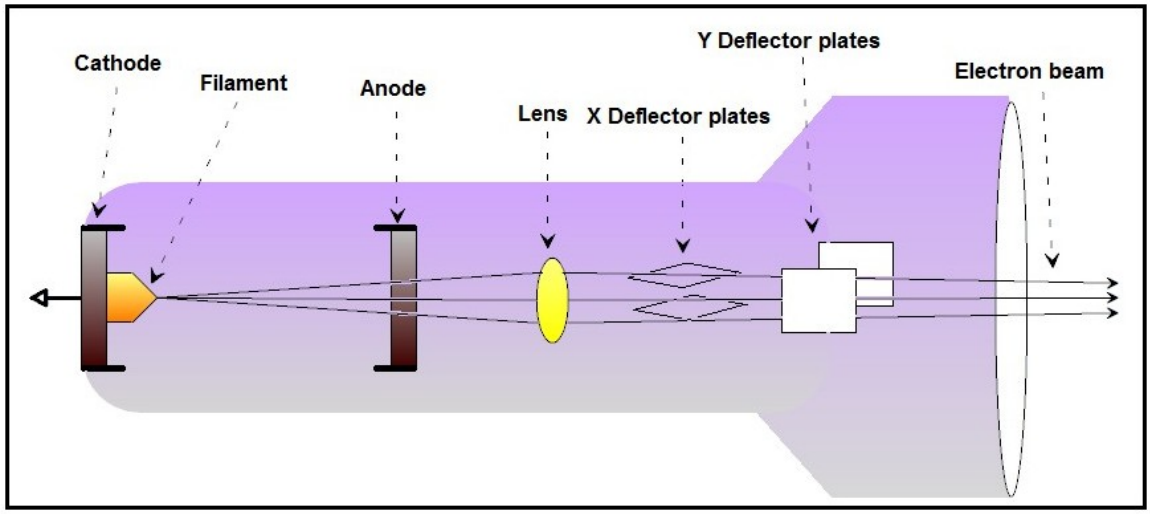

Figure 4.66: Schematic of electron gun ion optics from [138].

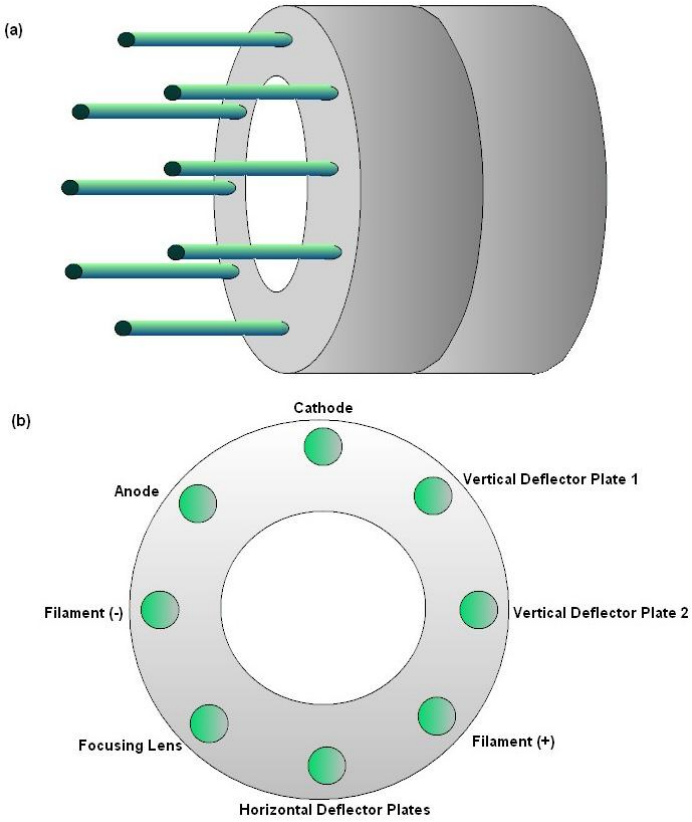

Figure 4.67: Illustration of UHV chamber electrical feedthrough for the electron gun from [138].

Table 4.6: Table of typical electron gun settings.

Parameter	Value (oriented axially)	Value (oriented radially)
Filament current I_{fil}	4 A	4 A
Filament voltage V_{fil}	-66 V	-530 V
Anode	0 V	-457 V
Cathode	-55 V	-516 V
Focusing einzel lens	1250 V	1700 V
Horizontal deflection plate	0 V	35 V
Vertical deflection plate	0 V	10 V

with two resistors so the filament center voltage V_{fil} is held by separate supply [138], as seen Fig. 4.68 (a).

Paraphrasing Ref. [138], to determine the initial electron gun potentials, an Ampere Keithley 602 meter capable of measuring very low currents is used to measure the electrons current at the anode. The cathode voltage and V_{fil} are adjusted to maximize current to the anode. The remaining electron gun ion optic potentials are determined by running the LPT and maximizing the trapped ion signal. A circuit built with PNP transistors shown in Fig. 4.68 (b), is used to pulse the filament voltage between ground (off) and the desired negative voltage (on) using the same TTL signal that can alternatively be used to turn on and off the PI laser.

The electron gun has two major drawbacks – indiscriminate ionization and lack of LPT penetration. Unlike PI, the electron beam will indiscriminately ionize all the background Na and Ca getter produced gas, as well as small but measurable quantities of of background CO, CO_2, N_2, and H_2O, present due to the high but imperfect vacuum within the UHV chamber. Although the electron energy can be controlled by changing V_{fil}, the ionization cross sections of all the background gases mentioned are still fairly sizable near the minimum required for the electron beam to penetrate the trapping fields, ionizing the gas within the trapping region.

When the electron gun is oriented along the trap's x_3 axis (axially oriented) the electron beam has little trouble penetrating the end segments' field $V_{\text{end}} \sim 10$ V, resulting in efficient indiscriminate ionization. For the results presented in Sec. 6.1 the electron gun is oriented with the beam pointing down the x_3 axis.

However, in future experiments we would like to laser cool Ca^+, as discussed in Sec. 4.3.9. Ideally, we would send the ion laser cooling beams down the x_3 axis of the LPT, as illustrated in Fig. 4.2. Therefore, we recently tried orienting the electron gun normal to the side of the LPT (radially oriented). Unfortunately, we found that very few electrons could penetrate the radial trapping fields, unless the rf voltage amplitude was

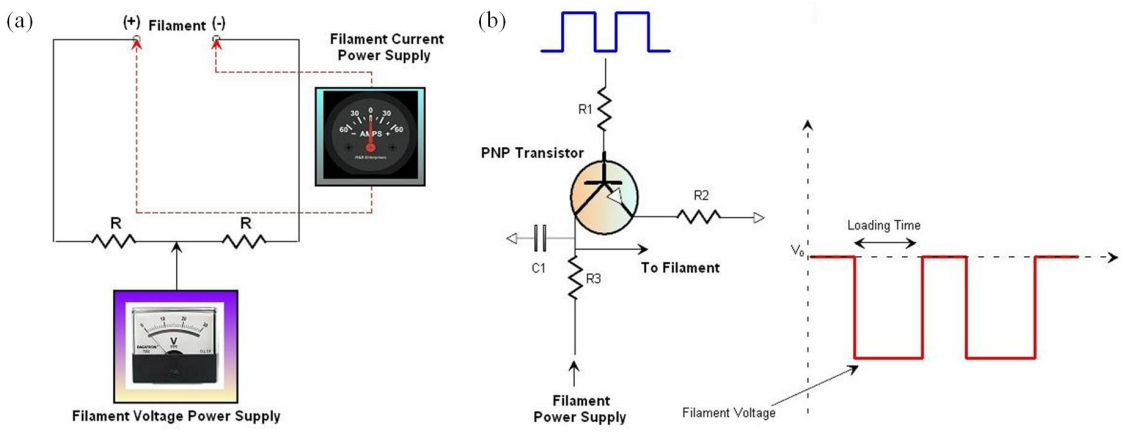

Figure 4.68: Panel (a) shows the schematic of filament current and voltage power supplies and panel (b) shows the pulsing V_{fil} circuit. This is a modified version of two figures from [138].

greatly reduced $V_{\text{rf}} \approx 20$ V compared to our typical operating voltages in the range of $30-80$ V. Even at low V_{rf} amplitude, many of the electrons are deflected and hit the middle electrodes producing a large copper ion signal and inefficiently ionizing the background Ca gas.

A better way to ionize Ca^+ would be to use a two-step PI process similar to the ionization of Na^+. A practical ionization scheme that uses diode lasers would be to resonantly exciting the 423 nm $4S_0 \rightarrow 4P_1$ transition in Ca and then ionize the excited atom with a second 390 nm PI photon. Hopefully, we will implement this PI scheme for Ca^+ in the near future.

Initial ion temperature Both PI and EI result in negligible recoil on the subsequently ionized atom, so the ion's initial kinetic energy is approximately equivalent to the neutral atom's kinetic energy. Therefore, knowledge of the MOT (~ 1 mK) or neutral background atomic temperature (~ 100 K) immediately gives the creation $t = 0$ s temperature of the ion

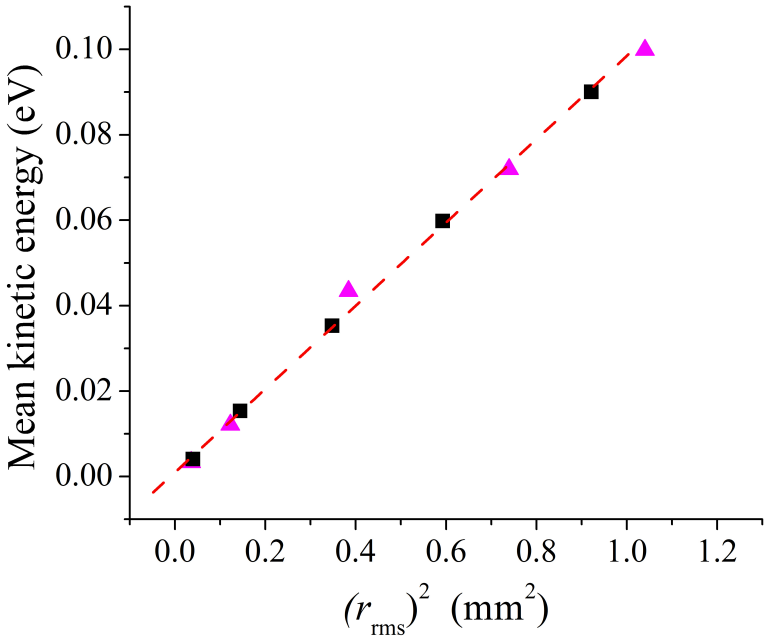

Figure 4.69: The average kinetic energy (after one axial secular oscillation) of a Na^+ ion cloud vs. r_{rms}^2 of the MOT from which Na^+ ions are created at $t = 0$ s. Magenta triangles are for $N_I = 10$ and black circles are for $N_I = 100$. The initial kinetic energy of the ion cloud after two secular oscillations is almost entirely dependent on the initial spatial extent of the loading regions and not the cloud's $t = 0$ s creation temperature $T = 70$ μK or 10^{-8} eV. The mean energy is only approximately quadratically dependent on the 3D position, since the LPT secular potential is cylindrically symmetric and not spherically symmetric.

cloud. However, the *creation* temperature of the cloud is fairly meaningless, since the ions are created within the pseudopotential. The presence of the pseudopotential means that the cloud's mean kinetic energy at the moment of creation is only a small fraction of its total energy given the modest creation temperatures considered here. A more meaningful definition of the ion cloud's *initial* temperature is the mean kinetic energy time-averaged over the first secular period.

Paraphrasing Ref. [37], our SIMION simulations showed that when ionizing from the MOT, the mean (time-averaged over one secular period) kinetic energy is highly sensitive to the initial size of the MOT cloud and not the velocity of the MOT atoms, as seen in

Fig. 4.69. In the SIMION simulation the mean time-averaged kinetic energy of the ion cloud containing N_I ions each with mass m_I is defined as the nested loop

$$\langle E_T \rangle = \sum_{s=1}^{S_0} \sum_{i=1}^{N_I} \frac{m_I v_{I,(i,s)}^2}{2 S_0 N_I}, \tag{4.78}$$

where the index i refers to the ith ion, the index s refers to the sth SIMION time step $\Delta t \ll 2\pi/\Omega_{\rm rf}$, and $v_{I,(i,s)}$ is the simulated speed of the ith ion at time-step s. The kinetic energy is averaged over a user specified time interval, e.g., for one axial secular period $S_0 \Delta t = 2\pi/\omega_a$. Similarly, the time-averaged root mean-squared position is defined by the nested loop

$$\langle r_{\rm rms} \rangle = \sum_{s=1}^{S_0} \frac{\sqrt{\sum_{i=1}^{N_I} \frac{r_{(i,s)}^2}{N_I}}}{S_0}, \tag{4.79}$$

where $r_{(i,s)}$ is the 3D position of the ith ion on time step s relative to the center of the LPT.

The total energy of an ion at the moment it is born is primarily determined by its large potential energy due to its pre-ionization position relative to the trap's center, not its negligible kinetic energy determined by its pre-ionization neutral atom velocity. Therefore, the size of either the MOT or ionization beam (whichever is smallest) is what primarily determines the time averaged energy of an ion cloud after one secular oscillation. In Ref. [37] we concluded that ions created directly from a MOT inside a Paul trap will not have cold initial time-averaged translational energy, despite the cold creation temperature. Therefore, ionizing from a cold neutral source that spatially extends beyond the trap's nodal line does not automatically yield a translationally cold source of ions. Reference [61] draws a similar conclusion.

The same is true for ions created from the background gas. Although background gas

atoms have greater creation temperatures, they also typically have even larger cylindrical creation spatial distributions, the size of which are determined by the size of the PI laser beam or election beam. Again, the cloud's mean creation potential energy is approximately the cloud's total creation energy, which is proportional to the cloud's initial time-averaged kinetic energy.

In the MOT-loaded experiment presented in Sec. 6.2, we take advantage of the correlation between MOT size and initial ion cloud temperature in that we determine the initial ion cloud temperature via SIMION simulation rather than through direct experimentation. This is because dark Na^+ ion thermometry is experimentally challenging, but determining the size of the bright Na MOT is easy with our current setup.

4.3.6 Detection of ions

Once the trap is loaded, detecting the ion population is a necessary aspect of any subsequent measurement. Figure 4.70 shows a schematic of the timing sequence for LPT loading, trapping, extraction, and ion detection, while operating the LPT without a MOT.

To detect the ion population we employ a destructive method rather than an optical laser induced fluorescence method [156]. The Na^+ ions are optically dark due to the closed shell structure seen in Fig. 3.2, making optical detection impossible. Although we plan to optically excite Ca^+ ions in the future, we currently just use ground state Ca^+ and destructive detection must suffice. In short, the destructive method involves forcing the ions out of the trap so that they strike a HV Channeltron electron multiplier (CEM) creating a detectable current proportional to the number of ions that had been trapped. A picture of the CEM is shown in the right panel of Fig. 4.71

To extract the ions out of the trap for detection, the end segment voltages are changed to an extraction voltage configuration, as seen in Fig. 4.70. The configuration currently used

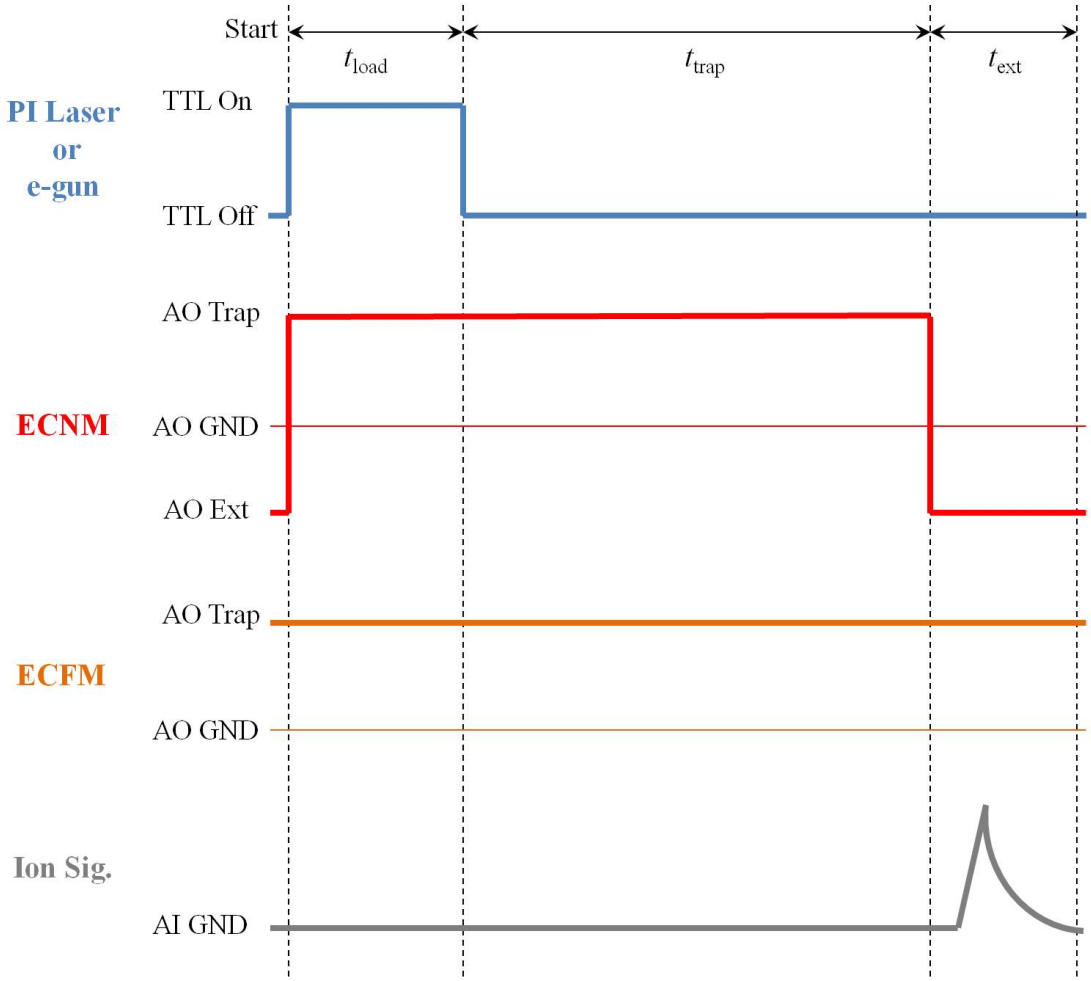

Figure 4.70: Schematic for LabVIEW controlled timing and voltage of the LPT loading, trapping, extraction, and detection of ions. The ions are loaded via PI or EI with a TTL pulse for loading time t_{load}. The ions are trapped for a time t_{trap} and then extracted for a time t_{ext}. To extract the ions the dipole field is created by lowering the potential of the end cap near the mesh (ECNM). Finally, the ions hit the CEM producing an output signal.

with our second generation trap and most recent ion optic geometry keeps $V_{\text{end, FM}}$ at 30 V, which is also the trapping FM end segment voltage. However, the opposite end segment goes from $V_{\text{end, FM}} = 30$V to -20 V, creating a dipole field that launches the ions axially out the trap along x_3 toward the electrified mesh and Channeltron electron multiplier

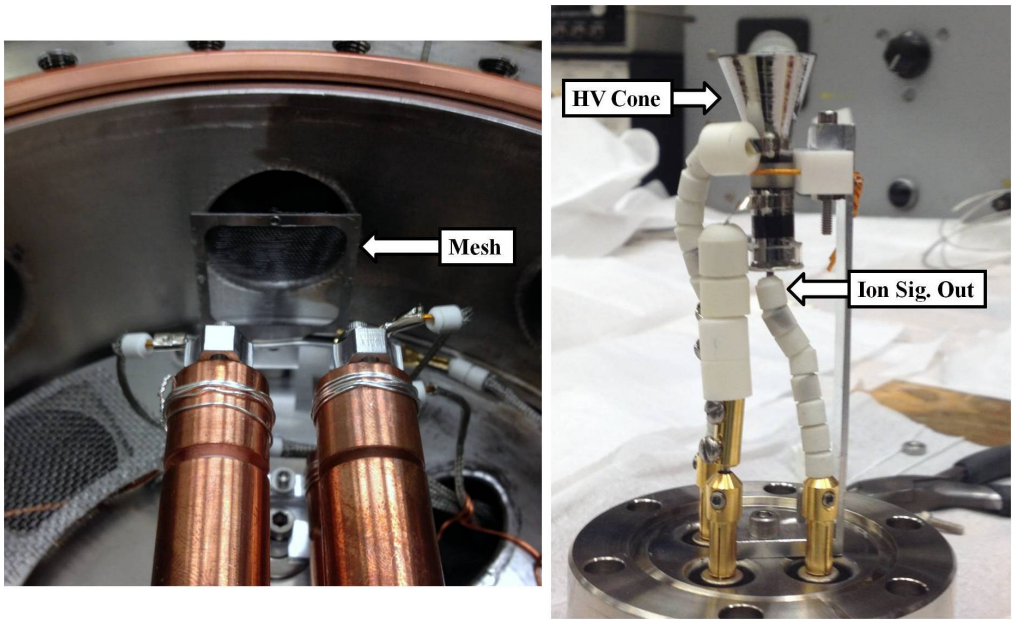

Figure 4.71: Digital image of mesh within UHV chamber (left) and CEM mounted on electrical feedthrough port before being placed into the UHV chamber (right).

(CEM) detector.[30] The ions pass through the mesh (mounted on a wire frame) with 83% transmission and then strike the CEM's HV cone. A picture of the mesh is shown in the left panel of Fig. 4.71. The ion pulse incident on the CEM is amplified by the CEM and a pre-amplifier, where the resulting current measurement becomes an analog voltage measurement that is read out by our NI DAQ board and recorded to file using our LabVIEW data acquisition program. An illustration of the mesh and CEM's position relative to the LPT is shown in Figs. 4.50 and 4.60.

To increase extraction efficiency, the second generation LPT was redesigned with a segmented trap style in lieu of the first generation's end tube style. The segmented design has greater ion-extraction clearance resulting in a larger fraction of ions reaching the CEM, as seen in the SIMION rendered models of the first (left) and second (right) generation traps in Fig. 4.72

[30]The ion signal is not overly sensitive to choice in end segment voltages, $V_{\text{end, NM}}$ need only be negative.

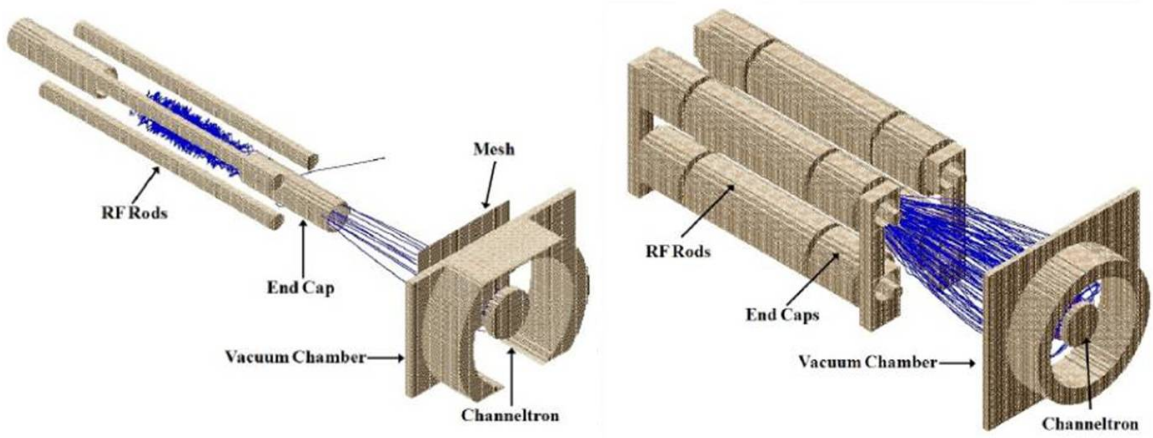

Figure 4.72: Isometric rendering using SIMION, of the ion trajectories (blue tracks) during extraction. With our original trap design (left) only a few ions reach the CEM detector. Using the new trap (right) 100% of the initially small cloud (with a 1 mm radius) trapped ions reach the CEM. The mesh is not shown in right panel.

After the ions leave the LPT they pass through an electrified mesh. The mesh shields the LPT trapping region from the high voltage fields on the CEM. The mesh also helps the CEM detector yield a more uniform ion signal response over the entirety of its detecting cone, as seen in Fig. 4.73. Mesh voltage settings used are typically in the -1 to -10 V range. Our earlier experiments discussed in Secs. 5.3.4 and 6.1 use a mesh setting of -10 V, which maximized the ion signal [38, 39, 138]. However, in later experiment we found that a mesh setting of -1 V yielded a somewhat smaller, but more linearly responsive ion signal. The details of that realization will be discussed in Sec. 6.2.

To test the robustness of our ion extraction system we increased the SIMION simulated initial cloud size to $\varnothing = 10$ mm, allowed the ions to evolve within the trap for several secular periods and then extracted the ions. A screen shot of the simulated ion tracks is shown in Fig. 4.74. Even with the unusually large ion cloud[31] we found that 95% of the ions impact the CEM cone, which suggests excellent extraction efficiency.[32]

[31]The maximum ion cloud size for our LPT is only about a 2 mm radius, as discussed in Sec. 6.2.5.
[32]In the SIMION simulations the mesh is assumed to be an ideal mesh with 100% transmission.

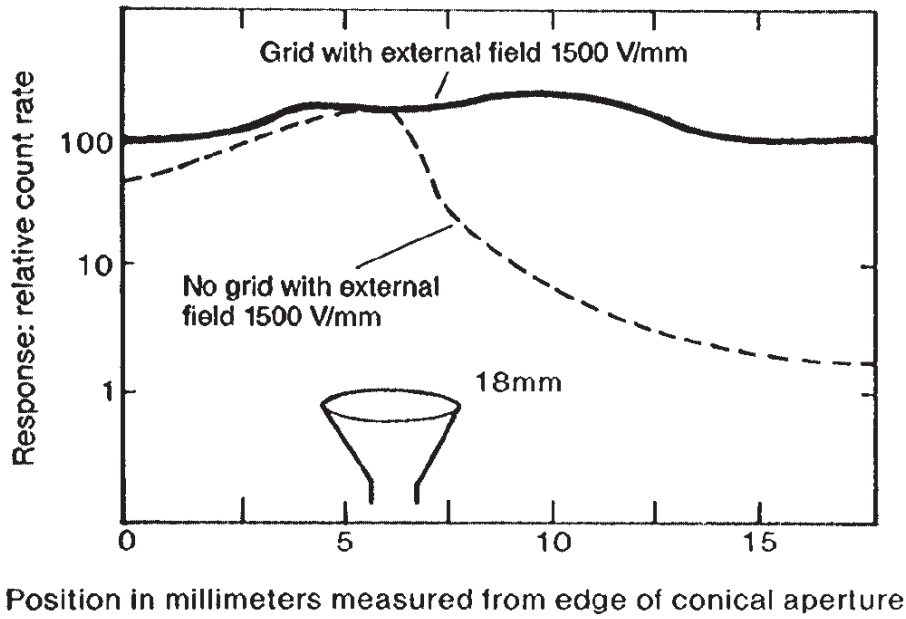

Figure 4.73: Originally from Ref. [157], plot showing that an electrified mesh placed in front of a CEM reduces ion impact position sensitivity yielding a more uniform response.

We can also use the SIMION simulation to establish the extraction timing and width of the detected ion pulse. Figure 4.75 shows a histogram of 200 simulated Na^+ ions striking the CEM. We find that it takes about 64 μs for the ion cloud to reach the CEM and the pulse width is about 8 μs wide.

Our group uses an analog CEM 4230 MEGASPIRALTRON manufactured by Photonis USA, Inc. The CEM HV detection cone has a $\varnothing = 13.5$ mm detection aperture held at a HV in the range of V_c = -1100 to -2500 V.

For each ion that strikes the CEM HV cone, 2 to 3 secondary electrons are produced [157]. The electrons are attracted to the opposite end of the channel due to the bias voltage between the cone and ground V_c. As they propagate down the channel they scatter off the semiconductor-coated glass channel walls, with resistance R_{CEM} creating additional electrons, as depicted in Fig. 4.76.

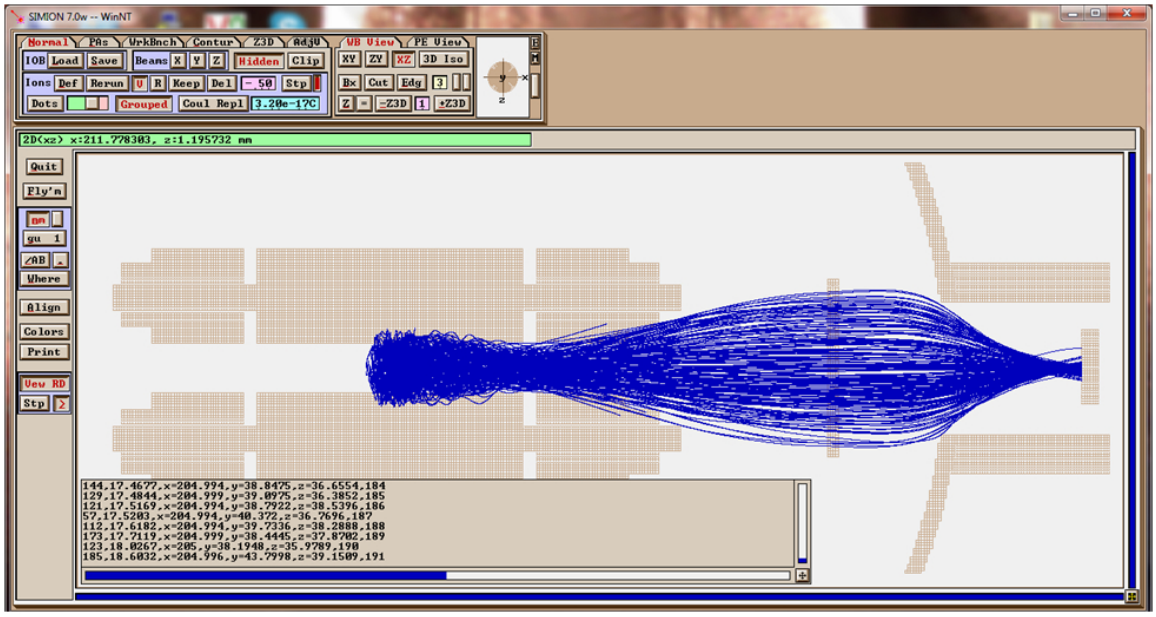

Figure 4.74: Top view of SIMION simulated ion extraction showing 95% of the 200 ions initialized in a sphere with a 5 mm radius extracted after being trapped for one secular period.

The HV power supply for the cone draws a bias current $I_b = V_c/R_{\text{CEM}}$. The output electron signal current I_o is proportional to the input ion current by the amplification gain factor G in

$$I_o = I_i G \propto I_i \times 10^{|V_c/V_0|}, \tag{4.80}$$

where V_0 is the cone voltage for which $G = 10$. As far as most CEMs go, the MEGASPIRALTRON has a particularly large $I_b \approx 160$ μA at $V_c =$ -2500 V with a gain of $G \approx 10^7$. The large bias current is helpful for measuring large ion populations, since the dynamic linear range of most analog CEMs ends once the output current $I_o > 20\%$ of the bias current I_b [40, 157]. When the output current is too high it saturates the CEM and Eq. (4.80) is no longer valid.

For experiments like the one discussed in Sec. 6.2 where we use a large ion population, $\sim 10^6$ ions, we operate at a low cone voltage $V_c =$ -1250 V, which reduces the gain ex-

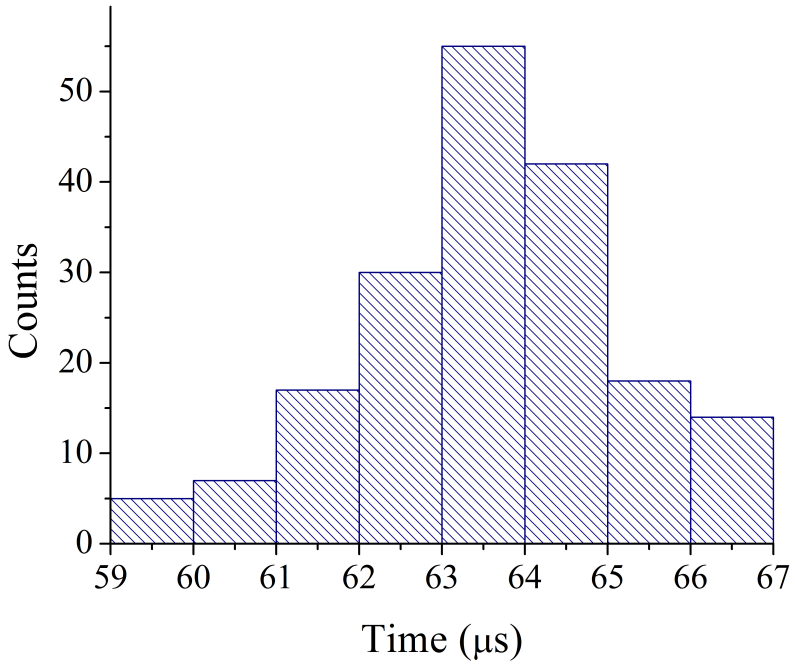

Figure 4.75: Simulated TOF histogram for ions striking the CEM.

ponentially while reducing the bias current linearly. Because the bias current is reduced more slowly than the output current, we can find a range of HV settings where $I_o < 0.2I_b$.

We measured the LPT saturated output ion signal for a fixed I_i as a function of V_c. We found that the log of the ion signal was linear with V_c within the experimental uncertainty,

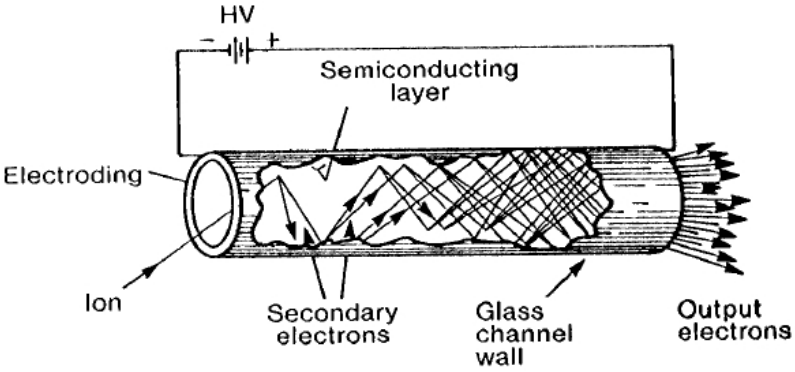

Figure 4.76: Diagram of basic operation of CEM originally from [157]. Incident ion signal is amplified yielding a large output current.

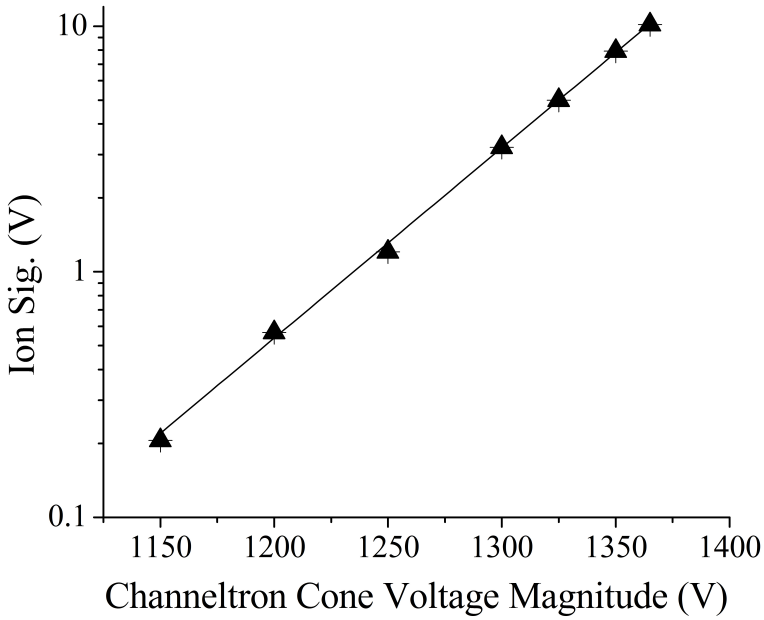

Figure 4.77: We tested for deviation from the expected exponential behavior of Eq. (4.80) at a fixed ion input current. We find that the output ion signal (which is proportional to the gain) looks linear when plotted with a log-linear plot scaling, indicating that we are not saturating the CEM. The uncertainty in the magnitude of the power supply voltage $|V_c|$ and the ion signal is approximately the size of the plot markers.

which suggests that we can operate in a range where the CEM is not saturating, as seen in Fig. 4.77. We repeated this test at several PI intensities, loading the LPT from both MOTs, and at several different ion optic settings. In all cases we found no evidence of CEM saturation [40].

A back-of-the-envelope calculation of the CEM output ion signal current is estimated. We use a reasonable order-of-magnitude guess for the gain, $G \sim 10^5$ or 10^4, with an input ion pulse $\approx 10^6$ ions/8 μs $\implies I_i \approx 2\times 10^{-8}$ A, yielding $I_o = 200 - 20$ μA according to Eq. (4.80). This output current range exceeds the 20% dynamic range limit of the CEM bias current specification of 160 μA. In Ref. [40], we rationalized that the ion extraction process has sub-unity efficiency, in contrast to the idealized SIMON simulation results. Thus

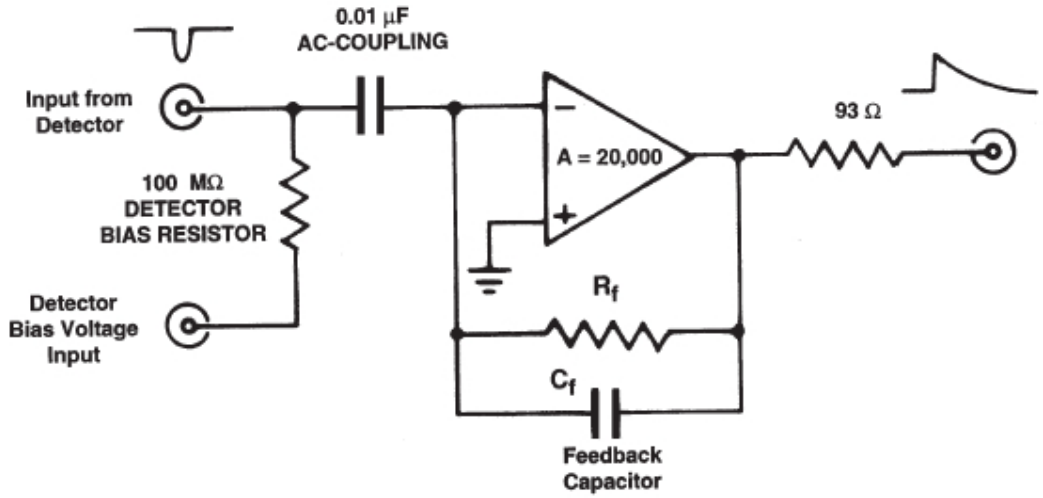

Figure 4.78: Circuit diagram of ORTEC 142C charge-sensitive integrating pre-amplifier. Output's peak is proportional to the total input charge from a current pulse and the rise time is proportional to the current pulse's width in time. See text for details.

we may trap $\sim 10^6$ ions, but only a fraction of them reach the CEM.[33] The sub-unity efficiency is not a problem, as long as it remains constant, it will simply become a constant multiplicative factor in the overall effective CEM calibration [40].

The output of the CEM goes directly to an ORTEC 142C charge sensitive pre-amplifier via a short BNC connector, reducing the detector capacitance.[34] The pre-amplifier actively integrates the CEM's output current pulse with a feedback time constant $\tau_f = R_f C_f$, as defined in the manufacturer's circuit diagram, Fig. 4.78.

The output integral is a pulse with a linear rising voltage, whose rise time is approximately equal to the ion pulse width, followed by a slow decay, as seen in the red trace in Fig. 4.79. The peak integrated voltage V_0 is proportional to the total number of ions that strike the CEM according to

[33]This is not so unreasonable seeing as the mesh alone is only $\approx 80\%$ transmissive, so even under ideal circumstances at least $\approx 20\%$ of the ions are lost during extraction.

[34]The cable between the CEM output and the pre-amplifier input acts like a parallel capacitor. For a given amount of charge, the largest possible input voltage on the pre-amplifier requires the smallest possible cable capacitance.

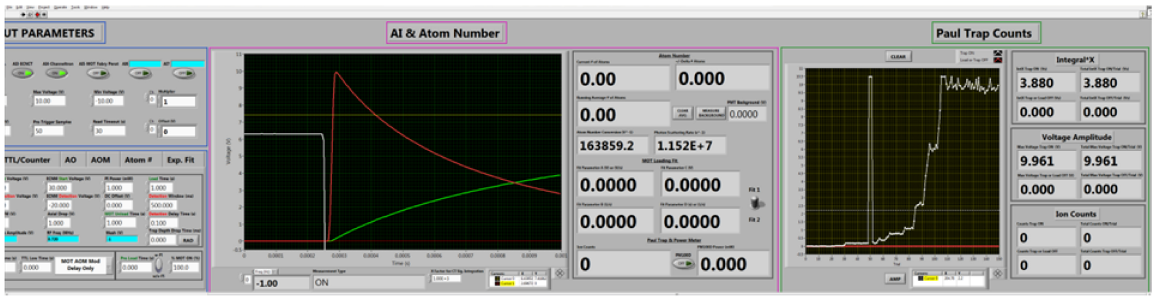

Figure 4.79: Front panel of LabVIEW data acquisition program showing pre-amplifier's analog output (red). On the right, the program also plots the amplitude of each data point in sequence.

$$V_0 = \frac{qN_e}{C_f} \propto \frac{qN_I G}{C_f}, \tag{4.81}$$

where $N_e \propto I_o$ is the number of electrons in the CEM's output current pulse.

The power supply to the pre-amplifier and the NI DAQ board specifications put a maximum signal limit of 12 V and 10 V on V_0, respectively. By changing the HV on the CEM cone we can reduce the CEM gain, so as to keep the DAQ input signal below 10 V.

4.3.7 Mass selective resonance quenching

A Na MOT can produce atomic and molecular ions via photoassociative ionization. A Na_2 molecule absorbs two MOT beam photons while initially in the large internuclear separation $Na_2(3S_{1/2}, 3S_{1/2})$ molecular limit, and becomes a Na_2^+ molecular ion [158–162]. Additionally, the trapping laser's wavelength is resonant with a photodissociative molecular transition, $Na_2^+ + h\nu \longrightarrow Na + Na^+$, where the dissociated Na^+ has, on average ~ 0.5 eV of kinetic energy [163]. Although Na is the only alkali that undergoes this photoassociative ionization from its own MOT beams, alkaline earth MOTs (e.g., Ca, Sr, Yb) can also act as ion sources due to photoassociative ionization from their MOT beams [37, 45].

The production within the MOT of Na_2^+ (produced via photoassociative ionization) and Na^+ (produced via photodissociation) results in an uncontrolled source of ions that can interfere with the controlled study of any other ions created within the hybrid trap, e.g., Na^+ created using PI [37].

In our experiments that involve PI-produced Na^+, our CEM indiscriminately detects photoassociated Na_2^+, photodissociated Na^+, and the photoionized Na^+. Although the Paul trap stability parameters a and q are mass dependent, the trap works over a wide enough range of masses that all of these ions can be trapped simultaneously.

We also have an uncontrolled mixture of trapped ions in our Ca^+ experiments, where EI indiscriminately and simultaneously creates several different ionic species within the trapping region. Again, many of the EI produced species can be trapped simultaneously over a wide range of trap settings.

We needed a method to selectively remove ions of a particular mass, so as to better control the purity of our ion cloud. For example, by continuously quenching the MOT born Na_2^+ ions at a rate faster than or comparable to the Na_2^+ production rate, the unwanted Na_2^+ ions will no longer remain trapped in the LPT. Only the PI produced Na^+ ions will remain in the LPT, on which we can perform controlled experiments.

On resonance MSRQ One can continuously quench the unwanted ions from the Paul trap via a well established mass selective resonance quenching (MSRQ)[35] experimental technique [24, 45, 143, 145, 164]. By applying a small additional ac field $V_{\text{rad}}\cos(\omega_{\text{rad}}t)$ to the middle LPT electrode segments on resonance with an ions secular motion $\omega_{\text{rad}} = \omega_r$, the trapped ion will be undergo driven, resonant harmonic motion. The ion absorbs energy from the MSRQ driving field, increasing its secular amplitude until it is driven above the

[35]This technique goes by many names, e.g., the "tickling" method.

trap depth and ejected from the LPT.

Because the ion's secular frequency is mass-dependent, the MSRQ driving field can selectively eject species by mass. The physical implementation of the ac voltage sources was discussed in Sec. 4.3.3. Alternatively, the axial end segments can also be given an MSRQ field $V_{\rm ax}\cos(\omega_{\rm rad}t)$ resonant with the ion's axial secular motion ω_3.

Typically, only one MSRQ field is used at a time. When radially quenching ions Eq. (4.58) becomes

$$\begin{aligned}\mathscr{V}(x_i,t) \approx [V_{\rm rf}\cos(\Omega_{\rm rf}t) + V_{\rm rad}\cos(\omega_{\rm rad}t) + V_{\rm dc}]\frac{x_1^2-x_2^2}{r_0^2} + \\ + \frac{\eta V_{\rm end}}{z_0^2}\left(x_3^2 - \frac{x_1^2+x_2^2}{2}\right).\end{aligned} \tag{4.82}$$

In Eq. (4.82) the dc voltage $V_{\rm dc}$ can be added in a quadrupole configuration, which shifts the radial secular frequency $\omega_r \to \tilde{\omega}_r$, as discussed in Ref. [145]. Although our setup is capable of adding a dc potential to the LPT electrodes, we do not use this feature in the experiments presented here, so it is safe to assume that $V_{\rm dc} = 0$ V.

When applying the axial MSRQ field the end segments get an oscillating dipole potential and the $V_{\rm ax}$ term in Eq. (4.58) becomes

$$V_{\rm ax}(x_i,t) \approx V_{\rm ax}\cos(\omega_{\rm ax}t)\left(\frac{x_3}{z_0} - \frac{x_1^2+x_2^2}{2z_0^2}\right), \tag{4.83}$$

by making the FM and NM segments 180° out-of-phase.

Although our setup is capable of axial MSRQ, for all the experiments presented here we only use radial MSRQ. This is done for three reasons: (i) the theoretical single ion axial trap depth defined in Eq. (4.61) is larger than the radial trap depth given the typical trap settings used by our group. This means that one must apply a greater axial MSRQ field or suffer slower ejection rates, as compared to radial quenching. Large MSRQ fields

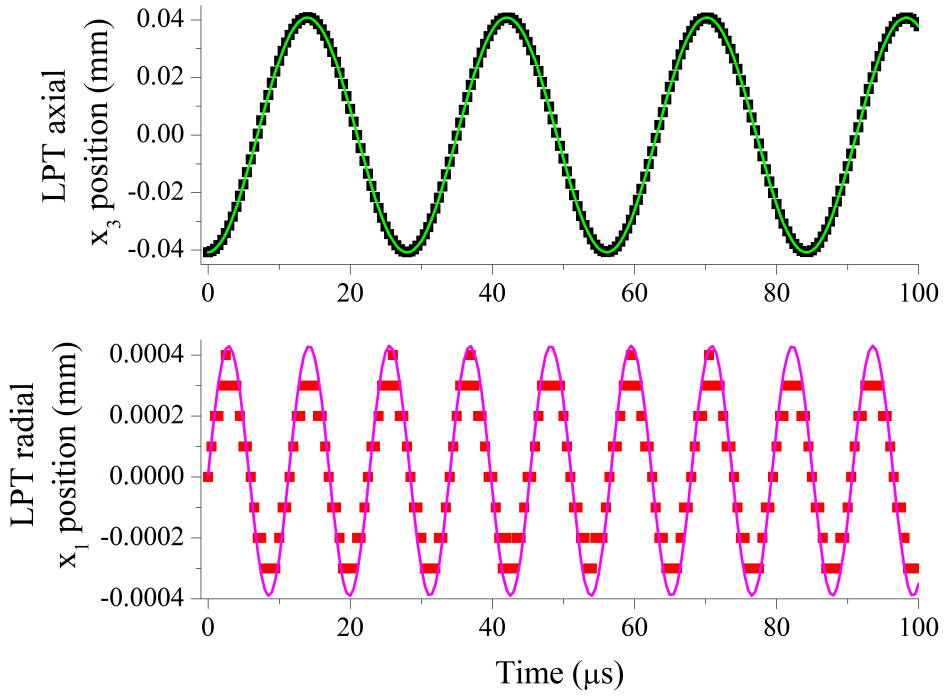

Figure 4.80: Plot of simulated axial (top) and radial (bottom) position of a single Na^+ ion within the LPT with $V_{rf} = 40$ V and $\Omega_{rf} = (2\pi)720$ kHz. The simulated data are fit to a sine function (solid green and magenta curves).

or slow ion ejection can lead to undesirable heating effects discussed later in this section. (ii) The trap is longer in the x_3 dimension, so the ion has to travel a larger distance before being ejected. Therefore, it takes longer to leave the trap axially as compared to radially.[36] (iii) Because our actual axial potential is more quartic then quadratic, the ion cloud has a weak kinetic energy dependence on its axial secular frequency, as discussed in Sec. 4.3.3. Therefore, a cloud of ions with a distribution of energy has an ill-defined secular frequency, which means that the quenching technique would rely heavily on sympathetic heating [24] between ions rather than directly driving all the ions out of the trap simultaneously. Because

[36] Admittedly, items (i) and (ii) are redundant since energy and position are proportional within the LPT's secular potential.

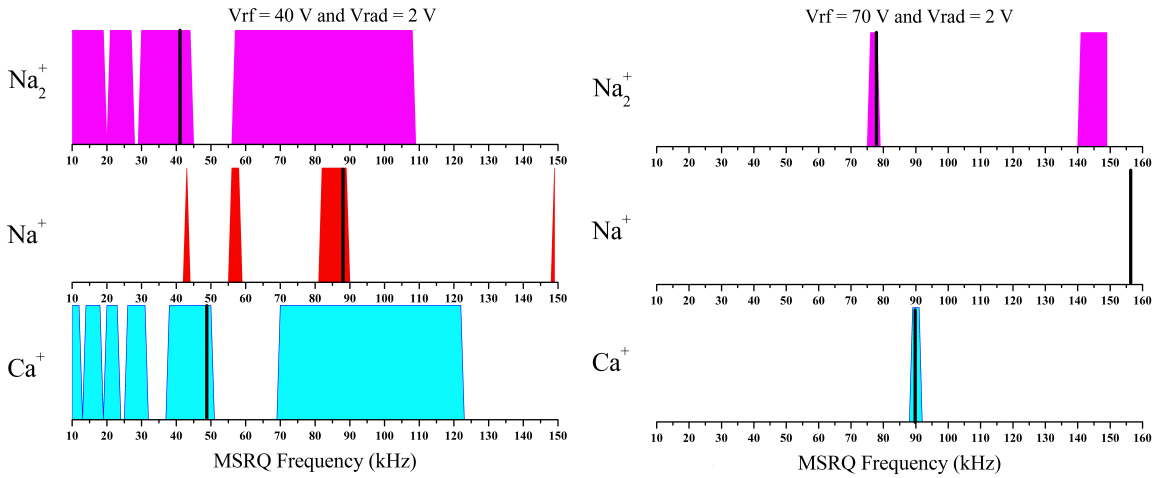

Figure 4.81: Plot of simulated MSRQ scan for a single Na_2^+, Na^+, or Ca^+ ion at two different V_{rf} values and $\Omega_{rf} = (2\pi)720$ kHz. The shaded regions represent the frequencies for which ion ejection was observed. The solid black lines represent the theoretically predicted secular frequencies ω_r according to Eq. (4.70). In the right plot (at $V_{rf} = 70$ V) the $V_{rad} = 2$ V is not strong enough to observe any first harmonic Na^+ quenching. The x-axes are in units of circular frequency not angular.

we do not use axial MSRQ in our experiments we will not mention it for the remainder of this section.

Using our SIMION simulations we can measure the secular motion by fitting the time dependent position output, as seen in Fig. 4.80. The fit secular frequencies have good agreement with the theoretically predicted secular frequencies from Eq. (4.70), typically $< 2\%$ difference. Our SIMION simulations model the real electrode geometry, so some discrepancy between the idealized model in Sec. 4.3.4 and our simulation results is to be expected.

Alternatively, the trapping program can simulate the ion's motion in the presence of the additional MSRQ fields discussed in Eqs (4.82) and (4.83). Figure 4.81 highlights the ω_{rad} frequencies associated with resonant Na^+, Na_2^+, or Ca^+ ion extraction, where an ion is considered ejected if it leaves the trap within 3 ms (or ≈ 100 axial secular periods for Na^+).

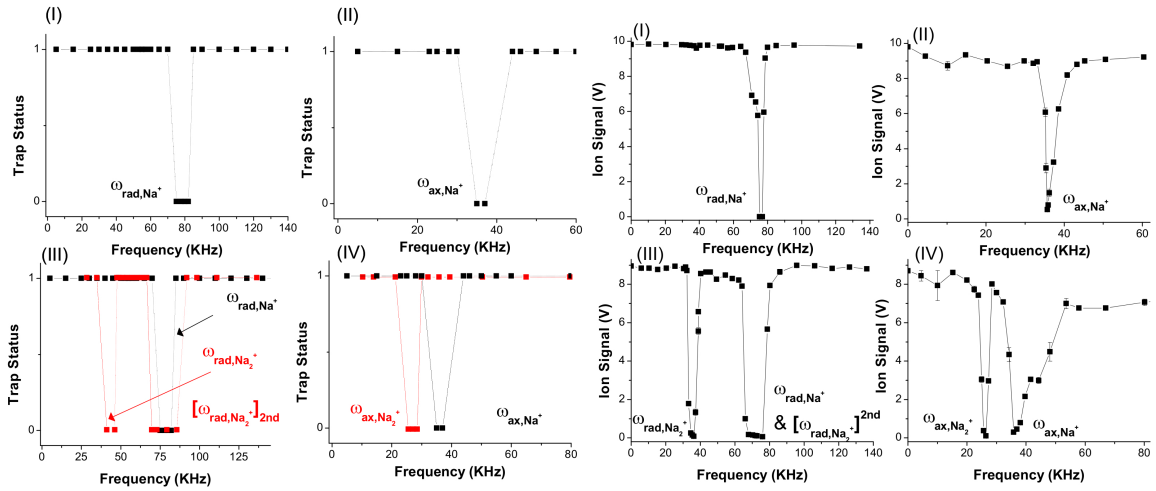

Figure 4.82: Plots originally from Ref. [143], showing agreement between SIMION simulation data (I) - (IV) on the left and experimental data (I) - (IV) on the right of MSRQ frequency scans on Na^+ and Na_2^+ ions. Both radial (I) and (III), and axial (II) and (IV) scans are shown. In the simulation plots, the binary trap status of 0 means that the ion was ejected at that frequency and the trap status of 1 means that the ion remained trapped. The x-axes are in units of circular frequency not angular. The solid lines are there to guide the eye (not fits).

We note that at lower rf amplitudes (left plot in Fig. 4.81) there are additional observable resonances associated with different linear combinations of secular harmonics [164].

We also observe excellent agreement between simulated secular scans (left side of Fig. 4.82) and experimental scans (right side of Fig. 4.82), as discussed in Refs [38, 143]. We find that driving the ions at their second harmonic gives stronger quenching compared to the first, as was observed in simulations and experiments by us [38, 143] and others [145].

The MSRQ scans of the EI loaded LPT (with the electron gun normally incident to the side of the LPT) reveal that several different ionic species are produced in addition to Ca^+, as seen in Fig. 4.83. These scan results demonstrate the necessity for Ca ionization via PI rather than EI, since Fig. 4.83 shows an inefficient production of Ca^+ and a fairly large amount of background (unwanted) ionic species.

For each ionic species we observe a widening of the ejection frequency range at a

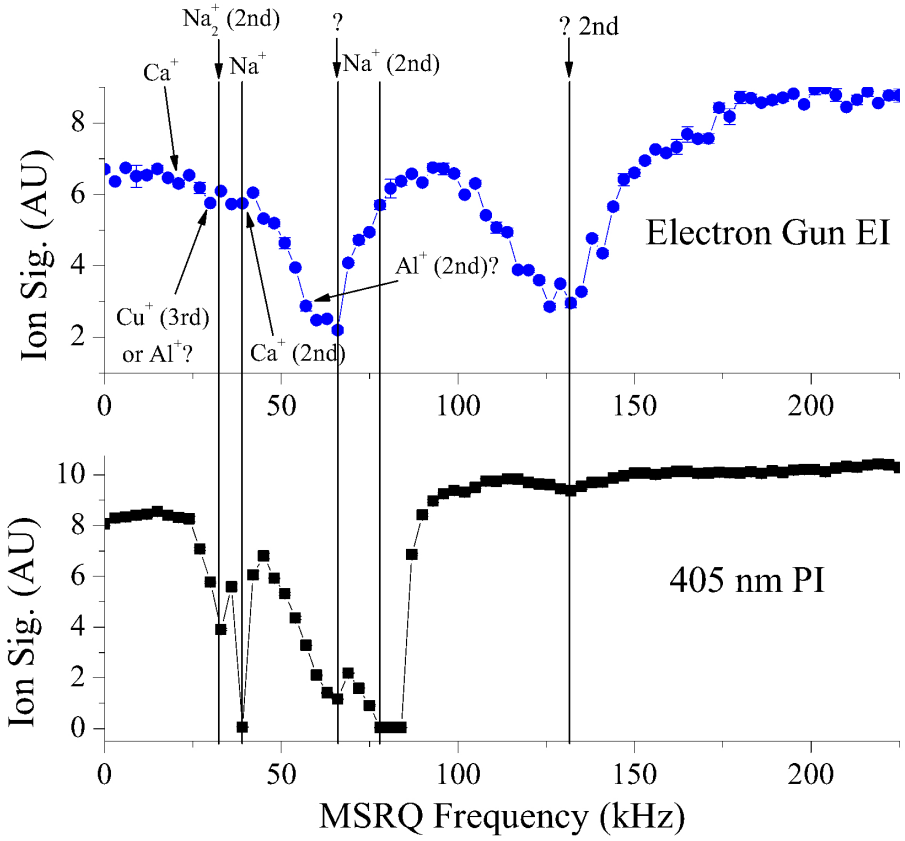

Figure 4.83: Top panel shows radial MSRQ scan of EI produced ions on Na MOT and background Ca vapor (with the electron gun normally incident to the side of the LPT). Bottom panel shows an MSRQ scan using only 405 nm PI radiation under the same conditions. The x-axes are in units of circular frequency not angular. PI radiation produces a cleaner MSRQ specutrum and ionizes with greater efficiency. The electron gun spectrum yields more mysteries than answers. Both spectra show dips near 66 kHz and 132 kHz, which we think might be an issue with our trap causing mass *insensitve* energy absoption at that MSRQ frequency.

given V_{rf} when increasing V_{rad}, as can be seen by comparing the two plots in Fig. 4.84. Increasing V_{rad} also asymmetrically shifts the middle of the frequency range toward lower frequencies.[37] The asymmetry's dependence on the applied MSRQ amplitude arises from both the perturbation caused by the MSRQ field itself and the fact that the actual trap electrodes do not create a perfect quadrupole field [143, 145].

[37]The asymmetry in the resonance curve is similar to that of an anharmonic driven oscillator.

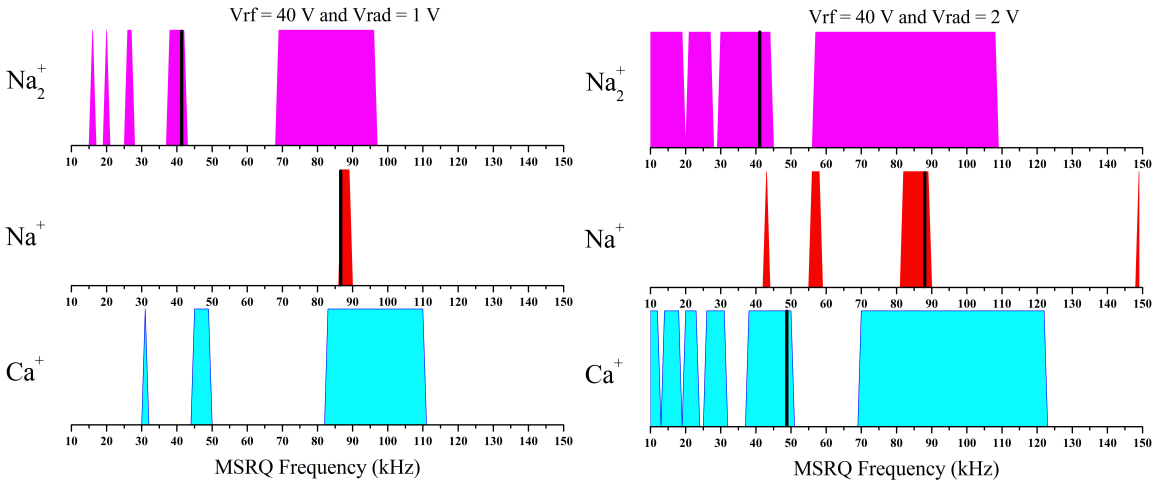

Figure 4.84: Same kind of plots as Fig. 4.81, but the left panel uses a lower V_{rad} than the right. The lower V_{rad} gives a narrower ejection frequency range. The x-axes are in units of circular frequency not angular.

Ejection rates per ion increase exponentially [143] with increasing V_{rad}, as seen in SIMION simulations [Fig. 4.85 (a) and (b)]. We can relate the ejection time per ion $t_{\text{eject}} = 1/R_{\text{eject}}$ to the fraction of ions remaining in the trap f_R by

$$t_{\text{eject}} \propto \frac{1}{1-e^{-V_{\text{rad}}}} \implies R_{\text{eject}} \propto 1-e^{-V_{\text{rad}}} \propto 1-f_R \implies f_R \propto e^{-V_{\text{rad}}}. \tag{4.84}$$

Our experimental measurement [Fig. 4.85 (c)] of f_R for a fixed trapping time and depth also shows exponential decay with respect to MSRQ amplitude, which is consistent with Eq. (4.84) and confirms the simulation results [Fig. 4.85 (b)].

Off resonance MSRQ Ideally, the MSRQ precisely heats ions of a single mass. However, we found in both simulations and experiments that this is not the case. Both the MSRQ fields and sympathetic heating from quenched ions [24, 143] can cause ions that are off-resonance from ω_{rad} to be heated as well. We call this problematic MSRQ side-effect off-resonance energy absorption (OREA) [143].[38]

[38] Previously referred to as side-effect heating in our earlier manuscript Ref. [37].

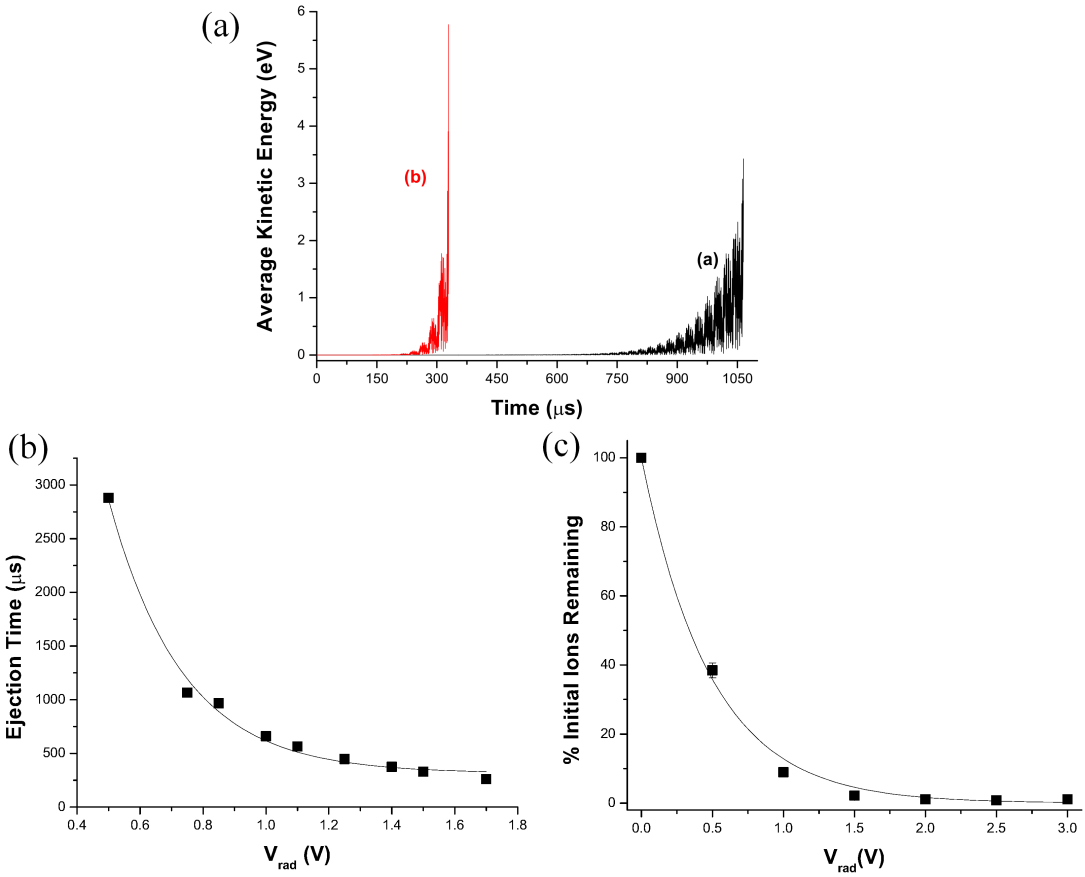

Figure 4.85: Plots (a) - (c) are originally from Ref. [143]. Plot (a) shows the kinetic energy evolution of a Na_2^+ ion quenched by two different radial MSRQ amplitudes. The larger MSRQ amplitude [the red curve (b)] ejects the ion more quickly. Plot (b) shows that the ejection time has an exponential dependence on MSRQ amplitude. Experimental data in plot (c) shows that the fraction of ions remaining in the trap will also decay exponentially with increasing MSRQ amplitude, confirming the simulation result. The uncertainty in the experimental data points is smaller than the plot markers.

The experimental scans of LPT decay seen in the right plot of Fig. 4.86 showed a noticeably greater trap loss rate of Na^+ ions in the presence of an off-resonant MSRQ field, as compared to no MSRQ fields. Here, when we say the MSRQ field is "off-resonance" for Na^+, it is considered on-resonance for Na_2^+, where $\omega_{\text{rad}} = \omega_{r,\ Na_2^+}$ and $\omega_{\text{r},\ Na^+} \approx 2.2\omega_{\text{r},\ Na_2^+}$.

We also observed the OREA of a single ion in a simulation, as seen in the left plot of Fig. 4.86. A simulated Na^+ ion's mean (micromotion averaged) kinetic energy and spread

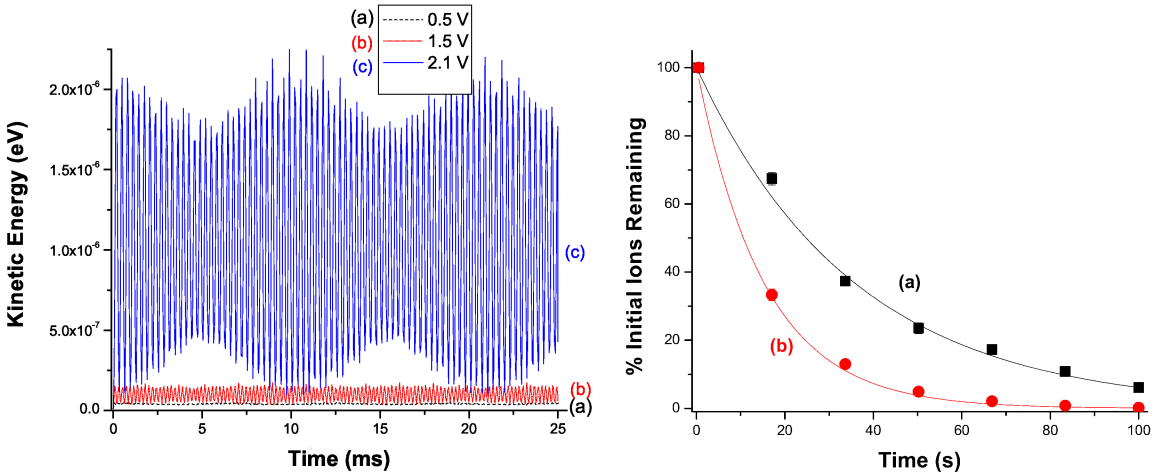

Figure 4.86: Originally from Ref. [143]. Left plot shows simulated Na^+ ion kinetic energy evolution with continuous MSRQ at $\omega_{\text{rad}} = \omega_{r,\ Na_2^+}$. Three different MSRQ amplitudes (a) - (c) are shown. The right plot shows the experimental LPT trap loss evolution of PI loaded Na^+ without MSRQ (a) and with continuous Na_2^+ off-resonant MSRQ (b). The uncertainty in the experimental data points is smaller than the plot markers.

in kinetic energy increases with increasing (off-resonance) MSRQ amplitude.[39]

We also investigated OREA's dependence on the number of ions. Simulations showed that the cloud's quasi steady-state mean energy increased with increasing ion number and density, as seen in the left plot of Fig. 4.87. As the ions coherently absorb energy from the (off-resonant) MSRQ field, the ion cloud's incoherent motional energy also increases due to ion-ion collisions. The cumulative effect is ion cloud heating.

Experimentally we confirmed this effect by measuring the fraction of trapped Na^+ ions remaining after 30 s of trapping time while subjected to off-resoncnat Na_2^+ MSRQ conditions as a funciton of the initial number of ions loaded into the trap, as seen in the right plot of Fig. 4.87. As the initial ion population was increased, we found that a larger fraction of that initial population was lost due to OREA, suggesting a collective ion cloud heating effect.

[39] Axial quenching appeared to have even more dramatic OREA, as seen experimentally and within simulations [38].

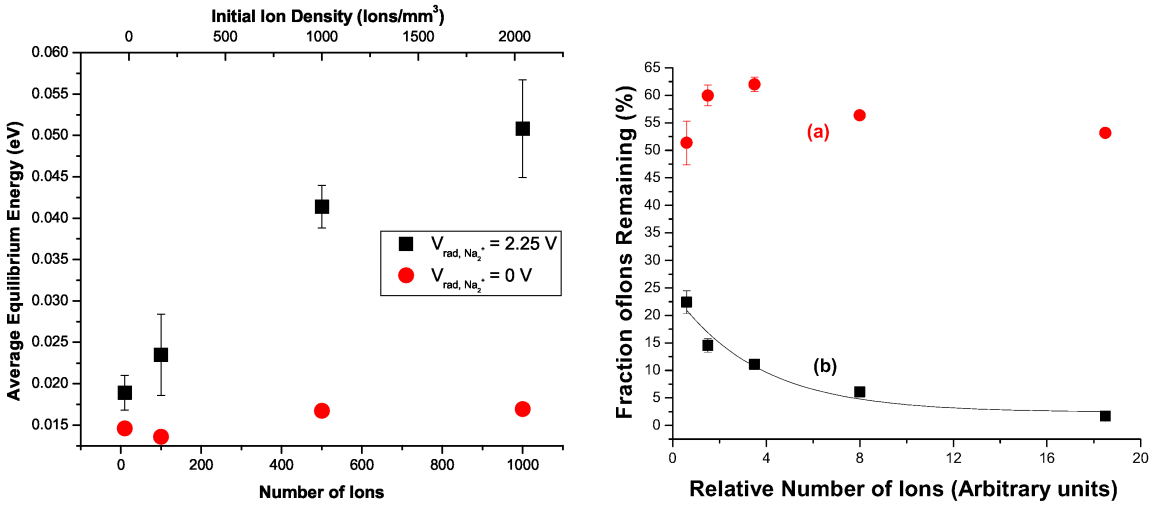

Figure 4.87: Originally from Ref. [143]. The left plot shows a simulated Na^+ ion cloud's quasi-steady-state mean kinetic energy after 3 ms of trapping as a function of the number of ions within an initially 0.5 mm cloud with (black squares) and without (red circles) off-resonant Na_2^+ MSRQ. The error bars represent the standard deviation of the energy fluctuations in steady-state. The right plot shows experimental detection of the fraction of remaining ions for fixed trap settings after 30 s of trapping. Without off-resonant Na_2^+ (a), the ion decay is insensitive to the number of ions initially loaded. With off-resonant Na_2^+ (b), the fraction of remaining ions decreases with increasing initial ion population.

4.3.8 Ion trap heating mechanisms

In the last section we discussed actively heating ions out of the LPT. Howerver, LPTs are also susceptible to a variety of inherent heating mechanisms, such as instantaneous collisional heating [37], two types of rf heating (atom-ion and ion-ion heating) [165–172], and excess micromotion heating [146]. In the absence of any active ion cloud cooling, these heating mechanisms can be significant enough to cause trap loss despite the LPT's deep $\sim$ 1 eV trap depth.

Atom-ion rf heating Both instantaneous collisional heating and atom-ion rf heating within a low-temperature neutral buffer gas are nicely explained by S. Schwarz using phase space diagrams [166]. A modified version of his explanation is illustrated in Fig. 4.88.

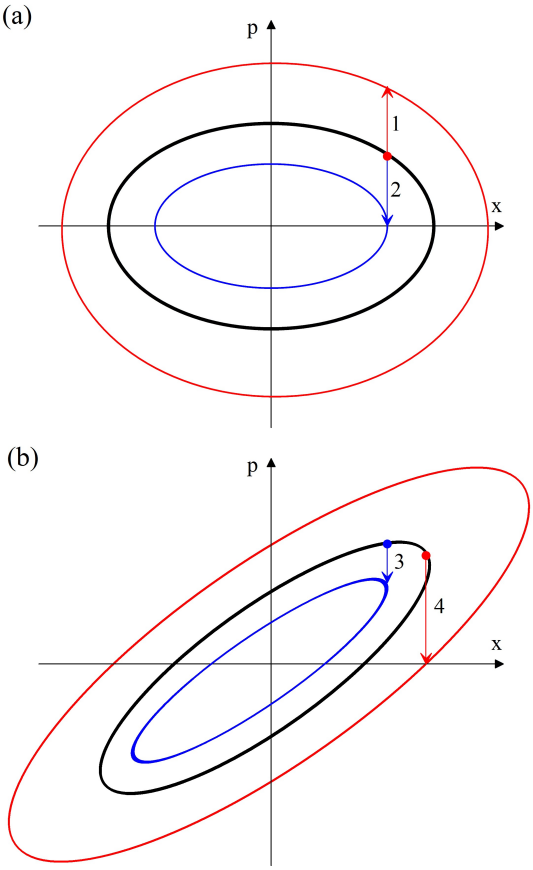

Figure 4.88: Sketch of 1D atom-Ion rf heating phase space diagrams from [166]. Panel (a) shows the ion phase space trajectory following simple harmonic motion at instance of rf phase $= 0$. Arrows 1 and 2 show instantaneous collisional heating (red) and cooling (blue) pathways, respectively. Panel (b) shows ion phase space trajectory at instance of rf phase $\neq 0$. Arrow 4 shows an atom-ion rf heating collision pathway, where an instantaneous speed decrease results in a larger (red) phase space ellipse and an increase in total energy.

Each phase space diagram shows the 1D momentum-position relationship of a single ion's secular motion in a Paul trap during a specific instance of the rf driving field's phase (i.e., at a single instance during the micromotion). The total energy of the ion is equal to the area of the phase space ellipse. At any instant in time, the ion has a distinct position in phase space constrained to a point on a closed path. Simultaneously, as the phase of the rf potential evolves in time, the closed phase space path rotates and stretches.

We will assume that the interaction time during a collision between an ion and atom is much shorter than the period of the ion's secular motion or micromotion. Therefore, collisions are represented as vertical arrows in Fig. 4.88, where each collision event (beginning with a solid dot and ending with an arrow head) instantaneously moves the ion to a new path in phase space consistent with the ion's new post-collision total energy.

A collision causing an instantaneous speed increase, represented by arrows 1 in Fig. 4.88 (a), always results in a total energy increase (independent of rf phase). We will define this event as instantaneous collisional heating, which leads to a larger (red) phase space ellipse. For example, this type of collision might occur because the ion had a head-on classical collision with a hotter background gas atom. Alternatively, it could have had an impact from behind by a faster moving atom traveling in the same direction.

If a collision causes an instantaneous speed decrease (depicted by arrows 2 - 4 in Fig. 4.88), then the ion does not necessarily result in an energy decrease. It depends on the instance of the rf phase at the moment of the collision. Unlike the neutral atom trap, the LPT is a dynamic trap with non-conservative forces that can pump energy into the system if the ion's motion is disrupted [43].

When the ion follows a 1D harmonic phase space ellipse like the one depicted in Fig. 4.88 (a), any instantaneous speed decrease will result in a lower energy phase space ellipse. For example, this instantaneous collisional cooling pathway is represented by arrow 2 in in Fig. 4.88 (a).

Atom-ion rf heating results from collisions that occur during an instance when the initial rf phase space path looks like Fig. 4.88 (b). Classical collisions causing a large instantaneous speed decrease (dramatically interrupting the ion's micromotion) can actually result in a total energy increase. For example, when $m_I \approx m_N$, according to Eq. (2.5) a head-on collision with a zero velocity neutral atom yields a zero velocity post collision ion.

Arrow 4 in Fig. 4.88 (b) is associated with that equal mass collision pathway, where energy is absorbed by the rf field during the collision, leading to a larger post-collision total energy phase space ellipse. Atom-ion rf heating collisions typically occur near the turning points of the ion's motion, like arrow 4 in Fig. 4.88 (b).

For the case where $m_I/m_N \gg 1$, a head-on collision may result in more modest instantaneous speed changes per collision according to Eq. (2.5). The massive ion two-body collisions lead to more collision events like that of pathway 3 in Fig. 4.88 (b) on average, where a modest instantaneous energy decrease results in a lower energy post collision phase space path.

We can quantify the heating for a two-body collision within an rf field originally developed by Major and Dehmelt [165]. Starting from our analysis of classical scattering from Sec. 2.1.1, we can write the post ion-neutral velocity of an ion as

$$\vec{v}_I\,' = u_I\left[\sin(\theta)\hat{x} + \cos(\theta)\hat{z}\right] + v_{\mathrm{COM}}\hat{z}, \tag{4.85}$$

according to Eq. (2.6) in the laboratory reference frame. First, we will redefine the term in brackets from Eq. (4.86) as $[...] \equiv \hat{\theta}$. Next, we note that according to Eqs (2.1) and (2.2) we can write

$$v_{\mathrm{COM}}\hat{z} = \frac{m_I\vec{v}_I}{m_I+m_N} \quad \text{and} \quad \vec{u}_I = \vec{v}_I - \frac{m_I\vec{v}_I}{m_I+m_N} = \frac{m_N v_I}{m_I+m_N}\hat{z}. \tag{4.86}$$

Substituting these results and definition into Eq. (4.86) gives the post collision velocity in the form stated in Ref. [165], namely

$$\vec{v}_I\,' = \frac{m_N v_I}{m_I+m_N}\hat{\theta} + \frac{m_I\vec{v}_I}{m_I+m_N}. \tag{4.87}$$

Here, $\hat{\theta}$ is the unit vector pointing along the ion's final trajectory direction.

From Eq. (4.52), which separates the slow macromotion and the fast micromtion, we can take a time derivative and represent the ion's velocity as

$$\vec{v}_I = \dot{\vec{X}}_s + \dot{\vec{X}}_m \text{ and } \vec{v}_I{}' = \dot{\vec{X}}_s{}' + \dot{\vec{X}}_m, \tag{4.88}$$

a linear combination of secular velocity $\dot{\vec{X}}_s$ and micromotion velocity $\dot{\vec{X}}_m \propto \vec{\mathscr{E}}\sin(\phi_{\text{rf}})$ according to Eq. (4.57).

Substituting Eq. (4.88) into Eq. (4.87) and taking a time average over the rf phase of the quantity $\langle(\dot{X}_s')^2 - (\dot{X}_s)^2\rangle$ gives the change in kinetic energy

$$\begin{aligned}\langle \Delta E_T\rangle &= \frac{1}{2} m_I \langle (\dot{\vec{X}}_s{}')^2 - (\dot{\vec{X}}_s)^2\rangle \\ &= m_I[1-\cos(\theta)]\left\{\frac{m_n}{m_N+m_I}\langle \dot{\vec{X}}_m^2\rangle - \frac{m_I m_N}{(m_I+m_N)^2}\langle \dot{\vec{X}}_s^2 + \dot{\vec{X}}_m^2\rangle\right\},\end{aligned} \tag{4.89}$$

as discussed in Ref. [165]. In Ref. [60], Ravi *et al*. point out that in arriving at Eq. (4.89), Major and Dehmelt make the approximation that the collision occurs at the ion's turning point (where it spends most of its time), specifically

$$\langle \dot{\vec{X}}_s\rangle \to 0 \text{ and } \langle \dot{\vec{X}}_m\rangle \gg \langle \dot{\vec{X}}_s\rangle \implies v_I \hat{\theta}\cdot \dot{\vec{X}}_m \approx \dot{\vec{X}}_m^2 \cos(\theta). \tag{4.90}$$

As we saw in Sec. 4.3.4 we can equate the micromotion and secular motion mean energy. So assuming $\dot{\vec{X}}_s^2 = \dot{\vec{X}}_m^2$, we arrive at the following conditions:

$$\begin{aligned} m_N > m_I &\implies \langle \Delta E_T\rangle > 0 \implies \text{ atom-ion rf heating,} \\ m_N < m_I &\implies \langle \Delta E_T\rangle < 0 \implies \text{ cooling,} \\ \text{and } m_N = m_I &\implies \langle \Delta E_T\rangle = 0. \end{aligned} \tag{4.91}$$

We can relate the conditions of Eq. (4.91) to the phase space model. When $m_N \gg m_I$, a head-on collision with a $v_N \approx 0$ atom results in a large instantaneous speed change as compared to the equivalent collision in the $m_I = m_N$ case. On average this results in a net absorption of energy [pathway 4 in Fig. 4.88 (b)] from the rf field and leads to heating.

Alternatively, when $m_N \ll m_I$, even a head-on collision causes small instantaneous speed changes [pathway 3 in Fig. 4.88 (b)] resulting in a net cooling effect. In the equally massive ion-neutral case, which always yields $v_I' \approx 0$ post head-on collision, half of the time the intermediate speed decrease causes cooling and the other half of the time it causes heating, giving null net energy change.

More recent studies by R. DeVoe [173] showed that a single ion within a neutral background buffer gas yields a non-Gaussian spatial probability density. Instead the tails of the spatial distirbution follow a power-law Tsallis function, whose exponent depends on the mass ratio m_N/m_I. R. DeVoe found that when the exponent falls below unity for $m_N > 1.55 m_I$, a runaway atom-ion rf heating would result.

Ion-ion rf heating The heating mechanism known as ion-ion rf heating is nicely explained by R. Blümel *et al.* and we show their main results in Fig. 4.89 to briefly illustrate this effect [167, 168, 171, 172].

For simplification, let us temporarily assume there is no atom-ion interaction, so only ions are present within the LPT's trapping region. The ions are initially far enough apart that they do not experience any heating. We assume they are in the weakly coupled Mathieu regime, $\Gamma_c \ll 1$. As these ions are cooled (by any means) the axial amplitude decreases according to Eq. (4.72), thus decreasing the root-mean-square position $\langle r_{\rm rms} \rangle$ of the ion cloud.

Eventually, collisions between ions cause ion-ion rf heating once the $\langle r_{\rm rms} \rangle$ becomes small enough that Coulomb interactions between ions perturb the ions' motion, resulting in chaos [174]. The chaos smears the well defined frequency spectrum indicative of the Mathieu regime, and allows for resonant absorption of the rf driving field's energy, which causes the ions to heat up. Blümel called this region the "chaotic regime." If the cooling

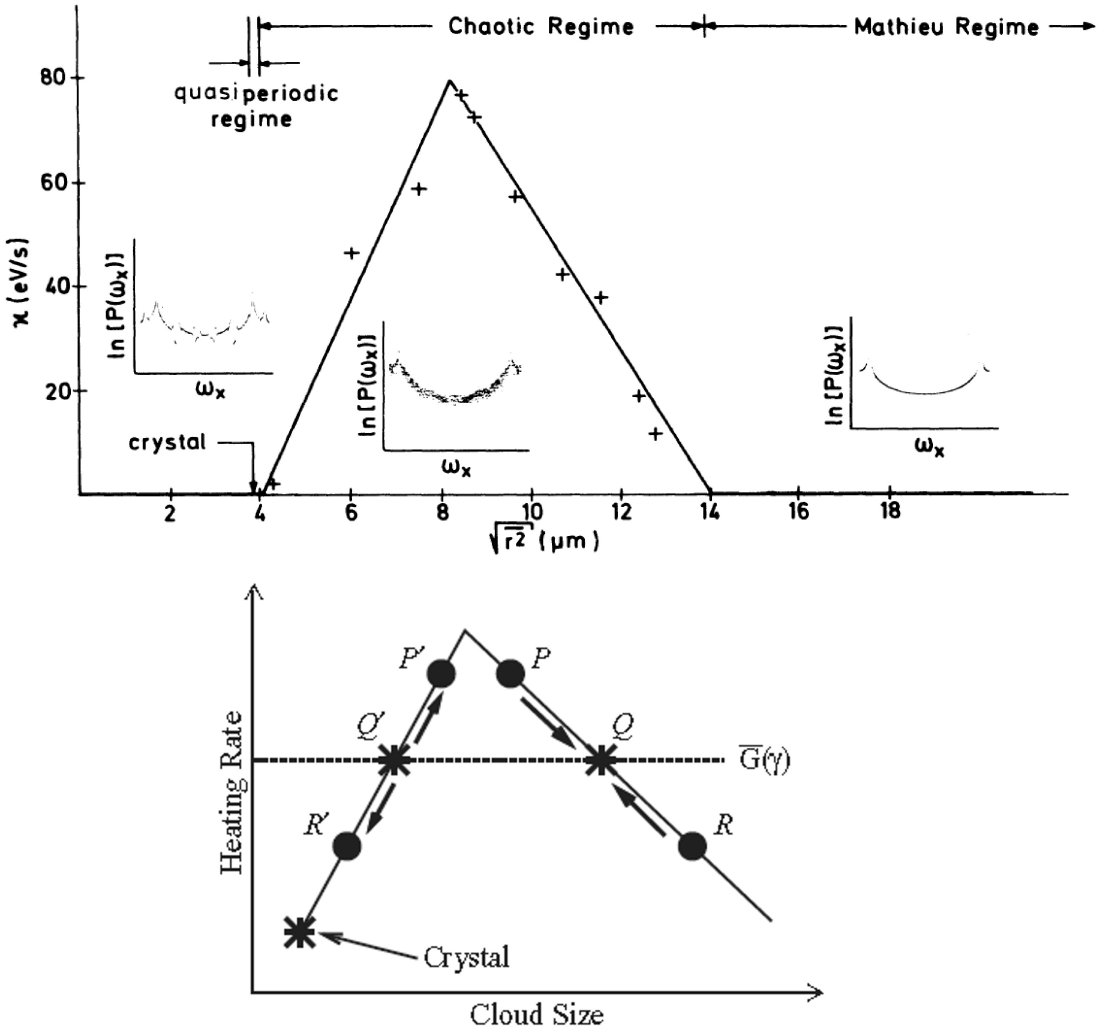

Figure 4.89: Top plot of ion-ion rf heating rate, heating rate vs. root-mean-square position of an ion cloud originally from [167]. To reach the crystalline quasiperiodic regime, one must actively cool the cloud beyond the point of maximum ion-ion rf heating. The bottom plot, originally from [171], shows the same "tent" structure. The position Q represents a stable equilibrium associated with a balance between active ion cooling ion-ion rf heating. The point Q′ is an unstable equilibrium that leads to a cloud or ion crystal formation.

rate ($\bar{G}$ in Fig. 4.89) is not large enough, a stable equilibrium is reached when the cooling and heating rates become equivalent [171] at position Q on Fig. 4.89.

If the cooling capacity is great enough to overcome the rf heating then a phase transition can occur, resulting in an ion crystal also known as a Wigner crystal [175, 176], as seen in

Figure 4.90: Image of 19 Ca^+ ions in a 1D crystal at the center of a LPT from Ref. [175].

Fig 4.90. The crystal phase is associated with strong coupling $\Gamma_c \gg 1$. At the boundary between crystallization and the chaotic regime, ions undergo quasiperiodic motion which Blümel called the "quasiperiodic regime." Only after getting beyond the ion-ion rf heating hurdle can crystallization and continued ion cooling occur.

Blümel *et al.* [171, 172] also showed that the macroscopic picture of the ion-ion heating mechanism in a 3D trap (not an LPT) can be described by a universal heating curve.

The scaled heating rate,

$$h \equiv \frac{\langle E_{\rm kin} \rangle}{\langle E_{\rm kin}^{\rm nig} \rangle}, \tag{4.92}$$

is a ratio of the (long) time-averaged kinetic energy of the cloud in the electrodynamic potential to that of the non-interacting gas held in the equivalent harmonic pseudopotential trap, as defined in Ref [171]. The absolute heating rate is defined as

$$H \equiv G\langle E_{\rm kin} \rangle, \tag{4.93}$$

where G is the chosen damping or cooling rate that when balanced with the heating results in an equilibrated cloud at temperature T_I and cloud size $r_{\rm rms}$.

Figure 4.91 shows the resulting absolute heating rate for different numbers of trapped ions versus the equlibrium cloud size. The heating rate for a fixed number of (non-crystalized) ions falls with increasing cloud size, as seen by the parallel red lines in Fig. 4.91. To move from one red line to the next we connect the lines by a vertical blue line, whose intersection with the red gives the approximate power-law relationship

$$H \propto (N_I - 1)^{3.7} \tag{4.94}$$

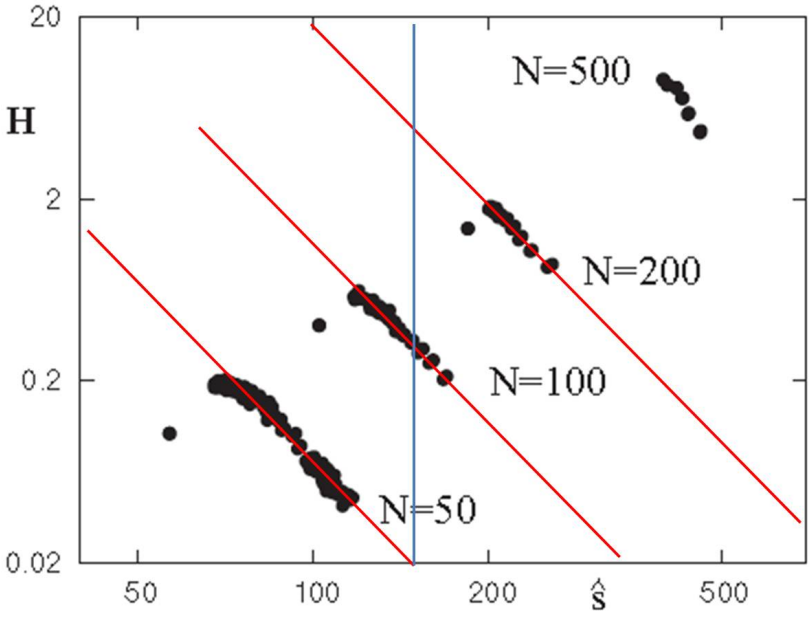

Figure 4.91: Modified figure originally from Ref. [172]. Absolute heating rate as a function of the root-mean-square size of the spherical ion cloud for different numbers of trapped ions. The points that do not fall along the red lines correspond to the crystalized cloud with size $r^c_{\rm rms}$. Each point for a given N_I corresponds to a different choice for G.

between the absolute heating rate and the number of ions in the trap.

When the data from Fig. 4.91 is plotted vs. a cloud size scaled by the size of the crystal,

$$\sigma \equiv \frac{r_{\rm rms}}{r^c_{\rm rms}} = \frac{[(3q_r^2/4)\sqrt{\pi}]^{1/3}}{w(\lambda)^{1/2}}, \tag{4.95}$$

all the data sit along a universal curve, as seen in Fig. 4.92. Here, $w(\lambda)$ is a scaling paramter associated with size of the cloud's assumed Gaussian distribution, which is a function of the universal λ parameter

$$\lambda \equiv \frac{[(N_I-1)q_r]^{2/3}}{T_I}. \tag{4.96}$$

The scaling parameter's dependence on λ must satisfy the relationship

$$w = \frac{\lambda}{2} - \frac{2\lambda w^{3/2}}{3\sqrt{\pi}}. \tag{4.97}$$

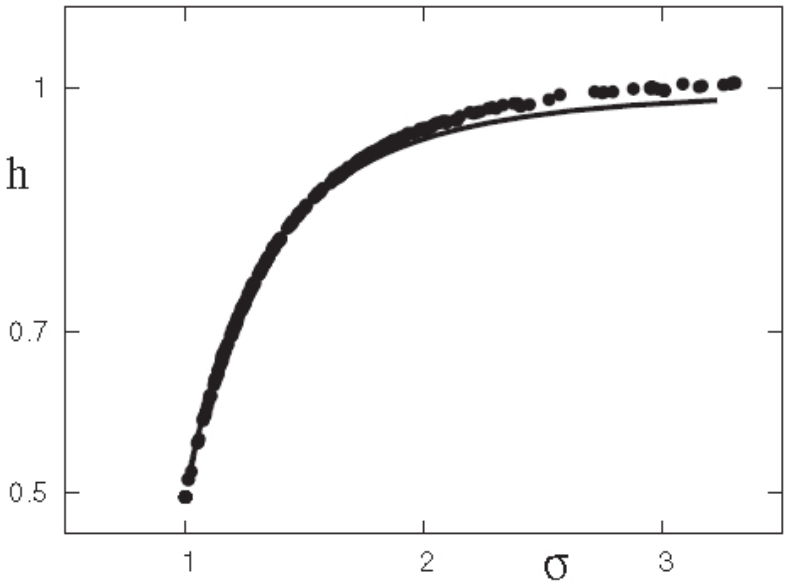

Figure 4.92: Originally from Ref. [171]. Plot shows that for $N_I = 50$, 100, 200, 500 ions at different equilibrium temperatures T_I, and at two different values of q_r, all the ion trap heating rate data collapse to a single universal curve when expressed in terms of the scaled heating rate h and the scaled cloud size σ. The solid line corresponds to the anylitical model in Eq. (4.98) and the data points are from numberical simulations.

Reference [171] shows that the scaled heating rate can be analytically expressed as a function of the scaled cloud size

$$\begin{aligned} h = \frac{2w(\lambda)(1+q_r^2/4)+\lambda}{2\lambda(1+q_r^2/8)} &= \frac{-(1+q_r^2/4)[2/(3\sqrt{\pi})w^{3/2}]+3/2}{2(1+q_r^2/8)} \\ &= \frac{-(1+q_r^2/4)[q_r^2/(2\sigma^3)]+3/2}{2(1+q_r^2/8)} \end{aligned} \tag{4.98}$$

and thus the single parameter λ. The analytical model shows good agreement with the numerical data, as seen in Fig. 4.92.

Excess micromotion heating Excess micromotion [146] occurs when an ion is displaced away from the quadrupole field's nodal line (along the x_3 axis of the trap) leading to micromotion in excess of the unavoidable micromotion described by Eqs. (4.69) and (4.71).

Experimentally, the displacement can be caused by stray or actively produced electric fields within the laboratory.[40] For example, in our LPT setup we can induce excess micromotion by applying separate dc voltages to each of the middle segments. One possible dipole voltage configuration places a positive potential on rod V2 (as defined in Fig. 4.51), making the approximate electrical potential near the center of the trap

$$\begin{aligned}\mathscr{V}(x_i,t) \approx & V_{\rm rf}\cos(\Omega_{\rm rf}t)\,\frac{x_1^2-x_2^2}{r_0^2}+V_{dc}\,\frac{x_1}{r_0}\\ & +\frac{\eta V_{\rm end}}{z_0^2}\left(x_3^2-\frac{x_1^2+x_2^2}{2}\right).\end{aligned} \tag{4.99}$$

The dc field displaces the average position of the ion [146], leading to an excess micromotion amplitude (to lowest order in a_i and q_i) of

$$\frac{q_i}{2}\left(\frac{qV_{\rm dc}}{r_0 m\omega_i^2}\right) \tag{4.100}$$

in addition to the unavoidable amplitude $X_{0i}\cos(\omega_i t+\phi_{0i})(q_i/2)$ from Eq. (4.69). The additional amplitude increases the kinetic energy in Eq. (4.71) by

$$\frac{4}{m_I}\left(\frac{qq_iV_{\rm dc}}{r_0(2a_i+q_i^2)\Omega_{\rm rf}}\right)^2. \tag{4.101}$$

Experimentally, the dipole potential can be strategically incorporated to actively heat an ion cloud in a controlled manner [51] via excess micromotion heating. Alternatively it can be added to counteract stray electric fields, thus reducing excess micromotion [140].

We differentiate this mechanism from rf heating, as it can occur in the absence of any ion-ion or atom-ion collisions.[41]

[40] Alternatively, the excess micromotion can result from the phase relationship between each diagonal pair of rf segments being different from the ideal 180° [146].

[41] Technically, this is a coherent absorption of energy from the rf field. For heating to occur ions must transfer the coherently absorbed excess micromotion energy into incoherent motion via ion-ion collisions.

4.3.9 Cooling of Ca^+ ions and cooling laser stabilization

Doppler laser cooling the trapped ions opens doors to a large number of possible experiments (discussed in Ch. 7) and experimental techniques, such as ion-fluorescence based thermometry, electronic state control, and ion density measurements. Furthermore, by laser cooling ions we can counteract many of the heating mechanisms discussed in Sec. 4.3.8. In this section we will briefly discuss our progress toward laser cooling Ca^+ ions.

The Doppler cooling scheme for Ca^+ is depicted in Fig. 4.93 and requires a cooling laser at 397 nm and a repumping laser at 866 nm to keep atoms out of the metastable 3D state. We use a homebuilt 866 nm diode laser [138] and a Toptica DL100 397 nm diode laser. Each laser delivers about 10 mW of power.[42] Using anamorphic prism pairs to correct for

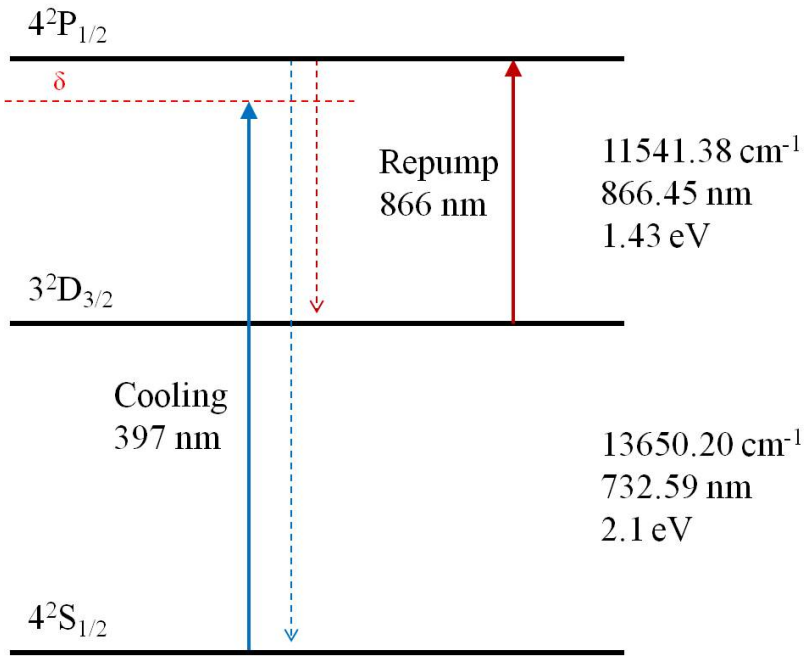

Figure 4.93: Energy level diagram for Doppler laser cooling Ca^+.

[42]Power is measured after the output optical isolator for the 397 nm laser head.

the diode lasers' elliptical beam mode, we get fairly collimated and circular beams with $r_{1/e} \approx 0.6$ mm for the 397 nm beam and $r_{1/e} \approx 0.3$ mm for the 866 nm beam, as measured with a razor-blade test.

The natural linewidth for the cooling cycle [177] is $\Gamma_{P_{1/2}} = \Gamma_{ps} + \Gamma_{pd}$, which is $\approx 2\pi(20.7 + 1.7) = (2\pi)22.4$ MHz. According to Eq. (3.86) the saturation intensity for a polarized (Q=1) 397 nm beam is $I_s = 43.3$ mW/cm^2, which we can achieve with our current setup. The Doppler cooling limit suggests that we should reach ion cloud temperatures $T_D \sim 0.5$ mK, according to Eq. (4.15).

In the setup illustrated in Fig. 4.2, we uses a single collinear pair of 397 nm + 866 nm beams, combined with a dichroic mirror and sent down the x_3 axis of the trap. This is in contrast to the two counter-propagating beam approach discussed in Sec. 4.2.1 for the MOT. However, because the ions are trapped by the LPT, they will periodically oscillate with secular motion that is sometimes parallel to and anti-parallel to the cooling laser propagation. By again red detuning the 397 nm cooling laser, the ion has the greatest likelihood of absorbing photons during the half of its secular oscillatory motion that coincides with counter-propagation to the cooling laser. Again, this creates a damping force that is present during half of the ion's secular period and no force during the other half of the period, which has a net cooling effect, as depicted in Fig. 4.94.

Due to a lack of UV spectral lines, frequency stabilization of the 397 nm radiation via saturation spectroscopy [as is done for the 589 nm radiation discussed in Sec. 4.2.3] is not practical. Instead, we have begun to employ a scanning FPI top-of-fringe lock for both the 397 nm laser and the 866 nm laser. Like the 589 nm laser, we send a separate PID error signal to tune the piezo-controlled diode laser gratings in the separate 397 nm and 866 nm

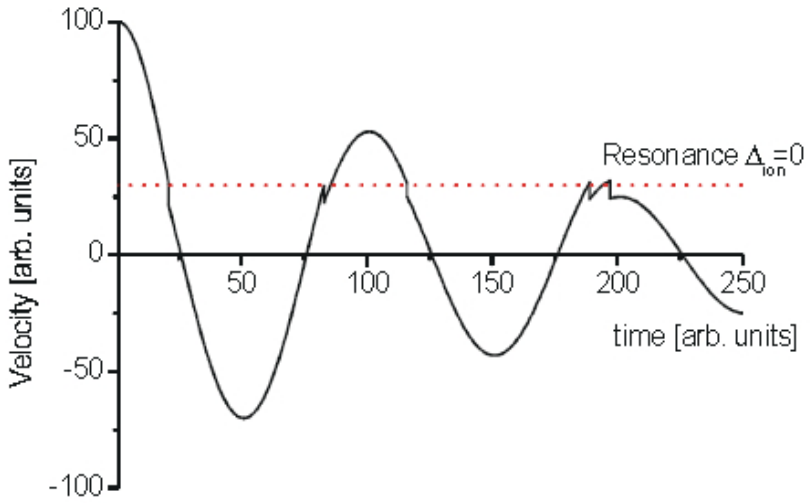

Figure 4.94: Originally from Ref. [84], showing a plot of a trapped ion undergoing periodic secular motion (neglecting micromotion). The ion is also laser cooled by a single red-detuned beam pointing in the negative velocity direction. When the ion has a velocity of $v_I = 30$ AU, there is a high probability of absorption since the detuning $\delta = 0$ in Eq. (4.4). On average, the absorption emission events decrease the ions momentum by $\hbar k_L$, reducing the ions maximum velocity.

laser heads.[43]

The error signal for the 397 nm is derived by comparing the relative Fabry-Perot peak position of the 397 nm laser and the 589 nm laser. Both beams are combined using a dichroic mirror, sent collinearly through a single FPI, split again, and sent to two separate photodiode detectors, as shown in Fig. 4.2. By fixing the relative peak position, we are locking the 397 nm laser to the independently Na-cell-locked 589 nm laser and not to the FPI cavity itself. This avoids systematic frequency shift errors due to thermal drift of the FPI cavity. An identical procedure is simultaneously performed on the 866 nm laser using another Thorlabs FPI, whose mirrors have greater reflectivity in the IR - visible part of the spectrum.

[43]The PID error signal calculation, top of fringe analysis, and analog error signal generation are all controlled by a LabVIEW program. Instead of using a lock-in to perform a top of fringe lock, a LabVIEW peak finding VI is used.

One drawback to this approach is that we have to continually scan the FPI cavity, thus making the speed of the lock limited to the scan speed of the cavity ~ 1 kHz. However, the diode laser heads have decent short-term stability, so a slow long-term lock is more than adequate for precise detuning from the wide Ca^+ natural linewidth $\Gamma_{P_{1/2}} \approx (2\pi)22.4$ MHz. Preliminary results suggest laser lock linewidths of ~ 10 MHz.

Chapter 5

Sympathetic cooling

One of the original motivations for developing the hybrid ion-neutral trap was to utilize the intermediate range ion-neutral scattering to sympathetically cool the translational and internal degrees-of-freedom of trapped ions, as discussed in Sec. 1.3. In this chapter we will discuss our investigation of translational sympathetic cooling within a hybrid system, both through SIMON simulations [37] and experimentation [38]. In Ch. 7 we will discuss possible furture experiments involving the cooling of molecular ions' internal degrees-of-freedom.

5.1 Sympathetic cooling model

Sympathetic cooling [83, 84, 84, 150, 170, 178] involves mixing at least two species of atoms or molecules – presumably, one species can easily be actively cooled and the other cannot. Ideally, through collisions with the actively cooled gas, the gas mixture does not reach an intermediate temperature, but rather it equilibrates at the actively cooled species' initial temperature. We can think of the active cooling as creating an ideal heat sink with a large heat capacity. Because sympathetic cooling relies on universal collisions physics and

not the electronic structure of the ion, sympathetic cooling allows physicists to cool species that might otherwise be nearly impossible to actively cool, e.g., optically dark atomic ions and nearly all molecular ions.

For example, ion clouds can be sympathetically cooled by a background noble buffer gas (e.g., He or Ar) that has been cryogenically cooled to low temperatures ~ 1 K [88, 89]. However, at best, that ion cloud's lowest possible equilibrium temperature is that of the buffer gas ~ 1 K. To sympathetically cool ions to cold or ultracold temperatures, one must use a cold or ultracold buffer gas (~ 1 mk - ~ 100 nk).

For instance, in our hybrid system the Na atoms are actively laser cooled and the co-trapped Na^+ ion cloud cannot be actively laser cooled, due to its closed electronic structure. Ideally, through elastic and charge-exchange collisions with the actively cooled MOT atoms, the Na^+ ions should be sympathetically cooled to cold MOT temperatures $\sim 100\ \mu$K. It was originally proposed [35, 36, 71] that, due to the large ion-(alkali) neutral cross sections, efficient sympathetic cooling would be realizable in the hybrid trap, despite the orders of magnitude lower atomic densities within cold atom traps as compared to typical buffer gas cooling apparatuses.

The hybrid trap sympathetic cooling process should even be possible for equally massive ions, despite the atom-ion rf heating conditions discussed in Sec. 4.3.8, namely that $m_N < m_I$ according to Ref. [165] or more specifically $m_N > 1.55 m_I$ according to [173].

Following the theory originally formulated in a collaboration between G. Werth and S.A. Rangwala's group [60, 179], the hybrid trap has a localized atomic density at the *center* of the LPT, unlike a typical buffer gas that uniformly fills the entire UHV system. As was assumed in Sec. 4.3.8, the buffer gas collisions most frequently occur at the turning points of an ion's motion [165], where the ion spends most of its time in the secular cycle. This leads to the condition of Eq. (4.91). However, in the hybrid system, ion-neutral collisions

will most frequently occur near the center of the trap where the micromotion is minimal and atom-ion heating cannot occur. Reformulating the time average over the phase of the change in secular velocities due to an ion-neutral collision, $\langle(\dot{\vec{X}}_s{}')^2 - (\dot{\vec{X}}_s)^2\rangle$, discussed in Sec. 4.3.8, for small micromotion velocities yields

$$\begin{aligned}\lim_{\dot{\vec{X}}_m \to 0} \langle \Delta E_T \rangle &= \lim_{\dot{\vec{X}}_m \to 0} \frac{1}{2} m_I \langle (\dot{\vec{X}}_s{}')^2 - (\dot{\vec{X}}_s)^2 \rangle \\ &= \frac{-2 m_I m_N}{m_I + m_N} \langle \dot{\vec{X}}_s \rangle^2 [1 - \cos(\theta)],\end{aligned} \tag{5.1}$$

which always leads to cooling, regardless of ion-neutral mass ratio [60, 179].

Equation (5.1) opens the possibility of translational sympathetic elastic scattering cooling between equally massive ion-neutral systems, like the Na^+-Na system studied by our group [37, 38], or the Rb-Rb^+ system studed by Rangwala's [60]. The equally massive ion-neutral system also offers the unique cooling pathway of resonant charge-exchange collisions discussed in Secs. 2.2.3 and 2.2.4. Rangwala's group called this "swap cooling" [60], owing to the fact that the hot ion swaps its electron with the cold atom, instantaneously reducing the ion's energy to that of the former MOT atom's. A very efficient instantaneous cooling collision.

As the ion cools its secular amplitude is reduced, eventually becoming smaller than the finite extent of the MOT. At that point the MOT is no different from a buffer gas according to the ion's perspective. Therefore, collisions will eventually frequent the ion's new (reduced) turning points ultimately resulting in atom-ion rf heating. Thus the ion is bound to have an equilibrium secular amplitude less than but approximately the size of the MOT, which corresponds to equilibrium ion energies equivalent to temperatures above that of the MOT's temperature [37].

Shortly after we published Ref. [37], V. Vuletić's MIT hybrid trap group published a paper [43] on the atom-ion rf heating fundamental limit to sympathetic cooling. They found that including the long-range interaction potential, Eq. (2.22), in the atom-ion collision between an atom that approaches an ion initially at rest on the LPT nodal line leads to absorption of energy from the rf field characterized by the energy scale

$$W_0 = \frac{r_c}{R}\left(\frac{8m_N}{m_N+m_I}\right)^{5/6}\frac{E_R}{(3q_r)^{2/3}} \tag{5.2}$$

per collision. In Eq. (5.2) the ion collides with the atom at position r_c relative to the trap's center. The parameters R and E_R are the characteristic length $R=(C_4/m_I\omega_r)^{1/6}$ and energy $E_R=(1/2)m_I\omega_r^2R^2$ scales, where the magnitude of the long-range interaction equals the total pseudopotential energy [43]. Their study suggested that sympathetic cooling within a hybrid trap cannot result in ultracold translational temperatures as a consequence of this atom-ion rf heating. We reached similar conclusions in our study [37], which also considered the limiting factors due to ion-ion rf heating too. Additionally, they concluded that light atoms like Na and Li yield the least atom-ion rf heating, making them the best candidates for sympathetic cooling, which is qualitatively consistent with Major and Dehmelt's original model [165].

5.2 SIMON user programming[1]

As originally discussed in Ref. [37], the SIMION 7.0 software uses a fourth order Runge-Kutta method to numerically solve for the ion trajectories generated by the fields produced by the Paul trap's electrodes and the Coulomb repulsion between ions [142, 180]. As a result, the program simulates the fully dynamic potential and generates time dependent

[1]The majority of the text and figures from this section are directly reproduced from our manuscript [37] with permission. Copyright 2012 The American Physical Society.

trajectories including the slow secular motion and the fast micromotion.

We have written a script for our LPT's specific electrode geometry, the vacuum chamber, and our ion detection system (as described in Secs. 4.3.3 and Sec. 4.3.6). The SIMION software not only allows the user to build custom electrode geometries, but also contains a user programming interface that can be customized to control time-dependent fields, ion-neutral collision effects, and initial conditions [181]. The ion motion and electrode models are visualized by the SIMION graphical user interface, whose output was shown in Figs. 4.62, 4.72, and 4.74.

Our single trapped ion simulations are always initialized at the center of the trap with an initial azimuthal and polar velocity angle of 45°. In multi-ion simulations, the ions' initial velocity directions are isotropically distributed. For the results presented in this chapter, the energy of an ion at $t = 0$ s is always set to the mean energy associated with the temperature of the neutral gas from which the ion is born.

The current version of the program allows the user to initialize the cloud in a cylindrical or a spherical isotropic distribution that models PI loading from the background gas or MOT, respectively. Additionally, the user can specify a $t = 0$ s creation temperature and the ions will be assigned creation speeds that adhere to the MB distribution associated with that temperature via a Monte Carlo accept and reject method (MCAR) [182].

The program's iterative time step Δt is continually adjusted such that the ion moves a specified number of grid units per time step. This is specified by the SIMION parameter called the "computation quality" [142]. Typically, $\Delta t \sim 10^{-3} - 10^{-1}$ μs $<$ rf period ~ 1 μs. Should too small a computation quality be chosen, the ion simulation accumulates numerical errors that yield an erroneous runaway heating effect, as seen in Fig. 5.1. However, increasing the computation quality parameter increases the computational intensity. Due to the simulated two-body Coulomb interaction associated with

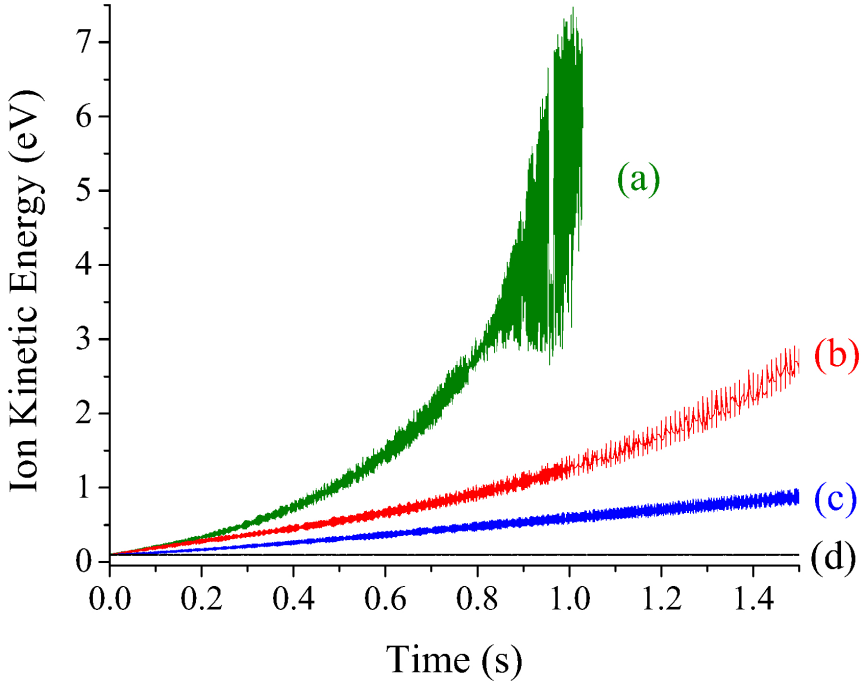

Figure 5.1: Single ion simulated in the absence of heating mechanisms (ideal vacuum conditions) with progressively larger computation qualities for curves (a) - (d), respectively. For curve (a) with a computation quality of 7, numerical errors accumulate resulting in larger and larger secular trajectories and an erroneous runaway increase in time-averaged kinetic energy. For curve (d) with a computation quality of 150, the ion's mean kinetic energy remains constant.

multi-ion simulations, the computation time scales like N_I^2, making simulations of more than 500 ions very computationally intensive.

Unless otherwise specified, the kinetic energy values and root mean squared positions reported throughout this chapter are time averaged over ≈ 15 secular oscillations queried once per time step, as defined in Eqs. (4.78) and (4.79), respectively.

The program simulates three environments: ideal vacuum conditions, a hot low-density neutral background gas, or both a background gas and high-density cold MOT. When running in either of the non-ideal vacuum environments, the probability of an ion-neutral collision is calculated within each time step according to

$$\mathscr{P}_{\Delta t} = 1 - e^{-nk_x\Delta t} \tag{5.3}$$

where n is the density of the gas [181, 183]. In Eq. (5.3), the program uses either the background gas's density or the MOT's density for n depending on the mode of operation and the instantaneous position of the ion. For example, it uses the MOT density if the ion is inside a small sphere specified by a user input parameter r_a, the size of the MOT. The parameter

$$k_x(E) = \sigma_x(E)v = \sigma_x(E)\sqrt{\frac{2E}{\mu}} \tag{5.4}$$

is the instantaneous rate coefficient. As defined in Eqs. (2.75) and (2.26), σ_x is the semiclassical power-law ion-neutral elastic ($x = \text{el}$) or non-radiative charge exchange ($x = \text{ce}$) scattering cross sections,[2] which are a function of the instantaneous collision energy E, instantaneous relative velocity v, and reduced mass μ. The cross sections' power-law coefficients used in our simulations are the same ground state Na cross sections previously discussed in Sec. 2.2.4 from Refs. [68, 71].[3] Although our earlier sympathetic cooling studies presented in this chapter have assumed that there is a negligible Na-Ca^+ charge-exchange cross section [71], later experimental work suggests otherwise [39].

The excited state Na^* has larger cross sections due to the larger polarizability C_4. A more accurate simulation model would use the average of the excited state and ground state cross sections, since the MOT is made of a mixture of excited and ground state atoms. However, the mean cross sections are at most a factor of 1.4 larger than the ground state one, which is not much of a difference.[4] Having only used the ground state cross sections

[2]Technically, Eq. (2.75) is for the *total* cross section, but because the $\sigma_{\text{el}} \gg \sigma_{\text{ce}}$ we can make the approximate that $\sigma_{\text{tot}} \approx \sigma_{\text{el}}$ and $k_{\text{ia}} \approx k_{\text{el}}$.

[3]For the Na-Ca^+ elastic cross section we just use the smaller C_{tot} value associated with the $a\,^3\Sigma^+$ state.

[4]Not using the mean cross section was not a strategic choice, we just did not think of it at the time.

simply means that we can think of the simulation results presented here [37] as a worst case scenario or lower bound on cooling efficiency.

The program decides whether or not an instantaneous collision event has occurred during each time step by generating a random number and comparing that number to the current value of $\mathscr{P}$ from Eq. (5.3). If the random number is less than the current value of $\mathscr{P}$ the simulation assumes that there was no collision, if greater than $\mathscr{P}$ the simulation assumes a collision event has occurred and adjusts the ion's instantaneous velocity accordingly [181, 183].

When the program decides a collision has occurred, the neutral atom's initial speed and direction are chosen by random number generation. The generated speeds adhere to the Boltzmann distribution and the initial direction is isotropically distributed. The ion's post-collision velocity during a charge-exchange collision is determined by swapping the ion's current velocity with that of the randomly generated velocity of the neutral atom. In an elastic collision, within the center of mass frame, the post-collision velocity of the ion is calculated according to Eq. (2.7), where the scattering angle is chosen using MCAR with a pseudo-hard-sphere differential scattering cross section. The ion's azimuthal scattering angle is isotropically distributed and the COM polar angle θ is determined by the program such that it adheres to the distribution function described by Eq. (2.13).[5]

There is a precedent for using a hard sphere model in these types of simulations [90, 183–185]. However, when similar systems have been analyzed with a full quantal treatment (e.g., Yb-Yb^+), the differential cross sections have not been found to be isotropic within the temperature regime being considered (10^{-3} to 10^3 K) [72]. This has also been

[5] All the various randomly generated distribution functions [Boltzmann, isotropic, $\rho(E,\theta)$] are created via MCAR [182].

observed experimentally [166, 181].[6] A fully quantal treatment considers the higher order partial wave contributions, which generally results in a differential cross section that favors forward scattering[72]. To improve upon the hard sphere approximation, we still use a rectangular differential cross section, but it is only nonzero for angles less than 60°, which we call the pseudo-hard-sphere differential cross section. When results were compared using a true isotropic hard-sphere differential scattering cross section, we found thermalization times to be slightly shorter, but equilibrium energies to be approximately unchanged.

The settings for all simulations, unless otherwise specified, are the following: the Na MOT is concentric with the Paul trap (where there is zero micromotion amplitude), $T_{MOT} = 1$ mK (10^{-7} eV), $P_{back} = 1 \times 10^{-9}$ Torr, and $T_{back} = 1000$ K (0.1 eV). The LPT settings used were $V_{end} = 35$ V, $V_{rf} = 40$ V for Na^+ (or 70 V for Ca^+), and $\Omega = (2\pi)708$ kHz, as defined in Sec. 4.3.3. These values were chosen to match closely with our optimal experimental settings and actual trap geometry.

5.3 Sympathetic cooling results

5.3.1 Single ion simulations[7]

Our simulations, originally discussed in Ref. [37], reproduce results consistent with the existing Paul trap literature. For example, under ideal vacuum conditions, with no excess micromotion, and using optimal stability parameter settings, a single ion exhibits no heating, as seen in Fig. 5.2 curve (b).

When interacting with only a hot low-pressure neutral background gas the ion (initially

[6] The system must be in the $\lesssim 100$ nK regime to exhibit pure s-wave scattering described by Eq (2.44), where $a \ll \lambda_{dB}$.

[7] The majority of the text and figures from this section are directly reproduced from our manuscript [37] with permission. Copyright 2012 The American Physical Society.

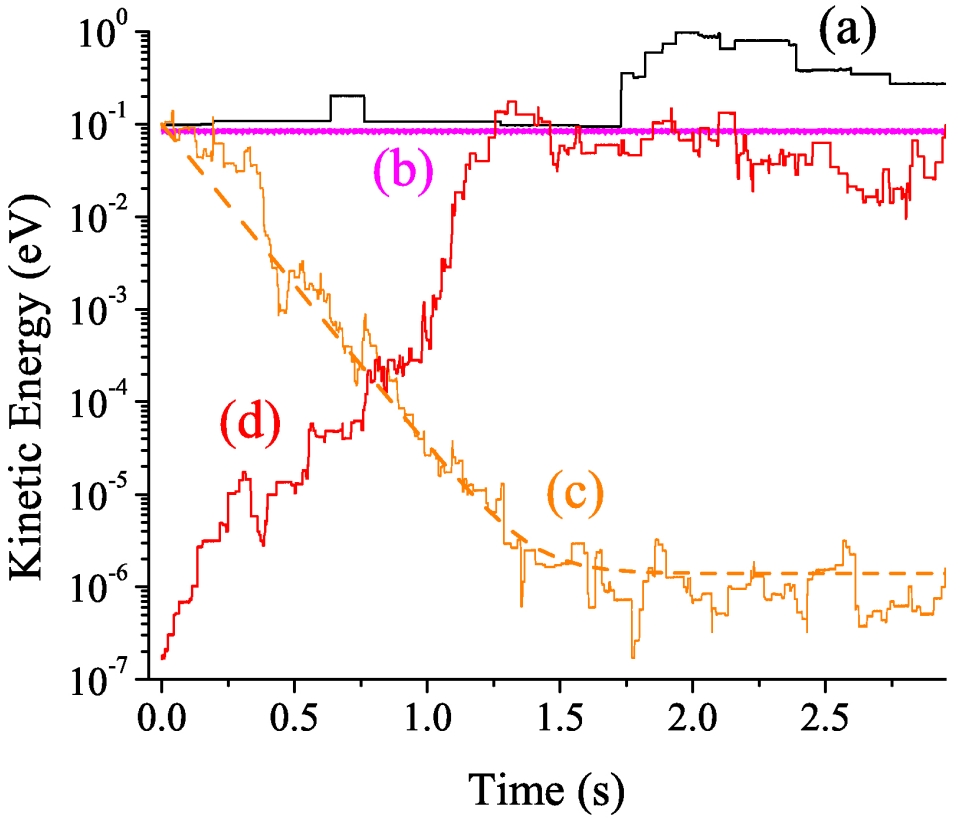

Figure 5.2: Plot of kinetic energy versus time of trapped single ion in different program environments. Curve (a) is from a Na^+ ion within background Na gas only (black). Curve (b) is from a Na^+ ion under ideal vacuum conditions (magenta). Curve (c) is from a Na^+ ion cooled by a MOT (orange). The curve is fit using Eq. (5.5). Curve (d) is from an initially cold heavy ion with $m_N/m_I \approx 3.8$ (red) heated by a MOT under the same neutral gas conditions as (c).

at the mean energy associated with the background gas's temperature) heats up due to atom-ion rf heating and instantaneous collisional heating. Additionally, a single ion has far fewer collisions with the background gas as compared to its interaction with both a background gas and a cold high density MOT. For example, 21 collision events with a background Na gas can be clearly seen as discontinuities in Fig. 5.2 curve (a). In contrast, curve (c) shows sympathetic cooling (from ~ 0.1 eV to $\sim 10^{-6}$ eV) after 256 elastic scattering collisions and 48 charge exchange collisions with atoms from the modestly dense

($n_{\mathrm{MOT}} = 5 \times 10^9$ cm^{-3}) and cold MOT [$T_{\mathrm{MOT}} = 1$ mK ($\sim 10^{-7}$ eV)]. We see that the hybrid trap can indeed yield sympathetic cooling consistent with the model in Eq. (5.1) from Ref. [60].

If the mass ratio is $m_N/m_I > 1.55$, atom-ion rf heating collisions with the cold MOT can actually heat an initially cold single ion, as seen in Fig. 5.2 curve (d). If the mass ratio becomes $m_N/m_I < 1$, atom-ion rf heating is reduced and greater cooling can be achieved, as depicted in Fig. 5.3, which shows the x_3 position of a single Ca^+ ion cooled under similar MOT conditions. As the Ca^+ ion is cooled the axial oscillations approach zero amplitude in accordance with Eq. (4.72).

Since the energy dependence in k_{el} is weak according to Eq. 2.76, we can approximate the net heating and cooling rates to be a constant κ. Therefore the time dependence of the ion's energy can be approximated as

$$E(t) \approx E_{\mathrm{final}} + (E_{\mathrm{initial}} - E_{\mathrm{final}})e^{-\kappa t}, \tag{5.5}$$

which our simulated ion's energy evolution follows in Fig. 5.2 curve (c).

We have found that the cooling rate and final temperature of the ions depend on several parameters with the MOT density being the most critical, due to the exponential n dependence in Eq. (5.3). Collisions with background gas atoms at pressures below 10^{-8} torr (easily obtainable experimentally) had a negligible effect on sympathetic cooling. We observe only one or two background gas collisions out of hundreds or thousands of MOT atom collisions at these densities.

As the MOT density increases, the thermalization time and equilibrium energy decrease. For example, a Ca^+ ion overlapped with a MOT of density 10^9 cm^{-3} as shown in Fig. 5.4 [curve (a)] does not thermalize until ~ 5 s and has a final energy of $\sim 10^{-6}$ eV, while Ca^+ cooled by a MOT with density 2.5×10^{10} cm^{-3} equilibrates at $\sim 10^{-7}$ eV in

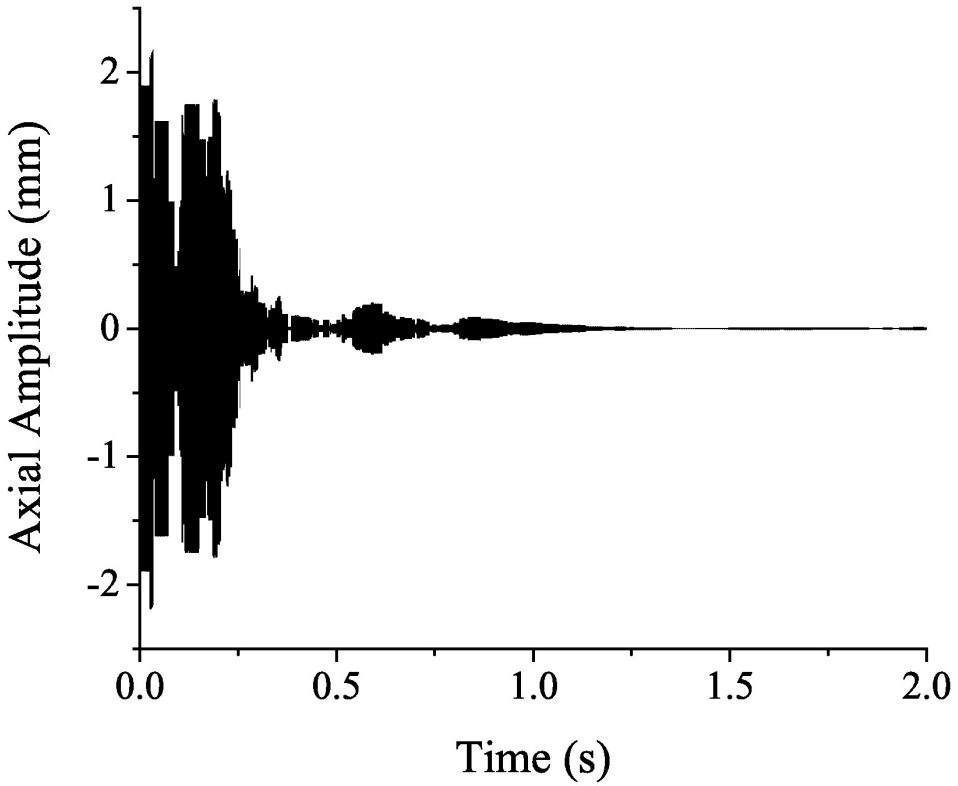

Figure 5.3: Plot of axial position of one Ca^+ ion relative to the trap's center versus time when overlapped with a MOT. As the ion is cooled the axial amplitude decreases.

~ 0.75 s [curve (c)]. A single Na^+ ion shows the same trend, as can be seen by comparing curves (b) and (d) in Fig. 5.4.

The jagged appearance of the curves in Fig. 5.4 can be attributed to the competing effects of instantaneous collisional heating, atom-ion rf heating, and instantaneous collisional cooling. The simulations show that the dominant heating mechanism is atom-ion rf heating. For example, only 7% of all elastic scattering collisions within the simulation associated with Fig. 5.4 curve (b) resulted in an instantaneous speed increase, i.e., instantaneous collisional heating. The infrequent number of instantaneous collisional heating events is likely due to the difference between the ion's equilibrium energy and the mean neutral atom energy associated with the MOT's temperature. Further support for this

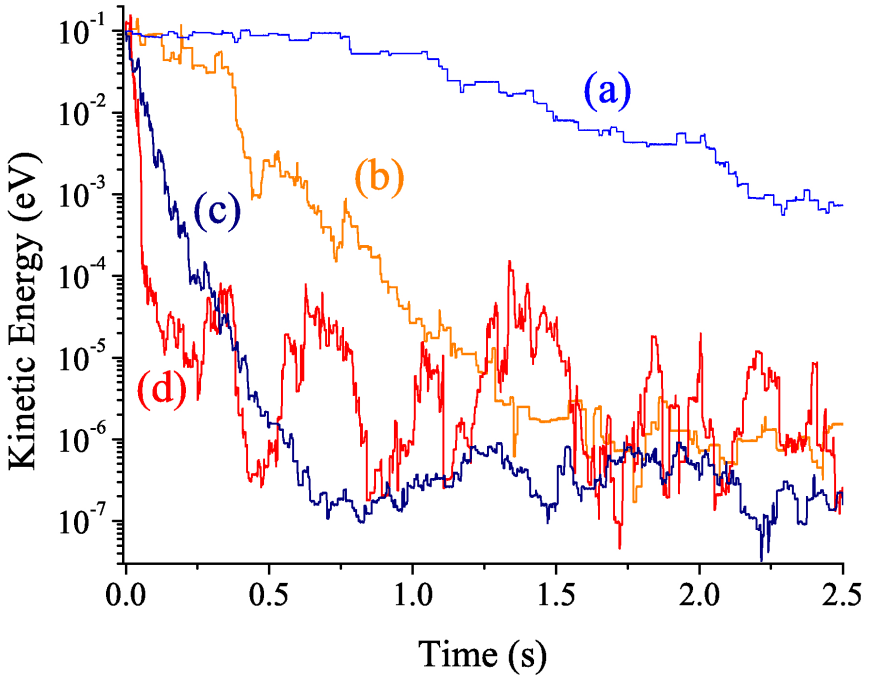

Figure 5.4: (Color online). Plot of kinetic energy versus time for a single ion showing the effect of MOT density on sympathetic cooling [$T_{MOT} = 1$ mK (10^{-7} eV) and $r_a = 1$ mm for all curves]. Curve (a) is from a Ca^+ ion cooled by a MOT with $n_{MOT} = 10^9$ cm^{-3}. Curve (b) is from a Na^+ ion cooled by a MOT with $n_{MOT} = 5 \times 10^9$ cm^{-3}. Curve (c) is from a Ca^+ ion cooled by a MOT with $n_{MOT} = 2.5 \times 10^{10}$ cm^{-3}. Curve (d) is from a Na^+ ion cooled by the same MOT density as (c). Higher MOT density results in lower final energy and faster thermalization.

explanation comes from the fact that if the ion's equilibration time and equilibrium energy is lower, the percentage of instantaneous collisional heating events increases (e.g., 20% within the simulation associated with $n_{MOT} \sim 5 \times 10^{11}$ cm^{-3} shown in Ref. [37]).

Due to the reduced atom-ion rf heating associated with a smaller mass ratio m_N/m_I we observed that sympathetically cooled Ca^+ outperfomed Na^+, with respect to equilibrium ion energy [as seen by comparing Fig. 5.4 (c) and (d)]. This suggested that the additional charge-exchange cooling pathway only available for the Na^+ sympathetic cooling case $m_N/m_I = 1$ may not be as important as the reduced atom-ion rf heating associated with the unequal mass $m_N/m_I < 1$ case.

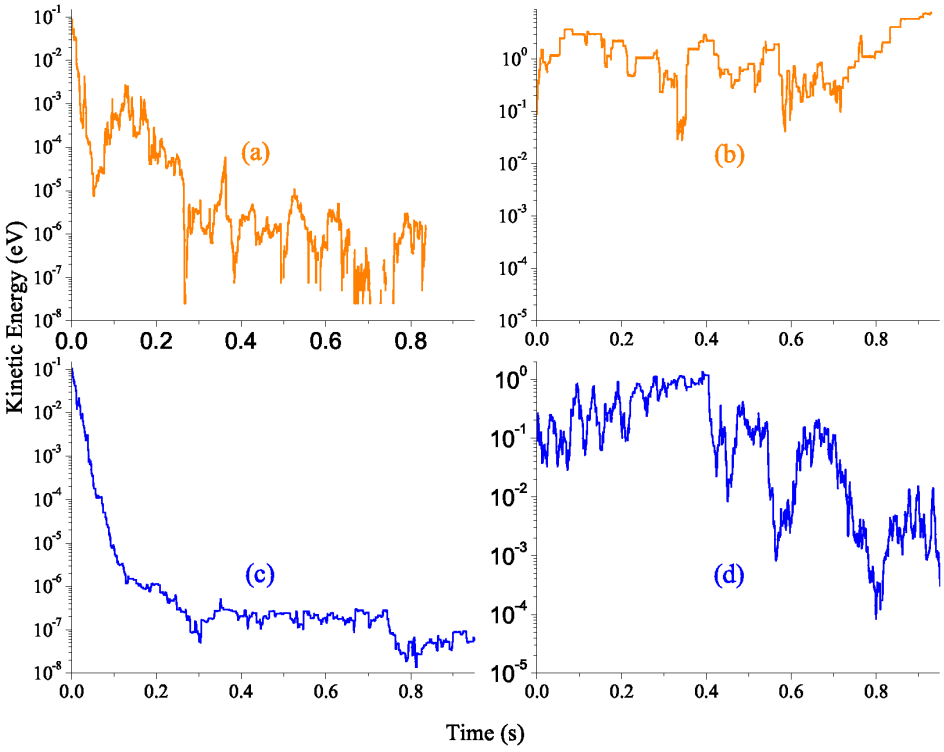

Figure 5.5: Plot of kinetic energy versus time for (a)-(b) single Na^+ (orange) and (c)-(d) single Ca^+ (blue) showing the effect of q_1 on sympathetic cooling and its dependence on ion species. (a) and (c) have the Paul trap stability parameter $q_1 \approx 0.4$, while (b) and (d) are at an increased V_{rf} resulting in Paul trap stability parameter $q_1 \approx 0.75$. The larger atom-ion rf heating associated with $q_1 \approx 0.75$ overwhelms the MOT cooling.

The atom-ion rf heating increases with increasing V_{rf} due to the micromotion's dependence on the stability parameter q_1, as seen in Eq. (4.71). By varying V_{rf} we found that absolute V_{rf} values were not a good metric for atom-ion rf heating rate comparison between different ion species, but q_1 was [169]. Figure 5.5 shows MOT sympathetic cooling of Na^+ or Ca^+ with $q_r = 0.4$ (low q_r) or $q_r = 0.75$ (high q_r). The difference between the left plot (low q_r) and the right plot (high q_r) for a given ion species is almost entirely due to atom-ion rf heating. The sympathetic cooling cannot combat the heating from high rf amplitudes. Therefore, it is necessary to use low q_1 values ($q_1 \lesssim 0.4$), provided the trap depth is not lowered below the initial energy of the ion. Single ion experiments within

hybrid ion-BEC traps have drawn similar conclusions [56].

Initially the ion's equilibrium energy decreases with decreasing MOT temperature, but not indefinitely (see Fig. 5.6). In fact, at low enough MOT temperatures the ion actually begins to equilibrate at higher energies. Again, at a given MOT temperature Ca^+ is cooled to a lower final energy than Na^+ due to reduced atom-ion rf heating.

As the temperature of the MOT is lowered each elastic head-on hard-sphere ion-neutral collision results in a greater change in speed for the ion on average, initially leading to greater cooling and lower equilibrium temperatures. Simultaneously, the ion-neutral collisions with increasingly colder atoms can also significant disruption of the ion's micromotion, resulting in more frequent atom-ion rf heating collisions. Hence, as the MOT temperature is lowered the atom-ion rf heating rate increases as well, resulting in a non-monotonically decreasing equilibrium energy. In addition, we found that lowering the MOT's temperature had little effect on decreasing the thermalization time of the ion.

The initial ion energy was varied as high as 0.7 eV ($\sim 10^4$ K), which resulted in little to no difference in final energy and thermalization time. DeVoe found similar results for buffer gas cooling of a single ion [173].

We found that with a fixed number of Na atoms in the MOT ($N_a = 5 \times 10^7$), a smaller MOT radius cooled faster and lower than a large MOT radius, i.e., increased MOT density is favorable despite decreased initial overlap between the MOT cloud and the single ion trajectory volume (i.e., the volume occupied by the ion's 3D orbit). The ion's initial secular axial amplitude was ≈ 2 mm (always larger than the MOT radii tested, e.g., 0.25 mm-1.5 mm).

This counter-intuitive result can be explained by the fact that with a higher density in the exponent of Eq. (5.3), there is a higher collision rate which is apparently more important than the reduced percentage of time spent initially overlapped with the MOT. Also, in the

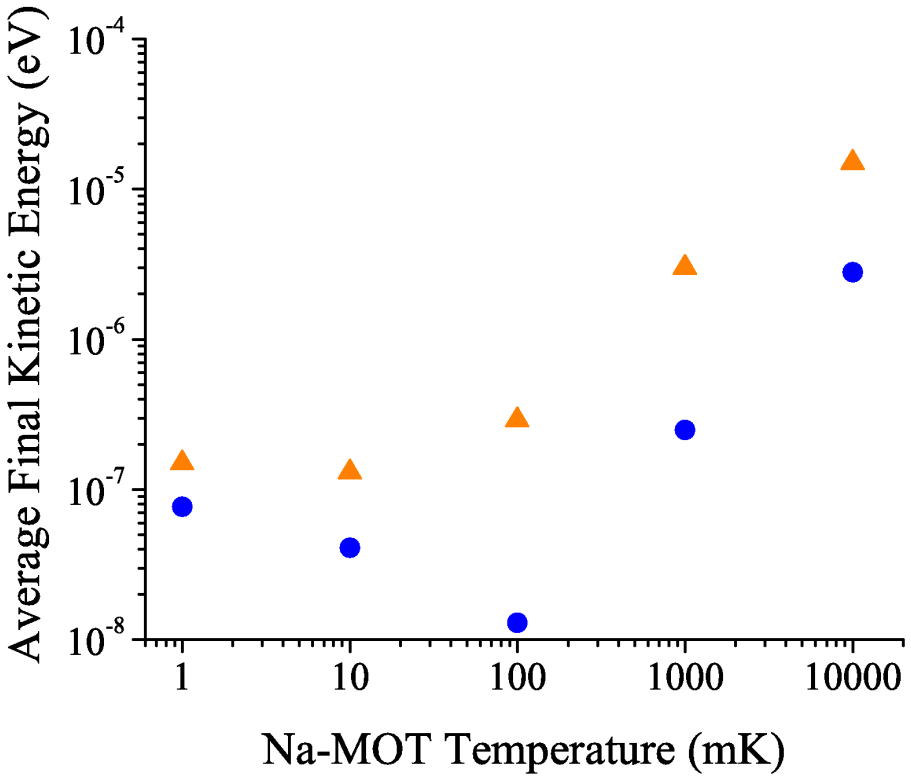

Figure 5.6: Plot of final thermalized energy of a single Ca^+ ion blue circles and Na^+ orange triangles versus the MOT's temperature. As the MOT temperature is lowered the final mean energy of the ion decreases, but not indefinitely, since the atom-ion rf heating rate increases as well.

cooling model from Sec. 5.1, the instantaneous collisional cooling can always occur at the center of the trap where there is little to no micromotion, so having a larger MOT should not be as important as having the MOT localized at the LPT's center. Furthermore, as we speculated in Sec. 5.1, the equilibrium secular amplitude of the sympathetically cooled ion should be reduced by using a smaller MOT.

To increase overlap without changing MOT characteristics, we compressed the initial ion trajectory volume by increasing the end segment voltage V_{end} (although the initial amplitude was still larger than the radius of the MOT). We found that increased overlap offered little improvement in thermalization time and final energy.

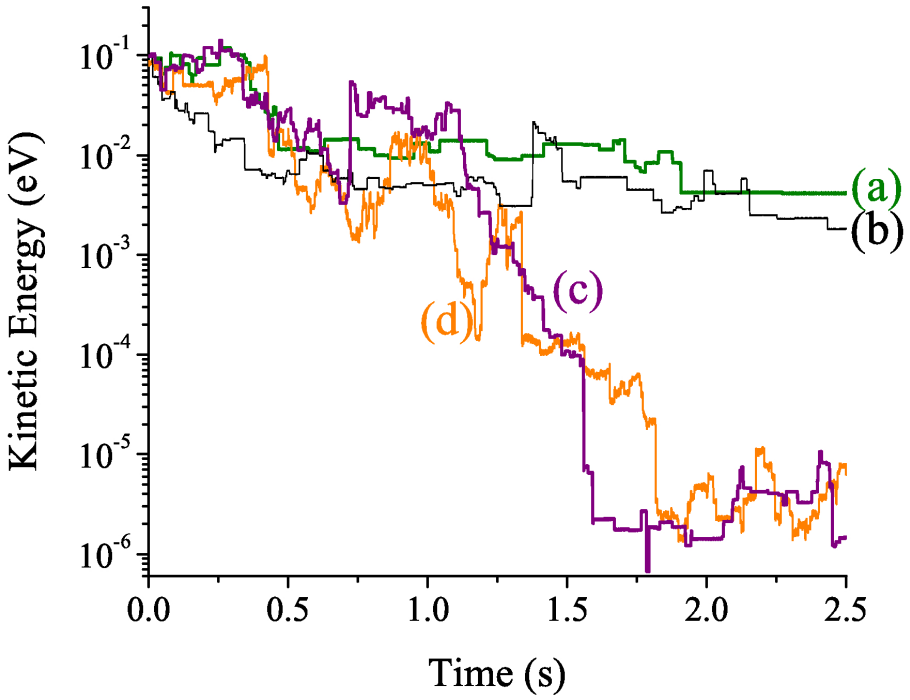

Figure 5.7: Plot of kinetic energy of a single Na^+ ion versus time showing the effect of MOT-Paul Trap concentricity on sympathetic cooling. Curves are from a MOT ($r_a =$ 1 mm and $n_{\mathrm{MOT}} = 5.7 \times 10^9$ cm^{-3}) (a) located 2 mm off center axially (green), (b) 1.5 mm off center axially (black), (c) 1 mm off center axially (purple), and (d) on center (orange). The ion's equilibrium energy is sensitive to reduced MOT concentricity greater than one MOT radius.

Overlap is improved automatically as collisions with the MOT cool the ion and decrease the ion's oscillation amplitude, as seen in Fig. 5.3. The fact that the ion's final energy is insensitive to MOT overlap is consistent with the lack of sensitivity to the initial ion energy, given the connection between ion energy and secular oscillation amplitude described by Eq. (4.72).

For ions with no laser-excitable transitions, such as Na^+, overlapping the MOT with the center of the ion trajectory volume becomes experimentally challenging, because there is no fluorescence to visually confirm ion-neutral concentricity. Therefore, we simulated the cooling of a single Na^+ ion by a non-concentric axially displaced MOT, as discussed in

Fig. 5.7. The MOT's ability to sympathetically cool is reduced if it is not concentric with the LPT's potential energy minimum. The ion will more frequently undergo collisions at its secular turning point resulting in more frequent atom-ion rf heating collisions, as discussed in Secs. 4.3.8 and 5.1.

Furthermore, as the cooled ion's axial amplitude decreases, the equilibrium energy is now limited (at best) to the energy equivalent to the secular oscillation amplitude that equals the distance between the edge of the MOT and the center of the ion trajectory volume. Therefore, the LPT-MOT concentricity significantly impedes the cooling efficiency once the MOT displacement is greater than one MOT radius, as seen in Fig. 5.7 curves (a) and (b). A secondary consequence of the offset is a reduction in overlap resulting in a smaller effective collision rate. Reference [56], using an ion-BEC hybrid trap, experimentally demonstrates that the effective collision rate is rather sensitive to ion-neutral concentricity which is in qualitative agreement with our findings. We also experimentally demonstrated that concentricity affects cooling efficiency in Ref. [38] and discussed later in Sec. 5.3.4.

5.3.2 Multiple ion simulations[8]

When considering multi-ion simulations we wanted to incorporate the complexity of the extra co-trapped MOT born Na_2^+ ions and MSRQ fields used to remove them, as discussed in Sec. 4.3.7. We believed that these additional ions and quenching fields were likely to affect our sympathetic cooling experiments because of OREA and possible sympathetic heating, as discussed in Sec. 4.3.7.

Fortunately, while sympathetically cooling and trapping 10 Na^+, we simulated the birth and simultaneous quenching of Na_2^+ ions and found the process did not impede the cooling

[8]The majority of the text and figures from this section are directly reproduced from our manuscript [37] with permission. Copyright 2012 The American Physical Society.

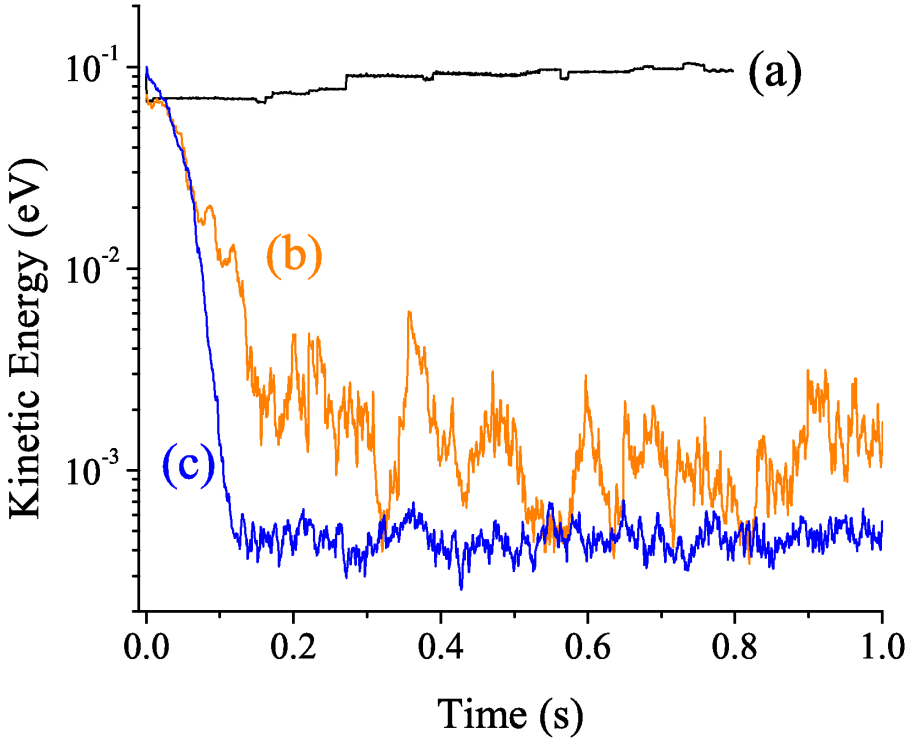

Figure 5.8: Plot of kinetic energy versus time for Na^+ (orange) and Ca^+ (blue). (a) 10 Na^+ ions with only a Na background gas ($P_{back} = 7 \times 10^{-9}$ Torr), (b) 10 Na^+ with 1 mK (10^{-7} eV) MOT $n_{MOT} = 5 \times 10^{10}$ cm^{-3} and r = 0.5 mm. (c) 10 Ca^+ under the same MOT conditions. Ten ions can be cooled to a few Kelvin, but not to ultracold temperatures.

of the 10 Na^+. Although an encouraging result, we should note that we could not simulate the actual Na_2^+ birth rate [158], because of computational limitations.

We find a dramatic difference in the hybrid trap's ability to sympathetically cool one ion (Fig. 5.2) compared to two or more ions (Fig. 5.8). The main factor limiting the equilibrium energy of cooled multiple co-trapped ions is ion-ion rf heating, although atom-ion rf heating still persists. We believe that as the ion cloud is reduced in size due to secular ampltudue decrease from sympathetic cooling, the ion-ion rf heating rate increases and a equilibrium between cooling and heating is reached, as illustrated in Fig. 4.89.

In the presence of only a background gas, atom-ion heating contributes to a mean energy

increase of 10 Na^+ seen in Fig. 5.8 curve (a) [similar to single ion results in Fig. 5.2, curve (a)]. The heating is not due to ion-ion rf heating since $\langle r_{\rm rms} \rangle$ is large enough that the ions are within the Mathieu regime [167] with $\Gamma_c \gg 1$ from Eq. (4.73).

Ten Na^+ (or Ca^+) ions [curve (b) and curve (c) of Fig. 5.8, respectively] cooled with a MOT density of $n_{\rm MOT} = 5 \times 10^{10}$ cm^{-3} do not equilibrate at energies equivalent to sub-Kelvin temperatures (the ions are only cooled to energies equivalent to a few Kelvin due to ion-ion rf heating). However, the MOT sympathetic cooling should cause a significant extension in trapping lifetime since the ions are cooled well below the pseudopotential's radial and axial trap depths defined in Eq. (4.61), as was seen experimentally in Refs. [38, 60] . Due to the ion-neutral mass ratio resulting in weaker atom-ion rf heating, Ca^+ equilibrates at a lower energy than Na^+. At this MOT density we found little difference in the equilibrium energies for 2, 5, or 10 sympathetically cooled ions.

When trapping and cooling multiple ions a cold, nearly crystallized center was found with one or two hotter atoms orbiting around the periphery (see Fig. 5.9). Attempts to improve overlap with the hotter orbiting ions by increasing the end segment voltage and placing a positive bias on all four rf segments (effectively squeezing the cloud and increasing the overlap), did not significantly decrease the equilibrium energy. The lack of improvement was consistent with the results discussed in the single ion case.

Decreasing the MOT temperature to 500 nK (6×10^{-11} eV) slightly lowered the final energy of the ions but did not increase the cooling capacity enough to crystallize the entire ion cloud. Only a high density MOT ($n_{\rm MOT} > 10^{11}$ cm^{-3}) can produce crystallization. Once cold enough to crystallize, we find a difference in final energies between the 2, 5, and 10 ion simulations. The minimum density needed for crystallization for 2 ions with a 100 μK (10^{-8} eV) MOT was 4×10^{11} cm^{-3}, 5 ions [shown in Fig. 5.10 curve (b)] required at least 8×10^{11} cm^{-3}, and 10 ions were never observed to crystallize, even at densities as

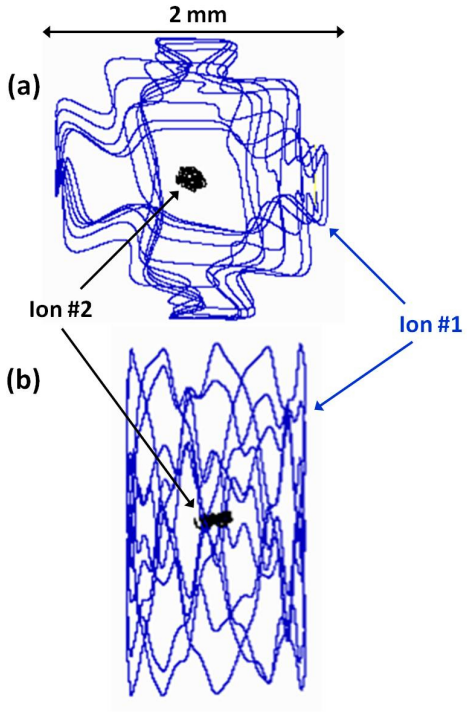

Figure 5.9: SIMION trajectories of two ions' equilibrating with the MOT (ion #1 in blue and ion #2 in black). (a) View along the axis of hybrid trap. (b) View from the side of the hybrid trap. The cooled ions initially result in a colder ion in the trap's center (ion #2) and a hotter ion (ion #1) in an orbit that is poorly overlapped with the MOT ($r_a = 0.5$ mm).

high as 10^{14} cm^{-3}. When the MOT density is above the required minimum crystallization MOT density, further cooling can be realized.

To support the claim that ion-ion rf heating is the mechanism that determines the final energy for sympathetic cooling of multiple ions, we examined the correlation between mean energy of the cooled ions and the ion cloud's $\langle r_{\rm rms} \rangle$ (see Fig. 5.11). While at initially large $\langle r_{\rm rms} \rangle$ and kinetic energy (i.e., within the Mathieu regime) there is little difference in the cooling by the high or low density MOT, except for small fluctuation due to atom-ion rf heating. As the $\langle r_{\rm rms} \rangle$ decreases, we begin to enter the chaotic regime; the heating rate begins to fluctuate as a function of the ion cloud $\langle r_{\rm rms} \rangle$ resulting in both a loss of clear position and energy correlation [shown by marker (1) in Fig. 5.11]. This could be thought

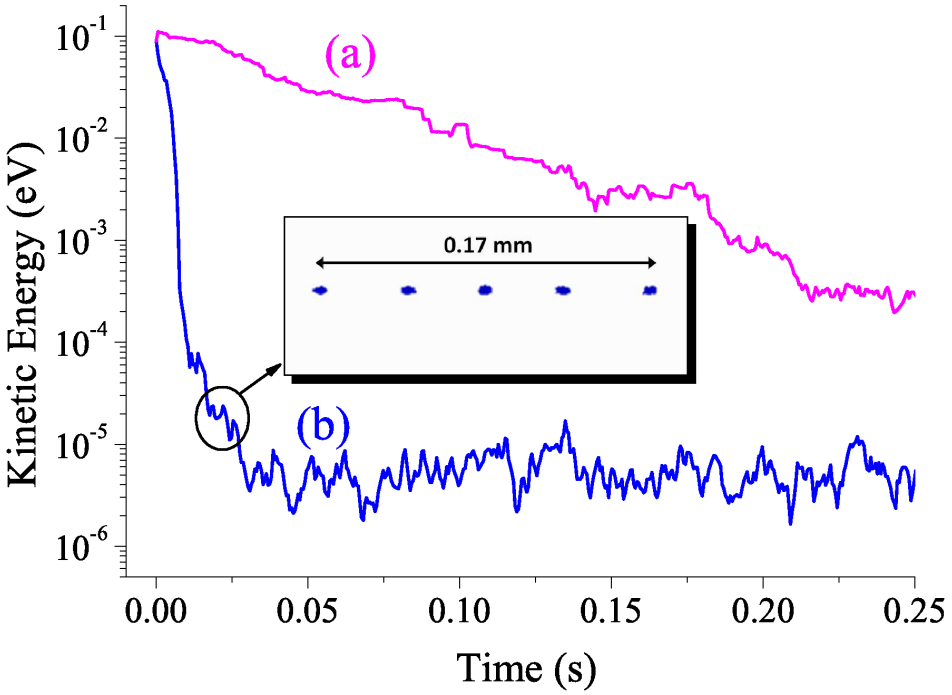

Figure 5.10: (Color online). Plot of kinetic energy versus time for 5 Ca^+ ions. Curve (a) shows sympathetic cooling without crystallization (magenta) where $T_{MOT} = 100\,\mu$K (10^{-8} eV) and $n_{\rm MOT} = 5\times10^{10}$ cm^{-3}. Curve (b) shows sympathetic cooling with crystallization (blue) $n_{\rm MOT} = 8\times10^{11}$ cm^{-3}, where the image shows SIMION's rendering of 5 crystallized ions.

of as an energy – $\langle r_{\rm rms}\rangle$ barrier. Only with the cooling capacity of the higher MOT density can the ion cloud move past the ion-ion rf heating barrier into an ion-crystal phase. Once in the approximately constant $\langle r_{\rm rms}\rangle$ crystal state [shown by marker (2) in Fig. 5.11] the ions can then be cooled further (by reducing the small oscillation amplitudes).

To specifically test the effect of atom-ion rf heating on crystallization, we simulated the sympathetic cooling of 5 ions that were more massive than Ca^+ ($m_I/m_N \simeq 7.52$), but assumed the same elastic scattering rate coefficient as that of Na-Ca^+. We found that these more massive ions cool to a lower final energy than Ca^+ (as can be expected with reduced atom-ion rf heating), but that the minimum MOT density required to crystallize the ions

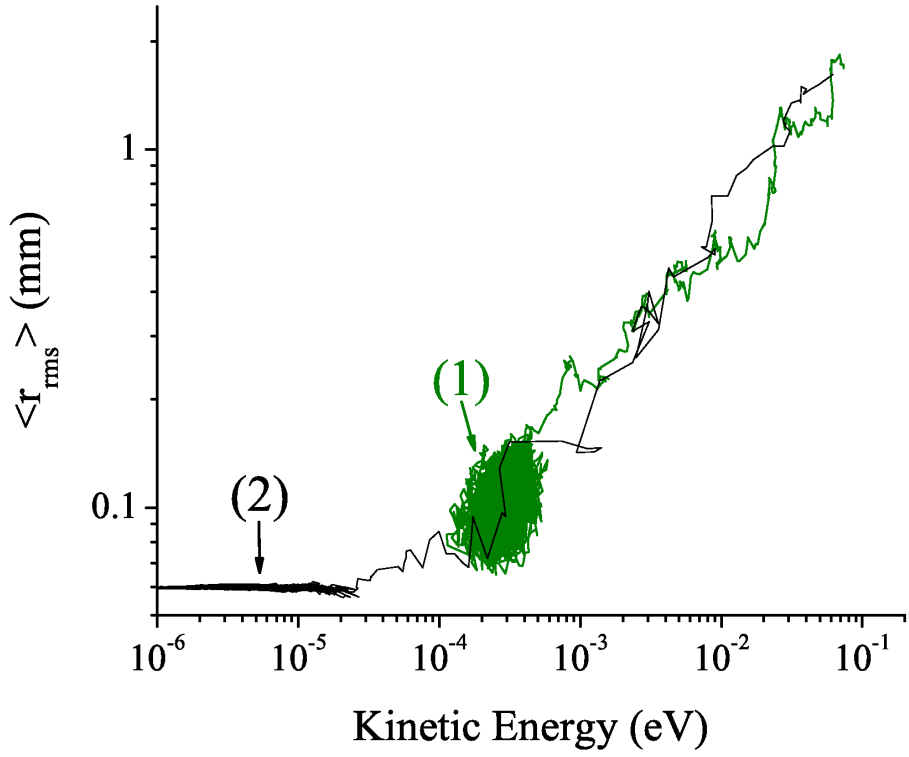

Figure 5.11: Plot of $\langle r_{\rm rms} \rangle$ versus 5 ions average kinetic energy for two MOT densities $n_{\rm MOT} = 5 \times 10^{10}$ cm^{-3} (green or light gray) which does not crystallize and $n_{\rm MOT} = 8 \times 10^{10}$ cm^{-3} (black) which does crystallize. Marker (1) denotes the ion-ion rf heating barrier, that is not breached at the lower MOT density. At higher MOT density crystallization is reached at marker (2).

is approximately the same. Hence, the only way to achieve cold or ultracold ion cloud temperatures is to have a high enough MOT density to overcome the ion-ion rf heating hurdle.

5.3.3 Simulation conclusions

In short, our simulations suggest that a MOT with a low number density $\sim 10^9$ cm^{-3} and modest 1 mK MOT temperature can cool a single ion to cold energies within seconds, even in instances of equal ion and neutral mass. The efficient single ion hybrid system sympathetic cooling should yield lower equilibrium temperatures than chilled noble buffer

gas sympathetic cooling ever could. This result should be of interest to the ion atomic clock community because cold ion atomic clocks typically consist of a single trapped ion.

To achieve the most effective cooling, we found that it is critical that the MOT be concentric with the ion cloud and as dense as possible. The MOT cooling rate is larger than the atom-ion rf heating rate for only part of the full range of stable $q_r < 0.4$ values. Decreasing the MOT temperature does decrease the final ion energy. However, it does not do so indefinitely, since the atom-ion rf heating rate also increases.

Modest MOT conditions can also sympathetically cool more than one trapped ion, although not to sub-Kelvin temperatures. Due to the total reaction rate's dependence on density, high MOT densities ($n_{\mathrm{MOT}} > 10^{11}$ cm^{-3}) or BEC densities are needed to overcome the ion-ion rf heating, crystallize the ions, and allow for the possibility of further cooling toward ultracold temperatures up to the fundamental cooling limit discussed in Ref. [43].[9] However, even at such large neutral atom number densities, crystallization appears to be experimentally feasible only for a small number of ions ($\mathrm{N_{ion}} < 10$).[10]

5.3.4 Experiment[11]

In the previous section we have considered the ion-neutral hybrid sympathetic cooling simulation results originally presented in Ref. [37]. Here we will discuss the sympathetic cooling experimental results originally presented in Ref. [38] for the Na^+- Na system. These results are also discussed in detail in Ilamaran Sivarajah's doctoral dissertation [138], so we only briefly outline the major results here.

[9] BEC peak number densities are typically $\sim 10^{13} - 10^{15}$ cm^{-3} [2, 9] and some of the largest Na MOT densities reported are $\sim 10^{11} - 10^{12}$ cm^{-3} for dual MOTs [122] and dark spot MOTs [186], respectively.

[10] The SIMION customized user programming scripts were developed by me. Both graduate students, I. Sivarajah and J. E. Wells, assisted in running the simulations, debugging, and interpreting the simulation results in Secs. 5.3.1 and 5.3.2.

[11] The majority of the text and figures from this section are directly reproduced from our manuscript [38] with permission.

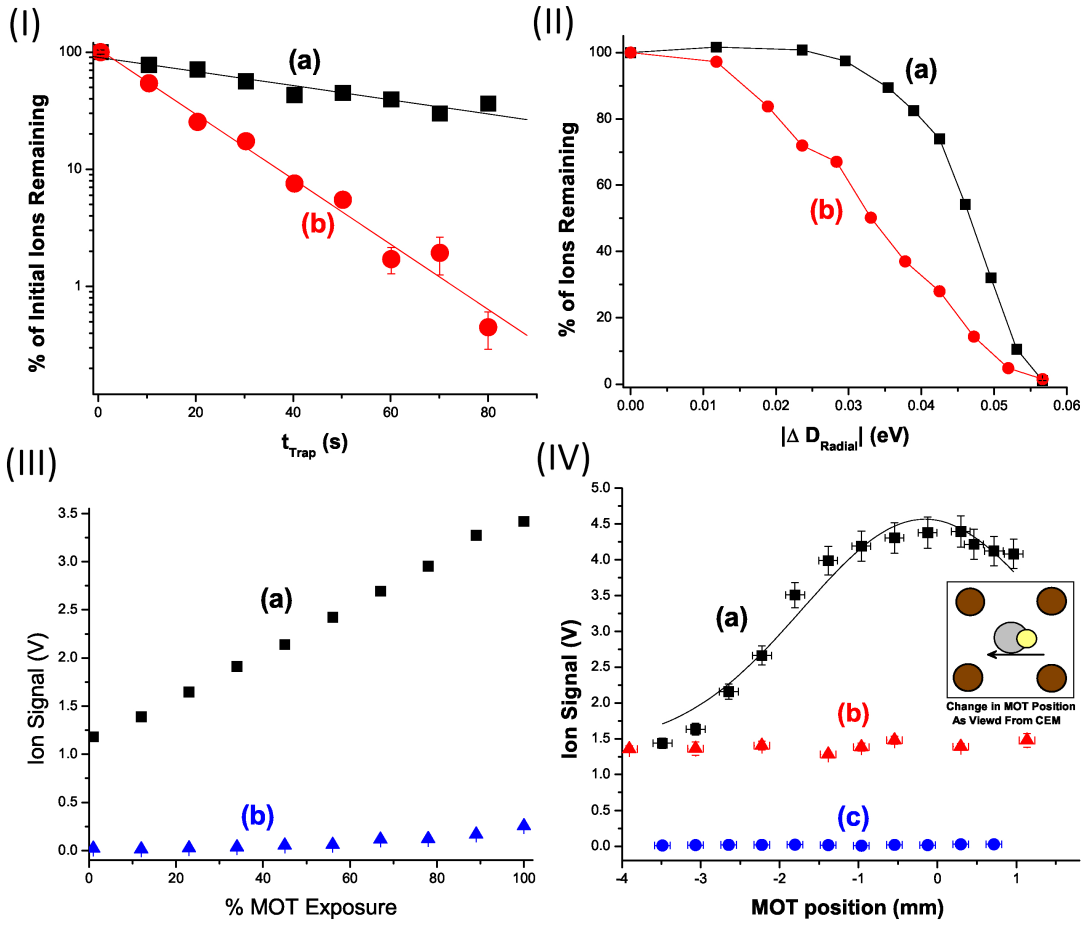

Figure 5.12: Panels (I) to (IV) (originally from Ref. [38]) show four different forms of indirect experimental evidence suggesting hybrid trap sympathetic cooling of $\sim$ 1000 ions.

Because direct thermometry of optically dark ions proved experimentally difficult, we demonstrated sympathetic cooling of dark Na^+ by four different inderect means, as shown in Fig. 5.12.

The ions were always PI produced from the background Na gas [discussed in Sec. 4.3.5] resulting in an initial time-averaged mean ion cloud kinetic energy of $\approx$ 1 eV (according to SIMION simulations).

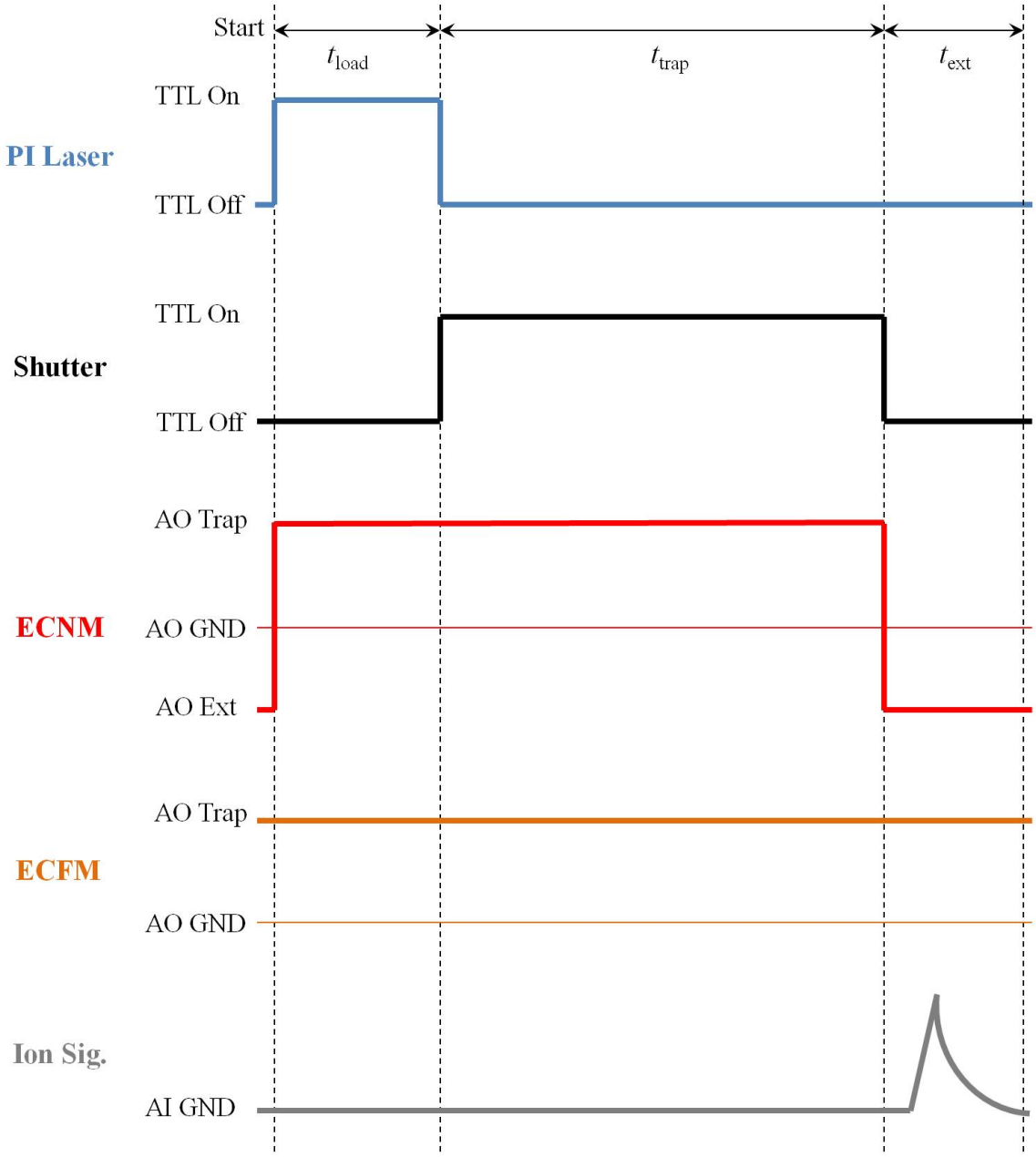

Figure 5.13: Schematic for LabVIEW controlled timing and voltage of the LPT loading, trapping, extraction, detection of ions, and MOT shutter, similar to Fig. 4.70. The ions are PI loaded from the background Na vapor for a fixed loading time t_{load} and held in the trap for a variable time t_{trap} until extracted for detection. While the ions are held in the trap they are exposed to the MOT by adjusting the shutter time. The shutter blocks one retro-reflected MOT beam [as seen in Fig. 4.2], thus turning on and off the MOT.

The MSRQ quenching of MOT-born Na_2^+ ions [discussed in Sec. 4.3.7] was continuously implemented during this process at $\omega_{rad} = (2\pi)35 \pm 1$ kHz and any residual background signal was subtracted from the final experimental values to eliminate any contributions from ions produced during the trapping time t_{Trap}. The experimental sequence of loading the LPT and sympathetically cooling the ion cloud with the MOT during t_{trap} is shown in Fig. 5.13. The LPT settings used were $\Omega_{rf} = (2\pi)729$ kHz, $V_{rf} = 36 \pm 1$ V, and $V_{end} = 35.0 \pm 0.5$ V, as defined in Sec. 4.3.3. Due to the closed electronic shell structure of Na^+ we cannot optically detect the ion cloud. Alternatively, the trapped ion population was destructively detected using a CEM and pre-amplifier, as discussed in Sec. 4.3.6. The type II Na MOT used in the experiment is characterized in Sec. 4.2.5.

As shown in Panel (I) of Fig. 5.12, Na^+ ions that were sympathetically cooled by the Na MOT [curve (a)] stayed in the trap longer than those trapped without cooling [curve (b)]. The sympathetic cooling reduced the effective LPT heating rate, thus extending the lifetime. Similar results were obtained for a smaller number of ions in Ref. [60] with Rb^+ ions and a Rb MOT.

The decay rates for MOT loaded and background gas loaded ion clouds are very similar. Therefore the temperature of the source of the neutrals from which the ions are produced has little effect on the trap lifetime or the final temperature, consistent with simulation results [37] discussed earlier in Sec. 4.3.5.

The second test (panel II) used to demonstrate sympathetic cooling measures the trap loss as a function of changing single particle trap depth D_r defined in Eq. (4.61) . When the ion cloud is cooled by the MOT the energy distribution of the ion cloud changes. Therefore, a hotter ion cloud should yield a larger fraction of ions lost after a sudden drop of the LPT's trap depth [187].

After t_{Trap} = 5 s with a $D_r = 0.6$ eV, the radial trap depth was lowered suddenly by

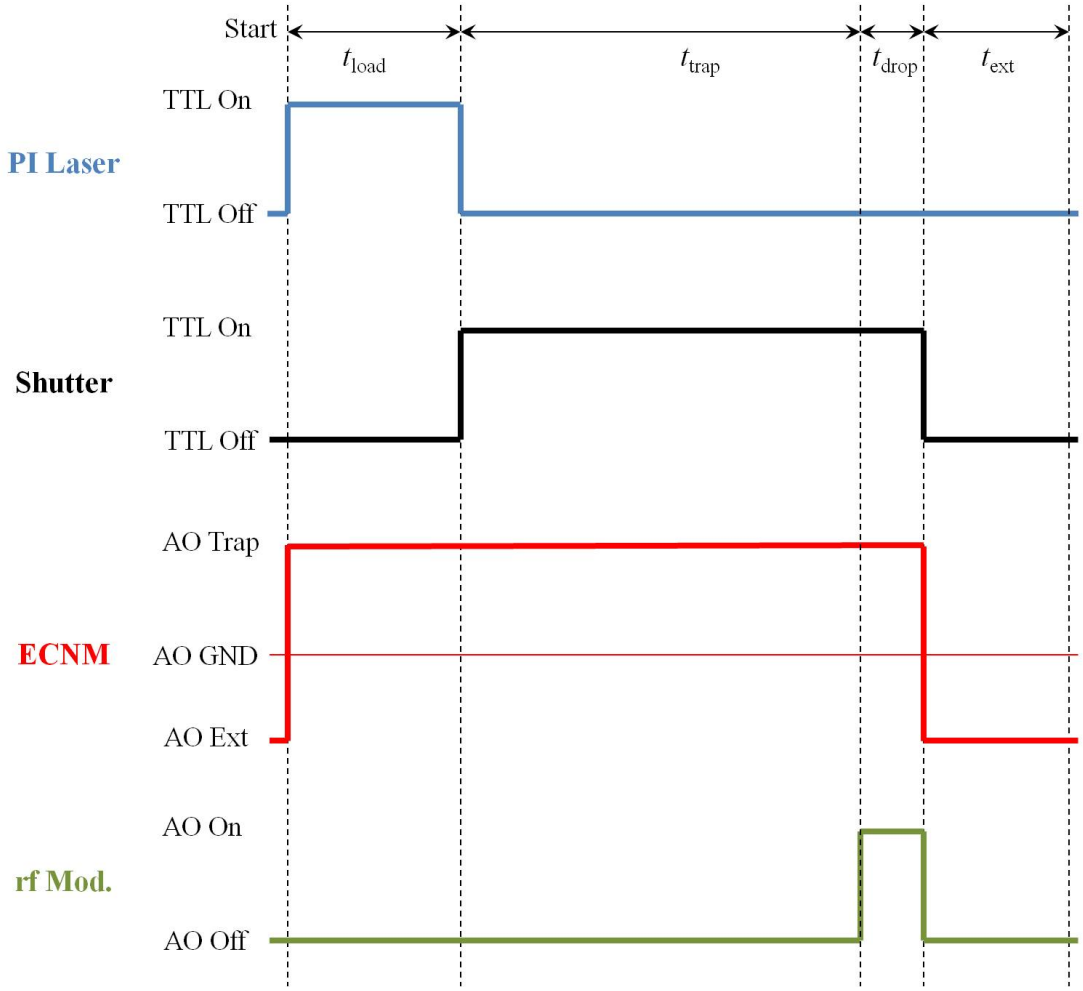

Figure 5.14: Same schematic as Fig. 5.13, but showing the modulation of the rf amplitude for a time t_{drop}, during which ions with energy greater than the suddenly reduced trap depth are evaporated out of the trap. The ECFM and Ion signal waveforms are the same as Fig. 5.13 and are not included here to reduce clutter.

ΔD_{Radial} for a 10 ms duration (t_{drop}) by modulating V_{rf} immediately prior to extraction. The experimental sequence is shown in Fig. 5.14. After suddenly lowering V_{rf} the ions were detected using the CEM. By varying the modulated depth, we are approximately measuring the ion cloud's speed cumulative distribution function. We call this the "depth-drop-test".

The results are shown in panel (II) of Fig. 5.12. As ΔD_{Radial} is increased, the ions that are not cooled [curve (b)] begin to evaporate from the trap at a much smaller ΔD_{Radial} than

when the ions are sympathetically cooled [curve (a)].

The third measurement (panel III) involved changing the percentage of trapping time an ion cloud was exposed to the MOT during a fixed $t_{\text{Trap}} = 8$ s. The ion signal increases linearly as a function of increased MOT exposure time, i.e., increased exposure time leads to a larger fraction of ions cooled below the trap depth, as seen in panel (III) of Fig. 5.12 curve (a). The second (blue) curve in panel (III) shows the corresponding unquenched negligible Na_2^+ background signal.

The overlap of the MOT with the ion cloud, which was demonstrated to have a significant effect on sympathetic cooling in Refs. [37, 56], was tested and provided a fourth and final test to demonstrate cooling (panel IV). Moving the MOT with respect to the ion cloud was accomplished by using a magnetic shim coil. The trapped ion signal is obtained after a fixed $t_{\text{Trap}} = 7$ s. As portrayed in panel (IV) of Fig. 5.12 (a), the ion signal reached a maximum as the MOT was translated across the $x_1 - x_2$ plane. When the sympathetic cooling efficiency is at a maximum the ion cloud temperature is reduced and a larger fraction of atoms will have energies below the trap depth after seven seconds of trapping, resulting in a relatively larger ion signal.

Although the ion cloud cannot be optically imaged, the relative MOT position at which the maximum ion signal occurs is likely where the MOT is concentric with the ion cloud. The top of the curve is fairly flat. We believe that this is due to the fact that sympathetic cooling is not significantly reduced by poor LPT-MOT concentricity until the center-to-center distance is $\approx r_a$, as was seen in our simulation result shown in Fig. 5.7. Once the center-to-center distance is greater than r_a the sympathetic cooling efficiency is reduced.

A Gaussian fit of curve (a) yields a full width at half maximum of 3.2 ± 0.2 mm. This measurement can be interpreted as an upper-bound of the size of the MOT along the MOT translation direction. The shim coil itself does not dramatically affect the ion signal, as seen

in curve (b), which corresponds to the same experimental conditions curve (a), but without any MOT cooling. Curve (c) shows that the background Na_2^+ ion signal remains negligible due to the continuous MSRQ.

5.3.5 Experiment conclusions

In Ref. [38], we demonstrated sympathetic cooling of Na^+ ions by a cold Na MOT in a hybrid trap via four different methods: trap lifetime, trap loss due to changing trap depth, variable MOT exposure time, and MOT overlap. Our results were qualitatively consistent with our previously discussed numerical simulation [37]. Although we did not take a direct temperature measurement, the sympathetic cooling of a large number of ions within the hybrid trap did not yield cold temperatures anywhere near the MOT's temperature, in agreement with our expectations from our simulation studies. Otherwise, we would have observed effectively infinite trapping lifetimes, given the large LPT trap depths ~ 1 eV.[12]

Our results were consistent with sympathetic cooling experiments on Rb^+ ion clouds conducted by Rangwala's group Ref. [60], who also could not achieve sub-Kelvin equilibrium temperatures. To the best of our knowledge, the only hybrid trap experiment that showed sympathetic cooling down to near sub-Kelvin equilibration was in Ref. [50], for a single trapped Yb^+ within a could neutral Rb BEC rather than a MOT. This is also qualitatively consistant with our simulation results [37], in that single ion cooling was predicted to be significantly more efficient than cooling of an ion cloud.

[12]The graduate students who participated in designing and conducting the experiments presented in Sec. 5.3.4 other than myself were I. Sivarajah and J. E. Wells.

Chapter 6

Measurements of collision rates

In this chapter we will discuss some experimental measurements of ion-neutral collision rate coefficients, whose theoretical treatment was previously discussed in Sec. 2.2.4. The first section of this chapter discusses some preliminary results on Ca^+- Na charge-exchange interaction and the second discusses the total collision rate for the Na^+- Na system.

6.1 Ca^+- Na measurement[1]

In Ref. [39] we found evidence of strong charge-exchange pathway between ground state Ca^+ and a mixture of excited Na^* and ground state Na. We were surprised by the experimental evidence, given our earlier theoretical work Ca^+- Na(3s) measurement that suggested slow charge-exchange reaction rates, as previously discussed in Sec. 2.2.4. However, new theoretical curves from the Côté group suggested a possible reaction pathway via an avoided crossing between the entrance channel $Ca^+(4s) + Na^*(3p)$ and exit channel $Na^+ + Ca(4^1P)$, as previously discussed in Sec. 2.2.4. However, more recent unpublished data from the Côté group may suggest that the exit channel may

[1]The majority of the text and figures from this section are directly reproduced from our manuscript [39] with permission. Copyright 2014 Springer Berlin Heidelberg.

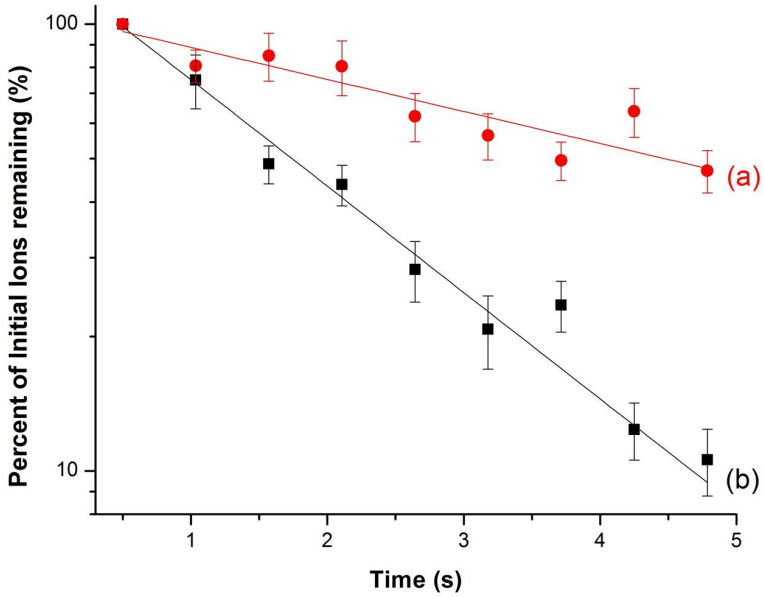

Figure 6.1: Originally from Ref. [39], showing decay of trapped (normalized) Ca^+ ion population vs. time. Curve (a) shows a slow decay due to inherent multi-ion heating mechanisms [discussed in Sec. 4.3.8] with the MOT off. Curve (b) shows that the Ca^+ ions decay faster due to a charge-exchange reaction when the Na MOT is turned on and Ca^+-Na collisions can occur. Solid lines show fits to a simple exponential decay.

actually be $Na^+ + Ca(3^1D)$.

The experimental discovery of this charge-exchange pathway was accidental. In an attempt to reproduce the sympathetic cooling decay curve shown in panel (I) of Fig. 5.12, but for the Ca^+- Na system, we observed the reverse effect - faster trap loss when the ion cloud was exposed to the MOT compared to when it was not, as seen in Fig. 6.1. We attributed the difference in net loss rate, $R_{ce} = 0.37 \pm 0.03$ Hz,[2] to an exothermic, non-resonant ion-neutral charge-exchange process and not some form of hybrid system heating.

In these measurements, $\sim 10^3$ Ca^+ ions[3] were loaded via EI with the electron gun

[2]This is a slightly different result than the one reported in Ref. [39]. We subsequently decided that it was better to determine the time constant by fitting a simple exponential decay without an offset fitting parameter, which slightly changed the fit value of the time constants in Fig. 6.1.

[3]The calibration of the CEM is described in Ref. [38], which utilizes the known PI rate of the Na MOT as a standard. A much more reliable calibration measurement based on the same standard was conducted in our more recent work [40], which is discussed in Sec. 6.2.4 of this dissertation.

oriented down the x_3 axis, as discussed in Sec. 4.3.5. The LPT used $\Omega_{\rm rf} = (2\pi)737$ kHz, $V_{\rm rf} = 37 \pm 1$ V, and $V_{\rm end} = 35$ V, as defined in Sec. 4.3.3. The type II Na MOT used in the experiment is characterized in Sec. 4.2.5.

According to Eq. (2.28) we can determine the charge-exchange reaction rate coefficient $k_{\rm ce}$ if we know the total collision rate $R_{\rm ec}$, as well as the number of ions N_I and atoms N_a within the volume of overlap V. In other hybrid trap experiments [42, 45, 46, 53, 54, 58] determining N_I and V can easily be measured using ion fluorescence measurements. However, with our current setup Ca^+ fluorescence measurements are not feasible and we use a destructive detection method described in Sec. 4.3.6.

Instead of optically imaging the ions we estimated the overlap. Because the ion cloud is larger than the MOT we can assume that $N_a \approx \tilde{N}_a \hat{\rho}_{22}$, the steady-state number of excited atoms (previously discussed in Secs. 4.2.5 and 4.2.7) and $V \approx V_{\rm MOT}$, the peak MOT volume (previously discussed in Sec. 4.2.5).

By performing a depth-drop-test [previously discussed in Sec. 5.3.4], we could determine the depth-drop at which half the ions were lost from the trap, as seen in Fig. 6.2. This gives us an estimate of the mean Ca^+ ion cloud's energy per ion to be ~ 0.7 eV, corresponding to ~ 5300 K.The initial ion temperature is larger than the neutral background gas temperature because most of the ions are not born at the LPT's center, as previously discussed in Sec. 4.3.5.

A significant fraction of the ions have an energy greater than the activation barrier height (~ 0.17 eV) seen in Fig. 2.20, so the reaction can proceed. From this energy measurement and the spring constant of the trapping potential, we can estimate the volume of the ion cloud V_I using Eq. (4.72). We determined the number of ions within the overlap volume by assuming a uniform ion density $n_I = 10^3$ ions$/V_I$, which means that $N_I = n_I V_{\rm MOT} \rho_I$. Here, $\rho_I \approx 0.9$ is the fraction of ions with energy greater than the activation barrier. Putting this

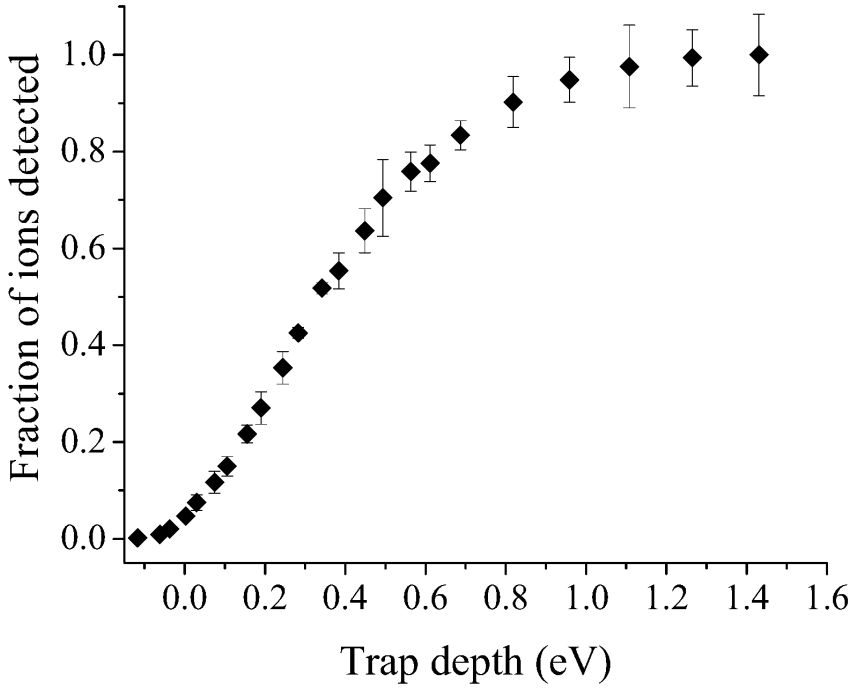

Figure 6.2: Depth-drop-test performed on (axial) EI loaded Ca^+ ions.

all together using Eq. (2.28), we arrive at

$$k_{\mathrm{ce}} = \frac{R_{\mathrm{ce}} V}{N_a N_I} \approx \frac{R_{\mathrm{ce}}}{\tilde{N}_a \hat{\rho}_{22} n_I \rho_I}, \tag{6.1}$$

for the charge-exchange collision coefficient.

From Eq. (6.1), we estimate the rate coefficient to be $\sim 7 \pm 6 \times 10^{-11}$ cm^3/s, which is two orders of magnitude smaller than the Langevin rate of $\approx 4.5 \times 10^{-9}$ cm^3/s according to Eq. (2.27). The discrepancy is comparable to that found by others for non-resonant charge exchange [53]. This discrepancy is not surprising, since based on the potential curves the Langevin assumption of unit efficiency in the reaction region is certainly too high. In the future, we plan to measure the rate constant's dependence on collision energy, as well as on ionic and atomic excited state populations.[4]

[4]The graduate students who participated in the designing and conducting the experiments presented in Sec. 6.1 other than myself were I. Sivarajah and J. E. Wells.

6.2 Na^+- Na measurement

In this section we will discuss our most recent measurement of the low-energy total Na^+-Na collision rate coefficient [40].

6.2.1 MOT and LPT experimental methods

Like the experiments presented in Secs. 5.3.4 and 6.1 we again load ions into the LPT, creating an ion cloud that is overlapped with the MOT, as depicted in Fig. 4.60.

MOT For the results presented here, we separately use the type I and II MOTs, previously introduced in Sec. 4.2.2. Again, we assume both MOTs have a spherical Gaussian spatial distribution, as previously discussed in Sec. 4.2.5. We also assume the trapped atoms adhere to a MB speed distribution with temperatures $T_{\mathrm{MOT}} = 0.38 \pm 0.18$ mK for the type I MOT and $T_{\mathrm{MOT}} = 2.3 \pm 1.0$ mk for the type II MOT, as previously discussed in Sec. 4.2.6. The type I MOT has a $\hat{\rho}_{22} \approx 33\%$ excited-state population and the type II MOT has $\hat{\rho}_{22} \approx 23\%$. We have established the excited state population using a two-level model-dependent measurement of the effective saturation intensity of the Na MOT [116]. The

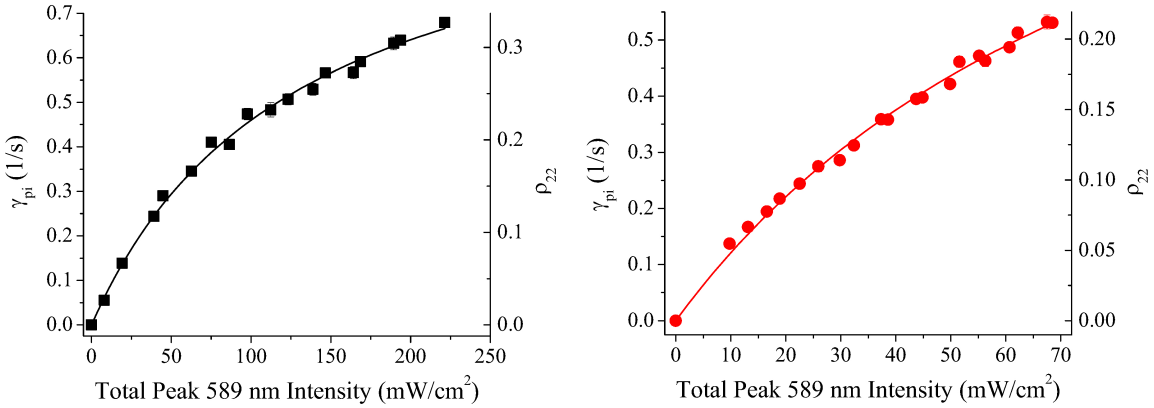

Figure 6.3: Model-dependent measurement of excited state population and fits to Eq. (6.2) for the type I MOT (left) and type II MOT (right).

results of that measurement is shown in Fig. 6.3 for both the type I and II MOTs.

According to Eq. (4.77), the photoionization rate per MOT atom $\gamma_{\rm pi}$ is linearly proportional to the fraction of MOT atoms within the excited state $\hat{\rho}_{22}$. By using a fixed PI intensity, $I_{\rm pi} = 103$ mW/cm^2 (type I) or $I_{\rm pi} = 259$ mW/cm^2 (type II), we can scan the excited state population by adjusting the total 589 nm MOT beam intensity $I_{\rm tot}$. Substituting Eq. (3.76) into Eq. (4.77) we get

$$\gamma_{\rm pi} = \left(\frac{\sigma_{\rm pi} I_{\rm pi}}{2h\nu_{\rm pi}}\right) \frac{I_{\rm tot}/I_s}{1+4(\delta/\Gamma)^2 + I_{\rm tot}/I_s} = A \frac{I_{\rm tot}/I_s}{1+4(\delta/\Gamma)^2 + I_{\rm tot}/I_s}, \tag{6.2}$$

where the detuning δ is independently determined and given in Table 4.2. Again, Γ is the natural linewidth of the atomic transition. By directly measuring $\gamma_{\rm pi}$ as a function of $I_{\rm tot}$, we can fit the data to Eq. (6.2) leaving A and I_s as fitting parameter.

Experimentally, the determination of $\gamma_{\rm pi}$ is accomplished by taking the difference of the measured total MOT loading rates with (γ_t) and without (γ_b) PI, where $\gamma_{\rm pi} = \gamma_t - \gamma_b$. An example of a MOT loading rate measurements can be seen in the left panel of Fig. 4.65. A detailed discussion of our MOT loading model can be found in Sec. 4.2.7.

After averaging results of several data runs like the ones shown in Fig. 6.3, we found that the effective saturation intensity $I_s = 17 \pm 2$ mW/cm^2 and 38 ± 4 mW/cm^2 for the type I and II MOTs, respectively. As previously discussed in Sec. 4.2.5, it is not surprising that the measured effective saturation intensities are larger than the theoretically calculated two-level model values. This is because leakage to additional relaxation pathways requires greater intensity to saturate the actual transition, as compared to an ideal two-level cycling transition. Similar results were seen for Rb MOTs in Refs. [115–117].

LPT The ion cloud was PI loaded Na^+ from either the type I or II MOT Na MOT, as previously discussed in Sec. 4.3.5. Due to the closed electronic shell structure of Na^+ we

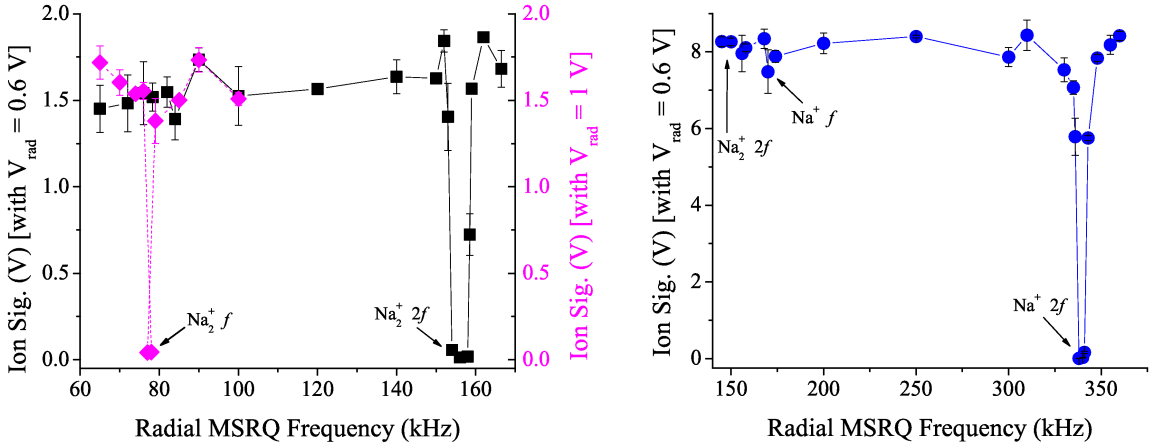

Figure 6.4: Left panel shows radial MSRQ scan of Na^+ and Na_2^+ mixture at $V_{rad} \approx 0.6$ V peak-to-peak (black) and $V_{rad} \approx 1$ V peak-to-peak (magenta) over the lower frequency range only. Right panel shows an MSRQ scan of Na^+ only.

cannot optically detect the ion cloud. Instead, the trapped ion population is destructively detected using a CEM $V_c = 1250$ V and pre-amplifier, as discussed in Sec. 4.3.6. The LPT settings were $\Omega_{rf} = (2\pi)720$ kHz, $V_{rf} = 80 \pm 2$ V, and $V_{end} = 30.0 \pm 0.2$ V, as defined in Sec. 4.3.3.

To remove the unwanted background MOT-born Na_2^+ ions discussed in Sec. 4.3.7, we continuously quench the Na_2^+ from the LPT with an MSRQ field having $V_{rad} = 0.625 \pm 0.005$ V peak-to-peak at a frequency $\omega_{rad} = (2\pi)157 \pm 1$ kHz, which corresponds to the measured second harmonic secular frequency for Na_2^+. The MSRQ spectrum is shown in Fig. 6.4 for the trap settings used in this experiment.

The equilibrium temperature of the trapped ion cloud T_I, loaded from either the type I or the type II MOT, was determined using SIMION 7.0 simulations, as previously discussed in Sec. 4.3.5. Clouds with different ion populations N_I were simulated, up to 1000 interacting ions, as seen in Fig. 6.5.

The most important factor in predicting the ion cloud's thermalized mean secular energy (from which one can assign a temperature, assuming a MB speed distribution) is the size

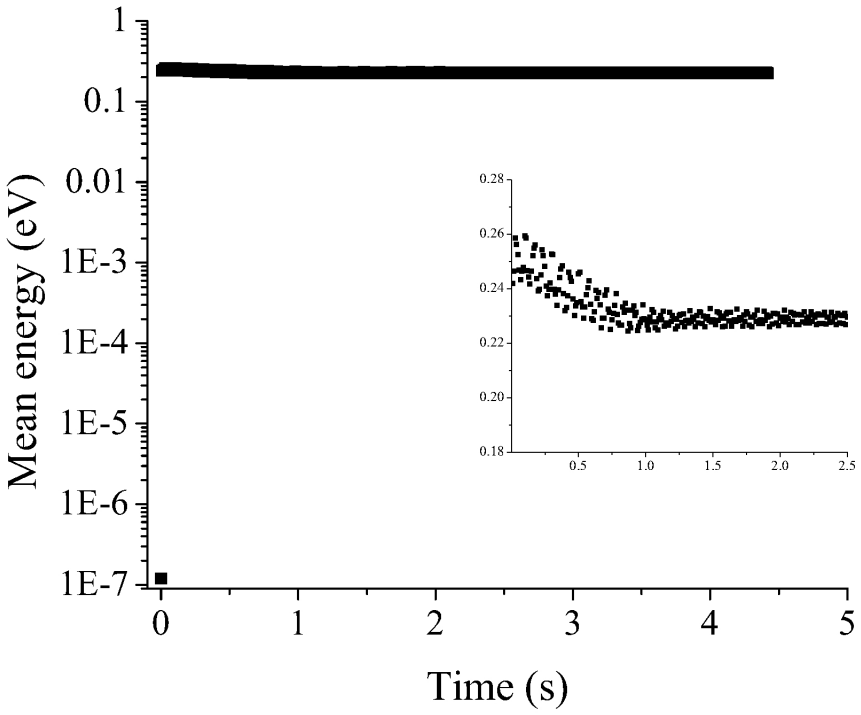

Figure 6.5: Simulation of mean kinetic energy [as defined by Eq. (4.78)] of type II MOT-loaded $N_I = 1000$ interacting ions, with creation temperature $\sim T_{\mathrm{MOT}}$. The cloud equilibrates at ≈ 0.23 eV, which corresponds to an ion cloud temperature of $T_I = 1070$ K according to Eq. (4.72). The inset shows the energy dependence with a linear y-axis scale for the first few seconds of trapping (excluding the $t = 0$ s data point).

of the MOT when the LPT is loaded via PI from a MOT [37, 61], as previously discussed in Sec. 4.3.5. Therefore, because we can accurately measure the size of the Na MOT, we can accurately initialize our simulations. The simulation determined the thermalized temperature of the ion cloud loaded from the type I and II MOTs to be $T_I = 140 \pm 10$ K and $T_I = 1070 \pm 30$ K, respectively. The uncertainty in T_I is only based on the precision of camera measurements of the MOTs' dimensions and does not include possible systematic errors with our model.

We assumed that the trapped ions adhere to a prolate Gaussian spatial distribution with $1/e$ radii $r_{I,1} = r_{I,2}$ in the transverse dimensions and $r_{I,3} > r_{I,1}$ in the axial dimension. The

calibration of the LPT and the size of the ion cloud will be discussed later in Secs. 6.2.4 and 6.2.5, respectively [40].

6.2.2 Experimental model[5]

When the Na MOT is overlapped with the ion cloud in the hybrid trap, the Na^+ and Na will undergo elastic and resonant non-radiative charge-exchange collisions previously discussed in Sec. 2.2.4 within the volume of overlap. Because the trap depth of the MOT defined in Eq. (4.22) is fairly small ~ 0.1 K, we can make the approximation that every elastic or charge-exchange collision with ions from a hot ion cloud $T_I \sim 10^2 - 10^3$ K, will result in the loss of a MOT atom [62].

We can check the validity of this approximation with a simple calculation. Let us consider two-body hard sphere collisions [185] between $T \approx 0$ K (near delta function speed distribution) Na atoms held within a 0.1 K deep MOT and a $T_I = 500$ K Na^+ ion cloud. For charge-exchange collisions we need only integrate over the Na^+ ion cloud MB speed distribution from the trap depth to infinity. The result is that more than 99.9% of the ion population has a velocity large enough to cause an atom to be lost from the trap after a charge-exchange collision.

According to Eq. (2.5),[6] a two-body equal-mass elastic scattering event has a post-collision final Na atom energy in the laboratory reference frame

$$E_a' = \frac{m v_I^2}{4} \left[1 + \cos(\theta)\right], \tag{6.3}$$

where v_I is the laboratory reference frame initial ion velocity and θ is the scattering angle in the center-of-mass (COM) reference frame [90]. If we assume an isotropic solid angle

[5]The majority of the text and figures from this section are directly reproduced from our manuscript [40] with permission. Copyright 2015 The American Physical Society.

[6]Because $m_I = m_N$, $2\chi = \theta$ according to Eq. (2.9).

COM scattering distribution, then the (polar) scattering angle probability distribution is $\rho(\theta) = \sin(\theta)/2$ according to Eq. (2.13). By integrating over the MB speed distribution $f(v_I)$ and the scattering angle distribution $\rho(\theta)$,

$$\int_0^{\pi} \int_{\sqrt{\frac{4(0.1)k_B}{m[1+\cos(\theta)]}}}^{\infty} f(v_I)\rho(\theta)\, dv_I d\theta, \tag{6.4}$$

we find that on average more than 99.9% of the ion population will eject a MOT atom during an elastic ion-atom collision. The only consequence of assuming ion-atom collisional MOT loss with unit efficiency is that the experimental result will be systematically underestimated, but our simple calculations suggest this systematic error should be negligible.

We define the loss rate per atom from the MOT due to ion-atom collisions γ_{ia} to be

$$\begin{aligned} \gamma_{\text{ia}} &= k_{\text{ia}} \langle n \rangle \\ &= k_{\text{ia}} N_I \prod_{i=1}^{3} \int_{-\infty}^{\infty} \left(\frac{e^{-(x_i - x_{0,i})^2/r_a^2}}{r_a\sqrt{\pi}} \right) \left(\frac{e^{-x_i^2/r_{I,i}^2}}{r_{I,i}\sqrt{\pi}} \right) dx_i \end{aligned} \tag{6.5}$$

where $\langle n \rangle$ is the average ion density experienced by the MOT [42], x_i is the distance from the center of the ion cloud in the $i = 1, 2,$ or 3 dimension, and $x_{0,i}$ is the center position of the MOT relative to the center of the ion cloud in the i^{th} dimension. Upon integrating over the ion and atom cloud Gaussian spatial distributions, we arrive at

$$\gamma_{\text{ia}} = \frac{k_{\text{ia}} N_I C}{V_{\text{ia}}}, \tag{6.6}$$

which shows that the loss rate is proportional to the total trapped number of ions N_I, the relative concentricity function

$$C = e^{-\left(x_{0,1}^2 + x_{0,2}^2\right)/\left(r_a^2 + r_{I,1}^2\right)} e^{-x_{0,3}^2/\left(r_a^2 + r_{I,3}^2\right)}, \tag{6.7}$$

and inversely proportional to the addition in quadrature of the effective volumes of the ion

and atom clouds

$$V_{\text{ia}} = \pi^{3/2} \left(r_a^2 + r_{I,1}^2\right) \sqrt{r_a^2 + r_{I,3}^2}. \tag{6.8}$$

Equation (6.7) is equal to unity when the MOT is perfectly centered on the ion cloud. If we also approximate $r_a \ll r_I$ and $C = 1$, we arrive at a similar expression for γ_{ia} used in a similar experiment on the Rb^+- Rb system [62]. Under the same approximation, if we multiply through by the number of atoms N_a, we also reproduce the approximate total rate R_{ia} given in Eq. (2.28), which assumes a uniform density with a hard (non-Gaussian) cloud edge.

We can experimentally measure the loss rate γ_{ia}, the number of ions N_I, and the volumes that make up V_{ia}, which gives enough information to solve for k_{ia} using Eq. (6.6). We followed Ref. [62]'s choice to measure the loss rate γ_{ia} when the LPT is saturated, which has three advantages. First, the saturated ion cloud volume $\tilde{V}_I$ remains constant for each measurement, thereby making the saturated addition in quadrature of the ion and atom cloud volumes $\tilde{V}_{\text{ia}}$ time independent. Second, because the LPT is in steady-state, the ion population $\tilde{N}_I$ can be approximated as time independent. Third, the saturated LPT holds the largest possible number of ions $\tilde{N}_I$ (for a given cloud temperature T_I and trap settings). Therefore, the saturated LPT maximizes γ_{ia}, which gives the greatest experimental resolution of k_{ia}.

6.2.3 Na MOT measurements[7]

Figure 4.34 shows the Na fluorescence measured by the PMT and fit with Eq. (4.43) when the type II MOT is loaded at three different loss rates γ_t, as defined in Sec. 4.2.7. The type I MOT loading curves are qualitatively identical to that of the type II MOT. The total loss

[7]The majority of the text and figures from this section are directly reproduced from our manuscript [40] with permission.Copyright 2015 The American Physical Society.

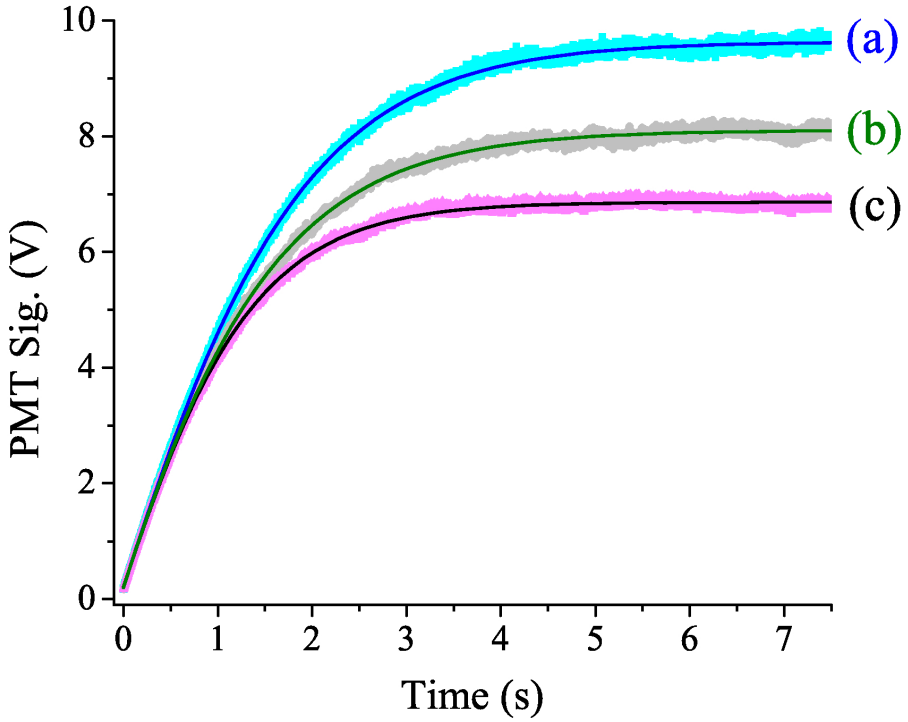

Figure 6.6: Fluorescence from a type II MOT as it loads, with the corresponding fits to Eq (4.43). Curve (a) shows the raw PMT data (light blue) and fit (royal blue) of an isolated MOT loaded with a total loss rate $\gamma_t = \gamma_b$. Curve (b) shows the raw PMT data (gray) and fit (green) of a MOT loaded with PI ($I_{\rm pi} \approx 80$ mW/cm^2), making $\gamma_t = \gamma_b + \gamma_{\rm pi}$. Curve (c) shows the raw PMT data (magenta) and fit (black) of a MOT loaded with the same PI intensity as curve (b), but the MOT is also immersed in a saturated LPT ion cloud, making $\gamma_t = \gamma_b + \gamma_{\rm pi} + \gamma_{\rm ia}$.

rate depends upon the loss mechanisms that are present at the time the MOT is loaded. Figure 6.6 curve (a) is for an isolated MOT loaded from background Na vapor $\gamma_t = \gamma_b$.

When the MOT is also experiencing PI, there is an additional loss rate $\gamma_{\rm pi}$, which increases the total loss rate $\gamma_t = \gamma_b + \gamma_{\rm pi}$, as is the case in Fig. 4.34 curve (b). The right panel of Figure 4.65 shows that at low enough PI intensity the PI loss rate $\gamma_{\rm pi}$ is linearly proportional to $I_{\rm pi}$.

The final loss mechanism is from ion-neutral collisions between the MOT and the saturated LPT ion cloud, as seen in Fig. 4.34 curve (c). These collisions introduce an

additional term intoduced in Sec. 6.2.2, which increases the loss rate to $\gamma_t = \gamma_b + \gamma_{\rm pi} + \gamma_{\rm ia}$. The ion-atom loss rate $\gamma_{\rm ia}$ at each PI intensity $I_{\rm pi}$ was determined by subtracting the loss rate measured with the PI laser on and the LPT turned off from measurements with both the PI laser and the LPT turned on.

Unlike the experimental sequence presented in Ref. [62], before taking the MOT loading data in Fig. 4.34 curve (c), the LPT is pre-loaded from the MOT until the LPT is saturated. The MOT is then briefly unloaded by blocking one of the retro-reflected 589 nm beams with an electronic shutter. Last, the MOT is reloaded while immersed in the saturated ion cloud. The PI laser remains on during the entire sequence to ensure the LPT remains saturated. The experimental sequence is schematically represented in Fig. 6.7. By pre-loading the LPT to saturation before taking the PMT measurement, we can approximate the ion cloud surrounding the MOT as having a constant volume in each measurement $\tilde{V}_I$. We can also approximate the density $\tilde{N}_I/\tilde{V}_I$ as time independent during a loading measurement, making $\gamma_{\rm ia}$ time independent.

To better automate the process, we calibrated the relationship between the analog input to the PI laser and output power. In doing so, we could control the PI power via LabVIEW and automatically step through all of the PI intensities. However, to ensure accurate knowledge of the PI power on each data point, we picked off the PI beam with a microscope slide and measured the power with our Thorlabs meter at the start of each data point and recorded those readings to file in addition to PMT signals or ion signals.

To achieve the greatest experimental resolution for $\gamma_{\rm ia}$, we worked at a high rf voltage amplitude $V_{\rm rf}$ that puts us close to the edge of the Mathieu equation's stability region discussed in Sec. 4.3.4. We found that $\gamma_{\rm ia}$ increased approximately quadratically with $V_{\rm rf}$, as suggested in Fig. 6.8. We can rationalize the proportionality between $\gamma_{\rm ia}$ and $V_{\rm rf}$ through the following scaling arguments.

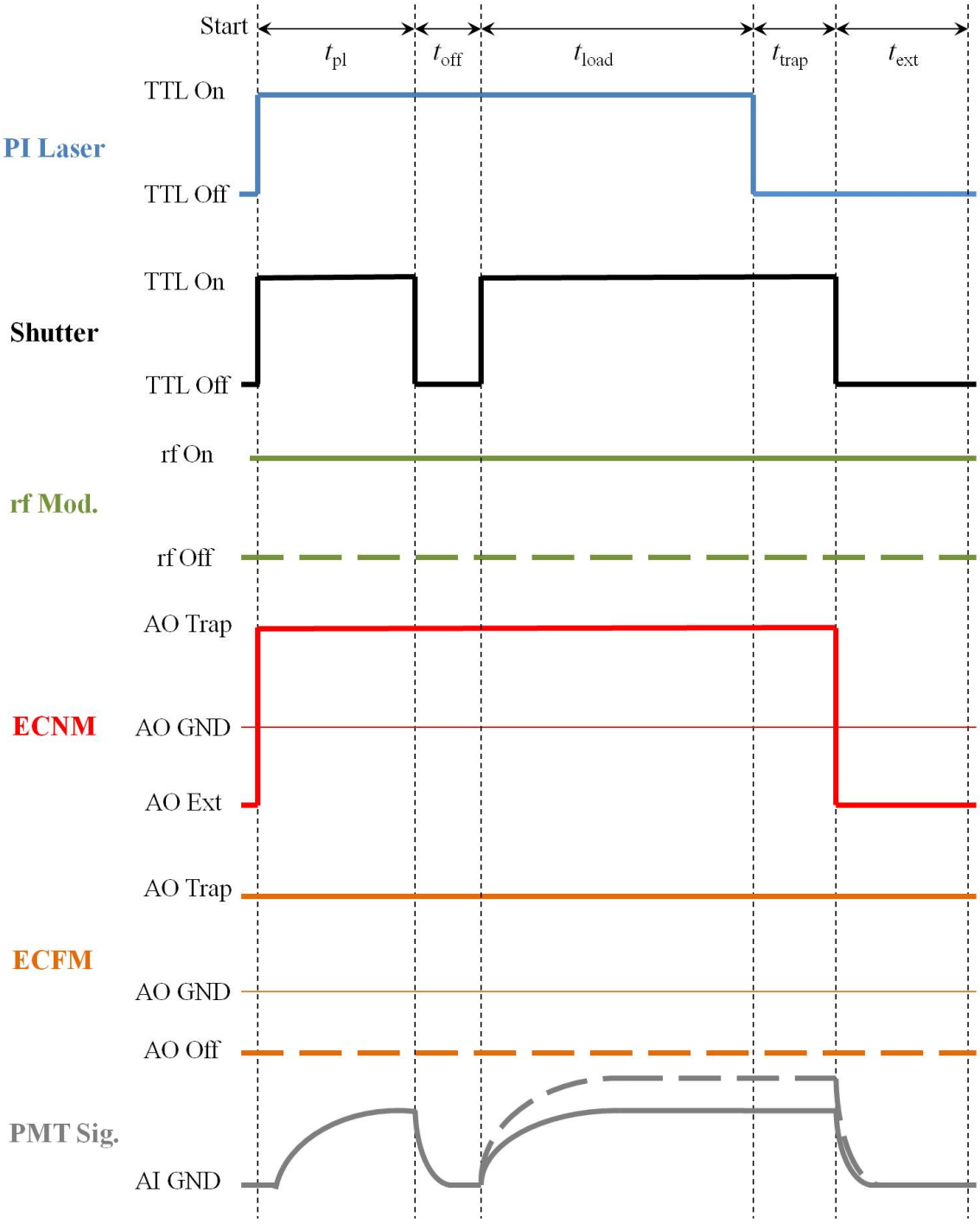

Figure 6.7: Schematic of experimental sequence of pre-loading the LPT and then loading the MOT with (solid) or without (dashed) the LPT turned on.

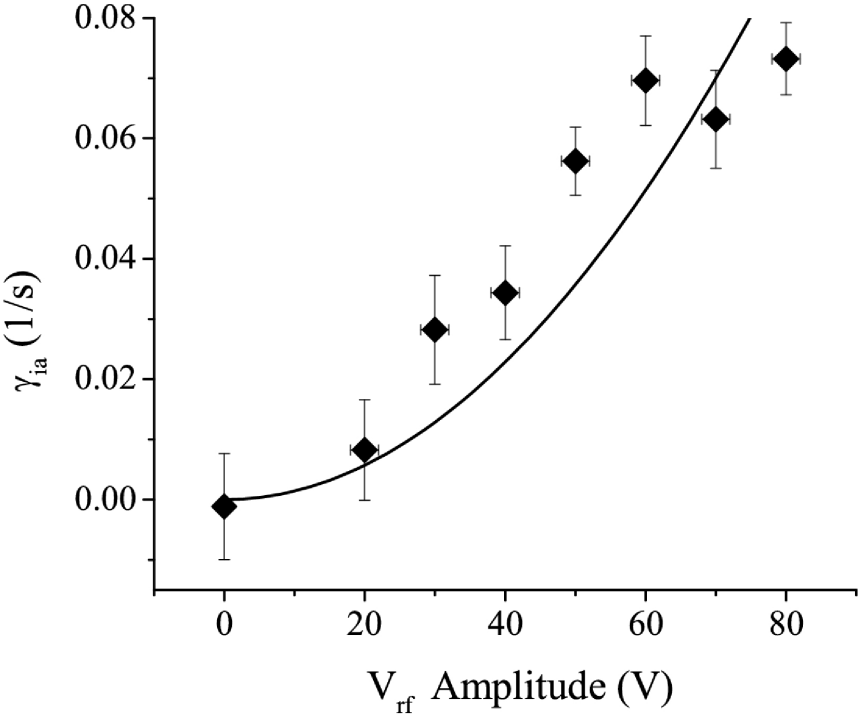

Figure 6.8: (Color online). Plot of the ion-atom loss rate γ_{ia} as a function of increasing rf voltage amplitude V_{rf}. Because the saturated LPT density increases quadratically with V_{rf}, the ion-atom loss rate also appears to increase quadratically. Although, the data could also be interpreted as being linearly proportional to V_{rf}.

When the LPT is saturated, we can determine the size of the ion cloud by equating the effective LPT trap depth D_r [defined in Eq. (4.61)] to the energy of the outermost ion in a simple harmonic potential [defined in Eq. (4.72)] with a frequency equal to the secular frequency [39, 62]

$$D_r = \frac{1}{2} m_I \omega_r^2 r_{I,1}^2 \implies r_{I,1} = \sqrt{\frac{2D}{m_I \omega_r^2}}. \tag{6.9}$$

According to Eqs. (4.61) and (4.63), for an idealized single particle in a perfect quadrupole field the LPT trap depth is proportional to $(V_{rf})^2$, as is the square of the secular frequency, respectively. Therefore, according to Eq. (6.9) we expect the saturated size of the cloud $r_{I,i}$, and thus $\tilde{V}_I$, to be insensitive to V_{rf}.

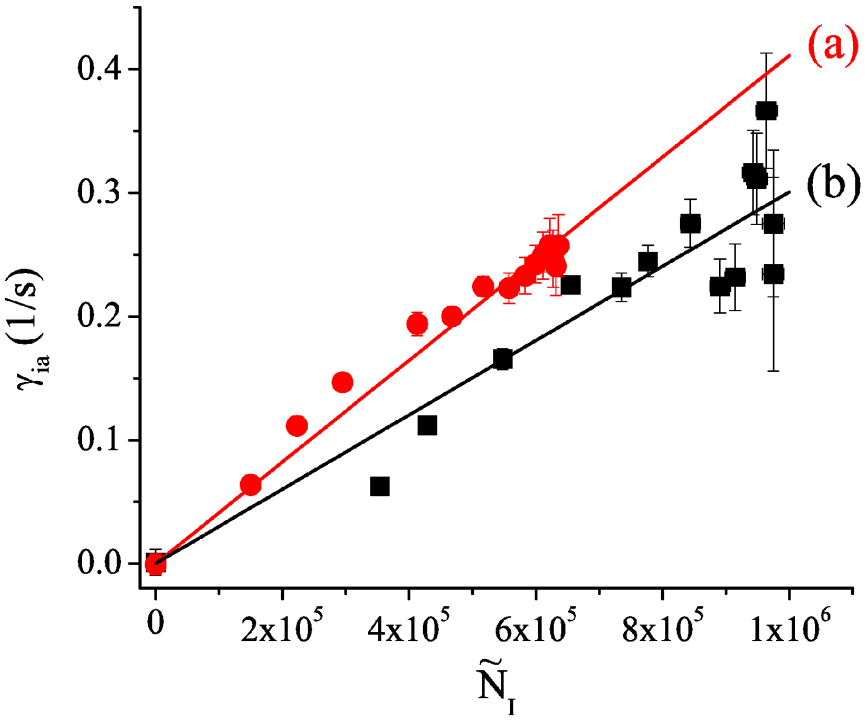

Figure 6.9: Plot of the ion-atom loss rate as a function of the saturated LPT steady-state ion population and corresponding linear fit to Eq. (6.6). Curve (a) shows type II MOT data and curve (b) shows type I MOT data. The type II MOT has larger loss rates and fewer steady-state ions at saturation because it produces a hotter lower density ion cloud that has a slightly larger k_{ia}. The uncertainty in the measurements are discussed in the text.

By equating the LPT's radial spring force to the ion cloud's Coulomb repulsion force,[8] it can be shown that the saturated number of trapped ions $\tilde{N}_I \propto (V_{rf})^2$, namely

$$m_I \omega_r^2 r_{I,1} = \left(\frac{\tilde{N}_I q}{2r_{I,3}}\right) \frac{q}{2\pi\varepsilon_0 r_{I,1}} \implies \tilde{N}_I \propto r_{I,1}^2 \omega^2 \propto V_{rf}^2. \tag{6.10}$$

We can approximate the Coulomb repulsion as that of an infinite cylinder [118] in Eq. (6.10) since $r_{I,1} \ll r_{I,3}$. Therefore, since $\gamma_{ia} \propto \tilde{N}_I/\tilde{V}_I \implies \gamma_{ia} \propto (V_{rf})^2$.

As seen in Fig. 6.9, we plot γ_{ia} as a function of the steady-state LPT ion population $\tilde{N}_I$. As predicted by Eq. (6.6), these quantities are linearly proportional. The observed linearity

[8]Technically, this argument only applies for an ion crystal $T_I \to 0$, where there is no thermal pressure. However, for this back-of-the-envelope type of calculation we do not care.

supports our assumption from Sec. 4.3.6 that the fraction of extracted ions that miss the CEM is fairly constant, if we assume Eq. (6.6) to be correct.

The fractional uncertainty in the measurement of γ_{ia} appears to increase with I_{pi} (shown later in Fig. 6.13) or steady-state ion population (shown here in Fig. 6.9). This can be explained by the fact that γ_{ia} is the difference of two measurements whose individual fractional uncertainty remains fairly constant. However, since the difference between these measurements saturates, as seen later in Fig. 6.13, the fractional uncertainty in the difference γ_{ia} must increase.

We will discuss the LPT loading behavior including how the steady-state ion population seen in Fig. 6.9 was determined in Sec. 6.2.4. Finally, using the slopes from Fig. 6.9 and the ion cloud size, which we will discuss in Sec. 6.2.5, we will have enough information to determine the rate coefficient k_{ia}.

6.2.4 Na^+ LPT measurements[9]

According to Eq. (6.6), γ_{ia}'s dependence on I_{pi} comes from $\tilde{N}_I$'s dependence on I_{pi}. Due to experimental difficulties with CEM saturation, Ref. [62] attempted to derive an LPT loading model that determined $\tilde{N}_I$ solely from MOT fluorescence measurable quantities, such as the MOT atom population $\tilde{N}_a$, the PI MOT loss rate γ_{pi}, and the ion-atom MOT loss rate γ_{ia}.

They modeled the LPT loading with the linear rate equation

$$\frac{dN_I}{dt} = L_I - \lambda N_I, \tag{6.11}$$

where L_I is the LPT ion loading rate and λ is the LPT ion loss rate. We find good agreement between Ref. [62]'s LPT rate equation [our Eq. (6.11)] and our experimental

[9]The majority of the text and figures from this section are directly reproduced from our manuscript [40] with permission. Copyright 2015 The American Physical Society.

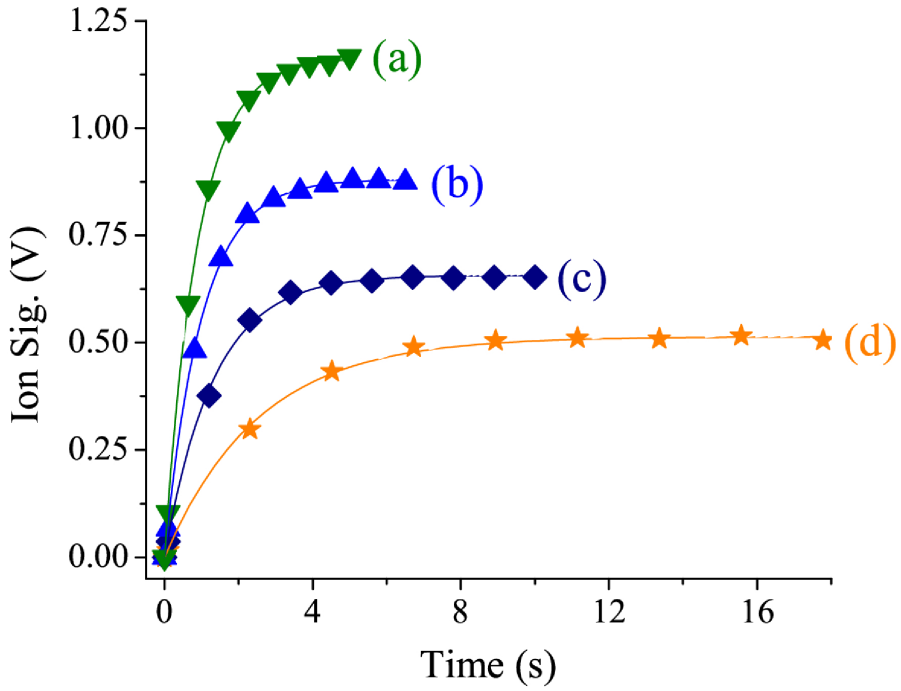

Figure 6.10: CEM measured LPT loading (from the type I MOT) as a function of time and corresponding two-parameter fits to the solution to rate Eq. (6.11). Each curve corresponds to a different PI intensity: Curve (a) is measured with $I_{\rm pi} \approx 670$ mW/cm^2, curve (b) is with $I_{\rm pi} \approx 108$ mW/cm^2, curve (c) is with $I_{\rm pi} \approx 42$ mW/cm^2, and curve (d) is with $I_{\rm pi} \approx 15$ mW/cm^2. The uncertainties are smaller than the size of the plot markers.

data, as seen in Fig. 6.10, which shows typical LPT loading curves taken with the CEM at four different $I_{\rm pi}$ intensities loaded from the type II MOT. The fits use L_I and λ as free fitting parameters, which makes the steady-state ion population the ratio of the two fitting parameters $\tilde{N}_I = L_I/\lambda$.

Experimentally, for each PI laser intensity we preset the MOT into a steady-state atom population $\tilde{N}_a$ with the PI laser on before turning on the LPT. The LPT is loaded from the MOT for a fixed time and then the ions are immediately extracted and detected. This procedure, schematically represented in Fig. 6.11, is repeated with increasing loading times until the LPT has reached its steady-state ion population.

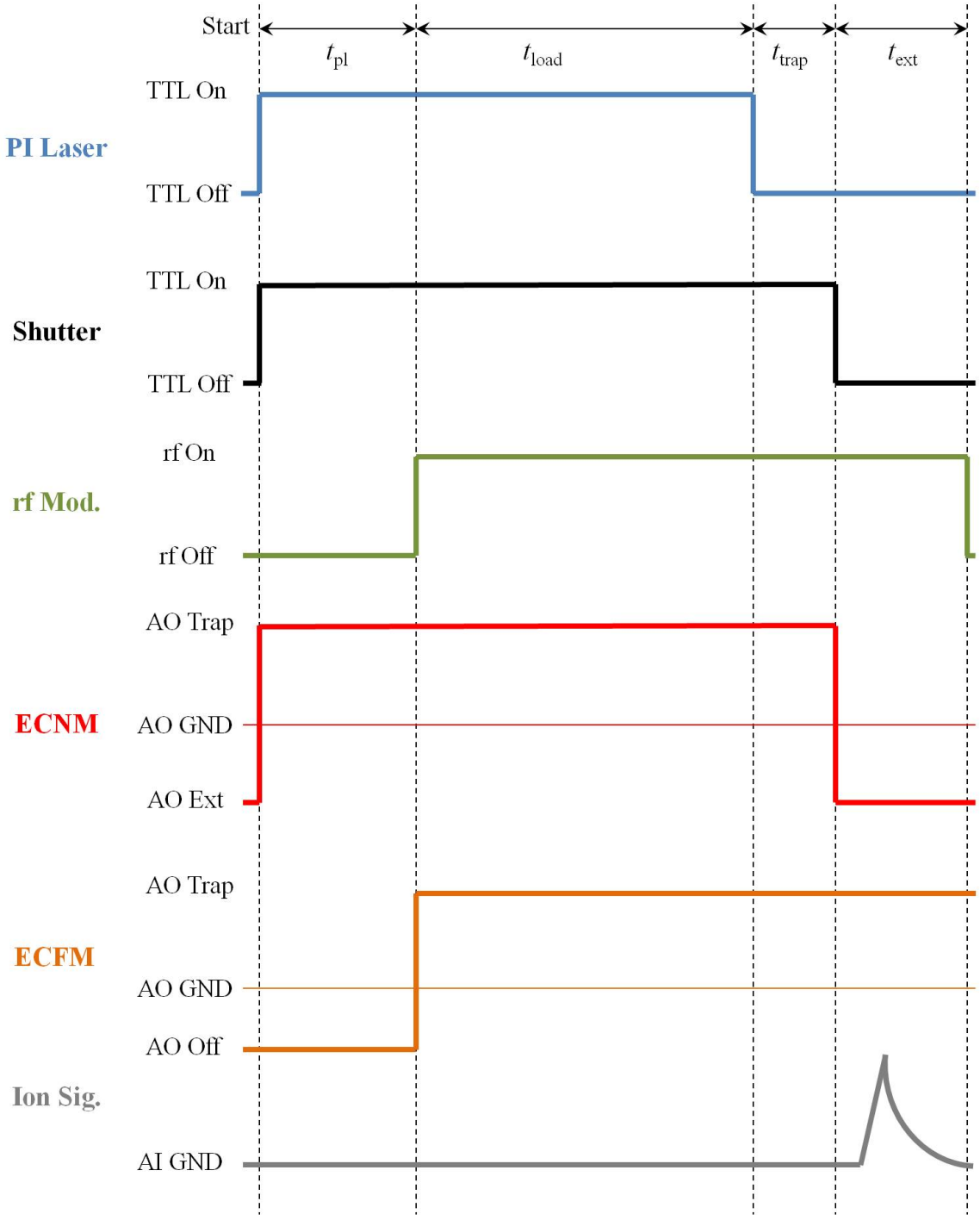

Figure 6.11: Schematic of experimental sequence of pre-loading the MOT into steady-state with the LPT turned off for a time t_{pl} and then loading the LPT at a constant rate L_I up to LPT saturation.

Reference [62] argues that the number of MOT atoms lost are proportional to the number of ions gained by the LPT. Accordingly, the loss rate λ is equated to the ion-atom MOT loss rate γ_{ia} and the loading rate is modeled with a linear dependence on I_{pi},

$$L_I = N_a \gamma_{\text{pi}} = N_a \zeta I_{\text{pi}}, \tag{6.12}$$

which diverges as $I_{\text{pi}} \to \infty$. Because the LPT cannot hold an infinite number of ions, they introduce an intensity loss coefficient κ and the PI intensity differential equation

$$\frac{dN_I}{dI_{\text{pi}}} = \frac{N_a \zeta}{\gamma_{\text{ia}}} \left(1 - e^{-\gamma_{\text{ia}} t}\right) - \kappa N_I. \tag{6.13}$$

In deriving Eq. 6.13 and its solution (as $t \to \infty$)

$$\tilde{N}_I = \frac{\tilde{N}_a \zeta}{\gamma_{\text{ia}} \kappa} \left(1 - e^{-\kappa I_{\text{pi}}}\right), \tag{6.14}$$

Ref. [62] appears to make the approximation that $dN_a/dI_{\text{pi}} = d\gamma_{\text{ia}}/dI_{\text{pi}} \approx 0$.

Because the MOT is much smaller than the trapping volume of the LPT, every PI ion created from the MOT can be considered loaded into the LPT. However, unlike Ref. [62], we consider PI intensity dependence of N_a according to Eq. (4.43), and we do not make the assumption that $dN_a/dI_{\text{pi}} \approx 0$. Also, because we allow the MOT to come to steady-state $\tilde{N}_a$ before turning on the LPT, our ion trap loading rate is

$$\begin{aligned} L_I &= \tilde{N}_a \gamma_{\text{pi}} \\ &\approx \frac{2 L_{\text{MOT}} \zeta I_{\text{pi}}}{\gamma_b + \zeta I_{\text{pi}} + \sqrt{\left(\gamma_b + \zeta I_{\text{pi}}\right)^2 + \frac{4\beta L_{\text{MOT}}}{V_{\text{MOT}}}}}. \end{aligned} \tag{6.15}$$

By including the atom number's PI intensity dependence we see that the ion trap loading rate already saturates as $I_{\text{pi}} \to \infty$ without the need for introducing an intensity-loss coefficient κ. For simplicity, like Ref. [62], we ignored $\tilde{N}_a$'s dependence on γ_{ia} in

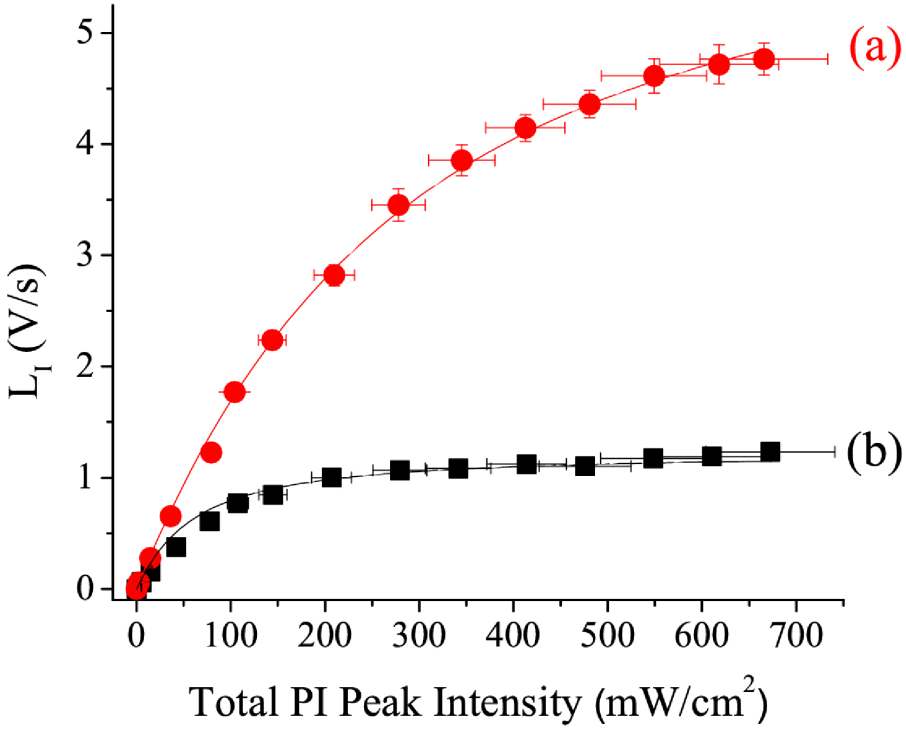

Figure 6.12: CEM measured LPT loading rate as a function of $I_{\rm pi}$ and corresponding fit to Eq. (6.15). Curve(a) shows the LPT loaded from the type II MOT and curve (b) shows the LPT loaded from the type I MOT. The fit to Eq. (6.15) is only a single parameter y-scaling constant, whose value is the CEM calibration. All other parameters are independently determined from MOT fluorescence measurements. The difference in steady state value between curves (a) and (b) is primarly due to the different values of $L_{\rm MOT}$ associated with each type of MOT.

Eq. (6.15), as this is only a small correction, since $\gamma_b + \gamma_{pi} \gg \gamma_{\rm ia}$. By ignoring this term, L_I does not depend on N_I, which makes solving Eq. (6.11) much easier.

Figure 6.12 shows the ion trap loading rate measured with the CEM as a function of $I_{\rm pi}$, when loaded from both the type I and II MOTs. We see that L_I is not linearly proportional to $I_{\rm pi}$, as Eq. (6.12) would suggest. We have fit L_I to Eq. (6.15), with only a single fitting parameter to scale the y-axis. All other parameters are independently determined from the MOT fluorescence measurements discussed in Sec. 6.2.3. The single parameter y-scaling fit result gives the CEM calibration. The type I MOT [curve (b)] has a calibration result of

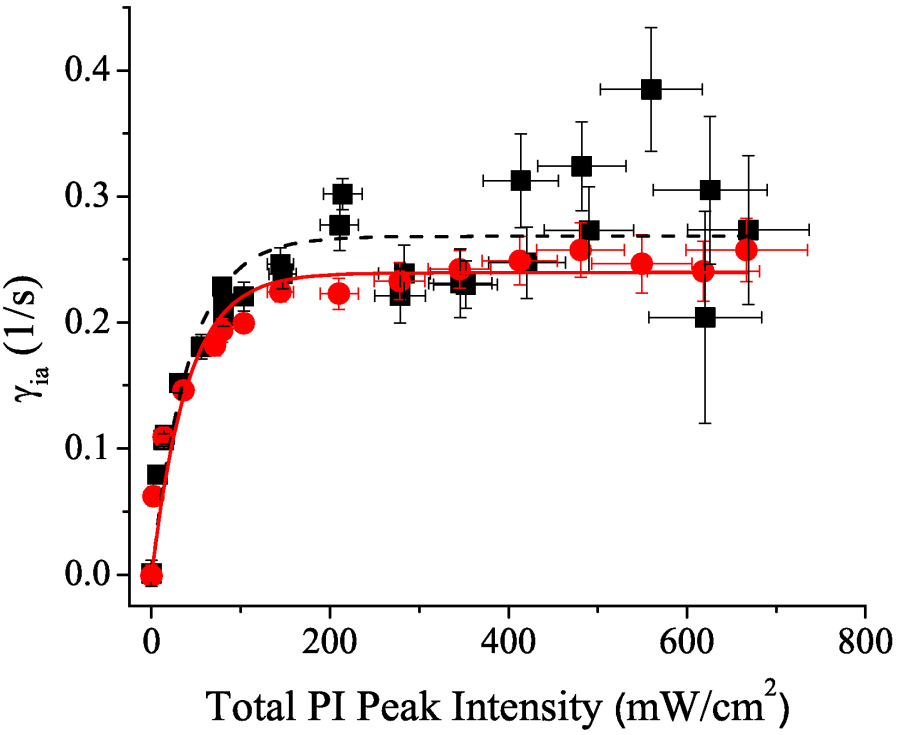

Figure 6.13: Plot of the ion-atom loss rate γ_{ia} as a function of PI intensity for the type I MOT (black) squares and the type II MOT (red) circles. We find that γ_{ia} measurements of the MOT fluorescence are not equivalent to the LPT loss rate measurements seen in Fig. 6.14. Furthermore, we show fits to the type I (black dashed line) and type II (solid red line) MOT data obtained as the solution of Ref. [62]'s intensity-loss rate equation.

$1.19 \pm 0.02 \times 10^{-6}$ V/ion and the type II MOT [curve (a)] gives $2.70 \pm 0.01 \times 10^{-6}$ V/ion. The calibrations are fairly close. However, we always used the corresponding calibration for each MOT type's data sets. The difference in the calibrations is likely due to different ion optics divergence associated with extraction from a type I MOT-born ion cloud that is systematically denser than a type II MOT-born ion cloud [188].

We find that the solution to Ref [62]'s intensity-loss coefficient model [our Eq. (6.14)] for determining the steady-state ion population, which is linearly proportional to γ_{ia} [according to our Eq. (6.6)], fits within the experimental error, as shown in Fig. 6.13. We found the agreement to be surprising, since the model's derivation required that

$d\gamma_{ia}/dI_{pi} \approx 0$, which seems inconsistent with the lower PI intensity γ_{ia} results.

We do find a small systematic difference between our experimental data and the intensity-loss coefficient model. The fits slightly overshoot the data at the knee of the curve and then the fits undershoot the data at the high intensity end of the curve. The discrepancy is small (as compared with the error bars) but systematic, since it appears in every data run that we have performed for both MOTs. However, it is understandable that this small discrepancy was not observed in Ref. [62], since the PI intensities used were two orders of magnitude smaller in that study and thus the nearly saturated regime seen in Fig. 6.13 was not reached.

As we mentioned before, the LPT loss rate λ was equated with γ_{ia} in Ref. [62]. Unfortunately, we find this to be inconsistent with our data. By comparing Fig. 6.13 and Fig. 6.14, we see that λ does not have the same I_{pi} dependence as γ_{ia}. Additionally, λ is an order of magnitude larger than γ_{ia}. The ion-atom MOT loss γ_{ia} goes to zero as PI intensity is decreased. By equating λ with γ_{ia}, Ref. [62] suggests that the trap loss would also go to zero without PI or without the MOT, which is inconsistent with the fact that the LPT always exhibits some trap loss.

A resonant charge-exchange collision results in a Na^+ with an energy close to that of a MOT atom. Elastic collisions with MOT atoms may cause the ion to gain energy but more often result in a lower energy. Because collisions with neutrals, on average, reduce the energy of an ion, only a very small fraction of these collisions cause an ion to be ejected from the very deep (as compared to the MOT) trapping potential of the LPT. Also, elastic and resonant charge-exchange collisions cause no net increase in the number of trapped ions, so a saturated LPT ion-atom collisions does not necessarily lead to ion loss. Therefore, it is unlikely that an ion-neutral collision will cause an ion to be ejected suggesting that γ_{ia} should not be equivalent to λ.

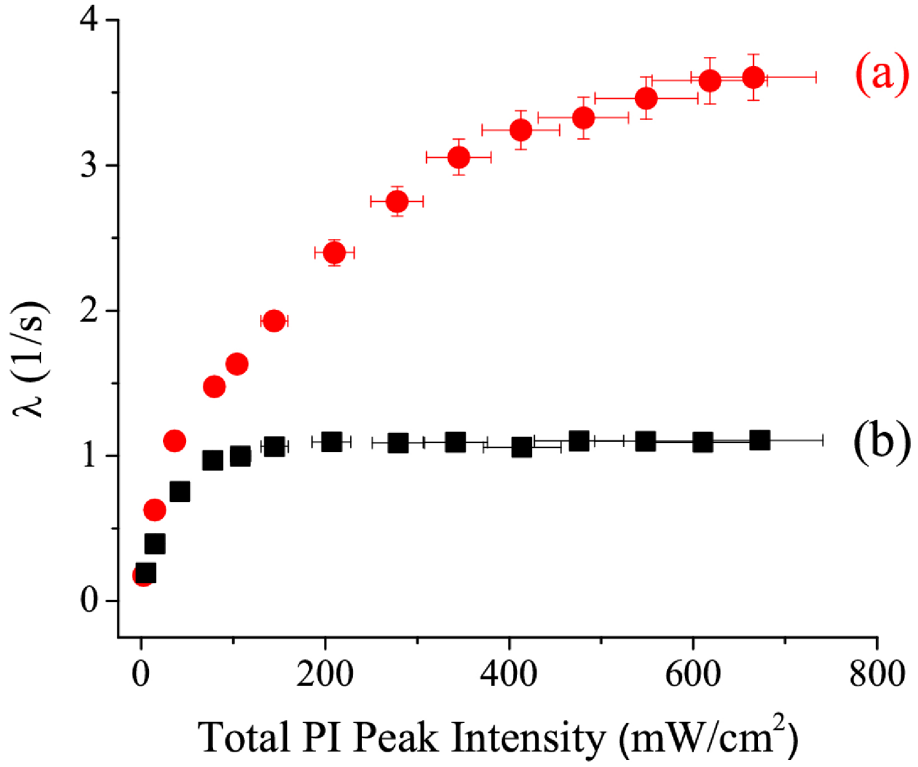

Figure 6.14: Plot of the LPT loss rate λ as a function of I_{pi}. Each value is determined from fits to loading curves like the ones seen in Fig. 6.10. Curve (a) is the λ fitting value when the LPT is loaded with the type II MOT and curve (b) is the λ fitting value when the LPT is loaded with the type I MOT.

We suggest that λ's apparent PI intensity dependence is actually due to a dependence on N_I. Therefore, the LPT steady-state population I_{pi} dependence comes entirely from L_I. If λ depends on N_I, this would mean that the LPT loss has a space charge dependence, despite the fact that we are operating in the low coupling regime $\Gamma \ll 1$, where Γ is the ratio of the nearest-neighbor Coulomb repulsion to the average thermal energy [137].

To incorporate the effects of two-body collisions, which to lowest order are proportional to the number of trapped ions, we approximated λ's ion number dependence as

$$\lambda \approx \lambda_1 + \lambda_2 N_I, \tag{6.16}$$

where λ_1 is the linear loss rate constant and λ_2 is the non-linear loss rate constant. Substituting Eq. (6.16) into Eq. (6.11) gives a rate equation with the same form as the temperature-limited MOT loading rate Eq. (4.42),

$$\frac{dN_I}{dt} = L_I - \lambda_1 N_I - \lambda_2 N_I^2. \tag{6.17}$$

We found that the solution to Eq. (6.17) fit the time dependent loading data slightly better than the fits shown in Fig. 6.10, probably because of the additional fitting parameter. Because the fits were slightly better, we used the steady-state ion population fitting results from the solution to rate Eq. (6.17) as the independent variable in Fig. 6.9. However, we found that there was little to no difference in the fit results of L_I or $\tilde{N}_I$ when we used the solution to rate Eq. (6.11) vs. that of Eq. (6.17). The uncertainty in the steady-state values comes from propagating the uncertainty in the ion loading fit results and the CEM calibration fit results.

Unfortunately, we find that the LPT loss rates λ_1 and λ_2 still have an I_{pi} dependence, which suggests that Eq (6.17) is also not the correct rate equation model for LPT saturation. However, with the CEM calibrated, we do not need the loss rate model to determine k_{ia}, only the steady-state population for each measured value of γ_{ia} in Sec. 6.2.3.

Even without an analytical model, we determined the optimal mesh setting by using the linear proportionality between the measured γ_{ia} signal and saturated ion signal $\tilde{N}_I$ according to Eq. (6.6). By measuring γ_{ia} and then separately measuring $\tilde{N}_I$ at different mesh voltages we used a y-axis scaling parameter to match the two curves at the right most point seen in Fig. 6.15. Clearly, the scaled γ_{ia} and $\tilde{N}_I$ data sets for the mesh setting of -1 V shown in the left panel of Fig. 6.15 qualitatively appear to be part of the same (scaled) curve, while the right panel at -50 V shows that the improperly chosen mesh setting yields a nonlinear ion signal response that cannot be scaled.

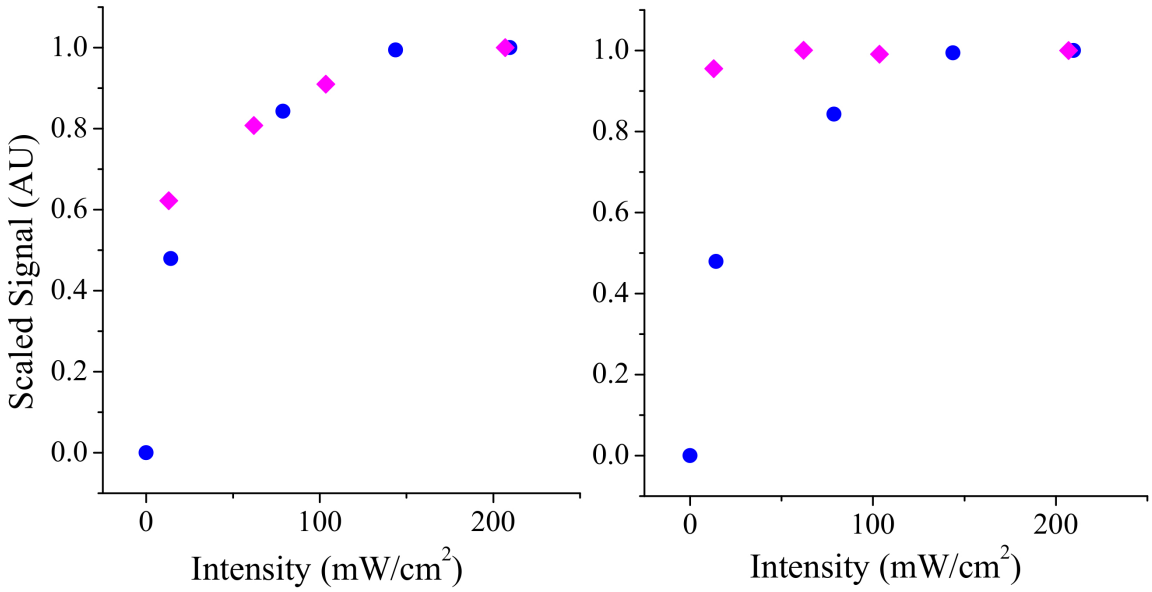

Figure 6.15: Left panel shows the scaled ion-atom loss rate in blue and the scaled steady-state ion signal in magenta, both as a function of intensity at a -1 V mesh setting. Right panel shows the same thing but with the ion signal measured using a -50 V mesh setting. The -1 V setting qualitatively appears to yield an ion signal that can be linearly scaled to match the ion-atom loss rate and -50 V setting does not.

Looking back, in this section we have revised the loading model from Ref. [62]. In doing so, we are confident that we can accurately model the LPT loading rate L_I and the steady-state ion population $\tilde{N}_I$ needed to determine k_{ia}. However, we have yet to determine a completely satisfactory closed-form analytic solution to both the LPT loading and decay rate equations and hope to solve this mystery in the future.

6.2.5 Na^+ cloud size measurement[10]

To determine k_{ia} we must also determine the dark Na^+ ion cloud size. For optically accessible ion clouds this can be accomplished by simply imaging the ion cloud in the same way we image the MOT, but for a dark ion cloud this is not an option. In principle,

[10]The majority of the text and figures from this section are directly reproduced from our manuscript [40] with permission. Copyright 2015 The American Physical Society.

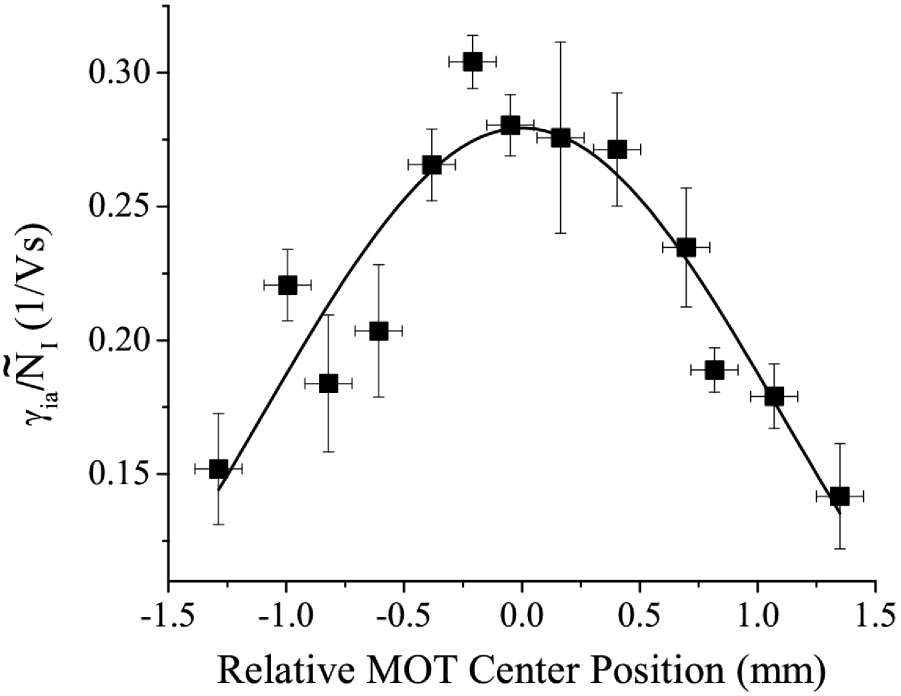

Figure 6.16: MOT ion-atom loss rate γ_{ia} normalized by the steady-state ion population $\tilde{N}_I$ as a function of the center position of the type I MOT (as measured with the CMOS camera) relative to the geometric center of the LPT [$x_{0,1}$ in Eq. (6.7)]. The data are fit to Eq (6.6) and the fitted ion cloud radius is $r_{I,1} = 1.6 \pm 0.1$ mm.

if the trap is saturated and the radial trap depth D_r is known then the maximum transverse radius of the ion cloud is given by Eq. (6.9) in the radial dimension [39, 40, 62, 63].

Because the radial depth is much greater than the axial trap depth previously discussed in Sec. 4.3.4, we can assume the cloud is limited by the equally partitioned [146] transverse secular energy mode, making the maximum axial extent $\tilde{r}_{I,3} = \omega_r \tilde{r}_{I,1}/\omega_a$, if we assume a harmonic axial potential. However, it is difficult to experimentally determine the effective trap depth, which can be quite different from the theoretical single ion idealized quadrupole radial trap depth in Eq. (4.61), as was the case in Ref. [60].

The first upper bound on the radial extent of the ion cloud is the mechanical inner electrode radius of the trap $r_0 \approx 9.5$ mm previously discussed in Sec. 4.3.3. We can reduce

this upper bound by using our SIMION simulations. We simulated an ion that is initialized with no initial kinetic energy at ever increasing transverse displacement from the LPT's nodal line [63]. If the ion starts at a distance ≥ 3 mm from the nodal line at the experimental trap settings, we find that the ion cannot remain trapped for more than two secular periods. If we consider this upper bound to be equivalent to the $1/e^2$ radius of the Gaussian distribution, then the upper bound on $r_{I,1} = 3/\sqrt{2} \approx 2.12$ mm.

Other groups [50, 51, 56] have used a single trapped ion in a hybrid trap to probe a neutral BEC. We have essentially employed the reverse process – we use the MOT to probe a dark ion cloud. By translating the MOT across the saturated ion cloud along one transverse dimension, we measured γ_{ia} as a function of the changing concentricity function $C(x_{0,1})$ in Eq. (6.7). As we translate the MOT the steady-state number of ions changes slightly, since the PI rate changes slightly as well as the temperature of the saturated ion cloud.[11] Therefore, we normalize γ_{ia} to the steady-state ion population point for point. We found the normalized ion-atom loss rate fit well to Eq. (6.6), as seen in Fig. 6.16, which supports our claim that the ion cloud had a Gaussian spatial distribution.

We have assumed that as the MOT is translated k_{ia} remains constant. Because the temperature of the ion cloud will change when the LPT is loaded from a MOT displaced off the nodal line, k_{ia} is technically different from point to point. However, since k_{ia} has a weak $T_I^{1/6}$ temperature dependence [according to Eq. 2.76] the model still fits well.

Measurements taken over several days found that the saturated ion cloud size did not depend on the PI intensity used. Typical fit results gave $r_{I,1} = 1.6 \pm 0.1$ to $r_{I,1} = 1.9 \pm 0.1$ mm, always less than but close to the simulation upper bound. Therefore, we will use the experimental data as a lower bound on the ion cloud radius of $r_{I,1} = 1.75$ mm.

[11] The 405 nm PI laser beam has a collimated intensity radius such that the region of PI is always larger than the MOT. This allows us to PI load from the MOT even when the MOT is translated off-axis from the beam as much as ≈ 0.125 cm.

Instead of using the ratio of the secular periods to determine the lower and upper bound on the axial extent of the ion cloud, we used our SIMION simulations with an ion initialized at the center of the trap having the kinetic energy equivalent to the potential energy at the maximum radial turning point for $r_{I,1} = 1.75$ mm and $r_{I,1} = 2.12$ mm, respectively. The SIMION simulations found the lower and upper bound axial extent to be $r_{I,3} = 10.57$ mm and $r_{I,3} = 12.10$ mm, respectively. Using the SIMION simulations should be more accurate because it models the actual LPT electrode geometry, which yields a more quartic axial electrical potential than harmonic, as previously discussed in Sec. 4.3.3.

As a quick back-of-the-envelope check for consistancy, according to Eq. (6.9) the saturated crystallized $T_I \to 0$ ion population associated with the predicted maximum ion volume is a little more than one order of magnitude higher than the maximum ion signal recorded in Fig. 6.9. Because Eq. (6.9) gives an upper bound on the ion population, the fact that we recorded smaller ion signals suggests that the predicted cloud size and CEM calibrations are reasonable.

Having determined the ion cloud size and the MOT dimensions via CMOS camera measurements, $\tilde{V}_{\text{ia}}$ can be determined. The final results are summarized in Table 6.1. The experimental k_{ia} is calculated using the slopes from Fig. 6.9 while the theoretically

Table 6.1: Table of total rate coefficient experimental [40] and theoretical [Table 6.2] results for the type I and type II MOTs. The saturated ion-atom volume $\tilde{V}_{\text{ia}}$ is determined using Eq. (6.8) with input from measurements discussed in Sec. 6.2.5. The uncertainty in the theoretical values is the propagated uncertainty from taking the weighted average of the theoretical values in Table 6.2.

MOT	$\tilde{V}_{\text{ia}}$ (cm^3)	Experimental $k_{\text{ia}}\left(\text{cm}^3/\text{s}\right)$	Theoretical $k_{\text{ia}}\left(\text{cm}^3/\text{s}\right)$
type I	0.247 ± 0.061	$7.4 \pm 1.9 \times 10^{-8}$	$8.62 \pm 0.07 \times 10^{-8}$
type II	0.267 ± 0.060	$1.10 \pm 0.25 \times 10^{-7}$	$1.14 \pm 0.01 \times 10^{-7}$

Table 6.2: Table of semiclassically predicted total (elastic and charge exchange) ion-atom scattering rate coefficients k_{ia} for both excited (3P) and ground state (3S) Na on ground state Na^+ at the experimentally relevant ion cloud temperatures T_I. The excited state C_{tot} is calculated using the ground state value [68] and the scaling of C_4 according to Eq. (2.75). The total rate coefficient is calculated using Eq. (2.76). The uncertainty in k_{ia} is due to the propagated uncertainty in T_I.

Species	C_4 (a.u.)	C_{tot} (a.u.)	T_I (K)	$k_{\mathrm{ia}}\left(\mathrm{cm}^3/\mathrm{s}\right)$
Na(3S)-Na^+	162.7[a]	4174[a]	140 ± 10	$7.00 \pm 0.08 \times 10^{-8}$
			1070 ± 30	$9.82 \pm 0.05 \times 10^{-8}$
Na(3P)-Na^+	361.4[b]	7106	140 ± 10	$1.19 \pm 0.01 \times 10^{-7}$
			1070 ± 30	$1.67 \pm 0.01 \times 10^{-7}$

[a] Reference [68]
[b] Reference [25]

determined k_{ia} values are weighted averages of the excited state and ground state theoretical cross sections shown in Table 6.2, based on the MOT f_e. Both theory [68] and experiment [40] show good agreement.

6.2.6 Conclusions[12]

We have demonstrated [40] a modified version of a method, originally reported in Ref. [62] for Rb^+– Rb, for measuring the total ion-atom collision rate coefficient of Na on optically dark Na^+. We have also developed a different LPT saturation model from the one presented in Ref. [62]. The experimental results show very good agreement with previously reported fully quantal *ab intio* calculations. In determining k_{ia} we demonstrated that the MOT can be used as a probe of a dark ion cloud spatial distribution.

For optically bright ion clouds, the charge-exchange rate coefficient can be determined by the ion decay alone. However, by also using the MOT ion-atom loss rate to determine

[12]The majority of the text and figures from this section are directly reproduced from our manuscript [40] with permission. Copyright 2015 The American Physical Society.

the total collision rate coefficient, the elastic scattering rate coefficient can be determined by subtracting the two results. We plan to implement this procedure in measurements on the Ca^+– Na system. Finally, we have presented some preliminary simulation and experimental results toward the development of an analytical closed-form model of LPT trap loss, saturation, and loading dynamics.[13]

[13]The graduate students who participated in the designing and conducting the experiments presented in Sec. 6.2 other than myself were J. E. Wells and J.M. Kwolek.

Chapter 7

Future work

In Chs. 5 and 6 we discussed sympathetic cooling within an ion-neutral hybrid trap and measurements of ion-neutral collision rate coefficients, respectively. In this final chapter we will discuss some of the proposed future experiments that are related to sympathetic cooling and ion-neutral rate coefficient measurements.

7.1 Molecular internal state sympathetic cooling

In Ch. 5, we considered the translational sympathetic cooling within an ion-neutral hybrid system. We found that sympathetic cooling was possible, but not to cold temperatures with the MOT densities currently achieved by our experimental setup. Ref. [47] was the first to show that the hybrid system can efficiently sympathetic cool heteronuclear molecular ions' internal degrees-of-freedom down to ground vibrational states.

We hope to demonstrate internal-state vibrational relaxation of initially vibrationally hot Na_2^+ (a band of vibrational exicitation centered near $v \approx 55$ about ~ 0.3 eV wide [189]) down to a low vibrational state ($v \approx$ 1-3) on exposure to neutral Na(3s or 3p) within the hybrid trap. This would be the first demonstration of ion-neutral sympathetic cooling of

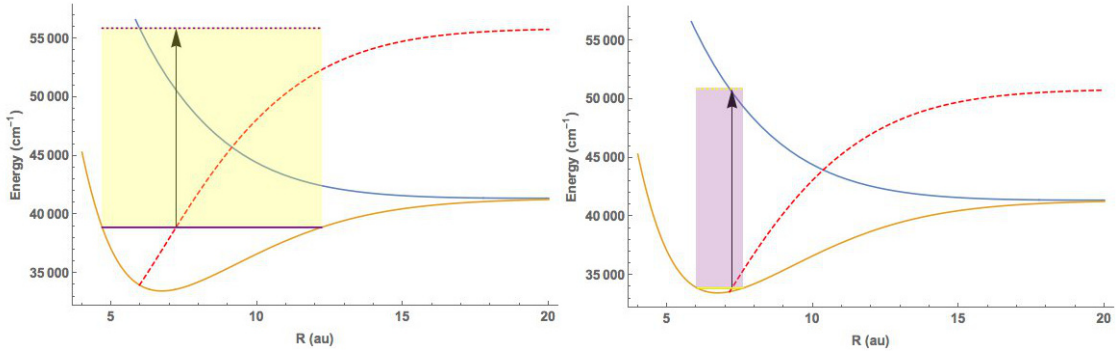

Figure 7.1: The two lowest Born-Oppenheimer potential curves of Na_2^+ (solid curves) with the $v = 3$ (right plot) and $v = 55$ (left plot) vibrational levels shown. The Mulliken Difference Potential, shown dotted, intersects with the vibrational level at the most likely point of an optical transition, other than the turning points. Each vertical arrow has a length corresponding to the energy of an ambient 589 nm photon (equal to the internal energy of an excited Na(3p) MOT atom). Na_2^+ population in a low vibrational state will be near-resonantly transferred to the dissociative state with a 589 nm photon, while population from the higher vibrational state will not.

the vibrational states of a *homonuclear* molecular ion. This is significant as homonuclear excited vibrational states have much longer lifetimes than the heteronuclear case because electric dipole (E1) transitions are forbidden.

As shown in Ref. [190] we can make Na_2^+ ions via stepwise excitation of one of the colliding MOT atoms, e.g., AI from Na(3p) + Na(3d) or Na(3p) + Na(5s) collisions. These processes yield strong vibrationally-excited Na dimer ion production with $v \approx 55$. Since the ion-neutral interaction is long-range attractive allowing for close-in collisions, it would not be surprising to see some internal vibrational relaxation with $Na_2^+ + Na(3s \text{ or } 3p)$ inelastic collisions.

In the case of Na on Na_2^+ , the symmetry of the colliding triatomic system Na_3^+ makes it difficult to calculate or even estimate quantum-mechanically the internal vibrational cooling by the MOT and a good measurement would be a stimulus to the theory. It is expected, as was the case in Ref. [47], that the rate should be approximately

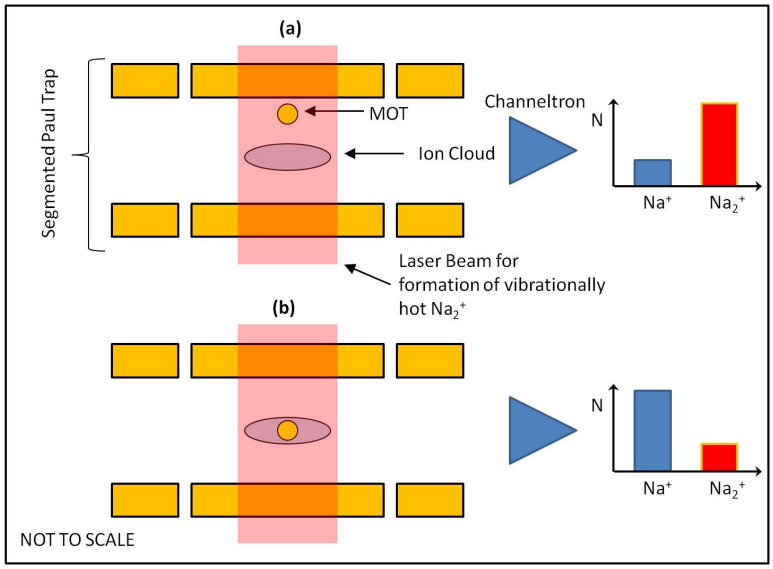

Figure 7.2: Internal-state vibrational cooling scenarios for trapped Na_2^+ at different ion-cloud overlap conditions. (a) No overlap between the MOT and ion cloud; (b) Maximum overlap between the MOT atoms and ion cloud. As the ion cloud overlap increases, vibrational cooling leads to a larger photodissociated Na^+ ion signal due to the increase in low vibrational Na_2^+ state population.

the Langevin rate.

The photodissociation rates for Na_2^+ in the presence of a 589 nm laser should depend strongly on the vibrational state. The Mulliken Difference Potential (MDP) provides an estimate for the internuclear distance where a dissociating collision is likely to occur, other than the turning points. Figure 7.1 shows that Na_2^+ ions in low vibrational states undergo near-resonant dissociation in the presence of a 589 nm photon. Vibrationally excited Na_2^+ is far off resonance, and the most likely internuclear distance predicted by the MDP is in a region of low probability of the wavefunction. This gives rise to a vibrationally dependent photodissociation due to the MOT beams.

The experimental process is shown schematically in Fig. 7.2. An excitation laser is used to excite Na(3p) to either the 3d (818 nm) or 5s states (616 nm), creating vibrationally hot Na_2^+. No cooling should take place if the MOT is radially displaced off the nodal line

(using a magnetic shim coil) so that there is no overlap with the ion cloud located at the center of the trap, as in Fig. 7.2 case (a). Therefore, the highly vibrationally excited Na_2^+ will not undergo much dissociation. When the MOT is in the center of the LPT where the trapped ions are located, as in Fig. 7.2 case (b), ion-neutral sympathetic cooling will relax the Na_2^+ to a low vibrational state, which will be dissociated by the 589 radiation.

We will monitor the ratio of Na_2^+ and Na^+ in the ion trap as a function of MOT and ion cloud overlap. The increase of Na^+ in the presence of sympathetic cooling can be established empirically by comparing the Na^+ production rate (from 589 nm photodissociation) with and without the second-step excitation laser, turning on and off the high vibrational excitation.

7.2 Ca^+- Na charge-exchange interaction

The logical extension to the preliminary study described in Sec. 6.1 is to use laser fluorescence to image the Ca^+ ion cloud, as previously discussed in Sec. 4.3.9.

First, laser cooling the Ca^+ ions would allow us to obtain much more accurate knowledge of the overlap volume, number of ions, and ion temperature. This would yield a much more precise measurement of the rate coefficient. Second, by using controlled excess micromotion heating (discussed in Sec. 4.3.8) in conjunction with laser cooling, we can control the cloud temperature and explore the rate coefficient's energy dependence. Third, controlling the ion cloud temperature allow us to precisely explore the reaction's activation barrier seen in Fig. 2.20. Fourth, we can explore reaction pathway branching ratios by adjusting the MOT's excited state population, the ion cloud's excited state population, or by optically pumping ions into the the metastable D state. Fifth, using the same total cross section measurement procedure that we demonstrated in Ref. [40], we can isolate the elastic scattering cross section and make a comparision with the theoretical treatment of Ref. [71].

7.3 Model-independent determination of $\hat{\rho}_{22}$

We have made Na MOT excited state fraction and effective saturation intensity measurement using a two-level atomic model as described earlier in Sec 6.2.1. A model-independent measurement of the excited-state fraction $\hat{\rho}_{22}$ could be conducted within the hybrid system by comparing two methods of measuring the number of ions created via PI: directly, with our Channeltron electron multiplier (CEM) and indirectly, by monitoring the MOT fluorescence when exposed to the PI laser.

Our CEM has been calibrated using the two-level MOT atom model. Therefore, we will independently calibrate the CEM using Ca^+ fluorescence. One possible method may be to count individual ions within an ion crystal [like the one seen in Fig. 4.90] before extracting those ions into the CEM. Then we can directly measure the number of Na^+ ions created via PI in the hybrid trap with an independent calibration.

According to Eq. (6.15) the number of Na^+ ions loaded N_I into the LPT during a duration t_{load} via PI can also be expressed as

$$N_I = \tilde{N}_a \gamma_{\text{pi}} t_{\text{load}}. \tag{7.1}$$

Because the LPT trap depth is much larger than the mean energy of the ions loaded into the LPT from the MOT, we can assume that all the ions created remain trapped within the LPT during the duration t_{load}. This assumption is valid when the number of ions loaded is small compared to the LPT saturation limit and t_{load} is much less than the LPT lifetime.

According to Eq. (4.39) the MOT's steady-state 589 nm fluorescence power P_{MOT} is related to the number of MOT atoms by

$$N_a = \frac{\kappa P_{\text{MOT}}}{\hbar \omega_L \Gamma \hat{\rho}_{22}}, \tag{7.2}$$

where κ is a geometric factor related to the experimental apparatus. Therefore, according to Eq. (7.2), by using MOT fluorescence measurements to find $\gamma_{\rm pi}$ and the steady state MOT fluorescence power $P_{\rm MOT}$, we can relate the number of ions loaded to $\hat{\rho}_{22}$.

Using the value of N_I measured with the CEM and combining Eq. (7.1) and Eq. (7.2), the excited state fraction is given by

$$\hat{\rho}_{22} = \frac{\kappa P_{\rm MOT}}{\hbar\omega_L \Gamma N_I}\gamma_{\rm pi} t_{\rm load}. \tag{7.3}$$

The right hand side contains quantities that are directly measurable and do not depend upon the two-level model theory in Eq. (3.76), thus giving a model-independent determination of the MOT's excited state population.

7.4 Conclusions

The hybrid ion-neutral trap offers an ideal setting to study ion-neutral interactions over a wide range of energies, including the relatively unexplored ultracold regime. In Chs. 2 and 3 we outlined the underlying physics associated with those ion-neutral scattering reactions and atomic interaction with electromagnetic radiation, respectively. In Ch. 4 we discussed the hybrid apparatuses construction, design, and operation.

In Ch. 5 we discussed experimental [38] and simulation [37] results pertaining to translational sympathetic cooling within the hybrid system. We found that sympathetic cooling was possible, but not likely able to equilibrate at cold temperatures with neutral number densities less than 10^{11} cm^{-3} or for large ion populations. In Ch. 6 we considered measurements of the charge-exchange rate coefficient for the Ca^+- Na system and the total collision rate for the Na^+- Na system. Preliminary measurements [39] suggest that a fast Ca^+- Na charge-exchange reaction pathway exists and its rate coefficient is approximately two orders of magnitude smaller than the equivalent Langevin rate. More

precise measurements [40] of the Na^+- Na system showed good agreement with previously reported fully quantal *ab initio* theoretical models and semiclassical power-law models [68].

Finally, in this chapter we have considered possible future experiments related to the vibrational sympathetic cooling of Na_2^+, laser fluorescence based measurements of the Ca^+-Na interaction, and using the hybrid system to perform a model-independent determination of a Na MOT's excited state population.

Appendices

Appendix A

Mechanical Drawings

In this section we document prints for several elements of the apparatus. These elements were designed by our group and machined by the UConn Physics Department machine shop.

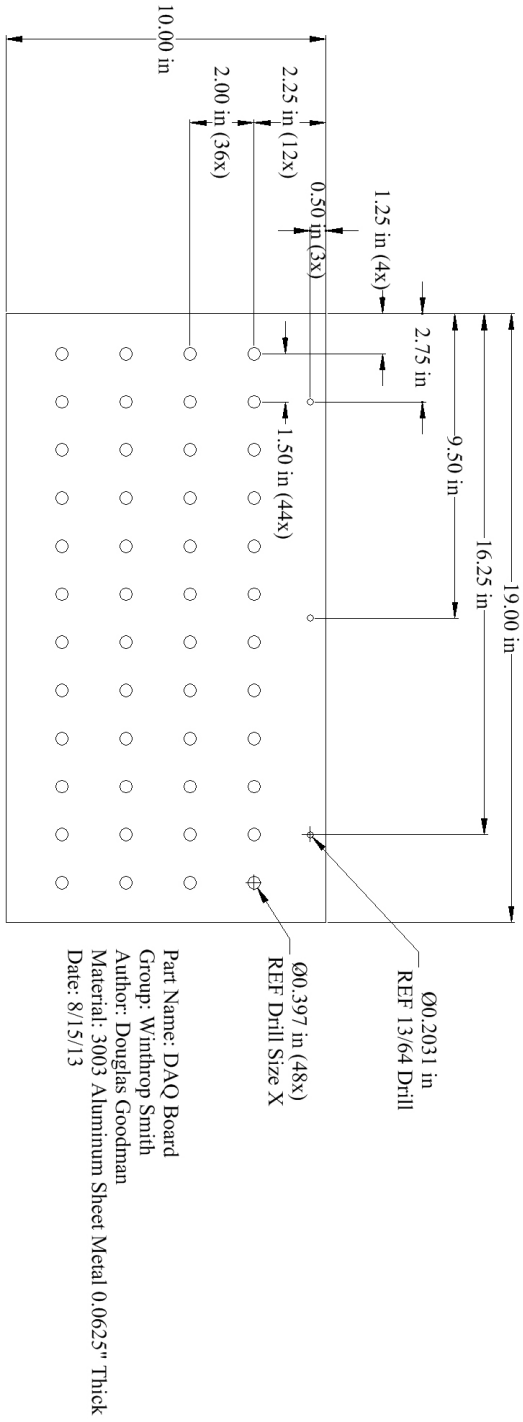

Figure A.1: DAQ board feethrough panel.

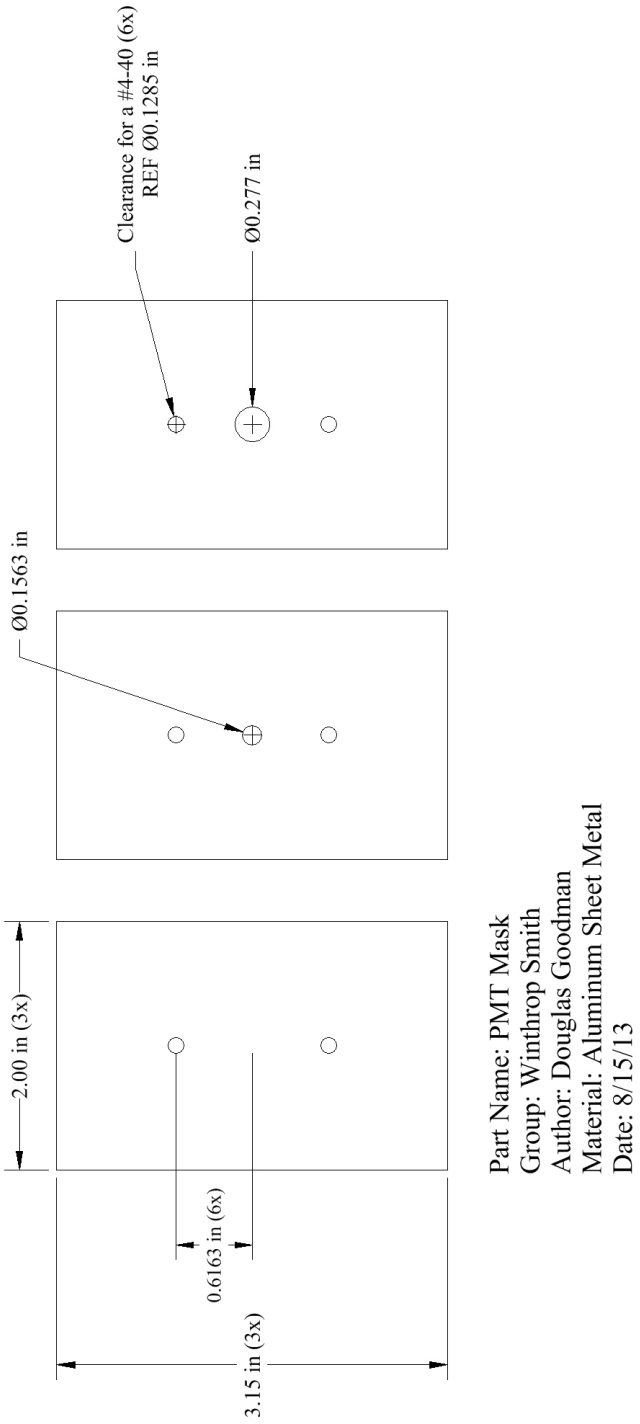

Figure A.2: PMT front mask.

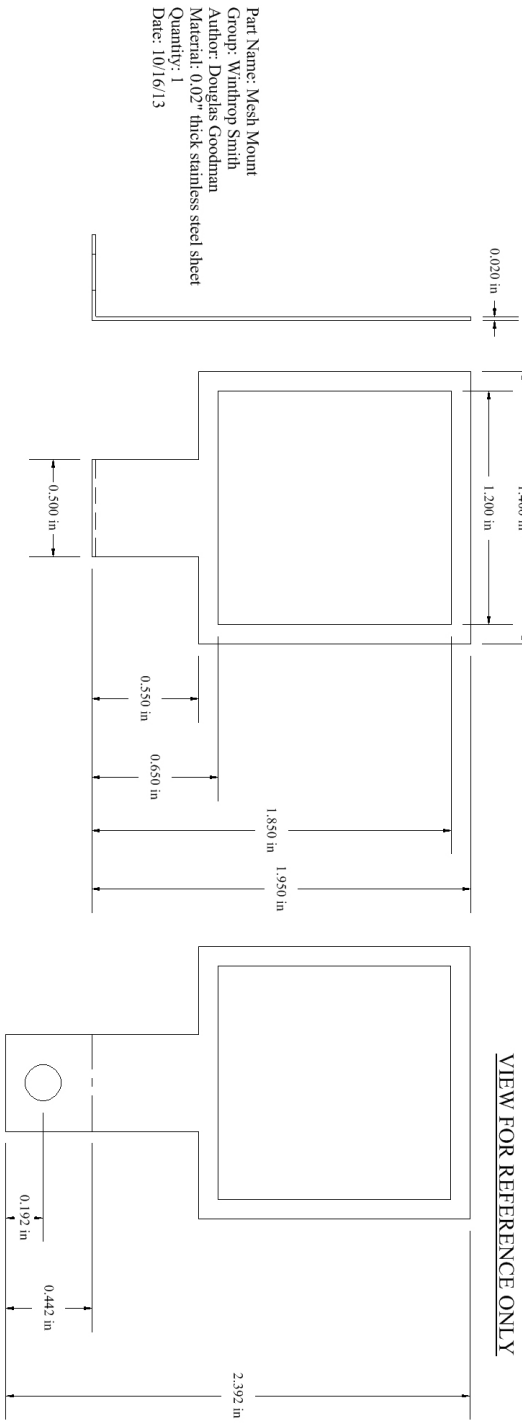

Figure A.3: Mesh mount.

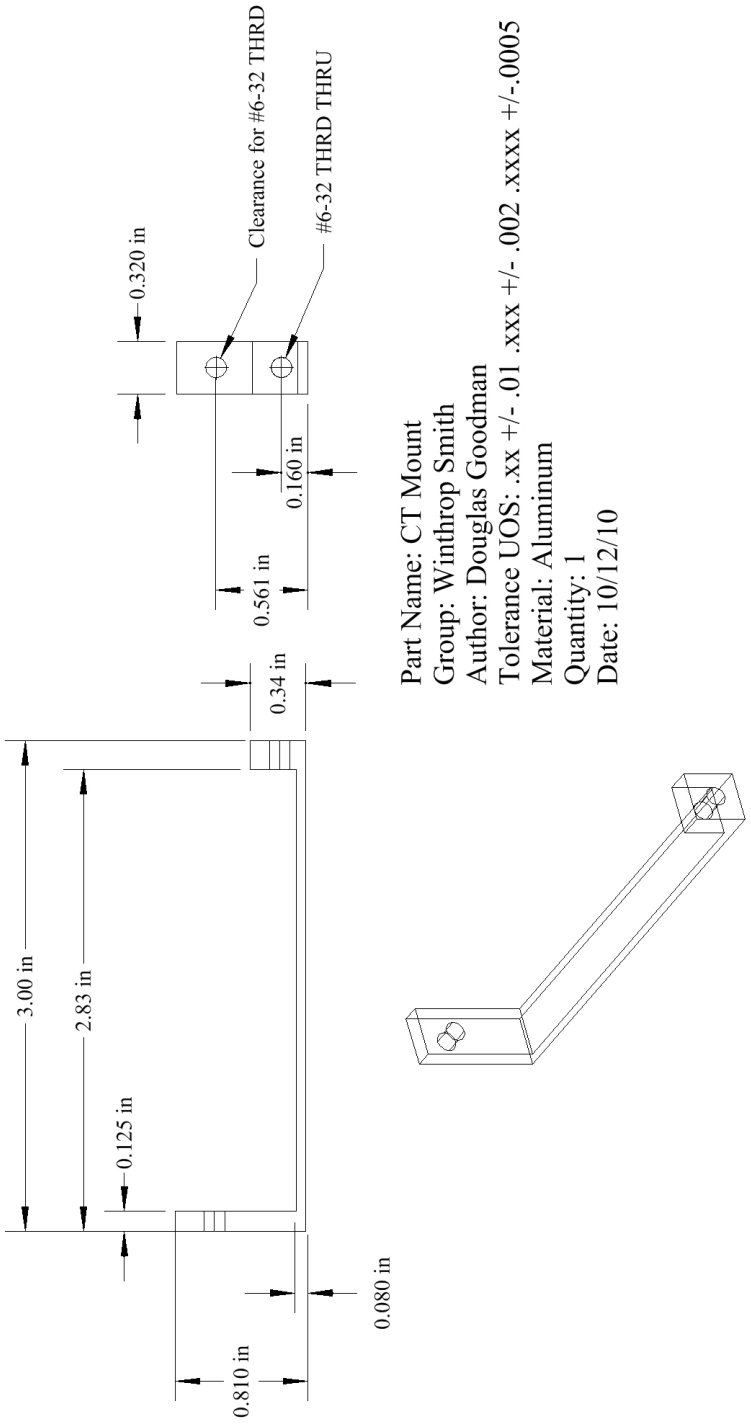

Figure A.4: CEM fixture.

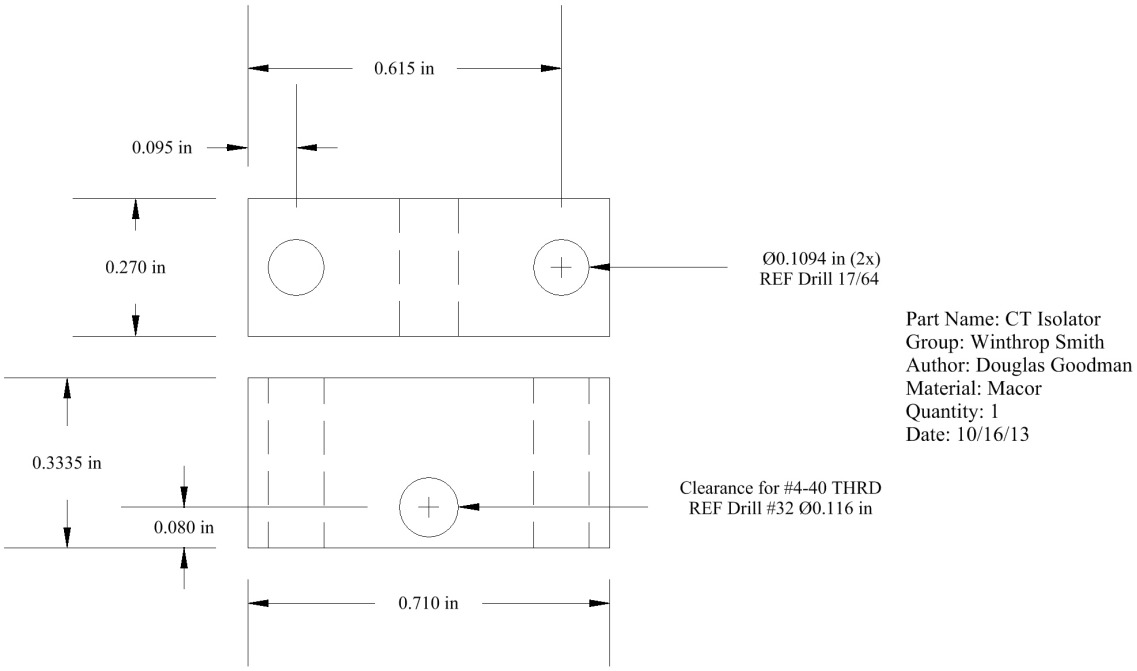

Figure A.5: Electrical isolator for CEM fixture.

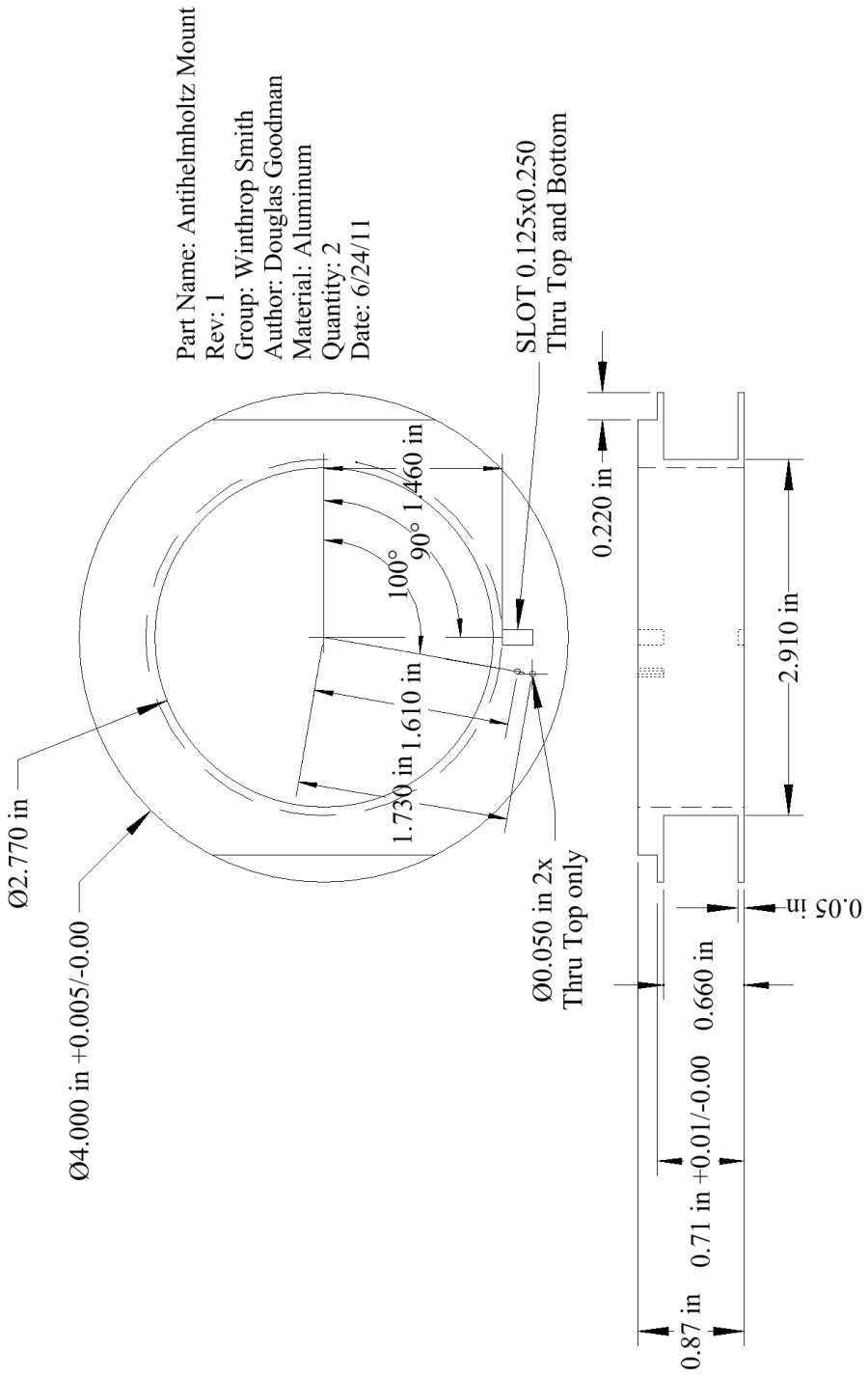

Figure A.6: Anti-Helmholtz coil fixture.

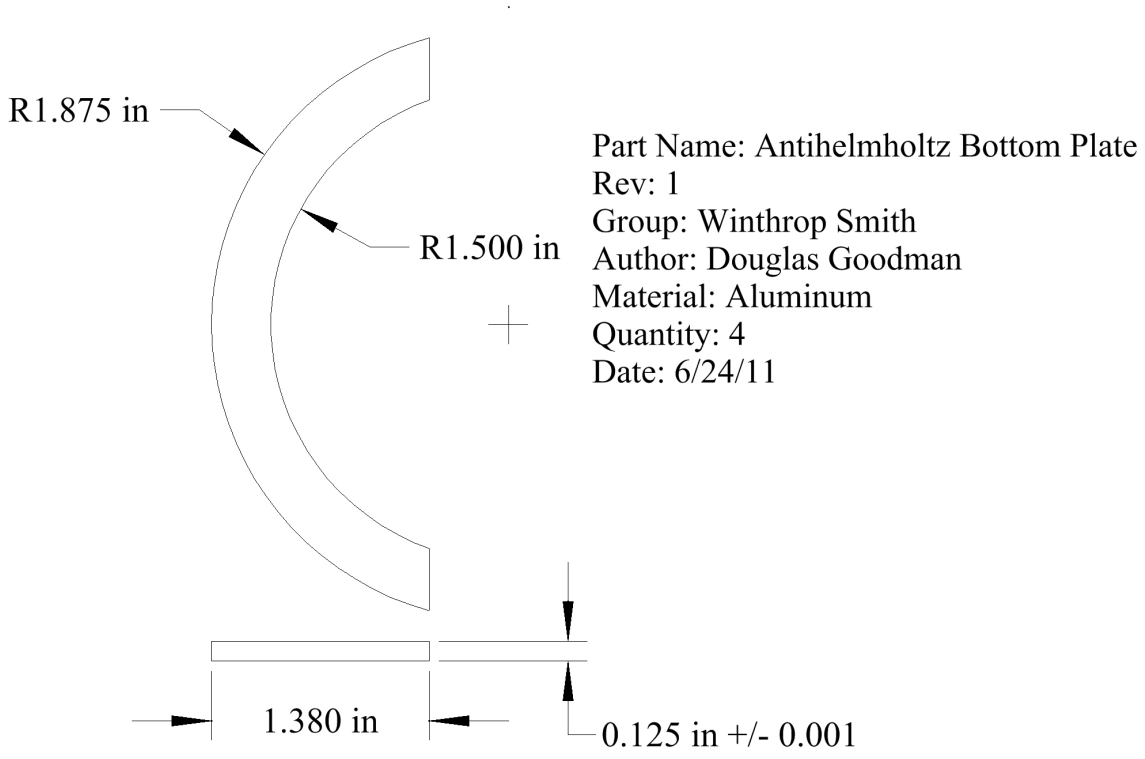

Figure A.7: Spacer plate for anti-Helmholtz coil that sits between coil fixture and UHV chamber.

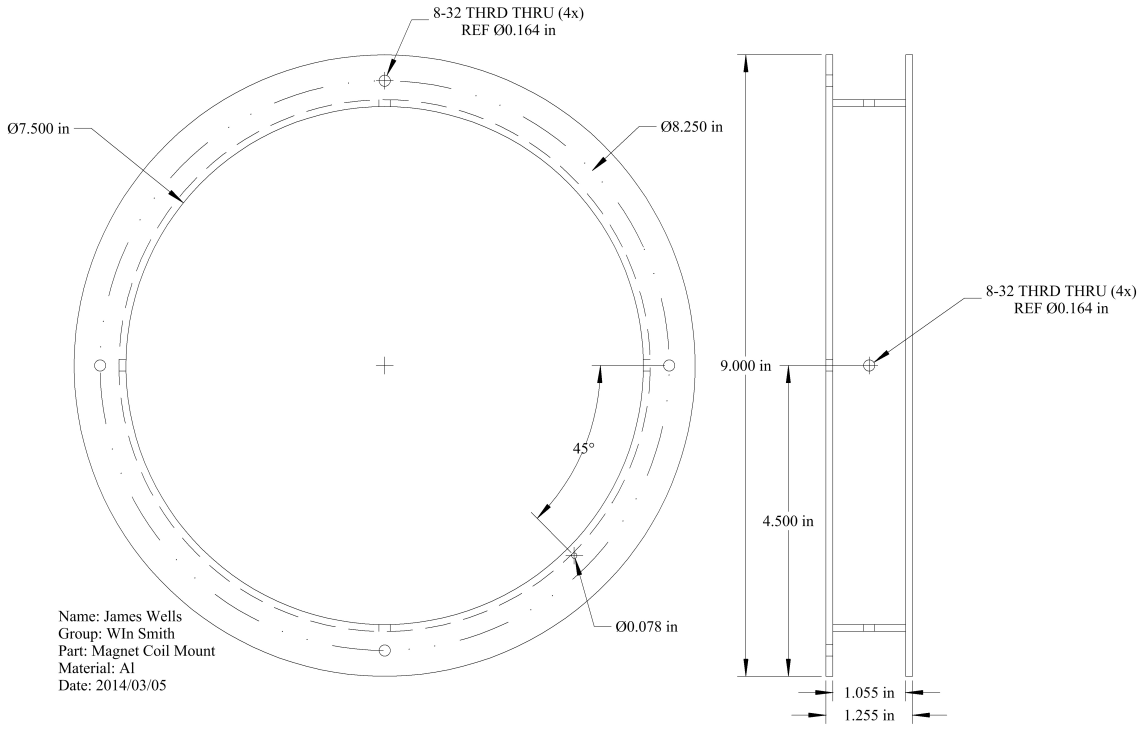

Figure A.8: Electromagnet shim coil fixture.

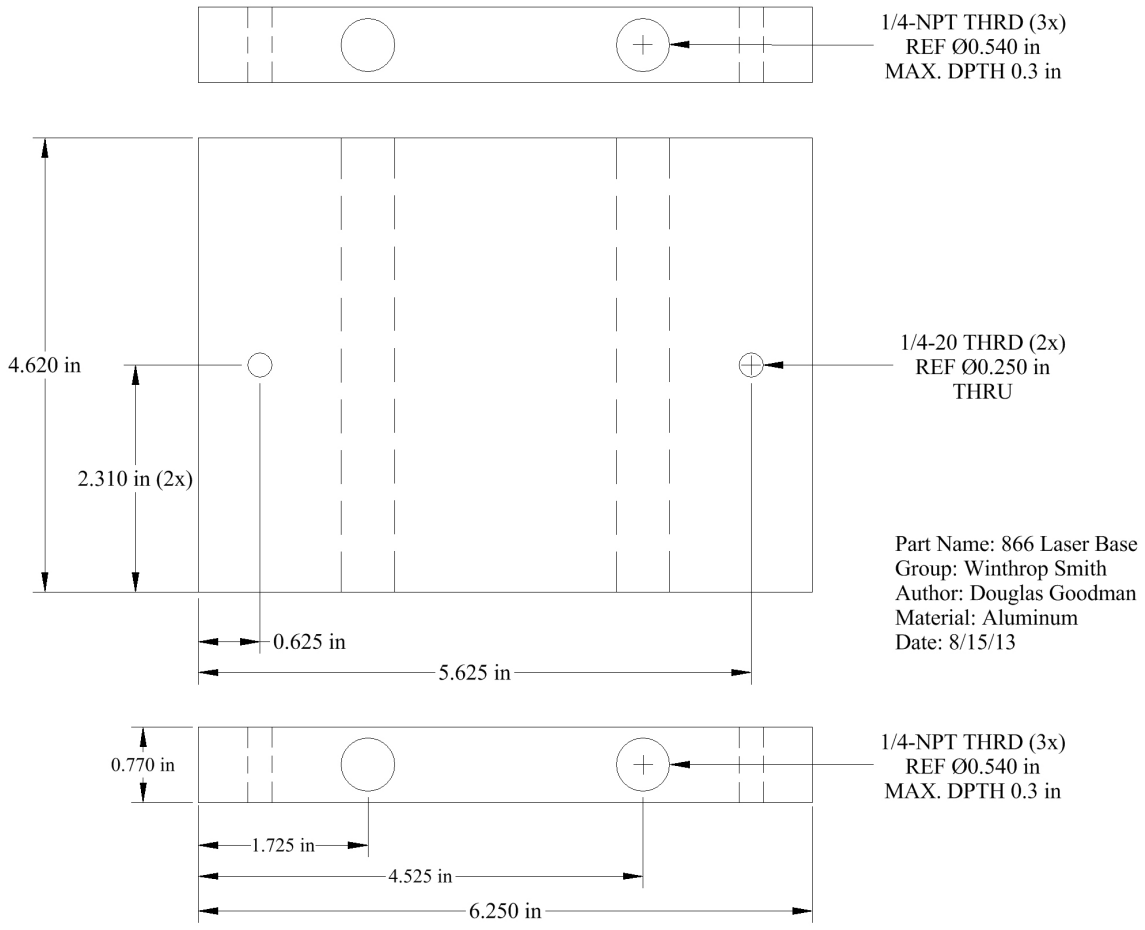

Figure A.9: Water cooling base for 866 nm laser head.

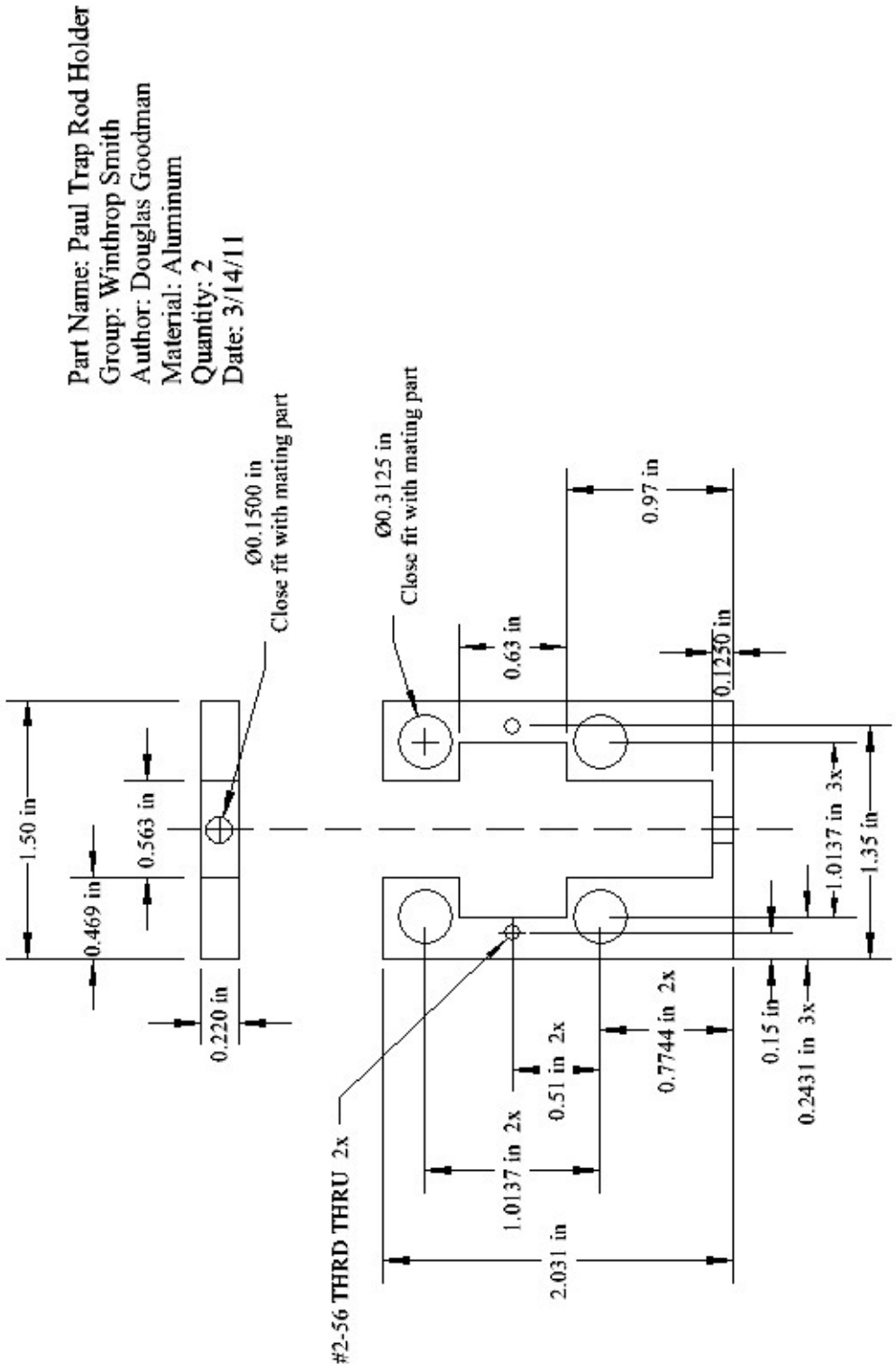

Figure A.10: LPT rod fixture.

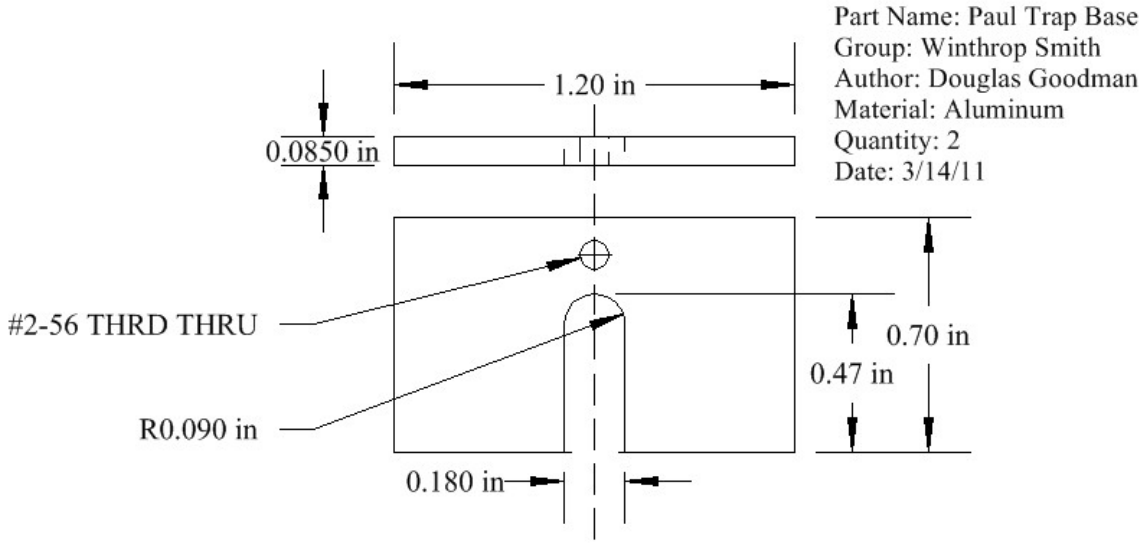

Figure A.11: LPT rod fixture base.

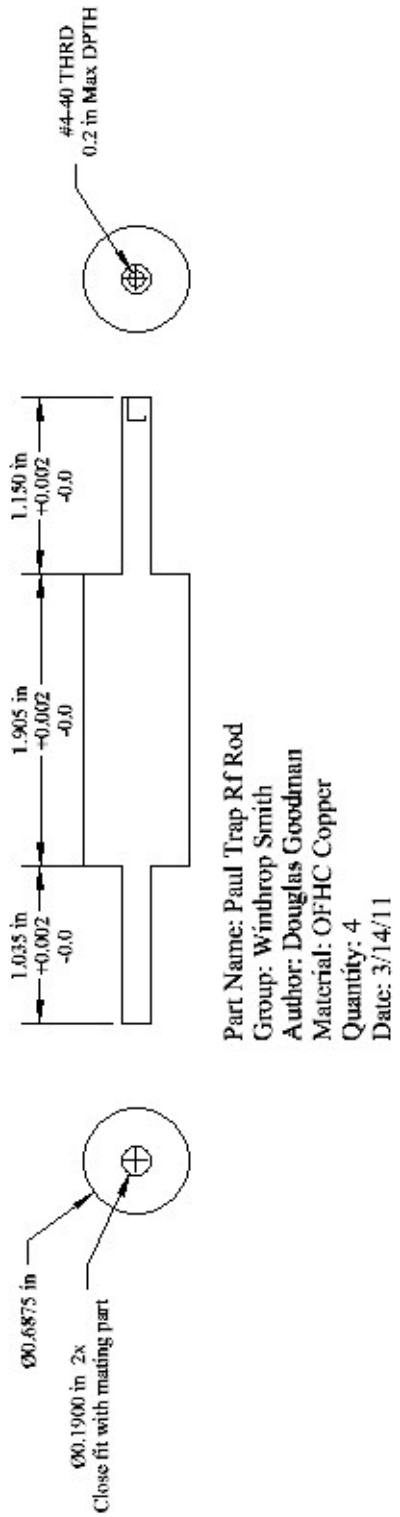

Figure A.12: LPT rf rod electrodes.

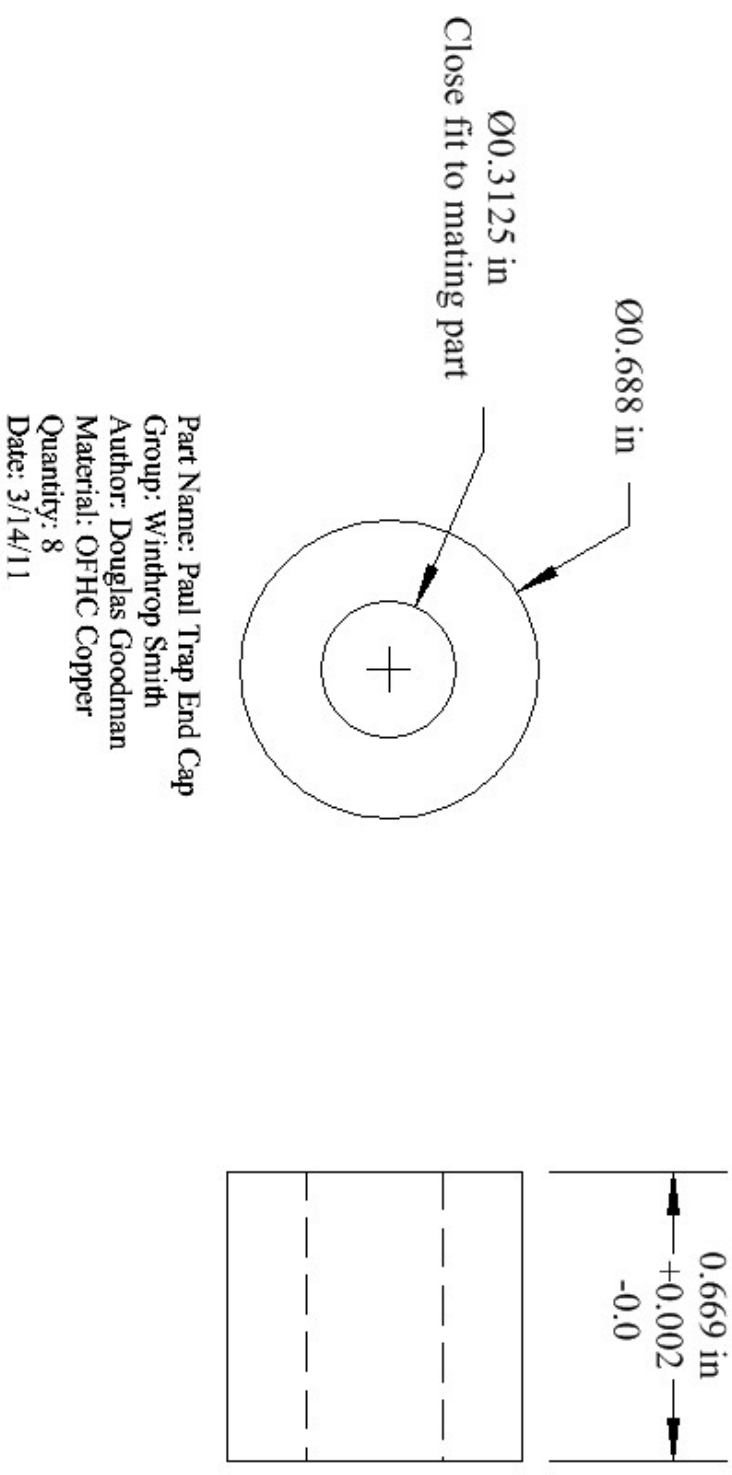

Figure A.13: LPT end cap electrodes.

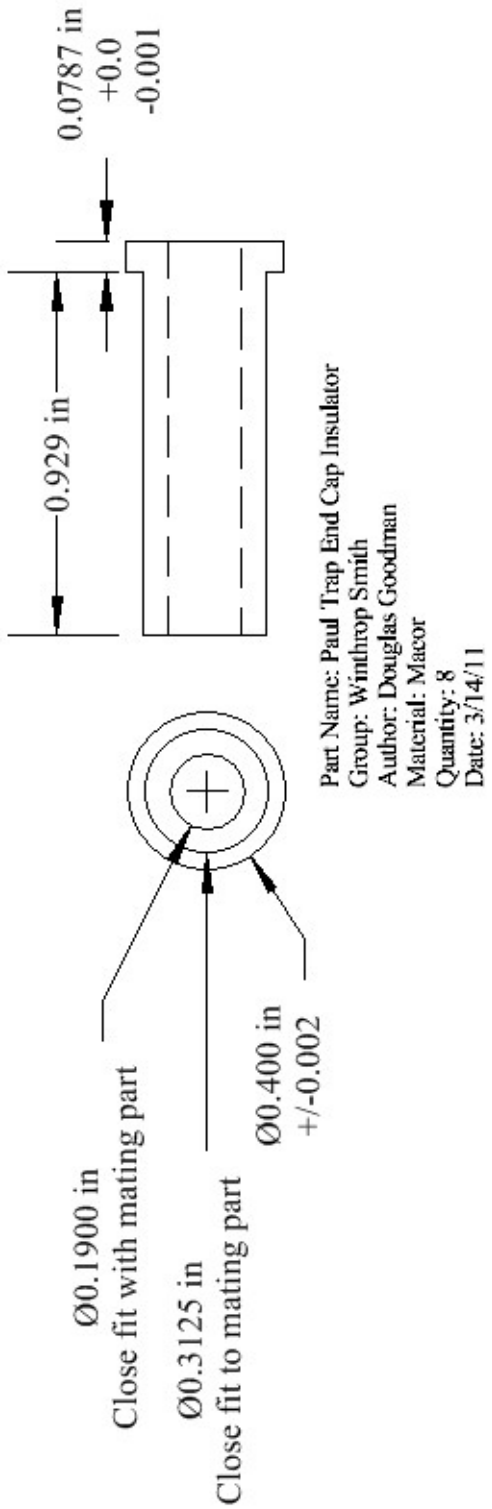

Figure A.14: LPT end cap insulator.

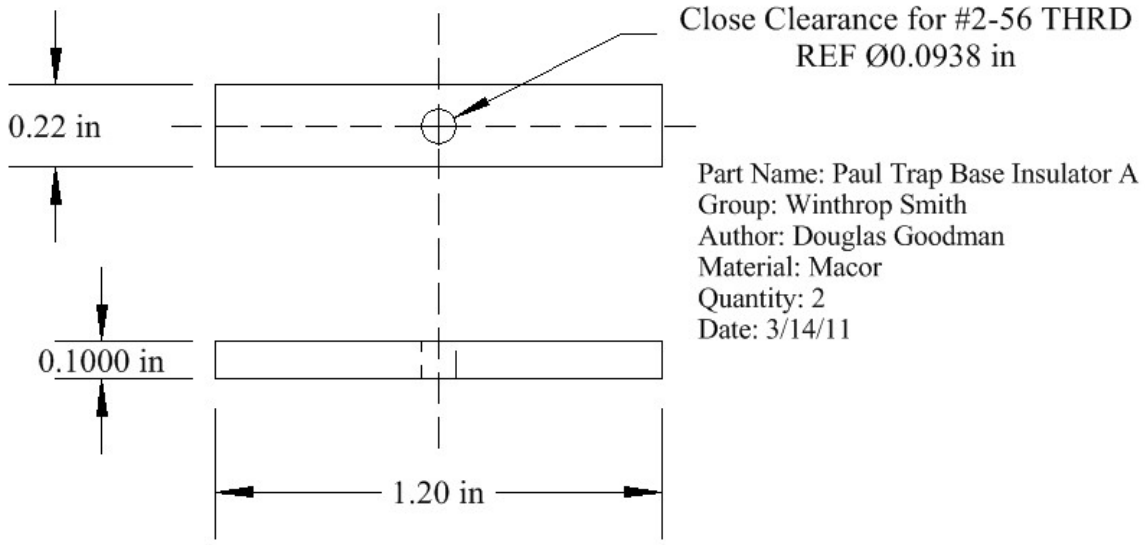

Figure A.15: LPT base insulator part A.

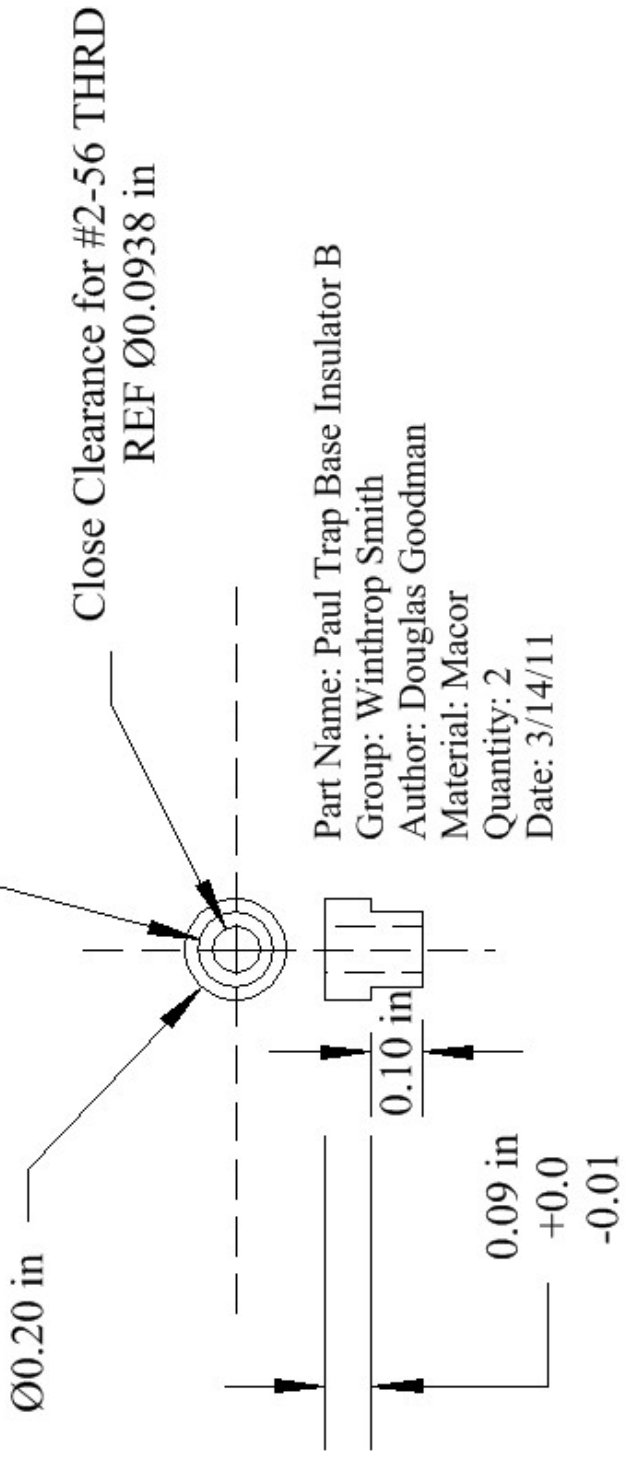

Figure A.16: LPT base insulator part B.

Appendix B

Electromagnets

Electromagnets play an important role in the operations and formation of our MOT. In this section we will discuss some of the technical details of our shim coil electromagnets, which adjust the position of the MOT's magnetic field minimum. We will also discuss the anti-Helmholtz electromagnets used to create the magnetic field gradient associated with the radiation pressure's spatial dependence.

B.1 Shim coils

The shim coils consist of a circular winding of N turns around a circular fixture. The mechanical drawings for the horizontal shim coil mounts can be seen in Fig. A.8. The vertical shim coil is a square fixture with dimensions 30 x 30 cm. For the remainder of this section we will restrict our discussion to that of the circular magnet coils.

When a current I runs through a wire the moving charges produces a magnetic field $\vec{\mathscr{B}}$. A single charge q moving at velocity $\vec{v}$ produces a field at position r

$$\vec{\mathscr{B}} = \left(\frac{\mu_0}{4\pi}\right) \frac{q\vec{v} \times \hat{r}}{r^2}, \tag{B.1}$$

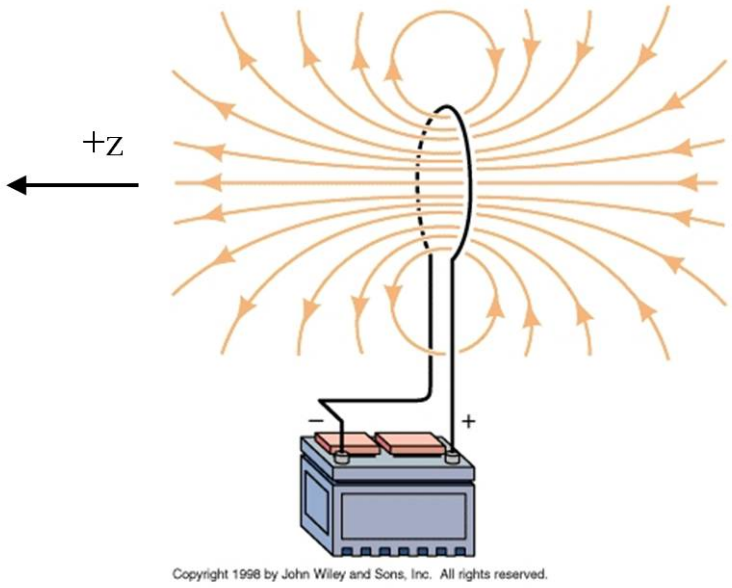

Figure B.1: Magnetic field lines (orange) produced by a single coil of wire hooked up to a dc power source. The field is strongest in the center where the field lines are close to each other. The field strength falls according Eq. (B.3) along the axial z direction. The field direction can be reversed by switching the power supply leads, thus reversing the current direction. The original figure is from John Wiley and Sons, Inc. website.

where μ_0 is the vacuum permeability magnetic constant. A wire carrying current is made up of many charges with number density n moving with a drift velocity v_d. If the wire has a cross section A then the total charge in an infinitesimal length of wire dl is $dq = nqAdl$. The infinitesimal field from dq according to Eq. (B.1) is

$$d\vec{\mathscr{B}} = \left(\frac{\mu_0}{4\pi}\right)\frac{(dq)\vec{v}_d \times \hat{r}}{r^2} = \left(\frac{\mu_0}{4\pi}\right)\frac{Id\vec{l} \times \hat{r}}{r^2}, \tag{B.2}$$

known as the Biot and Savart law. To obtain the total field at any point in space we need only integrate Eq. (B.2) over the length of wire.

For the case of a circular wire with radius R, the only net magnetic field component at any position along the wire's central z-axis lies parallel to that z-axis due to the symmetry of the loop [118], as illustrated in Fig. B.1. With a little trigonometry, we find that the

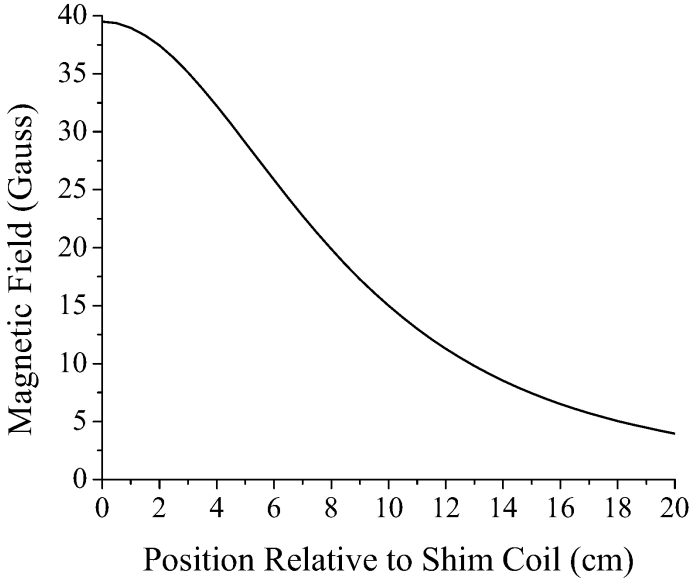

Figure B.2: Net shim coil magnetic field along centeral z-axis. The MOT is located approximately 16.5 cm from the shim coil.

integration of Eq. (B.2) for the z-component of the field for points along the z-axis yields

$$\mathscr{B}_z = \int \left(\frac{\mu_0}{4\pi}\right) \frac{IR}{(z^2+R^2)\sqrt{z^2+R^2}}\, dl = \frac{\mu_0 I R^2}{2(z^2+R^2)^{3/2}} \tag{B.3}$$

per wire at radius R.

Figure B.2 shows the magnetic field due to one of our shim coils according to Eq. (B.3) with $N = 220$ turns of 16 AWG wire at a current $I = 3$ A and 7 V.[1] By adding an additional (approximately) uniform magnetic field to that of the anti-Helmholtz field, the shim coil's field adjusts the location of the anti-Helmholtz field minimum, thus moving the location of the MOT's center. With the MOT at ≈ 16.5 cm from the coil and assuming a 22.5 Gauss/cm anti-Helmholtz coil horizontal magnetic field gradient near the MOT, the maximum displacement of the MOT by the shim coil is ≈ 0.3 cm, according to Fig. B.2.

[1] We do not use a current larger than 4 A because the shim coils are not actively cooled and we do not want to exceed the maximum current rating, so as to avoid overheating the coils.

B.2 Anti-Helmholtz coils

The anti-Helmholtz configuration uses two circular electromagnets to create a quadrupole magnetic field. There is a fairly uniform gradient dB/dz in each of the axial dimensions, where z points along the axis passing through both coils' centers, as shown in Fig. B.3. The gradient at points along the x and y directions is half that of z's, because of the system's symmetry and that the magnetic field must be divergenceless [73] according to Maxwell's equations

$$\vec{\nabla} \cdot \vec{\mathscr{B}} = 0 \implies \frac{1}{2}\frac{dB}{dz} = \frac{dB}{dx} = \frac{dB}{dy}. \tag{B.4}$$

Typically, the anti-Helmholtz coils are placed exactly one radius apart. However, in

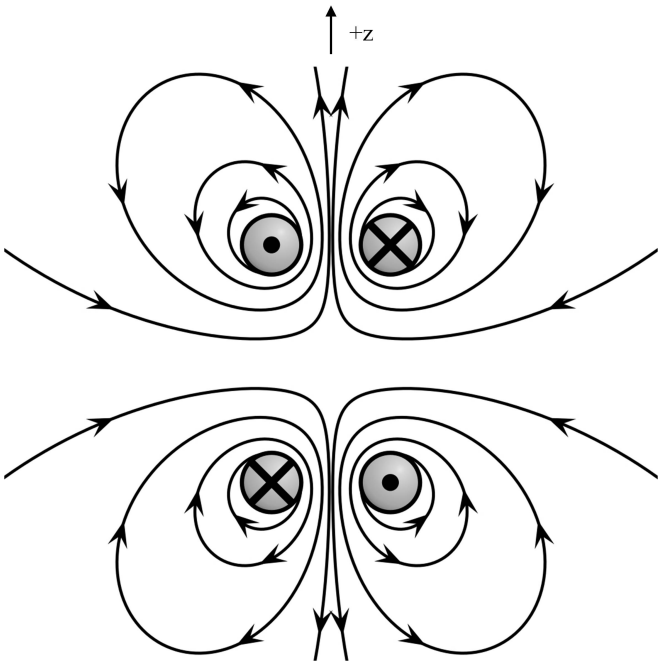

Figure B.3: Magnetic field lines of the anti-Helmholtz electromagnet configuration. The figure shows a 2D cross section through the central xz plane of the coils. The top coils has an opposing dc current direction relative to the bottom coil, producing a quadrupole magnetic field with zero field in the center.

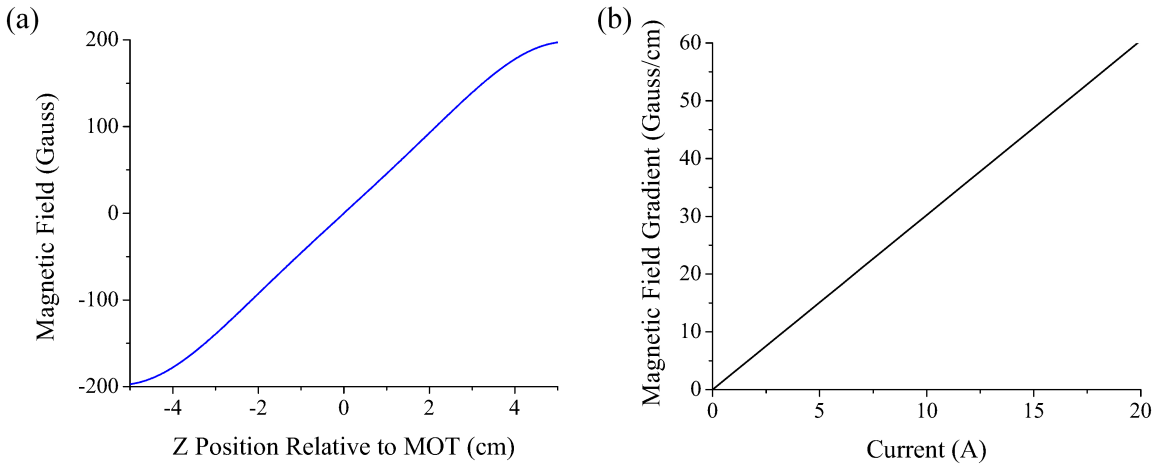

Figure B.4: Panel (a) shows the anti-Helmholtz magnetic field strength along z axis for two coils separated by $2R \approx 10$ cm with current $I = 15$ A as a function of position relative to the MOT. Panel (b) shows the anti-Helmholtz magnetic field gradient at the location of the MOT as a function of power supply current. We typically run in the 12 - 15 A range.

our setup they are placed one diameter apart because of practical limitations on the coils' construction and the dimensions of our UHV chamber. Nevertheless, the resulting magnetic field still has a linear gradient, as seen in Fig. B.4 (a).

Using Eq. (B.3), we can quantify the magnetic field along the z-axis of the anti-Helmholtz configuration as the sum of two electromagnets with opposite currents, namely,

$$\mathscr{B}_z = N\mu_0 R^2 \left(\frac{I}{2[(z-R)^2+R^2]^{3/2}} + \frac{-I}{2[(z+R)^2+R^2]^{3/2}} \right), \tag{B.5}$$

where we take the magnetic field minimum as the origin, which by definition is the location of the MOT's center. Equation (B.5) is consistent with our setup, which has the two coils $2R \approx 10$ cm apart and $N = 117$ turns of 18 AWG wire.

Typically we use coil currents in the range of $I = 12 - 15$ A and a supply voltage of $24 - 31$ V. Lower current produces a MOT with a larger size and atom number, but constant density over the $I = 12 - 15$ A range.

Figure B.4 (b) shows the corresponding z-axis gradient's dependence on the coil

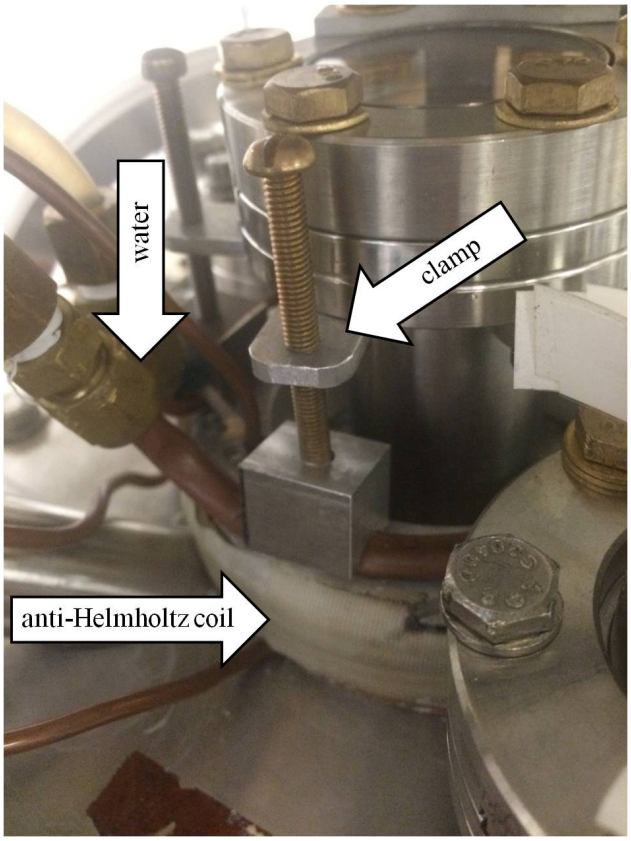

Figure B.5: Image of top anti-Helmholtz coil and mounting clamps.

current. To achieve the necessary gradients we must run the coils well above the ≈ 2 A rating for 18 AWG wire, so we actively water-cool the coils. We found that it was necessary to run a layer (3 windings) of 1/8" soft copper pipe along the inner diameter of the fixture and a layer of 1/8" tubing around the outer diameter, too. We also have one winding on top of each of the magnet fixture with 1/4" tubing. Water flows through the copper tubes with a flow rate of approximately 37 mL/s at an input temperature of 12° C. The water cooling provides enough power to combat the $144 - 233$ W per coil of resistive heating such that the coils feel warm, but not hot to the touch.

The coils are held to the chamber using custom clamps that use a stainless-steel #10-32 screw and a tapped tab that is mounted to the UHV window screws, as seen in Fig. B.5.

Appendix C

LabVIEW Programs

In this section we will discuss two of the LabVIEW programs that I wrote for data acquisition automation. We will call the first program "data acquisition" and the second "MOT image."

C.1 Data acquisition

The data acquisition program is part oscilloscope, part counter, and part voltage source. It was originally designed to control the the sequence of loading, trapping, and extraction of ions from the LPT. However, it quickly turned into a catch-all automation and data recording program that controls the majority of the laboratory hardware.

C.1.1 Analog input

The program interfaces with an NI analog input (AI) DAQ module 6363, which digitizes analog signals in the -10 to 10 V range. The front panel was created to look like an oscilloscope with the full array of oscilloscope controls, e.g., triggering, sample window timing, and basic waveform manipulation.

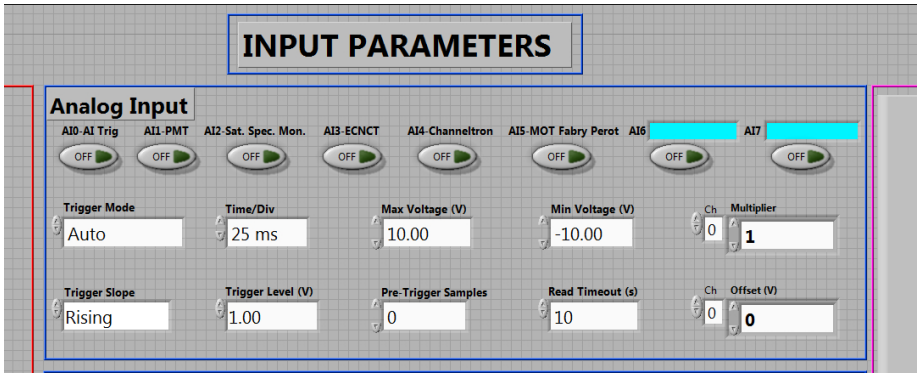

Figure C.1: Screen shot of data acquisition front panel's AI input controls.

Figure C.1 shows the input or "control" side of the AI front panel. By selecting the desired LED buttons, each AI channel can be switched on or off for waveform viewing and/or waveform signal recording to file. Examples of the various AI input signals include the CEM + pre-amplifier ion signal, PMT signal, and the FPI signals. The user can also add a custom channel name for any miscellaneous signals.

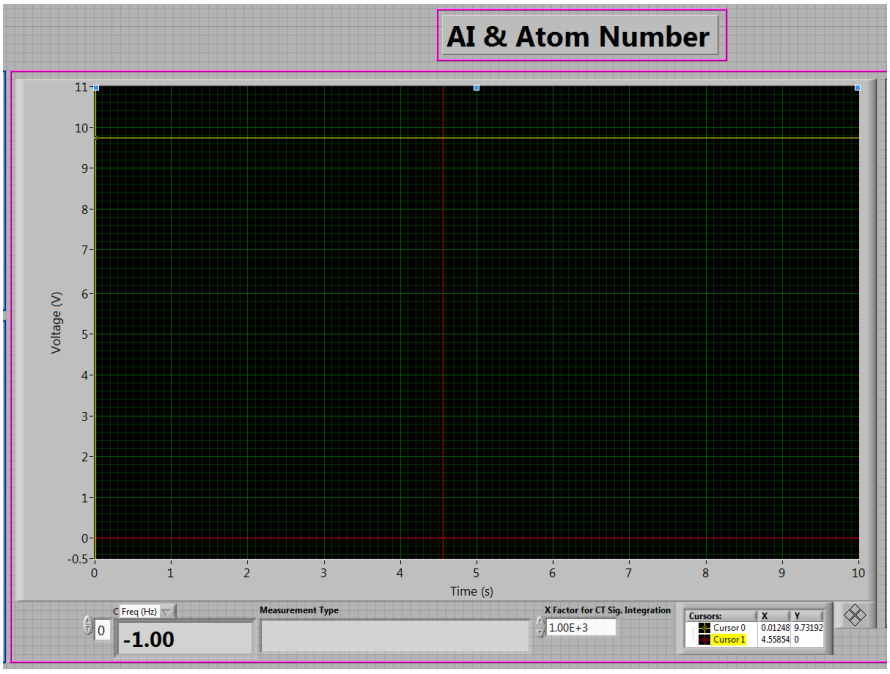

Figure C.2: Screen shot of data acquisition front panel's AI output plot indicator.

Figure C.2 shows the output or "indicator" waveform plot on the program's front panel. By connecting several monitors placed throughout the laboratory to the pc running the LabVIEW program, the AI output can conveniently be viewed simultaneously by several people at various locations within the laboratory.

C.1.2 Analog and TTL output

The program can also generate dc and waveform analog output, as well as TTL signals. The output signals come from interfacing with NI DAQ (TTL) 6602 and (AO) 6733 modules.

Figure C.3 shows the front panel controls for output signals, with seven different control

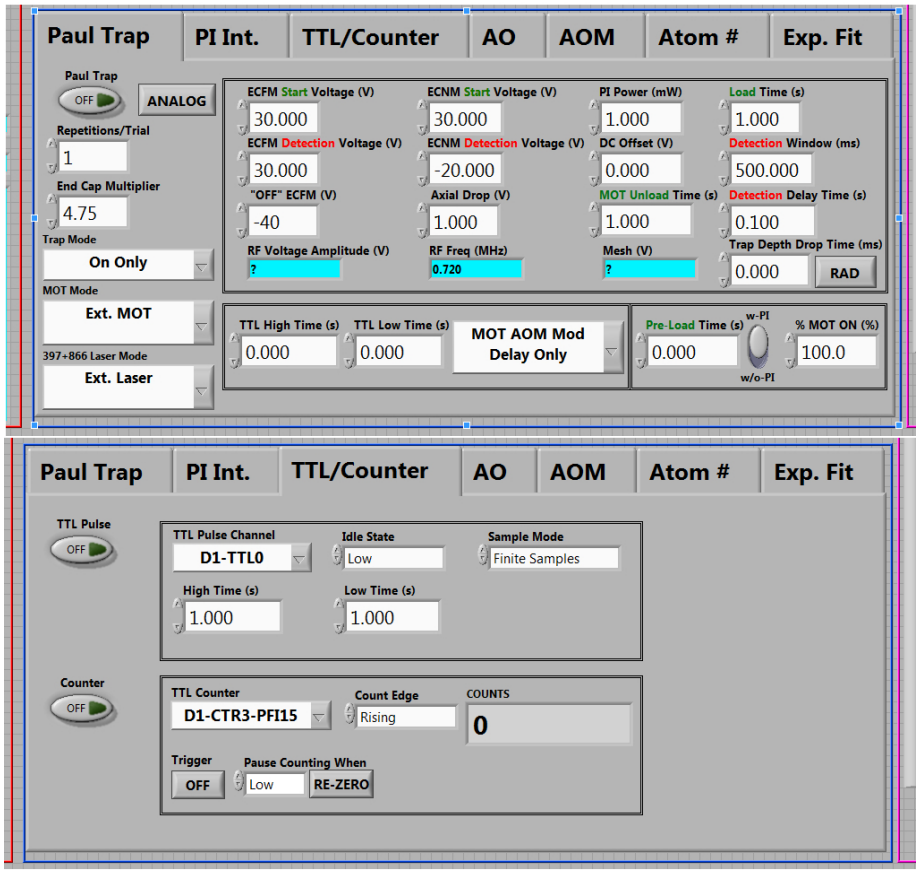

Figure C.3: Screen shot of data acquisition front panel's AO, TTL, and atom number input controls.

categories separated by tabs. Within each tab, the user can turn on and off or change settings associated with that tab's output signal generation. For example, the screen shot on the top of Fig. C.3 shows the various voltage and timing settings associated with running the LPT. The bottom screen shot shows the tab that controls the TTL signal (or TTL counter input) channels available for miscellaneous tasks that are not already reserved for LPT or AOM functions.

Additionally, the tabs "Atom #" and "Exp. Fit" are where the user inputs the setting associated with converting the PMT signal into an atom number and the settings associated with fitting MOT loading curves.

C.1.3 Recording to file

The default mode of the program is to not record data. This allows the user to test and control the automated hardware before recording to a text file. There are eleven different experiments or "recording sessions" that can be selected using the red dial knob seen in Fig. C.4. Before starting a recording session, the user can manually input comments to be included in the preamble of recorded text file, as well as choose the file name and directory within which the file will be saved.[1]

Once a recording session is chosen by switching on the "TAKE DATA" button, the user must answer a series of prompts associated with the particular data session chosen. For example, when selecting "PT time" measurement, the user is prompted to select an LPT timing parameter to automatically be incremented, e.g., the trapping time t_{trap}. The user must also specify a staring time, ending time, and number of steps to be taken. In this example, all the raw AI waveform data would be recorded to a series of text files. An additional text file with a summery of the main results is also created.

[1] Files automatically have dates and times appended to their names.

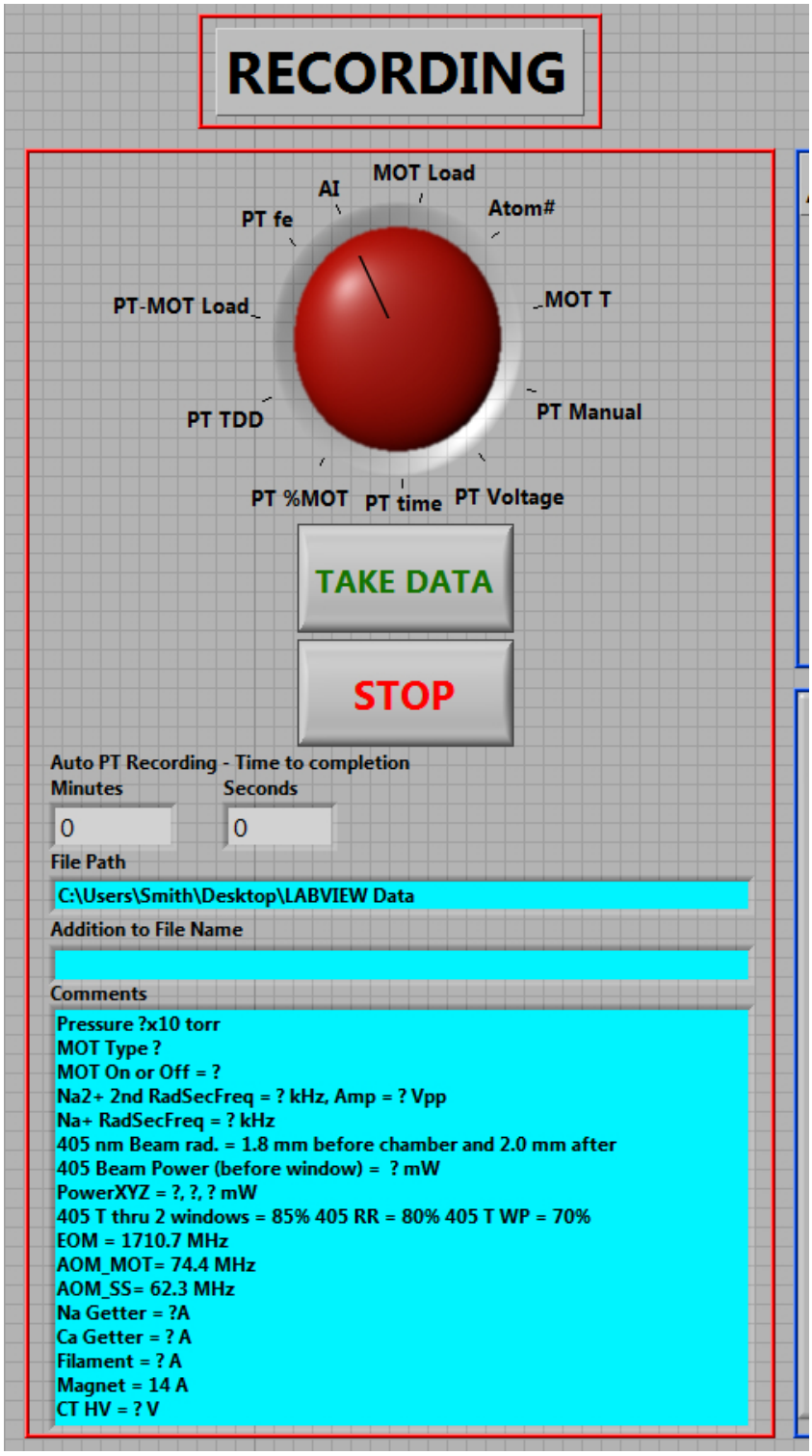

Figure C.4: Screen shot of data acquisition front panel's recording controls.

Another example is the "Atom #" recording session. Again, for this session the raw PMT waveform and atom number results are recorded to separate text files. Before starting, the user is prompted to choose one of three options: (i) a continuous data run, where the atom number data is recorded indefinitely until the user manually stops the program. (ii) a user defined fixed number of data runs or (iii) to have the program pause at regular intervals, allowing the user to periodically change input and record the value of some miscellaneous manual step parameter.

C.1.4 Additional output

Figure C.5 shows additional front panel output that gives useful realtime feedback on the atom number, MOT loading fitting parameters, power meter reading, or ion signal. These outputs come in handy when manually testing or tweaking something within the experiment or apparatus. They are also helpful when monitoring the progress of an active data session.

C.2 MOT image

The MOT image program interfaces with the Thorlabs CMOS camera. Input parameters are entered in the controls, similar to those seen in the data acquisition's "Atom #" control tab, but using the camera geometry and calibration. Like the data acquisition program, the file name and preamble comments can also be entered into text fields on the front panel.

Figure C.6 shows the three image panels used during a measurement. A snap shot of the MOT is taken by selecting the "Snap MOT or Laser" button. The image appears just below the button. The region of interest and the exposure time can be adjusted on the program's front panel until the desired image is acquired. Once at the desired settings, a background image must also be taken using the "Snap Background" button. The larger

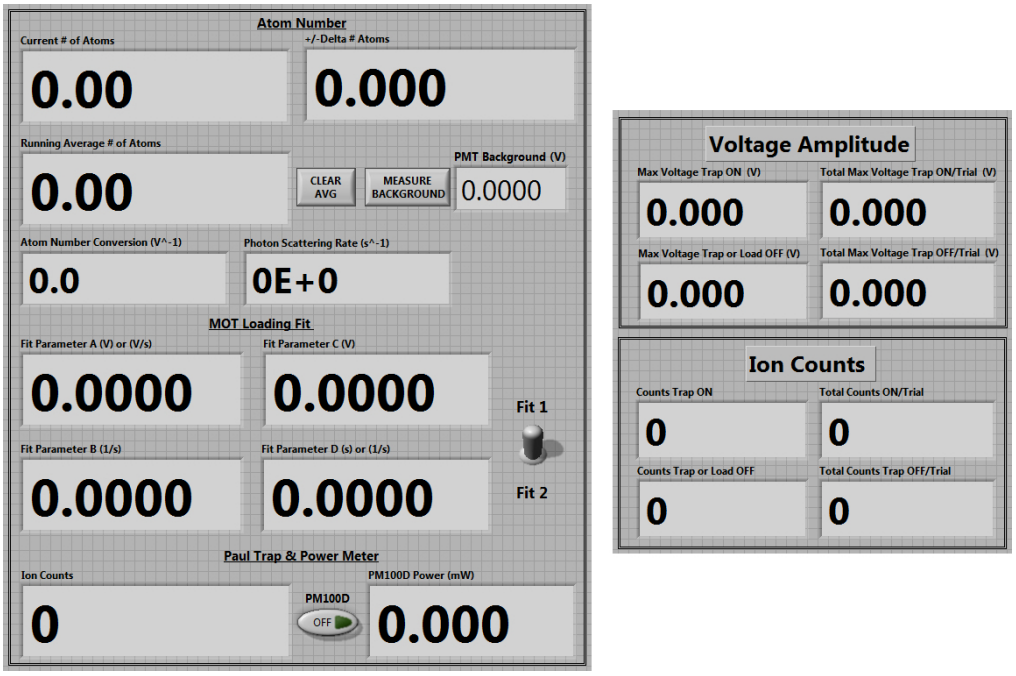

Figure C.5: Screen shot of data acquisition front panel's additional output indicators. Left panel shows MOT parameter output, power meter readings, and counter output. Right panel shows the voltage amplitude of the ion signal when running in an analog mode. Alternatively, the program can be also be run in a counting mode.

panel to the right displays the difference of the two images. If either image has pixels that are saturated, the "Camera Saturated" LED alarms, indicating that the picture should be taken again (possibly with a reduced exposure time) before recording to file.

When the "Write to File" button is selected the raw pixel data and a summary of the resulting atom number and density data are written to two separate text files. Subsequent pictures will not automatically be recorded to file, and the "Write to File" button must be selected each time. This allows the user to immediately discriminate which images should be recorded to file, making the post analysis less cumbersome.

Additional output numeric and graphical indicators including the atom number, peak density, and the spatial distribution of the MOT cloud are also seen on the front panel in Fig. C.7.

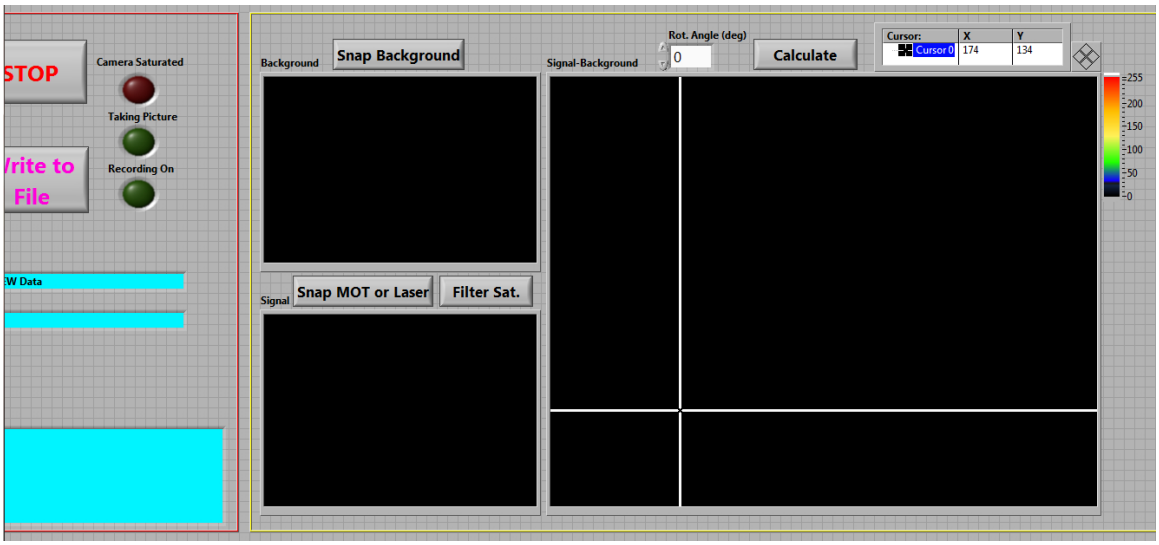

Figure C.6: Screen shot of the three image panels on the front panel of the MOT image program. The saturation and recording LED alarms are seen on the left hand side of the screen shot.

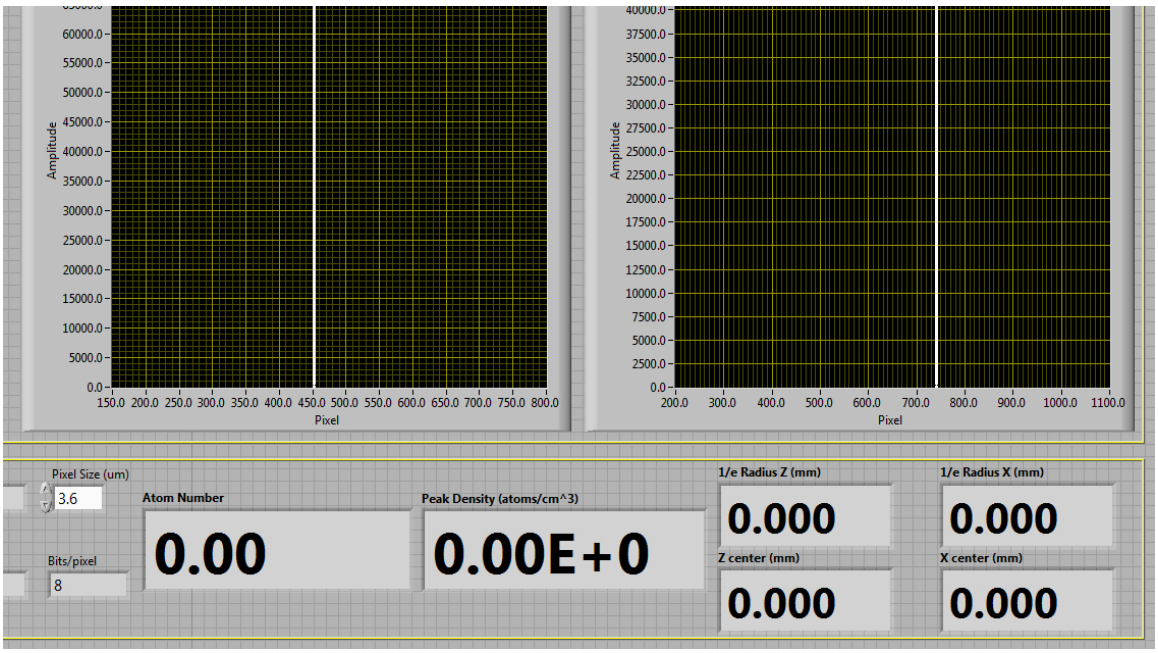

Figure C.7: Screen shot of additional MOT image output.

Appendix D

Lock-in amplifier

The lock-in amplifier is used experimentally to obtain the derivative of the Doppler-free saturation absoption spectrum signal. The resulting derivative signal is used for frequency-stablizing the TA-SHG Pro 589 nm laser head to the Na atomic spectra, as discussed in Sec. 4.2.3. In this section we will discuss how the lock-in generates the derivative signal.

When the laser is scanned using the Toptica scan control (discussed in Sec. 4.2.3), a sawtooth ramp waveform is generated. Let us just consider the rising linear half of the waveform, where the voltage $\mathscr{V}$ is linearly increasing with time t, thus the laser frequency is a linear function of time. We can express the spectrum signal as a function of time $S[\omega(t)]$, which has a Lorentzian lineshape.

We also modulate the laser frequency with the AOM by dithering the tuning voltage, which controls the AOM acoustic frequency with amplitude V_{dither} at dither frequency Ω. The net tuning voltage has the form

$$V_t + V_{\text{dither}} \sin(\Omega t) \equiv V_t + \mathscr{V}_{\text{ref}}(t). \tag{D.1}$$

At the sides of the Lorentzian ω far from ω_0, we can model the signal as being linear,

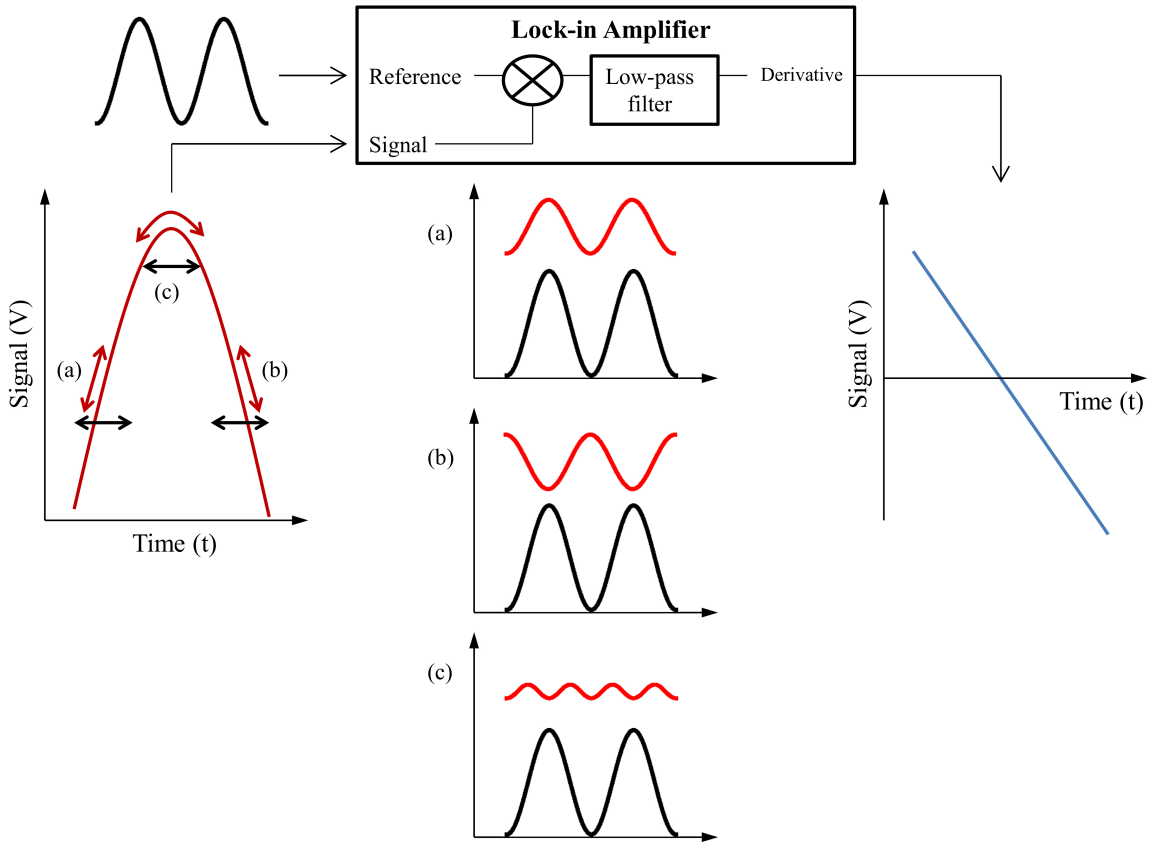

Figure D.1: Schematic of Lock-in amplifier. On the left we see the two inputs, the saturation spectrum's peak and the dither reference signal. The dither samples the local slope of the saturation spectrum. Location (a) and (b) are approximately linear and (c) corresponds to the top of the spectrum peak. In the middle we compare the local saturation spectrum signal (red) at each location in comparison with the reference signal (black). The lock-in measures the two signals' relative phase and amplitude and yields an output voltage proportional to the derivative of the original saturation spectrum signal.

as illustrated in Fig. D.1 (a) for a positive slope and Fig. D.1 (b) for a negative slope. The fast dithered signal samples the spectrum's local shape[1] and can be written as

$$S(t) \approx S[\sin(\Omega t)] = \zeta \sin(\Omega t) + V_o, \tag{D.2}$$

where ζ is the local slope and V_o is the offset. We can use the dither waveform as a reference

[1]Clearly, the dither voltage amplitude must be small compared to the size of the feature.

signal $\mathscr{V}_{\text{ref}}$, which will have a phase and amplitude difference relative to the spectrum signal. The positive slope $\zeta > 0$ is completely in phase and the negative slope $\zeta < 0$ is completely out of phase. This means that the derivative can be related to the phase difference and amplitude ratio between the reference and spectrum signal. At the top of the feature the amplitude is very small and the signal oscillates about twice as fast as the reference signal, as seen in Fig. D.1 (c).

We can generalize this observation by modeling the laser frequency shift as being linearly proportional to the tuning voltage. We can express the frequency controlled by the scan control and the AOM as

$$\omega(t) = \chi t + \xi V_{\text{dither}} \sin(\Omega t), \tag{D.3}$$

where χ is the frequency scan rate from the scan control and ξ is the conversion factor between tuning voltage and AOM double pass frequency shift. Again, since the dither frequency is much faster than the scan rate (~ 10 kHz $\gg 0.1$ Hz) we can think of the dither as sampling the local signal of the Lorentzian function $S[\omega(t_0)]$ at a specific time t_0. Taylor expansion of the signal about $\omega(t_0)$ gives

$$S[\omega(t)] = S[\omega(t_0)] + \left(\left. \frac{dS}{d\omega} \right|_{\omega=\omega(t_0)} \right) \xi V_{\text{dither}} \sin(\Omega t) + \ldots \tag{D.4}$$

To achieve a phase sensitive measurement of the derivative-proportional ac component in Eq. (D.4), the lock-in amplifier multiplies the reference and spectrum signal. The result of this multiplication is

$$\begin{aligned} S(t) \times \mathscr{V}_{\text{ref}}(t) = & S[\omega(t_0)] V_{\text{dither}} \sin(\Omega t + \phi) \\ & + \left(\left. \frac{dS}{d\omega} \right|_{\omega=\omega(t_0)} \right) \xi V_{\text{dither}}^2 \sin(\Omega t) \sin(\Omega t + \phi), \end{aligned} \tag{D.5}$$

where ϕ is the relative phase between the reference and spectrum signal. Using some trigonometry we can rewrite this as

$$S[\omega(t_0)]V_{\text{dither}}\sin(\Omega t+\phi)+\left(\left.\frac{dS}{d\omega}\right|_{\omega=\omega(t_0)}\right)\xi\frac{V_{\text{dither}}^2}{2}[\cos(\phi)-\cos(2\Omega t+\phi)]. \tag{D.6}$$

The lock-in amplifier's low-pass filter removes the high frequency 2Ω and Ω parts of the signal, outputting the phase sensitive measurement

$$\left(\left.\frac{dS}{d\omega}\right|_{\omega=\omega(t_0)}\right)\xi\frac{V_{\text{dither}}^2}{2}\cos(\phi) \tag{D.7}$$

proportional to the spectrum signal's derivative.

Appendix E

Acousto- and electro-optical modulation

The optical modulators are important optical elements used in the experiments presented here. Their purpose is to modulate their input laser light. As we will show, a large fraction of the output laser light is unchanged, still having the same input center-frequency called the carrier frequency. However, a smaller but significant fraction of the output has a shifted center-frequency relative to the carrier frequency by precisely the externally controlled and easily tunable modulation frequency. Here we will discuss the principles of electro-optical modulator (EOM) and acousto-optical modulator (AOM) operation.

E.1 Electro-optical modulation

Our group's EOM is a high-frequency phase modulator from New Focus. The EOM contains a MgO doped $LiNbO_3$ crystal with length L and width d. An electric field is applied across the crystal along the width perpendicular to the light propagation along length L.

The voltage applied $\mathscr{V}$ to the crystal (housed in a microwave cavity) causes electrical forces on the molecules in the crystal, thus distorting the crystal and consequently changing

its refractive index n. If we assume the voltage is applied using capacitor plate the electric field $\mathscr{E} = \mathscr{V}/d$, so the change in refractive index is

$$\Delta n = \frac{1}{2} n_e^3 r_{33} \frac{\mathscr{V}}{d} \tag{E.1}$$

known as the electro-optic effect. Here, n_e is the unperturbed refractive index and r_{33} is the proportionality element from the electro-optic tensor for the crystal's z-axis.

When light passes through the crystal it experiences a change in phase $\Delta\phi$ between the light exiting the crystal that traveled with speed v for time t through length

$$L = vt = v\frac{\phi_1}{\omega} = \frac{c}{n_e}\frac{\phi_1}{\omega}, \tag{E.2}$$

and that of light traveling with a reduced speed

$$L = \frac{c\phi_2}{\omega(n_e + \Delta n)}. \tag{E.3}$$

Using Eq. (E.1) we can express the phase modulation as

$$\Delta\phi = \frac{\omega}{c} L\Delta n = n_e^3 r_{33} \frac{\mathscr{V} L\omega}{2cd} = \beta\mathscr{V}, \tag{E.4}$$

where c is the speed of light in vacuum and ω is the angular frequency of the light.

Suppose some plane wave monochromatic radiation with electric field $\mathscr{E} \propto Ae^{i\omega t} + \text{c.c}$ enters the EOM. To keep the wave real we have included the complex conjugate c.c. However, to avoid clutter we will not continue to explicitly express it here. If a sinusoidal voltage at angular frequency Ω and amplitude $\mathscr{V}_0$ is applied to the crystal then the phase shift becomes $\beta\mathscr{V}_0\sin(\Omega t)$, according to Eq. (E.4). The radiation output becomes

$$\begin{aligned} Ae^{i[\omega t + \beta\mathscr{V}_0\sin(\Omega t)]} &\overset{\beta\ll 1}{\approx} Ae^{i\omega t}[1 + i\beta\mathscr{V}_0\sin(\Omega t)] \\ &= A\left(e^{i\omega t} + \frac{\beta\mathscr{V}_0}{2}e^{i(\omega+\Omega)t} - \frac{\beta\mathscr{V}_0}{2}e^{i(\omega-\Omega)t}\right). \end{aligned} \tag{E.5}$$

From Eq. (E.5) we see that the output field has some power at the carrier frequency ω and the rest of the power is at an up-shifted $\omega + \Omega$ and down-shifted $\omega - \Omega$ center-frequency.

E.2 Acousto-optical modulation

The AOM is manufactured with a piece of glass or crystal with a piezoelectric transducer on one end. A sinusoidal voltage driver is used to drive the transducer producing sound waves within the glass, as seen in Fig. E.1 (a). The sound wave's wavelength is

$$\Lambda = \frac{v_s}{f_a}, \tag{E.6}$$

where v_s is the speed of sound in the AOM medium. Although we do not know the exact v_s for the AOMs (not in specified by manufacturer), we can estimate it to be ≈ 4000 m/s.

The driving voltage supply is controlled by a dc tuning voltage in the range of $0-9$ V, which corresponds to a sinusoidal output at $f_a \approx 40-60$ MHz for the Brimrose AOM used in the saturation spectrum or $f_a \approx 70-90$ MHz for the Isomet AOM used with the MOT beams. The driving frequency f_a has an approximately linear proportionality with the tuning voltage V_t.

The longitudinal sound wave distorts the medium, thus periodically changing the medium's index of refraction. The changed index of refraction acts like a diffraction grating. The mechanical coupling between the sound wave and the light is called the acousto-optic effect.

The scattered light in the AOM follows the same geometry as x-ray Bragg diffraction between two atomic crystal planes, as seen by comparing Figs. E.1 (a) and (b). In Bragg diffraction, the light reflected off of consecutive atomic planes separated by a distance Λ constructively interfere (have no relative phase) if the path length is an integer n multiple of the light radiation's wavelength $n\lambda$. So the condition for constructive interference demands

(a)

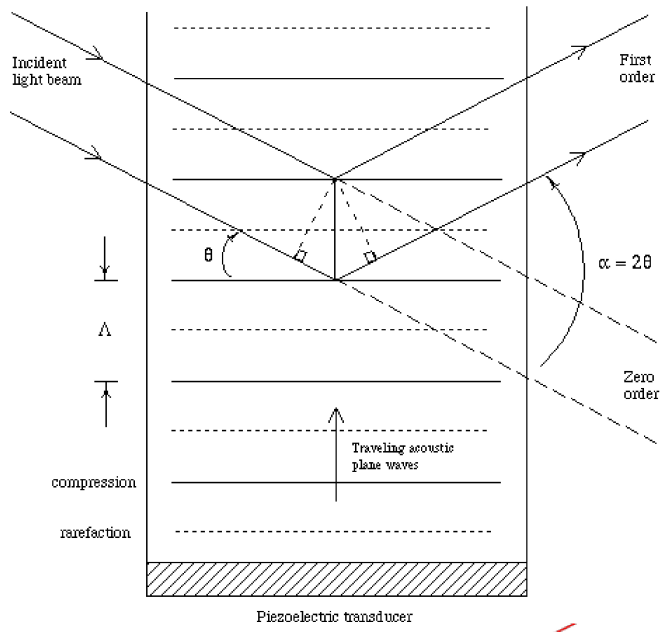

(b)

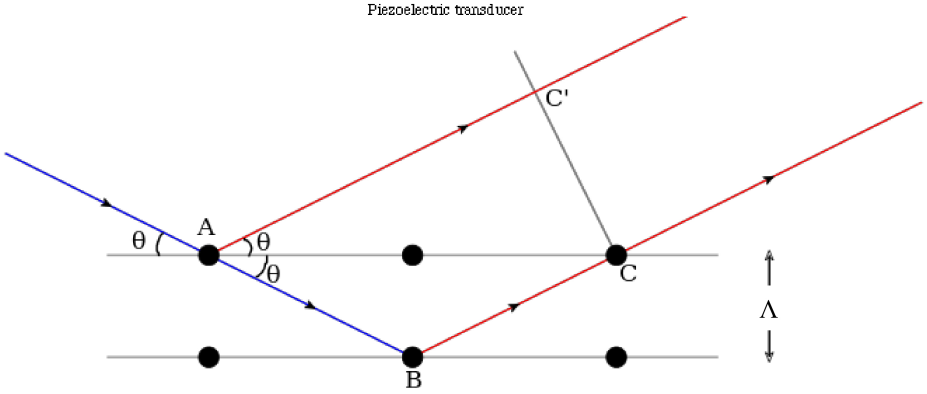

Figure E.1: Panel (a), originally from Ref. [128], shows light incident on the glass inside the AOM, which is diffracted by the traveling acoustic wave through the glass. Panel (b), originally drawn by M. Hadjiantonis, illustrates the geometry of Bragg scattering from two atomic planes. The two scattering geometries are identical except that the traveling wave in the AOM also Doppler shifts the diffracted light.

that the + first order maximum occurs at angle the Bragg angle $\theta_{n=1}$, where

$$(AB+AC)-AC' = (n=1)\lambda \implies 2\Lambda\sin(\theta) = \lambda\,. \tag{E.7}$$

The distances in Eq. E.9 are defined in Fig. E.1 (b).

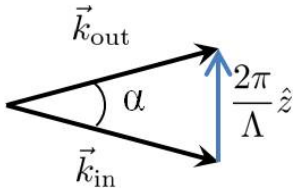

Figure E.2: Vector addition of the incident light momentum and the absorbed phonon momentum.

The Bragg angle is small. Using the small angle approximation in Eq. (E.1) we can estimate the angle between the + first order beam and the zeroth order (589 nm) beam α with $f_a = 70$ MHz as $\sim 1^\circ$, which is consistent with our small angle approximation.

If the sound wave was a standing wave then the diffracted light (out) would be at the same wavelength as the incident light (in). However, because the wave is traveling (in what we will call the +z direction) the output is Doppler shifted up in frequency for the + first order. Alternatively, we can think of the traveling wave diffraction as a photon-phonon scattering [191], where energy and momentum conservation demand that

$$\begin{aligned} \omega_{\text{out}} &= \omega_{\text{in}} + 2\pi f_a \\ \text{and } \vec{k}_{\text{out}} &= \vec{k}_{\text{in}} + \frac{2\pi}{\Lambda}\hat{z}. \end{aligned} \tag{E.8}$$

We can use the momentum condition depicted in Fig. E.2 and the fact that $\alpha \ll 1 \implies k_{\text{in}} \approx k_{\text{out}}$ to see that

$$\sin(\theta) = \frac{2\pi}{k_{\text{in}}\Lambda} \implies 2\Lambda\sin(\theta) = \lambda, \tag{E.9}$$

which confirms Eq. (E.9), as discussed in Ref. [191].

Appendix F

Laser beam size

F.1 Razor blade measurement

The "razor blade test" or "knife edge measurement" uses a razor blade with a sharp edge to measure the spatial profile of a laser beam with a Gaussian spatial mode. The laser spot is normally incident on a power meter, preferably one with a large enough sensor that nearly all of the beam appears to fit within the active area as seen by the naked eye. The larger the sensor the larger the area of analysis, which should improve accuracy. We typically use the Thorlabs S130C with a 9.5 mm active area and a measurement uncertainty of $\pm 5\%$.

Next, a razor blade is horizontally or vertically translated across the power meter (perpendicular to the beam and as close to the sensor as possible) a distance X , as illustrated in Fig. F.1 (a). The razor casts a sharp shadow on the power meter and the attenuated power reading as a function of X gives a measurement of the beam's spatial profile.

The intensity profile can be written as a function of the beam waist w where the beam's intensity drops to $1/e^2$ of its axial value as

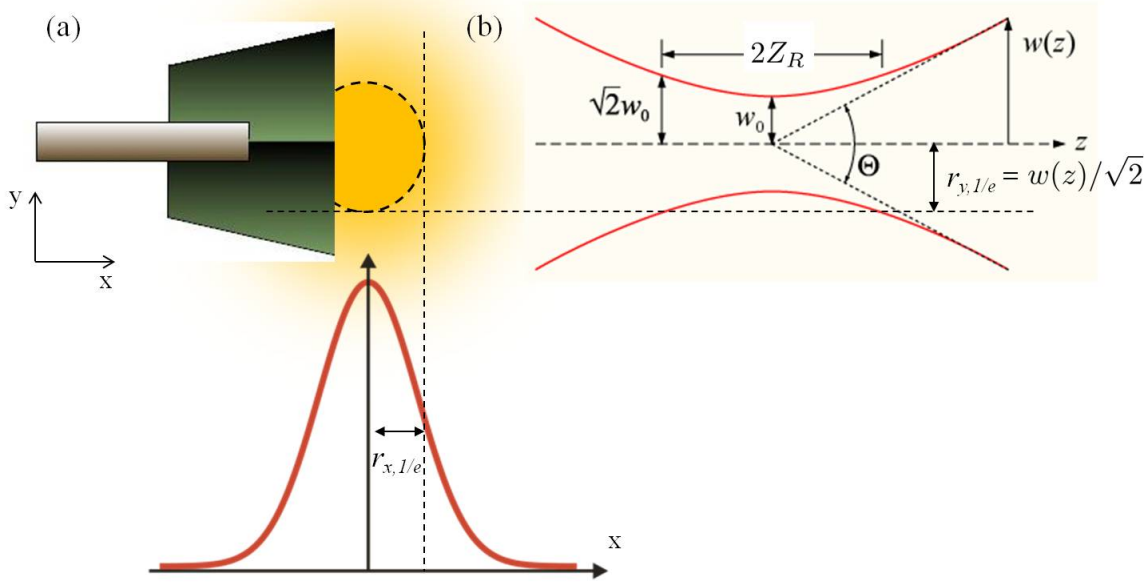

Figure F.1: Panel (a) shows the razor blade horizontally cutting across the beam spot and the corresponding 1D intensity profile (across the centerline) of a Gaussian beam. Panel (b) shows the Gaussian $1/e^2$ intensity profile along the vertical direction as a function of propagation distance along the beam z.

$$I(x,y,z) = \frac{2}{\pi w_x(z) w_y(z)} e^{-2\left(\left[\frac{x}{w_x(z)}\right]^2 + \left[\frac{y}{w_y(z)}\right]^2\right)} = I_0(z) e^{-2\left(\left[\frac{x}{w_x(z)}\right]^2 + \left[\frac{y}{w_y(z)}\right]^2\right)}, \tag{F.1}$$

where

$$w_{x,y}(z) = w_{0x,0y}\sqrt{1 + \left(\frac{z}{z_{Rx,y}}\right)^2}, \tag{F.2}$$

$z_{Rx,y} \equiv \pi\omega_{0x,0y}/\lambda$ is the Rayleigh range [125], $I_0(z)$ is the peak intensity at the location z, and z is the distance relative to the narrowest part of the beam waist w_0. The parameters are are also defined in Fig. F.1 (b). For our MOT beams z_R is typically $\sim 1-10$ m. From

basic geometry the beam divergence can be characterized by the far-field angle $\Theta = 2\theta_{FF}$ as

$$\theta_{\mathrm{FF}} = \frac{w_{\mathrm{FF}}}{z} = \frac{\lambda}{\pi w_0}, \tag{F.3}$$

where w_{FF} is the waist at z, as discussed in Ref. [125].

We will assume that the knife edge measurement is performed at a distance z_1 relative to w_0 with peak intensity $I_0(z_1)$. As the razor is moved across the beam spot horizontally, the power meter reads the integrated power that is not shadowed by the razor blade, namely

$$P(x) = P_{\mathrm{tot}} - I_0(z_1)\int_{-\infty}^{x} e^{-2\left[\frac{x'}{w_{x'}(z_1)}\right]^2} dx' \int_{-\infty}^{\infty} e^{-2\left[\frac{y}{w_y(z)}\right]^2} dy, \tag{F.4}$$

$$= \frac{P_{\mathrm{tot}}}{2}\left[1 - \mathrm{erf}\left(\frac{x}{r_{1/e}}\right)\right], \tag{F.5}$$

where

$$\begin{aligned} P_{\mathrm{tot}} = I_0(z_1)\int_{-\infty}^{\infty} e^{-2\left(\left[\frac{x}{w_x(z)}\right]^2+\left[\frac{y}{w_y(z)}\right]^2\right)} dxdy &= I_0(z_1)\frac{\pi\omega_x(z_1)\omega_y(z_1)}{\sqrt{2}} \\ &= I_0(z_1)\pi(r_{x,1/e})(r_{y,1/e}) \end{aligned} \tag{F.6}$$

is the total power.

The position of the razor blade starts at a an arbitrary distance $x = -x_0$, which we will redefine as $X = 0$, so Eq. (F.5) becomes

$$P(X) = \frac{P_{\mathrm{tot}}}{2}\left[1 - \mathrm{erf}\left(\frac{X - x_0}{r_{x,1/e}}\right)\right], \tag{F.7}$$

for an arbitrary origin.

To measure the vertical width we translate the razor blade in the y direction instead of the x direction, which gives the analog of Eq. (F.7),

$$P(Y) = \frac{P_{\text{tot}}}{2}\left[1 - \text{erf}\left(\frac{Y - y_0}{r_{y,1/e}}\right)\right]. \tag{F.8}$$

When determining the experimental beam size, we make a scatter plot of several power measurements and fit the results to Eqs. (F.7) or (F.8), where P_{tot}, x_0 (or y_0), and $r_{x,1/e}$ (or $r_{y,1/e}$) are fitting parameters. Typical results can be found in Figs. 4.15 and 4.64.

F.2 Telescoping procedure

With knowledge of the beam size at several locations, one can estimate the beam size everywhere by fitting those results to Eq. (F.2), with w_0 and its location as fitting parameters. Using Gaussian optics [125] we find that a biconvex lens located a distance d_o from w_0 with focal length f will create a new waist w_0' at distance d_i according to

$$\frac{1}{f} = \frac{1}{d_o + z_R^2/(d_o - f)} + \frac{1}{d_i}, \tag{F.9}$$

with magnification

$$M = \frac{w_0'}{w_0} = \frac{1}{\sqrt{(1 - d_0/f)^2 + (z_R/f)^2}}. \tag{F.10}$$

In the limit that $z_R^2 \ll (d_0 - f)$, Eqs. (F.13) and (F.15) are reduced to the geometric optics formulas

$$\frac{1}{f} = \frac{1}{d_0} + \frac{1}{d_i} \text{ and } M = \left|\frac{d_i}{d_o}\right|. \tag{F.11}$$

We can calculate the exact location and size of the waist w_0'' in Fig. F.2 using Eqs. (F.13) and (F.15) with the initial waist size and location before a pair of biconvex telescoping lenses. However, some useful approximations can be made to make the determination of w_0'' less experimentally tedious.

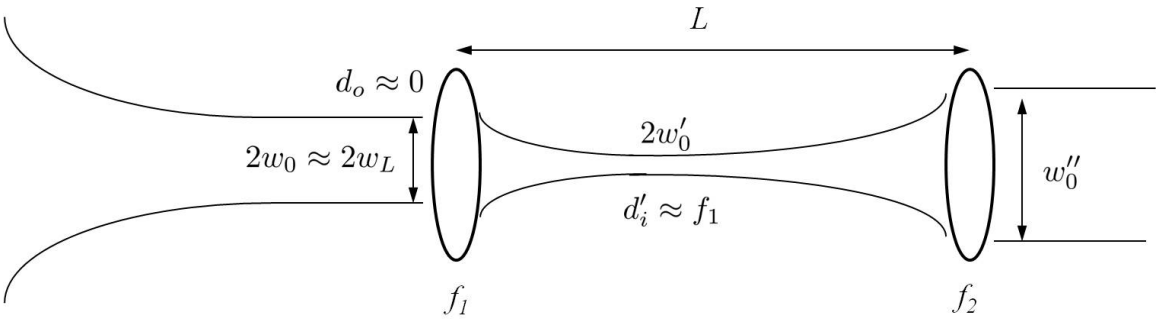

Figure F.2: Magnifying and re-collimating biconvex lens pair telescope for Gaussian optics. See text for details

If the incoming beam is fairly well collimated (which is often the case) and the first telescoping lens with focal length f_1 is at a position within the Rayleigh range where $z_R > d_o$, then we can take a single measurement of the beam size w_L at the location of the first telescoping lens and approximate $w_L \approx w_0$ making $d_o \approx 0$. These approximations along with the fact that $z_R \gg f_1$ reduces Eqs. (F.13) and (F.15) to

$$d_i' \approx f_1 \text{ and } M_1 \approx \frac{f_1}{z_R} \implies w_0' \approx \frac{f_1 \lambda}{\pi w_L} \tag{F.12}$$

at the middle of the telescope, as seen in Fig. F.2. Using Eqs. (F.13) and (F.15) again for the second lens (with focal length f_2 at a distance L from the first lens) gives the telescope's output waist location d_i'' and waist size w_0'' as

$$\frac{1}{f_2} \approx \frac{1}{(L-f_1)+(z_R')^2/[(L-f_1)-f_2)]} + \frac{1}{d_i''}, \tag{F.13}$$

with second lens magnification

$$M_2 = \frac{w_0''}{w_0'} \approx \frac{1}{\sqrt{[1-(L-f_1)/f_2]^2+(z_R'/f_2)^2}}. \tag{F.14}$$

The total telescope magnification is

$$M = M_1 M_2 = \frac{w_0''}{w_0} \approx \frac{w_0''}{w_L} = \frac{f_1}{z_R \sqrt{[1-(L-f_1)/f_2]^2 + (z_R'/f_2)^2}}. \tag{F.15}$$

When $L - f_1 = f_2$ we get perfect collimation, i.e., $d_i'' \to \infty$ and $M = f_1 f_2/(z_R z_R') = f_2/f_1$.

Appendix G

Waveplates

G.1 Principles of waveplates

Waveplates are optical elements that utilize birefringent crystals, such as quartz. A birefringent crystal has a different index of refraction along the crystal's ordinary or optical axis (fast axis) with index of refraction n_o and (larger or slower) extraordinary perpendicular axis with index of refraction n_e. Due to the different indices of refraction, the component of the electric field along the extraordinary axis will be retarded relative to the ordinary axis. Light propagating through a length of crystal L is associated with a phase shift ϕ_o along the optical axis traveling with a speed v_o for time t as

$$L = vt = v_o \frac{\phi_o}{\omega} = \frac{c}{n_e}\frac{\phi_o}{\omega} \implies \phi_o = \frac{\omega L n_e}{c}, \tag{G.1}$$

where c is the speed of light. Using a similar expression for the phase along the extraordinary axis gives the phase difference

$$\Delta\phi = \frac{\omega L(n_e - n_o)}{c} = \frac{\omega L \Delta n}{c}. \tag{G.2}$$

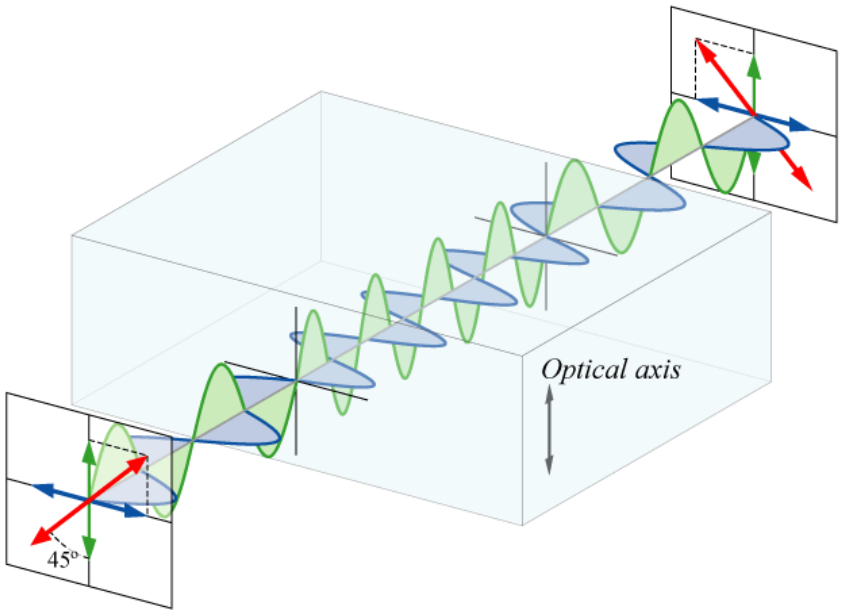

Figure G.1: Diagram of waveplate operation. The incident linearly-polarized light passes through a $\lambda/2$ waveplate. Due to the difference in refractive indices, the component of the wave's electric field traveling perpendicular to the crystal's optical axis lags behind the parallel component. The crystal's length is chosen so that the output beam causes exactly a π or $\lambda/2$ relative phase shift between the parallel and perpendicular components of the light, rotating the polarization 90°. This illustration was created Bob Mellish.

If the length L is chosen just right, the phase difference will be $\Delta\phi = \pi$, which will result in rotation of linear polarization, as illustrated in Fig G.1. When the manufactured waveplate length L is such that the light undergoes a total phase shift of $\pi + m2\pi$ (where m is an integer), the waveplate is called a multi-order half waveplate or $\lambda/2$ waveplate. When the waveplate causes a total phase shift of $\pi/4 + m2\pi$, it is called a multi-order quarter waveplate or $\lambda/4$ waveplate.

Manufacturing rigid and mountable zero-order $L = \lambda/2$ or $L = \lambda/4$ thick waveplates is not feasible. Instead, by combining two multi-order plates with their fast axes oriented perpendicular to each other, one multi-order plate partially undoes the retardation done by the other, giving a net zero-order effect. For example, a zero-order half waveplate's net

phase shift might be $\pi + m2\pi - m'2\pi$, where the first multi-order plate shifts $\pi + m2\pi$ and the second (with perpendicular fast axis orientation) shifts by $-m'2\pi$. With $m = m'$, the difference in length is $\Delta L = \lambda/2$.

To better understand the waveplate's effect on the light waves electric field, we begin by considering the electric field of a plane monochromatic light wave with frequency ω propagating with wave number $\vec{k}$ in the $\hat{k} = \hat{z}$ direction can be written as

$$\vec{\mathscr{E}}(z,t) = \hat{\varepsilon} E_0 e^{i(kr-\omega t)}, \tag{G.3}$$

where only the real part represents the physical wave. This is essentially the same expression as Eq. (3.31), where the amplitude E_0 is related to the intensity of the wave according to Eq. (3.33). We can represent the polarization vector as a column vector known as a Jones matrix with a relative phase δ between the x and y components as

$$\hat{\varepsilon} = A\hat{x} + B\hat{y}e^{i\delta} = \begin{pmatrix} A \\ Be^{i\delta} \end{pmatrix} \tag{G.4}$$

as discussed in Refs. [123, 124]. For example, if the x and y components of the field are equal in magnitude $A = B = 1$, but have a relative phase $\delta = \pi$, then the real Re[...] field is

$$\mathrm{Re}[\vec{\mathscr{E}}(z,t)] = Re[\hat{\varepsilon} E_0 e^{i(kr-\omega t)}] = \mathrm{Re}\left[E_0 \begin{pmatrix} 1 \\ i \end{pmatrix} e^{i(kr-\omega t)} \right] = E_0 \begin{pmatrix} \cos(kz-\omega t) \\ -\sin(kz-\omega t) \end{pmatrix}. \tag{G.5}$$

The x and y components are out of phase so that the polarization is rotating and in flux as it propagates, which is known as circularly polarized light. From Eq. (G.5) we see that to specify the field we need only the polarization information from Eq. (G.4), namely the

column vector $\begin{pmatrix} 1 \\ i \end{pmatrix}$, in our circularly polarized example. For convenience, we will drop the rest of the electric field expression $e^{i(kr-\omega t)}$ and just deal with the matrix algebra from here forward.

Some special cases of Eq. (G.4) with normalized vectors are

$$\begin{aligned} |H\rangle &= \begin{pmatrix} 1 \\ 0 \end{pmatrix}, \qquad |V\rangle = \begin{pmatrix} 0 \\ 1 \end{pmatrix} \\ |R\rangle &= \frac{1}{\sqrt{2}} \begin{pmatrix} 1 \\ i \end{pmatrix}, \quad |L\rangle = \frac{1}{\sqrt{2}} \begin{pmatrix} 1 \\ -i \end{pmatrix}, \end{aligned} \tag{G.6}$$

for horizontal, vertical, right circular, and left circular polarization, respectively.

We need to develop an operator to represent the waveplates, such that it correctly manipulates the Jones vectors. The light field is already expressed in a basis x - y and the waveplate has its fast axis at an angle θ relative to the x-axis. The waveplate defines a new basis along the crystal's fast and slow axis e_1 - e_2, where

$$\begin{aligned} \vec{\mathscr{E}} &= \mathscr{E}_1 \hat{e}_1 + \mathscr{E}_2 \hat{e}_2, \\ \mathscr{E}_1 &= E_0[A\cos(\theta) + Be^{i\delta}\sin(\theta)], \\ \mathscr{E}_2 &= E_0[-A\sin(\theta) + Be^{i\delta}\cos(\theta)], \\ \hat{e}_1 &= \cos(\theta)\hat{x} + \sin(\theta)\hat{y}, \\ \text{and } \hat{e}_1 &= -\sin(\theta)\hat{x} + \cos(\theta)\hat{y}. \end{aligned} \tag{G.7}$$

It is convenient to change to the waveplate basis because we can express the electric field after the waveplate [124] as

$$\vec{\mathscr{E}} = \mathscr{E}_1 \hat{e}_1 + \mathscr{E}_2 e^{i\Delta\phi} \hat{e}_2, \tag{G.8}$$

where $\Delta\phi$ is defined in Eq. (G.2). Using Eqs. (G.7) and (G.8) we can express the electric field by the matrix equation

$$\vec{\mathscr{E}} = E_0 \begin{pmatrix} \cos^2(\theta) + e^{i\Delta\phi}\sin^2(\theta) & (1-e^{i\Delta\phi})\sin(\theta)\cos(\theta) \\ (1-e^{i\Delta\phi})\sin(\theta)\cos(\theta) & e^{i\Delta\phi}\cos^2(\theta) + \sin^2(\theta) \end{pmatrix} \begin{pmatrix} A \\ Be^{i\delta} \end{pmatrix}, \tag{G.9}$$

as shown in Ref. [124].

The the quarter-waveplate ($\Delta\phi = \pi/2$) operator reduces to

$$\begin{pmatrix} \cos^2(\theta) + i\sin^2(\theta) & (1-i)\sin(\theta)\cos(\theta) \\ (1-i)\sin(\theta)\cos(\theta) & i\cos^2(\theta) + \sin^2(\theta) \end{pmatrix} \tag{G.10}$$

and the half waveplate ($\Delta\phi = \pi$) operator reduces to

$$\begin{pmatrix} \cos(2\theta) & \sin(2\theta) \\ \sin(2\theta) & -\cos(2\theta). \end{pmatrix} \tag{G.11}$$

For $\theta = 45^\circ$, Eqs. (G.10) and (G.11) reduce to

$$\frac{1}{\sqrt{2}} \begin{pmatrix} 1 & -i \\ -i & 1 \end{pmatrix} \text{ and } \frac{1}{\sqrt{2}} \begin{pmatrix} 0 & 1 \\ 1 & 0 \end{pmatrix}, \tag{G.12}$$

respectively, when we ignore overall phase factors.

G.2 MOT waveplate setting procedure

To set the MOT beam waveplates we need only set the first waveplate in each of the three MOT beams, as discussed in Sec. 4.2.2. Furthermore, we need only correctly set the relative handedness of the three beams, where the z beam must have the opposite handedness as the x and y beams, so as to match the opposite magnetic field gradients. The z gradient is always opposite to that of the x and y, since $\vec{\nabla} \cdot \vec{\mathscr{B}} = 0$, as discussed in Sec. 4.2.1.

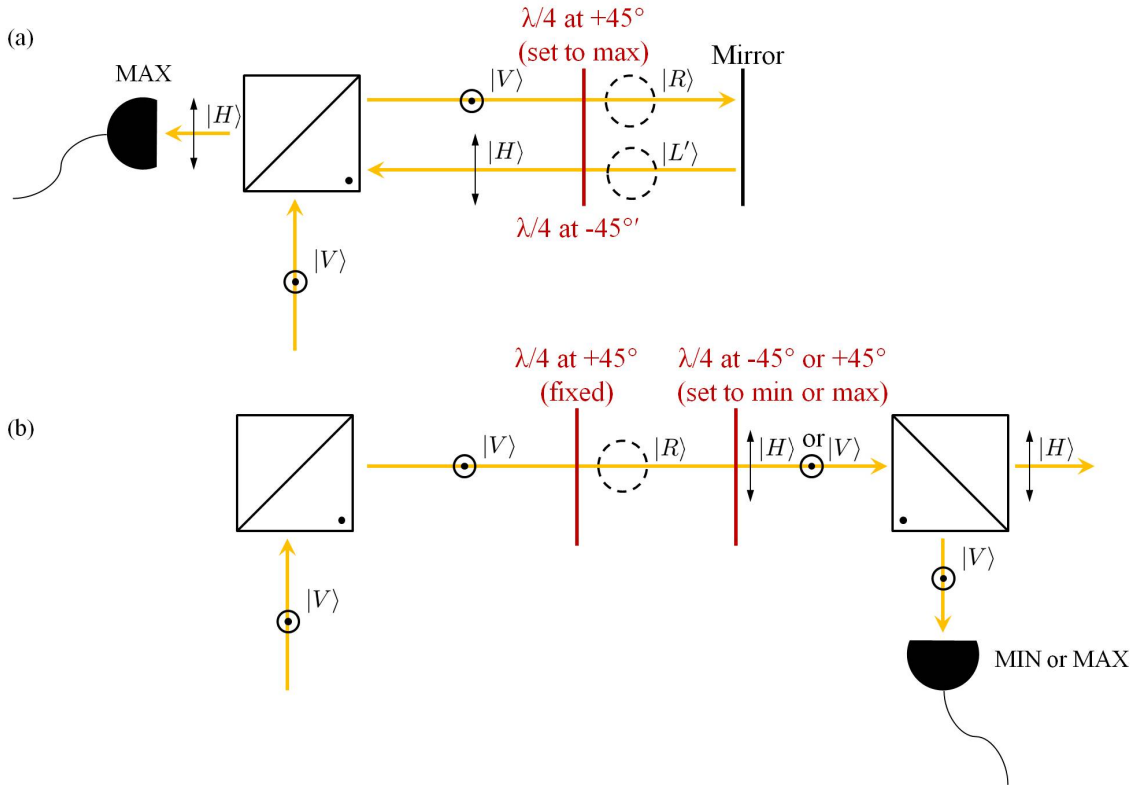

Figure G.2: Schematic of waveplate setting procedure for initial x, y, and z MOT beam waveplates. Panel (a) shows the schematic for setting the x beam waveplate. Panel (b) is the schematic for setting the y and z beams, such that the three beams have correct relative handedness.

To set the relative handedness we begin by setting the x MOT beam's $\lambda/4$ waveplate, as illustrated in Fig. G.2 (a). Vertically polarized light passes through a polarization beamsplitting cube, passes through a waveplate, is retro-reflected back through the waveplate, and then a photo-detector measures the amount of resulting horizontally polarized light. When the waveplate has a relative angle of $+45°$ to its incident vertical polarization the waveplate produces right circularly polarized light, which is indicated by a maximum in the photo-detector signal.

The sequence of optical elements can be represented by the Jones matrix operations

$$\frac{1}{\sqrt{2}}\begin{pmatrix}1 & -i\\ -i & 1\end{pmatrix}\begin{pmatrix}0\\ 1\end{pmatrix}=\frac{1}{\sqrt{2}}\begin{pmatrix}-i\\ 1\end{pmatrix}=-i\,|R\rangle \tag{G.13}$$

for the first pass and

$$\frac{1}{\sqrt{2}}\begin{pmatrix}1 & i\\ i & 1\end{pmatrix}\begin{pmatrix}1 & 0\\ 0 & -1\end{pmatrix}\frac{1}{\sqrt{2}}\begin{pmatrix}-i\\ 1\end{pmatrix}=i\begin{pmatrix}1\\ 0\end{pmatrix}=i\,|H\rangle \tag{G.14}$$

for the retro-reflection and second pass. For convenience, we have assumed the angle is $+45^\circ$ in the first pass, which yields $|R\rangle$ after the waveplate. For the second pass we used the mirror operator (which inverts the y axis so $-\hat{k}\rightarrow\hat{k}$) and the $\lambda/4$ waveplate operator for $\theta=-45^\circ$ as viewed by the retro-reflected beam.[1]

To set the y and z waveplates we use the scheme illustrated in Fig. G.2 (b). Using the already set x-beam waveplate we replace the mirror with y or z waveplates and another polarization beamsplitting cube. By maximizing or minimizing the vertical output of the second beamsplitter we can ensure that the second waveplate's fast axis is anti-aligned (off by 90°) or aligned with the first waveplate, respectively.

Again the sequence of optical elements can be represented by the Jones matrix operations. For example, when the two $\lambda/4$ waveplates are aligned they act like a single $\lambda/2$ waveplate and we have

$$\frac{1}{2}\begin{pmatrix}1 & -i\\ -i & 1\end{pmatrix}\begin{pmatrix}1 & -i\\ -i & 1\end{pmatrix}\begin{pmatrix}0\\ 1\end{pmatrix}=i\,|H\rangle\,, \tag{G.15}$$

which minimizes the signal at the photo-detector.

[1] A $\lambda/4$ waveplate and a retro-reflecting mirror have the same net effect as a single half waveplate.

We choose to match or align the z waveplate with the x, because they have perpendicular incident linear polarization in our setup, which results in opposite circular handedness output. We anti-align the y and x waveplates so that they yield the same handedness, since they too have perpendicular incident linear polarization.

Appendix H

Abbreviations

1D – One dimensional
3D – Three dimensional
AC – Alternating current
AMO – Atomic, molecular, and optical physics
AO – Analog output
AOM – Acousto-optic modulator
AR – Anti-reflection
BO – Born-Oppenheimer approximation
CCW – Counterclockwise
CEM – Channeltron electron multiplier
CMOS – Complementary metal-oxide semiconductor
COM – Center of mass
CW – Clockwise
cw – Continuous wave
DAQ – Data acquisition hardware
EOM – Electro-optic modulator
ECFM – End cap far from mesh
ECNM – End cap near mesh
FPI – Fabry-Perot interferometer
FSR – Free spectral range
HV – High voltage
IA (ia) – Ion-atom
LCAO – Linear combination of atomic orbitals
LPT – Linear Paul trap
MB – Maxwell Boltzmann
MIT – Massachusetts Institute of Technology
MOT – Magneto-optical trap
MCAR – Monte Carlo accept and reject
MSRQ – Mass selective resonance quenching
ND – Neutral density
NI – National Instruments
OFHC – Oxygen free high conductivity
PDF – Probability distribution function
PI or pi – Photoionization
PMT – Photomultiplier tube
QED – Quantum electrodynamics
rf – Radio frequency
rms – root mean squared
TISE – Time independent Schröedinger equation
TTL – Transistor transistor logic
UCLA – University of California Los Angeles
UConn – University of Connecticut
UHV – Ultra-high vacuum

Bibliography

[1] Steven Chu, L. Hollberg, J. E. Bjorkholm, Alex Cable, and A. Ashkin. Three-dimensional viscous confinement and cooling of atoms by resonance radiation pressure. *Phys. Rev. Lett.*, 55(1):48–51, Jul 1985.

[2] Eric Cornell. Very cold indeed: The nanokelvin physics of Bose-Einstein condensation. *Journal of Research of the National Institute of Standards and Technology*, 101(4):419–434, 1996.

[3] William D. Phillips. Nobel lecture: Laser cooling and trapping of neutral atoms. *Rev. Mod. Phys.*, 70(3):721–741, Jul 1998.

[4] L.M. Duan, E. Demler, and M. D. Lukin. Controlling spin exchange interactions of ultracold atoms in optical lattices. *Phys. Rev. Lett.*, 91:090402, Aug 2003.

[5] Lothar Ratschbacher, Christoph Zipkes, Carlo Sias, and Michael Köhl. Controlling chemical reactions of a single particle. *Nature Physics Letters*, 8(9):649–652, 2012.

[6] A. Galindo and M. A. Martín-Delgado. Information and computation: Classical and quantum aspects. *Rev. Mod. Phys.*, 74:347–423, May 2002.

[7] Immanuel Bloch, Jean Dalibard, and Wilhelm Zwerger. Many-body physics with ultracold gases. *Rev. Mod. Phys.*, 80:885–964, Jul 2008.

[8] Andrei Derevianko and Hidetoshi Katori. *Colloquium* : Physics of optical lattice clocks. *Rev. Mod. Phys.*, 83:331–347, May 2011.

[9] Wolfgang Ketterle. Nobel lecture: When atoms behave as waves: Bose-einstein condensation and the atom laser. *Rev. Mod. Phys.*, 74(4):1131–1151, Nov 2002.

[10] J. F. Barry, D. J. McCarron, E. B. Norrgard, M. H. Steinecker, and D. DeMille. Magneto-optical trapping of a diatomic molecule. *Nature*, 512(7514):286–289, Aug 2014.

[11] D. Leibfried, E. Knill, S. Seidelin, J. Britton, R. B. Blakestad, J. Chiaverini, D. B. Hume, W. M. Itano, J. D. Jost, C. Langer, R. Ozeri, R. Reichle, and D. J. Wineland. Creation of a six-atom 'Schrödinger cat' state. *Nature*, 438(7068):639–642, 2005.

[12] J. I. Cirac and P. Zoller. Quantum computations with cold trapped ions. *Phys. Rev. Lett.*, 74(20):4091–4094, May 1995.

[13] Kilian Singer, Ulrich Poschinger, Michael Murphy, Peter Ivanov, Frank Ziesel, Tommaso Calarco, and Ferdinand Schmidt-Kaler. *Colloquium* : Trapped ions as quantum bits: Essential numerical tools. *Rev. Mod. Phys.*, 82(3):2609–2632, Sep 2010.

[14] M. Saffman, T. G. Walker, and K. Mølmer. Quantum information with rydberg atoms. *Rev. Mod. Phys.*, 82:2313–2363, Aug 2010.

[15] D. DeMille. Quantum computation with trapped polar molecules. *Phys. Rev. Lett.*, 88(6):067901, Jan 2002.

[16] D. Hucul, I. V. Inlek, G. Vittorini, C. Crocker, S. Debnath, S. M. Clark, and C. Monroe. Modular entanglement of atomic qubits using photons and phonons. *Nature Physics*, 11(1):37–42, Jan 2015.

[17] J. D. Prestage, G. J. Dick, and L. Maleki. New ion trap for frequency standard applications. *Journal of Applied Physics*, 66(3):1013–1017, 1989.

[18] S. A. Diddams, J. C. Bergquist, E. A. Curtis, R. E. Drullinger, L. Hollberg, W. M. Itano, W. D. Lee, C. W. Oates, K. R. Vogel, and D. J. Wineland. An optical clock based on a single trapped $^{199}Hg^{+}$ ion. *Science*, 293(5531):825–828, 2001.

[19] R Wynands and S Weyers. Atomic fountain clocks. *Metrologia*, 42(3):S64, 2005.

[20] Susannah M. Dickerson, Jason M. Hogan, Alex Sugarbaker, David M. S. Johnson, and Mark A. Kasevich. Multiaxis inertial sensing with long-time point source atom interferometry. *Phys. Rev. Lett.*, 111:083001, Aug 2013.

[21] D.A. Braje, S.A. DeSavage, C.L. Adler, J.P. Davis, and F.A. Narducci. A frequency selective atom interferometer magnetometer. *Journal of Modern Optics*, 61(1):61–71, 2014.

[22] M. G. Raizens, J. M. Gilligan, J. C. Bergquist, W. M. Itano, and D. J. Wineland. Linear trap for high-accuracy spectroscopy of stored ions. *Journal of Modern Optics*, 39(2):233–242, 1992.

[23] R. Blatt, P. Gill, and R. C. Thompson. Current perspectives on the physics of trapped ions. *Journal of Modern Optics*, 39(2):193–220, 1992.

[24] Takashi Baba and Izumi Waki. Cooling and mass-analysis of molecules using laser-cooled atoms. *Japanese Journal of Applied Physics*, 35(Part 2, No. 9A):L1134–L1137, 1996.

[25] J Mitroy, M S Safronova, and Charles W Clark. Theory and applications of atomic and ionic polarizabilities. *Journal of Physics B: Atomic, Molecular and Optical Physics*, 43(20):202001, 2010.

[26] The ACME Collaboration, J. Baron, W. C. Campbell, D. DeMille, J. M. Doyle, G. Gabrielse, Y. V. Gurevich, P. W. Hess, N. R. Hutzler, E. Kirilov, I. Kozyryev, B. R. OLeary, C. D. Panda, M. F. Parsons, E. S. Petrik, B. Spaun, A. C. Vutha, and A. D. West. Order of magnitude smaller limit on the electric dipole moment of the electron. *Science*, 343(6168):269–272, 2014.

[27] J A Behr and G Gwinner. Standard model tests with trapped radioactive atoms. *Journal of Physics G: Nuclear and Particle Physics*, 36(3):033101, 2009.

[28] M. V. DePalatis and M. S. Chapman. Production of translationally cold barium monohalide ions. *Phys. Rev. A*, 88(2):023403, Aug 2013.

[29] A.E. Leanhardt, J.L. Bohn, H. Loh, P. Maletinsky, E.R. Meyer, L.C. Sinclair, R.P. Stutz, and E.A. Cornell. High-resolution spectroscopy on trapped molecular ions in rotating electric fields: A new approach for measuring the electron electric dipole moment. *Journal of Molecular Spectroscopy*, 270(1):1 – 25, 2011.

[30] G Werth, Th Beier, S Djekic, H.-J Kluge, W Quint, T Valenzuela, J Verdu, and M Vogel. Precision studies in traps: Measurement of fundamental constants and tests of fundamental theories. *Nuclear Instruments and Methods in Physics Research Section B: Beam Interactions with Materials and Atoms*, 205(0):1 – 8, 2003. 11th International Conference on the Physics of Highly Charged Ions.

[31] E. L. Raab, M. Prentiss, Alex Cable, Steven Chu, and D. E. Pritchard. Trapping of neutral sodium atoms with radiation pressure. *Phys. Rev. Lett.*, 59(23):2631–2634, Dec 1987.

[32] Lowell S. Brown and Gerald Gabrielse. Geonium theory: Physics of a single electron or ion in a Penning trap. *Rev. Mod. Phys.*, 58:233–311, Jan 1986.

[33] Wolfgang Paul. *Nobel Lectures in Physics 1981-1990/Including Presentation Speeches and Laureates' Biographies*. World Scientific Pub Co Inc, 1993.

[34] W. Neuhauser, M. Hohenstatt, P. E. Toschek, and H. Dehmelt. Localized visible Ba^+ mono-ion oscillator. *Phys. Rev. A*, 22(3):1137–1140, Sep 1980.

[35] Winthrop W. Smith, E. Babenko, R. Côté, and Harvey H. Michels. On the collisional cooling of co-trapped atomic and molecular ions by ultracold atoms: Ca^+ + Na and $Na_2^+(v^*, J^*)$ + Na. In N.P. Bigelow, J.H. Eberly, C.R. Stroud Jr., and I.A. Walmsley, editors, *Coherence and Quantum Optics VIII (No.8)*, pages 623–624. Kluwer Academic/Plenum, 2003.

[36] Winthrop W. Smith, Oleg P. Makarov, and Jian Lin. Cold ion-neutral collisions in a hybrid trap. *Journal of Modern Optics*, 52(16):2253–2260, 2005.

[37] D. S. Goodman, I. Sivarajah, J. E. Wells, F. A. Narducci, and W. W. Smith. Ion-neutral-atom sympathetic cooling in a hybrid linear rf Paul and magneto-optical trap. *Phys. Rev. A*, 86(3):033408, Sep 2012.

[38] I. Sivarajah, D. S. Goodman, J. E. Wells, F. A. Narducci, and W. W. Smith. Evidence of sympathetic cooling of Na^+ ions by a Na magneto-optical trap in a hybrid trap. *Phys. Rev. A*, 86(6):063419, Dec 2012.

[39] W. W. Smith, D. S. Goodman, I. Sivarajah, J. E. Wells, S. Banerjee, R. Côté, H. H. Michels, J. A. Mongtomery Jr., and F. A. Narducci. Experiments with an ion-neutral hybrid trap: cold charge-exchange collisions. *Applied Physics B*, 114(1-2):75–80, 2014.

[40] D. S. Goodman, J. E. Wells, J. M. Kwolek, R. Bümel, F. A. Narducci, and W. W. Smith. Measurement of the low-energy Na^+- Na total collision rate in an ion-neutral hybrid trap. *Phys. Rev. A*, 91(1):012709, Jan 2015. arXiv:1412.5141v1 [physics.atom-ph].

[41] Marko Cetina, Andrew Grier, J. Campbell, I. Chuang, and Vladan Vuletić. Bright source of cold ions for surface electrode traps. *Phys. Rev. A*, 76:041401, 2007.

[42] Andrew T. Grier, Marko Cetina, Fedja Oručević, and Vladan Vuletić. Observation of cold collisions between trapped ions and trapped atoms. *Phys. Rev. Lett.*, 102(22):223201, Jun 2009.

[43] Marko Cetina, Andrew T. Grier, and Vladan Vuletić. Micromotion-induced limit to atom-ion sympathetic cooling in paul traps. *Phys. Rev. Lett.*, 109(25):253201, Dec 2012.

[44] Eric R. Hudson. Method for producing ultracold molecular ions. *Phys. Rev. A*, 79(3):032716, Mar 2009.

[45] Scott T. Sullivan, Wade G. Rellergert, Svetlana Kotochigova, Kuang Chen, Steven J. Schowalter, and Eric R. Hudson. Trapping molecular ions formed via photo-associative ionization of ultracold atoms. *Phys. Chem. Chem. Phys.*, 13(42):18859, 2011.

[46] Wade G. Rellergert, Scott T. Sullivan, Svetlana Kotochigova, Alexander Petrov, Kuang Chen, Steven J. Schowalter, and Eric R. Hudson. Measurement of a large chemical reaction rate between ultracold closed-shell ^{40}Ca atoms and open-shell $^{174}Yb^{+}$ ions held in a hybrid atom-ion trap. *Phys. Rev. Lett.*, 107(24):243201, Dec 2011.

[47] Wade G. Rellergert, Scott T. Sullivan, Steven J. Schowalter, Svetlana Kotochigova, Kuang Chen, and Eric R. Hudson. Evidence for sympathetic vibrational cooling of translationally cold molecules. *Nature*, 495(7442):490–494, 2013.

[48] Scott T. Sullivan, Wade G. Rellergert, Svetlana Kotochigova, and Eric R. Hudson. Role of electronic excitations in ground-state-forbidden inelastic collisions between ultracold atoms and ions. *Phys. Rev. Lett.*, 109(22):223002, Nov 2012.

[49] Kuang Chen, Scott T. Sullivan, and Eric R. Hudson. Neutral gas sympathetic cooling of an ion in a paul trap. *Phys. Rev. Lett.*, 112(14):143009, Apr 2014.

[50] Christoph Zipkes, Stefan Palzer, Carlo Sias, and Michael Köhl. A trapped single ion inside a Bose-Einstein condensate. *Nature*, 464:388–391, Mar 2010.

[51] Christoph Zipkes, Stefan Palzer, Lothar Ratschbacher, Carlo Sias, and Michael Köhl. Cold heteronuclear atom-ion collisions. *Phys. Rev. Lett.*, 105(13):133201, Sep 2010.

[52] L. Ratschbacher, C. Sias, L. Carcagni, J. M. Silver, C. Zipkes, and M. Köhl. Decoherence of a single-ion qubit immersed in a spin-polarized atomic bath. *Phys. Rev. Lett.*, 110:160402, Apr 2013.

[53] Felix H. J. Hall, Mireille Aymar, Nadia Bouloufa-Maafa, Olivier Dulieu, and Stefan Willitsch. Light-assisted ion-neutral reactive processes in the cold regime: Radiative molecule formation versus charge exchange. *Phys. Rev. Lett.*, 107(24):243202, Dec 2011.

[54] Felix H.J. Hall, Pascal Eberle, Gregor Hegi, Maurice Raoult, Mireille Aymar, Olivier Dulieu, and Stefan Willitsch. Ion-neutral chemistry at ultralow energies: dynamics of reactive collisions between laser-cooled Ca^{+} ions and Rb atoms in an ion-atom hybrid trap. *Molecular Physics*, 111(14-15):2020–2032, 2013.

[55] Stefan Willitsch. Ion-atom hybrid systems. *arXiv:1401.1699v1 [physics.atom-ph]*, 2014.

[56] Stefan Schmid, Arne Härter, and Johannes Hecker Denschlag. Dynamics of a cold trapped ion in a Bose-Einstein condensate. *Phys. Rev. Lett.*, 105(13):133202, Sep 2010.

[57] A. Hrter and J. Hecker Denschlag. Cold atomion experiments in hybrid traps. *Contemporary Physics*, 55(1):33–45, 2014.

[58] Shinsuke Haze, Sousuke Hata, Munekazu Fujinaga, and Takashi Mukaiyama. Observation of elastic collisions between lithium atoms and calcium ions. *Phys. Rev. A*, 87(5):052715, May 2013.

[59] J. Deiglmayr, A. Göritz, T. Best, M. Weidemüller, and R. Wester. Reactive collisions of trapped anions with ultracold atoms. *Phys. Rev. A*, 86(4):043438, Oct 2012.

[60] K. Ravi, Seunghyun Lee, Arijit Sharma, G. Werth, and S. A. Rangwala. Cooling and stabilization by collisions in a mixed ion-atom system. *Nature Communications*, 3:1126, 2012.

[61] K. Ravi, S. Lee, A. Sharma, G. Werth, and S. Rangwala. Combined ion and atom trap for low-temperature ion-atom physics. *Applied Physics B: Lasers & Optics*, 107(4):971 – 981, 2012.

[62] Seunghyun Lee, K. Ravi, and S. A. Rangwala. Measurement of collisions between rubidium atoms and optically dark rubidium ions in trapped mixtures. *Phys. Rev. A*, 87(5):052701, May 2013.

[63] Tridib Ray, S. Jyothi, N.Bhargava Ram, and S.A. Rangwala. A thin wire ion trap to study ionatom collisions built within a fabryperot cavity. *Applied Physics B*, 114(1-2):267–273, 2014.

[64] B. M. McLaughlin, H. D. L. Lamb, I. C. Lane, and J F McCann. Ultracold, radiative charge transfer in hybrid Yb ion-Rb atom traps. *Journal of Physics B: Atomic, Molecular and Optical Physics*, 47(14):145201, 2014.

[65] Zbigniew Idziaszek, Tommaso Calarco, Paul S. Julienne, and Andrea Simoni. Quantum theory of ultracold atom-ion collisions. *Phys. Rev. A*, 79(1):010702, Jan 2009.

[66] Ming Li and Bo Gao. Quantum-defect theory of resonant charge exchange. *Phys. Rev. A*, 86(1):012707, Jul 2012.

[67] M. Tacconi, F. A. Gianturco, and A. K. Belyaev. Computing charge-exchange cross sections for ca+ collisions with Rb at low and ultralow energies. *Phys. Chem. Chem. Phys.*, 13(42):19156–19164, 2011.

[68] R. Côté and A. Dalgarno. Ultracold atom-ion collisions. *Phys. Rev. A*, 62(1):012709, Jun 2000.

[69] Robin Côté. From classical mobility to hopping conductivity: Charge hopping in an ultracold gas. *Phys. Rev. Lett.*, 85:5316–5319, Dec 2000.

[70] R. Côté, V. Kharchenko, and M. D. Lukin. Mesoscopic molecular ions in Bose-Einstein condensates. *Phys. Rev. Lett.*, 89(9):093001, Aug 2002.

[71] Oleg P. Makarov, R. Côté, H. Michels, and W. W. Smith. Radiative charge-transfer lifetime of the excited state of $(NaCa)^+$. *Phys. Rev. A*, 67(4):042705, Apr 2003.

[72] Peng Zhang, Alex Dalgarno, and Robin Côté. Scattering of Yb and Yb^+. *Phys. Rev. A*, 80(3):030703, Sep 2009.

[73] Christopher J. Foot. *Atomic Physics (Oxford Master Series in Atomic, Optical and Laser Physics)*. Oxford University Press, USA, 2005.

[74] R. V. Krems, W. C. Stwalley, and B. Friedrich, editors. *Cold Molecules: Theory, Experiment, Applications*. CRC Press, Taylor and Francis, 2009. see Paul Julienne pp 221-244.

[75] George Gioumousis and D. P. Stevenson. Reactions of gaseous molecule ions with gaseous molecules. v. theory. *The Journal of Chemical Physics*, 29(2):294–299, 1958.

[76] U. Bissbort, D. Cocks, A. Negretti, Z. Idziaszek, T. Calarco, F. Schmidt-Kaler, W. Hofstetter, and R. Gerritsma. Emulating solid-state physics with a hybrid system of ultracold ions and atoms. *Phys. Rev. Lett.*, 111:080501, Aug 2013.

[77] Peng Zhang, Alexander Dalgarno, Robin Cote, and Enrico Bodo. Charge exchange in collisions of beryllium with its ion. *Phys. Chem. Chem. Phys.*, 13(42):19026–19035, 2011.

[78] A. Dalgarno and M. R. H. Rudge. Cooling of interstellar gas. *Astrophysical Journal*, 140:800, 1964.

[79] N. Balakrishnan and A. Dalgarno. Chemistry at ultracold temperatures. *Chemical Physics Letters*, 341(56):652 – 656, 2001.

[80] P. C. Stancil, S. Lepp, and A. Dalgarno. The lithium chemistry of the early universe. *Astrophysical Journal*, 458, 1996.

[81] V. Kharchenko and A. Dalgarno. Variability of cometary x-ray emission induced by solar wind ions. *The Astrophysical Journal Letters*, 554(1):L99, 2001.

[82] S. C. Glover, D. W. Savin, and A.-K. Jappsen. Cosmological implications of the uncertainty in h destruction rate coefficients. *The Astrophysical Journal*, 640(2):553, 2006.

[83] D. J. Larson, J. C. Bergquist, J. J. Bollinger, Wayne M. Itano, and D. J. Wineland. Sympathetic cooling of trapped ions: A laser-cooled two-species nonneutral ion plasma. *Phys. Rev. Lett.*, 57(1):70–73, Jul 1986.

[84] K. Mølhave and M. Drewsen. Formation of translationally cold MgH^+ and MgD^+ molecules in an ion trap. *Phys. Rev. A*, 62(1):011401, Jun 2000.

[85] M. D. Barrett, B. DeMarco, T. Schaetz, V. Meyer, D. Leibfried, J. Britton, J. Chiaverini, W. M. Itano, B. Jelenković, J. D. Jost, C. Langer, T. Rosenband, and D. J. Wineland. Sympathetic cooling of $^9be^+$ and $^{24}mg^+$ for quantum logic. *Phys. Rev. A*, 68(4):042302, Oct 2003.

[86] C. W. Chou, D. B. Hume, J. C. J. Koelemeij, D. J. Wineland, and T. Rosenband. Frequency comparison of two high-accuracy al^+ optical clocks. *Phys. Rev. Lett.*, 104:070802, Feb 2010.

[87] A. Ostendorf, C. B. Zhang, M. A. Wilson, D. Offenberg, B. Roth, and S. Schiller. Sympathetic cooling of complex molecular ions to millikelvin temperatures. *Phys. Rev. Lett.*, 97(24):243005, Dec 2006.

[88] M. Green, J. Wodin, R. DeVoe, P. Fierlinger, B. Flatt, G. Gratta, F. LePort, M. Montero Díez, R. Neilson, K. O'Sullivan, A. Pocar, S. Waldman, D. S. Leonard, A. Piepke, C. Hargrove, D. Sinclair, V. Strickland, W. Fairbank, K. Hall, B. Mong, M. Moe, J. Farine, D. Hallman, C. Virtue, E. Baussan, Y. Martin, D. Schenker, J.-L. Vuilleumier, J.-M. Vuilleumier, P. Weber, M. Breidenbach, R. Conley, C. Hall, J. Hodgson, D. Mackay, A. Odian, C. Y. Prescott, P. C. Rowson, K. Skarpaas, and K. Wamba. Observation of single collisionally cooled trapped ions in a buffer gas. *Phys. Rev. A*, 76(2):023404, Aug 2007.

[89] John M. Doyle, Bretislav Friedrich, Jinha Kim, and David Patterson. Buffer-gas loading of atoms and molecules into a magnetic trap. *Phys. Rev. A*, 52:R2515–R2518, Oct 1995.

[90] Ken Takase, Rahn T. Larry, and David W. Chandler. The kinematic cooling of molecules with laser-cooled atoms. *New Journal of Physics*, 11(5):055033, May 2009.

[91] Herbert Goldstein, Charles Poole, and John Safko. *Classical Mechancis*. Addison Wesley, 2002.

[92] David J. Griffiths. *Introduction to Quantum Mechanics (2nd Edition)*. Addison-Wesley, 2004.

[93] John R. Taylor. *Classical Mechanics*. University Science Books, 2005.

[94] David J. Griffiths. *Introduction to Electrodynamics (3rd Edition)*. Addison Wesley, 1998.

[95] J. E. Jones. On the determination of molecular fields. ii. from the equation of state of a gas. *Proceedings of the Royal Society of London A: Mathematical, Physical and Engineering Sciences*, 106(738):463–477, 1924.

[96] R. A. Buckingham. The classical equation of state of gaseous helium, neon and argon. *Proceedings of the Royal Society of London A: Mathematical, Physical and Engineering Sciences*, 168(933):264–283, 1938.

[97] Harald Siegfried Friedrich. *Theoretical Atomic Physics*. Springer, 2005.

[98] Jean Dalibard. Collisional dynamics of ultra-cold atomic gases. In *Proceedings of the International School of Physics-Enrico Fermi*, volume 321, 1999.

[99] N. F. Mott and H. S. W. Massey. *Theory of Atomic Collisions*. Oxford, 1965.

[100] A. Dalgarno, M. R. C. McDowell, and A. Williams. The mobilities of ions in unlike gases. *Philosophical Transactions of the Royal Society of London A: Mathematical, Physical and Engineering Sciences*, 250(982):411–425, 1958.

[101] H. S. W. Massey and C. B. O. Mohr. Free paths and transport phenomena in gases and the quantum theory of collisions. ii. the determination of the laws of force between atoms and molecules. *Proceedings of the Royal Society of London A: Mathematical, Physical and Engineering Sciences*, 144(851):188–205, 1934.

[102] George B. Arfken and Hans J. Weber. *Mathematical Methods for Physicists, Seventh Edition: A Comprehensive Guide*. Academic Press, 2012.

[103] S. Magnier, Ph.D. thesis, University of Paris, Orsay, France, 1993 (unpublished).

[104] S. Banerjee *et al. Chemical Physics Letters*, 542:138, 2012.

[105] Sandipan Banerjee. Electronic structure calculations and properties of alkaline-earth molecular ions, April 2013. Ph.D. thesis, see http://digitalcommons.uconn.edu/dissertations/26/.

[106] M. Aymar and O. Dulieu. *Journal of Chemical Physics*, 122:204302, 2005.

[107] M. Krosnicki E. Czuchaj and H. Stoll. *Theo. Chem. Accts.*, 110:28, 2003.

[108] L. I. Schiff. *Quantum Mechanics (Pure & Applied Physics)*. Mcgraw-Hill College, 1968.

[109] John David Jackson. *Classical Electrodynamics Third Edition*. Wiley, 1998.

[110] E. Arimondo, M. Inguscio, and P. Violino. Experimental determinations of the hyperfine structure in the alkali atoms. *Rev. Mod. Phys.*, 49(1):31–75, Jan 1977.

[111] Daniel Adam Steck. *Sodium D Line Data*. Jan 2010. Available online at http://steck.us/alkalidata (revision 2.1.4, 23 December 2010).

[112] Daniel Adam Steck. *Quantum and Atom Optics*. April 2010. Available online at http://steck.us/teaching (revision 0.10.1, 30 April 2015).

[113] G. K. Woodgate. *Elementary Atomic Structure*. Oxford University Press, 1983.

[114] Albert Einstein. The quantum theory of radiation. *Phys. Z.*, 18:121, 1917.

[115] M. H. Shah, H. A. Camp, M. L. Trachy, G. Veshapidze, M. A. Gearba, and B. D. DePaola. Model-independent measurement of the excited fraction in a magneto-optical trap. *Phys. Rev. A*, 75(5):053418, May 2007.

[116] Timothy P. Dinneen, Christopher D. Wallace, Kit-Yan N. Tan, and Phillip L. Gould. Use of trapped atoms to measure absolute photoionization cross sections. *Opt. Lett.*, 17(23):1706–1708, Dec 1992.

[117] G. Veshapidze, J.-Y. Bang, C. W. Fehrenbach, H. Nguyen, and B. D. DePaola. Model-free measurement of the excited-state fraction in a ^{85}Rb magneto-optical trap. *Phys. Rev. A*, 91:053423, May 2015.

[118] Hugh D. Young, Roger A. Freedman, and A. Lewis Ford. *University Physics with Modern Physics (13th Edition)*. Addison-Wesley, 2011.

[119] Dmitry Budker, Derek Kimball, and David DeMille. *Atomic physics: An exploration through problems and solutions*. Oxford University Press, 2008.

[120] C. Monroe, W. Swann, H. Robinson, and C. Wieman. Very cold trapped atoms in a vapor cell. *Phys. Rev. Lett.*, 65(13):1571–1574, Sep 1990.

[121] V. Wippel, C. Binder, W. Huber, L. Windholz, M. Allegrini, F. Fuso, and E. Arimondo. Photoionization cross-sections of the first excited states of sodium and lithium in a magneto-optical trap. *Eur. Phys. J. D*, 17(3):285–291, 2001.

[122] Hideki Tanaka, Hiromitsu Imai, Katsuki Furuta, Yukihide Kato, Susumu Tashiro, Masayuki Abe, Ryousuke Tajima, and Atsuo Morinaga. Dual magneto-optical trap of sodium atoms in ground hyperfine F = 1 and F = 2 states. *Japanese Journal of Applied Physics*, 46(20):L492–L494, 2007.

[123] Grant R. Fowles. *Introduction to Modern Optics (Dover Books on Physics)*. Dover Publications, 1989.

[124] J. Peatross and M. Ware. *Physics of Light and Optics*. 2015. available at http://optics.byu.edu/.

[125] Sidney A. Self. Focusing of spherical gaussian beams. *Appl. Opt.*, 22(5):658–661, Mar 1983.

[126] R.A. Meyers. *Encyclopedia of Physical Science and Technology*. Number v. 14 in Encyclopedia of Physical Science and Technology. Academic Press, 1987.

[127] Frank J Durate and Lloyd William Hillman (editor). *Dye Laser Principles: With Applications*. Academic Press, 1990.

[128] J. Wilson and J.F.B. Hawkes. *Optoelectronics: An Introduction (Prentice Hall International Series in Optoelectronics)*. Prentice Hall, 1989.

[129] F. P. Schäfer (editor). *Dye Lasers*. Springer, 1977.

[130] Eric D. Black. An introduction to pounddreverhall laser frequency stabilization. *American Journal of Physics*, 69(1), 2001.

[131] Horowitz & Hill. *The Art of Electronics*. Cambridge University Press, 1989.

[132] O. W. Richardson. *(Thermionic) Emission From Hot Bodies*. Wexford College Press, 2003.

[133] C. G. Townsend, N. H. Edwards, C. J. Cooper, K. P. Zetie, C. J. Foot, A. M. Steane, P. Szriftgiser, H. Perrin, and J. Dalibard. Phase-space density in the magneto-optical trap. *Phys. Rev. A*, 52(2):1423–1440, Aug 1995.

[134] M. Prentiss, A. Cable, J. E. Bjorkholm, Steven Chu, E. L. Raab, and D. E. Pritchard. Atomic-density-dependent losses in an optical trap. *Opt. Lett.*, 13(6):452–454, Jun 1988.

[135] B. C. Duncan, V. Sanchez-Villicana, P. L. Gould, and H. R. Sadeghpour. Measurement of the Rb($5D_{5/2}$) photoionization cross section using trapped atoms. *Phys. Rev. A*, 63(4):043411, Mar 2001.

[136] Wolfgang Paul. Electromagnetic traps for charged and neutral particles. *Reviews of Modern Physics*, 62:531–540, 1990.

[137] C Champenois. About the dynamics and thermodynamics of trapped ions. *Journal of Physics B: Atomic, Molecular and Optical Physics*, 42(15):154002, 2009.

[138] Ilamaran Sivarajah. Studies of sympathetic cooling of Na^+ ions by ultracold neutral Na atoms, 2012.

[139] D. R. Denison. Operating parameters of a quadrupole in a grounded cylindrical housing. *Journal of Vacuum Science and Technology*, 8(1):266–269, 1971.

[140] Felix H. J. Hall, Eberle Pascal, Gregor Hegi, Maurice Roault, Mirelle Aymar, Olivier Dulieu, and Stefan Willitsch. Ion-neutral chemistry at ultralow energies: Dynamics of reactive collisions between laser cooled Ca^+ ions and Rb atoms in an ion-atom hybrid trap. *arXiv:1302.4682 [physics.atom-ph]*, 2013.

[141] M. Drewsen and A. Brøner. Harmonic linear Paul trap: stability diagram and effective potentials. *Phys. Rev. A*, 62(4):045401, Sep 2000.

[142] D. Manura and D. Dahl. *SIMION 3D version (R) 7.0 User Manual*. Scientific Instrument Services, Inc., Ringoes, NJ 08551, 2007.

[143] I. Sivarajah, D. S. Goodman, J. E. Wells, F. A. Narducci, and W. W. Smith. Off-resonance energy absorption in a linear paul trap due to mass selective resonant quenching. *Review of Scientific Instruments*, 84(11):113101, 2013.

[144] Yoshinori Hashimoto, Leo Matsuoka, Hiroyuki Osaki, Yu Fukushima, and Shuichi Hasegawa. Trapping laser ablated Ca^+ ions in linear Paul trap. *Japanese Journal of Applied Physics*, 45(9A):7108–7113, 2006.

[145] A. Drakoudis, M. Sllner, and G. Werth. Instabilities of ion motion in a linear Paul trap. *International Journal of Mass Spectrometry*, 252(1):61 – 68, 2006.

[146] D. J. Berkeland, J. D. Miller, J. C. Bergquist, W. M. Itano, and D. J. Wineland. Minimization of ion micromotion in a Paul trap. *Journal of Applied Physics*, 83(10):5025–5033, 1998.

[147] David Acheson. *From Calculus to Chaos: An Introduction to Dynamics*. Oxford University Press, 1998.

[148] J. C. Gutirrez-Vega, R. M. Rodrguez-Dagnino, M. A. Meneses-Nava, and S. Chvez-Cerda. Mathieu functions, a visual approach. *American Journal of Physics*, 71(3), 2003.

[149] T. Baba and I. Waki. Sympathetic cooling rate of gas-phase ions in a radio-frequency-quadrupole ion trap. *Applied Physics B: Lasers and Optics*, 74(4):375–382, 2002. 10.1007/s003400200829.

[150] T. J. Harmon, N. Moazzan-Ahmadi, and R. I. Thompson. Instability heating of sympathetically cooled ions in a linear Paul trap. *Phys. Rev. A*, 67(1):013415, Jan 2003.

[151] S. Gulde, D. Rotter, P. Barton, F. Schmidt-Kaler, R. Blatt, and W. Hogervorst. Simple and efficient photo-ionization loading of ions for precision ion-trapping experiments. *Applied Physics B: Lasers and Optics*, 73:861–863, 2001. 10.1007/s003400100749.

[152] R. Davis, Martin Frearson, and R. Davies. *Mass Spectrometry (Analytical Chemistry by Open Learning)*. John Wiley & Sons Ltd, 1987.

[153] J. M Preses, C. E. Burkhardt, R. L. Corey, D. L. Earsom, T. L. Daulton, W. P. Garver, J. J. Leventhal, A. Z. Msezane, and S. T. Manson. Photoionization of the excited $3p$ state of sodium: Experiment and theory. *Phys. Rev. A*, 32(2):1264–1266, Aug 1985.

[154] John R. Taylor. *An Introduction to Error Analysis: The Study of Uncertainties in Physical Measurements*. University Science Books, 1997.

[155] John H. Moore, Christopher C. Davis, and Michael A. Coplan. *Building Scientific Apparatus*. Cambridge University Press, 2009.

[156] Jürgen Eschner, Giovanna Morigi, Ferdinand Schmidt-Kaler, and Rainer Blatt. Laser cooling of trapped ions. *J. Opt. Soc. Am. B*, 20(5):1003–1015, May 2003.

[157] *Channeltron electron multiplier handbook for mass spectrometry applications*. Burle Electro-Optics, Inc. www.triumf.ca/sites/default/files/ChannelBookBurle.pdf.

[158] P. L. Gould, P. D. Lett, P. S. Julienne, W. D. Phillips, H. R. Thorsheim, and J. Weiner. Observation of associative ionization of ultracold laser-trapped sodium atoms. *Phys. Rev. Lett.*, 60(9):788–791, Feb 1988.

[159] V. S. Kushawaha and J. J. Leventhal. Energy pooling in Na $3p$ – Na $3p$ collisions. *Phys. Rev. A*, 22(6):2468–2473, Dec 1980.

[160] Paul S. Julienne and Robert Heather. Laser modification of ultracold atomic collisions: Theory. *Phys. Rev. Lett.*, 67(16):2135–2138, Oct 1991.

[161] A. Amelink, K. M. Jones, P. D. Lett, P. van der Straten, and H. G. M. Heideman. Single-color photoassociative ionization of ultracold sodium: The region from 0 to -5 GHz. *Phys. Rev. A*, 62(1):013408, Jun 2000.

[162] M. L. Trachy, G. Veshapidze, M. H. Shah, H. U. Jang, and B. D. DePaola. Photoassociation in cold atoms via ladder excitation. *Phys. Rev. Lett.*, 99(4):043003, Jul 2007.

[163] Charles Tapalian and Winthrop W. Smith. Resonant collisional dissociation of Na_2^+ by Na(3P) in an effusive beam. *Phys. Rev. A*, 49(2):921–926, Feb 1994.

[164] Fouad G. Major, Viorica N. Gheorghe, and Gnther Werth. *Charged Particle Traps: Physics and Techniques of Charged Particle Field Confinement (Springer Series on Atomic, Optical, and Plasma Physics)*. Springer, 2004.

[165] F. G. Major and H. G. Dehmelt. Exchange-collision technique for the rf spectroscopy of stored ions. *Phys. Rev.*, 170(1):91–107, Jun 1968.

[166] S. Schwarz. Simulations for ion traps buffer gas cooling. In *Trapped Charged Particles and Fundamental Interactions*, volume 749 of *Lecture Notes in Physics*, pages 1–21. Springer Berlin / Heidelberg, 2008.

[167] R. Blümel, C. Kappler, W. Quint, and H. Walther. Chaos and order of laser-cooled ions in a Paul trap. *Phys. Rev. A*, 40(2):808–823, Jul 1989.

[168] R. Blümel, J. M. Chen, E. Peik, W. Quint, W. Schleich, Y. R. Shen, and H. Walther. Phase transitions of stored laser-cooled ions. *Nature*, 334(6180):309–313, 1988.

[169] Vladimir L. Ryjkov, XianZhen Zhao, and Hans A. Schuessler. Simulations of the rf heating rates in a linear quadrupole ion trap. *Phys. Rev. A*, 71(3):033414, Mar 2005.

[170] C. B. Zhang, D. Offenberg, B. Roth, M. A. Wilson, and S. Schiller. Molecular-dynamics simulations of cold single-species and multispecies ion ensembles in a linear Paul trap. *Phys. Rev. A*, 76(1):012719, Jul 2007.

[171] Y. S. Nam, E. B. Jones, and R. Blümel. Analytical mean-field scaling theory of radio-frequency heating in a paul trap. *Phys. Rev. A*, 90:013402, Jul 2014.

[172] J. D. Tarnas, Y. S. Nam, and R. Blümel. Universal heating curve of damped coulomb plasmas in a paul trap. *Phys. Rev. A*, 88:041401, Oct 2013.

[173] Ralph G. DeVoe. Power-law distributions for a trapped ion interacting with a classical buffer gas. *Phys. Rev. Lett.*, 102(6):063001, Feb 2009.

[174] Heinz Georg Schuster and Wolfram Just. *Deterministic Chaos: An Introduction*. John Wiley & Sons, 2005.

[175] M Block, A Drakoudis, H Leuthner, P Seibert, and G Werth. Crystalline ion structures in a Paul trap. *J. Phys. B: At. Mol. Opt. Phys.*, 33(11):L375, 2000.

[176] E. Wigner. On the interaction of electrons in metals. *Phys. Rev.*, 46(11):1002–1011, Dec 1934.

[177] Alexander D. Gingell, Martin T. Bell, James M. Oldham, Timothy P. Softley, and Jeremy N. Harvey. Cold chemistry with electronically excited ca+ coulomb crystals. *The Journal of Chemical Physics*, 133(19):–, 2010.

[178] P. Blythe, B. Roth, U. Fröhlich, H. Wenz, and S. Schiller. Production of ultracold trapped molecular hydrogen ions. *Phys. Rev. Lett.*, 95(18):183002, Oct 2005.

[179] Krishnamurthy Ravi. Trapping and cooling of ions and the study of ion atom interactions, 2012.

[180] A.D. Appelhans and D.A. Dahl. Measurement of external ion injection and trapping efficiency in the ion trap mass spectrometer and comparison with a predictive model. *International Journal of Mass Spectrometry*, 216(3):269 – 284, 2002.

[181] Stefan Schwarz. IonCool - A versatile code to characterize gas-filled ion bunchers and coolers (not only) for nuclear physics applications. *Nuclear Instruments and Methods in Physics Research Section A: Accelerators, Spectrometers, Detectors and Associated Equipment*, 566(2):233 – 243, 2006.

[182] Rubin H. Landau, Manuel J. Pez, and Cristian C. Bordeianu. *Computational Physics: Problem Solving with Computers*. Wiley-VCH, 2007.

[183] B. Flatt, M. Green, J. Wodin, R. DeVoe, P. Fierlinger, G. Gratta, F. LePort, M. Montero Dez, R. Neilson, K. OSullivan, A. Pocar, S. Waldman, E. Baussan, M. Breidenbach, R. Conley, W. Fairbank Jr., J. Farine, C. Hall, K. Hall, D. Hallman, C. Hargrove, M. Hauger, J. Hodgson, F. Juget, D.S. Leonard, D. Mackay, Y. Martin, B. Mong, A. Odian, L. Ounalli, A. Piepke, C.Y. Prescott, P.C. Rowson, K. Skarpaas, D. Schenker, D. Sinclair, V. Strickland, C. Virtue, J.-L. Vuilleuimier, J.-M. Vuilleuimier, K. Wamba, and P. Weber. A linear rfq ion trap for the enriched xenon observatory. *Nuclear Instruments and Methods in Physics Research Section A: Accelerators, Spectrometers, Detectors and Associated Equipment*, 578(2):399 – 408, 2007.

[184] J. H. Parks and A. Szöke. Simulation of collisional relaxation of trapped ion clouds in the presence of space charge fields. *The Journal of Chemical Physics*, 103(4):1422–1439, 1995.

[185] Ling He and David M. Lubman. Simulation of external ion injection, cooling and extraction processes with simion 6.0 for the ion trap/reflectron time-of-flight mass spectrometer. *Rapid Communications in Mass Spectrometry*, 11(13):1467–1477, 1997.

[186] Wolfgang Ketterle, Kendall B. Davis, Michael A. Joffe, Alex Martin, and David E. Pritchard. High densities of cold atoms in a *Dark* spontaneous-force optical trap. *Phys. Rev. Lett.*, 70(15):2253–2256, Apr 1993.

[187] CHEN Liang, SHE Lei, LI Jiao-Mei, and GAO Ke-Lin. Kinetic energy of trapped ions cooled by buffer gas. *Chinese Physics Letters*, 27(6):063201, 2010.

[188] J.H. Whealton and J.C. Whitson. Space-charge ion optics including extraction from a plasma. *Particle Accelerators*, 10:235–251, 1980.

[189] E. Babenko, G. Ramos and W.W. Smith, ICAP 16 Abstracts, p. 488-489, Univ. of Windsor (1998).

[190] E. Babenko, C. Tapalian, and W.W. Smith. Associative ionization in laser-excited sodium 3p+3d collisions. *Chemical Physics Letters*, 244(12):121 – 126, 1995.

[191] E. A. Donley, T. P. Heavner, F. Levi, M. O. Tataw, and S. R. Jefferts. Double-pass acousto-optic modulator system. *Review of Scientific Instruments*, 76(6):–, 2005.